ION CHANNEL STRUCTURE AND DRUG DISCOVERY ACCELERATED BY CRYO-EM

EDITED BY: Shujia Zhu, Lei Chen, Changlin Tian, Chia-Hsueh Lee and Huaizong Shen

PUBLISHED IN: Frontiers in Pharmacology

frontiers Research Topics

ISSN 1664-8714
ISBN 978-2-83250-776-6
DOI 10.3389/978-2-83250-776-6

About Frontiers

Frontiers is more than just an open-access publisher of scholarly articles: it is a pioneering approach to the world of academia, radically improving the way scholarly research is managed. The grand vision of Frontiers is a world where all people have an equal opportunity to seek, share and generate knowledge. Frontiers provides immediate and permanent online open access to all its publications, but this alone is not enough to realize our grand goals.

Frontiers Journal Series

The Frontiers Journal Series is a multi-tier and interdisciplinary set of open-access, online journals, promising a paradigm shift from the current review, selection and dissemination processes in academic publishing. All Frontiers journals are driven by researchers for researchers; therefore, they constitute a service to the scholarly community. At the same time, the Frontiers Journal Series operates on a revolutionary invention, the tiered publishing system, initially addressing specific communities of scholars, and gradually climbing up to broader public understanding, thus serving the interests of the lay society, too.

Dedication to Quality

Each Frontiers article is a landmark of the highest quality, thanks to genuinely collaborative interactions between authors and review editors, who include some of the world's best academicians. Research must be certified by peers before entering a stream of knowledge that may eventually reach the public - and shape society; therefore, Frontiers only applies the most rigorous and unbiased reviews.
Frontiers revolutionizes research publishing by freely delivering the most outstanding research, evaluated with no bias from both the academic and social point of view. By applying the most advanced information technologies, Frontiers is catapulting scholarly publishing into a new generation.

What are Frontiers Research Topics?

Frontiers Research Topics are very popular trademarks of the Frontiers Journals Series: they are collections of at least ten articles, all centered on a particular subject. With their unique mix of varied contributions from Original Research to Review Articles, Frontiers Research Topics unify the most influential researchers, the latest key findings and historical advances in a hot research area! Find out more on how to host your own Frontiers Research Topic or contribute to one as an author by contacting the Frontiers Editorial Office: frontiersin.org/about/contact

ION CHANNEL STRUCTURE AND DRUG DISCOVERY ACCELERATED BY CRYO-EM

Topic Editors:
Shujia Zhu, Institute of Neuroscience, Shanghai Institute for Biological Sciences, Chinese Academy of Sciences (CAS), China
Lei Chen, Peking University, China
Changlin Tian, University of Science and Technology of China, China
Chia-Hsueh Lee, St. Jude Children's Research Hospital, United States
Huaizong Shen, Westlake University, China

Citation: Zhu, S., Chen, L., Tian, C., Lee, C.-H., Shen, H., eds. (2022). Ion Channel Structure and Drug Discovery Accelerated by Cryo-EM. Lausanne: Frontiers Media SA. doi: 10.3389/978-2-83250-776-6

Table of Contents

REVIEW
published: 11 May 2022
doi: 10.3389/fphar.2022.896532

Recent Advances in the Structural Biology of the Volume-Regulated Anion Channel LRRC8

Go Kasuya[1]*† and Osamu Nureki[2]*†

[1]Division of Integrative Physiology, Department of Physiology, Jichi Medical University, Shimotsuke, Japan, [2]Department of Biological Sciences, Graduate School of Science, The University of Tokyo, Tokyo, Japan

Members of the leucine-rich repeat-containing 8 (LRRC8) protein family, composed of five LRRC8A-E isoforms, are pore-forming components of the volume-regulated anion channel (VRAC), which is activated by cell swelling and releases chloride ions (Cl^-) or other osmolytes to counteract cell swelling. Although the LRRC8 protein family was identified as the molecular entity of VRAC only in 2014, due to recent advances in cryo-electron microscopy (cryo-EM), various LRRC8 structures, including homo-hexameric LRRC8A and LRRC8D structures, as well as inhibitor-bound and synthetic single-domain antibody-bound homo-hexameric LRRC8A structures, have been reported, thus extending our understanding of the molecular mechanisms of this protein family. In this review, we describe the important features of LRRC8 provided by these structures, particularly the overall architectures, and the suggested mechanisms underlying pore inhibition and allosteric modulation by targeting the intracellular leucine-rich repeat (LRR) domain.

Keywords: structural biology, cryo-EM, cell volume homeostasis, VRAC, LRRC8

Edited by:
Huaizong Shen,
Westlake University, China

Reviewed by:
Tobias Stauber,
Medical School Hamburg, Germany
Raimund Dutzler,
University of Zurich, Switzerland

***Correspondence:**
Go Kasuya
gokasuya@jichi.ac.jp
Osamu Nureki
nureki@bs.s.u-tokyo.ac.jp

†ORCID:
Go Kasuya
orcid.org/0000-0003-1756-5764
Osamu Nureki
orcid.org/0000-0003-1813-7008

Specialty section:
This article was submitted to
Pharmacology of Ion Channels and
Channelopathies,
a section of the journal
Frontiers in Pharmacology

Received: 15 March 2022
Accepted: 25 April 2022
Published: 11 May 2022

Citation:
Kasuya G and Nureki O (2022) Recent
Advances in the Structural Biology of
the Volume-Regulated Anion
Channel LRRC8.
Front. Pharmacol. 13:896532.
doi: 10.3389/fphar.2022.896532

INTRODUCTION

Maintenance of cell volume is a fundamental process for proper cell functions. Various membrane channels and transporters that are activated by cell swelling or cell shrinkage are associated with this process (Hoffmann et al., 2009). Among them, the volume-regulated anion channel (VRAC) is a particular type of anion channel (Jentsch, 2016). VRAC is activated by cell swelling and mediates the transport of Cl^- and small organic compounds that can serve as osmolytes. The VRAC-mediated transport of ions and osmolytes leads to water efflux and thereby returns the cell volume back to normal, a process that is called regulatory volume decrease (RVD) (Okada et al., 2019). In various eukaryotic cells including HEK293 cells, HeLa cells, and HCT116 cells, the VRAC-mediated currents are inhibited by the VRAC inhibitor DCPIB {4-[(2-Butyl-6,7-dichloro-2-cyclopentyl-2,3-dihydro-1-oxo-1H-inden-5-yl)oxy] butanoic acid} (Decher et al., 2001; Sato-Numata et al., 2016; Yamada et al., 2021). The existence of VRAC in human T lymphocytes and human intestinal epithelial cells was proposed in the 1980s (Nilius et al., 1997). Subsequent studies revealed various biophysical characteristics of VRAC, including high anion selectivity, weak outward rectification, permeability to organic osmolytes, and modulation by intracellular ATP (Pedersen et al., 2016; König and Stauber, 2019). However, despite extensive studies over the past decades, the molecular entity of VRAC had not been identified until recently mainly due to its ubiquitous expression and complex biophysical properties.

In 2014, using the high-throughput siRNA screening strategy combined with a halide-sensitive YFP, two independent groups found that leucine-rich repeat-containing 8A (LRRC8A), a mutation in which was found in a patient lacking B cells in peripheral blood (Sawada et al., 2003), is an essential component of VRAC (Qiu et al., 2014; Voss et al., 2014). LRRC8A is a member of the LRRC8 protein family composed of five LRRC8A-E isoforms. The LRRC8 protein family was thought to have a membrane topology similar to that of pannexin, connexin, and innexin (Abascal and Zardoya, 2012). These channels are permeable to small ions (e.g., Na^+, K^+, Ca^{2+}, and Cl^-) as well as larger molecules (e.g., ATP) (Ma et al., 2016; Chiu et al., 2018), and it has recently proposed that they should be classified as large-pore channels (Syrjanen et al., 2021) [Structural and functional comparisons between LRRC8 and other large-pore channels are well-summarized in a recent review (Syrjanen et al., 2021).] Hetero-hexameric assembly of LRRC8A and at least one other LRRC8 isoform is needed for the formation of a functional VRAC under physiological conditions (Voss et al., 2014; Syeda et al., 2016). The combination of LRRC8A and other LRRC8 isoforms determines the biophysical properties of VRAC including open probability (Syeda et al., 2016), gating kinetics (Voss et al., 2014; Ullrich et al., 2016), and substrate specificity (Planells-Cases et al., 2015; Gaitán-Peñas et al., 2016; Lutter et al., 2017; Schober et al., 2017; Lahey et al., 2020). In contrast, the LRRC8A homo-hexamer still retains channel activity in *LRRC8*$^{-/-}$ HEK293 cells (Deneka et al., 2018; Yamada et al., 2021) and in lipid-embedded conditions (Syeda et al., 2016; Kasuya et al., 2018), although the LRRC8A homomer is not observed under physiological conditions.

Identification of LRRC8 as the molecular entity of VRAC has also accelerated our understanding of the physiological and medical aspects of the LRRC8-mediated VRAC current (Osei-Owusu et al., 2018; Chen et al., 2019; Figueroa and Denton, 2022). For example, the LRRC8-mediated VRAC current is implicated in adipocyte development (Zhang et al., 2017), insulin secretion (Zhang et al., 2017; Kang et al., 2018; Stuhlmann et al., 2018; Gunasekar et al., 2022), and sperm development (Bao et al., 2018; Lück et al., 2018). VRAC in hippocampal astrocytes transports glutamates to regulate synaptic transmission and neuronal excitability (Yang et al., 2019). VRAC containing the LRRC8D isoform transports platinum-containing drugs, such as cisplatin and carboplatin, and thus is implicated in tumor drug resistance (Planells-Cases et al., 2015). VRAC containing LRRC8C and/or LRRC8E isoforms in macrophages transports an immunotransmitter, 2′3′cyclic-GMP-AMP (cGAMP), to regulate the stimulator of interferon genes (STING) pathway and the production of type I interferons (Lahey et al., 2020; Zhou et al., 2020). VRAC containing the LRRC8C isoform expressed in T cells transports cGAMP to regulate activation of the STING-p53 signaling pathway (Concepcion et al., 2022). These findings suggest that the LRRC8 protein family can be a potential therapeutic target for various diseases such as obesity, diabetes, and stroke.

The emergence of single-particle cryo-electron microscopy (cryo-EM) as a powerful tool for the structural determination of proteins had a great impact on the field of structural biology (Cao et al., 2013; Liao et al., 2013; Cheng, 2018). Due to recent advances in cryo-EM, the first structure of LRRC8 was reported in 2018, only 4 years after the identification of LRRC8 as the molecular entity of VRAC (Deneka et al., 2018). Since then, six studies reported the LRRC8 structures to date (Kasuya et al., 2018; Kefauver et al., 2018; Kern et al., 2019; Nakamura et al., 2020; Deneka et al., 2021; Gunasekar et al., 2022). In this review, we describe the structural and functional features of the LRRC8 protein family that were elucidated by those studies and discuss the possible directions of further research in this field.

Structure Determination

In 2018, the first overall structures of the LRRC8 protein family, mouse LRRC8A homo-hexamer (MmLRRC8A; "Mm" referring to *Mus musculus*) in detergent and low-resolution MmLRRC8A/8C hetero-hexamer in detergent, were determined by cryo-EM (Deneka et al., 2018) (**Figures 1A–C**). That paper also showed the intracellular LRR region structure of MmLRRC8A determined by X-ray crystallography (Deneka et al., 2018). Soon after publication of that paper, two overall structures of the human LRRC8A homo-hexamer (HsLRRC8A; "Hs" referring to *Homo sapiens*) in detergents were determined by cryo-EM (Kasuya et al., 2018; Kefauver et al., 2018). These MmLRRC8A and HsLRRC8A homo-hexamer structures revealed the overall architecture, ion permeation pathway, and selectivity filter. In 2019, the transmembrane (TM) region structures of DCPIB-bound and apo MmLRRC8A homo-hexamer in nanodiscs were determined by cryo-EM (Kern et al., 2019). Nanodiscs are self-assembling lipid bilayers that are stabilized by membrane scaffold proteins (MSP) (Ritchie et al., 2009; Autzen et al., 2019). The DCPIB-bound MmLRRC8A homo-hexamer structure revealed the binding sites of DCPIB and provided a possible DCPIB inhibition mechanism. In 2020, the overall structure of HsLRRC8D homo-hexamer in detergents was determined by cryo-EM (Nakamura et al., 2020), revealing the N-terminal helix involved in ion permeation. In 2021, the overall structures of MmLRRC8A homo-hexamer in complex with five different sybodies were determined by cryo-EM (Deneka et al., 2021). Sybodies are synthetic single-domain antibodies that bind to specific regions of target proteins (Zimmermann et al., 2018). These sybody-bound MmLRRC8A structures provided mechanistic insights into the allosteric modulation in the intracellular leucine-rich repeat (LRR) region. In 2022, the TM region structures of MmLRRC8A homo-hexamer in nanodiscs in complex with SN-407, a DCPIB analog, were determined by cryo-EM (Gunasekar et al., 2022). The DCPIB analog-bound MmLRRC8A homo-hexamer structures provided the structural basis for optimizing chemical compounds targeting the channel pore of LRRC8. The structures of LRRC8 that have been reported to date are listed in **Table 1**.

Overall Architecture

The overall architecture and subunit folding are the same in all of the LRRC8 structures that have been determined (Deneka et al., 2021, 2018; Gunasekar et al., 2022; Kasuya et al., 2018; Kefauver et al., 2018; Kern et al., 2019; Nakamura et al., 2020). The overall architecture of LRRC8 assembles into a hexamer (**Figure 1A**).

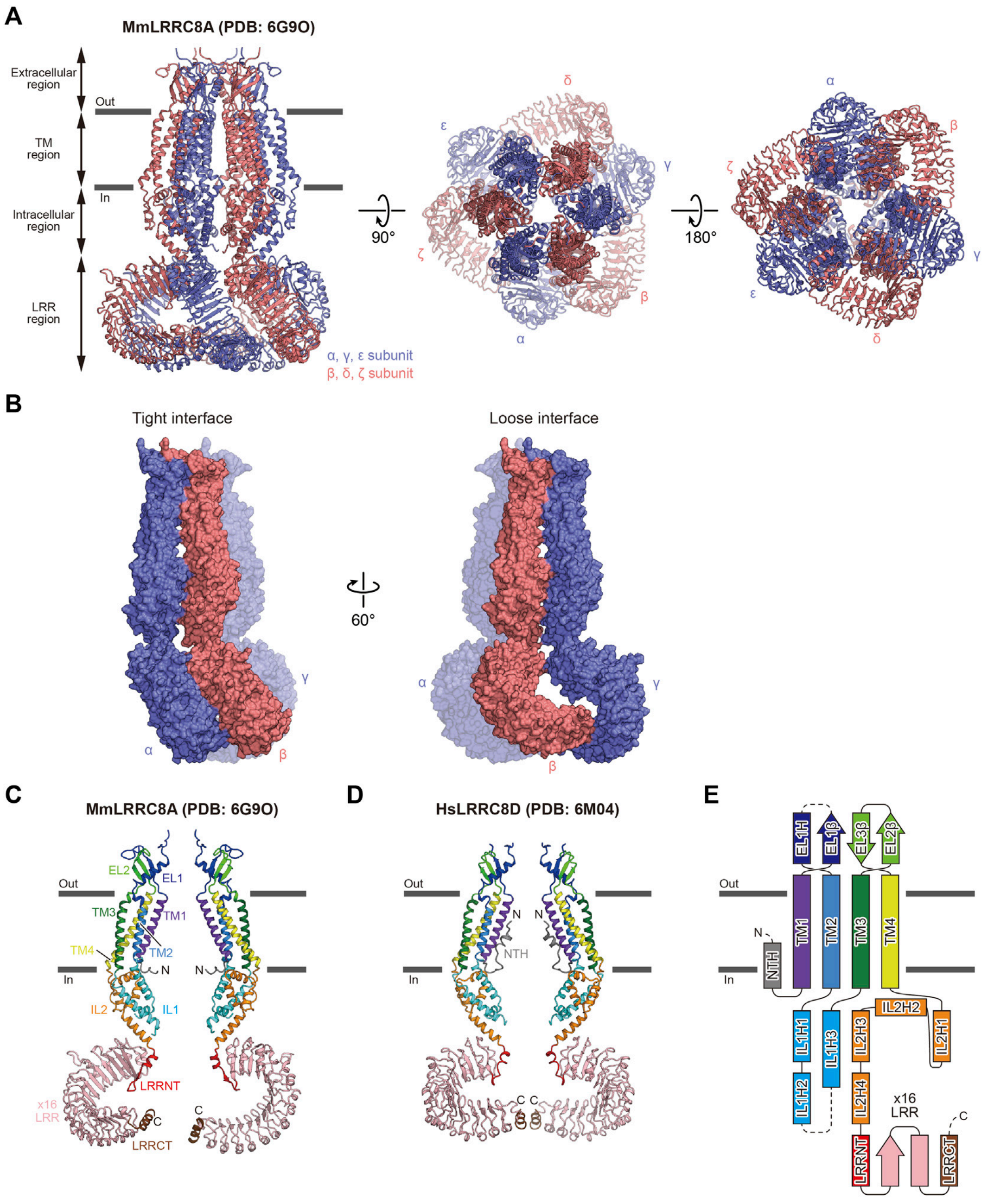

FIGURE 1 | Overall structure and subunit interactions of LRRC8. **(A)** Overall structure of the MmLRRC8A hexamer in detergent (PDB: 6G9O) (Deneka et al., 2018), viewed parallel to the membrane (left) and from the extracellular (middle) and intracellular (right) sides **(B)** Tight (left) and loose (right) subunit interfaces between the three neighboring subunits of the MmLRRC8A hexamer in detergent (PDB: 6G9O) (Deneka et al., 2018) **(C,D)** Two diagonal subunits of the MmLRRC8A hexamer in detergent (PDB: 6G9O) (Deneka et al., 2018) **(C)** and the HsLRRC8D hexamer in detergent (PDB: 6M04) (Nakamura et al., 2020) **(D)**. According to the previously proposed nomenclature (Kasuya et al., 2018; Nakamura et al., 2020), each region is colored as follows: NTH, N-terminal helix, gray; TM1, purple; EL1, blue; TM2, light blue; IL1, cyan; TM3, green; EL2, light green; TM4, yellow; IL2, orange; LRRNT, leucine-rich repeat N-terminal, red; LRR1–16, pink; and LRRCT, brown. The N and C termini are indicated by 'N' and 'C', respectively **(E)** Schematic representation of the LRRC8 membrane topology, colored as in **(C,D)**. The dotted lines indicate the disordered linkers. Figures prepared with CueMol (http://www.cuemol.org/).

The subunit consists of four regions: extracellular region, TM region, intracellular region, and LRR region (**Figures 1C–E**). The extracellular, TM, and intracellular regions are in the N-terminal half of the subunit, while the LRR region is in the C-terminal half of the subunit. The extracellular region protrudes above the cell membrane and forms the channel pore with the TM and intracellular regions. The extracellular region consists of two extracellular loops (EL1 and EL2). EL1 possesses one α-helix (EL1H) and one β-strand (EL1β), while EL2 possesses two β-strands (EL2β1 and EL2β2). EL1 is longer and more variable than

TABLE 1 | Structures of LRRC8 reported to date

Structure	Organism	Other molecule	Method	Resolution(Å)	LRR symmetry	PDB ID	EMDB ID	Reference
Full length								
LRRC8A homo-hexamer	Mus musculus	-	Cryo-EM	5.3	C3	6G9L	4366	Deneka et al (2018)
LRRC8A homo-hexamer	Mus musculus	-	Cryo-EM	4.3	C3	6G9O	4367	Deneka et al (2018)
LRRC8A/8C hetero-hexamer	Mus musculus	-	Cryo-EM	7.94(map)	C3	-	4361	Deneka et al (2018)
LRRC8A homo-hexamer	Homo saplens	-	Cryo-EM	4.4	C3	6DJB	7935	Kefauver et al (2018
LRRC8A homo-hexamer	Homo saplens	-	Cryo-EM	4.25	C3	5ZSU	6952	Kasuya et al (2018)
LRRC8D homo-hexamer	Homo saplens	-	Cryo-EM	4.36	C2	6M04	30029	Nakamura et al (2020)
LRRC8A homo-hexamer	Mus musculus	Sybody(Sb1)	Cryo-EM	3.26	C3	7P5V	13202	Deneka et al (2021)
LRRC8A homo-hexamer	Mus musculus	Sybody(Sb2)	Cryo-EM	3.8	C3	7P5W	13203	Deneka et al (2021)
LRRC8A homo-hexamer	Mus musculus	Sybody(Sb3)	Cryo-EM	3.5	C3	7P5Y	13208	Deneka et al (2021)
LRRC8A homo-hexamer	Mus musculus	Sybody(Sb4)	Cryo-EM	7.7(map)	C3	-	13212	Deneka et al (2021)
LRRC8A homo-hexamer	Mus musculus	Sybody(Sb4)	Cryo-EM	3.9	C3	7P60	13213	Deneka et al (2021)
LRRC8A homo-hexamer	Mus musculus	Sybody(Sb5)	Cryo-EM	5.7	C3	7P6K	13230	Deneka et al (2021)
Pore domain								
LRRC8A homo-hexamer	Mus musculus	-	Cryo-EM	3.7	-	6G8Z	4362	Deneka et al (2018)
LRRC8A homo-hexamer(constricted)	Mus musculus	DCPIB	Cryo-EM	3.32	-	6NZW	0562	Kern et al (2019)
LRRC8A homo-hexamer(expanded)	Mus musculus	DCPIB	Cryo-EM	3.47	-	6NZZ	0563	Kern et al (2019)
LRRC8A homo-hexamer(constricted	Mus musculus	-	Cryo-EM	3.8	-	6O00	0564	Kern et al (2019)
LRRC8A homo-hexamer	Mus musculus	SN-407(Pose-1)	Cryo-EM	3.72	-	7M17	23614	Gunasekar et al (2022)
	Mus musculus	SN-407(Pose-2)	Cryo-EM	3.75	-	7M19	23616	Gunasekar et al (2022)
LRR domain								
LRRC8A protomer	Mus musculus	-	X-ray	1.8	-	6FNW	-	Deneka et al (2018)

EL2 among the LRRC8 isoforms. The TM region consists of four transmembrane helices (TM1-4). TM1 and TM2 are connected by EL1 of the extracellular region, and TM2 and TM3 are connected by the intracellular loop (IL1) of the intracellular region. IL2 in the intracellular region connects TM4 and the LRR region. IL1 possesses three α-helices (IL1H1, IL1H2, and IL1H3), while IL2 possesses four α-helices (IL2H1, IL2H2, IL2H3, and IL2H4). The LRR region consists of the leucine-rich repeat N-terminal helix (LRRNT), up to 16 leucine-rich repeats (LRR1-16), and the leucine-rich repeat C-terminal helix (LRRCT). In all determined LRRC8 structures, the EL1 loop between EL1H and EL1β as well as the IL1 loop between IL1H2 and IL1H3 contain disordered regions, suggesting that these loops have conformational flexibility. In the structure of the HsLRRC8D hexamer, an additional N-terminal helix (NTH) formed by the N-terminal residues preceding TM1 is observed (Nakamura et al., 2020) (**Figures 1D,E**). One thing to note is that in most of the determined LRRC8 structures, while the extracellular and TM regions are sufficiently well resolved to place models, the other regions are not. Another thing to note is that since 3D reconstruction of protein structures by cryo-EM is generally achieved by using a fraction of the collected protein particles, it is difficult to exclude the possibility that the unused fractions contain other biologically important features, such as oligomeric symmetry or stoichiometry. Therefore, the readers need to take account of the resolution of each region and workflow of 3D reconstruction when evaluating the descriptions in each report.

The extracellular, TM, and intracellular regions have six-fold or three-fold (pseudo six-fold) symmetry in the LRRC8A structures (Deneka et al., 2018, Deneka et al., 2021; Kasuya et al., 2018; Kefauver et al., 2018; Kern et al., 2019; Gunasekar et al., 2022) and two-fold (pseudo six-fold) symmetry in the LRRC8D structure (Nakamura et al., 2020). In contrast, the symmetry of the LRR region is variable, suggesting its

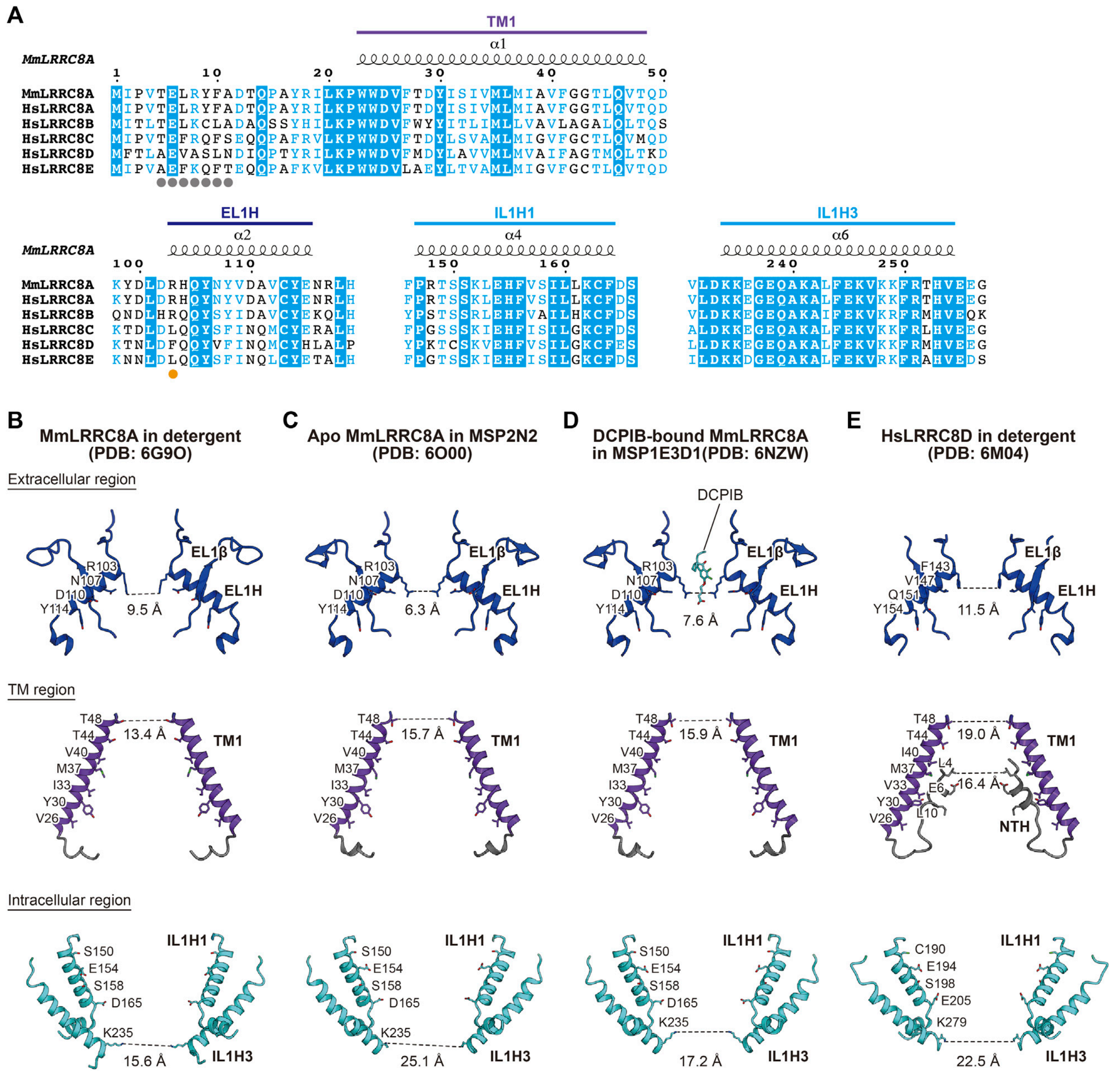

FIGURE 2 | Ion channel pore. **(A)** Sequence alignment around the ion channel pore of LRRC8 isoforms. Amino acid sequences were aligned using Clustal Omega (Sievers et al., 2011) and are shown using ESPript3 (Robert and Gouet, 2014). The secondary structure elements and the colors of the domains from the MmLRRC8A hexamer in detergent (PDB: 6G9O) (Deneka et al., 2018) are labeled above the alignments. The amino acid residue involved in the pore constriction on the extracellular side is highlighted with an orange dot and those involved in the NTH formation in HsLRRC8D (Nakamura et al., 2020) are highlighted with gray dots. For the sequence alignment, the following LRRC8 isoforms were used: mouse (MmLRRC8A, NCBI Reference sequence number: NP_808,393.1) and human (HsLRRC8A, NP_062,540.2; HsLRRC8B, NP_056,165.1; HsLRRC8C, NP_115,646.3; HsLRRC8D, NP_060,573.2; HsLRRC8E, NP_079,337.2) **(B–E)** Close-up views of the channel pore-forming regions of MmLRRC8A in detergent (PDB: 6G9O) (Deneka et al., 2018) **(B)**, apo MmLRRC8A in MSP2N2 nanodiscs (PDB: 6O00) (Kern et al., 2019) **(C)**, DCPIB-bound, constricted MmLRRC8A in MSP1E3D1 nanodiscs (PDB: 6NZW) (Kern et al., 2019) **(D)**, and HsLRRC8D in detergent (PDB: 6M04) (Nakamura et al., 2020) **(E)**. Only two diagonal subunits viewed parallel to the membrane are shown for clarity. The side chains of the pore-lining amino acid residues are depicted in stick representations. The distances between the atoms in PDB coordinates involved in the pore constrictions are shown.

conformational flexibility. While the LRR region has three-fold symmetry in the structures of MmLRRC8A in detergent (Deneka et al., 2018) and HsLRRC8A in detergent (Kasuya et al., 2018; Kefauver et al., 2018), it has two-fold symmetry in the structure of HsLRRC8D in detergent (Nakamura et al., 2020). The LRR region is not resolved well in the structures of MmLRRC8A in nanodiscs (Kern et al., 2019; Gunasekar et al., 2022). As a result of the structural difference in the LRR region, there are two manners of interactions observed at the interfaces between the subunits, termed “tight” interaction and “loose” interaction (**Figure 1B**).

For example, *α* and *β* subunits form a "tight" interaction, while *β* and *γ* subunits form a "loose" interaction. However, how these differences in interaction manners influence channel function is currently unknown.

Features for Ion Permeation

The channel pore of LRRC8 is located along the central axis. It is mainly formed by the EL1H helix in the extracellular region, the TM1 helix in the TM region, and the IL1H1 and IL1H3 helices in the intracellular region (Deneka et al., 2021, Deneka et al., 2018; Kasuya et al., 2018; Kefauver et al., 2018; Kern et al., 2019; Nakamura et al., 2020; Gunasekar et al., 2022) (**Figure 2**). These residues are mainly hydrophilic and positively charged, enabling anion permeation. A previous electrophysiological study demonstrated that the T44 residue of LRRC8A is involved in ion permeation (Syeda et al., 2016). In the LRRC8A structures, the T44 residue is located on TM1 and faces the channel pore (Deneka et al., 2018, Deneka et al., 2021; Kasuya et al., 2018; Kefauver et al., 2018; Kern et al., 2019; Gunasekar et al., 2022). The diameters of the pore are about 6.3–11.5 Å on the extracellular side, and the pore widens as it goes down to the TM region and then narrows to about 15.6–25.1 Å on the intracellular side (**Figures 2B–E**). The most constricted site at the extracellular side is formed by the side chains of Arg103 residues in LRRC8A and those of Phe143 residues in LRRC8D. These residues are located at the N-terminal tip of the EL1H helix (**Figure 2**). As a result of these differences in amino acid residues, the most constricted sites in the LRRC8A homo-hexamer structures are narrower than that in the LRRC8D homo-hexamer structure (**Figures 2B–E**). Importantly, the R103 residue is only conserved in LRRC8A and LRRC8B among the LRRC8 isoforms (**Figure 2A**). Although the LRRC8A/8B hetero-hexamer can form a functional VRAC in HCT116 cells, how the LRRC8B isoform is involved in the native VRAC is currently unknown. Therefore, considering that LRRC8A and at least one other LRRC8 isoform assemble into hetero-hexamers, the inclusion of the LRRC8C, LRRC8D, and/or LRRC8E isoforms into VRAC may change the pore diameter and pore polarity at the most constricted site and thereby affect the permeability of VRAC substrates (**Figures 2B–E**).

In the HsLRRC8D structure, an additional NTH helix is formed by the Ala5 to Asn11 residues at the N-terminal region (Nakamura et al., 2020) (**Figures 2A,E**). The NTH helix enters the channel pore from the intracellular side and lines the channel pore as in the case of other large-pore channels (Syrjanen et al., 2021). The importance of the N-terminal region is supported by the results of previous electrophysiological studies showing that the N-terminal region affects the biophysical properties of VRAC including conductance, ion permeability, and gating kinetics (Kefauver et al., 2018; Zhou et al., 2018).

It is notable that a recent electrophysiological study in which the functional property of the LRRC8A homo-hexamer was assessed suggested that these LRRC8A homo-hexameric structures should be used with caution as structure-based guides for mutagenesis studies (Yamada et al., 2021). That study showed that while the native VRAC and LRRC8A/8C hetero-hexamer are activated by either cell swelling or low intracellular μ or both but that the LRRC8A homo-hexamer is only activated by cell swelling under the condition of low intracellular μ. These differences suggest that the LRRC8A homo-hexamer forms a conformation with impaired sensing of cell volume or low intracellular μ or both.

Pore Inhibition

The structure of the DCPIB-bound MmLRRC8A homo-hexamer in nanodiscs revealed the DCPIB binding mode (Kern et al., 2019) (**Figures 3A–E**). DCPIB is positioned at the most constricted site in the extracellular region and is oriented vertically to the membrane. DCPIB is recognized by the side chains of the positively charged Arg103 residues through its carboxylic acid end. In contrast, the bulky hydrophobic end of DCPIB seems to be too large to pass the most constricted site formed by the side chains of Arg103 residues (**Figures 3A–C**). A structural comparison between the DCPIB-bound and apo MmLRRC8A homo-hexamers in nanodiscs showed that both structures are superimposed well (**Figure 3D**). Accordingly, these results suggest that the DCPIB molecule acts as a cork to plug the most constricted site from outside and that the DCPIB binding to the channel pore seems to have little effect on the overall conformation. Very recently determined structures of the MmLRRC8A homo-hexamer in nanodiscs in complex with SN-407 further support the DCPIB-dependent inhibition mechanism suggested by the structure of the DCPIB-bound MmLRRC8A homo-hexamer (Gunasekar et al., 2022). SN-407 is one of the DCPIB analogs that have been designed and synthesized according to the structure of the DCPIB-bound MmLRRC8A homo-hexamer (Kern et al., 2019). Compared to DCPIB, SN-407 has a longer carbon chain between the carboxylic acid and the bulky hydrophobic end, and it functions as a more potent inhibitor for the native VRAC in HEK293 cells (Gunasekar et al., 2022) (**Figure 3E**). While the SN-407 densities are not clear, there were two binding manners of SN-407, termed "vertical" and "tilted" forms, at the most constricted site in the extracellular region (**Figures 3F,G**). In the vertical form, SN-407 is oriented vertical to the membrane and is recognized by the side chains of Arg103 residues through its carboxylic acid end, as in the case of DCPIB (Kern et al., 2019) (**Figure 3F**). In the tilted form, the carboxylic acid end of SN-407 is recognized by the side chains of Arg103 residues, as in the case of the vertical form (**Figures 3F,G**). However, in addition, the bulky hydrophobic end of SN-407 tilts away from the central axis and is recognized by the hydrophobic interface between two neighboring subunits (**Figure 3G**). This additional hydrophobic interaction may explain the higher inhibitory activity of SN-407 than that of DCPIB. A recent electrophysiological study showed that the inhibitory activity of DCPIB on the LRRC8A homo-hexamer is much weaker than that on the native VRAC (Yamada et al., 2021), suggesting that the DCPIB binding mode observed in the structure of the DCPIB-bound MmLRRC8A homo-hexamer in nanodiscs may not represent the binding mode in the native VRAC. In addition, while studies using animal models suggested that DCPIB has a potential as a therapeutic agent for the treatment of obesity, diabetes, and stroke (Zhang et al., 2008; Gunasekar et al., 2022), there are significant challenges to

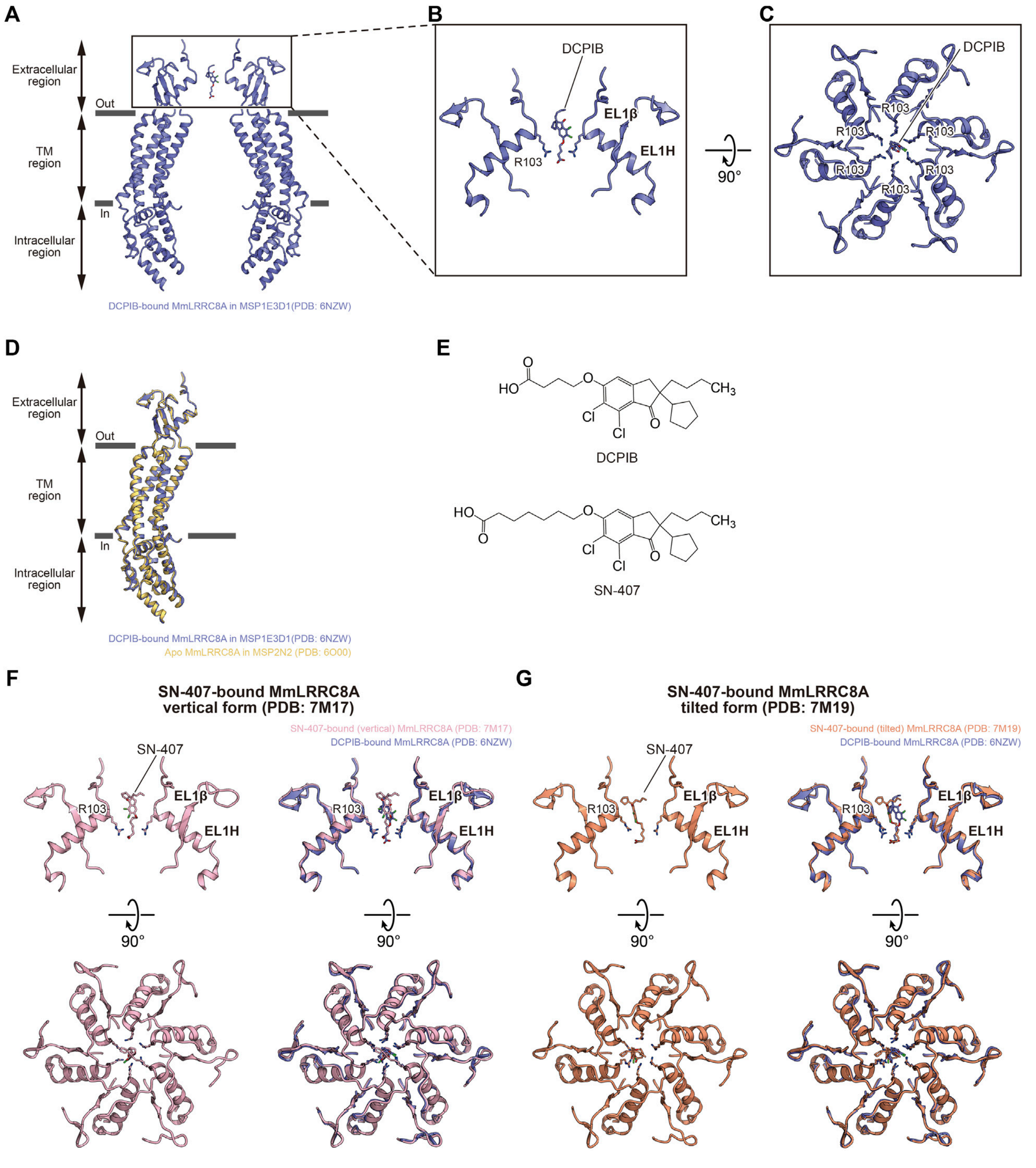

FIGURE 3 | Pore inhibition. **(A–C)** Overall **(A)** and close-up **(B,C)** views of the DCPIB binding site of DCPIB-bound, constricted MmLRRC8A in MSP1E3D1 nanodiscs (PDB: 6NZW) (Kern et al., 2019). The DCPIB molecule and side chains of R103 residues are depicted in stick representations. In **(A,B)** only two diagonal subunits viewed parallel to the membrane are shown for clarity. In **(C)**, all six subunits viewed from the extracellular side are shown. **(D)** Superimposition of DCPIB-bound, constricted MmLRRC8A in MSP1E3D1 nanodiscs (PDB: 6NZW) (Kern et al., 2019) (blue) and apo MmLRRC8A in MSP2N2 nanodiscs (PDB: 6O00) (Kern et al., 2019) (orange), using the Cα atoms (residues Pro15-Asn408) of the subunits. The root mean square deviation (RMSD) value is 0.50 Å for 303 Cα atoms. **(E)** Chemical structures of DCPIB and SN-407. **(F)** Close-up view of the SN-407 binding site of SN-407-bound MmLRRC8A in MSP1E3D1 nanodiscs (vertical form) (PDB: 7M17) (Gunasekar et al., 2022) (left). Superimposition of SN-407-bound MmLRRC8A in MSP1E3D1 nanodiscs (vertical form) (PDB: 7M17) (Gunasekar et al., 2022) and DCPIB-bound, constricted MmLRRC8A in MSP1E3D1 nanodiscs (PDB: 6NZW) (Kern et al., 2019) (right). **(G)** Close-up view of the SN-407 binding site of SN-407-bound MmLRRC8A in MSP1E3D1 nanodiscs (tilted form) (PDB: 7M19) (Gunasekar et al., 2022) (left). Superimposition of SN-407-bound MmLRRC8A in MSP1E3D1 nanodiscs (tilted form) (PDB: 7M19) (Gunasekar et al., 2022) and DCPIB-bound, constricted MmLRRC8A in MSP1E3D1 nanodiscs (PDB: 6NZW) (Kern et al., 2019) (right).

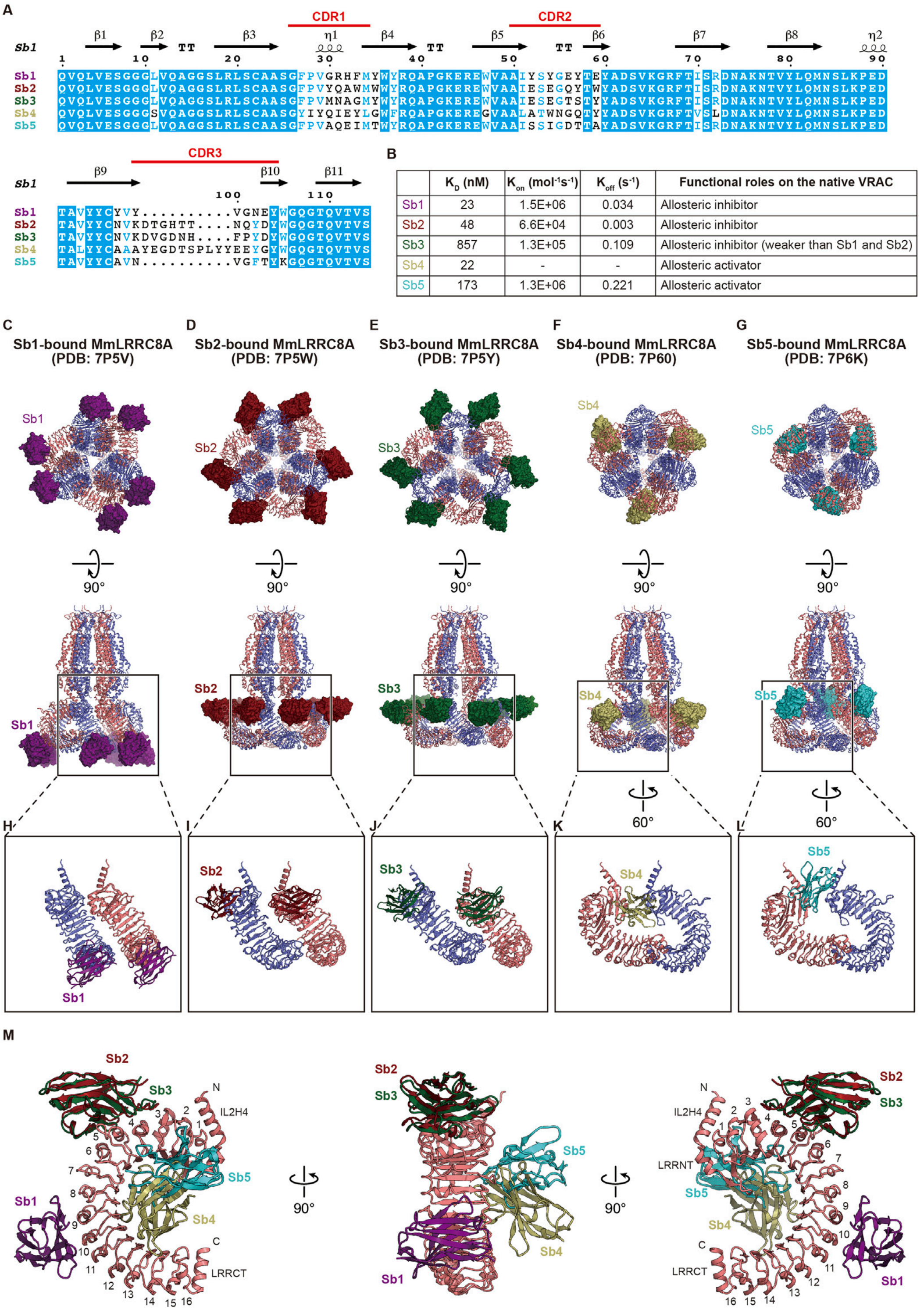

	K_D (nM)	K_{on} ($mol^{-1}s^{-1}$)	K_{off} (s^{-1})	Functional roles on the native VRAC
Sb1	23	1.5E+06	0.034	Allosteric inhibitor
Sb2	48	6.6E+04	0.003	Allosteric inhibitor
Sb3	857	1.3E+05	0.109	Allosteric inhibitor (weaker than Sb1 and Sb2)
Sb4	22	-	-	Allosteric activator
Sb5	173	1.3E+06	0.221	Allosteric activator

FIGURE 4 | Modulation of the LRR region. **(A)** Sequence alignment of the five sybodies screened by Deneka et al.(Deneka et al., 2021). The secondary structure elements from Sb1 (PDB: 7P5V) (Deneka et al., 2021) and their complementarity-determining regions (CDR) are labeled above the alignments **(B)** Summary of the kinetic and dissociation constants as well as functional roles on the native VRAC current in each sybody. The kinetic and dissociation constants were the average of two independent biological replicates obtained by surface plasmon resonance spectroscopy (SPR). For Sb4, the average K_{on} and K_{off} values were not obtained due to missing data from a replicate. For detailed information, see **Table 1** in Deneka et al. (Deneka et al., 2021) **(C–G)** Overall structure of the MmLRRC8A hexamer in complex with each sybody, viewed from the intracellular side (upper) and parallel to the membrane (lower). Each sybody is shown as the surface model and is colored as follows:

(Continued)

FIGURE 4 | Sb1, dark purple; Sb2, dark red; Sb3, dark green; Sb4, dark khaki; and Sb5, dark turquoise blue **(H–L)** Close-up views of the interaction between LRR and each sybody. In **(H–J)**, two neighboring LRR domains in complex with each sybody at the tight interface are shown. In **(K,L)** two neighboring LRR domains in complex with each sybody at the loose interface are shown **(M)** Superimposition of each sybody on an LRR domain. Sb2 to Sb5 are superimposed on LRR of the LRR-Sb1 complex using each LRR domain of Sb2 to Sb5. In the right and left panels, LRR numbers are labeled.

overcome. For example, it seems that DCPIB cannot cross the blood-brain barrier (BBB) (Zhang et al., 2008). Moreover, DCPIB is not just a specific VRAC inhibitor. At concentrations used to inhibit VRAC, various studies suggested that it regulates other membrane proteins including glutamate transporter GLT-1 (Bowens et al., 2013), Connexin 43 (Cx43) (Bowens et al., 2013), gastric H^+,K^+-ATPase (Fujii et al., 2015), components of mitochondrial electron transport chains (Afzal et al., 2019), K2P K^+ channels (Minieri et al., 2013; Lv et al., 2019), inward rectifying K^+ (Kir) channels (Deng et al., 2016), and BK K^+ channel (Zuccolini et al., 2022). Nevertheless, this successful result of the structure-based approach to design DCPIB analogs suggests that further potent inhibitors targeting the native VRAC pore can be designed using the SN-407- and DCPIB-bound MmLRRC8A homo-hexamer structures in the future.

Allosteric Modulation by Targeting Leucine-Rich Repeat

Binders that fix target proteins on specific conformations are powerful tools for basic biology and drug discovery. The synthetic single domain antibody (sybody) is a recently developed synthetic antibody that is engineered on the basis of prototypical camelid nanobody structures and has randomized amino-acid residues in all of the three complementarity-determining regions (CDR) (**Figure 4A**) (Zimmermann et al., 2018). Consequently, the sybody library, which contains about ~10^{12} sybodies, is an *in vitro* selection platform for specific binders against membrane proteins of interest. Using the sybody library, Deneka et al. (Deneka et al., 2021) identified five sybodies, termed Sb1 to Sb5, that form stable complexes with the LRR region of MmLRRC8A but not with the LRR regions of MmLRRC8C and MmLRRC8D (**Figure 4A**). When expressed in the cytoplasm of HEK 293 cells, while Sb1, Sb2, and Sb3 inhibited the native VRAC currents, Sb4 and Sb5 increased the currents by about 50% compared to WT. These results demonstrated that, Sb1, Sb2, and Sb3 function as allosteric inhibitors to MmLRRC8A, whreas Sb4 and Sb5 function as allosteric activators (**Figure 4B**). Deneka et al. (Deneka et al., 2021) determined the structures of the MmLRRC8A homo-hexamer in complex with each sybody (**Figures 4C–M**). In all of the sybody-bound structures, the overall architecture of MmLRRC8A has three-fold symmetry, being consistent with the structures of MmLRRC8A in detergent (Deneka et al., 2018) and HsLRRC8A in detergent (Kasuya et al., 2018; Kefauver et al., 2018). In contrast, the sybodies showed different binding manners. In the complexes with Sb1, Sb2, and Sb3, each sybody interacts with the individual MmLRRC8A subunit on the convex side of LRR with a stoichiometry of 1:1 LRRC8A:sybody (**Figures 4C–E, H–J**). Sb1 recognizes the LRR region on repeats 8–11. Sb2 and Sb3 recognize the same epitopes of the LRR region on repeats 3–6, which is closer to the TM region than Sb1 (**Figure 4M**). In the complexes with Sb4 and Sb5, each sybody interacts with the individual MmLRRC8A subunit on the edge between the flat face and the concave inside of LRR with a stoichiometry of 2:1 LRRC8A:sybody (**Figures 4F,G,K,L**). Sb4 recognizes the LRR region on repeats 2–14 and Sb5 recognizes the LRR region on repeats 2–7 (**Figure 4M**). A Förster resonance energy transfer (FRET) study using C-terminally CFP and YFP-fused HsLRRC8A subunits suggested that the VRAC activation induces a conformational change of the LRR region (König et al., 2019). In addition, an electrophysiological study demonstrated that the C-terminally Venus-fused HsLRRC8A and mCherry-fused HsLRRC8E expressed in *Xenopus* oocytes have increased activities, compared to the unfused counterparts (Gaitán-Peñas et al., 2018, Gaitán-Peñas et al., 2016). Considering these observations in FRET and electrophysiological studies, the sybody binding to the LRR region may affect the conformational mobility of the LRR region and thereby alter the channel activity, although further analyses are required to understand the precise effect of each sybody.

CONCLUSION AND PERSPECTIVES

In this review, we summarized the recent advances in structural biology of the LRRC8 family, the pore-forming component of VRAC. Although the summarized structural studies have greatly extended our understanding of the molecular mechanisms of this protein family, there are still various questions to be answered. In terms of biophysical properties of LRRC8, the precise stoichiometry and subunit arrangement are important questions, which may be answered by structural biology methods. Although the stoichiometry of LRRC8 isoforms forming VRAC is known to determine the biophysical properties of VRAC including open probability (Syeda et al., 2016), gating kinetics (Voss et al., 2014; Ullrich et al., 2016), and substrate specificity (Planells-Cases et al., 2015; Gaitán-Peñas et al., 2016; Lutter et al., 2017; Schober et al., 2017; Lahey et al., 2020), the precise stoichiometry and subunit arrangement of LRRC8 isoforms forming the native VRAC are currently unknown. Moreover, previous immunoblotting and efflux studies suggested that the incorporation of only one LRRC8A subunit into a hetero-hexamer is sufficient for the formation of a functional VRAC (Pervaiz et al., 2019) and that a functional VRAC hetero-hexamer may contain three or more LRRC8 isoforms (Lutter et al., 2017). For this question, structure determination of native LRRC8 proteins isolated from animal origins by using specific binders (e.g., Fab, scFv, and Sybody) may be one of the effective approaches, as in the case of the structure determination of native AMPA receptors from the rat brain (Zhao et al., 2019) and mouse brain (Yu et al., 2021) as well as the native glycine receptor from pig spinal cord and brainstem (Zhu and Gouaux, 2021). Another important question is the gating mechanism. For example, while VRAC activity has been shown to be modulated by low intracellular μ (Chen et al., 2019; Strange et al., 2019), a recent FRET study suggested that VRAC activity is not modulated by intracellular μ change but rather by diacylglycerol (DAG)-dependent protein kinase D (PKD) activity in the cellular environment (König et al., 2019). For this discrepancy regarding the gating mechanism, structure determination of LRRC8 embedded in liposomes under the conditions of similar lipid compositions to those found in cell membranes and mimicking cell swelling or cell shrinkage may be one of the effective approaches. The structure determination of a membrane protein embedded in liposomes was achieved in the case of the well-studied multidrug-resistant transporter AcrB (Yao et al., 2020).

In contrast, there are several questions that seem to be difficult for structural biology methods to answer. For example, we previously determined the structure of the HsLRRC8D homo-hexamer (Nakamura et al., 2020) in an attempt to reveal the mechanisms underlying LRRC8D-dependent VRAC activity such as selective transports of uncharged osmolytes (Lutter et al., 2017) and platinum-containing drugs (Planells-Cases et al., 2015). However, it mostly did not go well since the extracellular and intracellular regions, especially the EL1 and IL1 loops, were not resolved in the HsLRRC8D structure (Nakamura et al., 2020). Notably, these loops are highly variable among the LRRC8 isoforms (Abascal and Zardoya, 2012) and a previous electrophysiological study using chimeric homo-hexamer constructs, in which IL1 or EL1 was replaced with the corresponding sequence of other isoforms, suggested that these loops are important for the biophysical properties of VRAC including substrate permeability, rectification, and voltage sensitivity as well as the subunit-subunit interactions (Yamada and Strange, 2018). Considering that the EL1 and IL1 loops are also not resolved in the MmLRRC8A (Deneka et al., 2018) and HsLRRC8A (Kasuya et al., 2018; Kefauver et al., 2018) structures, it seems to be difficult to resolve these loops in detail by structural biology methods.

Overall, considering that the physiological and medical importance of LRRC8 has been gradually revealed in recent years, additional structures and structure-based functional analyses of LRRC8 are necessary to extend our understanding of the molecular mechanisms of this protein family.

AUTHOR CONTRIBUTIONS

GK and ON wrote the manuscript.

ACKNOWLEDGMENTS

We thank Dr. Koichi Nakajo (Jichi Medical University) for valuable comments on this manuscript. This work was supported by JSPS KAKENHI (Grant No. 19K23833 to GK.).

REFERENCES

Abascal, F., and Zardoya, R. (2012). LRRC8 Proteins Share a Common Ancestor with Pannexins, and May Form Hexameric Channels Involved in Cell-Cell Communication. *BioEssays* 34, 551–560. doi:10.1002/bies.201100173

Afzal, A., Figueroa, E. E., Kharade, S. V., Bittman, K., Matlock, B. K., and Flaherty, D. K., (2019). The LRRC8 Volume-Regulated Anion Channel Inhibitor, DCPIB, Inhibits Mitochondrial Respiration Independently of the Channel. *Physiol. Rep.* 7, e14303. doi:10.14814/phy2.14303

Autzen, H. E., Julius, D., and Cheng, Y. (2019). Membrane Mimetic Systems in CryoEM: Keeping Membrane Proteins in Their Native Environment. *Curr. Opin. Struct. Biol.* 58, 259–268. doi:10.1016/j.sbi.2019.05.022

Bao, J., Perez, C. J., Kim, J., Zhang, H., Murphy, C. J., and Hamidi, T., (2018). Deficient LRRC8A-dependent Volume-Regulated Anion Channel Activity Is Associated with Male Infertility in Mice. *JCI insight* 3, e99767. doi:10.1172/jci.insight.99767

Bowens, N. H., Dohare, P., Kuo, Y. H., and Mongin, A. A. (2013). DCPIB, the Proposed Selective Blocker of Volume-Regulated Anion Channels, Inhibits Several Glutamate Transport Pathways in Glial Cells. *Mol. Pharmacol.* 83, 22–32. doi:10.1124/mol.112.080457

Cao, E., Liao, M., Cheng, Y., and Julius, D. (2013). TRPV1 Structures in Distinct Conformations Reveal Activation Mechanisms. *Nature* 504, 113–118. doi:10.1038/nature12823

Chen, L., König, B., Liu, T., Pervaiz, S., Razzaque, Y. S., and Stauber, T. (2019). More Than Just a Pressure Relief Valve: Physiological Roles of Volume-Regulated LRRC8 Anion Channels. *Biol. Chem. 0* 400, 1481–1496. doi:10.1515/hsz-2019-0189

Cheng, Y. (2018). Single-particle Cryo-EM-How Did it Get Here and where Will it Go. *Science* 361, 876–880. doi:10.1126/science.aat4346

Chiu, Y. H., Schappe, M. S., Desai, B. N., and Bayliss, D. A. (2018). Revisiting Multimodal Activation and Channel Properties of Pannexin 1. *J. Gen. Physiol.* 150, 19–39. doi:10.1085/jgp.201711888

Concepcion, A. R., Wagner, L. E., Zhu, J., Tao, A. Y., Yang, J., Khodadadi-Jamayran, A., et al. (2022). The Volume-Regulated Anion Channel LRRC8C Suppresses T Cell Function by Regulating Cyclic Dinucleotide Transport and STING-P53 Signaling. *Nat. Immunol.* 23, 287–302. doi:10.1038/s41590-021-01105-x

Decher, N., Lang, H. J., Nilius, B., Brüggemann, A., Busch, A. E., and Steinmeyer, K. (2001). DCPIB Is a Novel Selective Blocker of I(Cl,swell) and Prevents Swelling-Induced Shortening of guinea-pig Atrial Action Potential Duration. *Br. J. Pharmacol.* 134, 1467–1479. doi:10.1038/sj.bjp.0704413

Deneka, D., Rutz, S., Hutter, C. A. J., Seeger, M. A., Sawicka, M., and Dutzler, R. (2021). Allosteric Modulation of LRRC8 Channels by Targeting Their Cytoplasmic Domains. *Nat. Commun.* 12, 5435–5514. doi:10.1038/s41467-021-25742-w

Deneka, D., Sawicka, M., Lam, A. K. M., Paulino, C., and Dutzler, R. (2018). Structure of a Volume-Regulated Anion Channel of the LRRC8 Family. *Nature* 558, 254–259. doi:10.1038/s41586-018-0134-y

Deng, W., Mahajan, R., Baumgarten, C. M., and Logothetis, D. E. (2016). The ICl,swell Inhibitor DCPIB Blocks Kir Channels that Possess Weak Affinity for PIP2. *Pflugers Arch.* 468, 817–824. doi:10.1007/s00424-016-1794-9

Figueroa, E. E., and Denton, J. S. (2022). A SWELL Time to Develop the Molecular Pharmacology of the Volume-Regulated Anion Channel (VRAC). *Channels (Austin)* 16, 27–36. doi:10.1080/19336950.2022.2033511

Fujii, T., Takahashi, Y., Takeshima, H., Saitoh, C., Shimizu, T., and Takeguchi, N., (2015). Inhibition of Gastric H+,K+-ATPase by 4-(2-Butyl-6,7-Dichloro-2-Cyclopentylindan-1-On-5-Yl)oxybutyric Acid (DCPIB), an Inhibitor of Volume-Regulated Anion Channel. *Eur. J. Pharmacol.* 765, 34–41. doi:10.1016/j.ejphar.2015.08.011

Gaitán-Peñas, H., Gradogna, A., Laparra-Cuervo, L., Solsona, C., Fernández-Dueñas, V., Barrallo-Gimeno, A., et al. (2016). Investigation of LRRC8-Mediated Volume-Regulated Anion Currents in Xenopus Oocytes. *Biophys. J.* 111, 1429–1443. doi:10.1016/j.bpj.2016.08.030

Gaitán-Peñas, H., Pusch, M., and Estévez, R. (2018). Expression of LRRC8/VRAC Currents in Xenopus Oocytes: Advantages and Caveats. *Ijms* 19, 719. doi:10.3390/ijms19030719

Gunasekar, S. K., Xie, L., Kumar, A., Hong, J., Chheda, P. R., Kang, C., et al. (2022). Small Molecule SWELL1 Complex Induction Improves Glycemic Control and Nonalcoholic Fatty Liver Disease in Murine Type 2 Diabetes. *Nat. Commun.* 13, 784. doi:10.1038/s41467-022-28435-0

Hoffmann, E. K., Lambert, I. H., and Pedersen, S. F. (2009). Physiology of Cell Volume Regulation in Vertebrates. *Physiol. Rev.* 89, 193–277. doi:10.1152/physrev.00037.2007

Jentsch, T. J. (2016). VRACs and Other Ion Channels and Transporters in the Regulation of Cell Volume and beyond. *Nat. Rev. Mol. Cell Biol.* 17, 293–307. doi:10.1038/nrm.2016.29

Kang, C., Xie, L., Gunasekar, S. K., Mishra, A., Zhang, Y., and Pai, S., (2018). SWELL1 Is a Glucose Sensor Regulating β-cell Excitability and Systemic Glycaemia. *Nat. Commun.* 9, 367. doi:10.1038/s41467-017-02664-0

Kasuya, G., Nakane, T., Yokoyama, T., Jia, Y., Inoue, M., and Watanabe, K., (2018). Cryo-EM Structures of the Human Volume-Regulated Anion Channel LRRC8. *Nat. Struct. Mol. Biol.* 25, 797–804. doi:10.1038/s41594-018-0109-6

Kefauver, J. M., Saotome, K., Dubin, A. E., Pallesen, J., Cottrell, C. A., and Cahalan, S. M., (2018). Structure of the Human Volume Regulated Anion Channel. *Elife* 7, e38461. doi:10.7554/eLife.38461

Kern, D. M., Oh, S., Hite, R. K., and Brohawn, S. G. (2019). Cryo-EM Structures of the DCPIB-Inhibited Volume-Regulated Anion Channel LRRC8A in Lipid Nanodiscs. *Elife* 8, 1–23. doi:10.7554/elife.42636

König, B., Hao, Y., Schwartz, S., Plested, A. J., and Stauber, T. (2019). A FRET Sensor of C-Terminal Movement Reveals VRAC Activation by Plasma Membrane DAG Signaling rather Than Ionic Strength. *Elife* 8, 1–20. doi:10.7554/eLife.45421

König, B., and Stauber, T. (2019). Biophysics and Structure-Function Relationships of LRRC8-Formed Volume-Regulated Anion Channels. *Biophysical J.* 116, 1185–1193. doi:10.1016/j.bpj.2019.02.014

Lahey, L. J., Mardjuki, R. E., Wen, X., Hess, G. T., Ritchie, C., and Carozza, J. A., (2020). LRRC8A:C/E Heteromeric Channels Are Ubiquitous Transporters of cGAMP. *Mol. Cell* 80, 578–e5. doi:10.1016/j.molcel.2020.10.021

Liao, M., Cao, E., Julius, D., and Cheng, Y. (2013). Structure of the TRPV1 Ion Channel Determined by Electron Cryo-Microscopy. *Nature* 504, 107–112. doi:10.1038/nature12822

Lück, J. C., Puchkov, D., Ullrich, F., and Jentsch, T. J. (2018). LRRC8/VRAC Anion Channels Are Required for Late Stages of Spermatid Development in Mice. *J. Biol. Chem.* 293, 11796–11808. doi:10.1074/jbc.RA118.003853

Lutter, D., Ullrich, F., Lueck, J. C., Kempa, S., and Jentsch, T. J. (2017). Selective Transport of Neurotransmitters and Modulators by Distinct Volume-Regulated LRRC8 Anion Channels. *J. Cell Sci.* 130, 1122–1133. doi:10.1242/jcs.196253

Lv, J., Liang, Y., Zhang, S., Lan, Q., Xu, Z., Wu, X., et al. (2019). DCPIB, an Inhibitor of Volume-Regulated Anion Channels, Distinctly Modulates K2P Channels. *ACS Chem. Neurosci.* 10, 2786–2793. doi:10.1021/acschemneuro.9b00010

Ma, Z., Tanis, J. E., Taruno, A., and Foskett, J. K. (2016). Calcium Homeostasis Modulator (CALHM) Ion Channels. *Pflugers Arch.* 468, 395–403. doi:10.1007/s00424-015-1757-6

Minieri, L., Pivonkova, H., Caprini, M., Harantova, L., Anderova, M., and Ferroni, S. (2013). The Inhibitor of Volume-Regulated Anion Channels DCPIB Activates TREK Potassium Channels in Cultured Astrocytes. *Br. J. Pharmacol.* 168, 1240–1254. doi:10.1111/bph.12011

Nakamura, R., Numata, T., Kasuya, G., Yokoyama, T., Nishizawa, T., and Kusakizako, T., (2020). Cryo-EM Structure of the Volume-Regulated Anion Channel LRRC8D Isoform Identifies Features Important for Substrate Permeation. *Commun. Biol.* 3, 240. doi:10.1038/s42003-020-0951-z

Nilius, B., Eggermont, J., Voets, T., Buyse, G., Manolopoulos, V., and Droogmans, G. (1997). Properties of Volume-Regulated Anion Channels in Mammalian Cells. *Prog. Biophys. Mol. Biol.* 68, 69–119. doi:10.1016/S0079-6107(97)00021-7

Okada, Y., Okada, T., Sato-Numata, K., Islam, M. R., Ando-Akatsuka, Y., and Numata, T., (2019). Cell Volume-Activated and Volume-Correlated Anion Channels in Mammalian Cells: Their Biophysical, Molecular, and Pharmacological Properties. *Pharmacol. Rev.* 71, 49–88. doi:10.1124/pr.118.015917

Osei-Owusu, J., Yang, J., Vitery, M. d. C., and Qiu, Z. (2018). *Current Topics in Membranes*. Elsevier, 177–203. Amsterdam, Netherlands. doi:10.1016/bs.ctm.2018.07.005

Pedersen, S. F., Okada, Y., and Nilius, B. (2016). Biophysics and Physiology of the Volume-Regulated Anion Channel (VRAC)/Volume-Sensitive Outwardly Rectifying Anion Channel (VSOR). *Pflugers Arch. - Eur. J. Physiol.* 468, 371–383. doi:10.1007/s00424-015-1781-6

Pervaiz, S., Kopp, A., von Kleist, L., and Stauber, T. (2019). Absolute Protein Amounts and Relative Abundance of Volume-Regulated Anion Channel (VRAC) LRRC8 Subunits in Cells and Tissues Revealed by Quantitative Immunoblotting. *Int. J. Mol. Sci.* 20, 5879. doi:10.3390/ijms20235879

Planells-Cases, R., Lutter, D., Guyader, C., Gerhards, N. M., Ullrich, F., and Elger, D. A., (2015). Subunit Composition of VRAC Channels Determines Substrate Specificity and Cellular Resistance to Pt-Based Anti-cancer Drugs. *EMBO J.* 34, 2993–3008. doi:10.15252/embj.201592409

Qiu, Z., Dubin, A. E., Mathur, J., Tu, B., Reddy, K., and Miraglia, L. J., (2014). SWELL1, a Plasma Membrane Protein, Is an Essential Component of Volume-Regulated Anion Channel. *Cell* 157, 447–458. doi:10.1016/j.cell.2014.03.024

Ritchie, T. K., Grinkova, Y. V., Bayburt, T. H., Denisov, I. G., Zolnerciks, J. K., and Atkins, W. M., (2009). Reconstitution of Membrane Proteins in Phospholipid Bilayer Nanodiscs. *Methods in Enzymology*. 464, 211. doi:10.1016/S0076-6879(09)64011-8

Robert, X., and Gouet, P. (2014). Deciphering Key Features in Protein Structures with the New ENDscript Server. *Nucleic Acids Res.* 42, W320–W324. doi:10.1093/nar/gku316

Sato-Numata, K., Numata, T., Inoue, R., and Okada, Y. (2016). Distinct Pharmacological and Molecular Properties of the Acid-Sensitive Outwardly Rectifying (ASOR) Anion Channel from Those of the Volume-Sensitive Outwardly Rectifying (VSOR) Anion Channel. *Pflugers Arch.* 468, 795–803. doi:10.1007/s00424-015-1786-1

Sawada, A., Takihara, Y., Kim, J. Y., Matsuda-Hashii, Y., Tokimasa, S., and Fujisaki, H., (2003). A Congenital Mutation of the Novel Gene LRRC8 Causes Agammaglobulinemia in Humans. *J. Clin. Invest.* 112, 1707–1713. doi:10.1172/JCI20031893710.1172/JCI18937

Schober, A. L., Wilson, C. S., and Mongin, A. A. (2017). Molecular Composition and Heterogeneity of the LRRC8-Containing Swelling-Activated Osmolyte Channels in Primary Rat Astrocytes. *J. Physiol.* 595, 6939–6951. doi:10.1113/JP275053

Sievers, F., Wilm, A., Dineen, D., Gibson, T. J., Karplus, K., and Li, W., (2011). Fast, Scalable Generation of High-Quality Protein Multiple Sequence Alignments Using Clustal Omega. *Mol. Syst. Biol.* 7, 539. doi:10.1038/msb.2011.75

Strange, K., Yamada, T., and Denton, J. S. (2019). A 30-year Journey from Volume-Regulated Anion Currents to Molecular Structure of the LRRC8 Channel. *J. Gen. Physiol.* 151, 100–117. doi:10.1085/jgp.201812138

Stuhlmann, T., Planells-Cases, R., and Jentsch, T. J. (2018). LRRC8/VRAC Anion Channels Enhance β-cell Glucose Sensing and Insulin Secretion. *Nat. Commun.* 9, 1974. doi:10.1038/s41467-018-04353-y

Syeda, R., Qiu, Z., Dubin, A. E., Murthy, S. E., Florendo, M. N., Mason, D. E., et al. (2016). LRRC8 Proteins Form Volume-Regulated Anion Channels that Sense Ionic Strength. *Cell* 164, 499–511. doi:10.1016/j.cell.2015.12.031

Syrjanen, J., Michalski, K., Kawate, T., and Furukawa, H. (2021). On the Molecular Nature of Large-Pore Channels. *J. Mol. Biol.* 433, 166994. doi:10.1016/j.jmb.2021.166994

Ullrich, F., Reincke, S. M., Voss, F. K., Stauber, T., and Jentsch, T. J. (2016). Inactivation and Anion Selectivity of Volume-Regulated Anion Channels (VRACs) Depend on C-Terminal Residues of the First Extracellular Loop. *J. Biol. Chem.* 291, 17040–17048. doi:10.1074/jbc.M116.739342

Voss, F. K., Ullrich, F., Münch, J., Lazarow, K., Lutter, D., and Mah, N., (2014). Identification of LRRC8 Heteromers as an Essential Component of the Volume-Regulated Anion Channel VRAC. *Science* 344, 634–638. doi:10.1126/science.1252826

Yamada, T., Figueroa, E. E., Denton, J. S., and Strange, K. (2021). LRRC8A Homohexameric Channels Poorly Recapitulate VRAC Regulation and Pharmacology. *Am. J. Physiol. Cell Physiol.* 320, C293–C303. doi:10.1152/ajpcell.00454.2020

Yamada, T., and Strange, K. (2018). Intracellular and Extracellular Loops of LRRC8 Are Essential for Volume-Regulated Anion Channel Function. *J. Gen. Physiol.* 150, 1003–1015. doi:10.1085/jgp.201812016

Yang, J., Viterydel, M. D. C. C., Chen, J., Osei-Owusu, J., Chu, J., and Qiu, Z. (2019). Glutamate-Releasing SWELL1 Channel in Astrocytes Modulates Synaptic Transmission and Promotes Brain Damage in Stroke. *Neuron* 102, 813–e6. doi:10.1016/j.neuron.2019.03.029

Yao, X., Fan, X., and Yan, N. (2020). Cryo-EM Analysis of a Membrane Protein Embedded in the Liposome. *Proc. Natl. Acad. Sci. U. S. A.* 117, 18497–18503. doi:10.1073/pnas.2009385117

Yu, J., Rao, P., Clark, S., Mitra, J., Ha, T., and Gouaux, E. (2021). Hippocampal AMPA Receptor Assemblies and Mechanism of Allosteric Inhibition. *Nature* 594, 448–453. doi:10.1038/s41586-021-03540-0

Zhang, Y., Xie, L., Gunasekar, S. K., Tong, D., Mishra, A., and Gibson, W. J., (2017). Erratum: SWELL1 Is a Regulator of Adipocyte Size, Insulin Signalling and Glucose Homeostasis. *Nat. Cell Biol.* 19, 873–517. doi:10.1038/ncb351410.1038/ncb3556

Zhang, Y., Zhang, H., Feustel, P. J., and Kimelberg, H. K. (2008). DCPIB, a Specific Inhibitor of Volume Regulated Anion Channels (VRACs), Reduces Infarct Size in MCAo and the Release of Glutamate in the Ischemic Cortical Penumbra. *Exp. Neurol.* 210, 514–520. doi:10.1016/j.expneurol.2007.11.027

Zhao, Y., Chen, S., Swensen, A. C., Qian, W.-J., Gouaux, E., and Zhao, Y., (2019). Architecture and Subunit Arrangement of Native AMPA Receptors Elucidated by Cryo-EM. *Science* 364, 355–362. doi:10.1126/science.aaw8250

Zhou, C., Chen, X., Planells-Cases, R., Chu, J., Wang, L., and Cao, L., (2020). Transfer of cGAMP into Bystander Cells via LRRC8 Volume-Regulated Anion Channels Augments STING-Mediated Interferon Responses and Anti-viral Immunity. *Immunity* 52, 767–e6. doi:10.1016/j.immuni.2020.03.016

Zhou, P., Polovitskaya, M. M., and Jentsch, T. J. (2018). LRRC8 N Termini Influence Pore Properties and Gating of Volume-Regulated Anion Channels (VRACs). *J. Biol. Chem.* 293, 13440–13451. doi:10.1074/jbc.RA118.002853

Zhu, H., and Gouaux, E. (2021). Architecture and Assembly Mechanism of Native glycine Receptors. *Nature* 599, 513–517. doi:10.1038/s41586-021-04022-z

Zimmermann, I., Egloff, P., Hutter, C. A., Arnold, F. M., Stohler, P., and Bocquet, N., (2018). Synthetic Single Domain Antibodies for the Conformational Trapping of Membrane Proteins. *Elife* 7, 1–32. doi:10.7554/eLife.34317

Zuccolini, P., Ferrera, L., Remigante, A., Picco, C., Barbieri, R., and Bertelli, S., (2022). The VRAC Blocker DCPIB Directly Gates the BK Channels and Increases Intracellular Ca 2+ in Melanoma and Pancreatic Duct Adenocarcinoma Cell Lines. *Br. J Pharmacol* [Epub ahead of print]. doi:10.1111/bph.15810

Conflict of Interest: The authors declare that the research was conducted in the absence of any commercial or financial relationships that could be construed as a potential conflict of interest.

frontiers | Frontiers in Pharmacology

REVIEW
published: 16 May 2022
doi: 10.3389/fphar.2022.900623

Ligand-Binding Sites in Vanilloid-Subtype TRP Channels

*Maria V. Yelshanskaya and Alexander I. Sobolevsky**

Department of Biochemistry and Molecular Biophysics, Columbia University, New York, NY, United States

Vanilloid-subfamily TRP channels TRPV1-6 play important roles in various physiological processes and are implicated in numerous human diseases. Advances in structural biology, particularly the "resolution revolution" in cryo-EM, have led to breakthroughs in molecular characterization of TRPV channels. Structures with continuously improving resolution uncover atomic details of TRPV channel interactions with small molecules and protein-binding partners. Here, we provide a classification of structurally characterized binding sites in TRPV channels and discuss the progress that has been made by structural biology combined with mutagenesis, functional recordings, and molecular dynamics simulations toward understanding of the molecular mechanisms of ligand action. Given the similarity in structural architecture of TRP channels, 16 unique sites identified in TRPV channels may be shared between TRP channel subfamilies, although the chemical identity of a particular ligand will likely depend on the local amino-acid composition. The characterized binding sites and molecular mechanisms of ligand action create a diversity of druggable targets to aid in the design of new molecules for tuning TRP channel function in disease conditions.

Keywords: TRP channels, ligand, agonist, inhibitor, antagonist, blocker, cryo-EM, X-ray crystallography

Edited by:
Lei Chen,
Peking University, China

Reviewed by:
Ye Yu,
China Pharmaceutical University, China
Fan Yang,
Zhejiang University, China

Correspondence:
Alexander I. Sobolevsky
as4005@cumc.columbia.edu

Specialty section:
This article was submitted to Pharmacology of Ion Channels and Channelopathies,
a section of the journal Frontiers in Pharmacology

Received: *21 March 2022*
Accepted: *06 April 2022*
Published: *16 May 2022*

Citation:
Yelshanskaya MV and Sobolevsky AI (2022) Ligand-Binding Sites in Vanilloid-Subtype TRP Channels. Front. Pharmacol. 13:900623. doi: 10.3389/fphar.2022.900623

INTRODUCTION

Transient receptor potential (TRP) channels are regulated by a broad range of stimuli, including chemicals, temperature, mechanical stress, and membrane voltage, and are directly involved in sensory perception such as thermal perception, nociception, taste, olfaction, vision, hearing, and touch (Clapham, 2003). TRP channels are implicated in the pathogenesis of numerous human diseases, including various types of cancer, asthma, hypertension, osteoporosis, pancreatitis, cystitis, allergy, psoriasis, taste dysfunction, neuropathic and inflammatory pain, stroke, migraine, neurodegenerative disorders, and schizophrenia, and represent important drug targets (Nilius et al., 2007; Moran et al., 2011; Arbabian et al., 2020). This superfamily of cation-selective ion channels includes seven subfamilies: TRPV (vanilloid), TRPC (canonical), TRPM (melastatin), TRPN (NOMPC-like), TRPA (ankyrin), TRPP (polycystic), and TRPML (mucolipin). The TRPV subfamily contains six members, TRPV1-6. TRPV1 represents the founding member of the TRP channel superfamily, being the first mammalian TRP channel to be cloned (Caterina et al., 1997) and the first TRP channel to be resolved structurally (Cao et al., 2013; Liao et al., 2013). The first four members of the TRPV subfamily, TRPV1-4, represent temperature-activated TRP channels or thermo-TRPs (Islas, 2014; Voets, 2014; Arrigoni and Minor, 2018; Castillo et al., 2018; Lamas et al., 2019; Yuan, 2019). All thermo-TRPVs are activated by heat but in different temperature ranges, from warm for TRPV4 (>27°C) (Güler et al., 2002) and TRPV3 (>31°C) (Peier et al., 2002; Smith et al., 2002; Xu et al., 2002) to noxiously hot for TRPV1 (>43°C) (Caterina et al., 1997) and TRPV2 (>52°C) (Caterina et al., 1999). TRPV5 and TRPV6 are not activated by temperature. Instead, they are highly

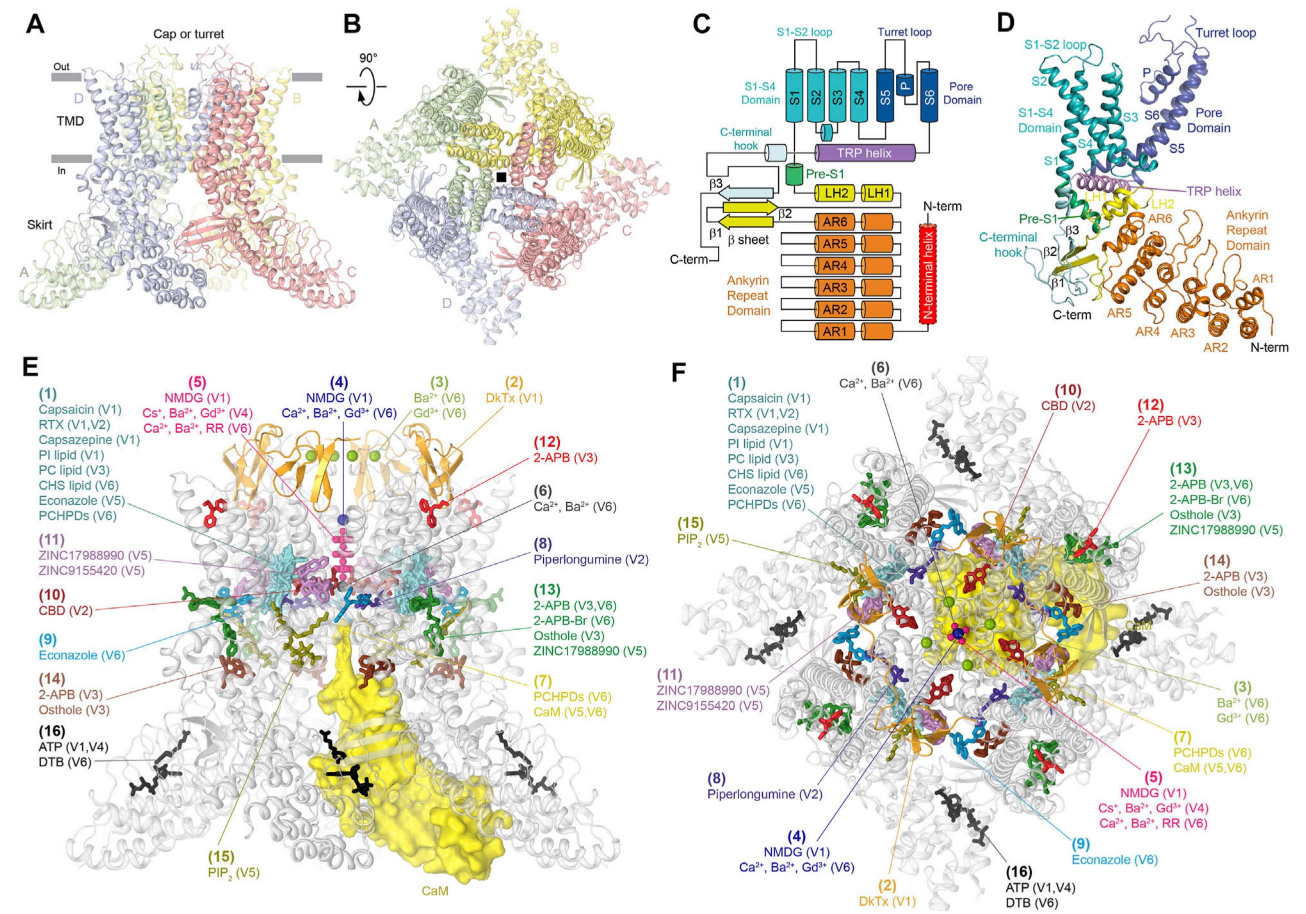

FIGURE 1 | Vanilloid-subfamily TRP channel architecture and mapping of binding sites. **(A–B)** Side **(A)** and top **(B)** views of the TRPV1 tetramer (PDB ID: 7LQY) with each subunit shown in a different color. (C) Domain organization diagram of TRPV subunit. The N-terminal helix (red) is only present in TRPV5 and TRPV6. **(D)** Structure of the TRPV1 subunit with domains colored as in **(C)**. **(E)–(F)** Side **(E)** and top **(F)** views of the TRPV1 tetramer (gray) with 16 unique binding sites mapped by differently colored ligands.

calcium-selective, representing calcium uptake channels in epithelial tissues (Hoenderop et al., 1999; Peng et al., 1999; Yelshanskaya et al., 2021; Khattar et al., 2022). Despite diverse contributions of TRPV subfamily members to physiology and disease, they share structural architecture, which in turn determines common ligand-binding sites for pharmacological interventions.

TRPV Channel Structural Architecture

Four 700 to 970 residue-long TRPV channel subunits assemble a four-fold symmetrical tetramer that includes two main compartments: a transmembrane domain (TMD) with a central ion channel pore and an intracellular skirt in which ankyrin repeat domains (ARDs) of four subunits connected by three-stranded β-sheets comprise walls enclosing a wide cavity underneath the ion channel (**Figures 1A,B**). TRPV1 also includes an extracellular cap or turret that forms a dome above the pore's extracellular entrance, with four portals leading to the ion conductance pathway and is critical for channel function (Grandl et al., 2010; Yang et al., 2010; Nadezhdin et al., 2021a).

Each individual TRPV subunit (**Figures 1C, D**) has peripheral regions of N- and C-termini that are not resolved in crystal or cryo-EM structures and are likely disordered. The most N-terminally structured region in TRPV1-4 is the ARD. In TRPV5-6, the ARD is preceded by an additional structural element, the N-terminal helix, which is important for the assembly of these channels (Saotome et al., 2016). The ARD of TRPV channels contains six ankyrin repeats and is followed by the ARD-TMD linker domain that includes a β-hairpin (composed of β-strands, β1 and β2) and a helix-turn-helix motif (composed of linker helices, LH1 and LH2), resembling a seventh ankyrin repeat. The last C-terminal part of the ARD-TMD linker domain, the pre-S1 helix, connects this domain to the TMD, which crudely resembles the TMDs in voltage-gated potassium (Long et al., 2005; Long et al., 2007), sodium (Payandeh et al., 2011; Shen et al., 2017), and calcium (Wu et al., 2015) channels and includes six transmembrane helices (S1-S6) and a pore loop (P-loop) between S5 and S6. The first four transmembrane helices form a bundle to comprise the S1-S4 domain. In voltage-gated ion channels, the S1-S4 domain plays the role of a voltage sensor, in which positively charged arginine or lysine residues of S4 move relative to the membrane plane during activation and deactivation of these channels. In TRPV channels, S4 does not contain positively charged residues, thus explaining why these channels are not activated by membrane voltage.

S5, P-loop, and S6 comprise the pore domain. The pore domains of all four TRPV subunits assemble together in a four-fold symmetrical manner to form an ion conduction pathway or pore in the middle that connects two sides of the membrane, with the outside entry facing an extracellular vestibule and the cytoplasmic side entry facing the intracellular cavity. The extended region of each subunit re-entrant P-loop lines the extracellular part of the pore and contributes to a selectivity filter, which determines channel permeability and ion selectivity. The intracellular part of the pore is lined by the S6 helices with the narrow part of their bundle forming the gate. Between the gate and the selectivity filter is the pore's central cavity, which is connected to the membrane environment surrounding the channel by four side portals between S5 and S6 of the neighboring subunits.

The S1-S4 and pore domains interact with each other in a domain-swapped arrangement, similar to classical voltage-gated channels but different from the non-swapped arrangement observed in CNG channels (Li et al., 2017), HCN channels (Lee and MacKinnon, 2017), and potassium channels such as Eag1 (Whicher and MacKinnon, 2016), Slo1 (Tao et al., 2017), and Slo2.2 (Hite and MacKinnon, 2017). Interestingly, the non-swapped arrangement was first discovered in the crystal structure of TRPV6 that had a single residue mutation L495Q in the TMD but showed nearly identical channel function to wild type (Saotome et al., 2016). The reversal of glutamine to leucine produced a remarkable conversion of TRPV6 to the natural domain-swapped architecture (Singh et al., 2017). A similar conversion can also happen as a result of deletions in the S4-S5 linker connecting the S1-S4 and pore domains (Singh et al., 2017), something that has likely happened in the course of evolution with CNG, HCN, Eag1, Slo1, and Slo2.2 channels (Whicher and MacKinnon, 2016; Hite and MacKinnon, 2017; Lee and MacKinnon, 2017; Li et al., 2017; Tao et al., 2017).

Following S6 is the amphipathic TRP helix, which runs parallel to the membrane and creates a hub for interactions between hydrophobic elements of the TMD and hydrophilic elements of the intracellular skirt. After the TRP helix, the polypeptide forms a loop structure named the C-terminal hook, which typically starts with a short α-helix and ends with a β-strand (β3) that tethers to the β-hairpin in the linker domain to create the three-stranded β-sheet. The latter, together with the C-terminal hook, participates in intersubunit interactions with the ARDs that glue the elements of the intracellular skirt together. In TRPV5-6, at the center of these interactions is the N-terminal helix, which is positioned as a pillar along the corners of the intracellular skirt (Saotome et al., 2016; Hughes et al., 2018a; Dang et al., 2019). Deletions of the N-terminal helix or mutations of its conserved residues in TRPV5 abolished or significantly impaired its Ca^{2+} uptake function (de Groot et al., 2011), suggesting that the intersubunit interactions are both structurally and functionally important. In TRPV1-3, which lack the N-terminal helix, intersubunit interactions are strengthened by the C-terminus, which wraps around the three-stranded β-sheet (Singh et al., 2018a; Zubcevic et al., 2018; Nadezhdin et al., 2021a).

The similarity in structural architecture of different TRPV channels allows generalized mapping and classification of ligand-binding sites that have been discovered in individual subfamily members (**Figures 1E, F**; **Table 1**). We identified 16 distinct binding sites, which form several groups based on contribution of specific structural elements: the vanilloid site (1); sites associated with ion channel pore, such as DkTx site (2); the permeant ions recruitment site in the extracellular vestibule (3); the extracellular pore entry site (4); the selectivity filter site (5); the central cavity site (6) and the intracellular pore entry site (7); the deep (8) and shallow (9) S4-S5 sites; the deep (10) and shallow (11) portal sites; the sites at the top (12) and base (13) of the S1-S4 helical bundle; the ARD-TMD linker (14) and S2-S3 (15) sites at the ARD–TMD interface; and the ARD sites (16).

Vanilloid Site

The first ligand-binding site that has been identified structurally in TRP channels is the vanilloid site (**Figure 2**). This site (1) is located in the TMD region that faces the cytoplasmic leaflet of the membrane, in the crevice between S1-S4 and pore domains and is contributed mainly by S3, S4, S4-S5 linker, S5, and S6, often involving domains at the TMD–skirt interface, including LH2, S2-S3 loop, and TRP helix (**Figures 2A, B**; **Table 1**). The vanilloid site harbors agonists such as the active component of hot chili peppers, capsaicin, and its potent functional analog, resiniferatoxin (RTX), a naturally occurring chemical found in cactus-like resin spurge plants in Morocco and Northern Nigeria. Structures in complex with capsaicin were solved for rat (Cao et al., 2013; Kwon et al., 2021) and squirrel (Nadezhdin et al., 2021a) TRPV1 (**Figure 2C**, **Supplementary Figure S1A**). Interestingly, despite robust capsaicin-induced opening of TRPV1 in physiological experiments (Caterina et al., 1999; McIntyre et al., 2001; Premkumar et al., 2002; Savidge et al., 2002; Nadezhdin et al., 2021a), structures of TRPV1 bound to capsaicin alone have a non-conducting pore, unless another activating stimulus, heat, has been applied at the same time (Kwon et al., 2021). Even in this latter case, the pore is less open than in TRPV1 bound to two agonists simultaneously, RTX and double-knot toxin (DkTx) (Cao et al., 2013; Gao et al., 2016; Zhang et al., 2021). While certain conformational changes induced by capsaicin alone, including widening of the S6 bundle-crossing gate region (Cao et al., 2013) and π-to-α transition in S6 (Nadezhdin et al., 2021a), have been documented, the inability of capsaicin to open the channel completely suggests that as of now, preparations of TRPV1 protein for structural studies are not able to reproduce the natural environment of the plasma membrane or capture the channel action on the physiologically relevant time scale.

The situation with capsaicin is somewhat similar to the situation with RTX (**Figure 2D**, **Supplementary Figure S1B**), which is either ineffective or induces only partial opening of TRPV1 pore, being much less effective itself than in combination with DkTx (Cao et al., 2013; Gao et al., 2016; Zhang et al., 2021). The same is true for TRPV2, in which RTX induces conformational changes in the selectivity filter and gate region, often deviating from the four-fold rotational symmetry but has

TABLE 1 | Ligand binding sites in TRPV channels.

Site	Ligand	Channel	Function	Affinity (µM) and references	Method: resolution	PDB IDs and references	Domains: residues
(1) Vanilloid site	Capsaicin	Rat TRPV1	Agonist	EC$_{50}$ 0.2–1.9 Caterina et al. (1997); McIntyre et al. (2001); Vriens et al. (2009); Laursen et al. (2016)	Cryo-EM: 3.37–4.20 Å	3J5R, 7LPA, 7LPB, 7LPD, and 7LPE Cao et al. (2013); Kwon et al. (2021)	**S3:** Y511, S512, and L515 **S4:** F543, T550, N551, and Y554 **S4-S5:** I573 **S6:** L662
		Squirrel TRPV1	Agonist	EC$_{50}$ 0.53 ± 0.03 Laursen et al. (2016)	Cryo-EM: 3.81 Å	7LR0 Nadezhdin et al. (2021a)	**S3:** S514, L517, and F518 **S4:** F545, T552, N553, L555, and Y556 **S5:** F593 **S6:** L664 and L671
	Resiniferatoxin (RTX)	Rat TRPV1	Agonist	EC$_{50}$ 0.007–0.1 Caterina et al. (1997); Szallasi et al. (1999); Vriens et al. (2009); Zhang et al. (2016)	Cryo-EM: 2.76–3.84 Å	3J5Q, 5IRX, 7L2L, 7L2M, 7L2N, 7L2O, 7L2V, 7L2W, 7L2X, 7MZ5, 7MZ7, 7MZ9, 7MZA, 7MZB, 7MZC, 7MZD, and 7MZE Cao et al. (2013); Gao et al. (2016); Zhang et al. (2021)	**S3:** Y511, S512, I514, and L515 **S4:** A546, M547, T550, N551, L553, Y554, and R557 **S4-S5:** A566, I569, and I573 **S5:** F591 **S6:** A665, I668, and L669
		Rabbit TRPV2	Agonist	–	X-ray:3.10 Å Cryo-EM: 2.90–4.20 Å	6BWJ, 6OO3, 6OO4, 6OO5, and 6OO7 Zubcevic et al. (2018); Zubcevic et al. (2019a)	**S3:** Y469, S470, L473 **S4:** S501, V504, M505, T508, L511, and R515 **S4-S5:** S524 **S5:** I531, L539, and F545 **S6:** L630 **TRP:** Q661
		Squirrel TRPV1	Agonist	–	Cryo-EM 3.41 Å	7LQZ Nadezhdin et al. (2021a)	**S3:** Y513, S514, M516, L517, and F518 **S4:** A548, M549, T552, N553, and Y556 **S4-S5:** I575 and L579 **S5:** F593 **S6:** I670 and L671
	Capsazepine	Rat TRPV1	Competitive antagonist	IC$_{50}$ 0.3 - 2.4 Bevan et al. (1992); Caterina et al. (1997); Szallasi et al. (1999)	Cryo-EM: 3.43 Å	5IS0 Gao et al. (2016)	**S3:** Y511, S512, and L515 **S4:** M547, T550, N551, L553, and Y554 **S4-S5:** E570 **S5:** F591 **S6:** L669
	Phosphatidyl-inositol (PI) lipid	Rat TRPV1	Unknown	–	Cryo-EM: 2.60–3.70 Å	5IRZ, 7L2H, 7L2I, 7L2J, 7L2P, 7L2R, 7L2S, 7L2T, 7L2U, 7LP9, 7LPC, and 7MZ6 Gao et al. (2016); Kwon et al. (2021); Zhang et al. (2021)	**LH2:** R409 **S2-S3:** D511 **S3:** S512, S514, Y513, and L517 **S4:** A548, M549, T552, and L555 **S4-S5:** E572, I575, and L576 **S5:** F593 **S6:** A667 and L671 **TRP:** I698, L701, Q702, and I705
		Squirrel TRPV1	Unknown	–	Cryo-EM: 3.19 Å	7LQY Nadezhdin et al. (2021a)	**LH2:** R411 and H412 **S2-S3:** D509 and Y511 **S3:** S512 and L515 **S4:** T550, L553, Y554, and R557 **S4-S5:** E570 **S6:** L669 **TRP:** L699, Q700, and I703
	Phosphatidyl-choline (PC) lipid	Mouse TRPV3	Inhibitor	–	Cryo-EM: 1.98–3.42 Å	6LGP, 7MIJ, 7MIK, 7MIM, and 7MIN Shimada et al. (2020); Nadezhdin et al. (2021b)	**S2-S3:** L517, S518, and D519 **S3:** W521, F522, and F524 **S4:** A556, A560, L563, and R567 **S4-S5:** S576, V577, I579, Q580, and L584 **S5:** F601 **TRP:** Q695
	Cholesteryl hemisuccinate (CHS) lipid	Human TRPV6	Unknown	–	Cryo-EM: 2.43–3.26 Å	7K4A, 7S88, 7S89, 7S8B, and 7S8C Bhardwaj et al. (2020) Neuberger et al. (2021a)	**S3:** P424 and F425 **S4:** S455, V459, C463, and M466 **S4-S5:** T479, I480, I482, and Q483 **S6:** I557, T558, A561, and I565 **TRP:** Q596

(Continued on following page)

TABLE 1 | (*Continued*) Ligand binding sites in TRPV channels.

Site	Ligand	Channel	Function	Affinity (μM) and references	Method: resolution	PDB IDs and references	Domains: residues
	Econazole	Rabbit TRPV5	Inhibitor	IC$_{50}$ 1.3 - 2.0 Nilius et al. (2001); Hughes et al. (2018b)	Cryo-EM: 4.80 Å	6B5V Hughes et al. (2018b)	**S4:** L460 **S6:** A561
	PCHPDs (cis-22a, Br-cis-22a, 3OG, 30, 31)	Human TRPV6	Inhibitors	IC$_{50}$ 0.08 - 1.7 Simonin et al. (2015); Cunha et al. (2019); Bhardwaj et al. (2020); Cunha et al. (2020)	Cryo-EM: 3.10–4.34 Å	7K4B, 7K4C, 7K4D, 7K4E, and 7K4F Bhardwaj et al. (2020)	**S3:** P424, F425, and L428 **S4:** F456, V459, C463, and M466 **S4-S5:** T479, I482, Q483, and I486 **S6:** M554, I557, T558, A561, and I565
	PCHPD (Br-cis-22a)	Rat TRPV6	Inhibitor	IC$_{50}$ 0.96 ± 0.03 Bhardwaj et al. (2020)	X-ray: 3.70 Å	7D2K Bhardwaj et al. (2020)	**S3:** P424, F425, and L428 **S4:** F456, V459, C463, and M466 **S4-S5:** T479, I482, Q483, and I486 **S6:** M554, I557, T558, A561, and I565
(2) DkTx site	DkTx	Rat TRPV1	Agonist	EC$_{50}$ 0.14–0.24 Bohlen et al. (2010)	Cryo-EM: 2.95–3.84 Å	3J5Q, 5IRX, 7L2M, 7L2R, 7L2T, and 7L2U Cao et al. (2013); Gao et al. (2016); Zhang et al. (2021)	**P:** S629 and Y631 **P-S6:** F649, N652, D654, and F655 **S6:** K656, A657, V658, I660, and I661
(3) Extracellular vestibule recruitment sites	Ba^{2+}	Rat TRPV6	Permeant ion	EC$_{50}$ 1.91 ± 0.74 Saotome et al. (2016)	X-ray: 3.85 Å	5IWR Saotome et al. (2016)	**S1-S2:** D363 **S5-P:** E518 **P-S6:** D547
	Gd^{3+}	Rat TRPV6	Channel blocker	IC$_{50}$ 3.87 ± 0.83 Saotome et al. (2016)	X-ray: 3.80–3.90 Å	5IWT and 5WOA Saotome et al. (2016); Singh et al. (2017)	**S5-P:** D519 and E518 **P-S6:** D547
(4) Extracellular pore entry site	NMDG	Rat TRPV1	Permeant ion	–	Cryo-EM: 3.64 Å	7L2V Zhang et al. (2021)	**P:** G645
	Ca^{2+}	Rat TRPV6	Permeant ion	EC$_{50}$ 1.47 ± 0.80 Saotome et al. (2016)	X-ray: 3.65–3.70 Å	5IWP and 5WO9 Saotome et al. (2016); Singh et al. (2017)	**P:** D541
	Ba^{2+}	Rat TRPV6	Permeant ion	EC$_{50}$ 1.91 ± 0.74 Saotome et al. (2016)	X-ray: 3.85 Å	5IWR Saotome et al. (2016)	**P:** D541
	Gd^{3+}	Rat TRPV6	Channel blocker	IC$_{50}$ 3.87 ± 0.83 Saotome et al. (2016)	X-ray: 3.80–3.90 Å	5IWT and 5WOA Saotome et al. (2016); Singh et al. (2017)	**P:** D541
(5) Selectivity filter site	NMDG	Rat TRPV1	Permeant ion	–	Cryo-EM: 3.26 Å	7L2X Zhang et al. (2021)	**P:** G643, M644, and G645
	Ca^{2+}	Rat TRPV6	Permeant ion	EC$_{50}$ 1.47 ± 0.80 Saotome et al. (2016)	X-ray: 3.65–3.70 Å	5IWP and 5WO9 Saotome et al. (2016); Singh et al. (2017)	**P:** T538
	Ba^{2+}	Rat TRPV6	Permeant ion	EC$_{50}$ 1.91 ± 0.74 Saotome et al. (2016)	X-ray: 3.85 Å	5IWR Saotome et al. (2016)	**P:** T538
	Ba^{2+}	Frog TRPV4	Permeant ion	–	X-ray: 6.31 Å	6C8G Deng et al. (2018)	**P:** G675
	Cs^{+}	Frog TRPV4	Permeant ion	–	X-ray: 6.50 Å	6C8F Deng et al. (2018)	**P:** G675
	Gd^{3+}	Frog TRPV4	Channel blocker	–	X-ray: 6.50 Å	6C8H Deng et al. (2018)	**P:** G675
	Ruthenium red (RR)	Human TRPV6	Channel blocker	IC$_{50}$ 9 ± 1 Hoenderop et al. (2001)	Cryo-EM: 2.43 Å	7S8B Neuberger et al. (2021a)	**P:** T539 and D542
(6) Central cavity site	Ca^{2+}	Rat TRPV6	Permeant ion	EC$_{50}$ 1.47 ± 0.80 Saotome et al. (2016)	X-ray: 3.65–3.70 Å	5IWP and 5WO9 Saotome et al. (2016); Singh et al. (2017)	**P:** T538 **S6:** T566, M569, and L573
	Ba^{2+}	Rat TRPV6	Permeant ion	EC$_{50}$ 1.91 ± 0.74 Saotome et al. (2016)	X-ray: 3.85 Å	5IWR Saotome et al. (2016)	**P:** T538 **S6:** T566, M569, and L573

(Continued on following page)

TABLE 1 | (*Continued*) Ligand binding sites in TRPV channels.

Site	Ligand	Channel	Function	Affinity (μM) and references	Method: resolution	PDB IDs and references	Domains: residues
(7) Intracellular pore entry site	PCHPDs (cis-22a, Br-cis-22a, 3OG, 30, 31)	Human TRPV6	Inhibitors	IC_{50} 0.08 - 1.7 Simonin et al. (2015); Cunha et al. (2019); Bhardwaj et al. (2020); Cunha et al. (2020)	Cryo-EM: 3.10–4.34 Å	7K4B, 7K4C, 7K4D, 7K4E, and 7K4F Bhardwaj et al. (2020)	**S6:** I575, A576, G579, and W583
	PCHPD (Br-cis-22a)	Rat TRPV6	Inhibitor	IC_{50} 0.96 ± 0.03 Bhardwaj et al. (2020)	X-ray: 3.70 Å	7D2K Bhardwaj et al. (2020)	**S6:** I575, A576, G579, and W583
	Calmodulin (CaM)	Rabbit TRPV5	Inactivator, channel blocker	–	Cryo-EM: 3.30–4.40 Å	6DMW and 6O20 Hughes et al. (2018a); Dang et al. (2019)	**S6:** W583
		Human TRPV6	Inactivator, channel blocker	–	Cryo-EM: 3.90 Å	6E2F Singh et al. (2018b)	**S6:** W583
		Rat TRPV6	Inactivator, channel blocker	–	Cryo-EM: 3.60 Å	6E2G Singh et al. (2018b)	**S6:** W582
(8) Deep S4-S5 site	Piperlongumine (PL)	Rat TRPV2	Inhibitor	IC_{50} 4.6 ± 0.13 Conde et al. (2021)	Cryo-EM: 3.46 Å	6WKN Conde et al. (2021)	**S4:** L513 and T516 **S4-S5:** T522, Y525, S526, I529, and Q530 **S5:** R539 and V543 **S6:** V635, L636, and N639
(9) Shallow S4-S5 site	Econazole	Human TRPV6	Inhibitor	IC_{50} 4.39 ± 0.31 Neuberger et al. (2021a)	Cryo-EM: 2.85 Å	7S8C Neuberger et al. (2021a)	**S4:** V465, F468, and A469 **S4-S5:** F472, M474, and L475 **S5:** W495
(10) Deep portal site	Cannabidiol (CBD)	Rat TRPV2	Agonist	EC_{50} 3.7 Pumroy et al. (2019)	Cryo-EM: 3.20–3.40 Å	6U88 and 6U8A Pumroy et al. (2019)	**S5:** I533, L537, F540, L541, and Y544 **P:** F601 **S6:** L631, L632, Y634, V635, L637, L638, and M640
(11) Shallow portal site	ZINC17988990	Rabbit TRPV5	Inhibitor	IC_{50} 0.106 ± 0.027 Hughes et al. (2019)	Cryo-EM: 3.78 Å	6PBE Hughes et al. (2019)	**S4-S5:** F487, L490, and M491 **S5:** C494 and W495 **S6:** I565
	ZINC9155420	Rabbit TRPV5	Inhibitor	IC_{50} 2.91 ± 0.56 Hughes et al. (2019)	Cryo-EM: 4.20 Å	6PBF Hughes et al. (2019)	**S4-S5:** L490 and M491 **S5:** C494 **S6:** I564
(12) S1-S4 top site	2-APB	Mouse TRPV3	Agonist	EC_{50} 9–34 Singh et al. (2018a), Hu et al. (2009), Chung et al. (2004); Hu et al. (2004)	Cryo-EM: 4.24 Å	6DVZ Singh et al. (2018a)	**S1:** V458 and R462 **S1-S2:** R464 **S2:** R487 **S3:** Y540
(13) S1-S4 base site	2-APB	Mouse TRPV3	Agonist	EC_{50} 9–34 Singh et al. (2018a), Hu et al. (2009), Chung et al. (2004); Hu et al. (2004)	Cryo-EM: 4.00–4.24 Å	6DVY and 6DVZ Singh et al. (2018a)	**S1:** S444 **S2:** W493, K500, and E501 **S3:** F526 **S4:** Y565
		Human TRPV6	Inhibitor	IC_{50} 274 ± 27 Singh et al. (2018c)	Cryo-EM: 4.44 Å	6D7T Singh et al. (2018c)	**S2-S3:** Q418 and G422 **S3:** G423 and H426 **S4:** R470 **TRP:** M603
		Rat TRPV6	Inhibitor	IC_{50} 184 ± 8 Singh et al. (2018c)	X-ray: 3.45–3.497 Å	6D7O and 6D7Q Singh et al. (2018c)	**S2:** E402 **S3:** G422, F424, H425, and I428 **S4:** N463, Y466, and R469 **TRP:** M602
	2-APB-Br	Rat TRPV6	Inhibitor	–	X-ray: 3.60–4.30 Å	6D7V and 6D7X Singh et al. (2018c)	**S2:** E402 **S3:** G422, F424, H425, and I428 **S4:** N463, Y466, and R469 **TRP:** M602
	Osthole	Mouse TRPV3	Competitive antagonist	IC_{50} 20–37 Sun et al. (2018); Neuberger et al. (2021b)	Cryo-EM: 3.64–3.99 Å	7RAS and 7RAU Neuberger et al. (2021b)	**S1:** S444 **S2:** C496, I497, K500, and E501 **S4:** Y565 **TRP:** M706

(Continued on following page)

TABLE 1 | (*Continued*) Ligand binding sites in TRPV channels.

Site	Ligand	Channel	Function	Affinity (μM) and references	Method: resolution	PDB IDs and references	Domains: residues
	ZINC17988990	Rabbit TRPV5	Inhibitor	*IC_{50}* 0.106 ± 0.027 Hughes et al. (2019)	Cryo-EM: 3.78 Å	6PBE Hughes et al. (2019)	**LH1:** E294 **S2:** L402, E403, and D406 **S2-S3:** Y415 and L421 **S3:** I429 **S4:** Y467 and F468 **TRP:** M603 and R606
(14) ARD-TMD linker site	2-APB	Mouse TRPV3	Agonist	EC_{50} 9–34 Singh et al. (2018a), Hu et al. (2009), Chung et al. (2004); Hu et al. (2004)	Cryo-EM: 4.00–4.24 Å	6DVY and 6DVZ Singh et al. (2018a)	**LH2:** H417, L420, and T421 **Pre-S1:** H426 and H430 **TRP:** R693 and L694
		Human TRPV3	Agonist	EC_{50} 28–78 Chung et al. (2004); Deering-Rice et al. (2014)	Cryo-EM: 3.60 Å	6OT5 Zubcevic et al. (2019b)	**LH2:** H417 and L420 **Pre-S1:** H426 and L429 **TRP:** R693
	Osthole	Mouse TRPV3	Competitive antagonist	IC_{50} 20–37 Sun et al. (2018); Neuberger et al. (2021b)	Cryo-EM: 3.64–3.99 Å	7RAS and 7RAU Neuberger et al. (2021b)	**LH2:** T421 **Pre-S1:** H426, H430, and W433 **TRP:** R693 and R696
(15) S2-S3 site	PIP_2	Rabbit TRPV5	Agonist	–	Cryo-EM: 4.00 Å	6DMU Hughes et al. (2018a)	**ARD:** R302 **S2-S3:** F416, G417, and Q418 **S6:** R584
(16) ARD site	ATP	Rat TRPV1	Positive allosteric modulator	–	X-ray: 2.70–3.20 Å	2NYJ and 2PNN Lishko et al. (2007)	**ARD:** R115, F118, K155, K160, L163, N164, Y199, Q202, E210, and R211
		Human TRPV4	Positive allosteric modulator	–	X-ray: 2.95 Å	4DX2 Inada et al. (2012)	**ARD:** K192, K197, L200, N201, F231, Y236, Q239, and R248
	Desthiobiotin (DTB)	Rat TRPV6	Unknown	–	X-ray: 3.246–3.85 Å	5WO6, 5WO7, 5WO8, 5WO9, 5IWK, 5IWP, 5IWR, and 5IWT Saotome et al. (2016); Singh et al. (2017)	**ARD:** Q40, L88, M110, Y115, V151, and N158

never produced the full opening of the ion channel pore (Zubcevic et al., 2018; Zubcevic et al., 2019a). The working hypothesis for the mechanism of vanilloid agonist action is that agonist binding induces movement of the S1-S4 bundle relative to the pore domain, which involves pulling the S4-S5 linker away from the central axis, altering the network of interactions between the P-loop, S5, and S6 and allowing the P-loop helices and S6 bundle crossing gate to widen the pore (Cao et al., 2013; Gao et al., 2016; Zubcevic et al., 2018; Zubcevic et al., 2019a; Zhang et al., 2021). This putative activation mechanism will likely become more precise and specific as one succeeds to identify structural conditions in which binding of a vanilloid agonist alone will lead to the channel pore opening.

In the absence of agonists (apo condition), the vanilloid-binding site is typically occupied by a lipid. In total, three types of lipids have been identified in the vanilloid site so far, and they appear to be TRPV subtype-specific. Indeed, in all apo-state TRPV1 structures with more or less clearly resolved density in the vanilloid site, the bound lipid was interpreted as phosphatidylinositol (PI) (Nadezhdin et al., 2021a; Kwon et al., 2021; Gao et al., 2016; Zhang et al., 2021) (**Figure 2E**, **Supplementary Figure S1C**). Since agonists have to expel PI from its binding site to activate TRPV1, PI might be considered an endogenous inhibitor of this channel. However, to test this hypothesis, one would have to activate TRPV1 in the absence of ligands by removing PI from the vanilloid site. More apparent inhibitory role can be assigned to the vanilloid site lipid in TRPV3, which resides in this site in the cold apo conditions but completely dissociates from this site upon activation by heat (Singh et al., 2019; Nadezhdin et al., 2021b). The vanilloid site lipid in TRPV3 has been modeled as phosphatidylcholine (PC) (Nadezhdin et al., 2021b; Shimada et al., 2020) (**Figure 2F**, **Supplementary Figure S1D**), but molecular dynamics (MD) simulations suggested rather low specificity of this site to different types of lipids (Nadezhdin et al., 2021b), which requires further studies. In higher resolution TRPV5-6 structures, the vanilloid site is occupied by densities of the characteristic shape that were modeled by either cholesterol or its soluble analog used in protein purifications, namely, cholesteryl hemisuccinate (CHS) (McGoldrick et al., 2018; Dang et al., 2019; Bhardwaj et al., 2020; Neuberger et al., 2021a) (**Figure 2G**, **Supplementary Figure S2A**). Whether the lipid at the vanilloid site plays a role of an agonist or inhibitor of TRPV5 and TRPV6 is currently unclear and will require additional functional experiments and structures at high resolution but in the absence of cholesterol/CHS.

The vanilloid site in TRPV channels not only binds agonists and lipids but also inhibitors, such as capsazepine in TRPV1 (**Figure 2H, Supplementary Figure S2B**) and cis22a in TRPV6 (**Figure 2I, Supplementary Figure S2C**). Capsazepine was proposed to act by displacing the resident PI lipid and stabilizing the interface between the S1-S4 and pore domains in the apo (closed) state-like conformation, which prevents pulling the S4-S5 linker away from the central axis to trigger conformational rearrangements that can lead to opening of the channel gate (Gao et al., 2016). For cis22a, as well as other representatives of (4-phenylcyclohexyl)piperazine derivatives (PCHPDs) that inhibit TRPV6-mediated currents with submicromolar affinity, the vanilloid site is modulatory, with the main inhibitory site located at the ion pore intracellular entrance (Bhardwaj et al., 2020). Because of the weak contribution of the vanilloid site to PCHPD inhibition, the mechanism of allosteric regulation through this site is not completely clear and requires additional studies. It has also been reported that the antifungal drug econazole binds to the vanilloid site in TRPV5 (Hughes et al., 2018b) (**Supplementary Figure S2D**). The corresponding 4.8-Å resolution structure allowed only an approximate placement of the compound into cryo-EM density (Hughes et al., 2018b), while more precise and confident fitting would require a higher resolution structure of the TRPV5–econazole complex. Such structure would be interesting to see, as the recent 2.85-Å resolution structure of the TRPV6–econazole complex has not identified the vanilloid site as a binding site for econazole (Neuberger et al., 2021a). Instead, the TRPV6 structure shows econazole binding to the shallow S4-S5 site, which is contributed by residues that are highly conserved between TRPV5 and TRPV6 channels (Neuberger et al., 2021a).

Pore Sites

The pore sites are contributed by the pore-forming P-loop and S6 as well as the extracellular loops (S1-S2, S5-P, and P-S6) that shape the ion channel extracellular vestibule (**Figures 3A, B**; **Table 1**). In TRPV1, two copies of the agonist DkTx bind to the extracellular side of the channel in a two-fold symmetrical manner, with each knot of this double-knot toxin binding to a site (2) composed of residues in the P-loop and S6 of two neighboring subunits (Cao et al., 2013; Gao et al., 2016; Zhang et al., 2021) (**Figure 3C**). The proposed mechanism of DkTx-induced TRPV1 opening suggests that DkTx binding induces a large backward tilting of the S1-S4 domain away from the channel central axis, which allosterically moves S5/S6 by pulling at the S4-S5 linker and opens the channel gate (Zhang et al., 2021). At the moment, it is unclear how DkTx interacts with the cap domain of TRPV1 and whether it affects permeation through the four portals leading to the ion conductance pathway (Nadezhdin et al., 2021a). Answering these questions will require structure determination of the full-length TRPV1 in complex with DkTx and with the completely resolved cap domain.

TRPV2-6 channels do not have a cap domain and instead have an extracellular vestibule leading to the pore entry. This vestibule contains binding sites for permeant cations, which in TRPV6 were resolved by X-ray crystallography (Saotome et al., 2016; Singh et al., 2017). Four symmetry-related cation binding sites or recruitment sites (3) were identified in TRPV6 as anomalous difference peaks for Ba^{2+} and Gd^{3+} (**Figure 3D**). These sites are contributed by negatively charged residues and have somewhat different locations, probably due to the difference in charge density. Although the anomalous difference peaks at the recruitment sites were not observed for Ca^{2+}, presumably due to lower affinity, reduced occupancy, or weaker anomalous signal, the highly electronegative outer vestibule is likely involved in the general recruitment of cations toward the extracellular vestibule of the TRPV6 channel (Saotome et al., 2016). Consistent with the results of isothermal titration calorimetry experiments for Gd^{3+}, the affinity of cations to the recruitment sites is lower than that to the binding sites in the pore (Saotome et al., 2016).

The next distinct binding site associated with the conductance pathway is the site at the pore extracellular entrance (4). In TRPV1, this site has been shown to bind a molecule of N-methyl-D-glucamine (NMDG), which appears as a blob of density in the cryo-EM map (Zhang et al., 2021). Strong blobs of density of a smaller size, interpreted as representing permeant cations, were observed at this location in the crystallographic and cryo-EM maps of TRPV5 (Hughes et al., 2018a; Dang et al., 2019; Hughes et al., 2018b; Hughes et al., 2019) and TRPV6 (Saotome et al., 2016; Singh et al., 2017; McGoldrick et al., 2018; Bhardwaj et al., 2020; Neuberger et al., 2021a; Singh et al., 2018b; Singh et al., 2018c). Solid evidence about the chemical identity of the pore entry site binders came from the crystallographic studies of TRPV6. Indeed, strong anomalous peaks at this location, contributed by side chains of the highly conserved aspartates (D542 in hTRPV6 and D541 in rTRPV6), were identified for the permeant cations Ca^{2+} and Ba^{2+} and for the channel blocker Gd^{3+} (Saotome et al., 2016), (Singh et al., 2017) (**Figure 3D**). The distance of 2.4 Å between Ca^{2+} and carboxylate oxygen of aspartate at this site matches the reported average Ca^{2+}–oxygen distance in Ca^{2+}-binding proteins (Yang et al., 2002), suggesting that the bound Ca^{2+} ion is at least partially dehydrated. Tight coordination of cations by the aspartates suggested a "knock-off" mechanism of ion permeation, strongly supported by MD simulations, which revealed 2 to 3 permeant ions continuously moving around the pore entry site to create the strong averaged density observed in crystallographic or cryo-EM maps (Sakipov et al., 2018). Because of the strong positive charge of Gd^{3+}, its binding to the pore entry site is so tight that it cannot leave this site to permeate the channel (Sakipov et al., 2018).

Tight binding to the pore entry site not only explains the mechanism of TRPV6 block by Gd^{3+} but also why Gd^{3+} ions were not found 6–8 Å deeper in the pore, at the selectivity filter site (5), formed by backbone carbonyls and side chain hydroxyl groups of T538 in the lower parts of the P-loop extended region (**Figure 3D**). This selectivity filter site binds permeant cations Ca^{2+} and Ba^{2+}, which were detected in the crystal structures of TRPV6 using anomalous difference Fourier maps (Saotome et al., 2016; Singh et al., 2017). The selectivity filter site in TRPV6 also binds the inorganic dye and low-specificity ion channel blocker ruthenium red (RR) (Neuberger et al., 2021a) (**Figure 3E, Supplementary Figure S3A**). RR occupies the entire selectivity filter, being surrounded by the carboxyl groups of D542 residues, the backbone carbonyl oxygens of I541, I540, and T539 residues, and the hydroxyl groups of T539 residues, which all together

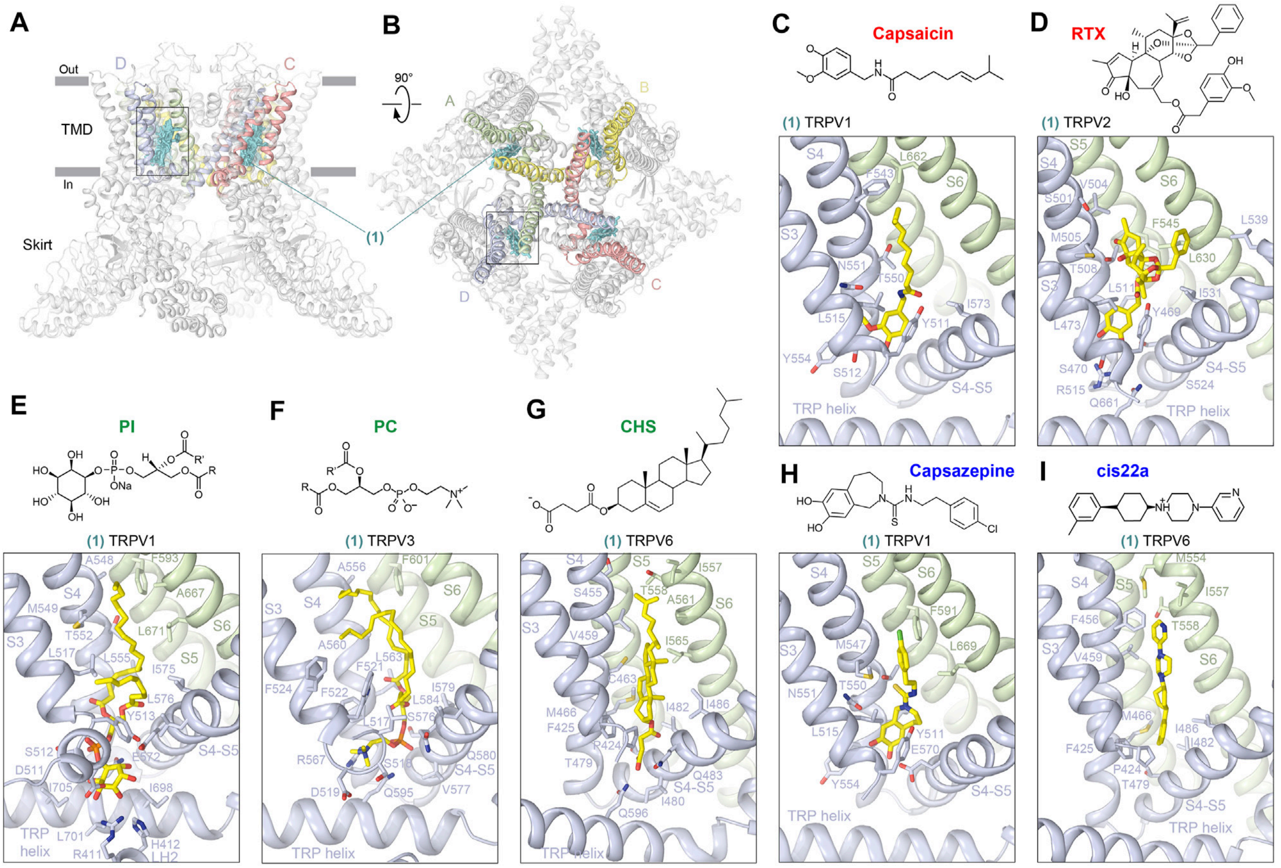

FIGURE 2 | Vanilloid site. **(A–B)** Side **(A)** and top **(B)** views of the TRPV1 tetramer (gray; PDB ID: 7LQY) with the vanilloid site (1) ligands shown in cyan and domains contributing to this site (S3, S4, S4-S5, S5, and S6) shown in subunit colors (see **Figures 1A,B**). Rectangles indicate the region expanded in close-up views. **(C–I)** Close-up views of the vanilloid site in TRPV1 with bound capsaicin (**C**, PDB ID: 7LPA), in TRPV2 with bound RTX (**D**, PDB ID: 6BWJ), in TRPV1 with bound PI (**E**, PDB ID: 7LQY), in TRPV3 with bound PC (**F**, PDB ID: 7MIJ), in TRPV6 with bound CHS (**G**, PDB ID: 7S8B), in TRPV1 with bound capsazepine (**H**, PDB ID: 5IS0), and in TRPV6 with bound cis22a (**I**, PDB ID: 7K4B). Residues contributing to ligand binding are shown in sticks. The chemical structures of the corresponding ligands are shown above the close-up views.

create a highly electronegative environment favorable for the positively charged RR that carries a 6^+ total charge. RR not only plugs the pore to prevent ion conductance, but it also causes the closure of the lower gate, with the characteristic π-to-α transition in S6 that typically accompanies channel closure (McGoldrick et al., 2018; Neuberger et al., 2021a). A possible explanation of why this happens is that RR creates an electric field inside the pore's central cavity that interacts with the electric dipole of the S6 helix. This interaction causes a repulsion of the lower portion of S6 away from RR, which results in rotation of the lower portion of S6 and helps S6 to become entirely α-helical (Neuberger et al., 2021a).

Another binding site in the TRPV6 pore (6) is 6–7 Å below the selectivity filter site, in the middle of the central cavity (**Figure 3D**). The corresponding anomalous difference peaks were found for both Ca^{2+} and Ba^{2+}, although the anomalous peak for Ca^{2+} was less robust, presumably due to its weaker anomalous diffraction properties. The anomalous signal at the central cavity site also suggests that cations bound here are ordered by water molecules, which can be held in place by weak hydrogen-bonding interactions and pore helix dipoles, pointing their partial negative charges toward the middle of the central cavity, similar to K^+ channels (Doyle et al., 1998).

There is also a site at the pore intracellular entrance (7), which is formed by the S6 helices and represents the main site of TRPV6 inhibition by PCHPDs (Bhardwaj et al., 2020) (**Figure 3F**, **Supplementary Figure S3B**). When bound to this site, PCHPDs plug the TRPV6 pore and prevent ion conductance. In addition, interactions of the positive charge of PCHPDs with the π orbitals of tryptophan (W583 in hTRPV6 and W582 in rTRPV6) indole rings, which form a cubic cage at the intracellular pore entrance, pull the S6 helices toward the pore center. This pore narrowing brings isoleucines (I575 in hTRPV6 and I574 in rTRPV6) close to each other to hydrophobically seal the channel, mimicking the pore conformation of the TRPV6-inactivated state. Indeed, when calcium-binding protein calmodulin (CaM) binds at the intracellular pore entrance to inactivate the channel, it inserts the side chain of its lysine K115 into the center of the cubic tryptophan cage (Singh et al., 2018b). The positively charged ε-amino group of K115 makes an atypically strong cation–π interaction with the π-

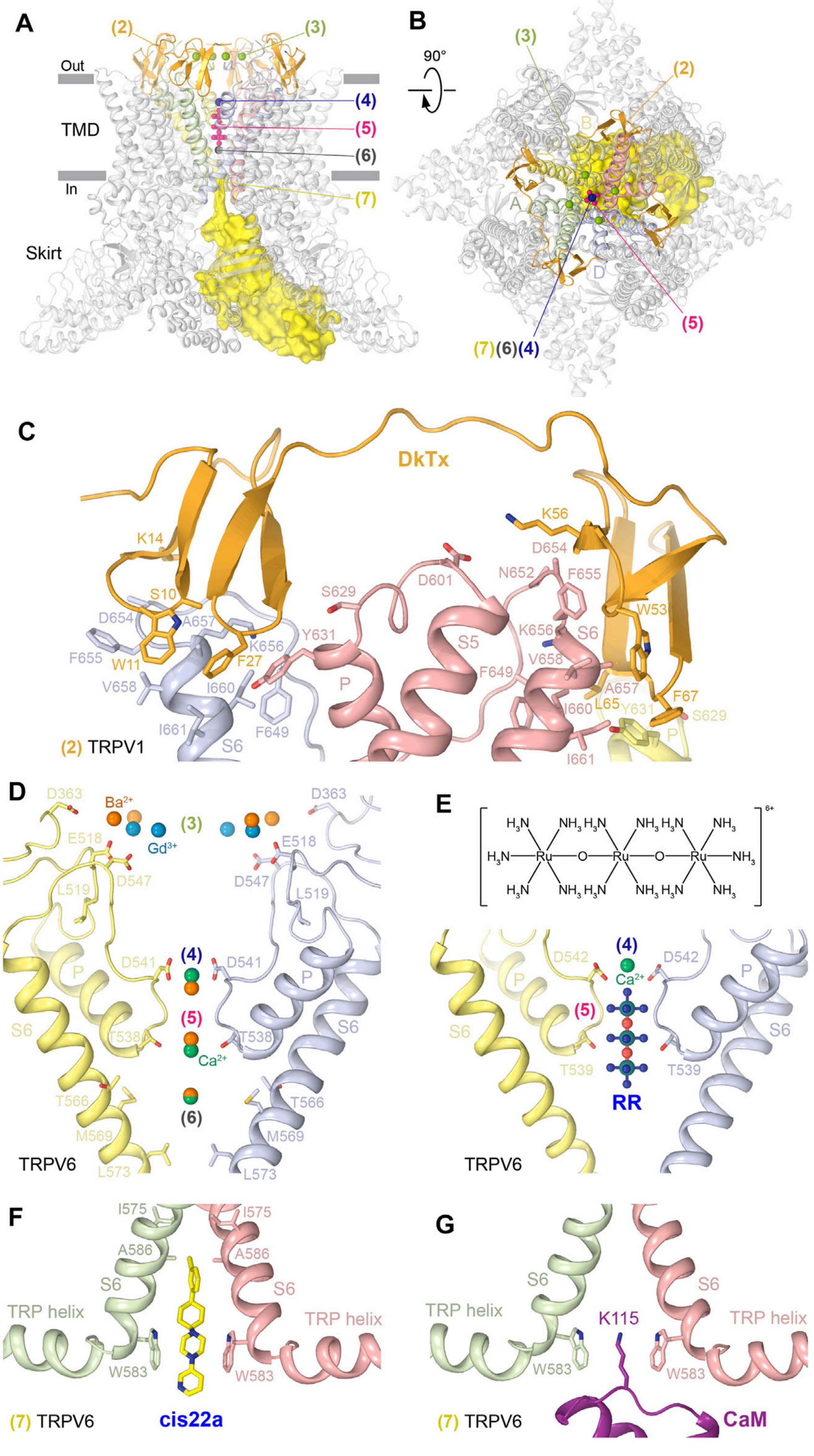

FIGURE 3 | Pore sites. (A–B) Side **(A)** and top **(B)** views of the TRPV1 tetramer (gray; PDB ID: 7LQY) with the DkTx (2), extracellular vestibule recruitment (3), extracellular pore entry (4), selectivity filter (5), central cavity (6), and intracellular pore entry (7) sites illustrated by ligands in orange, green, blue, pink, gray, and yellow, respectively. **(C–G)** Close-up views of the DkTx site in TRPV1 with bound DkTx (**C**, PDB ID: 5IRX); extracellular vestibule recruitment, extracellular pore entry, selectivity filter, and central cavity sites in TRPV6 **(D)** with bound Ca^{2+} (PDB ID: 5WO9), Ba^{2+} (PDB ID: 5IWR), and Gd^{3+} (PDB ID: 5WOA); extracellular pore entry and selectivity filter sites in TRPV6 with bound Ca^{2+} and RR (**E**, PDB ID: 7S8B); and intracellular pore entry sites in TRPV6 with bound cis22a (**F**, PDB ID: 7K4B) or CaM (**G**, PDB ID: 6E2F). Residues contributing to ligand binding are shown in sticks. The chemical structure of RR is shown above the corresponding close-up view **(E)**.

system of four tryptophan indole rings (**Figure 3G**). TRPV5 has a mechanism of inactivation by CaM similar to TRPV6 (Hughes et al., 2018a; Dang et al., 2019), while structures of other TRPVs in complex with CaM have not been solved, and it remains to be discovered whether they have a similar mechanism of inactivation.

S4-S5 Sites

Two types of sites are located right above the S4-S5 linker, where ligands bind at the interface between S4 and S5 of two neighboring subunits (**Figures 4A,B**; **Table 1**). At one site (8), the ligand wedges deeper into the interface and reaches residues on S6. An example of such ligand is the alkaloid piperlongumine (PL), which produces potent allosteric inhibition of TRPV2, presumably underlying the anticancer activity of PL in mouse models of glioblastoma (Conde et al., 2021). PL makes contacts with residues in S4 and S4-S5 linker of one TRPV2 subunit and S5 and S6 of the neighboring subunit (**Figure 4C**, **Supplementary Figure S4A**). By wedging itself between S4 and S5 of the neighboring subunits, PL pushes the S4-S5 linker down, shifting it by ~4 Å toward S5 and causing a downward movement of the entire intracellular skirt by ~3 Å. According to the proposed mechanism of PL action, PL inhibits TRPV2 by immobilizing the S4-S5 linker and locking the channel in a desensitized state (Conde et al., 2021).

At the second, shallower site (9), ligands do not wedge deeply into the interface between S4 and S5 of two neighboring subunits and correspondingly do not reach S6. An example is the binding site of the antifungal drug econazole, which produces strong inhibition of TRPV6-mediated currents (Nilius et al., 2001) (**Figure 4D**, **Supplementary Figure S4B**). By binding to the shallow S4-S5 site in TRPV6, where it is sandwiched between W495 of S5 and F472 of S4 and surrounded by hydrophobic side chains of L496 and V499 of S5 as well as M466, A469, M474, and L475 of S4, econazole replaces a lipid that is otherwise present at this location (Neuberger et al., 2021a). Because of the smaller size of econazole than the lipid, econazole binding creates a void that allows Q473 and M474 side chains to move closer to D472 and W495 and correspondingly away from R589. Separation of Q473 and R589 results in breakage of the salt bridge connecting these residues in the open state (McGoldrick et al., 2018). The loss of this salt bridge, which energetically compensates for the unfavorable α-to-π transition in S6, reverses the transition. Concurrently, the lower parts of S6 helices rotate by ~100°, leading to the separation of D489 and T581 and the loss of the open-state-stabilizing hydrogen bond between them (McGoldrick et al., 2018). The rotated lower parts of S6 expose the side chains of L574 and M578 toward the pore center, and they hydrophobically seal the pore to prevent ion conductance, thus converting the channel into the closed, non-conducting state (Neuberger et al., 2021a).

Portal Sites

There are two types of sites that bind to deep or shallow parts of the portals that connect the membrane environment surrounding the channel to the central cavity of the channel pore (**Figures 5A,B**; **Table 1**). The deep portal site (10) is contributed by S6 of one subunit and S5, P-loop and S6 of the neighboring subunit, and in TRPV2 is occupied by the agonist cannabidiol (CBD), a natural product of the *Cannabis sativa* plant (Pumroy et al., 2019). The CBD site in TRPV2 is lined with mostly hydrophobic and aromatic residues, including L631, L632, Y634, V635, and L638 from S6 of one protomer and L537, F540, L541, and Y544 from S5, L637 and M640 from S6, and F601 from the P-loop of another protomer (**Figure 5C**, **Supplementary Figure S5A**). While CBD-bound TRPV2 structures showed structural differences compared to apo structures, they nevertheless had a non-conducting pore and the corresponding channel conformations were interpreted as pre-open or desensitized states (Pumroy et al., 2019). Accordingly, understanding of the mechanism of TRPV2 activation by CBD awaits additional structural studies.

The shallow portal site (11) is contributed by S6 of one subunit and S4-S5 linker and S5 of the neighboring subunit, and in TRPV5 it is occupied by synthetic inhibitors ZINC9155420 and ZINC17988990 identified through structure-based virtual screening (Hughes et al., 2019). Similar to the deep portal site, the shallow portal site in TRPV5 is lined with mostly hydrophobic and aromatic residues, which for ZINC17988990 include I565 from S6 of one protomer, F487, L490, and M491 from S4-S5 linker, and C494 and W495 from S5 of another protomer (**Figure 5D**, **Supplementary Figure S5B**). Mutation of M491 to alanine produced only a small decrease in the inhibitory potency of ZINC17988990, suggesting that the shallow portal site is unlikely to play a major role in ZINC17988990-mediated inhibition of TRPV5, which instead is accomplished through binding to another site at the base of the S1-S4 bundle (Hughes et al., 2019) (see the following).

S1-S4 Sites

The top and base of the S1-S4 domain represent two locations at the membrane–solute interface convenient for binding different chemical nature compounds to regulate the function of TRPV channels (**Figures 6A,B**; **Table 1**). The top S1-S4 site (12) has been shown to be important for the activation of mouse TRPV3 by 2-APB (Singh et al., 2018a). 2-APB binds at this site by substituting the S1-S2 loop, which resides in the S1-S4 top pocket in the apo state. 2-APB binding involves residues V458 and R462 from S1, R464 from the S1-S2 loop, R487 from S2, and Y540 from S3 (**Figure 6C**, **Supplementary Figure S6A**). Mutations of R487 and Y540 as well as of the close-proximity residue Q483 to alanine produced strong reduction in potency of 2-APB activation, supporting an important role of this site in mouse TRPV3 activation (Singh et al., 2018a). According to the proposed mechanism of TRPV3 activation, 2-APB outcompetes the S1-S2 loop and wedges into and expands the top of the S1-S4 bundle. As the top of the S1-S4 bundle expands, the cleft between S4 and the neighboring S6 narrows, squeezing out a lipid from the vanilloid site, and the S1-S4 and pore domain interface rearranges in a manner that supports channel opening (Singh et al., 2018a). Interestingly, 2-APB binding to the top S1-S4 site was not observed in human TRPV3, where it was only identified bound to one of the other two 2-APB binding sites identified in mouse TRPV3, the ARD-TMD site (see below).

The second binding site of agonist 2-APB in mouse TRPV3 is at the base of the S1-S4 bundle (13), which is contributed by

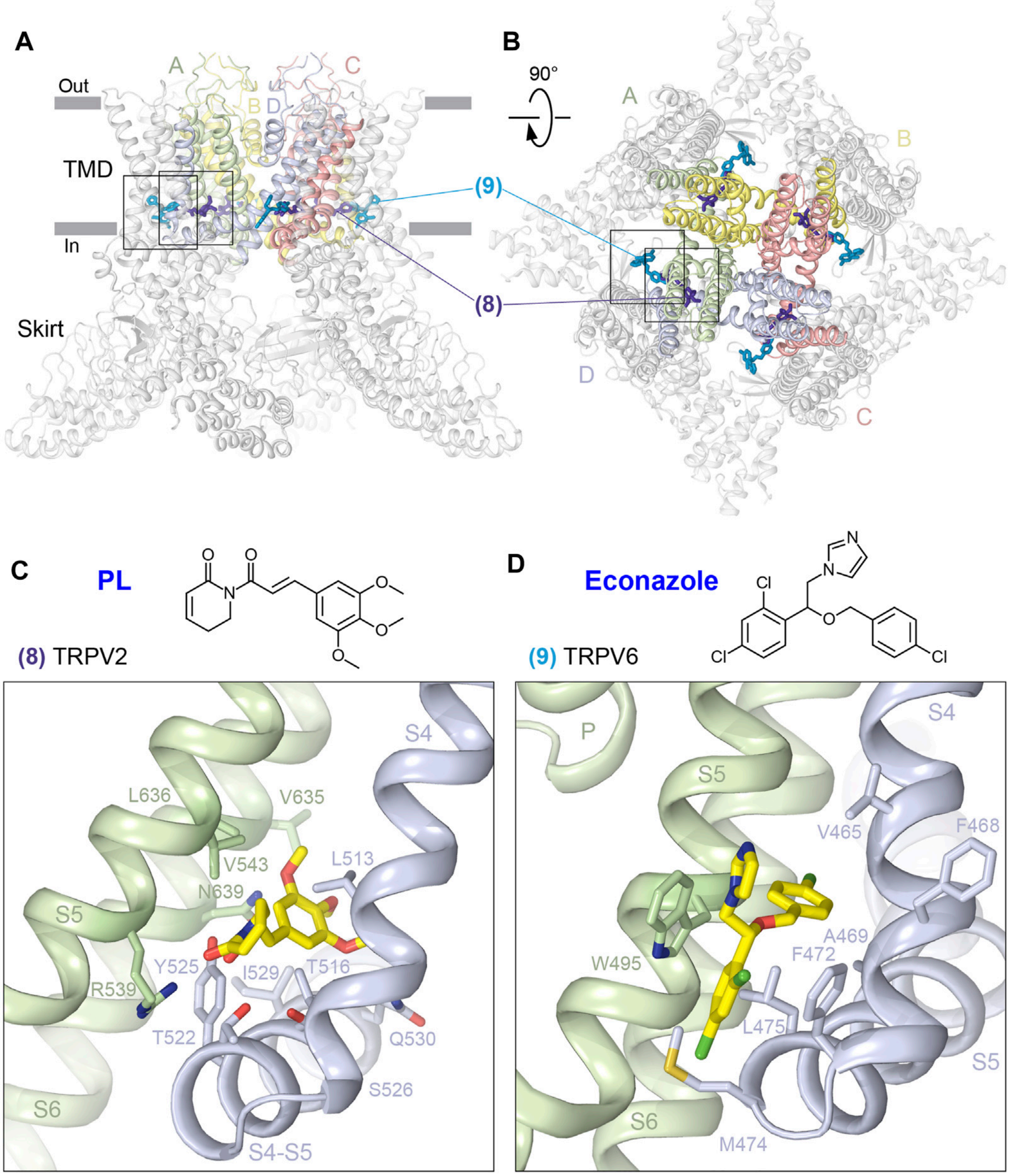

FIGURE 4 | S4-S5 sites. **(A–B)** Side **(A)** and top **(B)** views of the TRPV1 tetramer (gray; PDB ID: 7LQY) with the S4-S5 deep (8) and shallow (9) sites illustrated by ligands in dark and light blue, respectively. Rectangles indicate the regions expanded in close-up views. **(C-D)** Close-up views of the deep S4-S5 site in TRPV2 with bound piperlongumine **(C)** (PDB ID: 6WKN) and shallow S4-S5 site in TRPV6 with bound econazole **(D)** (PDB ID: 7S8C). Residues contributing to ligand binding are shown in sticks. The chemical structures of the ligands are shown above the close-up views.

residues in S1, S2, S3, and S4 (**Table 1**). Binding of 2-APB to this site in mouse TRPV3 does not introduce strong conformational changes but is likely necessary for the relative stability of the pore, S1-S4 and skirt domains during channel opening. Supporting the important role of this site in activation of mouse TRPV3, the Y564A mutation produces a strong increase in 2-APB potency (Singh et al., 2018a). In TRPV6, 2-APB and its brominated analog, 2-APB-Br, bind to the base S1-S4 site to produce inhibition of this ion channel. Along with contribution of residues from S2 (E402), S3 (G422, F424, H425, and I428), and S4 (N463, Y466, and R469), like in TRPV3, the inhibitor binding also involves the residue M602 from the TRP helix (**Figure 6D**, **Supplementary Figure S6B**). Similar to the activation of TRPV3, the mechanism of TRPV6 inhibition by 2-APB assumes an active role of lipids. Presumably, 2-APB binding displaces a lipid that resides at this site, thus promoting the formation of a hydrophobic cluster contributed by residues from S3, S4, and the S4-S5 linker. The formation of the cluster displaces the activating lipid from the vanilloid site and eliminates hydrogen bonds, which stabilize the open state by energetically compensating the unfavorable α-to-π transition in S6. As S6 turns α-helical, the

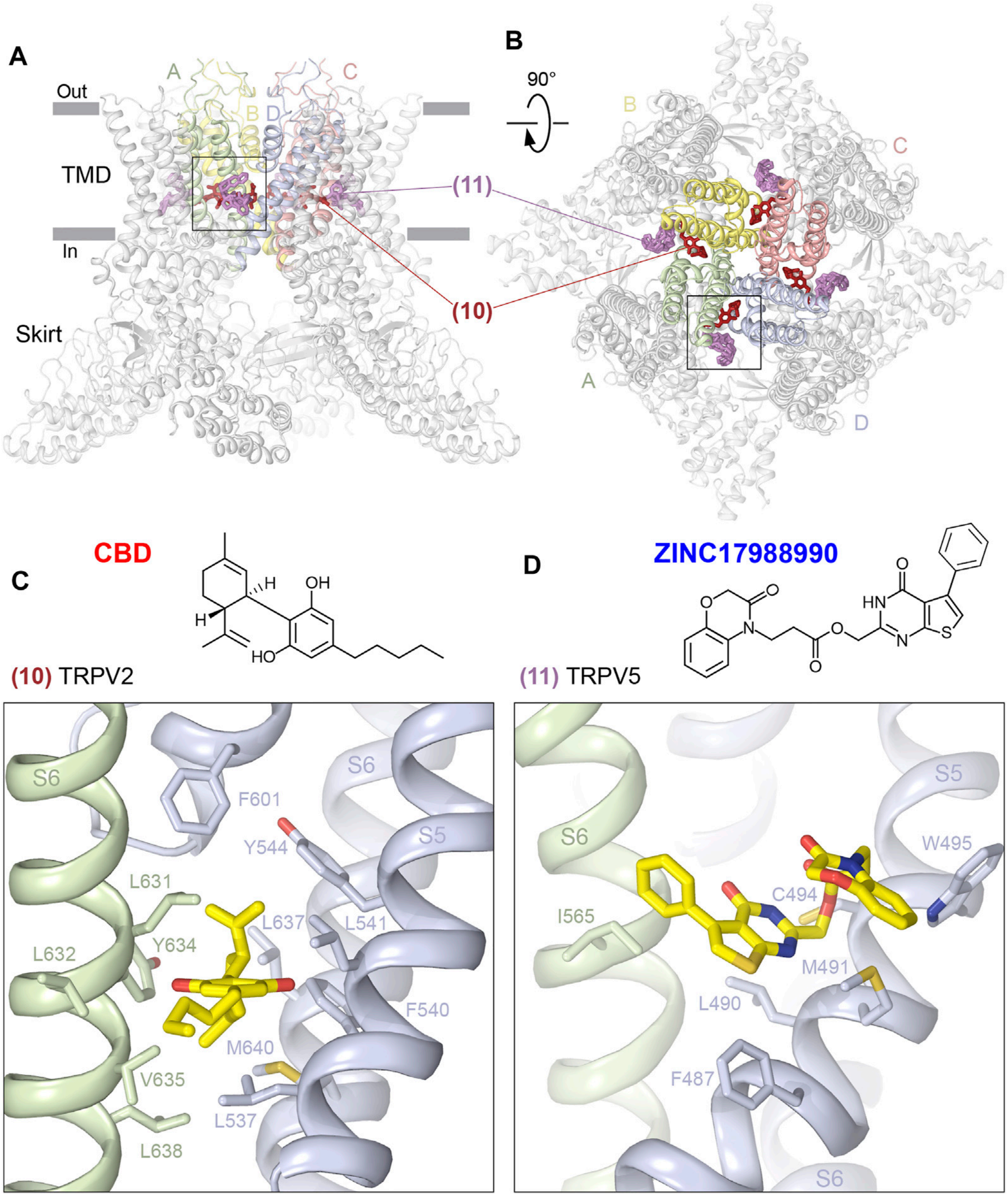

FIGURE 5 | Portal sites. **(A–B)**, Side **(A)** and top **(B)** views of the TRPV1 tetramer (gray; PDB ID: 7LQY) with the deep (10) and shallow (11) portal sites illustrated by ligands in brown and pink, respectively. Rectangles indicate the region expanded in close-up views. **(C–D)**, Close-up views of the deep portal site in TRPV2 with bound cannabidiol (**C**, PDB ID: 6U8A) and the shallow portal site in TRPV5 with bound ZINC17988990 (**D**, PDB ID: 6PBE). Residues contributing to ligand binding are shown in sticks. The chemical structures of the ligands are shown above the close-up views.

channel closes and its pore becomes impermeable to ions (Singh et al., 2018c).

Interestingly, the base S1-S4 site in TRPV3 harbors not only the agonist 2-APB but also the inhibitor osthole, which thus can be considered as a competitive antagonist (**Figure 6E, Supplementary Figure S6C**). The coumarin osthole is an active ingredient of *Cnidium monnieri* as well as other medicinal plants, which shows antipruritic and anticancer activity and is used in traditional Chinese medicine for the treatment of skin-related diseases (You et al., 2009; Zhang et al., 2015; Yang et al., 2016; Shokoohinia et al., 2018; Sun et al., 2018). Osthole binding at the base of S1-S4 involves S444 from S1, C496, I497, K500, and E501 from S2, Y565 from S4, and M706 from the TRP helix, and produces separations of S1 and S2 as well as pre-S1 and the TRP helix (Neuberger et al., 2021b). These separations lead to movement of S3 and S4 away from the pore center, followed by movement of S5 and S6, which in turn has two consequences. First, it results in a dramatic widening of the upper pore, including the selectivity filter. Second, S5 and S6 dislocation leads to movement of the TRP helix and a kink in the

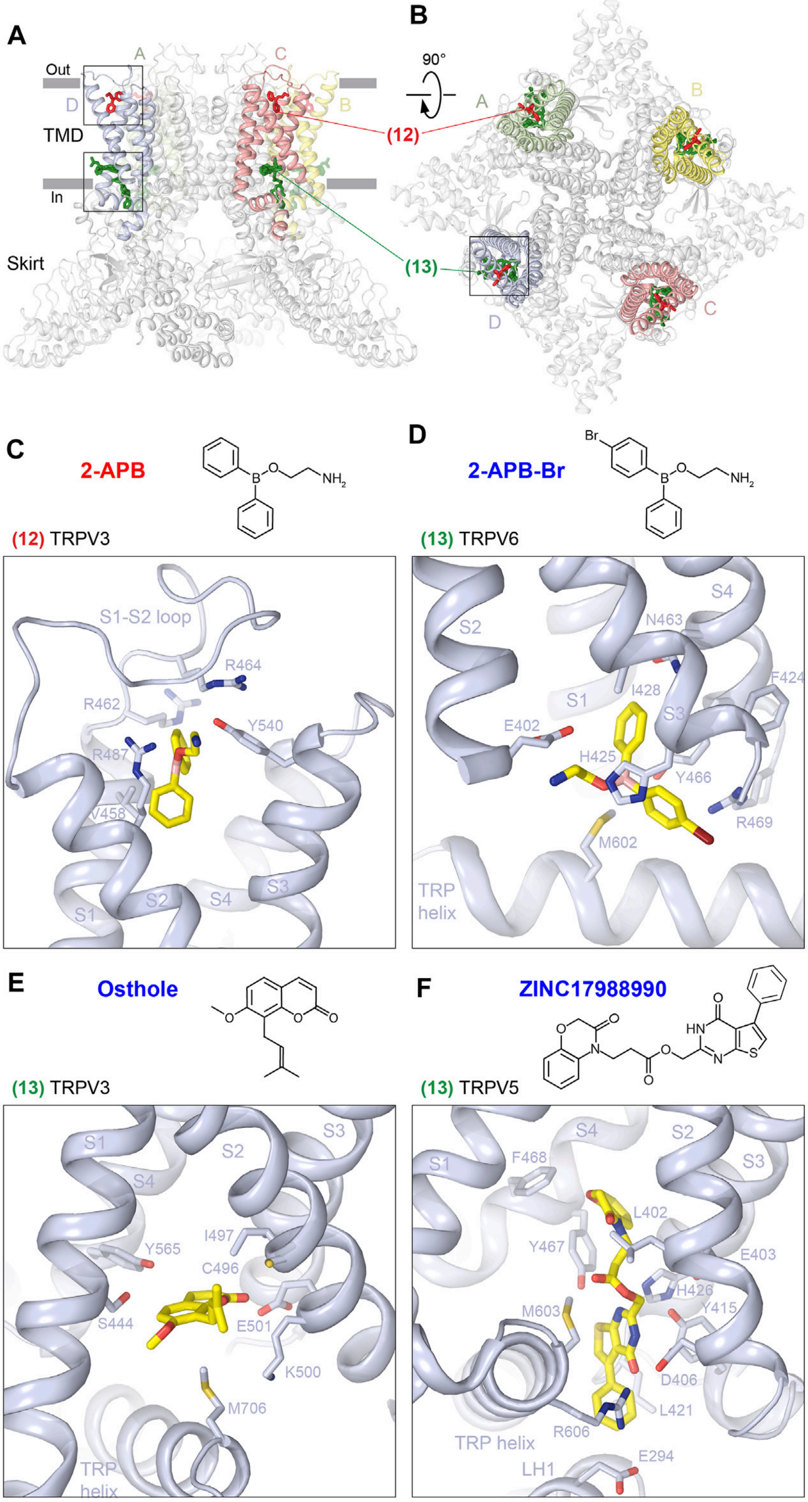

FIGURE 6 | S1-S4 sites. **(A–B)**, Side **(A)** and top **(B)** views of the TRPV1 tetramer (gray; PDB ID: 7LQY) with the S1-S4 top (12) and base (13) sites illustrated by ligands in red and green, respectively. Rectangles indicate the regions expanded in close-up views. **(C–F)** Close-up views of the S1-S4 top site in TRPV3 with bound 2-APB (**C**, PDB ID: 6DVZ) and S1-S4 base site in TRPV6 with bound 2-APB-Br (**D**, PDB ID: 6D7V), in TRPV3 with bound osthole (**E**, PDB ID: 7RAS), and in TRPV5 with bound ZINC17988990 (**F**, PDB ID: 6PBE). Residues contributing to ligand binding are shown in sticks. The chemical structures of the corresponding ligands are shown above the close-up views.

S4-S5 linker, which allows to disconnect the upper pore from the gate region. A concomitant increase in separation of S5 and S6 is accompanied by a π-to-α transition in S6 and rotation of its lower portion by ~100°, with M677 side chains now facing the pore center, hydrophobically sealing it for ion conduction and finalizing the open to closed state conversion. During all these changes, the structural environment of the base S1-S4 site when it binds to 2-APB and osthole appears to be similar (Singh et al., 2018a; Neuberger et al., 2021b), suggesting that this site is modulatory and unlikely to cause drastic structural rearrangements. In contrast, the top S1-S4 site appears to be structurally different in 2-APB- and osthole-bound structures and likely plays the most critical role in the osthole-induced TRPV3 inhibition, even though osthole density at this site was not resolved. More work is required to better understand the mechanism of TRPV3 inhibition by osthole.

In TRPV5, the base S1-S4 site was proposed to bind a synthetic inhibitor, ZINC17988990 (Hughes et al., 2019). Because of the larger size of ZINC17988990, its binding pocket is larger than the one for 2-APB, 2-APB-Br, and osthole (**Figures 6D, E**), extends intracellularly, and along with the residues from S2 (L402, E403, and D406), S2-S3 loop (Y415 and L421), S3 (I429), S4 (Y467 and F468), and TRP helix (M603 and R606) involves E294 from LH1 (**Figure 6F**, **Supplementary Figure S6D**). In contrast to the shallow portal site, which appears to play a minor role in TRPV5 inhibition by ZINC17988990, the base S1-S4 site was proposed to serve as the primary binding pocket through which ZINC17988990 exerts its inhibitory effect (Hughes et al., 2019). Indeed, mutations D406A and Y415F resulted in reduced potency of ZINC17988990 inhibition (Hughes et al., 2019). According to the proposed mechanism of TRPV5 inhibition by ZINC17988990, positioning of the inhibitor at the base S1-S4 site limits the activation-associated conformational changes in the channel induced by PI(4,5)P_2, including movement of the S1-S4 domain away from the pore axis, with the largest translation observed for the lower halves of the S1 and S2 helices, a counterclockwise rotation of the bundle, and a pivot of the TRP helix (Hughes et al., 2018a). Consequently, the antagonist plays the role of a molecule that locks the channel in the inhibited state, which is inconsistent with the putative activation-associated conformational changes (Hughes et al., 2019).

Ankyrin Repeat Domain–Transmembrane Domain Interface Sites

The ARD–TMD interface sites (14 and 15) are located more intracellularly than all the sites described previously (**Figure 1**), but they remain in close proximity to the intracellular membrane border and are contributed by the closest to the TMD regions of the ARD, the LH2, and pre-S1 elements of the ARD-TMD linker domain, the S2-S3 linker, and the TRP helix (**Figures 7A, B**; **Table 1**). In TRPV3, the ARD–TMD interface site (14) is located at the nexus of the linker domain, contributing LH2 and pre-S1, and TRP helix, and binds to the agonist 2-APB (**Figure 7C**, **Supplementary Figure S7A**) and antagonist osthole (**Figure 7D**, **Supplementary Figure S7B**). This site was first identified through mutagenesis (Hu et al., 2009), and in mouse TRPV3 appears to play a modulatory role (Singh et al., 2018a; Neuberger et al., 2021b). In contrast, the ARD-TMD linker site is the only site in human TRPV3 that binds 2-APB and was correspondingly proposed to drive activation-associated conformational changes (Zubcevic et al., 2019b). According to the putative mechanism of human TRPV3 activation by 2-APB, binding of the agonist between pre-S1 and TRP helix increases coupling between the linker domain and the TRP helix. The increased coupling is associated with a swivel of the TRP helix relative to S6, which causes S6 movement and conversion of the closed state to the open state (Zubcevic et al., 2019b).

The second representative of the ARD-TMD interface sites is the S2-S3 site (15) that in TRPV5 was proposed to bind PI(4,5)P_2 (Hughes et al., 2018a) (**Figure 7E**, **Supplementary Figure S7C**). Apart from the S2-S3 linker itself (F416, G417, and Q418), this PI(4,5)P_2 binding site is contributed by the ARD (R302) and S6 (R584). Binding of PI(4,5)P_2 to the S2-S3 site was supported by MD simulations and mutagenesis (Hughes et al., 2018a). Comparing the PI(4,5)P_2-bound and apo state structures, it was proposed that PI(4,5)P_2 uses its phosphate group to form a salt bridge with R584 and pulls S6 away from the center of the pore. According to the proposed mechanism, the resulting extension and rotation of S6 pulls W583 out of the pore and stabilizes its position through interaction with Q587, thus opening the lower gate (Hughes et al., 2018a).

Ankyrin Repeat Domain Site

Among all the sites discovered in TRPV channels, the only one that is distal from the TMD is the ARD site (16). Correspondingly, this site is contributed by the ARD residues only (**Figures 8A, B**; **Table 1**). Using crystal structures of the isolated ARD, the ARD site was shown to bind ATP at similar locations in TRPV1 (Lishko et al., 2007) (**Figure 8C**, **Supplementary Figure S8A**) and TRPV4 (Inada et al., 2012). When mapped on the full-length channels, this site is somewhat close to the three-stranded β-sheet but makes no direct contact with its residues and is fairly distal from the channel gate. It was hypothesized that ATP competes for binding to the ARD site with CaM, which causes desensitization of TRPV1 (Lishko et al., 2007). Unfortunately, no structures of CaM- or ATP-bound full-length TRPV1 or 4 are available, making it difficult to speculate about the possible structural mechanism of channel regulation by ATP.

The ARD site in TRPV6 is similar to the ATP-binding sites in TRPV1 and 4 and has been proposed to bind desthiobiotin (DTB) (Saotome et al., 2016; Singh et al., 2017) (**Figure 8D**, **Supplementary Figure S8B**). DTB was included as an eluent in the rat TRPV6 affinity purification procedure and has not been shown to play physiologically relevant roles. It is possible that the same site can be occupied by endogenous molecules such as ATP or synthetic molecules of a similar size to DTB. TRPV function may be affected by such binding through altering the intersubunit contacts mediated by the ARD and the three-stranded β-sheet. Future studies are required to explore the potential of the ARD site for TRPV regulation for scientific and medicinal purposes.

Outlook

We described 16 unique ligand-binding sites that have been structurally identified in TRPV channels using X-ray crystallography and cryo-EM. Many of these sites have been

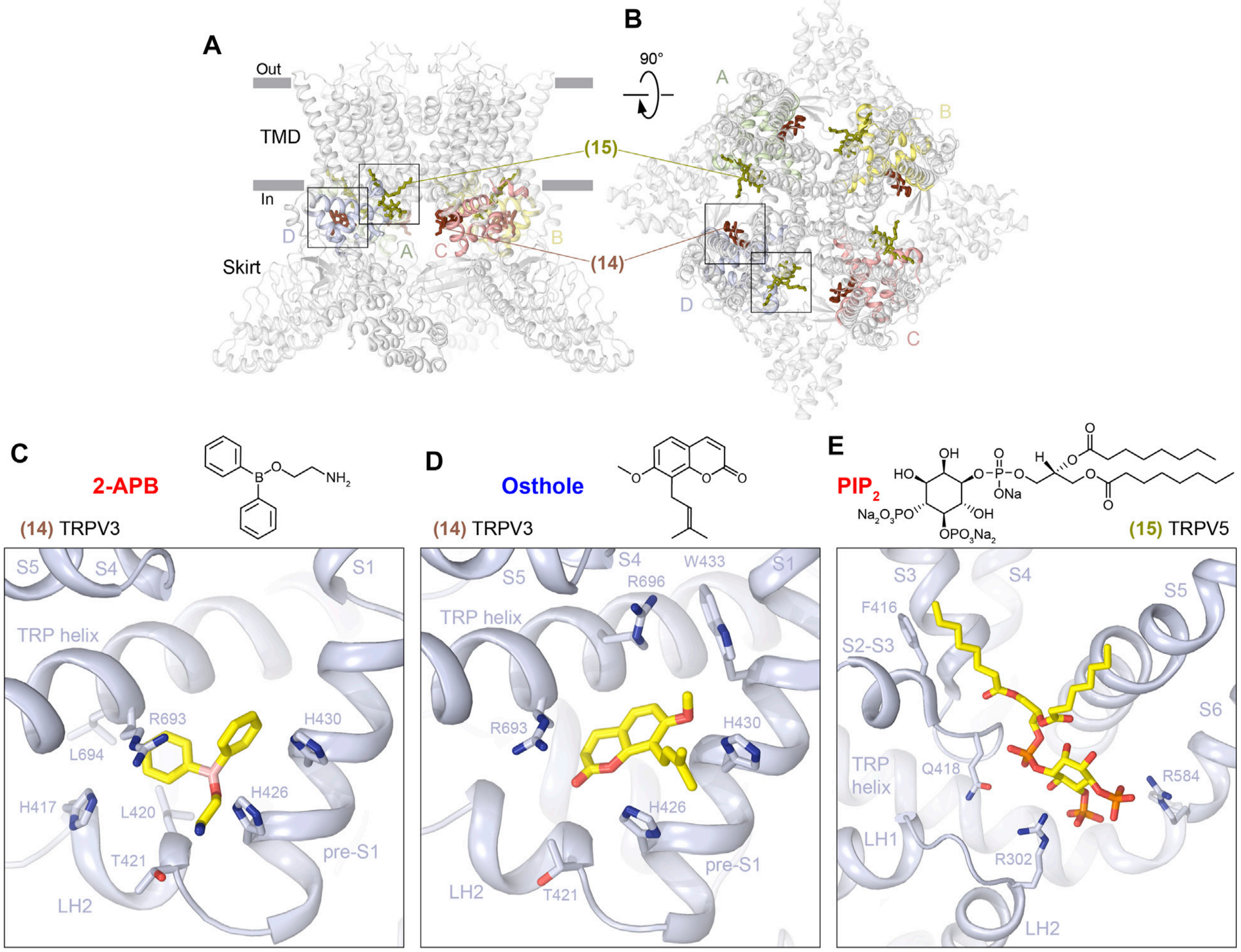

FIGURE 7 | ARD–TMD interface sites. **(A–B)** Side **(A)** and top **(B)** views of the TRPV1 tetramer (gray; PDB ID: 7LQY) with the ARD-TMD linker (14) and S2-S3 (15) sites illustrated by ligands in brown and olive, respectively. Rectangles indicate the regions expanded in close-up views. **(C–E)** Close-up views of the ARD-TMD linker site in TRPV3 with bound 2-APB (**C**, PDB ID: 6DVZ) or osthole (**D**, PDB ID: 7RAS) and the S2-S3 site in TRPV5 with bound PIP$_2$ (**E**, PDB ID: 6DMU). Residues contributing to ligand binding are shown in sticks. The chemical structures of the corresponding ligands are shown above the close-up views.

discovered very recently, and we look forward to seeing more examples of ligands that bind to these sites and perhaps the discovery of new sites in the near future. With the progress in genome sequencing, it became obvious that some of these sites can change due to altered amino-acid composition as a result of single nucleotide polymorphisms (SNPs) and disease mutations. Many of these changes result in altered trafficking, expression, and gain or loss of channel function and include mutations in TRPV3 causing Olmsted syndrome, mutations in TRPV4 leading to skeletal diseases, such as dysplasias, and neuropathies, such as Charcot–Marie–Tooth disease type 2C, and mutations in TRPV6 associated with pancreatitis and skeletal abnormalities as well as SNPs in TRPV5 and TRPV6 causing altered calcium transport (Na et al., 2009; Cantero-Recasens et al., 2010; Loh et al., 2013; Nilius and Voets, 2013; Na and Peng, 2014; Loukin et al., 2015; Sadofsky et al., 2017; Wang and Wang, 2017; Nett et al., 2021; Zhong et al., 2021). These changes in the ligand-binding sites have to be taken into account when designing new ligands to target specific disease conditions or SNPs.

It has also become clear that due to similarity in structural architecture, especially in the TMD, many of the 16 unique sites identified in TRPV channels are also present in other subfamilies of TRP channels and bind ligands, which are often different and specific to those subfamilies or their select members. For the vanilloid site, examples include TRPA1 agonist GNE551 (Liu et al., 2021) and TRPM5 antagonist NDNA. A homologous to the DkTx site in TRPC6 binds the agonist AM-0883 (Bai et al., 2020). The deep S4-S5 site in TRPC6 harbors the inhibitor BTDM (Guo et al., 2022). The deep portal site binds the agonist ML-SA1 (Schmiege et al., 2017; Zhou et al., 2017) and inhibitor ML-SI3 (Schmiege et al., 2021) in TRPML1, inhibitors HC-070 (Song et al., 2021) and Pico145 (Wright et al., 2020) in TRPC5, and A-967079 (Paulsen et al., 2015) in TRPA1. Many ligands have been found to bind to the S1-S4 base site, including Ca^{2+} that plays a role of an activator in TRPC3, TRPM2, and TRPM4 and an

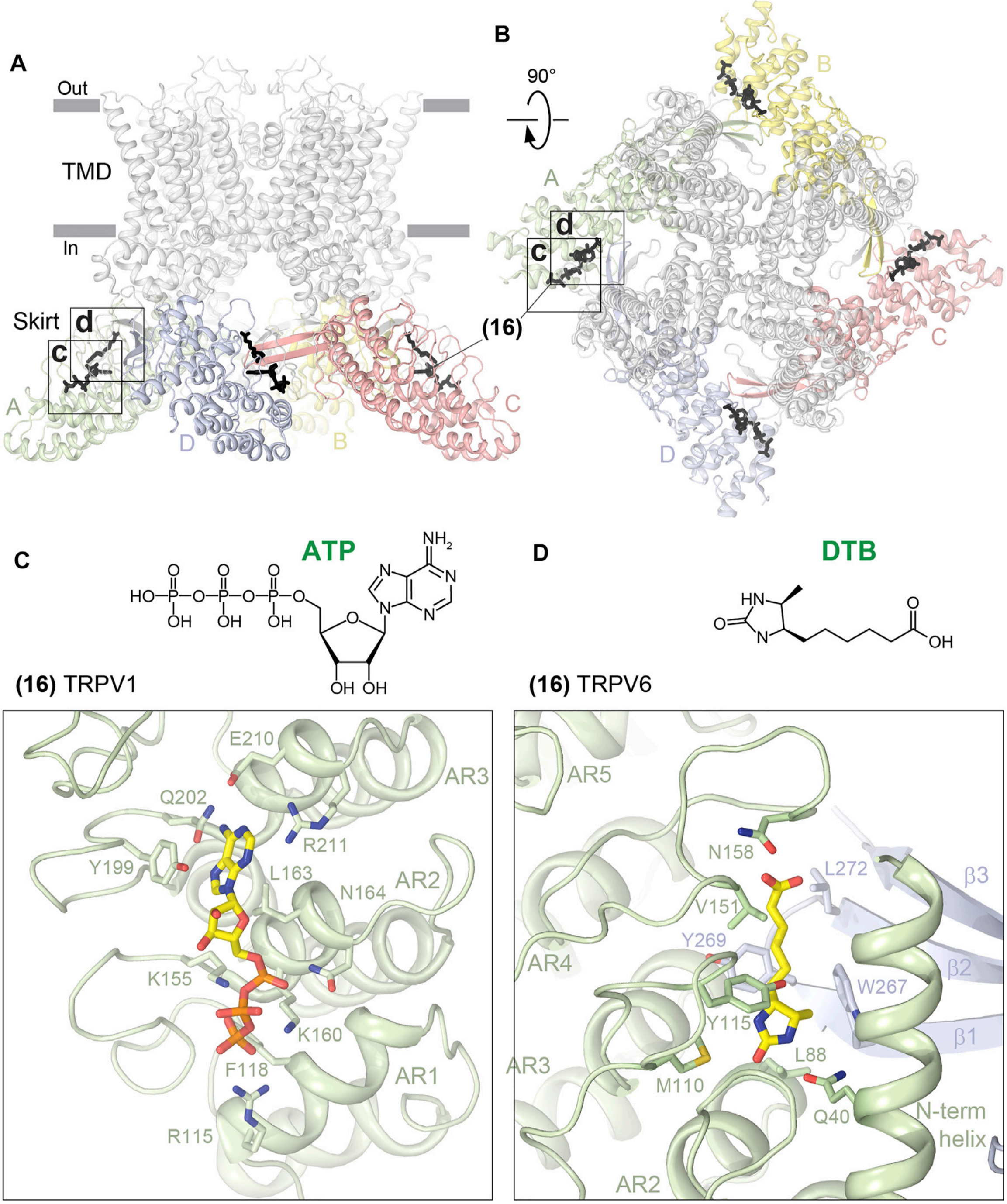

FIGURE 8 | ARD site. Side **(A)** and top **(B)** views of the TRPV1 tetramer (gray; PDB ID: 7LQY) with the ARD site (16) illustrated by ligands in black. Rectangles indicate the regions expanded in close-up views. **(C–D)** Close-up views of the ARD site in TRPV1 with bound ATP (**C**, PDB ID: 2PNN) and in TRPV6 with bound desthiobiotin (**D**, PDB ID: 5WO9). Residues contributing to ligand binding are shown in sticks. The chemical structures of the ligands are shown above the close-up views.

inhibitor in TRPM5 (Autzen et al., 2018; Huang et al., 2018; Wang et al., 2018; Zhang et al., 2018; Ruan et al., 2021; Guo et al., 2022), Na^+ in TRPC4 (Duan et al., 2018), a cation in TRPC5 (Duan et al., 2019), the inhibitors clemizole in TRPC5 (Song et al., 2021), and SAR7334 (Guo et al., 2022) and AM-1473 (Bai et al., 2020) in TRPC6 as well as the agonists WS-12 and icilin (Yin et al., 2019) and inhibitors TC-I 2014 and AMTB (Diver et al., 2019) in TRPM8. Therefore, the described 16 sites can be used as templates for the structure-based drug design not only in TRPV channels but also in all representatives of the TRP channel family.

Rapid development of structural pharmacology, combined with recent advances in computation, structure prediction, artificial intelligence, and machine-learning methods, will foster the discovery of new pharmacological agents to combat human diseases.

AUTHOR CONTRIBUTIONS

Both authors listed have made a substantial, direct, and intellectual contribution to the work and approved it for publication.

FUNDING

AS was supported by the NIH (R01 AR078814, R01 CA206573, R01 NS083660, and R01 NS107253) and NSF (1818086).

ACKNOWLEDGMENTS

The authors thank K. Nadezhdin and A. Neuberger for useful discussions and comments on the article.

SUPPLEMENTARY MATERIAL

The Supplementary Material for this article can be found online at: https://www.frontiersin.org/articles/10.3389/fphar.2022.900623/full#supplementary-material

Supplementary Figure S1 | LigPlot$^+$ analysis for the vanilloid site (part 1). LigPlot$^+$ diagrams for capsaicin bound to TRPV1 **(A)** (PDB ID: 7LPA), RTX bound to TRPV2 **(B)** (PDB ID: 6BWJ), PI bound to TRPV1 **(C)** (PDB ID: 7LQY), and PC bound to TRPV3 **(D)** (PDB ID: 7MIJ). Residues that belong to a specific structural domain are grouped in highlighted islands (green) and labeled. The analysis was performed using LigPlot$^+$ software (https://www.ebi.ac.uk/thornton-srv/software/LigPlus/).

Supplementary Figure S2 | LigPlot$^+$ analysis for the vanilloid site (part 2). LigPlot$^+$ diagrams for CHS bound to TRPV6 **(A)** (PDB ID: 7S8B), capsazepin bound to TRPV1 **(B)** (PDB ID: 5IS0), cis22a bound to TRPV6 **(C)** (PDB ID: 7K4B), and econazole bound to TRPV5 **(D)** (PDB ID: 6B5V). Residues that belong to a specific structural domain are grouped in highlighted islands (green) and labeled. The analysis was performed using LigPlot$^+$ software (https://www.ebi.ac.uk/thornton-srv/software/LigPlus/).

Supplementary Figure S3 | LigPlot$^+$ analysis for the pore site. LigPlot$^+$ diagrams for RR bound to the selectivity filter site **(A)** (PDB ID: 7S8B) and cis22a bound to the intracellular pore entry site **(B)** (PDB ID: 7K4B) in TRPV6. Residues that belong to a specific structural domain are grouped in highlighted islands (green) and labeled. The analysis was performed using LigPlot$^+$ software (https://www.ebi.ac.uk/thornton-srv/software/LigPlus/).

Supplementary Figure S4 | LigPlot$^+$ analysis for the S4-S5 sites. LigPlot$^+$ diagrams for piperlongumine bound to the deep S4-S5 site in TRPV2 **(A)** (PDB ID: 6WKN) and econazole bound to the shallow S4-S5 site in TRPV6 **(B)** (PDB ID: 7S8C). Residues that belong to a specific structural domain are grouped in highlighted islands (green) and labeled. The analysis was performed using LigPlot$^+$ software (https://www.ebi.ac.uk/thornton-srv/software/LigPlus/).

Supplementary Figure S5 | LigPlot$^+$ analysis for the portal sites. LigPlot$^+$ diagrams for cannabidiol bound to the deep portal site in TRPV2 **(A)** (PDB ID: 6U8A) and ZINC17988990 bound to the shallow portal site in TRPV5 **(B)** (PDB ID: 6PBE). Residues that belong to a specific structural domain are grouped in highlighted islands (green) and labeled. The analysis was performed using the LigPlot$^+$ software (https://www.ebi.ac.uk/thornton-srv/software/LigPlus/).

Supplementary Figure S6 | LigPlot$^+$ analysis for the S1-S4 sites. LigPlot$^+$ diagrams for 2-APB bound to the S1-S4 top site in TRPV3 **(A)** (PDB ID: 6DVZ), 2-APB-Br bound to the S1-S4 base site in TRPV6 **(B)** (PDB ID: 6D7V), osthole bound to the S1-S4 base site in TRPV3 **(C)** (PDB ID: 7RAS), and ZINC17988990 bound to the S1-S4 base site in TRPV5 **(D)** (PDB ID: 6PBE). Residues that belong to a specific structural domain are grouped in highlighted islands (green) and labeled. The analysis was performed using LigPlot$^+$ software (https://www.ebi.ac.uk/thornton-srv/software/LigPlus/).

Supplementary Figure S7 | LigPlot$^+$ analysis for the ARD–TMD interface sites. LigPlot$^+$ diagrams for 2-APB bound to the ARD-TMD linker site in TRPV3 **(A)** (PDB ID: 6DVZ), osthole bound to the ARD-TMD linker site in TRPV3 **(B)** (PDB ID: 7RAS), and PIP_2 bound to the S2-S3 site in TRPV5 **(C)** (PDB ID: 6DMU). Residues that belong to a specific structural domain are grouped in highlighted islands (green) and labeled. The analysis was performed using LigPlot$^+$ software (https://www.ebi.ac.uk/thornton-srv/software/LigPlus/).

Supplementary Figure S8 | LigPlot$^+$ analysis for the ARD site. LigPlot$^+$ diagrams for ATP bound to TRPV1 **(A)** (PDB ID: 2PNN) and desthiobiotin bound to TRPV6 **(B)** (PDB ID: 5WO9). Residues that belong to a specific structural domain are grouped in highlighted islands (green) and labeled. The analysis was performed using LigPlot$^+$ software (https://www.ebi.ac.uk/thornton-srv/software/LigPlus/).

REFERENCES

Arbabian, A., Iftinca, M., Altier, C., Singh, P. P., Isambert, H., and Coscoy, S. (2020). Mutations in Calmodulin-Binding Domains of TRPV4/6 Channels Confer Invasive Properties to colon Adenocarcinoma Cells. *Channels (Austin)* 14, 101–109. doi:10.1080/19336950.2020.1740506

Arrigoni, C., and Minor, D. L. (2018). Global versus Local Mechanisms of Temperature Sensing in Ion Channels. *Pflugers Arch.* 470, 733–744. doi:10.1007/s00424-017-2102-z

Autzen, H. E., Myasnikov, A. G., Campbell, M. G., Asarnow, D., Julius, D., and Cheng, Y. (2018). Structure of the Human TRPM4 Ion Channel in a Lipid Nanodisc. *Science* 359, 228–232. doi:10.1126/science.aar4510

Bai, Y., Yu, X., Chen, H., Horne, D., White, R., Wu, X., et al. (2020). Structural Basis for Pharmacological Modulation of the TRPC6 Channel. *Elife* 9, e53311. doi:10.7554/eLife.53311

Bevan, S., Hothi, S., Hughes, G., James, I. F., Rang, H. P., Shah, K., et al. (1992). Capsazepine: a Competitive Antagonist of the Sensory Neurone Excitant Capsaicin. *Br. J. Pharmacol.* 107, 544–552. doi:10.1111/j.1476-5381.1992.tb12781.x

Bhardwaj, R., Lindinger, S., Neuberger, A., Nadezhdin, K. D., Singh, A. K., Cunha, M. R., et al. (2020). Inactivation-mimicking Block of the Epithelial Calcium Channel TRPV6. *Sci. Adv.* 6, eabe1508. doi:10.1126/sciadv.abe1508

Bohlen, C. J., Priel, A., Zhou, S., King, D., Siemens, J., and Julius, D. (2010). A Bivalent Tarantula Toxin Activates the Capsaicin Receptor, TRPV1, by Targeting the Outer Pore Domain. *Cell* 141, 834–845. doi:10.1016/j.cell.2010.03.052

Cantero-Recasens, G., Gonzalez, J. R., Fandos, C., Duran-Tauleria, E., Smit, L. A., Kauffmann, F., et al. (2010). Loss of Function of Transient Receptor Potential Vanilloid 1 (TRPV1) Genetic Variant Is Associated with Lower Risk of Active Childhood Asthma. *J. Biol. Chem.* 285, 27532–27535. doi:10.1074/jbc.C110.159491

Cao, E., Liao, M., Cheng, Y., and Julius, D. (2013). TRPV1 Structures in Distinct Conformations Reveal Activation Mechanisms. *Nature* 504, 113–118. doi:10.1038/nature12823

Castillo, K., Diaz-Franulic, I., Canan, J., Gonzalez-Nilo, F., and Latorre, R. (2018). Thermally Activated TRP Channels: Molecular Sensors for Temperature Detection. *Phys. Biol.* 15, 021001. doi:10.1088/1478-3975/aa9a6f

Caterina, M. J., Rosen, T. A., Tominaga, M., Brake, A. J., and Julius, D. (1999). A Capsaicin-Receptor Homologue with a High Threshold for Noxious Heat. *Nature* 398, 436–441. doi:10.1038/18906

Caterina, M. J., Schumacher, M. A., Tominaga, M., Rosen, T. A., Levine, J. D., and Julius, D. (1997). The Capsaicin Receptor: a Heat-Activated Ion Channel in the Pain Pathway. *Nature* 389, 816–824. doi:10.1038/39807

Chung, M. K., Lee, H., Mizuno, A., Suzuki, M., and Caterina, M. J. (2004). 2-aminoethoxydiphenyl Borate Activates and Sensitizes the Heat-Gated Ion Channel TRPV3. *J. Neurosci.* 24, 5177–5182. doi:10.1523/JNEUROSCI.0934-04.2004

Clapham, D. E. (2003). TRP Channels as Cellular Sensors. *Nature* 426, 517–524. doi:10.1038/nature02196

Conde, J., Pumroy, R. A., Baker, C., Rodrigues, T., Guerreiro, A., Sousa, B. B., et al. (2021). Allosteric Antagonist Modulation of TRPV2 by Piperlongumine Impairs Glioblastoma Progression. *ACS Cent. Sci.* 7, 868–881. doi:10.1021/acscentsci.1c00070

Cunha, M. R., Bhardwaj, R., Lindinger, S., Butorac, C., Romanin, C., Hediger, M. A., et al. (2019). Photoswitchable Inhibitor of the Calcium Channel TRPV6. *ACS Med. Chem. Lett.* 10, 1341–1345. doi:10.1021/acsmedchemlett.9b00298

Cunha, M. R., Bhardwaj, R., Carrel, A. L., Lindinger, S., Romanin, C., Parise-Filho, R., et al. (2020). Natural Product Inspired Optimization of a Selective TRPV6 Calcium Channel Inhibitor. *RSC Med. Chem.* 11 (9), 1032–1040. doi:10.1039/d0md00145g

Dang, S., van Goor, M. K., Asarnow, D., Wang, Y., Julius, D., Cheng, Y., et al. (2019). Structural Insight into TRPV5 Channel Function and Modulation. *Proc. Natl. Acad. Sci. U S A.* 116, 8869–8878. doi:10.1073/pnas.1820323116

de Groot, T., van der Hagen, E. A., Verkaart, S., te Boekhorst, V. A., Bindels, R. J., and Hoenderop, J. G. (2011). Role of the Transient Receptor Potential Vanilloid 5 (TRPV5) Protein N Terminus in Channel Activity, Tetramerization, and Trafficking. *J. Biol. Chem.* 286, 32132–32139. doi:10.1074/jbc.M111.226878

Deering-Rice, C. E., Mitchell, V. K., Romero, E. G., Abdel Aziz, M. H., Ryskamp, D. A., Križaj, D., et al. (2014). Drofenine: A 2-APB Analogue with Greater Selectivity for Human TRPV3. *Pharmacol. Res. Perspect.* 2, e00062. doi:10.1002/prp2.62

Deng, Z., Paknejad, N., Maksaev, G., Sala-Rabanal, M., Nichols, C. G., Hite, R. K., et al. (2018). Cryo-EM and X-ray Structures of TRPV4 Reveal Insight into Ion Permeation and Gating Mechanisms. *Nat. Struct. Mol. Biol.* 25, 252–260. doi:10.1038/s41594-018-0037-5

Diver, M. M., Cheng, Y., and Julius, D. (2019). Structural Insights into TRPM8 Inhibition and Desensitization. *Science* 365, 1434–1440. doi:10.1126/science.aax6672

Doyle, D. A., Morais Cabral, J., Pfuetzner, R. A., Kuo, A., Gulbis, J. M., Cohen, S. L., et al. (1998). The Structure of the Potassium Channel: Molecular Basis of K^+ Conduction and Selectivity. *Science* 280, 69–77. doi:10.1126/science.280.5360.69

Duan, J., Li, J., Chen, G. L., Ge, Y., Liu, J., Xie, K., et al. (2019). Cryo-EM Structure of TRPC5 at 2.8-Å Resolution Reveals Unique and Conserved Structural Elements Essential for Channel Function. *Sci. Adv.* 5, eaaw7935. doi:10.1126/sciadv.aaw7935

Duan, J., Li, J., Zeng, B., Chen, G. L., Peng, X., Zhang, Y., et al. (2018). Structure of the Mouse TRPC4 Ion Channel. *Nat. Commun.* 9, 3102. doi:10.1038/s41467-018-05247-9

Gao, Y., Cao, E., Julius, D., and Cheng, Y. (2016). TRPV1 Structures in Nanodiscs Reveal Mechanisms of Ligand and Lipid Action. *Nature* 534, 347–351. doi:10.1038/nature17964

Grandl, J., Kim, S. E., Uzzell, V., Bursulaya, B., Petrus, M., Bandell, M., et al. (2010). Temperature-induced Opening of TRPV1 Ion Channel Is Stabilized by the Pore Domain. *Nat. Neurosci.* 13, 708–714. doi:10.1038/nn.2552

Güler, A. D., Lee, H., Iida, T., Shimizu, I., Tominaga, M., and Caterina, M. (2002). Heat-evoked Activation of the Ion Channel, TRPV4. *J. Neurosci.* 22, 6408–6414. doi:10.1523/JNEUROSCI.22-15-06408.2002

Guo, W., Tang, Q., Wei, M., Kang, Y., Wu, J.-X., and Chen, L. (2022). Structural Mechanism of Human TRPC3 and TRPC6 Channel Regulation by Their Intracellular Calcium-Binding Sites. *Neuron* 110, 1023–1035. doi:10.1016/j.neuron.2021.12.023

Hite, R. K., and MacKinnon, R. (2017). Structural Titration of Slo2.2, a Na^+-dependent K^+ Channel. *Cell* 168, 390–e11. e311. doi:10.1016/j.cell.2016.12.030

Hoenderop, J. G., van der Kemp, A. W., Hartog, A., van de Graaf, S. F., van Os, C. H., Willems, P. H., et al. (1999). Molecular Identification of the Apical Ca^{2+} Channel in 1,25-dihydroxyvitamin D3-Responsive Epithelia. *J. Biol. Chem.* 274, 8375–8378. doi:10.1074/jbc.274.13.8375

Hoenderop, J. G., Vennekens, R., Müller, D., Prenen, J., Droogmans, G., Bindels, R. J., et al. (2001). Function and Expression of the Epithelial Ca^{2+} Channel Family: Comparison of Mammalian ECaC1 and 2. *J. Physiol.* 537, 747–761. doi:10.1111/j.1469-7793.2001.00747.x

Hu, H., Grandl, J., Bandell, M., Petrus, M., and Patapoutian, A. (2009). Two Amino Acid Residues Determine 2-APB Sensitivity of the Ion Channels TRPV3 and TRPV4. *Proc. Natl. Acad. Sci. U S A.* 106, 1626–1631. doi:10.1073/pnas.0812209106

Hu, H. Z., Gu, Q., Wang, C., Colton, C. K., Tang, J., Kinoshita-Kawada, M., et al. (2004). 2-aminoethoxydiphenyl Borate Is a Common Activator of TRPV1, TRPV2, and TRPV3. *J. Biol. Chem.* 279, 35741–35748. doi:10.1074/jbc.M404164200

Huang, Y., Winkler, P. A., Sun, W., Lü, W., and Du, J. (2018). Architecture of the TRPM2 Channel and its Activation Mechanism by ADP-Ribose and Calcium. *Nature* 562, 145–149. doi:10.1038/s41586-018-0558-4

Hughes, T. E., Del Rosario, J. S., Kapoor, A., Yazici, A. T., Yudin, Y., Fluck, E. C., et al. (2019). Structure-based Characterization of Novel TRPV5 Inhibitors. *Elife* 8, e49572. doi:10.7554/eLife.49572

Hughes, T. E. T., Lodowski, D. T., Huynh, K. W., Yazici, A., Del Rosario, J., Kapoor, A., et al. (2018b). Structural Basis of TRPV5 Channel Inhibition by Econazole Revealed by Cryo-EM. *Nat. Struct. Mol. Biol.* 25, 53–60. doi:10.1038/s41594-017-0009-1

Hughes, T. E. T., Pumroy, R. A., Yazici, A. T., Kasimova, M. A., Fluck, E. C., Huynh, K. W., et al. (2018a). Structural Insights on TRPV5 Gating by Endogenous Modulators. *Nat. Commun.* 9, 4198. doi:10.1038/s41467-018-06753-6

Inada, H., Procko, E., Sotomayor, M., and Gaudet, R. (2012). Structural and Biochemical Consequences of Disease-Causing Mutations in the Ankyrin Repeat Domain of the Human TRPV4 Channel. *Biochemistry* 51, 6195–6206. doi:10.1021/bi300279b

Islas, L. D. (2014). Thermal Effects and Sensitivity of Biological Membranes. *Curr. Top. Membr.* 74, 1–17. doi:10.1016/B978-0-12-800181-3.00001-4

Khattar, V., Wang, L., and Peng, J. B. (2022). Calcium Selective Channel TRPV6: Structure, Function, and Implications in Health and Disease. *Gene* 817, 146192. doi:10.1016/j.gene.2022.146192

Kwon, D. H., Zhang, F., Suo, Y., Bouvette, J., Borgnia, M. J., and Lee, S. Y. (2021). Heat-dependent Opening of TRPV1 in the Presence of Capsaicin. *Nat. Struct. Mol. Biol.* 28, 554–563. doi:10.1038/s41594-021-00616-3

Lamas, J. A., Rueda-Ruzafa, L., and Herrera-Pérez, S. (2019). Ion Channels and Thermosensitivity: TRP, TREK, or Both? *Int. J. Mol. Sci.* 20, 2371. doi:10.3390/ijms20102371

Laursen, W. J., Schneider, E. R., Merriman, D. K., Bagriantsev, S. N., and Gracheva, E. O. (2016). Low-cost Functional Plasticity of TRPV1 Supports Heat Tolerance in Squirrels and Camels. *Proc. Natl. Acad. Sci. U S A.* 113, 11342–11347. doi:10.1073/pnas.1604269113

Lee, C. H., and MacKinnon, R. (2017). Structures of the Human HCN1 Hyperpolarization-Activated Channel. *Cell* 168, 120. doi:10.1016/j.cell.2016.12.023

Li, M., Zhou, X., Wang, S., Michailidis, I., Gong, Y., Su, D., et al. (2017). Structure of a Eukaryotic Cyclic-Nucleotide-Gated Channel. *Nature* 542, 60–65. doi:10.1038/nature20819

Liao, M., Cao, E., Julius, D., and Cheng, Y. (2013). Structure of the TRPV1 Ion Channel Determined by Electron Cryo-Microscopy. *Nature* 504, 107–112. doi:10.1038/nature12822

Lishko, P. V., Procko, E., Jin, X., Phelps, C. B., and Gaudet, R. (2007). The Ankyrin Repeats of TRPV1 Bind Multiple Ligands and Modulate Channel Sensitivity. *Neuron* 54, 905–918. doi:10.1016/j.neuron.2007.05.027

Liu, C., Reese, R., Vu, S., Rougé, L., Shields, S. D., Kakiuchi-Kiyota, S., et al. (2021). A Non-covalent Ligand Reveals Biased Agonism of the TRPA1 Ion Channel. *Neuron* 109, 273–e4. doi:10.1016/j.neuron.2020.10.014

Loh, N. Y., Bentley, L., Dimke, H., Verkaart, S., Tammaro, P., Gorvin, C. M., et al. (2013). Autosomal Dominant Hypercalciuria in a Mouse Model Due to a Mutation of the Epithelial Calcium Channel, TRPV5. *PLoS One* 8, e55412. doi:10.1371/journal.pone.0055412

Long, S. B., Campbell, E. B., and Mackinnon, R. (2005). Crystal Structure of a Mammalian Voltage-dependent Shaker Family K^+ Channel. *Science* 309, 897–903. doi:10.1126/science.1116269

Long, S. B., Tao, X., Campbell, E. B., and MacKinnon, R. (2007). Atomic Structure of a Voltage-dependent K^+ Channel in a Lipid Membrane-like Environment. *Nature* 450, 376–382. doi:10.1038/nature06265

Loukin, S. H., Teng, J., and Kung, C. (2015). A Channelopathy Mechanism Revealed by Direct Calmodulin Activation of TrpV4. *Proc. Natl. Acad. Sci. U S A.* 112, 9400–9405. doi:10.1073/pnas.1510602112

McGoldrick, L. L., Singh, A. K., Saotome, K., Yelshanskaya, M. V., Twomey, E. C., Grassucci, R. A., et al. (2018). Opening of the Human Epithelial Calcium Channel TRPV6. *Nature* 553, 233–237. doi:10.1038/nature25182

McIntyre, P., McLatchie, L. M., Chambers, A., Phillips, E., Clarke, M., Savidge, J., et al. (2001). Pharmacological Differences between the Human and Rat Vanilloid Receptor 1 (VR1). *Br. J. Pharmacol.* 132, 1084–1094. doi:10.1038/sj.bjp.0703918

Moran, M. M., McAlexander, M. A., Bíró, T., and Szallasi, A. (2011). Transient Receptor Potential Channels as Therapeutic Targets. *Nat. Rev. Drug Discov.* 10, 601–620. [pii]. doi:10.1038/nrd3456

Na, T., and Peng, J. B. (2014). TRPV5: a Ca^{2+} Channel for the fine-tuning of Ca^{2+} Reabsorption. *Handb Exp. Pharmacol.* 222, 321–357. doi:10.1007/978-3-642-54215-2_13

Na, T., Zhang, W., Jiang, Y., Liang, Y., Ma, H. P., Warnock, D. G., et al. (2009). The A563T Variation of the Renal Epithelial Calcium Channel TRPV5 Among African Americans Enhances Calcium Influx. *Am. J. Physiol. Ren. Physiol* 296, F1042–F1051. doi:10.1152/ajprenal.90771.2008

Nadezhdin, K. D., Neuberger, A., Nikolaev, Y. A., Murphy, L. A., Gracheva, E. O., Bagriantsev, S. N., et al. (2021a). Extracellular Cap Domain Is an Essential Component of the TRPV1 Gating Mechanism. *Nat. Commun.* 12, 2154. doi:10.1038/s41467-021-22507-3

Nadezhdin, K. D., Neuberger, A., Trofimov, Y. A., Krylov, N. A., Sinica, V., Kupko, N., et al. (2021b). Structural Mechanism of Heat-Induced Opening of a Temperature-Sensitive TRP Channel. *Nat. Struct. Mol. Biol.* 28, 564–572. doi:10.1038/s41594-021-00615-4

Nett, V., Erhardt, N., Wyatt, A., and Wissenbach, U. (2021). Human TRPV6-Pathies Caused by Gene Mutations. *Biochim. Biophys. Acta Gen. Subj* 1865, 129873. doi:10.1016/j.bbagen.2021.129873

Neuberger, A., Nadezhdin, K. D., and Sobolevsky, A. I. (2021a). Structural Mechanisms of TRPV6 Inhibition by Ruthenium Red and Econazole. *Nat. Commun.* 12, 6284. doi:10.1038/s41467-021-26608-x

Neuberger, A., Nadezhdin, K. D., Zakharian, E., and Sobolevsky, A. I. (2021b). Structural Mechanism of TRPV3 Channel Inhibition by the Plant-derived Coumarin Osthole. *EMBO Rep.* 22, e53233. doi:10.15252/embr.202153233

Nilius, B., Owsianik, G., Voets, T., and Peters, J. A. (2007). Transient Receptor Potential Cation Channels in Disease. *Physiol. Rev.* 87, 165–217. doi:10.1152/physrev.00021.2006

Nilius, B., Prenen, J., Vennekens, R., Hoenderop, J. G., Bindels, R. J., and Droogmans, G. (2001). Pharmacological Modulation of Monovalent Cation Currents through the Epithelial Ca^{2+} Channel ECaC1. *Br. J. Pharmacol.* 134, 453–462. doi:10.1038/sj.bjp.0704272

Nilius, B., and Voets, T. (2013). The Puzzle of TRPV4 Channelopathies. *EMBO Rep.* 14, 152–163. doi:10.1038/embor.2012.219

Paulsen, C. E., Armache, J. P., Gao, Y., Cheng, Y., and Julius, D. (2015). Structure of the TRPA1 Ion Channel Suggests Regulatory Mechanisms. *Nature* 520, 511–517. doi:10.1038/nature14367

Payandeh, J., Scheuer, T., Zheng, N., and Catterall, W. A. (2011). The crystal Structure of a Voltage-Gated Sodium Channel. *Nature* 475, 353–358. doi:10.1038/nature10238

Peier, A. M., Reeve, A. J., Andersson, D. A., Moqrich, A., Earley, T. J., Hergarden, A. C., et al. (2002). A Heat-Sensitive TRP Channel Expressed in Keratinocytes. *Science* 296, 2046–2049. doi:10.1126/science.1073140

Peng, J. B., Chen, X. Z., Berger, U. V., Vassilev, P. M., Tsukaguchi, H., Brown, E. M., et al. (1999). Molecular Cloning and Characterization of a Channel-like Transporter Mediating Intestinal Calcium Absorption. *J. Biol. Chem.* 274, 22739–22746. doi:10.1074/jbc.274.32.22739

Premkumar, L. S., Agarwal, S., and Steffen, D. (2002). Single-channel Properties of Native and Cloned Rat Vanilloid Receptors. *J. Physiol.* 545, 107–117. doi:10.1113/jphysiol.2002.016352

Pumroy, R. A., Samanta, A., Liu, Y., Hughes, T. E., Zhao, S., Yudin, Y., et al. (2019). Molecular Mechanism of TRPV2 Channel Modulation by Cannabidiol. *Elife* 8, e48792. doi:10.7554/eLife.48792

Ruan, Z., Haley, E., Orozco, I. J., Sabat, M., Myers, R., Roth, R., et al. (2021). Structures of the TRPM5 Channel Elucidate Mechanisms of Activation and Inhibition. *Nat. Struct. Mol. Biol.* 28, 604–613. doi:10.1038/s41594-021-00607-4

Sadofsky, L. R., Cantero-Recasens, G., Wright, C., Valverde, M. A., and Morice, A. H. (2017). TRPV1 Polymorphisms Influence Capsaicin Cough Sensitivity in Men. *J. Thorac. Dis.* 9, 839–840. doi:10.21037/jtd.2017.03.50

Sakipov, S., Sobolevsky, A. I., and Kurnikova, M. G. (2018). Ion Permeation Mechanism in Epithelial Calcium Channel TRVP6. *Sci. Rep.* 8, 5715. doi:10.1038/s41598-018-23972-5

Saotome, K., Singh, A. K., Yelshanskaya, M. V., and Sobolevsky, A. I. (2016). Crystal Structure of the Epithelial Calcium Channel TRPV6. *Nature* 534, 506–511. [pii]. doi:10.1038/nature17975

Savidge, J., Davis, C., Shah, K., Colley, S., Phillips, E., Ranasinghe, S., et al. (2002). Cloning and Functional Characterization of the guinea Pig Vanilloid Receptor 1. *Neuropharmacology* 43, 450–456. doi:10.1016/s0028-3908(02)00122-3

Schmiege, P., Fine, M., Blobel, G., and Li, X. (2017). Human TRPML1 Channel Structures in Open and Closed Conformations. *Nature* 550, 366–370. doi:10.1038/nature24036

Schmiege, P., Fine, M., and Li, X. (2021). Atomic Insights into ML-SI3 Mediated Human TRPML1 Inhibition. *Structure* 29, 1295–e3. doi:10.1016/j.str.2021.06.003

Shen, H., Zhou, Q., Pan, X., Li, Z., Wu, J., and Yan, N. (2017). Structure of a Eukaryotic Voltage-Gated Sodium Channel at Near-Atomic Resolution. *Science* 355, eaal4326. doi:10.1126/science.aal4326

Shimada, H., Kusakizako, T., Dung Nguyen, T. H., Nishizawa, T., Hino, T., Tominaga, M., et al. (2020). The Structure of Lipid Nanodisc-Reconstituted TRPV3 Reveals the Gating Mechanism. *Nat. Struct. Mol. Biol.* 27, 645–652. doi:10.1038/s41594-020-0439-z

Shokoohinia, Y., Jafari, F., Mohammadi, Z., Bazvandi, L., Hosseinzadeh, L., Chow, N., et al. (2018). Potential Anticancer Properties of Osthol: A Comprehensive Mechanistic Review. *Nutrients* 10, 36. doi:10.3390/nu10010036

Simonin, C., Awale, M., Brand, M., van Deursen, R., Schwartz, J., Fine, M., et al. (2015). Optimization of TRPV6 Calcium Channel Inhibitors Using a 3D Ligand-Based Virtual Screening Method. *Angew. Chem. Int. Ed. Engl.* 54, 14748–14752. doi:10.1002/anie.201507320

Singh, A. K., McGoldrick, L. L., Demirkhanyan, L., Leslie, M., Zakharian, E., and Sobolevsky, A. I. (2019). Structural Basis of Temperature Sensation by the TRP Channel TRPV3. *Nat. Struct. Mol. Biol.* 26, 994–998. doi:10.1038/s41594-019-0318-7

Singh, A. K., McGoldrick, L. L., and Sobolevsky, A. I. (2018a). Structure and Gating Mechanism of the Transient Receptor Potential Channel TRPV3. *Nat. Struct. Mol. Biol.* 25, 805–813. doi:10.1038/s41594-018-0108-7

Singh, A. K., McGoldrick, L. L., Twomey, E. C., and Sobolevsky, A. I. (2018b). Mechanism of Calmodulin Inactivation of the Calcium-Selective TRP Channel TRPV6. *Sci. Adv.* 4, eaau6088. doi:10.1126/sciadv.aau6088

Singh, A. K., Saotome, K., McGoldrick, L. L., and Sobolevsky, A. I. (2018c). Structural Bases of TRP Channel TRPV6 Allosteric Modulation by 2-APB. *Nat. Commun.* 9, 2465. doi:10.1038/s41467-018-04828-y

Singh, A. K., Saotome, K., and Sobolevsky, A. I. (2017). Swapping of Transmembrane Domains in the Epithelial Calcium Channel TRPV6. *Sci. Rep.* 7, 10669. doi:10.1038/s41598-017-10993-9

Smith, G. D., Gunthorpe, M. J., Kelsell, R. E., Hayes, P. D., Reilly, P., Facer, P., et al. (2002). TRPV3 Is a Temperature-Sensitive Vanilloid Receptor-like Protein. *Nature* 418, 186–190. doi:10.1038/nature00894

Song, K., Wei, M., Guo, W., Quan, L., Kang, Y., Wu, J. X., et al. (2021). Structural Basis for Human TRPC5 Channel Inhibition by Two Distinct Inhibitors. *Elife* 10, e63429. doi:10.7554/eLife.63429

Sun, X. Y., Sun, L. L., Qi, H., Gao, Q., Wang, G. X., Wei, N. N., et al. (2018). Antipruritic Effect of Natural Coumarin Osthole through Selective Inhibition of Thermosensitive TRPV3 Channel in the Skin. *Mol. Pharmacol.* 94, 1164–1173. doi:10.1124/mol.118.112466

Szallasi, A., Blumberg, P. M., Annicelli, L. L., Krause, J. E., and Cortright, D. N. (1999). The Cloned Rat Vanilloid Receptor VR1 Mediates Both R-type Binding and C-type Calcium Response in Dorsal Root Ganglion Neurons. *Mol. Pharmacol.* 56, 581–587. doi:10.1124/mol.56.3.581

Tao, X., Hite, R. K., and MacKinnon, R. (2017). Cryo-EM Structure of the Open High-Conductance Ca^{2+}-Activated K^+ Channel. *Nature* 541, 46–51. doi:10.1038/nature20608

Voets, T. (2014). TRP Channels and Thermosensation. *Handb Exp. Pharmacol.* 223, 729–741. doi:10.1007/978-3-319-05161-1_1

Vriens, J., Appendino, G., and Nilius, B. (2009). Pharmacology of Vanilloid Transient Receptor Potential Cation Channels. *Mol. Pharmacol.* 75, 1262–1279. doi:10.1124/mol.109.055624

Wang, G., and Wang, K. (2017). The Ca^{2+}-Permeable Cation Transient Receptor Potential TRPV3 Channel: An Emerging Pivotal Target for Itch and Skin Diseases. *Mol. Pharmacol.* 92, 193–200. doi:10.1124/mol.116.107946

Wang, L., Fu, T. M., Zhou, Y., Xia, S., Greka, A., and Wu, H. (2018). Structures and Gating Mechanism of Human TRPM2. *Science* 362, eaav4809. doi:10.1126/science.aav4809

Whicher, J. R., and MacKinnon, R. (2016). Structure of the Voltage-Gated K⁺ Channel Eag1 Reveals an Alternative Voltage Sensing Mechanism. *Science* 353, 664–669. doi:10.1126/science.aaf8070

Wright, D. J., Simmons, K. J., Johnson, R. M., Beech, D. J., Muench, S. P., and Bon, R. S. (2020). Human TRPC5 Structures Reveal Interaction of a Xanthine-Based TRPC1/4/5 Inhibitor with a Conserved Lipid Binding Site. *Commun. Biol.* 3, 704. doi:10.1038/s42003-020-01437-8

Wu, J., Yan, Z., Li, Z., Yan, C., Lu, S., Dong, M., et al. (2015). Structure of the Voltage-Gated Calcium Channel Cav1.1 Complex. *Science* 350, aad2395. doi:10.1126/science.aad2395

Xu, H., Ramsey, I. S., Kotecha, S. A., Moran, M. M., Chong, J. A., Lawson, D., et al. (2002). TRPV3 Is a Calcium-Permeable Temperature-Sensitive Cation Channel. *Nature* 418, 181–186. doi:10.1038/nature00882

Yang, F., Cui, Y., Wang, K., and Zheng, J. (2010). Thermosensitive TRP Channel Pore Turret Is Part of the Temperature Activation Pathway. *Proc. Natl. Acad. Sci. USA.* 107, 7083–7088. doi:10.1073/pnas.1000357107

Yang, N. N., Shi, H., Yu, G., Wang, C. M., Zhu, C., Yang, Y., et al. (2016). Osthole Inhibits Histamine-dependent Itch via Modulating TRPV1 Activity. *Sci. Rep.* 6, 25657. doi:10.1038/srep25657

Yang, W., Lee, H. W., Hellinga, H., and Yang, J. J. (2002). Structural Analysis, Identification, and Design of Calcium-Binding Sites in Proteins. *Proteins* 47, 344–356. doi:10.1002/prot.10093

Yelshanskaya, M. V., Nadezhdin, K. D., Kurnikova, M. G., and Sobolevsky, A. I. (2021). Structure and Function of the Calcium-Selective TRP Channel TRPV6. *J. Physiol.* 599, 2673–2697. doi:10.1113/JP279024

Yin, Y., Le, S. C., Hsu, A. L., Borgnia, M. J., Yang, H., and Lee, S. Y. (2019). Structural Basis of Cooling Agent and Lipid Sensing by the Cold-Activated TRPM8 Channel. *Science* 363, eaav9334. doi:10.1126/science.aav9334

You, L., Feng, S., An, R., and Wang, X. (2009). Osthole: a Promising lead Compound for Drug Discovery from a Traditional Chinese Medicine (TCM). *Nat. Prod. Commun.* 4, 297–302. doi:10.1177/1934578x0900400227

Yuan, P. (2019). Structural Biology of thermoTRPV Channels. *Cell Calcium* 84, 102106. doi:10.1016/j.ceca.2019.102106

Zhang, F., Hanson, S. M., Jara-Oseguera, A., Krepkiy, D., Bae, C., Pearce, L. V., et al. (2016). Engineering Vanilloid-Sensitivity into the Rat TRPV2 Channel. *Elife* 5, e16409. doi:10.7554/eLife.16409

Zhang, K., Julius, D., and Cheng, Y. (2021). Structural Snapshots of TRPV1 Reveal Mechanism of Polymodal Functionality. *Cell* 184, 5138–e12. e5112. doi:10.1016/j.cell.2021.08.012

Zhang, Z., Tóth, B., Szollosi, A., Chen, J., and Csanády, L. (2018). Structure of a TRPM2 Channel in Complex with Ca^{2+} Explains Unique Gating Regulation. *Elife* 7, e36409. doi:10.7554/eLife.36409

Zhang, Z. R., Leung, W. N., Cheung, H. Y., and Chan, C. W. (2015). Osthole: A Review on its Bioactivities, Pharmacological Properties, and Potential as Alternative Medicine. *Evid. Based Complement. Alternat Med.* 2015, 919616. doi:10.1155/2015/919616

Zhong, W., Hu, L., Cao, X., Zhao, J., Zhang, X., Lee, M., et al. (2021). Genotype–Phenotype Correlation of TRPV3-Related Olmsted Syndrome. *J. Invest. Dermatol.* 141, 545–554. doi:10.1016/j.jid.2020.06.035

Zhou, X., Li, M., Su, D., Jia, Q., Li, H., Li, X., et al. (2017). Cryo-EM Structures of the Human Endolysosomal TRPML3 Channel in Three Distinct States. *Nat. Struct. Mol. Biol.* 24, 1146–1154. doi:10.1038/nsmb.3502

Zubcevic, L., Borschel, W. F., Hsu, A. L., Borgnia, M. J., and Lee, S. Y. (2019b). Regulatory Switch at the Cytoplasmic Interface Controls TRPV Channel Gating. *Elife* 8, e47746. doi:10.7554/eLife.47746

Zubcevic, L., Hsu, A. L., Borgnia, M. J., and Lee, S. Y. (2019a). Symmetry Transitions during Gating of the TRPV2 Ion Channel in Lipid Membranes. *Elife* 8, e45779. doi:10.7554/eLife.45779

Zubcevic, L., Le, S., Yang, H., and Lee, S. Y. (2018). Conformational Plasticity in the Selectivity Filter of the TRPV2 Ion Channel. *Nat. Struct. Mol. Biol.* 25, 405–415. doi:10.1038/s41594-018-0059-z

Conflict of Interest: The authors declare that the research was conducted in the absence of any commercial or financial relationships that could be construed as a potential conflict of interest.

frontiers | Frontiers in Pharmacology

REVIEW
published: 23 May 2022
doi: 10.3389/fphar.2022.897494

Structural Insight Into Ryanodine Receptor Channelopathies

Hadiatullah Hadiatullah[1,2†], *Zhao He*[1,2†] *and Zhiguang Yuchi*[1,2*]

[1]*Tianjin Key Laboratory for Modern Drug Delivery and High-Efficiency, Collaborative Innovation Center of Chemical Science and Engineering, School of Pharmaceutical Science and Technology, Tianjin University, Tianjin, China,* [2]*Department of Molecular Pharmacology, National Clinical Research Center for Cancer, Key Laboratory of Cancer Prevention and Therapy, Tianjin's Clinical Research Center for Cancer, Tianjin Medical University Cancer Institute and Hospital, Tianjin, China*

The ryanodine receptors (RyRs) are large cation-selective ligand-gated channels that are expressed in the sarcoplasmic reticulum (SR) membrane. They mediate the controlled release of Ca^{2+} from SR and play an important role in many cellular processes. The mutations in RyRs are associated with several skeletal muscle and cardiac conditions, including malignant hyperthermia (MH), central core disease (CCD), catecholaminergic polymorphic ventricular tachycardia (CPVT), and arrhythmogenic right ventricular dysplasia (ARVD). Recent breakthroughs in structural biology including cryo-electron microscopy (EM) and X-ray crystallography allowed the determination of a number of near-atomic structures of RyRs, including wildtype and mutant structures as well as the structures in complex with different modulating molecules. This allows us to comprehend the physiological gating and regulatory mechanisms of RyRs and the underlying pathological mechanisms of the disease-causing mutations. In this review, based on the insights gained from the available high-resolution structures of RyRs, we address several questions: 1) what are the gating mechanisms of different RyR isoforms; 2) how RyRs are regulated by multiple channel modulators, including ions, small molecules, and regulatory proteins; 3) how do disease-causing mutations affect the structure and function of RyRs; 4) how can these structural information aid in the diagnosis of the related diseases and the development of pharmacological therapies.

Keywords: ryanodine receptor, cryo-EM, x-ray crystallography, channelopathies, disease mutations

Edited by:
Lei Chen,
Peking University, China

Reviewed by:
Shinichi Okuda,
Yamaguchi Prefectural Grand Medical Center, Japan
Yuequan Shen,
Nankai University, China

***Correspondence:**
Zhiguang Yuchi
yuchi@tju.edu.cn

†*These authors have contributed equally to this work*

Specialty section:
This article was submitted to Pharmacology of Ion Channels and Channelopathies,
a section of the journal Frontiers in Pharmacology

Received: *16 March 2022*
Accepted: *09 May 2022*
Published: *23 May 2022*

Citation:
Hadiatullah H, He Z and Yuchi Z (2022) Structural Insight Into Ryanodine Receptor Channelopathies. Front. Pharmacol. 13:897494.
doi: 10.3389/fphar.2022.897494

1 INTRODUCTION

The ryanodine receptor (RyR) is a giant allosteric ion channel that plays a crucial role in excitation-contraction (EC) coupling (Flucher and Franzini-Armstrong, 1996; Meissner, 2017; Ríos, 2018), neuron excitability (Albrecht et al., 2001; Bouchard et al., 2003; Arias-Cavieres et al., 2018), differentiation (Denda et al., 2012), and apoptosis (Tu et al., 2016; Bagur and Hajnóczky, 2017). RyR is mainly expressed on the membrane of endoplasmic reticulum (ER) or sarcoplasmic reticulum (SR) in muscle and mediates the release of calcium ions from ER/SR store. Mammals express three RyR isoforms (RyR1, RyR2, and RyR3), which share sequence identity of 63%–67% (Hakamata et al., 1992). RyR1 and RyR2 isoforms are predominantly found in skeletal and cardiac muscle, respectively (Takeshima et al., 1989; Otsu et al., 1990). However, the phrases "skeletal and cardiac isoforms" would be misleading since they are also expressed in a variety of cell types (Giannini et al., 1995). RyR3 was originally identified in the brain but later found to be distributed ubiquitously (Pessah et al., 1985). RyRs are also found in many lower organisms,

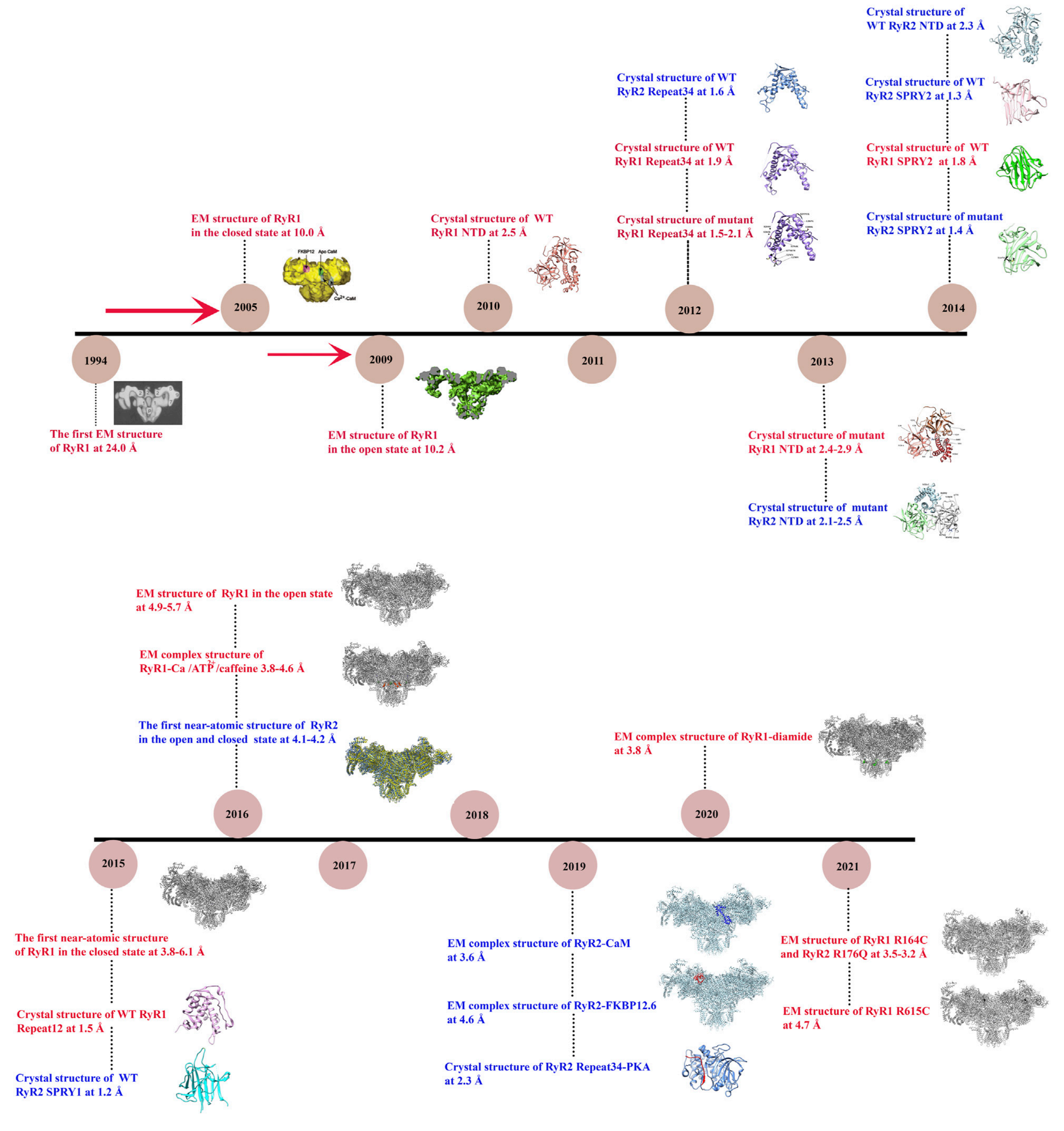

FIGURE 1 | Timeline of significant discoveries/milestones of RyR structural studies. The structures of RyR were adapted from (Radermacher et al., 1994; Samsó et al., 2005; Samsó et al., 2009; Tung et al., 2010; Yuchi et al., 2012; Kimlicka et al., 2013a; Kimlicka et al., 2013b; Lau and Van Petegem, 2014; Efremov et al., 2015; Yan et al., 2015; Yuchi et al., 2015; Zalk et al., 2015; Bai et al., 2016; Wei et al., 2016; Chi et al., 2019; Gong et al., 2019; Haji-Ghassemi et al., 2019; Iyer et al., 2020; Ma et al., 2020; Woll et al., 2021).

which are similar in size and complexity to their mammalian counterparts. Non-mammalian vertebrates have two RyR isoforms, usually named as RyRα and RyRβ (OTTINI et al., 1996), whereas insects and other invertebrates, such as nematodes, sea urchin, fruit fly, and lobster, have only one isoform (Lanner et al., 2010).

More than 700 inherited genetic mutations of RyRs have been identified and associated with several life-threating diseases (Lehnart et al., 2008; Betzenhauser and Marks, 2010; Lanner et al., 2010). For example, RyR1 mutations have been primarily linked to malignant hyperthermia (MH) (FuJII et al., 1991; Gillard et al., 1991), central core disease (CCD) (Zhang et al., 1993), multi-minicore disease (MmD), congenital fiber type disproportion (CFTD), and centronuclear myopathy (CMD) (Treves et al., 2008; Amburgey et al., 2011; Amburgey et al., 2013; Snoeck et al., 2015; Jungbluth et al., 2018), and account for more than 30% of total congenital myopathy cases (Zvaritch et al., 2009; Zhou et al., 2013). RyR2 mutations have been associated with several cardiac conditions such as catecholaminergic polymorphic ventricular tachycardia (CPVT) (Laitinen et al., 2001; Itoh et al., 2021), sudden cardiac death (Blayney and Lai, 2009; Aiba et al., 2016), heart failure (HF) (Ran et al., 2010), and other cardiac arrhythmias (Priori et al., 2001). RyR3 mutations have been linked to neurodegenerative and cardiac diseases (Supnet et al., 2010; Yang et al., 2017; Gong et al., 2018), but the evidence is less clear. In addition, the mutations in all three isoforms are also associated with cancer in several clinical studies (Kobylewski et al., 2012; Lu et al., 2017; Schmitt et al., 2019; Xu et al., 2019; Liu et al., 2021). These dysfunctions highlight the key role of RyRs in human physiology and diseases. Understanding the impacts of these mutations on RyRs at the molecular level would not only provide important insights into the disease mechanisms but also lay a foundation for the development of therapeutic avenues to tackle these debilitating diseases.

Recently, thanks to revolutionary advances in structural biology techniques, several structures at near-atomic resolutions have been solved for both mammalian RyR1 (Efremov et al., 2015; Yan et al., 2015; Zalk et al., 2015; Bai et al., 2016; Wei et al., 2016) and RyR2 (Peng et al., 2016), revealing the overall domain organization and the gating mechanisms. In addition, the structures of RyRs with disease-causing mutations (Iyer et al., 2020; Woll et al., 2021) or small molecule modulators have also been reported (des Georges et al., 2016; Chi et al., 2019; Gong et al., 2019; Ma et al., 2020), elucidating the underlying disease and regulation mechanisms. Several good review papers have been published in recent years on the structure, function, and modulations of RyRs (Gong et al., 2021; Ogawa et al., 2021; Samurkas et al., 2022; Woll and Van Petegem, 2021). In this paper, we will first review the history of the structural studies of RyRs (summarized in **Figure 1**), and then mainly focus on the latest discoveries in RyR-related channelopathies from a structural point of view. Specifically, we will discuss the distribution of disease-causing mutations in the 3D structures of RyRs and how these mutations affect the structure and function of the channel. In addition, we will discuss the current developments in the pharmacology of RyRs.

2 STRUCTURES OF RYRS REVEAL THE OVERALL CHANNEL ARCHITECTURE AND GATING MECHANISMS

2.1 Cryo-Electron Microscopy

In 1994, the first single-particle cryo-EM structure of the gigantic RyR isolated from rabbit skeletal muscle was solved by Wagenknecht group with a resolution of ~40 Å (Radermacher et al., 1994). Since then, the resolution is gradually increased to ~10 Å for the skeletal isoform with the efforts from several research groups during the next two decades (Samsó et al., 2005; Samsó et al., 2009; Ludtke and Serysheva, 2013). These medium-resolution structures revealed the overall shape of the channel as a giant tetrameric "mushroom" with four-fold symmetry, which contains ~5,000 residues per monomer (**Figure 2A**) (Samsó et al., 2009). The symmetry axis is along the Ca^{2+}-conducting pore of the channel and its transmembrane domain is like a classic voltage-gated ion channel such as Kv1.2 (Samsó et al., 2009). At this resolution, numerous distinct regions of the cytoplasmic part of RyR, including the clamp, the handle, and the central rim, could be resolved (**Figure 2B**), providing valuable information for the domain organization, although the exact corresponding sequences were still not clear.

Since the early 2010s, the "resolution revolution" in cryo-EM has dramatically improved the quality of RyR structures. The cryo-EM structures of rabbit RyR1 have been solved by several groups with resolutions of 3.2–6.1 Å, representing different functional states, including the closed-state (Efremov et al., 2015; Yan et al., 2015; Zalk et al., 2015; des Georges et al., 2016), the open-state (Bai et al., 2016; des Georges et al., 2016; Wei et al., 2016), the primed-state (des Georges et al., 2016), and several ligand-bound states, such as in complex with Ca^{2+}, ATP, caffeine, ryanodine (des Georges et al., 2016), calmodulin (CaM) (Gong et al., 2019; Ma et al., 2020), FK506-binding protein (FKBP) (Yan et al., 2015; des Georges et al., 2016; Peng et al., 2016; Chi et al., 2019; Gong et al., 2019), and diamide (Ma et al., 2020). With the improved resolution, a total of 20 individual domains from each protomer become discernible, including three N-terminal domains (NTDs) (NTD-A, NTD-B, and NTD-C), three SPRY domains (SPRY1, SPRY2, and SPRY3), three divergent regions (DR1, DR2, and DR3), two RYR repeat domains (Repeat12 and Repeat34), three solenoid (sol) domains (Bridging solenoid (Bsol), core solenoid [(Csol), and junctional solenoid (Jsol)], a shell-core linker peptide (SCLP) domain, an EF-hand domain (EF), a thumb and forefinger (TaF) domain, a pseudo voltage-sensor domain (pVSD), a channel pore domain (Pore), and a C-terminal domain (CTD) (**Figures 2A,C**). The last three domains form the transmembrane region enclosing a central Ca^{2+}-conducting pore, whereas the other domains located in the cytoplasmic region mainly sense the signals from diverse ligands. The activity of RyR is regulated by a wide range of stimuli from both cytosolic and luminal sides, including ions (Ca^{2+}, Mg^{2+}, and Zn^{2+}), proteins (CaM and FKBP12/12.6), and small molecules (ATP, caffeine, ryanodine, PCB95, and diamide insecticide) (**Figures 2D,E**) (Yan et al., 2015). The structural basis of channel gating and ligand-dependent activation has been established by comparing the open and closed structures of RyR1 (**Figures 3A–D**) (Bai et al., 2016; des Georges et al., 2016), which shows a coupled motion between the displacements of the cytoplasmic "O-ring" motif of the channel domain, the U-motif of the central domain, the central domain, and the dilation of the S6 helix bundle at the cytoplasmic side during pore opening (**Figure 3C**) (Bai et al., 2016). Des Georges et al. reported that either ATP, Ca^{2+}, or caffeine alone promotes conformational changes in the cytoplasmic assembly, allowing it to reach a "primed" state without pore dilation. In contrast, the presence of all three

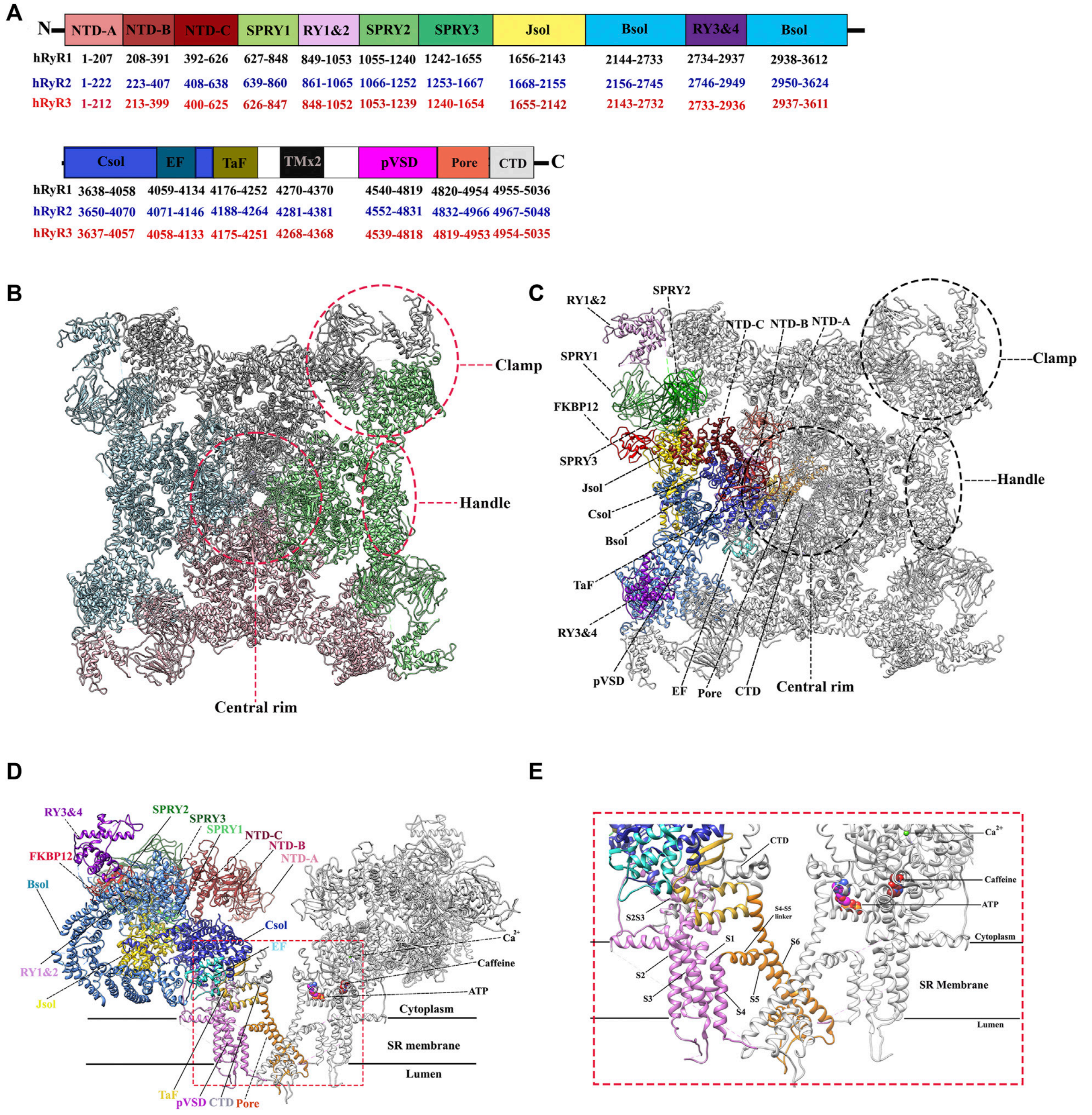

FIGURE 2 | Overall structure and domain organization of RyR. **(A)** Schematic illustration of domain organization of three human RyR isoforms. The residue numbers of the domain boundaries are labeled. **(B)** The top view of the cryo-EM structure of rabbit RyR1 (PDB: 5TAL). Four protomers are colored in green, pink, cyan, and grey, respectively. Several distinct areas of the cytoplasmic region, including the clamp, the handle, and the central rim, are also labeled. **(C,D)** The top view **(C)** and the side view. **(D)** of the cryo-EM structure of rabbit RyR1 in complex with FKBP12, Ca^{2+}, ATP, and caffeine (PDB: 5TAL). One of four protomers is colored by domain according to the schematic illustration in panel A. Two of the four protomers facing each other are shown for the side view. **(E)** A close-up view of the binding sites of Ca^{2+}, ATP, and caffeine, and the transmembrane region.

activating regulators causes the pore dilation and conformational changes in the cytosolic assembly and local changes in the transmembrane domain (**Figure 2E**) des Georges et al., 2016).

Shortly after the determination of the rabbit RyR1 structure, Yan group solved the cryo-EM structures of porcine RyR2 in both the open and closed states (apo-RyR2) with a resolution of 4.2 and 4.4 Å, respectively (**Figures 3E–H**) (Peng et al., 2016). The comparison of the open and closed states of RyR2 shows relative movements within the cytoplasmic domains, leading to breathing motion of the periphery of the cytoplasmic region and the rotation of the central domain (**Figure 3G**). The central domain was shown to be the major mediator of conformational

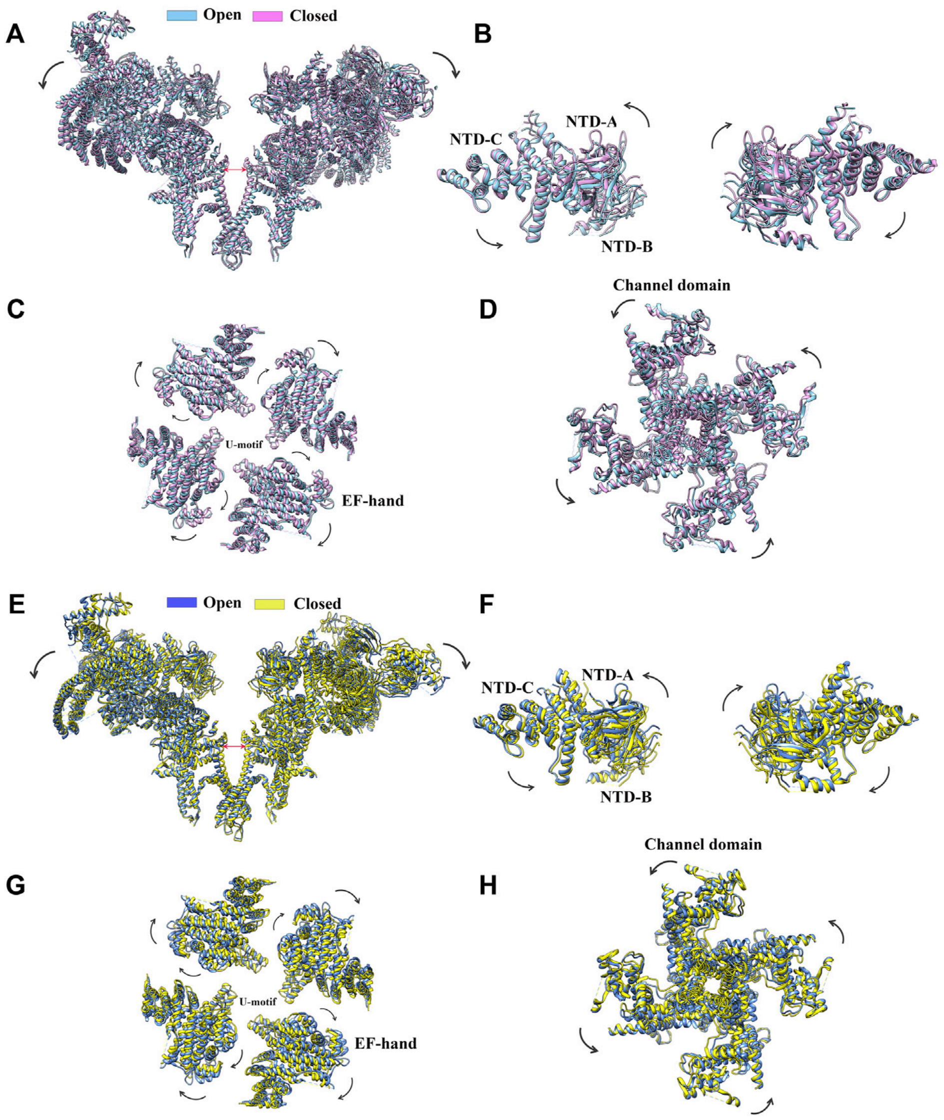

FIGURE 3 | Conformational changes of RyR upon channel gating. **(A)** Superimposition of RyR1 in the closed state (magenta, PDB: 5TB0) and the open state (sky blue, PDB: 5TAL). The structural movements of individual domains of RyR1, such as the NTD. **(B)**, the central domain. **(C),** and the channel domain. **(D)** are shown in a zoomed-in view. **(E)** Superimposition of RyR2 in the closed state (yellow, PDB: 5GO9) and the open state (light blue, PDB: 5GOA). Two of the four protomers facing each other are shown. The structural movements of individual domains of RyR2, such as the NTD. **(F)** The central domain. **(G)** and the channel domain. **(H)** are shown in a zoomed-in view.

changes, integrating the conformational changes of the cytoplasmic domains and converting them into channel gating (Peng et al., 2016). Recently, complex structures of RyR2 with allosteric regulators Ca^{2+}, PCB95, ATP, caffeine, FKBP12.6, and CaM were also determined in different configurations, gaining insight into the complex regulatory mechanisms of RyR2 (Chi et al., 2019; Gong et al., 2019). Aligning with their 70% sequence similarity, the overall structure and domain organization of RyR2 are almost identical to that of RyR1 (Yan et al., 2015), and the structural changes in the closed and open states of RyR2 are also largely similar to the ones in RyR1 (des Georges et al., 2016; Chi et al., 2019; Gong et al., 2019). However, many of the isoform-specific differences in function remain poorly defined, partially because that the non-conserved regions tend to be more flexible which are less resolved in the structures.

RyRs are known to form 2D lattice on ER membrane and their activity can be regulated by the crosstalk between neighboring RyR channels, or "coupled gating." The potential of long-range allosteric gating presents a fascinating view of the impact of nano- and microdomains on intracellular calcium dynamics (Chen-Izu et al., 2006; Hiess et al., 2018). Therefore, in addition to the high-resolution structure of single isolated RyRs, the determination of the super-complex structure that can describe the structural linkage with neighboring RyRs is crucial for the understanding of the "coupled gating" mechanism. Using direct stochastic optical reconstruction (dSTORM) imaging several groups

TABLE 1 | Structures of wild type and mutant RyRs mentioned in the paper.

Domain/isoform	Organism	WT/mutation	PDB	Experimental method	Resolution (Å)	References
RyR1-NTD	*Oryctolagus cuniculus*	WT	2XOA	X-ray Diffraction	2.05 Å	Tung et al. (2010)
RyR1-NTD	*Oryctolagus cuniculus*	L14R	4I7I	X-ray Diffraction	2.40–2.95 Å	Kimlicka et al. (2013a)
		G249R	4I1E			
		C36R	4I0Y			
		V219I	4I8M			
		I404M	4I2S			
		R45C	4I6I			
		D61N	4I3N			
		R402G	4I37			
RyR1-Repeat34	*Oryctolagus cuniculus*	WT	4ERT	X-ray Diffraction	1.95 Å	Yuchi et al. (2012)
RyR1-Repeat34	*Oryctolagus cuniculus*	R2939S	4ESU	X-ray Diffraction	1.59–2.19 Å	Yuchi et al. (2012)
		S2776M	4ETT			
		E2764K	4ETU			
RyR1-Repeat12	*Oryctolagus cuniculus*	WT	5C30	X-ray Diffraction	1.55 Å	Yuchi et al. (2015)
RyR1-SPRY2	*Oryctolagus cuniculus*	WT	4P9J	X-ray Diffraction	1.84 Å	Lau and Van Petegem, (2014)
Full-length RyR1	*Sus scrofa*	WT	6W1N	Cryo-EM	4.00 Å	Woll et al. (2021)
Full-length RyR1	*Sus scrofa*	R615C	6X34	Cryo-EM	4.70 Å	Woll et al. (2021)
Full-length RyR1	*Oryctolagus cuniculus*	R164C	6WOT	Cryo-EM	3.54 Å	Iyer et al. (2020)
Full-length RyR1	*Oryctolagus cuniculus*	Closed-state	5TB0	Cryo-EM	4.40 Å	des Georges et al. (2016)
Full-length RyR1	*Oryctolagus cuniculus*	Open-state	5TAL	Cryo-EM	4.40 Å	des Georges et al. (2016)
RyR2-NTD	*Homo sapiens*	WT	4JKQ	X-ray Diffraction	2.39 Å	Borko et al. (2014)
RyR2-NTD	*Mus musculus*	P164S	4KEI	X-ray Diffraction	2.14–2.55 Å	Kimlicka et al. (2013b)
		R169Q	4KEJ			
		R176Q	4KEK			
RyR2-NTD	*Mus musculus*	V186M; A77V	3IM6; 3IM7	X-ray Diffraction	1.70–2.21 Å	Lobo and Van Petegem, (2009)
RyR2-Repeat34	*Mus musculus*	WT	4ETV	X-ray Diffraction	1.65 Å	Yuchi et al. (2012)
RyR2-SPRY2	*Mus musculus*	WT	4P9I	X-ray Diffraction	1.34 Å	Lau and Van Petegem, (2014)
RyR2-SPRY2	*Mus musculus*	A1107M	4P9L	X-ray Diffraction	1.43 Å	Lau and Van Petegem, (2014)
RyR2-SPRY2	*Mus musculus*	P1124L	5VSN	X-ray Diffraction	1.43 Å	Alvarado et al. (2019)
RyR2-SPRY1	*Mus musculus*	WT	5C33	X-ray Diffraction	1.21 Å	Yuchi et al. (2015)
RyR2-SPRY1	*Mus musculus*	I784F	6J6L	X-ray Diffraction	1.21 Å	Touat-Hamici et al. (2021)
Full-length RyR2	*Homo sapiens*	WT	6WOV	Cryo-EM	5.10 Å	Iyer et al. (2020)
Full-length RyR2	*Homo sapiens*	R176Q	6WOU	Cryo-EM	3.27 Å	Iyer et al. (2020)
Full-length RyR2	Sus scrofa	Closed-state	5GO9	Cryo-EM	4.40 Å	Peng et al. (2016)
Full-length RyR2	Sus scrofa	Open-state	5GOA	Cryo-EM	4.20 Å	Peng et al. (2016)

demonstrated that RyR2 may be clustered into a broad variety of group dimensions in ventricular cardiomyocytes, which designated as "super-clusters" (Hou et al., 2015; Munro et al., 2016). These super-clusters are groups of individual clusters close enough to each other that Ca^{2+} release from one cluster can cause Ca^{2+}-induced Ca^{2+} release (CICR) from a neighboring cluster within the group (Macquaide et al., 2015). As clusters inside a super-cluster may be functionally connected, they are often referred to as calcium release units (CRUs). Along with inter-cluster spacing, the packing, or density, of RyR2 channels within individual clusters might influence their physiological Ca^{2+} handling. Reduced RyR2 channel density within a cluster increases the space between individual channels, reducing the possibility of RyR2–RyR2 interactions and thereby affecting coupled gating features and channel open probability (Walker et al., 2015). Recently, using a combination of line scan confocal imaging, dual-tilt electron tomography (ET), and dSTORM imaging, Asghari et al. (2020). reported that the arrangement of RyR2 super-complex is dynamic and can switch between different modes depending on the conditions of cellular environment, including the presence or absence of the regulatory proteins FKBP12 and FKBP12.6 as well as the post-translational modifications (PTMs) such as phosphorylation. Their findings prove that the long-range allosteric regulations by protein modulators or PTMs can change the size of RyR2 cluster and also the arrangement of RyR2 tetramers within clusters (Asghari et al., 2020). Advances in high-resolution techniques and approaches that can cover a broad range of dimensions, such as correlative light and electron microscopy (CLEM) that combines high-resolution structural data from cryo-electron tomography (cryo-ET) with spatiotemporal information from fluorescence light microscopy (FLM), would be necessary to solve the high-resolution structures of the super-complexes of RyRs, which would provide valuable information on the mechanism of "coupled gating."

2.2 X-Ray Crystallography

While cryo-EM structures shed light on the overall domain organization of RyRs and conformational changes associated with channel gating, x-ray crystallography has been extensively used to reveal the structural details of RyR domains at atomic resolutions. Several high-resolution structures of RyR1, RyR2, and RyR3 domains were determined by X-ray crystallography, including whole NTDs of RyR1 (Tung et al., 2010; Kimlicka et al.,

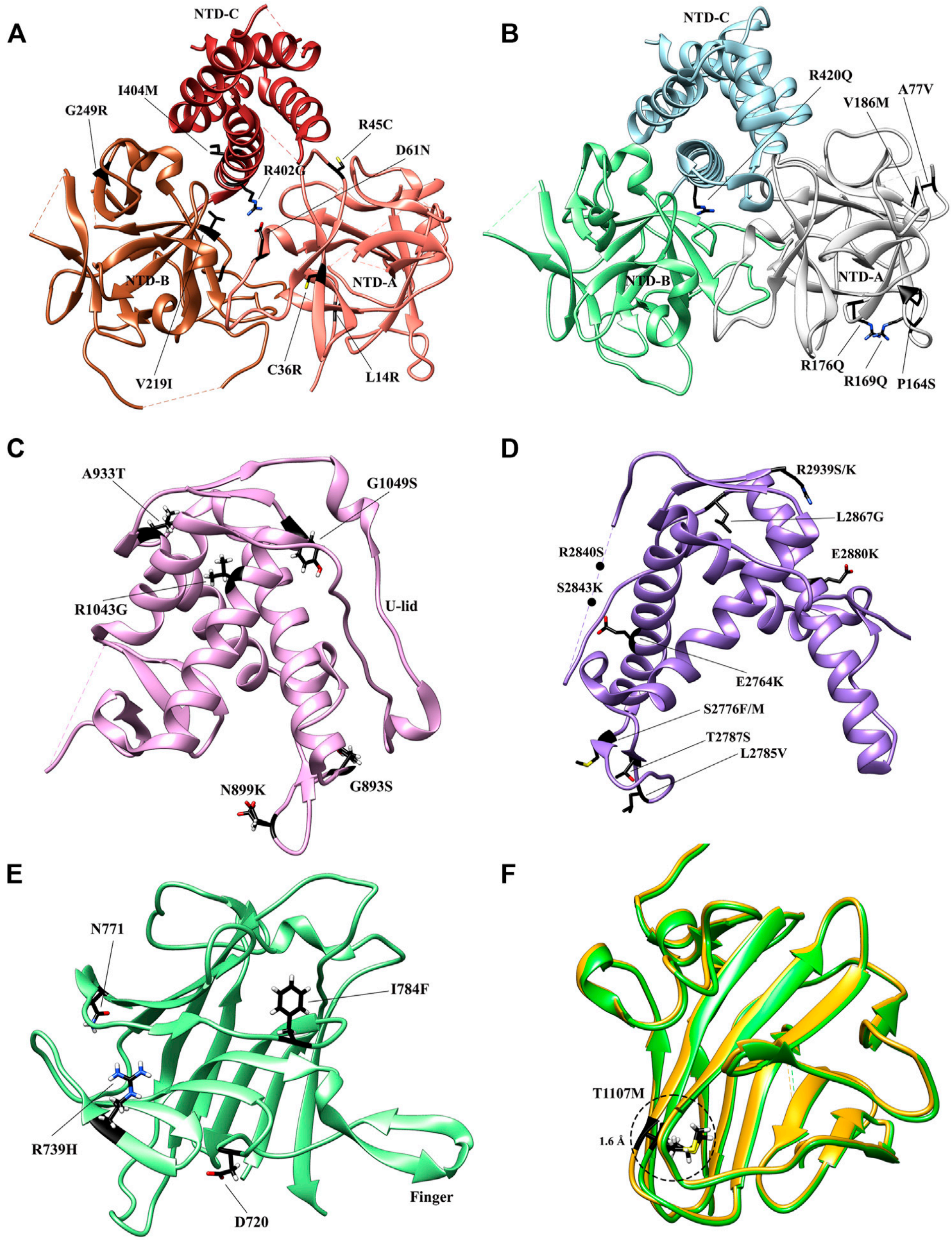

FIGURE 4 | Crystal structures of the RyR domains with disease mutations mapped. **(A)** The crystal structure of the N-terminal domain of rabbit RyR1 (PDB: 2XOA). The individual subdomains are colored in sandy brown (NTD-A), sienna (NTD-B), and dark brown (NTD-C), respectively. **(B)** The crystal structure of the N-terminal domain of human RyR2 (PDB: 4JKQ). The individual subdomains are colored in grey (NTD-A), light green (NTD-B), and light blue (NTD-C), respectively. **(C)** The crystal structure of Repeat 34 domain of rabbit RyR1 (PDB: 4ERT). **(D)** The crystal structure of Repeat 12 domain of rabbit RyR1 (PDB: 5C30). **(E)** The crystal structure of SPRY1 domain of mouse RyR2 (PDB ID: 6J6L). **(F)**. The superposition of the crystal structures of WT SPRY2 (green) (PDB: 4P9I) and SPRY2 A1107M (golden) (PDB: 4P9L) in RyR2. The locations of individual disease-causing mutations are shown as black sticks and labelled.

2013a) and RyR2 (Borko et al., 2014) and their individual subdomains (Amador et al., 2009; Lobo and Van Petegem, 2009; Amador et al., 2013), SPRY1 of RyR2 (Yuchi et al., 2015) and SPRY2s of RyR1 and RyR2 (Lau and Van Petegem, 2014; Yuchi et al., 2015), the Repeat12 of RyR1 (Yuchi et al., 2015), and the Repeat34 of RyR1, RyR2, and RyR3 (**Table 1**) (Yuchi et al., 2012; Yuchi et al., 2015).

2.2.1 NTD

Several reports have provided high-resolution details of the N-terminal domains (NTD) of RyR1 (**Figure 4A**) (Tung et al., 2010; Kimlicka et al., 2013a) and RyR2 (**Figure 4B**) (Borko et al., 2014). Based on the crystallographic studies of the N-terminal region of RyR, this region consists of three domains interacting with each other *via* a hydrophilic interface. NTD-A (residues

1–208 rabbit RyR1 numbering) and NTD-B (residues 209–392 rabbit RyR1 numbering) form β-trefoil domains, each containing 12 β-strands, while NTD-C (residues 393–627 rabbit RyR1 numbering) forms an armadillo repeat domain consisting of a bundle of five α-helices. These three domains are highly similar in sequence and structure to their counterparts of the inositol 1,4,5-triphosphate receptor (IP3R). NTD-B and NTD-C of IP3R form a ligand binding site for IP3, and the presence of NTD-A reduces the binding affinity of the ligand, hence named as ligand binding suppressor domain (Lin et al., 2011). In contrast, despite of the structural similarity, the ligand-binding property is not conserved in the RyR. According to the results of docking study, using several different RyR1 cryo-EM maps, the NTD is consistently docked in the center of the cytoplasmic region and forms a vestibule around the 4-fold symmetry axis (Tung et al., 2010). Albeit this position seems to be in contradiction with a GFP insertion study (Wang et al., 2007), the data can be aligned when the length of the linkers and the size of the insertion proteins are taken into account (Tung et al., 2010).

The overall structure of RyR2 NTD is similar to RyR1 (**Figures 4A,B**), but its NTD-A contains an additional α-helix, as revealed by an X-ray crystal/NMR hybrid structure (Amador et al., 2013). This mobile helix was not resolved in some other crystal structures (Lobo and Van Petegem, 2009; Kimlicka et al., 2013a; Borko et al., 2014), probably due to its high dynamics. According to the docking result, this α-helix is located at an interface with the pore region and might mediate the conformational changes between NTD and the pore (Amador et al., 2013).

Recently, the crystal structures of insect RyR NTD-A from two insect species, *Apis mellifera* and *Plutella xylostella,* have also been solved at the resolutions of 2.50 and 2.84 Å, respectively (Lin et al., 2018; Zhou et al., 2020). Several species-specific structural features were revealed at the inter-domain interfaces, which would alter conformation upon channel gating, making them excellent pest-specific insecticide-targeting sites.

2.2.2 Repeat12 and Repeat34

RyRs encode four tandem repeats existing in two pairs (Repeat12 and Repeat34). These domains are referred to as Repeat domains or RYR domains, and the Repeat34 domain is also named as the phosphorylation domain. Repeat12 (residues 850–1,054 rabbit RyR1 numbering), and Repeat34 (residues 2,735–2,938 rabbit RyR1 numbering), presumably evolved by gene-duplication, are ~1,700 residues apart in sequence (**Figure 2A**). Because of tandem repeats, both domains have a pseudo two-fold symmetry.

The high-resolution crystal structures of Repeat34 (phosphorylation domain) have been solved for all three mammalian isoforms (Sharma et al., 2012; Yuchi et al., 2012; Yuchi et al., 2015). Repeat34 is positioned in the center of the RyR sequence and comprises a phosphorylation hot-spot loop that links two halves of the domain (**Figure 2A**). It exhibits a high pseudosymmetry and a prominent horseshoe shape (**Figure 4C**). Multiple phosphorylation sites have been reported in the Repeat34 domain of RyR1 (S2843) and RyR2 (S2808 and S2814), but not in RyR3. The crystal structures show that the phosphorylation loops are largely unstructured in RyR1 and RyR2 but more rigid in RyR3, implicating some correlation between the flexibility of the loop and the substrate feasibility. The structure of the Repeat34 domain from the insect *P. xylostella* has also been determined (Xu and Yuchi, 2019). Interestingly, the phosphorylation pattern of insect Repeat34 is temperature-dependent, which might be related to their environmental adaptation. Insect Repeat34 was found to possess several distinct features, such as an extra α-helix after the phosphorylation loop.

Repeat12 is located between SPRY1 and SPRY2 domains near the N-terminal region of the RyR sequence (**Figure 2A**). Although Repeat12 and Repeat34 have some structural similarities, the former is less symmetrical. This is mainly owing to the existence of an extra three-stranded β-sheet that fills a cavity between the two repeats of Repeat12 (Yuchi et al., 2015). The two repeats of Repeat12 are separated by a highly structured 30-residue loop, the equivalent of the phosphorylation loop in Repeat34, generating a U-shaped lid ("U-lid") and interacting closely with an α-helix in Repeat12 (**Figure 4D**). According to the result of the docking experiment using the RyR1 cryo-EM maps, Repeat12 is located at the corners of the cytoplasmic domain, precisely above the SPRY2 domain. This location is corroborated by the high-resolution structures (Efremov et al., 2015; Yan et al., 2015; Yuchi et al., 2015). Because this corner region has been shown to be involved in the coupled gating of RyRs (Asghari et al., 2020), Repeat12 might play a role in this process.

2.2.3 SPRY

RyRs have three SPRY domains (SPRY1-3), which share high sequence identity between vertebrates and invertebrates. SPRY domains, located after the NTD of RyRs in sequence (**Figure 2A**), are named after two protein families, SPlA kinases and RYanodine receptors, where they were first identified. They have been implicated in protein-protein interactions in several protein families.

The crystal structures of the SPRY2 domains of RyR1 (residue 1,070–1,246 rabbit numbering) and RyR2 (residue 1,080–1,253 mouse numbering) isoforms have been determined with 1.34–1.84 Å resolution (Lau and Van Petegem, 2014). The structures reveal that two antiparallel β-sheets form a core, on which an N-terminal extension and a lid module further stabilize the folding of the domain (Lau and Van Petegem, 2014). The docking results reveal that the SPRY2 domain is located at a position connecting the NTD gating ring with the clamp region (**Figure 2C**).

The crystal structure of SPRY1 domain of RyR2 (residue 650–844 mouse numbering) was solved later at a resolution of 1.2 Å (Yuchi et al., 2015). SPRY1 shares similar core and lid modules with SPRY2, but it has a unique inserted "finger" module formed by a β-hairpin structure (**Figure 4E**). This "finger" protrudes out from the core and is stabilized by a conserved W713 residue at the base, which serves as an anchor point. The conformation of this finger is similar in both molecules of the asymmetric unit, and its residues are highly conserved among all three RyR isoforms, indicating that it has a key functional role as an anchor point for other RyR domains or auxiliary proteins. In addition, SPRY1 domain does not contain an "insertion loop," which breaks a β-strand in two halves in SPRY2 (Lau and Van Petegem, 2014). Overall, despite having a similar core structure, SPRY1 and SPRY2 have diverged significantly through numerous insertions that alter their overall shape.

Although three SPRY domains were predicted to fold independently, the cryo-EM structures showed that they are partially intertwined. In RyR1, SPRY1 comprises two pairs of anti-parallel β-sheets (residues 1,466–1,491 and 1,615–1,634) from SPRY3 in addition to its own core β-sheets (residues 639–826). Similarly, SPRY2 contains a pair of anti-parallel β-sheet (residues 827–845) from SPRY1 (Yan et al., 2015). SPRY3 has a special structure consisting of two large structurally linked regions (residues 1,242–1,465 and 1,492–1,614) that are separated by an extension from SPRY1. A similar pattern is also observed in the RyR2 structure (Peng et al., 2016). Because of this domain organization, the crystal structures of individual SPRY1 and SPRY2 domains produced from recombinant expression cannot represent the whole domains, but rather the largest continuous core-forming segments (Lau and Van Petegem, 2014; Yuchi et al., 2015).

3 STRUCTURES OF RYR REVEAL THE DISEASE MECHANISMS

3.1 Crystal Structures of RyR Domains Containing Disease Mutations

More than 700 disease-associated mutations have been associated with RyRs, many of which are located in some mutation hotspot domains. X-ray crystallography has its advantage in studying the subtle structural changes caused by disease-causing mutations due to the high-resolution information. So far, the crystal structures of several mutant RyR domains, including NTD (Lobo and Van Petegem, 2009; Tung et al., 2010; Kimlicka et al., 2013a; Amador et al., 2013; Kimlicka et al., 2013b), SPRY1 (Touat-Hamici et al., 2021), SPRY2 (Lau and Van Petegem, 2014; Alvarado et al., 2019), Repeat12 (Yuchi et al., 2015), and Repeat34 (Yuchi et al., 2012), have been solved and provided insights into the mechanisms of these disease-causing mutations (**Table 1**).

3.1.1 NTD Mutant

The NTD is known as one of the three so-called "mutation hotspot regions," containing fifty six mutations (http://www.hgmd.cf.ac.uk/ac/gene.php?gene=RYR) in both RyR1 (Amburgey et al., 2011; Snoeck et al., 2015) and RyR2 (Marjamaa et al., 2009). The structures of both mutant NTDs and their subdomains were studied thoroughly to acquire a better understanding of how a given mutation impacts the tertiary structure and consequently the gating of the channel. The NTD mutations are found to cluster in several main regions of both isoforms, including the central helix, various interfaces within and across subunits, and a hotspot (HS) loop (loop β8-β9 of NTD-A) (Amador et al., 2009; Tung et al., 2010; Kimlicka et al., 2013a; Kimlicka et al., 2013b; Borko et al., 2014). To date, fourteen crystal structures of mutant NTD have been solved, including L14R, G249R, C36R, V219I, I404M, R45C, D61N, and R402G mutants of RyR1 (**Figure 4A**) (Kimlicka et al., 2013a) and the A77V, V186M, R420Q, P164S, R169Q, and R176Q mutants of RyR2 (**Figure 4B**) (Lobo and Van Petegem, 2009; Amador et al. , 2013; Kimlicka et al., 2013b; Borko et al., 2014).

The RyR1 mutant NTD structures show that most disease-causing mutations affect either the intra-subunit or inter-subunit domain-domain interface and alter relative domain orientations (Kimlicka et al., 2013a). Specifically, R45C, D61N, and R402G target ionic pairs between NTD-A and NTD-C: R45C abolishes a salt bridge with D447 on NTD-C, while D61N and R402G completely disrupt the ionic pair network. In general, they cause a large structural changes by affecting inter-domain ionic pairs. In contrast, a small number of mutations buried within the NTD domains, such as G249R and L14R, indirectly affect the inter-subunit interface through inducing conformational changes of residues at the interfaces. These findings highlight the overall importance of these interfaces in channel opening. However, some other mutations, such as V219I, I404M, and C36R, do not appear to induce any significant structural changes, but rather affect the thermal stability of the NTD protein. The C36R mutation showed the largest impact, lowering the melting temperature of RyR1 NTD protein by more than 9°C (Kimlicka et al., 2013a).

Several RyR2 NTD crystal structures have also been determined at atomic resolutions (**Figure 4B**). The structures of A77V (2.2 Å) and V186M (1.7 Å), which were solved on the background of RyR2 NTD-A, reveal that the mutations cause distinct local changes in the protein surface (Lobo and Van Petegem, 2009), while the structure of R420Q, which was solved based on RyR2 full NTD, shows that this CPVT mutation abolishes the chloride ion binding and reorients the three NTD subdomains (Kimlicka et al., 2013b). Other mutations, such as L62F, F329L, T415R, and L433P, located at the intra-subunit domain interfaces or buried inside the specific domains, induced protein instability, resulting in extensively degraded products (Kimlicka et al., 2013b).

In general, three molecular mechanisms are proposed for NTD mutations: 1. causing the misfolding of the protein; 2. destabilizing the interactions between NTD-A, NTD-B, and NTD-C; 3. affecting the interfaces between NTD and other RyR domains.

3.1.2 Repeat12 and Repeat34 Mutants

Several disease mutations have been identified in Repeat12 and Repeat34 domains, which were mapped to the high-resolution crystal structures of these domains (Yuchi et al., 2012; Yuchi et al., 2015) and also some of the mutant structures were determined by x-ray crystallography. Seven mutations were identified in the Repeat12 domain (**Figure 4D**), among which five of them from RyR1 (G893S, N899K, A933T, R1043G, and G1049S) are associated with MH (Levano et al., 2009), while the other two from RyR2 (R1013Q and R1051P) are associated with CPVT (Medeiros-Domingo et al., 2009). Several of these mutations are distributed on the surface, which are unlikely to cause misfolding of the domain but rather affect some domain-domain interactions in the full-length RyR. One exception is RyR1

R1043C, which affects a hydrogen bond network that is important for the stabilization of U-lid motif and causes a clear destabilization effect (Yuchi et al., 2015). RyR2 R1051P is located in the middle of the second α-helix of Repeat12. Thus, the substitution of the arginine with a proline, a "helix-breaking" residue, would probably disrupt this helix and possibly the structure of at least part of the domain.

Eleven disease mutations, including E2764K, S2776F, S2776M, L2785V, T2787S, R2840W, S2843P, L2867G, E2880K, R2939S, and R2939K, have been found in the RyR1 Repeat34 domain and associated with MH and CCD (**Figure 4C**) (Yuchi et al., 2012). Their distribution is not random but rather clustering into three structural regions. One mutation, L2867G, which targets a buried hydrophobic residue, induces a significant thermal instability and aggregation at room temperature. All of other mutations are exposed to the surface. Seven of them cluster on the same side as the phosphorylation loop. Mutations in the phosphorylation loop can either directly abolish the S2843 phosphorylation (S2843P) site directly or remove a positive charge (R2840W). Removing a positive charge has the same effect as the adding a negative charge *via* phosphorylation. The proximity of the majority of the mutations in Repeat34 to the phosphorylation sites implies that the mutations may influence the same interaction with a neighboring domain or a regulatory subunit as phosphorylation does. The remaining three mutations, R2939S, R2939K, and E2880K, are located on the completely opposite side of the domain. Crystal structures reveal that R2939S and R2939K can affect intra-domain salt bridges and hydrogen bonds with E2870 and Q2877, while E2880K simply affects the local surface charge properties.

Four mutations (D708N, N759D, R739H, and I784F) identified in SPRY domains have been associated to myopathies (**Figure 4E**). D708N in RyR1 has been linked to MmD and atypical periodic paralysis (Zhou et al., 2010). Based on the crystal structure, the equivalent residue in RyR2, D720, forms a salt bridge with the equally conserved R694. D720 is part of the "finger" motif, mediating the SPRY1-SPRY2 interaction. Thus, a mutation to asparagine would weaken the interaction and consequently disrupt the SPRY1-SPRY2 interaction (Yuchi et al., 2015). Furthermore, considering the direct involvement of SPRY1 in FKBP binding, the question emerges whether the SPRY1 disease mutations directly affect FKBP binding. The mutation of SPRY1 N760D mutation [equivalent to the human N759D core myopathy mutation (Bharucha-Goebel et al., 2013)] lies at the FKBP interface. Interestingly, this mutation leads to a four-fold decrease in total FKBP binding at saturating levels without affecting FKBP binding affinity (Yuchi et al., 2012). The mutation significantly reduced the expression level of SPRY1 N760D, implicating that the residue is critical in folding of the domain, but is less important in maintaining this structure as a receptor of FKBP. Two mutations, including R739H associated with CPVT (Medeiros-Domingo et al., 2009) and I784F associated with short-coupled torsade de pointes Touat-Hamici et al. (2021), were identified in RyR2 SPRY1. Recently, Touat-Hamici et al. solved a crystal structure of RyR2 SPRY1 I784F at 1.21 Å. The structure revealed that I784F causes a conformational change in a loop at the interface with SPRY3 and Repeat12, which affects inter-domain interactions and alters channel gating. In addition, this mutation has shown to reduce the melting temperature of SPRY1 by 7°. The impacts in both structure and thermal stability might contribute to the increase of propensity for spontaneous Ca^{2+} release observed in the functional assays.

Five mutations, including R1075W, G1165D, R1179W, R1127H, and R1140C, have been identified in the SPRY2 domain (Lau and Van Petegem, 2014). G1165D and R1075W affect partially buried residues and were associated to CCD (Böhm et al., 2013). Despite both mutations were found in conjunction with other mutations elsewhere in RyR1, they interfere with proper folding and should either contribute or be entirely responsible for the disease phenotype (Lau and Van Petegem, 2014). For the three mutations at the domain surface, R1179W, R1127H, and R1140C, they likely lie at some interfaces with other RyR domains or an auxiliary protein to become disease causing. Generally, the mutations that interfere with the folding of SPRY2 result in loss-of-function phenotypes, whereas mutations on the surface result in gain-of-function ones. In RyR2 SPRY2, T1107M has been associated with hypertrophic cardiomyopathy as well as CPVT (**Figure 4F**) (Medeiros-Domingo et al., 2009). The functional experiments have convincingly demonstrated that it confers an uncommon loss-of-function phenotype with early termination of Ca^{2+} release (Tang et al., 2012). The crystal structure of RyR2 SPRY2 A1107M (equivalent mutation in mouse RyR2) shows that the mutation abolishes a surface salt bridge between two neighboring β-strands to accommodate this nearby bulky methionine residue, explaining the observed significant thermal destabilization, resulting in 22% unfolding at physiological temperatures and the loss-of-function phenotype (Lau and Van Petegem, 2014). Recently, another RyR2 mutation discovered in a patient from a genotype-negative Hypertrophic cardiomyopathy (HCM) cohort, P1124L, was structurally and functionally characterized (Alvarado et al., 2019). HEK293 cells expressing recombinant RyR2 P1124L displayed a cytosolic loss-of-function phenotype and a higher sensitivity to luminal Ca^{2+}. This mutation induces significant conformational changes in SPRY2, which might disrupt a nearby interface between SPRY2 and SPRY3 and alter the channel gating property.

3.2 Cryo-EM Structures of RyR Containing Disease-Associated Mutations

3.2.1 The Distribution of Disease-Causing Mutations in RyRs

To date, over 700 mutations have been identified in both RyR1 and RyR2, and these are distributed throughout the receptor (**Figure 5A**). Several attempts have been sought to establish a relationship between the 3D structural distribution of these disease-associated mutations and their disease phenotype and severeness with the aim to create some prognostic markers. Roston et al. created a 3D model based on the available crystal structures of RyR2 domains and cryo-EM structures of rabbit RyR1, which can be used to predict the structural and functional impacts of CPVT-related variants. Interestingly, they discovered

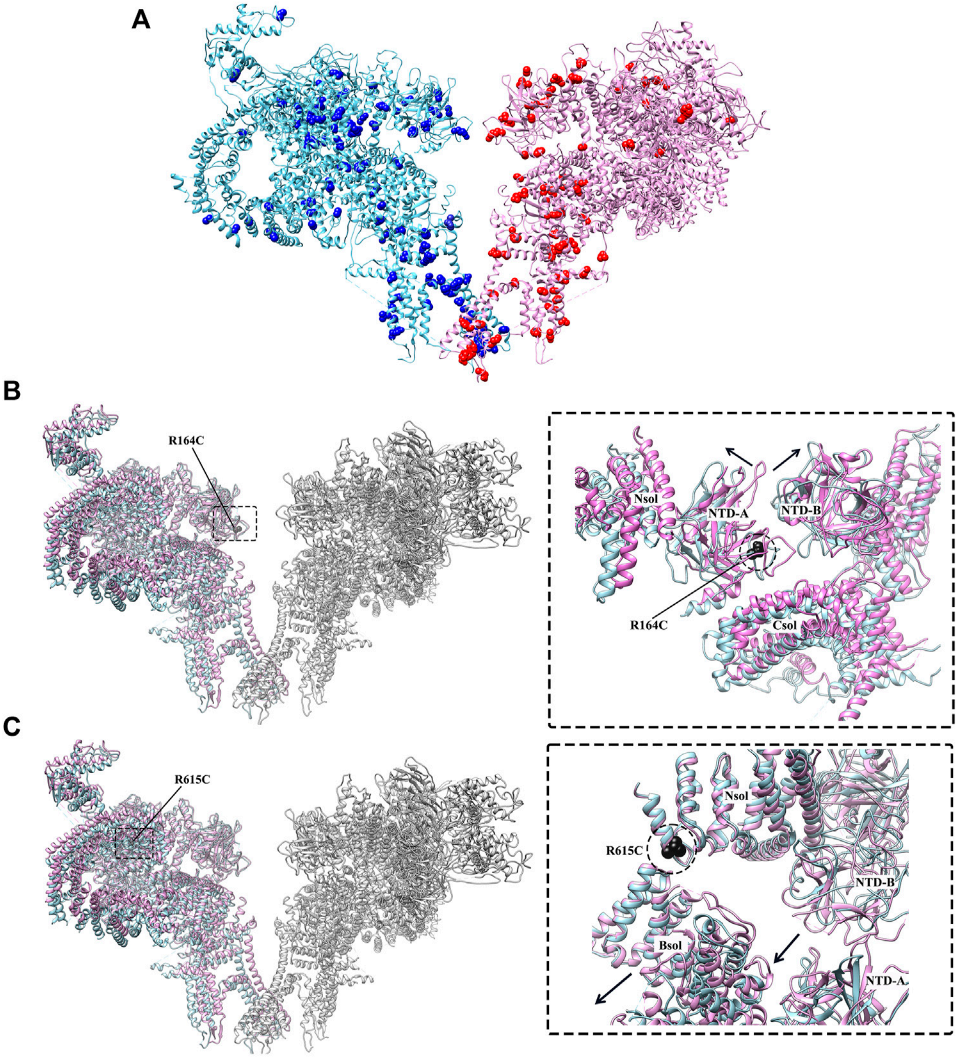

FIGURE 5 | Disease-causing mutations of RyR studied by cryo-EM. **(A)** The distribution of disease-causing mutations (spheres) in RyR1 (light blue) and RyR2 (magenta). One protomer is shown for each isoform. **(B)** Superposition of the structures of WT RyR1 (magenta) (PDB: 3J8H) and RyR1 R164C (light blue) (PDB: 6WOT). **(C)** Superposition of the structures of WT RyR1 (magenta) (PDB: 6W1N) and RyR1 R615C (light blue) (PDB: 6X34). Left panels of. **(B,C)** show the locations of the mutations in the full-length RyR1, and the right panels show the relative displacement induced by the disease-causing mutations in zoomed-in views.

that the majority of the CPVT mutations cluster along the four-fold symmetry axis with almost none in the peripheral region. The mutations with severe clinical phenotype, namely cardiac arrest, are distributed in a few important interfaces in RyR2 structure, including NTD, S4-S5 linker, and the pore-forming domain (Roston et al., 2018). NTD forms a continuous gating-ring structure surrounding the four-fold symmetry axis and is vital in regulating channel gating. The S4-S5 linker and the pore-forming domain belong to the transmembrane part of the channel that directly mediates calcium permeation. The linker between S4 and S5 has been demonstrated to be a key allosteric coupling element between the signal-sensing modules and the channel gates in several ion channel families (Blunck and Batulan, 2012), while the pore-forming domain, comprised of helices S5 and S6, creates the minimal "channel" through which calcium ions can permeate the SR membrane. In contrast, the mutations with relatively mild phenotype, such as syncope, are scattered in other interfaces. The distribution pattern of mutations in the 3D structure of RyR is useful in the prediction of the severeness of newly identified mutations during diagnosis in the future.

3.2.2 The Impacts of Disease-Causing Mutations Revealed by Cryo-EM Structures

Although the crystal structures of mutant RyR domains provide valuable information about their localization and impacts on the local structural changes, they were not able to reveal the global and long-range allosteric structural changes of the channel caused by these mutations. Recently, several disease-causing mutations of RyR1 were investigated through cryo-EM (Iyer et al., 2020; Woll et al., 2021), provided insights into their disease mechanisms. Iyer et al. solved the cryo-EM structures of two gain-of-function RyR mutations, RyR1 R164C and RyR2 R176Q, both located in an equivalent position of NTD-A, that are associated with MH and CPVT, respectively (Iyer et al., 2020). Despite a comparable loss of positive charge, the structures revealed that the mutations had an isoform-specific effect on the structure of RyR. A salt bridge network is disrupted by RyR1 R164C mutation, resulting in a 1 Å shift and 6° rocking of the NTD-A, which induces the channel into an altered pre-activated conformation (**Figure 5B**). This movement is similar to the movements in these domains that occur upon channel opening, but lesser in magnitude (6.5 Å shift and 8° rocking for channel opening). However, there was no significant change of the NTD-A^+/NTD-B distance for RyR2 R176Q, and the NTD-A did not shift in orientation.

In another recent study, Woll et al. solved the cryo-EM structure of a pig RyR1 containing an MH-associated mutation, R615C. The structure reveals that the mutation in the N-solenoid (Nsol) domain interacts with N1678 in junctional solenoid (Jsol) and E2175 in bridging solenoid (Bsol) (**Figure 5C**) (Woll et al., 2021). Previous cryo-EM studies revealed that the disruption of the interaction between Nsol and Bsol needs to occur upon channel opening. R615C mutation affects an interface between three solenoid domains and facilitates channel opening by causing a 2–3 Å shift in the Bsol near E2175 and a secondary movement of ~10 Å in the Bsol around residue 2,457 to reach an "intermediate" state (**Figure 3C**). Furthermore, Woll et al. also showed that apo-CaM binding abolishes the "intermediate" state caused by the mutation and induce the channel into the open state. In the WT channel, the apo-CaM N-lobe contacts the Bsol (residues 2,190–2,242, interface 1) and is close to a short loop in the Bsol (residues 2,595–2,600, interface 2). The apo-CaM C-lobe interacts with Bsol (residues 3,627–3,634, interface 3) immediately downstream of the Jsol (residues 1,975–1,999, interface 4). These interactions induce a conformational change in Jsol, bringing interface 4 closer to the apo-CaM C-lobe while having no discernible effect on the structure of the closed channel pore. In contrast, apo-CaM binding to R615C channels alters the tilt angle between the Nsol and Bsol, causing it to more similar to this region of the open channel. The R615C-induced change in the Nsol-Bsol interface reduces the energy barrier for channel opening, contributing to the increased sensitivity of the mutant channel to open in response to activators. The cryo-EM classification results showed that WT pRyR1 in the presence of apo-CaM and in the absence of ATP produced mostly closed channels (27% open), whereas under the same condition the R615C mutation increase the open state population by ~2.5-fold (69% open), suggesting that the mutation increases the opening probability of the channel (Woll et al., 2021). Overall, this finding highlights the role of the solenoid regions and CaM as key elements in propagating the effects of a disease-causing mutation. A common theme of gain-of-function RyR mutations revealed by Iyer et al. (2020) and Woll et al. (2021) is that the MH mutations can lead to some distinct "intermediate" pathological local conformations and cause the cytoplasmic regions of RyR1 to more closely resemble those of the open channel, thereby facilitating channel opening.

More mutations have been studied by molecular dynamic (MD) simulations based on the structural templates provided by cryo-EM and X-ray crystallography. MD simulations can provide information about dynamics that are difficult to capture by cryo-EM and X-ray crystallography. Zheng and Liu. (2017) studied the structural impacts of three disease mutations, K155E, R157Q, and R164Q (corresponding to mutations K167E, R169Q, and R176Q in RyR2), on the structure of RyR1 NTD tetramer. They revealed a dynamic network of inter-subunit salt bridges that critically control the relative motions and stability of the NTDs in RyR1, and are disrupted by the above mutations. Another study by Xiong et al. (2018). showed a CPVT mutation, A165D, located at the same inter-subunit interface of NTD can also perturb the conformation of the closed-state tetramer structure of NTD, suggesting that a similar disease mechanism of NTD mutations applies to both RyR1 and RyR2 given the strong conservation of NTD between them. Overall, structural analysis suggests that A165D, K167E, R169Q, and R176Q mutations all cause structural disruptions in a similar manner.

Different disease-causing mutations, depending on their locations in the structure of RyR, are likely to have different impacts on the local and global structures. Three mutation clusters, or so-called "hotspots," have been previously identified in the RyR, including the NTD (35–614, human RyR1 numbering), the central domain (2,129–2,458), and the CTD (3,916–4,942) (Betzenhauser and Marks, 2010), which implies a functional linkage between these domains. In the "zipping/unzipping" hypothesis raised in early 2000s, the mutations were proposed to be located in the interdomain interfaces and destabilize the closed state of the channel by impairing crucial interdomain interactions (Ikemoto and Yamamoto, 2002; Uchinoumi et al., 2010). As a result, these mutations cause an aberrant sensitivity of the channel to activating signals, including caffeine, halothane, and 4-chloro-m-cresol (Tong et al., 1999; Balog et al., 2001), or displaces the inhibitory proteins, such as CaM, to cause CPVT arrhythmogenesis (Nakamura et al., 2019). The "zipping/unzipping" hypothesis provides a reasonable explanation of disease mechanism. The high-resolution cryo-EM structures of RyR in the different functional and pathological states provided valuable information about the gating and disease mechanisms, but the limited numbers of snapshots are still not enough to provide high resolution at the time-scale and describe the detailed conformational changes related to long-range allosteric domain linkages and the regulation of this large protein with a variety of modifying factors. On one hand, more cryo-EM structures describing the impacts of mutations from different interfaces will give a more comprehensive view of the pathological mechanism. On the other hand, the time-resolved cryo-EM or long MD runs combined with cryo-EM structures might provide further insights into the "functional linkage" by revealing the dynamic changes.

4 ENDOGENOUS AND EXOGENOUS MODULATOR REGULATING CA^{2+} RELEASE IN RYR

RyR is one of the biggest known ion channels. It is activated predominantly by Ca^{2+} but also regulated by many factors,

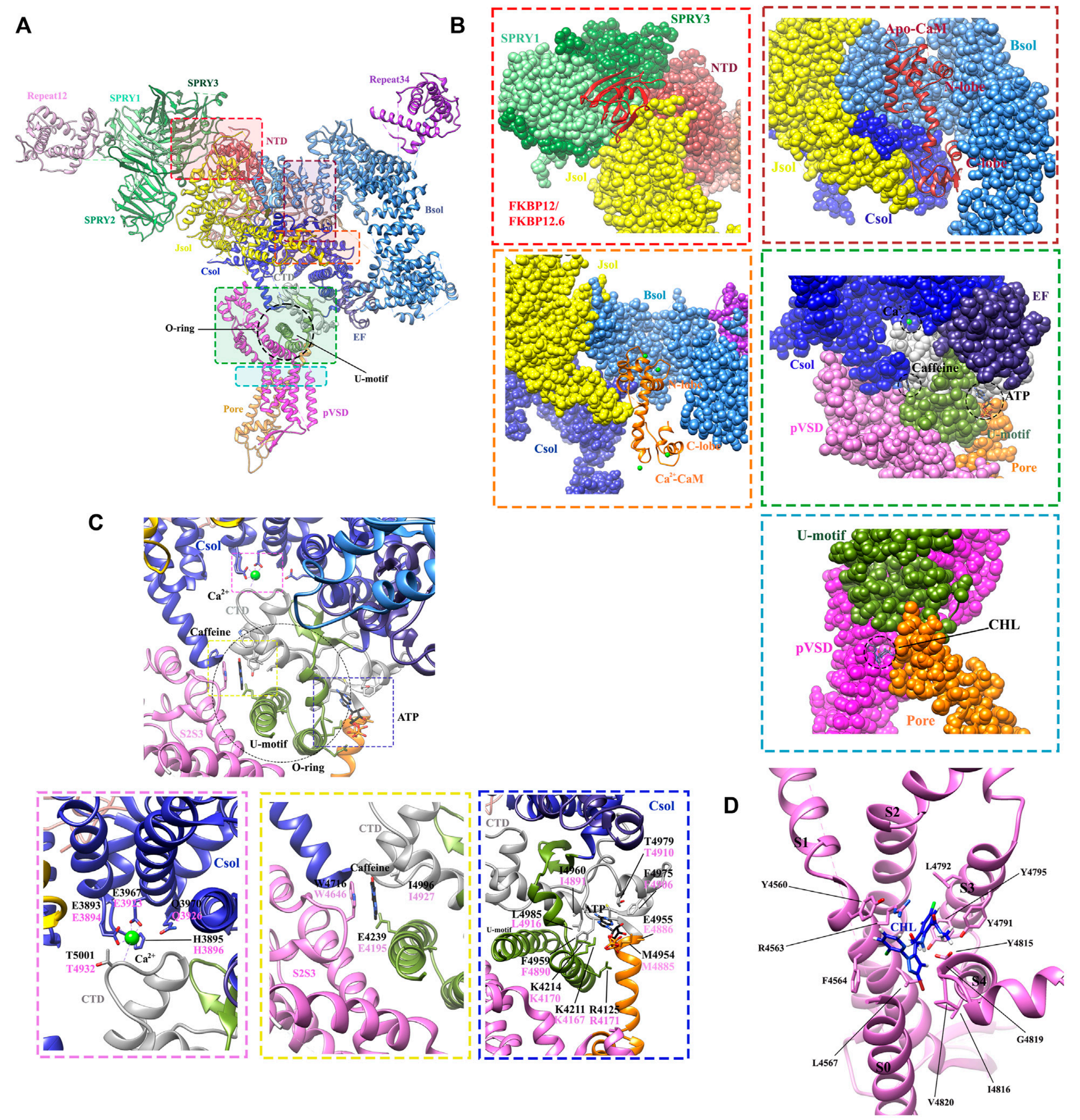

FIGURE 6 | Structures revealing the modulations of RyRs by the endogenous and exogenous modulators. **(A)** The locations of different ligand-binding sites within the full-length RyR1 (PDB: 6M2W) are indicated by colored boxes. A single protomer is shown. **(B)** The zoomed-in views of the binding sites for FKBPs (red dot square), apo-CaM (brown dot square), Ca^{2+}-CaM (orange dot square), Ca^{2+}, ATP, caffeine (green dot square), and chlorantraniliprole (CHL) (blue dot square). The different domains are displayed in surface view by the same color scheme as. **(A,C)** Zoomed-in view of the binding sites for Ca^{2+} (magenta dot square), caffeine (yellow dot square), and ATP (blue dot square) in RyR1. The contact residues are labelled in black (RyR1) and magenta (RyR2). **(D)** Zoomed-in view of the CHL binding site in RyR1. The detailed interactions and ligand-coordinating residues are labeled in. **(C,D)**.

including Mg^{2+}, ATP, phosphorylation, the redox potential, and via the interactions with several modulatory proteins, such as DHPR, FKBP, CaM, etc. The regulations of RyR by several proteins [calsequestrin (Beard and Dulhunty, 2015), sorcin (Meyers et al., 1995), triadin (Chopra et al., 2009), homer (Pouliquin and Dulhunty, 2009), histidine-rich Ca^{2+} binding protein (Arvanitis et al., 2018), S100A1 (Rebbeck et al., 2016), and junctin (Li et al., 2015)] and pharmacological agent [(Paul-Pletzer et al., 2002; Kobayashi et al., 2005; Oo et al., 2015; Diszházi et al., 2019), flecainide (Hilliard et al., 2010), K201 (Kaneko et al., 2009), S107 (Bellinger et al., 2008; Lehnart et al., 2008; Bellinger et al., 2009), scorpion toxins imperatoxin A (Gurrola et al., 2010), maurocalcine (Esteve et al., 2003), hemicalcin (Shahbazzadeh et al., 2007), hadrucalcin (Schwartz et al., 2009), ryanodine (Meissner, 1986), diamide (Ma et al., 2020), and carvedilol (Zhou et al., 2011)] have been extensively characterized by electrophysiological and biochemical experiments (Santulli et al., 2018), and reviewed elsewhere (Lanner et al., 2010; Van Petegem, 2012; Meissner, 2017; Woll and Van Petegem, 2021). Recently, several high-resolution structures of RyRs in complex with different modulators have been determined (Wu et al., 2015; Bai et al., 2016; des Georges et al., 2016; Wu et al., 2016; Chi et al., 2019; Gong et al., 2019; Ma et al., 2020), revealing a wealth of information about the ligand-binding sites, the detailed interaction modes, and the conformational changes induced by these molecules. In this section, we mainly focus on the recent structural studies of some important RyR modulators (**Figures 6A,B**), including both endogenous and exogenous ones.

4.1 Endogenous Modulators

4.1.1 Calcium Ion

The determination of the high-resolution cryo-EM structures of RyR1 and RyR2 isoforms has shed light on the intricate regulatory mechanism governing Ca^{2+} modulation (des Georges et al., 2016; Chi et al., 2019). Several studies previously reported that RyR channel contains a moderate-affinity micromolar Ca^{2+}-binding site for Ca^{2+}-dependent activation and a lower-affinity millimolar Ca^{2+}-binding site for Ca^{2+}-dependent inhibition (Watras and Ehrlich, 1991; Clapham, 1995). The cryo-EM structures of rabbit RyR1 solved by des Georges et al. showed that the moderate-affinity of Ca^{2+}-binding site at the interdomain interfaces between Csol and CTD is highly occupied at 30 μM Ca^{2+} concentration (**Figure 4A**), and the Ca^{2+}-coordinating residues (E3893, E3967, T5001, Q3970, and H3895) are conserved between RyRs and IP3Rs (des Georges et al., 2016). They propose that the binding of 30 μM Ca^{2+} primes the channel and makes it ready for activation, and the binding of other channel activators, e.g., ATP and caffeine, would induce the channel to a fully open-state (**Figure 6C**) (des Georges et al., 2016). This observation was supported by the reports from other independent structural studies on RyR1 (Efremov et al., 2015; Ma et al., 2020). Later, Yan's group investigated whether Ca^{2+} alone could open RyR2 in the absence of other modulators using cryo-EM. They discovered that the channel is inactivate in the absence of Ca^{2+}, but that increasing Ca^{2+} to 20 μM concentration with the addition of PCB95 in the absence of FKBP12.6 (Peng et al., 2016) or with the simultaneous addition of ATP and caffeine in the presence of FKBP12.6 (Gong et al., 2019) induces a contraction of the central domain, which applies a pulling force, facilitating the dilation of the S6 bundle and opens the pore. Overall, these studies reveal the location of the moderate-affinity Ca^{2+}-activation site and indicate that Ca^{2+} is essential for the opening of RyRs, and multiple modulators highly regulate the calcium-induced channel opening by stabilizing the open-state of the channel. In contrast, the location of the low-affinity Ca^{2+}-binding site remains elusive probably due to the low occupancy at the experimental condition, although a study using the chimeric channels between RyR1 and RyR2 suggests that it might be located in one of the two EF hands (Gomez and Yamaguchi, 2014).

4.1.2 ATP and Magnesium Ion

Adenine-derived nucleosides and nucleotides are competitive partial agonists of both RyR1 (Laver et al., 2001) and RyR2 (Kermode et al., 1998). ATP enhances the maximal opening probability (P_O) of the channel, without affecting its conductance (Kermode et al., 1998). des Georges et al. (2016). solved cryo-EM structure of ATP-binding site in RyR1 in the absence or presence of other modulators, revealing that ATP-binding site is constituted by the cytoplasmic extension of S6 and C-terminal components. M4954, F4959, T4979, and L4985 intimately interact with adenine-base; three positive residues, K4211, K4214, and R4215 contact with the negatively charged triphosphate tail; while E4955 appears to contact with the ribose ring. Similar to the structure of RyR in Ca^{2+} alone condition, ATP alone also primes the channel and the addition of other activators are required to open RyR1, especially Ca^{2+} (**Figure 6C**).

Mg^{2+} was proposed to have a complex role on RyR activity: it acts as a competitive inhibitor by binding to the moderate-affinity Ca^{2+} site which is essential for Ca^{2+}-dependent activation, but also shows inhibitory effects on RyRs by binding to the low-affinity inactivation site with similar affinity as Ca^{2+} (Laver, 2018). In addition, Mg^{2+} also binds to the luminal regulatory site and reduces the conductance of Ca^{2+} through the channel (Gusev and Niggli, 2008; Laver and Honen, 2008).

In addition, the majority of cellular ATP appears as MgATP complex, which is the most physiologically active form of ATP in cells. An increase in Mg^{2+} concentration, which increases MgATP and decreases non-complexed ATP, also decreases RyR activity (Walweel et al., 2014). However, whether MgATP or ATP is a physiological regulator of RyRs remains debatable. It is argued that RyR can be activated by "free" ATP because ATP activates RyRs in the absence of Mg^{2+} and because three positively charged amino acid residues in the ATP-binding site balance out the negatively charged triphosphate tail of ATP (des Georges et al., 2016). Experimental evidence on the preference of ATP or MgATP in physiological regulation of RyR has not yet been provided (des Georges et al., 2016)

4.1.3 Calmodulin

CaM binds to RyR under both apo-CaM and Ca^{2+}-CaM conditions and exhibits biphasic regulation of RyR1. Briefly, it inhibits both RyR1 and Gomez and Yamaguchi, 2014RyR2 at high Ca^{2+} concentrations, while activating RyR1 but inhibiting RyR2 at low Ca^{2+} concentrations (Fruen et al., 2000; Balshaw et al., 2001). As a result, CaM regulates RyRs in an isoform-specific manner. The binding of CaM has been widely investigated *via* X-ray crystallography and cryo-EM, demonstrating that both apo-CaM and Ca^{2+}-CaM may bind to the periphery of the cytosolic cap, although the exact binding mode relies on the Ca^{2+} concentrations (Samsó and Wagenknecht, 2002; Huang et al., 2012).

The crystal structures of Ca^{2+}-CaM bound to the calmodulin-binding domain (CaMBD2) of RyR1 and RyR2 have been solved

(Maximciuc et al., 2006; Holt et al., 2020). The binding modes of both isoforms are similar, with W3620 (RyR1 numbering) interacting with a hydrophobic pocket of the C-lobe and F3636 (RyR1 numbering) interacting with the N-lobe. This dual binding mode explains the nanomolar affinity of the CaMBD2 peptide for Ca^{2+}-CaM.

The recent cryo-EM structures of RyRs in complex with CaM confirmed the findings from the crystal structures and shed light on the regulation of RyR channel gating by CaM (**Figure 6B**). Gong et al. (2019) solved the cryo-EM structures of RyR2 in complex with apo-CaM (resolution of 3.6 Å) and Ca^{2+}-CaM (resolution of 4.4 Å). The structures show that apo-CaM and Ca^{2+}-CaM establish different but overlapping contacts in an elongated cleft formed by the handle, helical, and central domains, which is consistent with prior low-resolution structures of RyR1 (Samsó and Wagenknecht, 2002; Huang et al., 2012). Upon binding of Ca^{2+}-CaM, both N- and C-lobes of CaM wrap around an α-helix by interacting with the same two aromatic anchors (F3604 and W3588 in RyR2) in their hydrophobic cavities as revealed by the previous crystal structures (**Figure 6B**) (Maximciuc et al., 2006). In contrast, for apo-CaM, the N-lobe of CaM contacts with the region of BSol domain, whereas the C-lobe lies in the JSol domain, the binding and conformation of apo-CaM bound to the RyR2 are similar to the ones of CaM1234 bound to RyR1 (Ma et al., 2020). These structures were further validated *via* mutagenesis analysis (Gong et al., 2019). The binding of Ca^{2+}-CaM stabilizes the RyR in a closed-state. Ca^{2+}-PCB95, which normally facilitates channel opening, can be counteracted effectively by Ca^{2+}-CaM, which keeps the channel closed. However, the RyR in complex with Ca^{2+}-CaM remains open in the presence of caffeine and ATP. This suggests that CaM acts only as one modulator of the channel whose conformational and functional state is delicately regulated by the presence and absence of a combination of positive and negative regulators.

4.1.4 FKBP12 and FKBP12.6

Two FKBPs, FKBP12 (also named calstabin1) and FKBP12.6 (also named calstabin2), are generally regarded to be components of the massive RyR complexes and selectively associated with RyR1 (FKBP12) and RyR2 (FKBP12.6) in an isoform and tissue specific manner (Chelu et al., 2004; Santulli and Marks, 2015). They stabilize the closed state of the channel and prevent intracellular Ca^{2+} leak (Ahern et al., 1997; MacMillan, 2013; Santulli and Marks, 2015). An early investigation demonstrated that a hydrophobic cluster within SPRY1 is required for FKBP binding based on the combined results from crystal structures, FRET experiment, mutagenesis, and molecular docking to cryo-EM maps (Yuchi et al., 2015). Later, low and high resolution of cryo-EM studies has determined the binding sites of FKBP12 and FKBP12.6 on RyR1 at the periphery of the tetrameric assembly (Samsó et al., 2006; Yan et al., 2015; Zalk et al., 2015). FKBP binds at the N-terminus of the BSol (**Figure 6B**). It stabilizes the link between the pore and cytoplasmic region by rigidifying the interface between BSol and SPRY1/SPRY2 (Yan et al., 2015; Zalk et al., 2015; des Georges et al., 2016).

The regulation of RyR2 by FKBP is complicated and controversial. While FKBP12.6 has a higher affinity to RyR2, FKBP12 is more abundant in the heart (Galfre et al., 2012). Some studies showed that FKBP12 acts as a high-affinity activator of RyR2 to sensitize the channel to cytosolic Ca^{2+}, while FKBP12.6 has lower efficacy but can antagonize the effect of FKBP12 (Galfre et al., 2012). But other studies support that FKBP12.6-binding promotes the closed state of RyR2 and inhibits its function (Marx et al., 2000; Wehrens et al., 2003). This avenue of thought is corroborated by a number of studies showing that lack of binding of FKBPs causes leaky RyRs in pathologies such as muscular dystrophy (Fauconnier et al., 2010), sarcopenia (Andersson et al., 2011), cardiac arrhythmias (Wehrens et al., 2004a), and heart failure (Marx et al., 2000). In this scenario, overexpression of FKBP12.6 likely to serve as an inhibitor of arrhythmogenesis by lowering diastolic RyR2 Ca^{2+} leak and halting spontaneous Ca^{2+} release (Gómez et al., 2004; Guo et al., 2010; Zhang et al., 2016). Fernández-Morales et al. (2022) reported that RyR2 N771D mutation located in FKBP-binding site (corresponding to N760D in RyR1) has a minor effect on Ca^{2+} signaling but promotes "arrhythmogenesis" in human stem cells derived cardiomyocytes. In a recent study Chi et al. (2019), solved the cryo-EM structures of RyR2 in the absence or presence of FKBP12.6 at a resolution of 6.1 and 4.6 Å, respectively. FKBP12.6 causes relaxation in the central domain of the channel, stabilizing RyR2 in a closed state in the presence of Ca^{2+}-PCB95, Ca^{2+}-ATP, or Ca^{2+}-caffeine, indicating that FKBP12.6 is involved in pathophysiological regulation of RyR2 (Marx et al., 2000; Wehrens et al., 2003). In the presence of FKBP12.6, however, combining the synergistic effects of Ca^{2+}-ATP or Ca^{2+}-caffeine is sufficient to open the channel (Chi et al., 2019).

4.1.5 $Ca_v1.1$, STAC3, and Junctophilin

The voltage dependent Ca^{2+} channels ($Ca_V1.1$ and $Ca_V1.2$) are also referred as dihydropyridine receptors (DHPRs). $Ca_V1.1$ is expressed in skeletal muscle, whereas cardiac myocytes express $Ca_V1.2$ with a trace of $Ca_V1.3$ in atrial myocytes (Zamponi et al., 2015). $Ca_V1.1$ modulates RyR1 activity through direct mechanical interactions, while $Ca_V1.2$ modulates RyR2 by an indirect Ca^{2+}-induced Ca^{2+} release (CICR) release pathway. RyR1 is activated physiologically *via* direct physical interaction with the $Ca_V1.1$ complex and the surrounding RyR1 tetramers in the crystal line-like assembly (Tanabe et al., 1990; Protasi et al., 1997). Several domains of the cytoplasmic region of RyR1, such as SPRY3 domain, were shown to be involved in coupling with the $Ca_V1.1$ complex (Perez et al., 2003). The architecture organization of a pseudotetrameric eukaryotic Ca_V channel in complex with its auxiliary subunits has been solved (Wu et al., 2015; Wu et al., 2016), advancing our understanding of EC-coupling mechanism and providing a three-dimensional template for molecular interpretations of Ca_V and Na_V channel functions and disease mechanisms. Although, the structures of $Ca_V1.1$ (Wu et al., 2015; Wu et al., 2016; Zhao et al., 2019) and RyRs (Efremov et al., 2015; Yan et al., 2015; Zalk et al., 2015; Bai et al., 2016; Peng et al., 2016; Wei et al., 2016; Chi et al., 2019; Gong et al., 2019; Ma et al., 2020) have been solved individually, the detailed interaction mode between these two channels remains elusive. Furthermore, the key elements in Ca_V for RyR1 binding, such as the II-III loop of the α1 subunit and part of the β subunit, are still missing from the determined Ca_V structure. Bai et al. (2016). docked structures of the $Ca_V1.1$ complex (PDB: 3JBR) and RyR1, hypothesizing that domains of Cav1.1α1 would cause shifts of the β-subunit and other cytoplasmic segments of $Ca_V1.1$ upon depolarization, which might prompt movement of the neighboring cytoplasmic RyR1, such as SPRY3 domain. Perni et al. (2017) showed that the functional coupling can be reconstituted in tsA201 cells by expressing five junctional proteins, $Ca_V1.1$, RyR1, β1a, STAC3, and junctophilin2, highlighting the importance of these proteins in skeletal muscle EC-coupling. Ultimately, the determination of a cryo-EM structure of EC-coupling super-complex would provide a long-awaited answer to how this complex molecular machine works.

STAC3 is an essential protein for EC-coupling and acts as the auxiliary protein linking $Ca_V1.1$ and RyR1. The interactions between STAC3 and $Ca_V1.1$ are well-known and functionally validated (Polster et al., 2018; Rufenach et al., 2020). The crystal structures of tandem-SH3 domains of different STAC isoforms was solved up to 1.2 Å resolution. Combined with the results from ITC and calcium imaging experiments, they proved that STAC3 binds to $Ca_V1.1$ through interacting with the II-III loop of the α1 subunit of $Ca_V1.1$ (Yuen et al., 2017).

Junctophilins (JPHs) are known to stabilize the structure of the junctional membrane complex by bridging the plasma membrane and the sarcoplasmic membrane. In muscle tissue, JPHs allow for the communication between Ca_V, located in the transverse-tubule (T-tubule) membrane, and RyRs in the SR membrane. Currently, the structure of a JPH2 alone and in complex with $Ca_V1.1$ has been solved (Yang et al., 2022), showing that this interaction is required for clustering of these channels and for robust muscle EC-coupling. However, the complex structure of JPHs-RyRs is still a missing jigsaw piece, with which one can appreciate the assembly of the full Ca_V-JPH-RyR complex.

4.1.6 PKA and CaMKII

The large cytoplasmic region of RyRs has numerous phosphorylation sites (Takeshima et al., 1989) that can be targeted by protein kinases, including cAMP-dependent protein kinase (PKA) and CaM-dependent kinase II (CaMKII) (Dulhunty et al., 2001; Marx et al., 2001). However, the location and physiological importance of many phosphorylation target sites remains questionable. Among, the best studied sites are RyR2 S2808 (S2843 in RyR1) targeted by PKA (Witcher et al., 1991; Marx et al., 2000) and S2814 targeted by CaMKII (Wehrens et al., 2004b). These two residues are found within the Repeat34 domain, in a linker loop (phosphorylation loop) connecting Repeats3 and 4 (Yuchi et al., 2012). Crystal structures of the Repeat34 domain of all three mammalian isoforms have been determined (Yuchi et al., 2012). The electron density of the phosphorylation loop is low in both RyR1 and RyR2 crystal structures, preventing direct visualization of the phosphorylation target sites. The flexibility of the phosphorylation loop might be essential for the recognition by the kinases because the linker in non-phosphorylatable RyR3 is more structured.

Recently, Haji-Ghassemi et al. (2019) solved a crystal structure of the mouse RyR2 Repeat34 domain bound to the catalytic domain of PKA (PKAc) in complex with an ATP analogue, revealing the detailed interactions between the phosphorylation loop and the active site of PKAc. The activity of PKA can be positively or negatively regulated by different phosphorylation patterns of this loop. In addition, they solved the structure of PKAc in complex with the CaMKII phosphomimetic mutant (S2814D). The mutation induced the formation of a new α-helix which promotes the binding of PKAc to RyR2 Repeat34. This implies that there is substantial cross-talk between different kinase pathways: the phosphorylation by CaMKII at one site can enhance the phosphorylation level of another site by PKA.

In addition to phosphorylation, other types of post-translational modifications (PTM), such as oxidation, nitrosylation, and glutathiolation, can also modulate the open probability and gating behavior of RyRs (Sun et al., 2003; Denniss et al., 2018). RyR has 80–100 cysteines per monomer, of which about 25–50 cysteines are in the reduced state and 6–8 are regarded as "hyperreactive" (Xu et al., 1998; Dulhunty et al., 2000). The oxidation, nitrosylation or glutathiolation of critical sulfhydryls on the cytoplasmic region of RyR1 and RyR2 affects the gating properties and the sensitivity to modulators such as ATP, caffeine, Ca^{2+}, Mg^{2+}, calmodulin (Zhang et al., 1999), and FKBP (Aracena et al., 2005). Ca^{2+} efflux from the cardiac SR vesicles is increased by reactive oxygen, and calmodulin has been identified as a mediator of reactive oxygen-triggered Ca^{2+} release *via* the RyR (Kawakami and Okabe, 1998; Xu et al., 1998; Sun et al., 2003; Voss et al., 2004; Aracena-Parks et al., 2006; Gangopadhyay and Ikemoto, 2006; Gonzalez et al., 2010). The large number of PTMs and their heterogeneity make it difficult to obtain the high-resolution structures and study their specific impacts. The recent development of genetic code expansion technique could provide powerful tools to generate homogeneously modified proteins suitable for high-resolution structural studies.

4.2 Exogenous Modulators

4.2.1 Ryanodine and Caffeine

Ryanodine and caffeine have been extensively used in controlling cytoplasmic and ER luminal Ca^{2+} concentrations. The ryanodine, a plant alkaloid, affects RyR function in two ways: at low nanomolar concentrations it locks the channel in a subconductance state, while at high micromolar concentrations it blocks the conductance (Meissner, 1986). According to the results of $[^3H]$Ryanodine binding studies, binding to a single high-affinity site locks RyRs into an open subconductance state, while binding to one or more ryanodine to low-affinity sites totally abolishes the current (Lai et al., 1989; Pessah and Zimanyi, 1991). According to a cryo-EM structure (des Georges et al., 2016), the high-affinity ryanodine-binding site is located within the pore, close to Q4933, and ryanodine binding to this site causes the transmembrane pore to dilate. The density does not match the exact shape of ryanodine molecule. This is because only one molecule of ryanodine binds to the site in the pore. Due to the C4 symmetry applied during the data processing this ryanodine molecule was averaged over four symmetrically equivalent sites. However, the mutation in this site specifically reduces ryanodine binding without affecting channel function, proving this is the real high-affinity binding site of ryanodine (Fessenden et al., 2001).

The caffeine binds to a site located between the S2S3 domain and the CTD in RyR1 (**Figure 6C**). Caffeine is sandwiched by the hydrophobic side chains of W4716 from the helical bundle domain between transmembrane helices S2 and S3 (S2S3) and I4996 from CTD, and also stabilized by the hydrogen bonds between one of the two carbonyls and the carboxyl side chain of E4239 from TaF domain (des Georges et al., 2016). These interactions are also conserved in RyR2 (corresponding to RyR2 E4195, W4646, and I4927) (Murayama et al., 2018b). The caffeine-binding site is located directly below the Ca^{2+}-binding site. The close proximity of Ca^{2+}- and caffeine-binding sites suggests that the two sites play a direct role in regulating Ca^{2+} sensitivity. One of the CPVT mutation, RyR2 W4645R, corresponds to a caffeine-coordinating residues. It not only affects the caffeine binding, but also the structure of the neighboring Ca^{2+}-binding site regulating Ca^{2+} sensitivity (Murayama et al., 2018b), which represents a potential mechanism for CPVT.

4.2.2 Chlorantraniliprole

Chlorantraniliprole (CHL), belonging to the diamide insecticide family, is one of the top-selling insecticides on the global market. CHL has a novel mode of action: it can target pest RyRs and cause disruption of feeding and muscle paralysis and ultimately death of the treated insects. One merit of CHL is that it can selectively activate insect RyRs with high nanomolar affinity but binds mammalian RyRs only with a low micromolar affinity (Chen et al., 2019). Recently, the cryo-EM structure of rabbit RyR1 in complex with CHL was solved. It clearly revealed the binding site and the binding pose of CHL at a local resolution of 3.2 Å (Ma et al., 2020). The binding site of CHL was found in a pocket at the interface between the pseudo-voltage-sensor domain (pVSD) from the transmembrane region of RyR and the cytoplasmic core solenoid (CSol) (**Figure 6D**). The binding of CHL induces a conformational change of pVSD, causing a displacement of the S4-S5 linker to relax the constriction in the S6 bundle and open the pore.

Due to the heavy usage, many mutations have been identified in the insect RyRs, developing the resistance in several agricultural pests, such as diamondback moth (*P. xylostella*) (Nauen and Steinbach, 2016), tomato leafminer (*Tuta absoluta*) (Roditakis et al., 2017), and beet armyworm (*Spodoptera exigua*) (Zuo et al., 2020). The identification of the four resistant mutations (G4946E, I4790M, Y4701D, and Y4922F in DBM numbering) in the transmembrane domain of RyR suggested a potentially nearby diamide-binding pocket, but the exact mechanisms of these resistant mutations remained enigmatic. The RyR1-CHL cryo-EM structure reveals that these four resistance mutations are distributed at the CHL-binding site, but interestingly, they affect CHL binding in two distinct ways: G4946E and I4790M cause steric hindrance with the diamide, while Y4701D and Y4922F reduce the contacts. The Ca^{2+} imaging experiments and insect toxicity results confirm that the mutations cause the resistance in the order of Y4922F→G4946E→Y4701D→I4790M, which agrees with the computational docking results based on the structural model (Ma et al., 2020). The structural basis of diamide modulation of insect RyR provides new insights for the development of diamide derivatives to combat pest resistance.

In addition, as RyR activators, the diamide compounds are also shown to have potential therapeutic effects to treat CCD caused by some loss-of-function (LoF) mutations (Ma et al., 2020). Two cell lines stably expressing LoF CCD mutants, RyR1 R4824C and R4860C, could be activated by CHL with slightly increased EC_{50} values compared to the one expressing WT RyR1, implying that CHL may reduce the LoF effects of these mutations by increasing the opening probability (Ma et al., 2020).

4.2.3 Dantrolene

Dantrolene was used to treat MH and cardiomyopathies effectively by targeting skeletal muscle ryanodine receptors (RyR1) (Paul-Pletzer et al., 2001; Paul-Pletzer et al., 2002) and the cardiac ryanodine receptors (RyR2), respectively (Kobayashi et al., 2009; Uchinoumi et al., 2010). However, the molecular mechanism of dantrolene is mostly unclear. Inter-domain interactions between the N-terminal and central regions of RyRs may be stabilized by binding to the N-terminal residues 590–609 in RyR1 (Paul-Pletzer et al., 2002) and residues 601–620 in RyR2 (Paul-Pletzer et al., 2005). Direct structural evidence supporting these binding sites is missing. According to recent study, dantrolene has no intrinsic effect on purified RyR1 and only shows its effects on the channels pre-activated by other modulators, such as CaM, Mg^{2+}, and ATP (Oo et al., 2015; Diszházi et al., 2019).

Wang et al. (2011) used a combination of GFP as a structural marker, FRET, and three-dimensional cryo-EM structures to determine the dantrolene-binding motif in RyR1/RyR2. They proposed that the location of the dantrolene-binding site is located distal to the central region of RyR2 and dantrolene might allosterically modulate the interaction between the N-terminal and central domains. Insertion of GFP after R626, near the proposed dantrolene-binding site, abolished the binding of GST-FKBP12.6, implicating the dantrolene-binding site in close proximity to that for binding FKBP12.6 and the outer periphery of the cytoplasmic assembly (Wang et al., 2011). But the full extent of the functional relationship between these two sites was not investigated. This location was further supported by FRET analyses using 10 FRET pairs (Wang et al., 2011). Further clarification of the dantrolene-regulation on RyR will likely rely on the determination of some high-resolution cryo-EM complex structures or crystal structures of RyR dantrolene-binding domain.

4.3 Development of Therapeutic RyR-Targeting Drugs

As a key therapeutic target for many skeletal and cardiac muscle diseases, RyR has recently attracted a lot of attention in drug development. Considering the high structural similarity between RyR1 and RyR2, it is important to develop skeletal or cardiac specific drugs to treat these disease with low side effect. Dantrolene is the only clinically approved drug for MH (Kobayashi et al., 2009). However, it has significant drawbacks in clinical application, including poor water solubility that makes quick preparation difficult under emergency conditions and a long plasma half-life that causes long-lasting side effects such muscle weakness. To tackle this problem, Murayama group identified RyR1-selective inhibitor, oxolinic acid, with improved water solubility using fluoresence-based high-throughput screening (HTS) platform that monitors ER luminal [Ca^{2+}] change (Murayama et al., 2018a; Murayama and Kurebayashi, 2019). Following that, they developed a series of oxolinic acid derivatives and successfully developed a compound, 6,7-(methylenedioxy)-1-octyl-4-quinolone-3-carboxylic acid (Cpd1), with comparable potency as dantrolene in *in vitro* study (Mori et al., 2019). This compound effectively rescued mice with MH and heat stroke. Cpd1 has great advantages of higher water solubility and shorter plasma half-life compared to dantrolene, thus representing a promising new candidate drug for the treatment of patients carrying related RyR1 mutations (Yamazawa et al., 2021). In addition, Cornea group developed a series of delicate FRET-based HTS assays to screen isoform-specific inhibitors of RyRs by monitoring the changes of distances between different regulators of RyR, such as CaM, FKBP, DPc10, etc, using which they have identified several promising candidate compounds (Oda et al., 2015; Rebbeck et al., 2017; Rebbeck et al., 2020).

Mutations in RyR2 generally lead to the Ca^{2+} leak that is associated with heart failure and arrhythmias. Current therapy includes indirect inhibition of RyR2 through upstream blockage of β-adrenergic receptors, direct modulation of RyR2, or use of implantable cardioverter defibrillator (ICD). Because β-blockers and ICD devices often fail to prevent potentially lethal arrhythmias, the development of new therapeutic compounds targeting mutant RyR2 is urgently needed (van der Werf et al., 2012). The first compound identified using CPVT mice model was the 1,4-benzothiazepine derivative K201, also known as JTV519, which suppressed ventricular tachycardia caused by SR Ca^{2+} leak (Wehrens et al., 2004a). Subsequently, compound S107, an orally available 1,4-benzothiazepine derivative with high potency on RyR2 and no significant off-target effects, was shown to suppress ventricular arrhythmias in a RyR2 R2474S knock-in mouse model (Lehnart et al., 2008). JTV519 and S107 were proposed to treat CPVT by enhancing the binding of FKBP12.6 to the mutant RyR2 (Wehrens et al., 2004a; Lehnart et al., 2008). Other lead compounds tested for anti-arrhythmic effects in CPVT mouse models include flecainide and carvedilol derivatives (Watanabe et al., 2009; Zhou et al., 2011). But flecainide has some safety problem in patients with structural heart disease (Echt et al., 1991). Knollmann group discovered another antiarrhythmic drug, propafenone, that is effective for CPVT patients through the inhibition of RyR2, similarly to flecainide (Hwang et al., 2011). They also developed ent-1 verticilide, a RyR antagonist derived from a fungal cycloligomeric depsipeptide (Batiste et al., 2019). Compared to those treated with dantrolene, flecainide, and tetracaine, CPVT mice treated with ent-1 verticilide experienced less VT and fewer delayed afterdepolarisations (DADs) (Batiste et al., 2019). Recently, Wehrens group developed tetracaine and its derivatives (EL1-9) for the treatment of ventricular tachycardia (Li et al., 2017). The IC_{50} of EL9 was approximately 400-fold lower than that of JTV519 (Li et al., 2017). Later, a new derivative, known as EL20 [2-(diethylamino)ethyl 4-(butylamino)-2-methoxybenzoate], was discovered and showed similar effect to that of EL9 (Klipp et al., 2018). Furthermore this compound also showed good efficacy against CPVT in human induced pluripotent stem cell-derived cardiomyocytes (iPS-CMs) carrying the R176Q mutation (Word et al., 2021). In addition, Wan et al. 2(2022). reported the discovery that a natural product, Z16b, isolated from *Ganoderma cochlear*, has a potent therapeutic effect on CPVT. It reduces CPVT episodes not only in a mouse model of CPVT but also in iPS-CMs derived from a patient with CPVT. Functional analyses and molecular assays demonstrated that Z16b serves as an RyR2 stabilizer by enhancing the interaction between the CTD and NTD. Given their promising efficacy, the above mentioned compounds represent intriguing therapeutic options, and further development of those compounds may result in a viable therapy for SR Ca^{2+} leak-induced arrhythmia and heart failure. However, the exact binding sites and binding modes of these promising pharmacological compounds agent remain elusive. The determination of high-resolution cryo-EM structures of RyRs in complex with these compounds will clarify their modulatory mechanisms on RyR dysfunctions, thus facilitating the development of isoform-selective potent therapeutic molecules to treat RyR-associated diseases.

5 CONCLUDING REMARK AND FUTURE PROSPECT

Ryanodine receptors are one of the most complex classes of ion channels, highlighted by their large size and a large number of regulators. The combination of cryo-EM and crystal structures at near-atomic resolution, and biochemical analysis of RyR has provided major insights toward a detailed mechanistic understanding of their function in physiology and pathophysiology. Furthermore, the distribution pattern of mutations in the 3D structure of RyR has been used to generate an efficient tool for diagnosis purpose. Finally, the complex structures of RyR with different modulators not only revealed the positions of several druggable pockets but also provided accurate templates for the rational structure-based drug design. It should be noticed that the present cryo-EM models of RyRs cover only ~70% of the protein with still ~1,500 residues missing. Many critical functional domains are missing, including some transmembrane segments, luminal loops, and cytoplasmic fragments. The accurate binding sites of several modulatory small molecules and protein-binding partners are also called into question. Furthermore, the effects of many disease mutations on the full-length RyR structures remain enigmatic, preventing the structure-based rational design of new therapeutics. Determining the structures of recombinant RyRs with disease mutations or PTMs, the super-cluster of RyRs involved in “coupled-gating” and the EC-coupling super-complexes in the absence or presence of a combination of modulators will continue to be a significant focus of future research. The advance in structural biology, such as CLEM and time-resolved cryo-EM, combined with genetic code expansion and long-MD, would shed more light on the challenges in the field.

AUTHOR CONTRIBUTIONS

HH: Conceptualization, Designing and illustrating the figures, Writing-original draft; ZH: Writing-review and editing; ZY: Conceptualization, Supervision, Writing-review and editing. All authors have read and agreed to the submitted version of the manuscript.

FUNDING

This work was supported by the National Natural Science Foundation of China (No. 32022073 and 31972287 to ZY), and the Natural Science Foundation of Tianjin (No. 19JCYBJC24500 to ZY).

REFERENCES

Ahern, G. P., Junankar, P. R., and Dulhunty, A. F. (1997). Subconductance States in Single-Channel Activity of Skeletal Muscle Ryanodine Receptors after Removal of FKBP12. *Biophys. J.* 72 (1), 146–162. doi:10.1016/S0006-3495(97)78654-5

Aiba, I., Wehrens, X. H., and Noebels, J. L. (2016). Leaky RyR2 Channels Unleash a Brainstem Spreading Depolarization Mechanism of Sudden Cardiac Death. *Proc. Natl. Acad. Sci. U. S. A.* 113 (33), E4895–E4903. doi:10.1073/pnas.1605216113

Albrecht, M. A., Colegrove, S. L., Hongpaisan, J., Pivovarova, N. B., Andrews, S. B., and Friel, D. D. (2001). Multiple Modes of Calcium-Induced Calcium Release in Sympathetic Neurons I: Attenuation of Endoplasmic Reticulum Ca2+ Accumulation at Low [Ca2+](i) during Weak Depolarization. *J. Gen. Physiol.* 118 (1), 83–100. doi:10.1085/jgp.118.1.83

Alvarado, F. J., Bos, J. M., Yuchi, Z., Valdivia, C. R., Hernández, J. J., Zhao, Y. T., et al. (2019). Cardiac Hypertrophy and Arrhythmia in Mice Induced by a Mutation in Ryanodine Receptor 2. *JCI insight* 5 (7). doi:10.1172/jci.insight.126544

Amador, F. J., Kimlicka, L., Stathopulos, P. B., Gasmi-Seabrook, G. M., MacLennan, D. H., Van Petegem, F., et al. (2013). Type 2 Ryanodine Receptor Domain A Contains a Unique and Dynamic α-helix that Transitions to a β-strand in a Mutant Linked with a Heritable Cardiomyopathy. *J. Mol. Biol.* 425 (21), 4034–4046. doi:10.1016/j.jmb.2013.08.015

Amador, F. J., Liu, S., Ishiyama, N., Plevin, M. J., Wilson, A., MacLennan, D. H., et al. (2009). Crystal Structure of Type I Ryanodine Receptor Amino-Terminal β-trefoil Domain Reveals a Disease-Associated Mutation "hot Spot" Loop. *Proc. Natl. Acad. Sci. U.S.A.* 106 (27), 11040–11044. doi:10.1073/pnas.0905186106

Amburgey, K., Bailey, A., Hwang, J. H., Tarnopolsky, M. A., Bonnemann, C. G., Medne, L., et al. (2013). Genotype-phenotype Correlations in Recessive RYR1-Related Myopathies. *Orphanet J. Rare Dis.* 8 (1), 117–212. doi:10.1186/1750-1172-8-117

Amburgey, K., McNamara, N., Bennett, L. R., McCormick, M. E., Acsadi, G., and Dowling, J. J. (2011). Prevalence of Congenital Myopathies in a Representative Pediatric united states Population. *Ann. Neurol.* 70 (4), 662–665. doi:10.1002/ana.22510

Andersson, D. C., Betzenhauser, M. J., Reiken, S., Meli, A. C., Umanskaya, A., Xie, W., et al. (2011). Ryanodine Receptor Oxidation Causes Intracellular Calcium Leak and Muscle Weakness in Aging. *Cell Metab.* 14 (2), 196–207. doi:10.1016/j.cmet.2011.05.014

Aracena, P., Tang, W., Hamilton, S. L., and Hidalgo, C. (2005). Effects of S-Glutathionylation and S-Nitrosylation on Calmodulin Binding to Triads and FKBP12 Binding to Type 1 Calcium Release Channels. *Antioxid. Redox Signal* 7 (7-8), 870–881. doi:10.1089/ars.2005.7.870

Aracena-Parks, P., Goonasekera, S. A., Gilman, C. P., Dirksen, R. T., Hidalgo, C., and Hamilton, S. L. (2006). Identification of Cysteines Involved in S-Nitrosylation, S-Glutathionylation, and Oxidation to Disulfides in Ryanodine Receptor Type 1. *J. Biol. Chem.* 281 (52), 40354–40368. doi:10.1074/jbc.M600876200

Arias-Cavieres, A., Barrientos, G. C., Sánchez, G., Elgueta, C., Muñoz, P., and Hidalgo, C. (2018). Ryanodine Receptor-Mediated Calcium Release Has a Key Role in Hippocampal Ltd Induction. *Front. Cell Neurosci.* 12, 403. doi:10.3389/fncel.2018.00403

Arvanitis, D. A., Vafiadaki, E., Johnson, D. M., Kranias, E. G., and Sanoudou, D. (2018). The Histidine-Rich Calcium Binding Protein in Regulation of Cardiac Rhythmicity. *Front. Physiol.* 9, 1379. doi:10.3389/fphys.2018.01379

Asghari, P., Scriven, D. R., Ng, M., Panwar, P., Chou, K. C., van Petegem, F., et al. (2020). Cardiac Ryanodine Receptor Distribution Is Dynamic and Changed by Auxiliary Proteins and Post-translational Modification. *Elife* 9, e51602. doi:10.7554/eLife.51602

Bagur, R., and Hajnóczky, G. (2017). Intracellular Ca2+ Sensing: its Role in Calcium Homeostasis and Signaling. *Mol. Cell* 66 (6), 780–788. doi:10.1016/j.molcel.2017.05.028

Bai, X. C., Yan, Z., Wu, J., Li, Z., and Yan, N. (2016). The Central Domain of RyR1 Is the Transducer for Long-Range Allosteric Gating of Channel Opening. *Cell Res.* 26 (9), 995–1006. doi:10.1038/cr.2016.89

Balog, E. M., Fruen, B. R., Shomer, N. H., and Louis, C. F. (2001). Divergent Effects of the Malignant Hyperthermia-Susceptible Arg(615)-->Cys Mutation on the Ca(2+) and Mg(2+) Dependence of the RyR1. *Biophys. J.* 81 (4), 2050–2058. doi:10.1016/S0006-3495(01)75854-7

Balshaw, D. M., Xu, L., Yamaguchi, N., Pasek, D. A., and Meissner, G. (2001). Calmodulin Binding and Inhibition of Cardiac Muscle Calcium Release Channel (Ryanodine Receptor). *J. Biol. Chem.* 276 (23), 20144–20153. doi:10.1074/jbc.M010771200

Batiste, S. M., Blackwell, D. J., Kim, K., Kryshtal, D. O., Gomez-Hurtado, N., Rebbeck, R. T., et al. (2019). Unnatural Verticilide Enantiomer Inhibits Type 2 Ryanodine Receptor-Mediated Calcium Leak and Is Antiarrhythmic. *Proc. Natl. Acad. Sci. U. S. A.* 116 (11), 4810–4815. doi:10.1073/pnas.1816685116

Beard, N. A., and Dulhunty, A. F. (2015). C-terminal Residues of Skeletal Muscle Calsequestrin Are Essential for Calcium Binding and for Skeletal Ryanodine Receptor Inhibition. *Skelet. Muscle* 5 (1), 6–12. doi:10.1186/s13395-015-0029-7

Bellinger, A. M., Reiken, S., Carlson, C., Mongillo, M., Liu, X., Rothman, L., et al. (2009). Hypernitrosylated Ryanodine Receptor Calcium Release Channels Are Leaky in Dystrophic Muscle. *Nat. Med.* 15 (3), 325–330. doi:10.1038/nm.1916

Bellinger, A. M., Reiken, S., Dura, M., Murphy, P. W., Deng, S. X., Landry, D. W., et al. (2008). Remodeling of Ryanodine Receptor Complex Causes "Leaky" Channels: a Molecular Mechanism for Decreased Exercise Capacity. *Proc. Natl. Acad. Sci. U. S. A.* 105 (6), 2198–2202. doi:10.1073/pnas.0711074105

Betzenhauser, M. J., and Marks, A. R. (2010). Ryanodine Receptor Channelopathies. *Pflugers Arch.* 460 (2), 467–480. doi:10.1007/s00424-010-0794-4

Bharucha-Goebel, D. X., Santi, M., Medne, L., Zukosky, K., Zukosky, K., Dastgir, J., et al. (2013). Severe Congenital RYR1-Associated Myopathy: the Expanding Clinicopathologic and Genetic Spectrum. *Neurology* 80 (17), 1584–1589. doi:10.1212/WNL.0b013e3182900380

Blayney, L. M., and Lai, F. A. (2009). Ryanodine Receptor-Mediated Arrhythmias and Sudden Cardiac Death. *Pharmacol. Ther.* 123 (2), 151–177. doi:10.1016/j.pharmthera.2009.03.006

Blunck, R., and Batulan, Z. (2012). Mechanism of Electromechanical Coupling in Voltage-Gated Potassium Channels. *Front. Pharmacol.* 3, 166. doi:10.3389/fphar.2012.00166

Böhm, J., Vasli, N., Malfatti, E., Le Gras, S., Feger, C., Jost, B., et al. (2013). An Integrated Diagnosis Strategy for Congenital Myopathies. *PLoS One* 8 (6), e67527. doi:10.1371/journal.pone.0067527

Borko, L., Bauerová-Hlinková, V., Hostinová, E., Gašperík, J., Beck, K., Lai, F. A., et al. (2014). Structural Insights into the Human RyR2 N-Terminal Region

Involved in Cardiac Arrhythmias. *Acta Crystallogr. D. Biol. Crystallogr.* 70 (11), 2897–2912. doi:10.1107/S1399004714020343

Bouchard, R., Pattarini, R., and Geiger, J. D. (2003). Presence and Functional Significance of Presynaptic Ryanodine Receptors. *Prog. Neurobiol.* 69 (6), 391–418. doi:10.1016/s0301-0082(03)00053-4

Chelu, M. G., Danila, C. I., Gilman, C. P., and Hamilton, S. L. (2004). Regulation of Ryanodine Receptors by FK506 Binding Proteins. *Trends Cardiovasc Med.* 14 (6), 227–234. doi:10.1016/j.tcm.2004.06.003

Chen, J., Xue, L., Wei, R., Liu, S., and Yin, C. C. (2019). The Insecticide Chlorantraniliprole Is a Weak Activator of Mammalian Skeletal Ryanodine receptor/Ca2+ Release Channel. *Biochem. Biophys. Res. Commun.* 508 (2), 633–639. doi:10.1016/j.bbrc.2018.11.180

Chen-Izu, Y., McCulle, S. L., Ward, C. W., Soeller, C., Allen, B. M., Rabang, C., et al. (2006). Three-dimensional Distribution of Ryanodine Receptor Clusters in Cardiac Myocytes. *Biophys. J.* 91 (1), 1–13. doi:10.1529/biophysj.105.077180

Chi, X., Gong, D., Ren, K., Zhou, G., Huang, G., Lei, J., et al. (2019). Molecular Basis for Allosteric Regulation of the Type 2 Ryanodine Receptor Channel Gating by Key Modulators. *Proc. Natl. Acad. Sci. U. S. A.* 116 (51), 25575–25582. doi:10.1073/pnas.1914451116

Chopra, N., Yang, T., Asghari, P., Moore, E. D., Huke, S., Akin, B., et al. (2009). Ablation of Triadin Causes Loss of Cardiac Ca2+ Release Units, Impaired Excitation-Contraction Coupling, and Cardiac Arrhythmias. *Proc. Natl. Acad. Sci. U. S. A.* 106 (18), 7636–7641. doi:10.1073/pnas.0902919106

Clapham, D. E. (1995). Calcium Signaling. *Cell* 80 (2), 259–268. doi:10.1016/0092-8674(95)90408-5

Denda, S., Kumamoto, J., Takei, K., Tsutsumi, M., Aoki, H., and Denda, M. (2012). Ryanodine Receptors Are Expressed in Epidermal Keratinocytes and Associated with Keratinocyte Differentiation and Epidermal Permeability Barrier Homeostasis. *J. Invest Dermatol* 132 (1), 69–75. doi:10.1038/jid.2011.256

Denniss, A., Dulhunty, A. F., Beard, N. A., and Biology, C. (2018). Ryanodine Receptor Ca2+ Release Channel Post-translational Modification: Central Player in Cardiac and Skeletal Muscle Disease. *Int. J. Biochem. Cell Biol.* 101, 49–53. doi:10.1016/j.biocel.2018.05.004

des Georges, A., Clarke, O. B., Zalk, R., Yuan, Q., Condon, K. J., Grassucci, R. A., et al. (2016). Structural Basis for Gating and Activation of RyR1. *Cell* 167 (1), 145–e17. e117. doi:10.1016/j.cell.2016.08.075

Diszházi, G., Magyar, Z. É., Mótyán, J. A., Csernoch, L., Jóna, I., Nánási, P. P., et al. (2019). Dantrolene Requires Mg2+ and ATP to Inhibit the Ryanodine Receptor. *Mol. Pharmacol.* 96 (3), 401–407. doi:10.1124/mol.119.116475

Dulhunty, A., Haarmann, C., Green, D., and Hart, J. (2000). How Many Cysteine Residues Regulate Ryanodine Receptor Channel Activity? *Antioxid. Redox Signal* 2 (1), 27–34. doi:10.1089/ars.2000.2.1-27

Dulhunty, A. F., Laver, D., Curtis, S. M., Pace, S., Haarmann, C., and Gallant, E. M. (2001). Characteristics of Irreversible ATP Activation Suggest that Native Skeletal Ryanodine Receptors Can Be Phosphorylated via an Endogenous CaMKII. *Biophys. J.* 81 (6), 3240–3252. doi:10.1016/S0006-3495(01)75959-0

Echt, D. S., Liebson, P. R., Mitchell, L. B., Peters, R. W., Obias-Manno, D., Barker, A. H., et al. (1991). Mortality and Morbidity in Patients Receiving Encainide, Flecainide, or Placebo. The Cardiac Arrhythmia Suppression Trial. *N. Engl. J. Med.* 324 (12), 781–788. doi:10.1056/NEJM199103213241201

Efremov, R. G., Leitner, A., Aebersold, R., and Raunser, S. (2015). Architecture and Conformational Switch Mechanism of the Ryanodine Receptor. *Nature* 517 (7532), 39–43. doi:10.1038/nature13916

Estève, E., Smida-Rezgui, S., Sarkozi, S., Szegedi, C., Regaya, I., Chen, L., et al. (2003). Critical Amino Acid Residues Determine the Binding Affinity and the Ca2+ Release Efficacy of Maurocalcine in Skeletal Muscle Cells. *J. Biol. Chem.* 278 (39), 37822–37831. doi:10.1074/jbc.M305798200

Fauconnier, J., Thireau, J., Reiken, S., Cassan, C., Richard, S., Matecki, S., et al. (2010). Leaky RyR2 Trigger Ventricular Arrhythmias in Duchenne Muscular Dystrophy. *Proc. Natl. Acad. Sci. U. S. A.* 107 (4), 1559–1564. doi:10.1073/pnas.0908540107

Fernández-Morales, J.-C., Xia, Y., Renzo, T. J., Zhang, X.-H., and Morad, M. (2022). Mutation in RyR2-FKBP Binding Site Alters Ca2+ Signaling Modestly but Increases "arrhythmogenesis" in Human Stem Cells Derived Cardiomyocytes. *Cell Calcium* 101, 102500. doi:10.1016/j.ceca.2021.102500

Fessenden, J. D., Chen, L., Wang, Y., Paolini, C., Franzini-Armstrong, C., Allen, P. D., et al. (2001). Ryanodine Receptor Point Mutant E4032A Reveals an Allosteric Interaction with Ryanodine. *Proc. Natl. Acad. Sci. U. S. A.* 98 (5), 2865–2870. doi:10.1073/pnas.041608898

Flucher, B. E., and Franzini-Armstrong, C. (1996). Formation of Junctions Involved in Excitation-Contraction Coupling in Skeletal and Cardiac Muscle. *Proc. Natl. Acad. Sci. U. S. A.* 93 (15), 8101–8106. doi:10.1073/pnas.93.15.8101

Fruen, B. R., Bardy, J. M., Byrem, T. M., Strasburg, G. M., and Louis, C. F. (2000). Differential Ca(2+) Sensitivity of Skeletal and Cardiac Muscle Ryanodine Receptors in the Presence of Calmodulin. *Am. J. Physiol. Cell Physiol.* 279 (3), C724–C733. doi:10.1152/ajpcell.2000.279.3.C724

FuJII, J., Otsu, K., Zorzato, F., De Leon, S., Khanna, V. K., Weiler, J. E., et al. (1991). Identification of a Mutation in Porcine Ryanodine Receptor Associated with Malignant Hyperthermia. *Science* 253 (5018), 448–451. doi:10.1126/science.1862346

Galfré, E., Pitt, S. J., Venturi, E., Sitsapesan, M., Zaccai, N. R., Tsaneva-Atanasova, K., et al. (2012). FKBP12 Activates the Cardiac Ryanodine Receptor Ca2+-Release Channel and Is Antagonised by FKBP12.6. *PloS one* 7 (2), e31956. doi:10.1371/journal.pone.0031956

Gangopadhyay, J. P., and Ikemoto, N. (2006). Role of the Met3534-Ala4271 Region of the Ryanodine Receptor in the Regulation of Ca2+ Release Induced by Calmodulin Binding Domain Peptide. *Biophys. J.* 90 (6), 2015–2026. doi:10.1529/biophysj.105.074328

Giannini, G., Conti, A., Mammarella, S., Scrobogna, M., and Sorrentino, V. (1995). The Ryanodine Receptor/calcium Channel Genes Are Widely and Differentially Expressed in Murine Brain and Peripheral Tissues. *J. Cell Biol.* 128 (5), 893–904. doi:10.1083/jcb.128.5.893

Gillard, E. F., Otsu, K., Fujii, J., Khanna, V. K., de Leon, S., Derdemezi, J., et al. (1991). A Substitution of Cysteine for Arginine 614 in the Ryanodine Receptor Is Potentially Causative of Human Malignant Hyperthermia. *Genomics* 11 (3), 751–755. doi:10.1016/0888-7543(91)90084-r

Gomez, A. C., and Yamaguchi, N. (2014). Two Regions of the Ryanodine Receptor Calcium Channel Are Involved in Ca(2+)-dependent Inactivation. *Biochemistry* 53 (8), 1373–1379. doi:10.1021/bi401586h

Gómez, A. M., Schuster, I., Fauconnier, J., Prestle, J., Hasenfuss, G., and Richard, S. (2004). FKBP12.6 Overexpression Decreases Ca2+ Spark Amplitude but Enhances [Ca2+]i Transient in Rat Cardiac Myocytes. *Am. J. Physiol. Heart Circ. Physiol.* 287 (5), H1987–H1993. doi:10.1152/ajpheart.00409.2004

Gong, D., Chi, X., Wei, J., Zhou, G., Huang, G., Zhang, L., et al. (2019). Modulation of Cardiac Ryanodine Receptor 2 by Calmodulin. *Nature* 572 (7769), 347–351. doi:10.1038/s41586-019-1377-y

Gong, D., Yan, N., and Ledford, H. A. (2021). Structural Basis for the Modulation of Ryanodine Receptors. *Trends Biochem. Sci.* 46 (6), 489–501. doi:10.1016/j.tibs.2020.11.009

Gong, S., Su, B. B., Tovar, H., Mao, C., Gonzalez, V., Liu, Y., et al. (2018). Polymorphisms within RYR3 Gene Are Associated with Risk and Age at Onset of Hypertension, Diabetes, and Alzheimer's Disease. *Am. J. Hypertens.* 31 (7), 818–826. doi:10.1093/ajh/hpy046

Gonzalez, D. R., Treuer, A. V., Castellanos, J., Dulce, R. A., and Hare, J. M. (2010). Impaired S-Nitrosylation of the Ryanodine Receptor Caused by Xanthine Oxidase Activity Contributes to Calcium Leak in Heart Failure. *J. Biol. Chem.* 285 (37), 28938–28945. doi:10.1074/jbc.M110.154948

Guo, T., Cornea, R. L., Huke, S., Camors, E., Yang, Y., Picht, E., et al. (2010). Kinetics of FKBP12.6 Binding to Ryanodine Receptors in Permeabilized Cardiac Myocytes and Effects on Ca Sparks. *Circ. Res.* 106 (11), 1743–1752. doi:10.1161/CIRCRESAHA.110.219816

Gurrola, G. B., Capes, E. M., Zamudio, F. Z., Possani, L. D., and Valdivia, H. H. (2010). Imperatoxin A, a Cell-Penetrating Peptide from Scorpion Venom, as a Probe of Ca-Release Channels/Ryanodine Receptors. *Pharm. (Basel)* 3 (4), 1093–1107. doi:10.3390/ph3041093

Gusev, K., and Niggli, E. (2008). Modulation of the Local SR Ca2+ Release by Intracellular Mg2+ in Cardiac Myocytes. *J. Gen. Physiol.* 132 (6), 721–730. doi:10.1085/jgp.200810119

Haji-Ghassemi, O., Yuchi, Z., and Van Petegem, F. (2019). The Cardiac Ryanodine Receptor Phosphorylation Hotspot Embraces PKA in a Phosphorylation-dependent Manner. *Mol. Cell* 75 (1), 39–e4. e34. doi:10.1016/j.molcel.2019.04.019

Hakamata, Y., Nakai, J., Takeshima, H., and Imoto, K. (1992). Primary Structure and Distribution of a Novel Ryanodine Receptor/calcium Release Channel from

Rabbit Brain. *FEBS Lett.* 312 (2-3), 229–235. doi:10.1016/0014-5793(92)80941-9

Hiess, F., Detampel, P., Nolla-Colomer, C., Vallmitjana, A., Ganguly, A., Amrein, M., et al. (2018). Dynamic and Irregular Distribution of RyR2 Clusters in the Periphery of Live Ventricular Myocytes. *Biophys. J.* 114 (2), 343–354. doi:10.1016/j.bpj.2017.11.026

Hilliard, F. A., Steele, D. S., Laver, D., Yang, Z., Le Marchand, S. J., Chopra, N., et al. (2010). Flecainide Inhibits Arrhythmogenic Ca2+ Waves by Open State Block of Ryanodine Receptor Ca2+ Release Channels and Reduction of Ca2+ Spark Mass. *J. Mol. Cell Cardiol.* 48 (2), 293–301. doi:10.1016/j.yjmcc.2009.10.005

Holt, C., Hamborg, L., Lau, K., Brohus, M., Sørensen, A. B., Larsen, K. T., et al. (2020). The Arrhythmogenic N53I Variant Subtly Changes the Structure and Dynamics in the Calmodulin N-Terminal Domain, Altering its Interaction with the Cardiac Ryanodine Receptor. *J. Biol. Chem.* 295 (22), 7620–7634. doi:10.1074/jbc.RA120.013430

Hou, Y., Jayasinghe, I., Crossman, D. J., Baddeley, D., and Soeller, C. (2015). Nanoscale Analysis of Ryanodine Receptor Clusters in Dyadic Couplings of Rat Cardiac Myocytes. *J. Mol. Cell Cardiol.* 80, 45–55. doi:10.1016/j.yjmcc.2014.12.013

Huang, X., Fruen, B., Farrington, D. T., Wagenknecht, T., and Liu, Z. (2012). Calmodulin-binding Locations on the Skeletal and Cardiac Ryanodine Receptors. *J. Biol. Chem.* 287 (36), 30328–30335. doi:10.1074/jbc.M112.383109

Hwang, H. S., Hasdemir, C., Laver, D., Mehra, D., Turhan, K., Faggioni, M., et al. (2011). Inhibition of Cardiac Ca2+ Release Channels (RyR2) Determines Efficacy of Class I Antiarrhythmic Drugs in Catecholaminergic Polymorphic Ventricular Tachycardia. *Circ. Arrhythm. Electrophysiol.* 4 (2), 128–135. doi:10.1161/CIRCEP.110.959916

Ikemoto, N., and Yamamoto, T. (2002). Regulation of Calcium Release by Interdomain Interaction within Ryanodine Receptors. *Front. Biosci.* 7, d671–83. doi:10.2741/A803

Itoh, H., Murayama, T., Kurebayashi, N., Ohno, S., Kobayashi, T., Fujii, Y., et al. (2021). Sudden Death after Inappropriate Shocks of Implantable Cardioverter Defibrillator in a Catecholaminergic Polymorphic Ventricular Tachycardia Case with a Novel RyR2 Mutation. *J. Electrocardiol.* 69, 111–118. doi:10.1016/j.jelectrocard.2021.09.015

Iyer, K. A., Hu, Y., Nayak, A. R., Kurebayashi, N., Murayama, T., and Samsó, M. (2020). Structural Mechanism of Two Gain-Of-Function Cardiac and Skeletal RyR Mutations at an Equivalent Site by Cryo-EM. *Sci. Adv.* 6 (31), eabb2964. doi:10.1126/sciadv.abb2964

Jungbluth, H., Treves, S., Zorzato, F., Sarkozy, A., Ochala, J., Sewry, C., et al. (2018). Congenital Myopathies: Disorders of Excitation-Contraction Coupling and Muscle Contraction. *Nat. Rev. Neurol.* 14 (3), 151–167. doi:10.1038/nrneurol.2017.191

Kaneko, N., Matsuda, R., Hata, Y., and Shimamoto, K. (2009). Pharmacological Characteristics and Clinical Applications of K201. *Curr. Clin. Pharmacol.* 4 (2), 126–131. doi:10.2174/157488409788184972

Kawakami, M., and Okabe, E. (1998). Superoxide Anion Radical-Triggered Ca2+ Release from Cardiac Sarcoplasmic Reticulum through Ryanodine Receptor Ca2+ Channel. *Mol. Pharmacol.* 53 (3), 497–503. doi:10.1124/mol.53.3.497

Kermode, H., Williams, A. J., and Sitsapesan, R. (1998). The Interactions of ATP, ADP, and Inorganic Phosphate with the Sheep Cardiac Ryanodine Receptor. *Biophys. J.* 74 (3), 1296–1304. doi:10.1016/S0006-3495(98)77843-9

Kimlicka, L., Lau, K., Tung, C. C., and Van Petegem, F. (2013a). Disease Mutations in the Ryanodine Receptor N-Terminal Region Couple to a Mobile Intersubunit Interface. *Nat. Commun.* 4 (1), 1506–1510. doi:10.1038/ncomms2501

Kimlicka, L., Tung, C. C., Carlsson, A. C., Lobo, P. A., Yuchi, Z., and Van Petegem, F. (2013b). The Cardiac Ryanodine Receptor N-Terminal Region Contains an Anion Binding Site that Is Targeted by Disease Mutations. *Structure* 21 (8), 1440–1449. doi:10.1016/j.str.2013.06.012

Klipp, R. C., Li, N., Wang, Q., Word, T. A., Sibrian-Vazquez, M., Strongin, R. M., et al. (2018). EL20, a Potent Antiarrhythmic Compound, Selectively Inhibits Calmodulin-Deficient Ryanodine Receptor Type 2. *Heart rhythm.* 15 (4), 578–586. doi:10.1016/j.hrthm.2017.12.017

Kobayashi, S., Bannister, M. L., Gangopadhyay, J. P., Hamada, T., Parness, J., and Ikemoto, N. (2005). Dantrolene Stabilizes Domain Interactions within the Ryanodine Receptor. *J. Biol. Chem.* 280 (8), 6580–6587. doi:10.1074/jbc.M408375200

Kobayashi, S., Yano, M., Suetomi, T., Ono, M., Tateishi, H., Mochizuki, M., et al. (2009). Dantrolene, a Therapeutic Agent for Malignant Hyperthermia, Markedly Improves the Function of Failing Cardiomyocytes by Stabilizing Interdomain Interactions within the Ryanodine Receptor. *J. Am. Coll. Cardiol.* 53 (21), 1993–2005. doi:10.1016/j.jacc.2009.01.065

Kobylewski, S. E., Henderson, K. A., and Eckhert, C. D. (2012). Identification of Ryanodine Receptor Isoforms in Prostate DU-145, LNCaP, and PWR-1E Cells. *Biochem. Biophys. Res. Commun.* 425 (2), 431–435. doi:10.1016/j.bbrc.2012.07.119

Lai, F. A., Misra, M., Xu, L., Smith, H. A., and Meissner, G. (1989). The Ryanodine Receptor-Ca2+ Release Channel Complex of Skeletal Muscle Sarcoplasmic Reticulum. Evidence for a Cooperatively Coupled, Negatively Charged Homotetramer. *J. Biol. Chem.* 264 (28), 16776–16785. doi:10.1016/s0021-9258(19)84773-7

Laitinen, P. J., Brown, K. M., Piippo, K., Swan, H., Devaney, J. M., Brahmbhatt, B., et al. (2001). Mutations of the Cardiac Ryanodine Receptor (RyR2) Gene in Familial Polymorphic Ventricular Tachycardia. *Circulation* 103 (4), 485–490. doi:10.1161/01.cir.103.4.485

Lanner, J. T., Georgiou, D. K., Joshi, A. D., and Hamilton, S. L. (2010). Ryanodine Receptors: Structure, Expression, Molecular Details, and Function in Calcium Release. *Cold Spring Harb. Perspect. Biol.* 2 (11), a003996. doi:10.1101/cshperspect.a003996

Lau, K., and Van Petegem, F. (2014). Crystal Structures of Wild Type and Disease Mutant Forms of the Ryanodine Receptor SPRY2 Domain. *Nat. Commun.* 5 (1), 5397–5411. doi:10.1038/ncomms6397

Laver, D. R., and Honen, B. N. (2008). Luminal Mg2+, a Key Factor Controlling RYR2-Mediated Ca2+ Release: Cytoplasmic and Luminal Regulation Modeled in a Tetrameric Channel. *J. Gen. Physiol.* 132 (4), 429–446. doi:10.1085/jgp.200810001

Laver, D. R., Lenz, G. K., and Lamb, G. D. (2001). Regulation of the Calcium Release Channel from Rabbit Skeletal Muscle by the Nucleotides ATP, AMP, IMP and Adenosine. *J. Physiol.* 537 (3), 763–778. doi:10.1111/j.1469-7793.2001.00763.x

Laver, D. R. (2018). Regulation of the RyR Channel Gating by Ca2+ and Mg2. *Biophys. Rev.* 10 (4), 1087–1095. doi:10.1007/s12551-018-0433-4

Lehnart, S. E., Mongillo, M., Bellinger, A., Lindegger, N., Chen, B. X., Hsueh, W., et al. (2008). Leaky Ca2+ Release Channel/ryanodine Receptor 2 Causes Seizures and Sudden Cardiac Death in Mice. *J. Clin. Invest* 118 (6), 2230–2245. doi:10.1172/JCI35346

Levano, S., Vukcevic, M., Singer, M., Matter, A., Treves, S., Urwyler, A., et al. (2009). Increasing the Number of Diagnostic Mutations in Malignant Hyperthermia. *Hum. Mutat.* 30 (4), 590–598. doi:10.1002/humu.20878

Li, L., Mirza, S., Richardson, S. J., Gallant, E. M., Thekkedam, C., Pace, S. M., et al. (2015). A New Cytoplasmic Interaction between Junctin and Ryanodine Receptor Ca2+ Release Channels. *J. Cell Sci.* 128 (5), 951–963. doi:10.1242/jcs.160689

Li, N., Wang, Q., Sibrian-Vazquez, M., Klipp, R. C., Reynolds, J. O., Word, T. A., et al. (2017). Treatment of Catecholaminergic Polymorphic Ventricular Tachycardia in Mice Using Novel RyR2-Modifying Drugs. *Int. J. Cardiol.* 227, 668–673. doi:10.1016/j.ijcard.2016.10.078

Lin, C. C., Baek, K., and Lu, Z. (2011). Apo and InsP₃-Bound Crystal Structures of the Ligand-Binding Domain of an InsP₃ Receptor. *Nat. Struct. Mol. Biol.* 18 (10), 1172–1174. doi:10.1038/nsmb.2112

Lin, L., Liu, C., Qin, J., Wang, J., Dong, S., Chen, W., et al. (2018). Crystal Structure of Ryanodine Receptor N-Terminal Domain from Plutella Xylostella Reveals Two Potential Species-specific Insecticide-Targeting Sites. *Insect Biochem. Mol. Biol.* 92, 73–83. doi:10.1016/j.ibmb.2017.11.009

Liu, Z., Liu, L., Jiao, D., Guo, C., Wang, L., Li, Z., et al. (2021). Association of RYR2 Mutation with Tumor Mutation Burden, Prognosis, and Antitumor Immunity in Patients with Esophageal Adenocarcinoma. *Front. Genet.* 12, 651. doi:10.3389/fgene.2021.669694

Lobo, P. A., and Van Petegem, F. (2009). Crystal Structures of the N-Terminal Domains of Cardiac and Skeletal Muscle Ryanodine Receptors: Insights into Disease Mutations. *Structure* 17 (11), 1505–1514. doi:10.1016/j.str.2009.08.016

Lu, H., Chen, I., Shimoda, L. A., Park, Y., Zhang, C., Tran, L., et al. (2017). Chemotherapy-induced Ca2+ Release Stimulates Breast Cancer Stem Cell Enrichment. *Cell Rep.* 18 (8), 1946–1957. doi:10.1016/j.celrep.2017.02.001

Ludtke, S. J., and Serysheva, I. I. (2013). Single-particle Cryo-EM of Calcium Release Channels: Structural Validation. *Curr. Opin. Struct. Biol.* 23 (5), 755–762. doi:10.1016/j.sbi.2013.06.003

Ma, R., Haji-Ghassemi, O., Ma, D., Jiang, H., Lin, L., Yao, L., et al. (2020). Structural Basis for Diamide Modulation of Ryanodine Receptor. *Nat. Chem. Biol.* 16 (11), 1246–1254. doi:10.1038/s41589-020-0627-5

MacMillan, D. (2013). FK506 Binding Proteins: Cellular Regulators of Intracellular Ca2+ Signalling. *Eur. J. Pharmacol.* 700 (1-3), 181–193. doi:10.1016/j.ejphar.2012.12.029

Macquaide, N., Tuan, H. T., Hotta, J., Sempels, W., Lenaerts, I., Holemans, P., et al. (2015). Ryanodine Receptor Cluster Fragmentation and Redistribution in Persistent Atrial Fibrillation Enhance Calcium Release. *Cardiovasc Res.* 108 (3), 387–398. doi:10.1093/cvr/cvv231

Marjamaa, A., Laitinen-Forsblom, P., Lahtinen, A. M., Viitasalo, M., Toivonen, L., Kontula, K., et al. (2009). Search for Cardiac Calcium Cycling Gene Mutations in Familial Ventricular Arrhythmias Resembling Catecholaminergic Polymorphic Ventricular Tachycardia. *BMC Med. Genet.* 10 (1), 12–19. doi:10.1186/1471-2350-10-12

Marx, S. O., Reiken, S., Hisamatsu, Y., Gaburjakova, M., Gaburjakova, J., Yang, Y. M., et al. (2001). Phosphorylation-dependent Regulation of Ryanodine Receptors: a Novel Role for Leucine/isoleucine Zippers. *J. Cell Biol.* 153 (4), 699–708. doi:10.1083/jcb.153.4.699

Marx, S. O., Reiken, S., Hisamatsu, Y., Jayaraman, T., Burkhoff, D., Rosemblit, N., et al. (2000). PKA Phosphorylation Dissociates FKBP12.6 from the Calcium Release Channel (Ryanodine Receptor): Defective Regulation in Failing Hearts. *Cell* 101 (4), 365–376. doi:10.1016/s0092-8674(00)80847-8

Maximciuc, A. A., Putkey, J. A., Shamoo, Y., and MacKenzie, K. R. (2006). Complex of Calmodulin with a Ryanodine Receptor Target Reveals a Novel, Flexible Binding Mode. *Structure* 14 (10), 1547–1556. doi:10.1016/j.str.2006.08.011

Medeiros-Domingo, A., Bhuiyan, Z. A., Tester, D. J., Hofman, N., Bikker, H., van Tintelen, J. P., et al. (2009). The RYR2-Encoded Ryanodine Receptor/calcium Release Channel in Patients Diagnosed Previously with Either Catecholaminergic Polymorphic Ventricular Tachycardia or Genotype Negative, Exercise-Induced Long QT Syndrome: a Comprehensive Open Reading Frame Mutational Analysis. *J. Am. Coll. Cardiol.* 54 (22), 2065–2074. doi:10.1016/j.jacc.2009.08.022

Meissner, G. (1986). Ryanodine Activation and Inhibition of the Ca2+ Release Channel of Sarcoplasmic Reticulum. *J. Biol. Chem.* 261 (14), 6300–6306. doi:10.1016/s0021-9258(19)84563-5

Meissner, G. (2017). The Structural Basis of Ryanodine Receptor Ion Channel Function. *J. Gen. Physiol.* 149 (12), 1065–1089. doi:10.1085/jgp.201711878

Meyers, M. B., Pickel, V. M., Sheu, S. S., Sharma, V. K., Scotto, K. W., and Fishman, G. I. (1995). Association of Sorcin with the Cardiac Ryanodine Receptor. *J. Biol. Chem.* 270 (44), 26411–26418. doi:10.1074/jbc.270.44.26411

Mori, S., Iinuma, H., Manaka, N., Ishigami-Yuasa, M., Murayama, T., Nishijima, Y., et al. (2019). Structural Development of a Type-1 Ryanodine Receptor (RyR1) Ca2+-Release Channel Inhibitor Guided by Endoplasmic Reticulum Ca2+ Assay. *Eur. J. Med. Chem.* 179, 837–848. doi:10.1016/j.ejmech.2019.06.076

Munro, M. L., Jayasinghe, I. D., Wang, Q., Quick, A., Wang, W., Baddeley, D., et al. (2016). Junctophilin-2 in the Nanoscale Organisation and Functional Signalling of Ryanodine Receptor Clusters in Cardiomyocytes. *J. Cell Sci.* 129 (23), 4388–4398. doi:10.1242/jcs.196873

Murayama, T., and Kurebayashi, N. (2019). Assays for Modulators of Ryanodine Receptor (RyR)/Ca2+ Release Channel Activity for Drug Discovery for Skeletal Muscle and Heart Diseases. *Curr. Protoc. Pharmacol.* 87 (1), e71. doi:10.1002/cpph.71

Murayama, T., Kurebayashi, N., Ishigami-Yuasa, M., Mori, S., Suzuki, Y., Akima, R., et al. (2018a). Efficient High-Throughput Screening by Endoplasmic Reticulum Ca2+ Measurement to Identify Inhibitors of Ryanodine Receptor Ca2+-Release Channels. *Mol. Pharmacol.* 94 (1), 722–730. doi:10.1124/mol.117.111468

Murayama, T., Ogawa, H., Kurebayashi, N., Ohno, S., Horie, M., and Sakurai, T. (2018b). A Tryptophan Residue in the Caffeine-Binding Site of the Ryanodine Receptor Regulates Ca2+ Sensitivity. *Commun. Biol.* 1 (1), 98–12. doi:10.1038/s42003-018-0103-x

Nakamura, Y., Yamamoto, T., Kobayashi, S., Tamitani, M., Hamada, Y., Fukui, G., et al. (2019). Ryanodine Receptor-Bound Calmodulin Is Essential to Protect against Catecholaminergic Polymorphic Ventricular Tachycardia. *JCI insight* 4 (11). doi:10.1172/jci.insight.126112

Nauen, R., and Steinbach, D. (2016). “Resistance to Diamide Insecticides in Lepidopteran Pests,” in *Advances in Insect Control and Resistance Management* (Springer), 219–240. doi:10.1007/978-3-319-31800-4_12

Oda, T., Yang, Y., Uchinoumi, H., Thomas, D. D., Chen-Izu, Y., Kato, T., et al. (2015). Oxidation of Ryanodine Receptor (RyR) and Calmodulin Enhance Ca Release and Pathologically Alter, RyR Structure and Calmodulin Affinity. *J. Mol. Cell Cardiol.* 85, 240–248. doi:10.1016/j.yjmcc.2015.06.009

Ogawa, H., Kurebayashi, N., Yamazawa, T., and Murayama, T. (2021). Regulatory Mechanisms of Ryanodine receptor/Ca2+ Release Channel Revealed by Recent Advancements in Structural Studies. *J. Muscle Res. Cell Motil.* 42 (2), 291–304. doi:10.1007/s10974-020-09575-6

Oo, Y. W., Gomez-Hurtado, N., Walweel, K., van Helden, D. F., Imtiaz, M. S., Knollmann, B. C., et al. (2015). Essential Role of Calmodulin in RyR Inhibition by Dantrolene. *Mol. Pharmacol.* 88 (1), 57–63. doi:10.1124/mol.115.097691

Otsu, K., Willard, H. F., Khanna, V. K., Zorzato, F., Green, N. M., and MacLennan, D. H. (1990). Molecular Cloning of cDNA Encoding the Ca2+ Release Channel (Ryanodine Receptor) of Rabbit Cardiac Muscle Sarcoplasmic Reticulum. *J. Biol. Chem.* 265 (23), 13472–13483. doi:10.1016/s0021-9258(18)77371-7

Ottini, L., Marziali, G., Conti, A., Charlesworth, A., and Sorrentino, V. (1996). Alpha and Beta Isoforms of Ryanodine Receptor from Chicken Skeletal Muscle Are the Homologues of Mammalian RyR1 and RyR3. *Biochem. J.* 315 (Pt 1) (1), 207–216. doi:10.1042/bj3150207

Paul-Pletzer, K., Palnitkar, S. S., Jimenez, L. S., Morimoto, H., and Parness, J. (2001). The Skeletal Muscle Ryanodine Receptor Identified as a Molecular Target of [3H]azidodantrolene by Photoaffinity Labeling. *Biochemistry* 40 (2), 531–542. doi:10.1021/bi001502s

Paul-Pletzer, K., Yamamoto, T., Bhat, M. B., Ma, J., Ikemoto, N., Jimenez, L. S., et al. (2002). Identification of a Dantrolene-Binding Sequence on the Skeletal Muscle Ryanodine Receptor. *J. Biol. Chem.* 277 (38), 34918–34923. doi:10.1074/jbc.M205487200

Paul-Pletzer, K., Yamamoto, T., Ikemoto, N., Jimenez, L. S., Morimoto, H., Williams, P. G., et al. (2005). Probing a Putative Dantrolene-Binding Site on the Cardiac Ryanodine Receptor. *Biochem. J.* 387 (3), 905–909. doi:10.1042/BJ20041336

Peng, W., Shen, H., Wu, J., Guo, W., Pan, X., Wang, R., et al. (2016). Structural Basis for the Gating Mechanism of the Type 2 Ryanodine Receptor RyR2. *Science* 354 (6310). doi:10.1126/science.aah5324

Perez, C. F., Mukherjee, S., and Allen, P. D. (2003). Amino Acids 1-1,680 of Ryanodine Receptor Type 1 Hold Critical Determinants of Skeletal Type for Excitation-Contraction Coupling. Role of Divergence Domain D2. *J. Biol. Chem.* 278 (41), 39644–39652. doi:10.1074/jbc.M305160200

Perni, S., Lavorato, M., and Beam, K. G. (2017). De Novo reconstitution Reveals the Proteins Required for Skeletal Muscle Voltage-Induced Ca2+ Release. *Proc. Natl. Acad. Sci. U. S. A.* 114 (52), 13822–13827. doi:10.1073/pnas.1716461115

Pessah, I. N., Waterhouse, A. L., and Casida, J. E. (1985). The Calcium-Ryanodine Receptor Complex of Skeletal and Cardiac Muscle. *Biochem. Biophys. Res. Commun.* 128 (1), 449–456. doi:10.1016/0006-291x(85)91699-7

Pessah, I. N., and Zimanyi, I. (1991). Characterization of Multiple [3H]ryanodine Binding Sites on the Ca2+ Release Channel of Sarcoplasmic Reticulum from Skeletal and Cardiac Muscle: Evidence for a Sequential Mechanism in Ryanodine Action. *Mol. Pharmacol.* 39 (5), 679–689.

Polster, A., Nelson, B. R., Papadopoulos, S., Olson, E. N., and Beam, K. G. (2018). Stac Proteins Associate with the Critical Domain for Excitation-Contraction Coupling in the II-III Loop of CaV1.1. *J. Gen. Physiol.* 150 (4), 613–624. doi:10.1085/jgp.201711917

Pouliquin, P., and Dulhunty, A. F. (2009). Homer and the Ryanodine Receptor. *Eur. Biophys. J.* 39 (1), 91–102. doi:10.1007/s00249-009-0494-1

Priori, S. G., Napolitano, C., Tiso, N., Memmi, M., Vignati, G., Bloise, R., et al. (2001). Mutations in the Cardiac Ryanodine Receptor Gene (hRyR2) Underlie Catecholaminergic Polymorphic Ventricular Tachycardia. *Circulation* 103 (2), 196–200. doi:10.1161/01.cir.103.2.196

Protasi, F., Franzini-Armstrong, C., and Flucher, B. E. (1997). Coordinated Incorporation of Skeletal Muscle Dihydropyridine Receptors and Ryanodine

Receptors in Peripheral Couplings of BC3H1 Cells. *J. Cell Biol.* 137 (4), 859–870. doi:10.1083/jcb.137.4.859

Radermacher, M., Rao, V., Grassucci, R., Frank, J., Timerman, A. P., Fleischer, S., et al. (1994). Cryo-electron Microscopy and Three-Dimensional Reconstruction of the Calcium Release Channel/ryanodine Receptor from Skeletal Muscle. *J. Cell Biol.* 127 (2), 411–423. doi:10.1083/jcb.127.2.411

Ran, Y., Chen, J., Li, N., Zhang, W., Feng, L., Wang, R., et al. (2010). Common RyR2 Variants Associate with Ventricular Arrhythmias and Sudden Cardiac Death in Chronic Heart Failure. *Clin. Sci. (Lond)* 119 (5), 215–223. doi:10.1042/CS20090656

Rebbeck, R. T., Essawy, M. M., Nitu, F. R., Grant, B. D., Gillispie, G. D., Thomas, D. D., et al. (2017). High-throughput Screens to Discover Small-Molecule Modulators of Ryanodine Receptor Calcium Release Channels. *SLAS Discov.* 22 (2), 176–186. doi:10.1177/1087057116674312

Rebbeck, R. T., Nitu, F. R., Rohde, D., Most, P., Bers, D. M., Thomas, D. D., et al. (2016). S100A1 Protein Does Not Compete with Calmodulin for Ryanodine Receptor Binding but Structurally Alters the Ryanodine Receptor·Calmodulin Complex. *J. Biol. Chem.* 291 (30), 15896–15907. doi:10.1074/jbc.M115.713107

Rebbeck, R. T., Singh, D. P., Janicek, K. A., Bers, D. M., Thomas, D. D., Launikonis, B. S., et al. (2020). RyR1-targeted Drug Discovery Pipeline Integrating FRET-Based High-Throughput Screening and Human Myofiber Dynamic Ca2+ Assays. *Sci. Rep.* 10 (1), 1791–1813. doi:10.1038/s41598-020-58461-1

Ríos, E. (2018). Calcium-induced Release of Calcium in Muscle: 50 Years of Work and the Emerging Consensus. *J. Gen. Physiol.* 150 (4), 521–537. doi:10.1085/jgp.201711959

Roditakis, E., Steinbach, D., Moritz, G., Vasakis, E., Stavrakaki, M., Ilias, A., et al. (2017). Ryanodine Receptor Point Mutations Confer Diamide Insecticide Resistance in Tomato Leafminer, Tuta Absoluta (Lepidoptera: Gelechiidae). *Insect Biochem. Mol. Biol.* 80, 11–20. doi:10.1016/j.ibmb.2016.11.003

Roston, T. M., Yuchi, Z., Kannankeril, P. J., Hathaway, J., Vinocur, J. M., Etheridge, S. P., et al. (2018). The Clinical and Genetic Spectrum of Catecholaminergic Polymorphic Ventricular Tachycardia: Findings from an International Multicentre Registry. *Europace* 20 (3), 541–547. doi:10.1093/europace/euw389

Rufenach, B., Christy, D., Flucher, B. E., Bui, J. M., Gsponer, J., Campiglio, M., et al. (2020). Multiple Sequence Variants in STAC3 Affect Interactions with CaV1.1 and Excitation-Contraction Coupling. *Structure* 28 (8), 922–e5. e925. doi:10.1016/j.str.2020.05.005

Samsó, M., Feng, W., Pessah, I. N., and Allen, P. D. (2009). Coordinated Movement of Cytoplasmic and Transmembrane Domains of RyR1 upon Gating. *PLoS Biol.* 7 (4), e85. doi:10.1371/journal.pbio.1000085

Samsó, M., Wagenknecht, T., and Allen, P. D. (2005). Internal Structure and Visualization of Transmembrane Domains of the RyR1 Calcium Release Channel by Cryo-EM. *Nat. Struct. Mol. Biol.* 12 (6), 539–544. doi:10.1038/nsmb938

Samsó, M., and Wagenknecht, T. (2002). Apocalmodulin and Ca2+-Calmodulin Bind to Neighboring Locations on the Ryanodine Receptor. *J. Biol. Chem.* 277 (2), 1349–1353. doi:10.1074/jbc.M109196200

Samsó, M., Shen, X., and Allen, P. D. (2006). Structural Characterization of the RyR1-FKBP12 Interaction. *J. Mol. Biol.* 356 (4), 917–927. doi:10.1016/j.jmb.2005.12.023

Samurkas, A., Yao, L., Hadiatullah, H., Ma, R., Xie, Y., Sundarraj, R., et al. (2022). Ryanodine Receptor as Insecticide Target. *Curr. Pharm. Des.* 28 (1), 26–35. doi:10.2174/1381612827666210902150224

Santulli, G., and Marks, A. R. (2015). Essential Roles of Intracellular Calcium Release Channels in Muscle, Brain, Metabolism, and Aging. *Curr. Mol. Pharmacol.* 8 (2), 206–222. doi:10.2174/1874467208666150507105105

Santulli, G., Lewis, D., des Georges, A., Marks, A. R., and Frank, J. (2018). *Ryanodine Receptor Structure and Function in Health and Disease.* Membrane Protein Complexes: Structure Function, 329–352. doi:10.1007/978-981-10-7757-9_11

Schmitt, K., Molfenter, B., Laureano, N. K., Tawk, B., Bieg, M., Hostench, X. P., et al. (2019). Somatic Mutations and Promotor Methylation of the Ryanodine Receptor 2 Is a Common Event in the Pathogenesis of Head and Neck Cancer. *Int. J. Cancer* 145 (12), 3299–3310. doi:10.1002/ijc.32481

Schwartz, E. F., Capes, E. M., Diego-García, E., Zamudio, F. Z., Fuentes, O., Possani, L. D., et al. (2009). Characterization of Hadrucalcin, a Peptide from Hadrurus Gertschi Scorpion Venom with Pharmacological Activity on Ryanodine Receptors. *Br. J. Pharmacol.* 157 (3), 392–403. doi:10.1111/j.1476-5381.2009.00147.x

Shahbazzadeh, D., Srairi-Abid, N., Feng, W., Ram, N., Borchani, L., Ronjat, M., et al. (2007). Hemicalcin, a New Toxin from the Iranian Scorpion Hemiscorpius Lepturus Which Is Active on Ryanodine-Sensitive Ca2+ Channels. *Biochem. J.* 404 (1), 89–96. doi:10.1042/BJ20061404

Sharma, P., Ishiyama, N., Nair, U., Li, W., Dong, A., Miyake, T., et al. (2012). Structural Determination of the Phosphorylation Domain of the Ryanodine Receptor. *FEBS J.* 279 (20), 3952–3964. doi:10.1111/j.1742-4658.2012.08755.x

Snoeck, M., Van Engelen, B. G., Küsters, B., Lammens, M., Meijer, R., Molenaar, J. P., et al. (2015). RYR1-related Myopathies: a Wide Spectrum of Phenotypes throughout Life. *Eur. J. Neurol.* 22 (7), 1094–1112. doi:10.1111/ene.12713

Sun, J., Xu, L., Eu, J. P., Stamler, J. S., and Meissner, G. (2003). Nitric Oxide, NOC-12, and S-Nitrosoglutathione Modulate the Skeletal Muscle Calcium Release Channel/ryanodine Receptor by Different Mechanisms. An Allosteric Function for O2 in S-Nitrosylation of the Channel. *J. Biol. Chem.* 278 (10), 8184–8189. doi:10.1074/jbc.M211940200

Supnet, C., Noonan, C., Richard, K., Bradley, J., and Mayne, M. (2010). Up-regulation of the Type 3 Ryanodine Receptor Is Neuroprotective in the TgCRND8 Mouse Model of Alzheimer's Disease. *J. Neurochem.* 112 (2), 356–365. doi:10.1111/j.1471-4159.2009.06487.x

Takeshima, H., Nishimura, S., Matsumoto, T., Ishida, H., Kangawa, K., Minamino, N., et al. (1989). Primary Structure and Expression from Complementary DNA of Skeletal Muscle Ryanodine Receptor. *Nature* 339 (6224), 439–445. doi:10.1038/339439a0

Tanabe, T., Beam, K. G., Adams, B. A., Niidome, T., and Numa, S. (1990). Regions of the Skeletal Muscle Dihydropyridine Receptor Critical for Excitation-Contraction Coupling. *Nature* 346 (6284), 567–569. doi:10.1038/346567a0

Tang, Y., Tian, X., Wang, R., Fill, M., and Chen, S. R. (2012). Abnormal Termination of Ca2+ Release Is a Common Defect of RyR2 Mutations Associated with Cardiomyopathies. *Circ. Res.* 110 (7), 968–977. doi:10.1161/CIRCRESAHA.111.256560

Tong, J., McCarthy, T. V., and MacLennan, D. H. (1999). Measurement of Resting Cytosolic Ca2+ Concentrations and Ca2+ Store Size in HEK-293 Cells Transfected with Malignant Hyperthermia or Central Core Disease Mutant Ca2+ Release Channels. *J. Biol. Chem.* 274 (2), 693–702. doi:10.1074/jbc.274.2.693

Touat-Hamici, Z., Blancard, M., Ma, R., Lin, L., Iddir, Y., Denjoy, I., et al. (2021). A SPRY1 domain cardiac ryanodine receptor variant associated with short-coupled torsade de pointes. *Sci. Rep.* 11 (1), 5243–5313. doi:10.1038/s41598-021-84373-9

Treves, S., Jungbluth, H., Muntoni, F., and Zorzato, F. (2008). Congenital Muscle Disorders with Cores: the Ryanodine Receptor Calcium Channel Paradigm. *Curr. Opin. Pharmacol.* 8 (3), 319–326. doi:10.1016/j.coph.2008.01.005

Tu, M. K., Levin, J. B., Hamilton, A. M., and Borodinsky, L. N. (2016). Calcium Signaling in Skeletal Muscle Development, Maintenance and Regeneration. *Cell calcium* 59 (2-3), 91–97. doi:10.1016/j.ceca.2016.02.005

Tung, C. C., Lobo, P. A., Kimlicka, L., and Van Petegem, F. (2010). The Amino-Terminal Disease Hotspot of Ryanodine Receptors Forms a Cytoplasmic Vestibule. *Nature* 468 (7323), 585–588. doi:10.1038/nature09471

Uchinoumi, H., Yano, M., Suetomi, T., Ono, M., Xu, X., Tateishi, H., et al. (2010). Catecholaminergic Polymorphic Ventricular Tachycardia Is Caused by Mutation-Linked Defective Conformational Regulation of the Ryanodine Receptor. *Circ. Res.* 106 (8), 1413–1424. doi:10.1161/CIRCRESAHA.109.209312

van der Werf, C., Zwinderman, A. H., and Wilde, A. A. (2012). Therapeutic Approach for Patients with Catecholaminergic Polymorphic Ventricular Tachycardia: State of the Art and Future Developments. *Europace* 14 (2), 175–183. doi:10.1093/europace/eur277

Van Petegem, F. (2012). Ryanodine Receptors: Structure and Function. *J. Biol. Chem.* 287 (38), 31624–31632. doi:10.1074/jbc.R112.349068

Voss, A. A., Lango, J., Ernst-Russell, M., Morin, D., and Pessah, I. N. (2004). Identification of Hyperreactive Cysteines within Ryanodine Receptor Type 1 by Mass Spectrometry. *J. Biol. Chem.* 279 (33), 34514–34520. doi:10.1074/jbc.M404290200

Walker, M. A., Kohl, T., Lehnart, S. E., Greenstein, J. L., Lederer, W. J., and Winslow, R. L. (2015). On the Adjacency Matrix of RyR2 Cluster Structures. *PLoS Comput. Biol.* 11 (11), e1004521. doi:10.1371/journal.pcbi.1004521

Walweel, K., Li, J., Molenaar, P., Imtiaz, M. S., Quail, A., dos Remedios, C. G., et al. (2014). Differences in the Regulation of RyR2 from Human, Sheep, and Rat by Ca^{2+} and Mg^{2+} in the Cytoplasm and in the Lumen of the Sarcoplasmic Reticulum. *J. Gen. Physiol.* 144 (3), 263–271. doi:10.1085/jgp.201311157

Wan, J.-f., Wang, G., Qin, F.-y., Huang, D.-l., Wang, Y., Su, A.-l., et al. (2022). Z16b, a Natural Compound from Ganoderma Cochlear Is a Novel RyR2 Stabilizer Preventing Catecholaminergic Polymorphic Ventricular Tachycardia. *Acta Pharmacol. Sin.*, 1–11. doi:10.1038/s41401-022-00870-1

Wang, R., Chen, W., Cai, S., Zhang, J., Bolstad, J., Wagenknecht, T., et al. (2007). Localization of an NH(2)-terminal Disease-Causing Mutation Hot Spot to the "clamp" Region in the Three-Dimensional Structure of the Cardiac Ryanodine Receptor. *J. Biol. Chem.* 282 (24), 17785–17793. doi:10.1074/jbc.M700660200

Wang, R., Zhong, X., Meng, X., Koop, A., Tian, X., Jones, P. P., et al. (2011). Localization of the Dantrolene-Binding Sequence Near the FK506-Binding Protein-Binding Site in the Three-Dimensional Structure of the Ryanodine Receptor. *J. Biol. Chem.* 286 (14), 12202–12212. doi:10.1074/jbc.M110.194316

Watanabe, H., Chopra, N., Laver, D., Hwang, H. S., Davies, S. S., Roach, D. E., et al. (2009). Flecainide Prevents Catecholaminergic Polymorphic Ventricular Tachycardia in Mice and Humans. *Nat. Med.* 15 (4), 380–383. doi:10.1038/nm.1942

Watras, J., and Ehrlich, B. E. (1991). Bell-shaped Calcium-Response Curves of Lns (L, 4, 5) P 3-and Calcium-Gated Channels from Endoplasmic Reticulum of Cerebellum. *Nature* 351 (6329), 751–754.

Wehrens, X. H., Lehnart, S. E., Huang, F., Vest, J. A., Reiken, S. R., Mohler, P. J., et al. (2003). FKBP12.6 Deficiency and Defective Calcium Release Channel (Ryanodine Receptor) Function Linked to Exercise-Induced Sudden Cardiac Death. *Cell* 113 (7), 829–840. doi:10.1016/s0092-8674(03)00434-3

Wehrens, X. H., Lehnart, S. E., Reiken, S. R., Deng, S. X., Vest, J. A., Cervantes, D., et al. (2004a). Protection from Cardiac Arrhythmia through Ryanodine Receptor-Stabilizing Protein Calstabin2. *Science* 304 (5668), 292–296. doi:10.1126/science.1094301

Wehrens, X. H., Lehnart, S. E., Reiken, S. R., and Marks, A. R. (2004b). Ca2+/calmodulin-dependent Protein Kinase II Phosphorylation Regulates the Cardiac Ryanodine Receptor. *Circ. Res.* 94 (6), e61–70. doi:10.1161/01.RES.0000125626.33738.E2

Wei, R., Wang, X., Zhang, Y., Mukherjee, S., Zhang, L., Chen, Q., et al. (2016). Structural Insights into Ca(2+)-Activated Long-Range Allosteric Channel Gating of RyR1. *Cell Res.* 26 (9), 977–994. doi:10.1038/cr.2016.99

Witcher, D. R., Kovacs, R. J., Schulman, H., Cefali, D. C., and Jones, L. R. (1991). Unique Phosphorylation Site on the Cardiac Ryanodine Receptor Regulates Calcium Channel Activity. *J. Biol. Chem.* 266 (17), 11144–11152. doi:10.1016/s0021-9258(18)99140-4

Woll, K. A., Haji-Ghassemi, O., and Van Petegem, F. (2021). Pathological Conformations of Disease Mutant Ryanodine Receptors Revealed by Cryo-EM. *Nat. Commun.* 12 (1), 807–813. doi:10.1038/s41467-021-21141-3

Woll, K. A., and Van Petegem, F. (2022). Calcium-release Channels: Structure and Function of IP3 Receptors and Ryanodine Receptors. *Physiol. Rev.* 102 (1), 209–268. doi:10.1152/physrev.00033.2020

Wong King Yuen, S. M., Campiglio, M., Tung, C. C., Flucher, B. E., and Van Petegem, F. (2017). Structural Insights into Binding of STAC Proteins to Voltage-Gated Calcium Channels. *Proc. Natl. Acad. Sci. U. S. A.* 114 (45), E9520–E9528. doi:10.1073/pnas.1708852114

Word, T. A., Quick, A. P., Miyake, C. Y., Shak, M. K., Pan, X., Kim, J. J., et al. (2021). Efficacy of RyR2 Inhibitor EL20 in Induced Pluripotent Stem Cell-derived Cardiomyocytes from a Patient with Catecholaminergic Polymorphic Ventricular Tachycardia. *J. Cell. Mol. Med.* 25 (13), 6115–6124. doi:10.1111/jcmm.16521

Wu, J., Yan, Z., Li, Z., Qian, X., Lu, S., Dong, M., et al. (2016). Structure of the Voltage-Gated Calcium Channel Ca(v)1.1 at 3.6 Å Resolution. *Nature* 537 (7619), 191–196. doi:10.1038/nature19321

Wu, J., Yan, Z., Li, Z., Yan, C., Lu, S., Dong, M., et al. (2015). Structure of the Voltage-Gated Calcium Channel Cav1.1 Complex. *Science* 350 (6267), aad2395. doi:10.1126/science.aad2395

Xiong, J., Liu, X., Gong, Y., Zhang, P., Qiang, S., Zhao, Q., et al. (2018). Pathogenic Mechanism of a Catecholaminergic Polymorphic Ventricular Tachycardia Causing-Mutation in Cardiac Calcium Release Channel RyR2. *J. Mol. Cell Cardiol.* 117, 26–35. doi:10.1016/j.yjmcc.2018.02.014

Xu, L., Eu, J. P., Meissner, G., and Stamler, J. S. (1998). Activation of the Cardiac Calcium Release Channel (Ryanodine Receptor) by Poly-S-Nitrosylation. *Science* 279 (5348), 234–237. doi:10.1126/science.279.5348.234

Xu, N., Zhang, D., Chen, J., He, G., and Gao, L. (2019). Low Expression of Ryanodine Receptor 2 Is Associated with Poor Prognosis in Thyroid Carcinoma. *Oncol. Lett.* 18 (4), 3605–3612. doi:10.3892/ol.2019.10732

Xu, T., and Yuchi, Z. (2019). Crystal Structure of Diamondback Moth Ryanodine Receptor Repeat34 Domain Reveals Insect-specific Phosphorylation Sites. *BMC Biol.* 17 (1), 77–19. doi:10.1186/s12915-019-0698-5

Yamazawa, T., Kobayashi, T., Kurebayashi, N., Konishi, M., Noguchi, S., Inoue, T., et al. (2021). A Novel RyR1-Selective Inhibitor Prevents and Rescues Sudden Death in Mouse Models of Malignant Hyperthermia and Heat Stroke. *Nat. Commun.* 12 (1), 4293–4314. doi:10.1038/s41467-021-24644-1

Yan, Z., Bai, X., Yan, C., Wu, J., Li, Z., Xie, T., et al. (2015). Structure of the Rabbit Ryanodine Receptor RyR1 at Near-Atomic Resolution. *Nature* 517 (7532), 50–55. doi:10.1038/nature14063

Yang, F., Zhu, X. H., Zhang, Q., Sun, N. X., Ji, Y. X., Ma, J. Z., et al. (2017). Genomic Characteristics of Gender Dysphoria Patients and Identification of Rare Mutations in RYR3 Gene. *Sci. Rep.* 7 (1), 8339–9. doi:10.1038/s41598-017-08655-x

Yang, Z. F., Panwar, P., McFarlane, C. R., Tuinte, W. E., Campiglio, M., and Van Petegem, F. (2022). Structures of the Junctophilin/voltage-Gated Calcium Channel Interface Reveal Hot Spot for Cardiomyopathy Mutations. *Proc. Natl. Acad. Sci. U.S.A.* 119 (10), e2120416119. doi:10.1073/pnas.2120416119

Yuchi, Z., Lau, K., and Van Petegem, F. (2012). Disease Mutations in the Ryanodine Receptor Central Region: Crystal Structures of a Phosphorylation Hot Spot Domain. *Structure* 20 (7), 1201–1211. doi:10.1016/j.str.2012.04.015

Yuchi, Z., Yuen, S. M., Lau, K., Underhill, A. Q., Cornea, R. L., Fessenden, J. D., et al. (2015). Crystal Structures of Ryanodine Receptor SPRY1 and Tandem-Repeat Domains Reveal a Critical FKBP12 Binding Determinant. *Nat. Commun.* 6 (1), 7947–8013. doi:10.1038/ncomms8947

Zalk, R., Clarke, O. B., Des Georges, A., Grassucci, R. A., Reiken, S., Mancia, F., et al. (2015). Structure of a Mammalian Ryanodine Receptor. *Nature* 517 (7532), 44–49. doi:10.1038/nature13950

Zamponi, G. W., Striessnig, J., Koschak, A., and Dolphin, A. C. (2015). The Physiology, Pathology, and Pharmacology of Voltage-Gated Calcium Channels and Their Future Therapeutic Potential. *Pharmacol. Rev.* 67 (4), 821–870. doi:10.1124/pr.114.009654

Zhang, J. Z., Waddell, H. M., Wu, E., Dholakia, J., Okolo, C. A., McLay, J. C., et al. (2016). FKBPs Facilitate the Termination of Spontaneous Ca2+ Release in Wild-type RyR2 but Not CPVT Mutant RyR2. *Biochem. J.* 473 (14), 2049–2060. doi:10.1042/BCJ20160389

Zhang, J. Z., Wu, Y., Williams, B. Y., Rodney, G., Mandel, F., Strasburg, G. M., et al. (1999). Oxidation of the Skeletal Muscle Ca2+ Release Channel Alters Calmodulin Binding. *Am. J. Physiol.* 276 (1), C46–C53. doi:10.1152/ajpcell.1999.276.1.c46

Zhang, Y., Chen, H. S., Khanna, V. K., De Leon, S., Phillips, M. S., Schappert, K., et al. (1993). A Mutation in the Human Ryanodine Receptor Gene Associated with Central Core Disease. *Nat. Genet.* 5 (1), 46–50. doi:10.1038/ng0993-46

Zhao, Y., Huang, G., Wu, J., Wu, Q., Gao, S., Yan, Z., et al. (2019). Molecular Basis for Ligand Modulation of a Mammalian Voltage-Gated Ca2+ Channel. *Cell* 177 (6), 1495–e12. e1412. doi:10.1016/j.cell.2019.04.043

Zheng, W., and Liu, Z. (2017). Investigating the Inter-subunit/subdomain Interactions and Motions Relevant to Disease Mutations in the N-Terminal Domain of Ryanodine Receptors by Molecular Dynamics Simulation. *Proteins* 85 (9), 1633–1644. doi:10.1002/prot.25318

Zhou, H., Lillis, S., Loy, R. E., Ghassemi, F., Rose, M. R., Norwood, F., et al. (2010). Multi-minicore Disease and Atypical Periodic Paralysis Associated with Novel Mutations in the Skeletal Muscle Ryanodine Receptor (RYR1) Gene. *Neuromuscul. Disord.* 20 (3), 166–173. doi:10.1016/j.nmd.2009.12.005

Zhou, H., Rokach, O., Feng, L., Munteanu, I., Mamchaoui, K., Wilmshurst, J. M., et al. (2013). RyR1 Deficiency in Congenital Myopathies Disrupts Excitation-Contraction Coupling. *Hum. Mutat.* 34 (7), 986–996. doi:10.1002/humu.22326

Zhou, Q., Xiao, J., Jiang, D., Wang, R., Vembaiyan, K., Wang, A., et al. (2011). Carvedilol and its New Analogs Suppress Arrhythmogenic Store Overload-Induced Ca2+ Release. *Nat. Med.* 17 (8), 1003–1009. doi:10.1038/nm.2406

Zhou, Y., Wang, W., Salauddin, N. M., Lin, L., You, M., You, S., et al. (2020). Crystal Structure of the N-Terminal Domain of Ryanodine Receptor from the Honeybee, *Apis mellifera*. *Insect Biochem. Mol. Biol.* 125, 103454. doi:10.1016/j.ibmb.2020.103454

Zuo, Y. Y., Ma, H. H., Lu, W. J., Wang, X. L., Wu, S. W., Nauen, R., et al. (2020). Identification of the Ryanodine Receptor Mutation I4743M and its Contribution to Diamide Insecticide Resistance in Spodoptera Exigua (Lepidoptera: Noctuidae). *Insect Sci.* 27 (4), 791–800. doi:10.1111/1744-7917.12695

Zvaritch, E., Kraeva, N., Bombardier, E., McCloy, R. A., Depreux, F., Holmyard, D., et al. (2009). Ca2+ Dysregulation in Ryr1(I4895T/wt) Mice Causes Congenital Myopathy with Progressive Formation of Minicores, Cores, and Nemaline Rods. *Proc. Natl. Acad. Sci. U. S. A.* 106 (51), 21813–21818. doi:10.1073/pnas.0912126106

Conflict of Interest: The authors declare that the research was conducted in the absence of any commercial or financial relationships that could be construed as a potential conflict of interest.

frontiers | Frontiers in Pharmacology

REVIEW
published: 03 June 2022
doi: 10.3389/fphar.2022.908867

Structural Advances in Voltage-Gated Sodium Channels

Daohua Jiang[1,2]*, *Jiangtao Zhang*[1,3] *and Zhanyi Xia*[1,2]

[1]Laboratory of Soft Matter Physics, Institute of Physics, Chinese Academy of Sciences, Beijing, China, [2]University of Chinese Academy of Sciences, Beijing, China, [3]Key Laboratory of Molecular Biophysics of MOE, College of Life Science and Technology, Huazhong University of Science and Technology, Wuhan, China

Voltage-gated sodium (Na_V) channels are responsible for the rapid rising-phase of action potentials in excitable cells. Over 1,000 mutations in Na_V channels are associated with human diseases including epilepsy, periodic paralysis, arrhythmias and pain disorders. Natural toxins and clinically-used small-molecule drugs bind to Na_V channels and modulate their functions. Recent advances from cryo-electron microscopy (cryo-EM) structures of Na_V channels reveal invaluable insights into the architecture, activation, fast inactivation, electromechanical coupling, ligand modulation and pharmacology of eukaryotic Na_V channels. These structural analyses not only demonstrate molecular mechanisms for Na_V channel structure and function, but also provide atomic level templates for rational development of potential subtype-selective therapeutics. In this review, we summarize recent structural advances of eukaryotic Na_V channels, highlighting the structural features of eukaryotic Na_V channels as well as distinct modulation mechanisms by a wide range of modulators from natural toxins to synthetic small-molecules.

Keywords: voltage-gated sodium channel, cryo-EM, pharmocology, gating mechanism, drug modulation mechanism

OPEN ACCESS

Edited by:
Chia-Hsueh Lee,
St. Jude Children's Research Hospital,
United States

Reviewed by:
Rong Shen,
The University of Chicago,
United States
Heike Wulff,
University of California, Davis,
United States

***Correspondence:**
Daohua Jiang
jiangdh@iphy.ac.cn

Specialty section:
This article was submitted to
Pharmacology of Ion Channels and
Channelopathies,
a section of the journal
Frontiers in Pharmacology

Received: *31 March 2022*
Accepted: *23 May 2022*
Published: *03 June 2022*

Citation:
Jiang D, Zhang J and Xia Z (2022)
Structural Advances in Voltage-Gated
Sodium Channels.
Front. Pharmacol. 13:908867.
doi: 10.3389/fphar.2022.908867

INTRODUCTION

Voltage-gated sodium (Na_V) channels are a family of integrated membrane proteins, which selectively conduct sodium ions across cell membrane in response to depolarizing stimuli (Catterall, 2000; Hille, 2001). The primary function of Na_V channels was related to the generation of action potentials (Hodgkin And Huxley, 1952a; Hodgkin And Huxley, 1952b). Subsequently, the voltage-dependent activation, sodium selectivity, fast inactivation and components of Na_V channels were characterized by extensive biophysical and biochemical studies (Armstrong and Bezanilla, 1973; Tamkun and Catterall, 1981; Weigele and Barchi, 1982; Hartshorne and Catterall, 1984; Stühmer et al., 1987). Since the first Na_V channel gene was cloned by Noda in 1984 (Noda et al., 1984), nine highly conserved Na_V channel subtypes (Na_V1.1- Na_V1.9) in humans have been identified (Catterall et al., 2005). These channels have specific tissue-expression patterns. Na_V1.1, Na_V1.2 and Na_V1.3 are mainly expressed in the central nervous system (CNS), which are crucial for nerve excitability. Hundreds of mutations in these channels cause inherited epilepsy and other form diseases of hyperexcitability (Meisler and Kearney, 2005; Catterall et al., 2008; Catterall, 2014; Huang et al., 2017). Phenytoin, lamotrigine, and carbamazepine are clinical drugs for treatment of epilepsy that act as Na_V channel blockers (Zuliani et al., 2012; Catterall, 2014). Na_V1.4 and Na_V1.5 are predominantly expressed in skeletal muscle and cardiomyocytes, respectively. Malfunction of these two Na_V channels are associated with periodic paralysis,

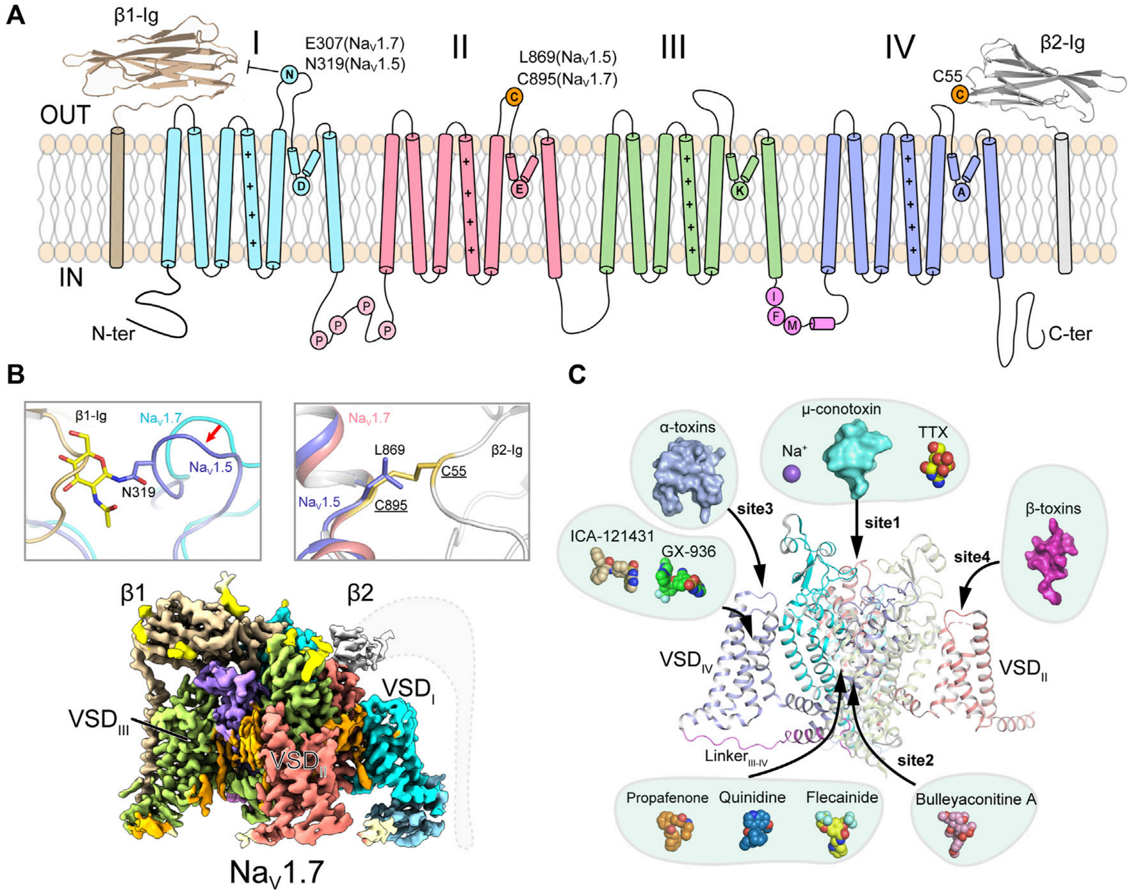

FIGURE 1 | Topology and architecture of mammalian Na$_V$ channels. **(A)** Topology of mammalian Na$_V$ channels. D$_I$, D$_{II}$, D$_{III}$, IFM-motif and D$_{IV}$ of α-subunit, β1 and β2 subunit are colored in cyan, red, green, purple, blue, brown and gray, respectively. A unique N-glycosylation site in Na$_V$1.5 and the cysteine residue for linking β2 are highlighted. P represents phosphorylation sites. **(B)** Subunits assembly of mammalian Na$_V$ channels. A sugar moiety of N319 glycosylation and L869 block the binding of β1 and β2 to Na$_V$1.5 (PDB code: 6UZ3), respectively (Upper panels). Cryo-EM map of human Na$_V$1.7/β1/β2 (lower panel, EMDB code: EMD-33292). Dashed lines indicate the invisible region of β2 subunit. **(C)** Multiple ligand binding sites in mammalian Na$_V$ channel α-subunit. Sodium ion and small-molecule modulators shown in spheres, polypeptide toxins shown in surface.

myotonia and cardiac arrhythmias (Sokolov et al., 2007; Catterall et al., 2020a). Class I anti-arrhythmic drugs, which block Na$_V$1.5 to remove the abnormal component, are broadly used for treating arrhythmias. Based on the rate of binding and unbinding, the Class I anti-arrhythmic drugs are divided into three subclasses: IA (*e.g.*, quinidine), IB (*e.g.*, lidocaine) and IC (*e.g.*, flecainide) (Kowey, 1998; Huang et al., 2020). Na$_V$1.6 is widely distributed in both CNS and the peripheral nervous system (PNS). The unique features of Na$_V$1.6 such as generating persistent current and resurgent current, contribute to neuronal excitability and repetitive neuronal firing (Raman and Bean, 1997; Raman et al., 1997). Mutations in Na$_V$1.6 are related to epilepsy, ataxia and dystonia (O'Brien and Meisler, 2013). Na$_V$1.7, Na$_V$1.8 and Na$_V$1.9 are highly expressed in PNS, which are closely related to pain perception (Bennett et al., 2019; Dib-Hajj and Waxman, 2019). Na$_V$1.7 was also reported to be essential for odour sensation (Weiss et al., 2011). Many programs have been established in searching for Na$_V$1.7 and Na$_V$1.8 selective inhibitors as potential analgesics (Kingwell, 2019; Alsaloum et al., 2020). In addition, a wide range of natural toxins from animal or plant venoms target the Na$_V$ channels and modulate channel functions by binding in at least six distinct receptor sites (Catterall et al., 2007).

Further studies revealed that Na$_V$ channels are widely distributed in eukaryotes, as well as in prokaryotes (Koishi et al., 2004; Ren et al., 2001) and marine unicellular phytoplankton (Helliwell et al., 2020; Helliwell et al., 2019), highlighting the evolutionary conservation of Na$_V$ channels. The metazoan Na$_V$ channels are composed of a large pore-forming α-subunit and one or two auxiliary β-subunits (β1-β4) (**Figure 1A**) (Catterall, 2000; Hartshorne and Catterall, 1984; Isom et al., 1994; O'Malley and Isom, 2015). The α-subunit consists of 24-transmembrane helices, which are divided into four homologous domains (D$_I$-D$_{IV}$). The four domains are connected by intracellular loops. The loop between D$_{III}$ and D$_{IV}$ contains a highly conserved fast inactivation gate, which mediates the fast inactivation of Na$_V$ channels (West et al., 1992; Goldin, 2003). The first four transmembrane segments (S1-S4) form the voltage-sensing domain (VSD), the S5 and S6 form the pore module (PM). Distinct from the metazoan Na_V channels, Na_V channels from bacteria and the unicellular phytoplankton are formed by four identical protomers in a homotetrameric organization (Ren et al., 2001; Helliwell et al., 2020). In 2001, Sato pioneered the structural study of Na_V channels reporting a ~19 Å cryo-electron microscopy (cryo-EM) map of Na_V channel from the electrical eel (Sato et al., 2001). However, the low-resolution map did not permit model building of the Na_V channel. The crystal structure of voltage-gated potassium (K_V) channel also provided useful homologous template for Na_V channels (Long et al., 2005). Since 2011, Catterall lab and other groups reported high-resolution crystal structures of prokaryotic Na_V ($BacNa_V$) channels (Payandeh et al., 2011; Payandeh et al., 2012; Zhang et al., 2012; Lenaeus et al., 2017; Sula et al., 2017; Wisedchaisri et al., 2019), which revealed structural basis for bacterial Na_V channel architecture, activation and inactivation, gating, ion conductance and selectivity at atomic level. These bacterial Na_V channels had also been used as templates to investigate the structural pharmacology of human Na_V channels (Bagnéris et al., 2014; Boiteux et al., 2014; Ahuja et al., 2015; Tang et al., 2016; Gamal El-Din et al., 2018; Wisedchaisri et al., 2021). Recent advances from cryo-EM structures of the eukaryotic Na_V channel Na_VPas (Shen et al., 2017; Shen et al., 2018; Clairfeuille et al., 2019), $Na_V1.4$ (Yan et al., 2017; Pan et al., 2018), $Na_V1.7$ (Shen et al., 2019), $Na_V1.2$ (Pan et al., 2019), $Na_V1.5$ (Jiang et al., 2020; Jiang et al., 2021a; Li et al., 2021a; Li et al., 2021b; Jiang et al., 2021c), $Na_V1.1$ (Pan et al., 2021) and $Na_V1.3$ (Li et al., 2022) reveal detailed structural basis for the eukaryotic Na_V channel subunits assembly, fast inactivation, modulation by natural animal toxins, and pore blockade by anti-arrhythmic drugs (**Figures 1B,C**). In this review, we highlight the structural features of the eukaryotic Na_V channels and the distinct molecular mechanisms for Na_V channel modulation by natural toxins and clinical drugs.

Assembly of Voltage-Gated Sodium Channels

The homotetrameric bacterial Na_VAb had been an ideal model for investigating molecular mechanisms of Na_V channel activation, inactivation, gating, electromechanical coupling and mutation induced channelopathies (Payandeh et al., 2011; Payandeh et al., 2012; Lenaeus et al., 2017; Jiang et al., 2018; Wisedchaisri et al., 2019) (Reviewed in Ref (Catterall et al., 2020b)). However, there are significant structural and functional differences between the homotetrameric $BacNa_V$ channels and the asymmetric eukaryotic Na_V channels. The eukaryotic Na_V channels withheld their detailed structural features owing to their extremely low yield of recombinant expression and sample heterogeneity. In 2017, Nieng Yan lab reported the ground breaking high-resolution cryo-EM structure of a eukaryotic Na_V channel Na_VPas from the American cockroach (Shen et al., 2017). Although Na_VPas was found to be non-functional in heterologous expression system and lack of the conserved fast inactivation gate, the Na_VPas structure does provide important insights into the architecture of Na_V channel α-subunit, four VSDs in distinct conformations and the asymmetric selectivity filter (SF). In addition, the structure proved that human Na_V channels could possibly be resolved to high-resolution by the advanced cryo-EM technique. After extensive efforts had been conducted to improve the sample quality (Jiang et al., 2021b; Shen et al., 2021), cryo-EM structures of the electrical eel and human $Na_V1.4$-β1, human $Na_V1.7$-β1-β2, human $Na_V1.2$-β2, rat and human $Na_V1.5$, human $Na_V1.1$-β4 and human $Na_V1.3$-β1-β2 were subsequently reported at 3–4 Å resolution (Yan et al., 2017; Pan et al., 2018; Pan et al., 2019; Shen et al., 2019; Jiang et al., 2020; Li et al., 2021b; Pan et al., 2021; Li et al., 2022). These structures reveal detailed insights into the assembly of Na_V channel α- and β-subunits, allosteric inhibition mechanism of the fast inactivation and multiple ligand binding sites (**Figures 1B,C**).

These high-resolution structures suggest that the overall structures of the Na_V channels are structurally conserved. The transmembrane core-regions closely resemble the bacterial Na_V channels, which are formed similarly in a domain-swapped manner, e.g., VSD and PM of one domain are separated by a S4S5 linker helix, thus VSD of one domain closely engages PM from the other domain. Distinct from the $BacNa_V$ channels, the metazoan Na_V channels possess large extracellular loops (ECLs) between S5 and S6 helices of each domain. Multiple glycosylation sites on the ECLs were visualized from these structures, which are important for the channel maturation and modulation. On the cytoplasmic side, the N-terminal domain (NTD), long loops of D_I-D_{II} and D_{II}-D_{III}, and the C-terminal domain (CTD) were invisible to cryo-EM, which are probably due to mobility of these regions. These intracellular regions were reported to be essential for Na_V channel function and modulation (West et al., 1991; Mantegazza et al., 2001; Scheuer, 2011; Clatot et al., 2012). However, it's challenging to capture a snapshot of the transient modulation state such as phosphorylation. The relative short loop between D_{III}-D_{IV} of the mammalian Na_V channels, which contains the fast inactivation particle Ile-Phe-Met (IFM) motif, were all clearly resolved in a nearly identical conformation (Pan et al., 2018; Pan et al., 2019; Shen et al., 2019; Jiang et al., 2020; Pan et al., 2021). The IFM-motif binds to a hydrophobic pocket adjacent to the intracellular activation gate, rather than directly blocking the activation gate, elucidating a unique local allosteric inhibition mechanism for the fast inactivation.

The β-subunits (β1-β4) bind to the α-subunit and regulate the Na_V channel properties such as cell surface expression, voltage-dependent activation and gating kinetics (Hartshorne and Catterall, 1984; Isom et al., 1994; O'Malley and Isom, 2015; Vijayaragavan et al., 2001). The four β-subunits share conserved topology of an extracellular immunoglobulin-like domain and a single transmembrane helix (Das et al., 2016; Gilchrist et al., 2013; Namadurai et al., 2014). The $Na_V1.4$-β1, $Na_V1.7$-β1-β2, $Na_V1.2$-β2, $Na_V1.1$-β4 and $Na_V1.3$-β1-β2 complex structures confirmed that the β1 noncovalently binds to the α-subunit, whereas β2 or β4 is linked to the α-subunit *via* a disulfide bond (**Figures 1A,B**). Surprisingly, the rat and human $Na_V1.5$ structures showed that the β1 binding is blocked by a sugar moiety of a unique glycosylation modification in the ECL_I, and

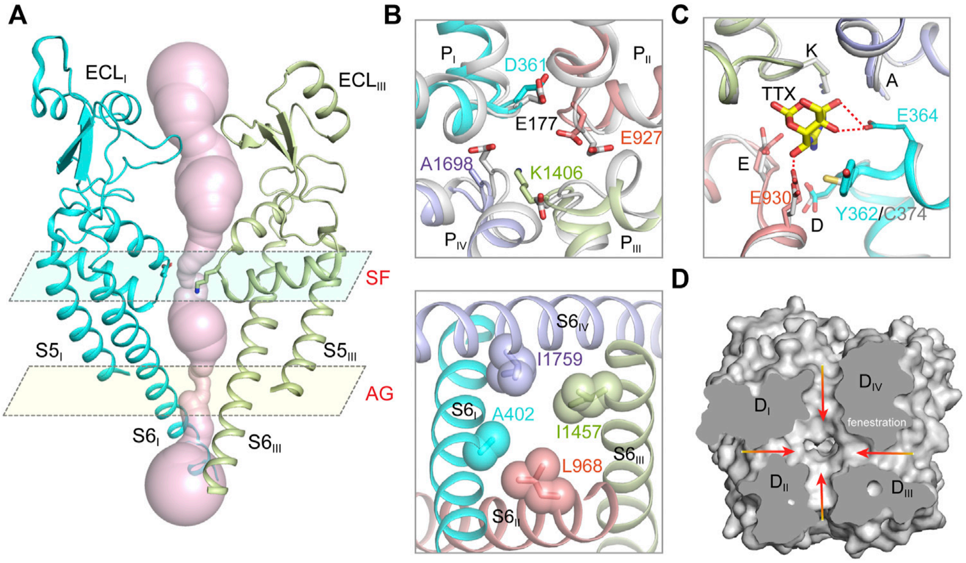

FIGURE 2 | The ion path of mammalian Na$_V$ channels. **(A)** The pore radii of human Na$_V$1.7 (PDB code: 7XM9) calculated by HOLE. Only two opposing subunits shown for clarity. The constriction sites of selectivity filter (SF) and intracellular activation gate (AG) are highlighted. **(B)** A close-up view of the SF (top panel) and AG (bottom panel) of human Na$_V$1.7 (PDB code: 7XM9). The SF of Na$_V$1.7 was aligned with the SF of Na$_V$Ab (gray, PDB code: 3RVY). The side-chains of key residues in the SF and the AG are depicted in sticks. **(C)** The TTX binding site in Na$_V$1.7 (PDB code: 6J8I). The TTX-insensitive channel Na$_V$1.5 (PDB code: 6UZ3) shown in gray. **(D)** Fenestrations of human Na$_V$1.7 (PDB code: 7XM9). Red arrows indicate potential access for lipids or pore-blockers.

the cysteine for linking β2 or β4 is substituted by a Leu869 in Na$_V$1.5 or an Ala822 in Na$_V$1.8 (**Figure 1B**) (Jiang et al., 2020; Li et al., 2021a). These structural observations demonstrate that the β subunits bind weakly to Na$_V$1.5, which is in agreement with previous biophysical reports that the β subunits have negligible effect on the kinetics or voltage-dependence of Na$_V$1.5 (Makita et al., 1994; Qu et al., 1995). However, pathogenic mutations in the Na$_V$ β-subunits were reported to be associated with cardiac arrhythmias (Ruan et al., 2009; Watanabe et al., 2009; Olesen et al., 2011). These results indicate that the β-subunits might be important for Na$_V$1.5 folding or trafficking to the plasma membrane, rather than modifying Na$_V$1.5 functional properties. It has also been reported that the β-subunits play other physiological functions unrelated to Na$_V$1.5, such as cell adhesion in the cardiomyocytes (Patino et al., 2011; Namadurai et al., 2015).

Ion Path of Na$_V$ Channels

Hille tested the sodium selectivity of Na$_V$ channels and estimated a ~3.0 Å by ~5.0 Å constriction site at the extracellular side (Hille, 1971a; b; 1972; 1975). Point-mutagenesis studies revealed that an Asp in D$_I$, Glu in D$_{II}$, Lys in D$_{III}$ and Ala in D$_{IV}$, often termed the DEKA-locus, are responsible for the sodium selectivity (Favre et al., 1996; Sun et al., 1997). The crystal structure of the bacterial Na$_V$Ab provides the first atomic model for investigating the molecular mechanism of sodium selectivity (Payandeh et al., 2011). At the center of Na$_V$ channels, four pore-loops (P-loop) and S6 helices form an ion conductance path across the membrane. The ion path consists of a narrow extracellular constriction site termed selectivity filter (SF), a large central cavity (CC) and a size-variable intracellular activation gate (AG) (**Figure 2A**). Unlike the asymmetric DEKA-locus of the metazoan Na$_V$ channels, four identical P-loops (TLESWSM) of Na$_V$Ab constitute the SF with diameter of ~4.6 Å by ~4.6 Å, close to Hille's estimation (Hille, 1975; Payandeh et al., 2011). The SF of Na$_V$Ab is significantly wider than that of potassium channels, suggesting that sodium may pass through the SF in partially hydrated form (Doyle et al., 1998; Hille, 1971a; Payandeh et al., 2011; Yellen, 2002). The four Glu at +3 position of the SF loop determine sodium selectivity, which form a high-field strength site to coordinate sodium ions (**Figure 2B**). Substitution of the TLESWSM with TLDSWDD converts the sodium channel to a highly calcium selective channel (Yue et al., 2002; Tang et al., 2014), suggesting that the ion path of sodium and calcium channels are closely related. Crystal structure of the chimeric calcium channel Ca$_V$Ab revealed high affinity binding sites for Ca^{2+} supporting the stepwise "knock-off" permeation mechanism, which are not observed in the BacNa$_V$ channel structures (Payandeh et al., 2011; Zhang et al., 2012; Tang et al., 2014). These observations suggested that the Na$_V$ and Ca$_V$ channel are evolutionarily highly-related, the subtle compositional differences in the SFs discriminate Na^+ and Ca^{2+} ions. Based on the BacNa$_V$ structures and molecular dynamics simulation studies, potential models had been proposed to explain the sodium selectivity (Corry and Thomas, 2012; Chakrabarti et al., 2013; Naylor et al., 2016). However, these possible mechanisms may not be fully applicable to the metazoan Na$_V$ channels, because the asymmetric DEKA-locus is absent in the BacNa$_V$ channels.

The cryo-EM structures of metazoan Na$_V$ channels revealed that the SF is comparable to that of the BacNa$_V$ structures (Jiang et al., 2020; Pan et al., 2019; Pan et al., 2018; Shen et al., 2019; Shen et al., 2017). The Asp in D_I and Glu in D_{II} of the DEKA-locus provide the high-field strength site similar to the $BacNa_V$ channels (**Figure 2B**), which coordinates and facilitates partially dehydration of sodium ions (Payandeh et al., 2011; Chakrabarti et al., 2013). The Lys in D_{III} of the DEKA-locus was consistently found pointing its sidechain deep inside the SF and narrowing the SF in one dimension, which meets Hille's estimation (Hille, 1971b, 1975; Jiang et al., 2020). A positively-charged Lys embedded in the SF would likely block the ion permeation rather than conduct. Considering pKa value of Lys-NH2 can be dramatically affected by its interacting chemical environments (Isom et al., 2011), one possibility is that the pKa of the Lys is significantly decreased and its positive charge is delocalized by nearby carbonyl groups (Jiang et al., 2020). In this case, the neutralized Lys may serve as an energetically favorable coordinating ligand for Na^+ or Li^+, whereas the larger alkali cations like K^+, Rb^+ and Cs^+ are energetically unfavorable.

The tetrodotoxin (TTX) from puffer fish is a highly Na_V channel specific and highly lethal neurotoxin, which was initially used to discriminate Na^+ and K^+ currents in the squid giant axons and to map the location of the SF (Kao, 1966; Noda et al., 1989). Based on the binding affinity, $Na_V1.1$, $Na_V1.2$, $Na_V1.3$, $Na_V1.4$, $Na_V1.6$ and $Na_V1.7$ are classified as TTX-sensitive channels with TTX affinity at nanomolar level; $Na_V1.5$, $Na_V1.8$ and $Na_V1.9$ are TTX-insensitive channels with micromolar affinity. A Tyr or Phe residue located in the D_I P-loop was found as the key determinant for the TTX sensitivity, this residue is substituted by a Cys or Ser in the TTX-insensitive Na_V channels (Sivilotti et al., 1997; Sunami et al., 2000). The detailed binding site for TTX and another guanidinium neurotoxin Saxitoxin (STX), termed site-1, was depicted by the high-resolution cryo-EM complex structures of Na_VPas and $Na_V1.7$ (Shen et al., 2018; Shen et al., 2019). The positively-charged TTX or STX forms extensive electrostatic interactions with the negatively-charged vestibule of the Na_V channels, that physically blocks ions entering the SF. The Tyr on D_I P-loop of $Na_V1.7$ forms an additional π-cation interaction with the TTX or STX, which is absent in $Na_V1.5$ (**Figure 2C**). Consequently, the affinity of TTX for $Na_V1.7$ is over 500-fold higher than that for $Na_V1.5$. These structures provide an excellent example showing that a single residue at the receptor site could confer isoform selectivity. Recently, guanidinium neurotoxin analogues ST-2262 and ST-2530 were discovered as potent and selective $Na_V1.7$ inhibitors (Pajouhesh et al., 2020), suggesting that the TTX receptor site is a potential therapeutic site. Because the blockade of the guanidinium neurotoxin is state-independent, high affinity and isoform selectivity is critical to minimize potential side effects. The structures of human Na_V channel complexed with the guanidinium neurotoxins should facilitate rational development of isoform selective candidate drugs.

The Central Cavity of Na_V Channels

The bulky central cavity of Na_V channels connects the extracellular SF and the intracellular activation gate, but also opens to four fenestrations formed by adjacent PMs (**Figure 2D**). Lipids or small-molecule drugs access the central cavity through these connecting tunnels to modulate channel properties. The central cavity accommodates multiple receptor sites for site-2 neurotoxins (Deuis et al., 2017), local anesthetic, anti-epilepsy and antiarrhythmic drugs (Hille, 1977; Hondeghem and Katzung, 1984). Batrachotoxin, veratridine and aconitine are natural alkaloids, which modulate the voltage-dependent activation, inactivation and ion selectivity of Na_V channels (Catterall et al., 2007; Quandt and Narahashi, 1982; Ulbricht, 1969). The site-2 neurotoxins usually activate Na_V channels at hyperpolarized membrane potential or increase the open probability, thus they are considered as Na_V channel activators (Deuis et al., 2017). Bulleyaconitine A (BLA), the active substance of the traditional herb *Aconitum bulleyanum* plant (Tang et al., 1986; Wang et al., 2007), exhibits strong inhibition of Na_V channels in a use-dependent manner. The complex structure of human $Na_V1.3$-β1-β2 with BLA reveals a binding site for the site-2 neurotoxin (Li et al., 2022). BLA binds tightly to the central cavity of $Na_V1.3$ *via* multiple polar and non-polar interactions with P-loops and S6 helices of D_I and D_{II} (**Figure 3A**). The BLA engages V416 and L420 on D_I-S6 helix, N972 and L976 on D_{II}-S6 helix (**Figure 3B**), which are in line with the biophysical studies that these residues are important for batrachotoxin, grayanotoxin or veratridine binding (Wang and Wang, 1998; Ishii et al., 1999; Wang et al., 2000; Wang et al., 2001). However, D_{III}-S6 and D_{IV}-S6 helices, which were reported to be involved in batrachotoxin binding (Wang and Wang, 1999; Deuis et al., 2017), have no direct contact with BLA in the $Na_V1.3$-BLA complex structure. These results suggest that the site-2 neurotoxins may bind to overlapping but not identical receptor sites in the central cavity. The binding of BLA partially blocks the ion path, which causes the strong inhibitory effect on $Na_V1.3$. The weak activation potency of BLA probably because BLA sticks into the D_I-D_{II} fenestration, which prevents the closure of the pore-lining S6 helices of D_I and D_{II} during state transition (**Figure 3C**). Owing to the shape and chemistry differences, site-2 neurotoxins with strong activation potency such as batrachotoxin and veratridine likely bind in the central cavity partially overlapping with the BLA site, which stabilize the pore in open conformation and cause less pore blockade.

The structures of $Na_V1.5$ in complex with antiarrhythmic drugs flecainide, propafenone and quinidine reveal antiarrhythmic drugs binding sites in the central cavity (Jiang et al., 2021a; Jiang et al., 2020; Li et al., 2021a), which are distinct from the BLA binding site (**Figures 3D,E**). All three drugs block $Na_V1.5$ in use-dependent manner. The Class IC drug flecainide binds in the central cavity close to D_{II}-D_{III} fenestration. Its positively-charged piperidine nitrogen lies beneath the SF, which prevents the exit of Na^+ from the SF. Meanwhile, the hydrophobic side of the piperidine ring faces the sidechain of Phe1759 (rat $Na_V1.5$), the key residue for antiarrhythmic and local anesthetic drugs binding (Ragsdale et al., 1994). Mutation of this Phe1759 to Ala significantly drops the affinity of flecainide (Liu et al., 2003; Ragsdale et al., 1996; Wang et al., 2003). One of the two hydrophobic trifluoromethoxy tails of flecainide is inserted into the D_{II}-D_{III} fenestration, which suggests that flecainide may access the binding sites through the fenestrations (Gamal El-Din et al., 2018; Nguyen et al., 2019).

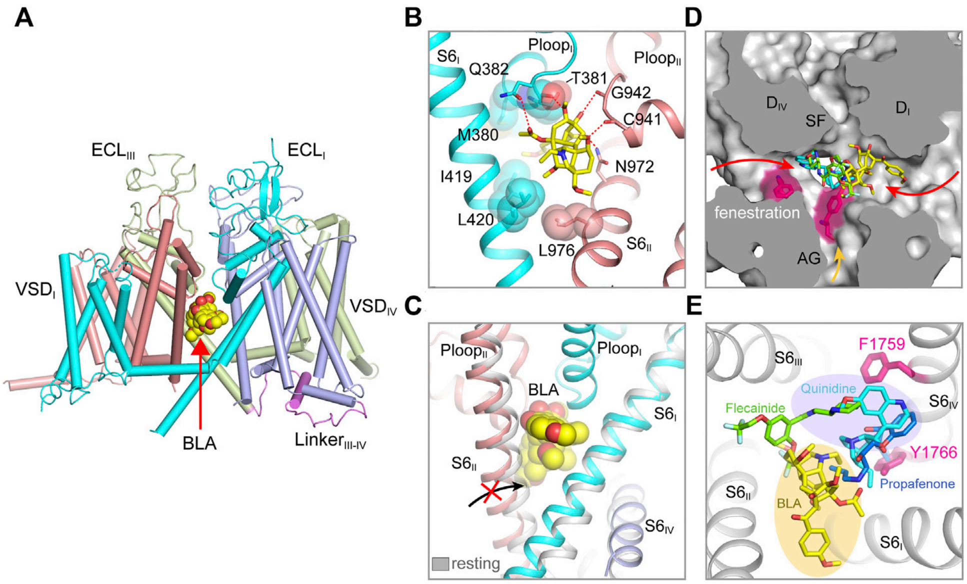

FIGURE 3 | Pore modulators of mammalian Na$_V$ channels. **(A)** The binding site of site-2 neurotoxin BLA in Na$_V$1.3 (PDB code: 7W77). BLA is depicted in spheres. **(B)** A close-up view of the BLA binding site. Key interacting residues are shown side chains in sticks. BLA is shown in sticks. **(C)** BLA binding prevents S6$_{II}$ helix shifting to the resting state. **(D)** Superposition of Na$_V$ structure bound BLA (PDB code: 7W77), Flecainide (PDB code: 6UZ0), Propafenone (PDB code: 7FBS) and Quinidine (PDB code: 6LQA) in the pore. Arrows indicate possible access path for the drugs. **(E)** Top-down view of the BLA binding site and the antiarrhythmic drug binding sites from panel **(D)**.

Compared to class IA (e.g., quinidine) and IB (e.g., lidocaine) drugs, flecainide is larger in size and more hydrophobic, the higher affinity and slower binding kinetics of flecainide and other class IC drugs likely reflect their stronger interaction with Na$_V$1.5. The structure of human Na$_V$1.5-quinidine reveals a quinidine binding site which is also located in the central cavity (Li et al., 2021a). Quinidine lies under the SF and physically blocks the ion path. The quinolone ring of quinidine overlaps with the piperidine ring of flecainide (**Figure 3D**). Unlike the flecainide binding without causing obvious local conformational changes, the quinidine binding was reported to induce the side chain rotation of Tyr1767 (human Na$_V$1.5) and a slightly smaller activation gate compared to the human Na$_V$1.5 structure with a Glu1784Lys mutation (Li et al., 2021a; Pan et al., 2021). However, similar "up" and "down" conformations of the Tyr1755 at the equivalent position were also observed in the Na$_V$1.7 structures (Shen et al., 2019). In addition, the side chain rotation of Tyr1767 could also be affected by the pathogenic Glu1784Lys mutation, which alters the Na$_V$1.5 gating by significantly shifting the voltage-dependent activation toward depolarized membrane potential and the voltage-dependent inactivation toward hyperpolarized membrane potential (Makita et al., 2008).

Class IC drug propafenone preferentially blocks open Na$_V$1.5 (Kohlhardt and Fichtner, 1988). The open state structure of Na$_V$1.5 was achieved by importing the IFM/QQQ mutations (termed Na$_V$1.5/QQQ) to remove the fast inactivation gate, also with the help of propafenone blocking the constant opening activity of the Na$_V$1.5/QQQ during protein expression (Jiang et al., 2021a). The Na$_V$1.5/QQQ structure revealed a high affinity binding site for propafenone in the central cavity. Propafenone engages both the Phe1762 and Tyr1769 (rat Na$_V$1.5) on D$_{IV}$ S6 helix by forming π-π stacking interaction and on-edge van der Waals interactions, respectively (**Figure 3E**). The positively-charged amino group blocks the exit of Na$^+$ from the SF, which is similar to the piperidine of flecainide and the quinolone ring of quinidine (Jiang et al., 2020; Li et al., 2021a). The open activation gate of Na$_V$1.5/QQQ is wide enough for propafenone passing through, which suggests that propafenone probably access its high affinity binding site through the open activation gate. In the resting state, the intracellular activation gate is closed, the antiarrhythmic and local anesthetic drugs may access their receptor sites through the fenestrations in a less efficient manner (**Figure 3D**) (Gamal El-Din et al., 2018; Catterall et al., 2020a), thus exhibiting low affinity blocking. Structural superposition of the Na$_V$ isoforms show that the wall of the central cavity is nearly identical, suggesting it's very difficult to achieve selective receptor site inside the central cavity. Thus, the state- and use-dependent block of the antiarrhythmic and local anesthetic drugs relies on the membrane potential and firing frequency (Hille, 1977; Hondeghem and Katzung, 1984), which allows the drugs to access their active sites in the favorable states without affecting the channels in unfavorable states (Catterall et al., 2020a).

Fast Inactivation of Sodium Channel

Fast inactivation is one of the hallmark features of eukaryotic Na$_V$ channels (Goldin, 2003). The fast inactivation of Na$_V$ channels is crucial for preventing hyperexcitability and priming firing frequency (Catterall, 2000; Catterall et al., 2017). In 1973,

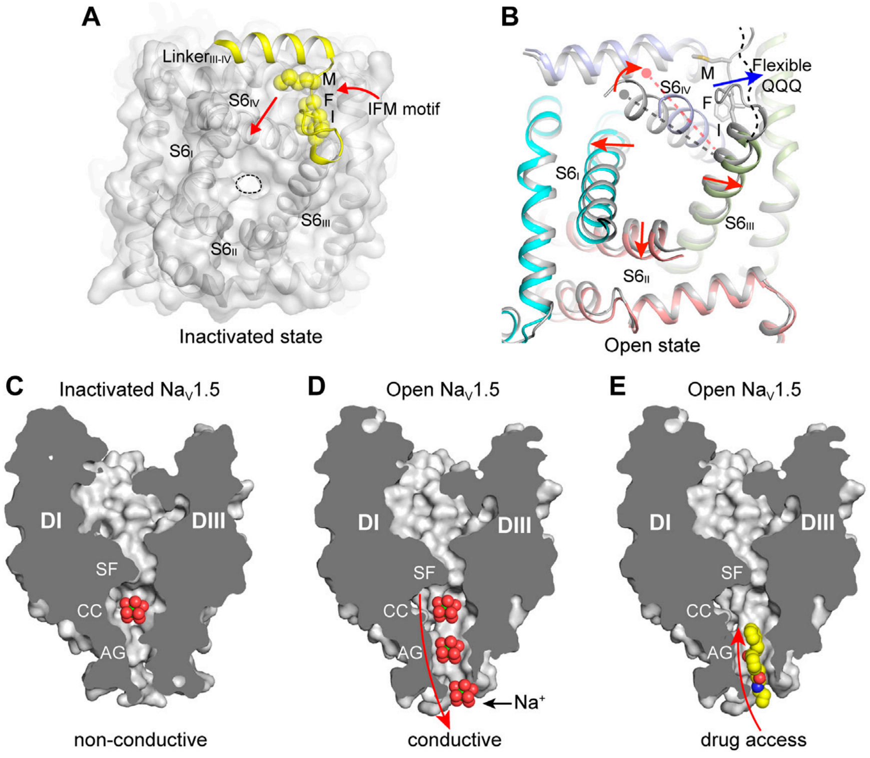

FIGURE 4 | The IFM-motif mediated fast inactivation and the open activation gate. **(A)** Allosteric inhibition of mammalian Na$_V$ channels by the IFM-motif (PDB code: 6J8I). The pore domain viewed from cytosol is shown in surface. The IFM-motif shown in yellow spheres. **(B)** Releasing of the IFM-motif leads to channel opening. Activation gate comparison between rat Na$_V$1.5 (PDB code: 6UZ3) and Na$_V$1.5/QQQ (PDB code: 7FBS). Red arrows indicate the S6 helix shift. **(C)** Non-conductive ion path of the inactivated state Na$_V$ channel (PDB code: 6UZ3). **(D)** Na$^+$ conductive ion path of the open-state Na$_V$ channel (PDB code: 7FBS). **(E)** The open activation gate of Na$_V$ channel provides potential accessing path for the open-state blockers. Propafenone is shown in spheres.

Armstrong found that the fast inactivation was dramatically destructed by intracellularly applying proteolytic enzyme in the squid giant axons (Armstrong et al., 1973), indicating that the fast inactivation gate is located in the cytosol. Site-direct antibody studies identified that the fast inactivation gate is located in the loop between D$_{III}$ and D$_{IV}$ (Vassilev et al., 1988; Stühmer et al., 1989). More detailed point mutagenesis studies confirmed a triple-hydrophobic Ile-Phe-Met (IFM) motif in the D$_{III}$-D$_{IV}$ loop is responsible for the fast inactivation (West et al., 1992; Eaholtz et al., 1994). The cysteine substitution accessibility results indicated that the IFM-motif is buried in a receptor site inaccessible to solvent during inactivation process (Kellenberger et al., 1996). Further extensive site-directed mutagenesis screening studies mapped the IFM-motif receptor site which is constituted by the S4-S5 linkers of D$_{III}$ and D$_{IV}$, and also the cytoplasmic end of D$_{IV}$-S6 helix (McPhee et al., 1994, 1998; Lerche et al., 1997; Smith and Goldin, 1997). Bases on these results, a hinged-lid mechanism for the fast inactivation was proposed, that is, the IFM-motif acts as a hydrophobic latch that binds to its receptor site to close the activation gate. Furthermore, the fast inactivation was found to be electromechanically coupled to the activation of the VSD$_{IV}$ (Chanda and Bezanilla, 2002; Capes et al., 2013).

The solution structure of the D$_{III}$ and D$_{IV}$ linker showed that the flexible IFM-motif is tethered to an α-helix (Rohl et al., 1999), suggesting that the IFM-motif is readily available to bind to its receptor site once close to it. The detailed binding mode of the IFM-motif was consistently revealed by the cryo-EM structures of the eukaryotic Na$_V$ channels (Jiang et al., 2020; Pan et al., 2019; Pan et al., 2018; Shen et al., 2019; Yan et al., 2017). In agreement with the mutagenesis studies and the hinged-lid model, the IFM-motif is embedded in a hydrophobic receptor site formed by the D$_{IV}$-S6 helix and the S4-S5 linkers of D$_{III}$ and D$_{IV}$, adjacent to the intracellular activation gate (**Figure 4A**). The binding pose of the IFM-motif is further stabilized by extensive hydrophobic interactions and hydrogen-bond network (Jiang et al., 2020; Pan et al., 2018). In particular, the activated conformation of VSD$_{III}$ and VSD$_{IV}$ are required for the formation of the IFM-motif receptor site (Jiang et al., 2020). These structures also showed that the activation gate is in the non-conductive state with a diameter of <5 Å, elucidating an allosteric inhibition mechanism for the fast inactivation (**Figures 2A, 4A**). Meanwhile, the electromechanical coupling was observed to be disrupted by α-Scorpion toxins, which specifically bind to the VSD$_{IV}$ and trap it in a deactivated state (Clairfeuille et al., 2019; Jiang et al., 2021c). There structures provide a structural

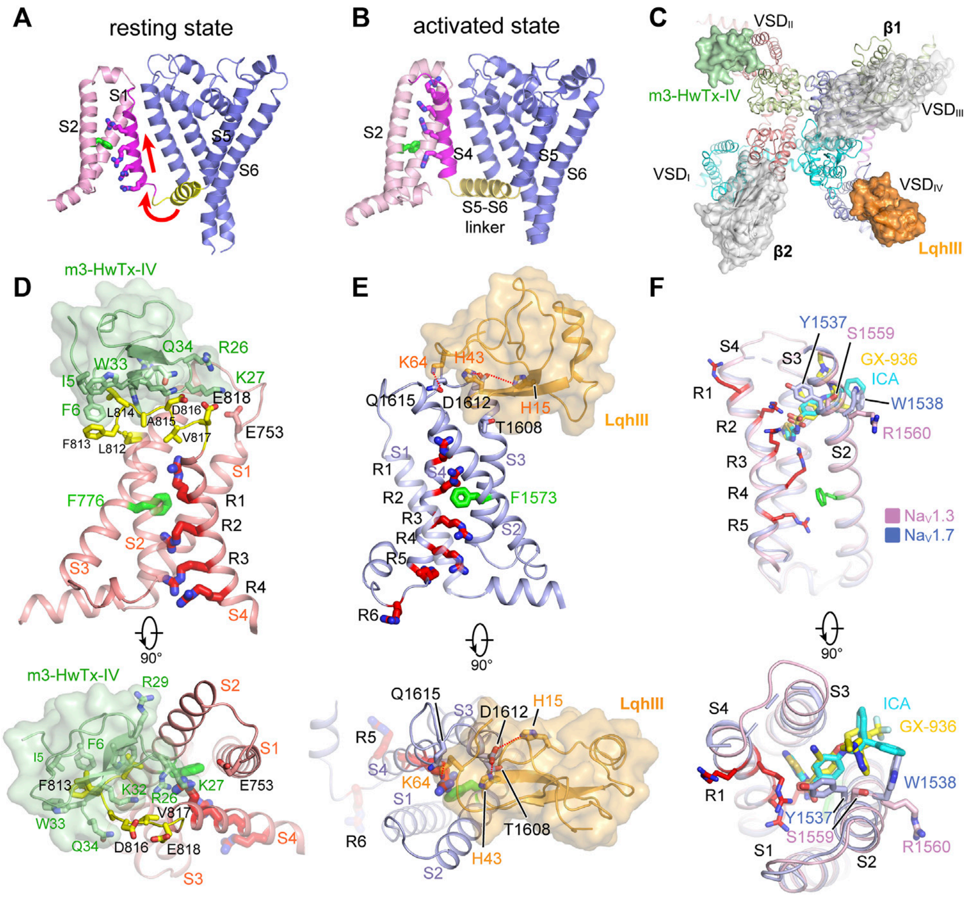

FIGURE 5 | GMTs bind to VSDs of Na$_V$ channels. **(A,B)** Resting (PDB code: 6P6W) and activated (PDB code: 3RVY) state structure of Na$_V$Ab. Red arrows indicate conformational shifts between resting and activated state Na$_V$Ab. The gating charges on the S4 helix shown side chains in sticks. **(C)** Site-3 toxin LqhIII (PDB code: 7K18) and site-4 toxin HwTxIV (PDB code: 7K48) bind to VSD$_{IV}$ and VSD$_{II}$ of Na$_V$ channel, respectively. The Ig-like domain of β1 and β2 subunits project on the VSD$_{III}$ and VSD$_{I}$, respectively, which block the accessibility for potential GMTs binding to VSD$_{III}$ and VSD$_{I}$. **(D)** High affinity binding site for site-4 toxin HwTxIV in the deactivated VSD$_{II}$ (PDB code: 7K48). **(E)** Detailed binding site for α-Scorpion toxin LqhIII in the deactivated VSD$_{IV}$ (PDB code: 7K18). **(F)** Detailed binding site for aryl sulfonamide derivatives ICA121431 and GX-936 in the activated VSD$_{IV}$ of Na$_V$1.3 (PDB code: 7W7F) and Na$_V$1.7 (PDB code: 5EK0), respectively.

framework for the fast inactivation of sodium channels. Pathogenic mutations target the fast inactivation gate and cause life-threatening diseases. For example, mapping the location of the arrhythmia associated mutations in Na$_V$1.5 revealed that the gain-of-function mutations are dense around the fast inactivation gate (Jiang et al., 2020). These gain-of-function mutations impair the fast inactivation, thus cause the channel to generate large abnormal persistent currents or repetitive firing that lead to arrhythmias such as Long-QT syndrome type-3 (Clancy and Kass, 2005).

Sodium ions across the ion path are believed to undergo de-hydration by the SF and re-hydration in the central cavity, then pass the activation gate in hydrated form. The open state structures of BacNa$_V$ channels have shown that the activation gate is wide enough for conducting hydrated Na$^+$ (Lenaeus et al., 2017; Sula et al., 2017). The overall structure of the open state Na$_V$1.5/QQQ is similar to the inactivated state Na$_V$1.5 structures (Jiang et al., 2021a; Jiang et al., 2020). However, releasing of the IFM-motif from its receptor site caused marked local conformational changes in the activation gate (**Figure 4B**). Especially, The D$_{IV}$-S6 helix shifts toward the receptor site by ~6 Å at the cytoplasmic end. The resulting dilated activation gate of the Na$_V$1.5/QQQ is sufficient for free passing of hydrated Na$^+$, also provides an access for pore-blocking drugs such as propafenone (**Figures 4C–E**) (Jiang et al., 2021a).

VSD and Gating Modifier Toxins

The VSDs control both the activation and inactivation of the eukaryotic Na$_V$ channels in response to membrane potential changes. The molecular gating mechanisms of Na$_V$ channels have been reviewed by Ahern (Ahern et al., 2016) and Catterall (Catterall et al., 2017; 2020b). The Na$_V$ channel amino acid sequence revealed that the fourth helix (S4) contains at least four positively-charged Arg or Lys (gating-charges) repeated in a pattern of every three-residues (Noda et al., 1984). In light of the sequence and the biophysical results, the "sliding-helix" and "helical-screw" models were soon proposed to explain the voltage sensing, both models suggest that the positive gating-charges on the S4 helix serve as voltage sensors which move up and down in the membrane in response to membrane potential changes (Catterall, 1986; Guy and Seetharamulu, 1986). The BacNa$_V$ structures captured in the resting and activated states show that the gating-charges underwent a two helical-turns shift, supporting the "sliding-helix" or "helical-screw" models (Payandeh et al., 2011; Sula et al., 2017; Wisedchaisri et al., 2019; Zhang et al., 2012). Because there is no membrane potential in purification conditions (0 mV), most Na$_V$ structures were determined in the activated state (**Figures 5A,B**). The S4 helix is wrapped by the S1-S3 helices, forming a V-shaped aqueous cleft toward the extracellular side. Three of the four gating-charges in the activated Na$_V$Ab structure adopt the activated "up" conformation, which are neutralized by extracellular negatively-charged clusters (ENC). Wisedchaisri obtained the resting state structure of Na$_V$Ab by a combination of importing positive voltage-shifting mutations and cysteine disulfide-bond lock (Wisedchaisri et al., 2019). Compared to the activated VSD, the VSD in the resting state shifts the S4 helix two helical-turns downward to the intracellular side, while the conformation of the S1-S3 helices remains unchanged (**Figures 5A,B**). The inward movement of the S4 helix further bends the S4-S5 linker helix *via* an elbow-like turn. The twisted S4-S5 linker directly causes the bending and rotation of the S6 helix to close the activation gate. These structures define a possible general mechanism for electromechanical coupling of voltage-gated ion channels.

Distinct from the homotetrameric BacNa$_V$ channels, metazoan Na$_V$ channels possess four non-identical VSDs (Noda et al., 1984; Catterall et al., 2017). The VSD$_I$ and VSD$_{II}$ have four gating-charges, VSD$_{III}$ has five gating-charges, and VSD$_{IV}$ has six to eight gating-charges. The four asymmetric VSDs response asynchronously to membrane depolarization (Chanda and Bezanilla, 2002; Ahern et al., 2016). This asynchronous activation is closely related to the voltage-dependent activation and fast inactivation of Na$_V$ channels. According to the asynchronous gating model (Ahern et al., 2016), activation of VSD$_I$-VSD$_{III}$ precedes VSD$_{IV}$ leading to channel opening, and VSD$_{IV}$ activates subsequently to induce the fast inactivation (Chanda and Bezanilla, 2002; Chanda et al., 2004; Capes et al., 2013). The mammalian Na$_V$ channel structures confirmed the asymmetric activation of the four VSDs (Pan et al., 2018; Pan et al., 2019; Shen et al., 2019; Jiang et al., 2020). The VSD$_I$ and VSD$_{II}$ closely resemble the activated VSD of Na$_V$Ab, R1-R3 adopt the "up" conformation above the hydrophobic constriction stie (HCS). The VSD$_{III}$ is more activated, K1-R4 point up and R5 is stuck in the HCS. In contrast, the VSD$_{IV}$ is less activated, R1-R4 are located above the HCS, whereas R5-R6 point downward interacting with the intracellular negatively-charged clusters (INC). The VSD$_{III}$ and VSD$_{IV}$ also recover slower than the VSD$_I$ and VSD$_{II}$, which is probably because the VSD$_{III}$ and VSD$_{IV}$ carry more gating charges that limit their moving rate across the HCS (Capes et al., 2013; Goldschen-Ohm et al., 2013; Jiang et al., 2020).

Modulation of Na$_V$ Channels by Site-4 Toxins

Many natural gating modifier toxins (GMTs) target the VSDs and alter Na$_V$ channel properties (Catterall et al., 2007). These GMTs are important tools to study the Na$_V$ channel properties because of their high-affinity and specific binding mode (Lazdunski et al., 1986). Among them, a group of polypeptide toxins from spiders or scorpions specifically bind to the VSD$_{II}$ of Na$_V$ channels, classified as site-4 neurotoxins, which are used as weapons to paralyze prey (Catterall et al., 2007; Dufton and Rochat, 1984; Rochat et al., 1979). The site-4 toxins were found to inhibit the activation of Na$_V$ channels (Sokolov et al., 2008; Xiao et al., 2008), or cause abnormal activation (Cestèle et al., 1998). The binding site for the site-4 toxins is located in the VSD$_{II}$, especially the extracellular loops linking S1-S2 and S3-S4 (Cestèle et al., 1998; Marcotte et al., 1997). Two site-4 toxins, Protoxin-II (β/ω-theraphotoxin-Tp2a; ProTx-II) from the Peruvian green velvet tarantula *Thrixopelma pruriens* (Middleton et al., 2002) and Huwentoxin-IV (μ-theraphotoxin-Hs2a; HwTx-IV) from the Chinese bird tarantula *Haplopelma schmidti* (Peng et al., 2002), show higher potency in inhibiting Na$_V$1.7 than other Na$_V$ isoforms. Shen reported the cryo-EM structures of human Na$_V$1.7 in complex with ProTx-II and HwTx-IV, showing that ProTx-II binds to both the VSD$_{II}$ and VSD$_{IV}$, whereas HwTx-IV only binds to the VSD$_{II}$ (**Figure 5C**) (Shen et al., 2019). However, the EM density for ProTx-II and HwTx-IV are insufficient to define a detailed binding site. The binding of the two toxins appear only to induce subtle local conformational changes in the activated VSDs (Shen et al., 2019). It has been shown that ProTx-II has higher affinity to the resting state of Na$_V$1.7 than the activated state (Sokolov et al., 2008; Xu et al., 2019). These observations suggest that the binding poses of ProTx-II and HwTx-IV in the Na$_V$1.7 structures may reflect a low-affinity binding state. Meanwhile, Xu reported the ProTx-II bound structures of a chimeric bacterial Na$_V$Ab with VSD$_{II}$ of Na$_V$1.7 (designated as Na$_V$Ab-Na$_V$1.7VSD$_{II}$) in different activation states (Xu et al., 2019). By sorting cryo-EM images of the Na$_V$Ab-Na$_V$1.7VSD$_{II}$-ProTxII yielded two maps in distinct conformations. The VSDs of the major class are in the activated conformation, while the structure of the minor class clearly showed that ProTx-II binding shifted the S4 helix ~10 Å downward into a deactivated state. The deactivated Na$_V$Ab-Na$_V$1.7VSD$_{II}$-ProTxII may represent the high-affinity binding state for ProTx-II. However, the limited resolution prevented revealing a clearer picture for the high-affinity binding site (Xu et al., 2019). Subsequently, Wisedchaisri refined the chimeric Na$_V$Ab-Na$_V$1.7VS2A construct by importing a voltage-shifting mutation to stabilize the channel in the resting state even under positive membrane potential (Wisedchaisri et al., 2021),

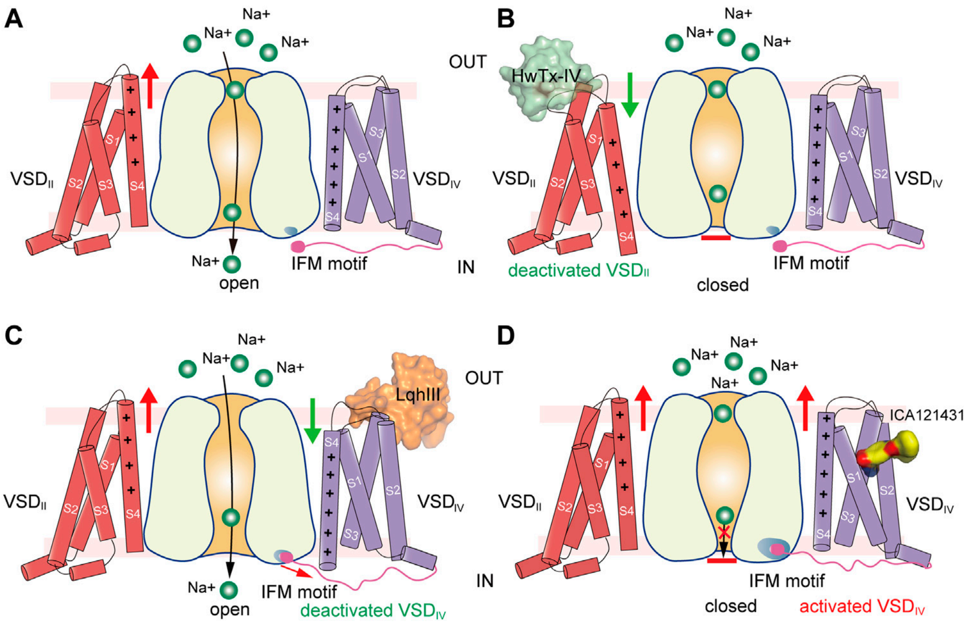

FIGURE 6 | Putative models for modulation of VSDs of Na$_V$ channels. **(A)** Activation of VSD$_I$ and VSD$_{II}$ cause channel opening. Green balls represent sodium ions. Red arrow indicates activation of the VSD. **(B)** Site-4 toxin HwTx-IV traps VSD$_{II}$ in a deactivated state and inhibits channel opening. Green arrow indicates deactivation of the VSD. **(C)** α-Scorpion toxin LqhIII traps VSD$_{IV}$ in a deactivated state and inhibits fast inactivation. **(D)** Aryl sulfonamide analogue ICA121431 binds to activated VSD$_{IV}$ and inhibits channel opening.

and reported the structure of the Na$_V$Ab-Na$_V$1.7VS2A complexed with a modified HwTx-IV (m3-HwTx-IV) (Rahnama et al., 2017; Revell et al., 2013). The Na$_V$Ab-Na$_V$1.7VS2A:m3-HwTx-IV structure unveiled the high affinity binding site for m3-HwTx-IV and demonstrated that the m3-HwTx-IV inhibits the channel by locking the VSD$_{II}$ in the resting state (Wisedchaisri et al., 2021). The m3-HwTx-IV forms extensive interactions with the S3-S4 loop ($_{811}$ELFLADVE$_{818}$) of the VSD$_{II}$, which is consistent with the deactivated Na$_V$Ab-Na$_V$1.7VSD$_{II}$-ProTxII structure (Xu et al., 2019) and the site-direct mutagenesis studies (Xiao et al., 2008; Xiao et al., 2010). Among the S3-S4 loop ($_{811}$ELFLADVE$_{818}$) of the VSD$_{II}$, the F813G mutation drops the affinity of ProTx-II by ~9-fold, but does not affect the binding of HwTx-IV (Xiao et al., 2010); by contrast, the E818C mutation significantly increases the affinity of HwTx-IV, whereas it has little effect on ProTx-II (Xiao et al., 2010; Xu et al., 2019). These opposite effects suggest that the detailed binding poses for the HwTx-IV and ProTx-II are different, despite both of the toxins bind to the same region of the VSD$_{II}$ (**Figure 5D**). The Na$_V$Ab-Na$_V$1.7VSD$_{II}$-ProTxII and Na$_V$Ab-Na$_V$1.7VS2A:m3-HwTx-IV structures elucidate a common inhibition mechanism for the site-4 toxins (**Figures 6A,B**), that is, the positively-charged residues in the C-terminus of the toxins insert their side-chains into the cleft of the VSD$_{II}$ and trap the VSD$_{II}$ in the resting state to prevent the activation (Xu et al., 2019; Wisedchaisri et al., 2021).

The site-4 toxins ProTxII and HwTx-IV are more potent in inhibiting Na$_V$1.7 than other Na$_V$ subtypes (Schmalhofer et al., 2008). Na$_V$1.7 plays crucial roles in pain sensation (Bennett et al., 2019; Dib-Hajj and Waxman, 2019), thus, selective inhibition of Na$_V$1.7 may bring potentially non-addictive medical benefits in treating chronic pain. Given the fact that Na$_V$1.7 are in the resting state for most of the time in the nociceptive afferents (Wisedchaisri et al., 2021), the resting-state trapping mechanism revealed by the above structures suggests that optimization of these gating-modifier toxins could potentially generate effective and selective analgesics. These structures also provide structural templates for future development of new analgesics targeting the resting-state Na$_V$ channels.

Modulation of Na$_V$ Channel by α-Scorpion Toxins

α-Scorpion toxins belong to a family of peptide neurotoxins which inhibit fast inactivation of Na$_V$ channels, causing prolonged and/or repetitive action potentials (Catterall et al., 2007; Jiang et al., 2021c; Kopeyan et al., 1974). Site-directed mutagenesis studies have localized the binding site of α-Scorpion toxins in the S3-S4 loop of VSD$_{IV}$, termed site-3 (Rogers et al., 1996; Thomsen and Catterall, 1989). In addition, a negatively-charged Asp or Glu residue on S3 of VSD$_{IV}$ was identified as the key determinant for the α-Scorpion toxins binding (Benzinger et al., 1998; Rogers et al., 1996). These findings also support the electromechanical coupling between the fast inactivation gate and the VSD$_{IV}$. The α-Scorpion toxin LqhIII and AaHII are lethal toxins extracted from venoms of the "deathstalker scorpion" *Leiurus quinquestriatus hebraeus* and the *Androctonus australis Hector* "man killer" scorpion (Chen and Heinemann, 2001; Martin et al., 1987), both of which dramatically inhibit the fast inactivation of the Na_V channels. In particular, LqhIII exhibits higher affinity to $Na_V1.5$ and extremely slow disassociation rate (Chen and Heinemann, 2001). The cryo-EM structures of rat $Na_V1.5$-LqhIII and the chimeric Na_VPas-$Na_V1.7VSD_{IV}$-AaHII reveal detailed binding site for the α-Scorpion toxins (Clairfeuille et al., 2019; Jiang et al., 2021c). Consistent with previous mutagenesis studies, LqhIII and AaHII engage the S3-S4 loop of VSD_{IV} by forming broad interaction interface (**Figure 5C**). The D1612 in D_{IV}-S3 of $Na_V1.5$ and D1586 in D_{IV}-S3 of $Na_V1.7$ form critical polar interactions with LqhIII and AaHII, respectively. The toxins binding shifts the S4 helix about two helical-turns inward and traps the VSD_{IV} in an intermediate activated state (**Figure 5E**). The relatively flexible positively-charged C-terminal tails of LqhIII and AaHII dock into the extracellular aqueous cleft of VSD_{IV}, displacing the gating-charges and preventing them moving upward. As expected, the two structures show very similar overall binding sites for the α-Scorpion toxins, and also similar conformational shifts in the VSD_{IV} induced the toxins binding (Clairfeuille et al., 2019; Jiang et al., 2021c). Furthermore, the $Na_V1.5$-LqhIII structure reveals a common gating mechanism for the α-Scorpion toxins (**Figure 6C**). That is, the α-Scorpion toxins specifically recognize the high-affinity binding site in the VSD_{IV} and trap the VSD_{IV} in the intermediate activated state, then deactivation of the VSD_{IV} destabilizes the fast inactivation gate thus favors the channel opening (Jiang et al., 2021c).

Although the site-3 toxins and site-4 toxins bind to distinct receptor sites and cause different effects on Na_V channels, these two types of neurotoxins use similar VSD trapping mechanism to modulation channel gating (**Figures 5D,E**). The different modulation effects are because that the activation and fast inactivation of Na_V channels rely on the activation of VSD_I-VSD_{II} and VSD_{IV}, respectively (Chanda and Bezanilla, 2002). From the $Na_V1.4$-β1, $Na_V1.7$-β1-β2, $Na_V1.2$-β2, $Na_V1.1$-β4 and $Na_V1.3$-β1-β2 complex structures, we have known that β1 subunit projects its Ig-like domain on the VSD_{III}, β2 and β4 project their Ig-like domain on the VSD_I, respectively (**Figures 1B**, **5C**). Consequently, the accessibility of VSD_{III} and VSD_I for potential neurotoxins are blocked by the β subunits, which may explain that only a few neurotoxins were reported to bind to VSD_{III} or VSD_I. For instance, Hm-3, from the crab spider *Heriaeus melloteei*, was reported to inhibit $Na_V1.4$ by binding to the VSD_I with micromolar affinity (Männikkö et al., 2018). Recently, a spider toxin Gr4b from *Grammostola rosea* appears to selectively impair fast inactivation of $Na_V1.9$ by binding to its VSD_{III} (Peng et al., 2021). However, the detailed binding sites and the underlying mechanisms for those toxins need further investigation. Meanwhile, because the β subunits bind loosely to $Na_V1.5$ and $Na_V1.8$ (Jiang et al., 2020), this raises a possibility that candidate modulators such as engineered neurotoxins or nanobodies can target $Na_V1.5$ or $Na_V1.8$ by binding to the VSD_{III} or VSD_I without affecting other β subunit-bound Na_V isoforms.

Aryl Sulfonamides Selectively Binds to VSD_{IV}

The apo-form Na_V channel structures show that activation of the VSD_{IV} tightens the fast inactivation gate to close the channel (Jiang et al., 2020; Pan et al., 2018; Yan et al., 2017). Thus, trapping the VSD_{IV} in the activated conformation inhibits the opening of Na_V channels. In agreement with this concept, a family of synthetic aryl sulfonamide derivatives exhibit potent and selective inhibition of Na_V channel isoforms *via* binding to the VSD_{IV} (McCormack et al., 2013). For instance, PF-04856264 and GX-936 selectively and potently inhibit $Na_V1.7$ (Ahuja et al., 2015; McCormack et al., 2013), whereas ICA121431 exhibits potent inhibition of $Na_V1.3/Na_V1.1$ with a factor of >1000-fold over other isoforms (McCormack et al., 2013). The promising selective inhibition is of great interest for developing potentially non-addictive analgesics (Alsaloum et al., 2020). The crystal structure of the chimeric Na_VAb-$Na_V1.7VSD_{IV}$ in complex with GX-936 revealed the first binding site for the aryl sulfonamide analogues (Ahuja et al., 2015). The GX-936 sticks deep into the extracellular aqueous cleft of the VSD_{IV}, and its negatively-charged warhead engages the fourth gating-charge (R4), locking the VSD_{IV} in the activated conformation (**Figure 5F**). Subsequently, the complex structure of human $Na_V1.3$/β1/β2-ICA121431 confirmed the conserved binding site for the aryl sulfonamide analogues (Li et al., 2022). The conserved warhead of the aryl sulfonamide derivatives determines the potency *via* strong electrostatic interactions with the positively-charges R4, which is supported by the R4A mutation dramatically decreasing the affinity of GX-936 by >2000-fold (Ahuja et al., 2015). In addition, the S1559/R1560 on S2 helix of the $Na_V1.3$-VSD_{IV} are responsible for recognizing the tail of ICA121431, and Y1537/W1538 at the equivalent position on $Na_V1.7$ are more favorable for GX-936 binding (Ahuja et al., 2015; Li et al., 2022; McCormack et al., 2013). Superposition of the ICA121431 bound $Na_V1.3$-VSD_{IV} with the deactivated LqhIII bound $Na_V1.5$-VSD_{IV} shows that the gating charges in the deactivated VSD_{IV} cannot form proper interactions with the anionic warhead, elucidating why the aryl sulfonamide derivatives are in favor of binding to the activated VSD_{IV}. In the $Na_V1.3$/β1/β2-ICA121431 structure, the fast inactivation gate binds tightly to its receptor site resulting in a non-conductive activation gate (**Figure 6D**), which provides a full-picture for understanding the allosteric inhibition mechanism of the aryl sulfonamide antagonists (Li et al., 2022).

Several aryl sulfonamide derivatives, such as PF-05089771, GDC-0276 and RG6029, which selectively inhibit $Na_V1.7$ (Alexandrou et al., 2016; McDonnell et al., 2018; Rothenberg et al., 2019; Alsaloum et al., 2020), have failed in Phase I or Phase II clinical trials because of low efficacy (Kingwell, 2019; Alsaloum et al., 2020). These discouraging results suggest that isoform selectivity is not the only challenge for developing candidate analgesics targeting pain related Na_V channels.

SUMMARY AND PROSPECTS

Na_V channels play fundamental roles in electrical signaling. Extensive studies on the biophysical characterization, gene sequence, physiological functions, ligands modulation and pharmacology of Na_V channels have greatly enriched the knowledge of Na_V channels. During the last a few years, cryo-EM structures of Na_V channels from nerve, cardiomyocytes and skeletal muscle were resolved in different functional states or with the binding of distinct modulators. These structures provide in-depth mechanistic insights into the architecture, activation, inactivation, ion selectivity, electromechanical coupling, ligand modulation, and structural pharmacology of Na_V channels. The structure-based drug design will be accelerated by those structural studies, which could potentially generate more efficient, safer and selective drugs for the treatment of Na_V channel associated diseases. The cryo-EM technique will have broader application prospects in validating the structural pharmacology of Na_V channels, also in expanding the fundamental understanding of Na_V channel structure and function. We anticipate that more mammalian Na_V channel structures in different functional states including the resting-state will be achieved, and high-resolution structures will also be very important to unveil more detailed information such as ion selectivity and lipid-channel interactions.

AUTHOR CONTRIBUTIONS

DJ wrote the manuscript, ZX and JZ prepared the figures, and all authors reviewed and revised the paper.

FUNDING

This work is supported by funding from the Institute of Physics, Chinese Academy of Sciences (E0VK101 to DJ).

REFERENCES

Ahern, C. A., Payandeh, J., Bosmans, F., and Chanda, B. (2016). The Hitchhiker's Guide to the Voltage-Gated Sodium Channel Galaxy. *J. Gen. Physiol.* 147, 1–24. doi:10.1085/jgp.201511492

Ahuja, S., Mukund, S., Deng, L., Khakh, K., Chang, E., Ho, H., et al. (2015). Structural Basis of Nav1.7 Inhibition by an Isoform-Selective Small-Molecule Antagonist. *Science* 350, aac5464. doi:10.1126/science.aac5464

Alexandrou, A. J., Brown, A. R., Chapman, M. L., Estacion, M., Turner, J., Mis, M. A., et al. (2016). Subtype-Selective Small Molecule Inhibitors Reveal a Fundamental Role for Nav1.7 in Nociceptor Electrogenesis, Axonal Conduction and Presynaptic Release. *PLoS One* 11, e0152405. doi:10.1371/journal.pone.0152405

Alsaloum, M., Higerd, G. P., Effraim, P. R., and Waxman, S. G. (2020). Status of Peripheral Sodium Channel Blockers for Non-addictive Pain Treatment. *Nat. Rev. Neurol.* 16, 689–705. doi:10.1038/s41582-020-00415-2

Armstrong, C. M., and Bezanilla, F. (1973). Currents Related to Movement of the Gating Particles of the Sodium Channels. *Nature* 242, 459–461. doi:10.1038/242459a0

Armstrong, C. M., Bezanilla, F., and Rojas, E. (1973). Destruction of Sodium Conductance Inactivation in Squid Axons Perfused with Pronase. *J. Gen. Physiol.* 62, 375–391. doi:10.1085/jgp.62.4.375

Bagnéris, C., DeCaen, P. G., Naylor, C. E., Pryde, D. C., Nobeli, I., Clapham, D. E., et al. (2014). Prokaryotic NavMs Channel as a Structural and Functional Model for Eukaryotic Sodium Channel Antagonism. *Proc. Natl. Acad. Sci. U. S. A.* 111, 8428–8433. doi:10.1073/pnas.1406855111

Bennett, D. L., Clark, A. J., Huang, J., Waxman, S. G., and Dib-Hajj, S. D. (2019). The Role of Voltage-Gated Sodium Channels in Pain Signaling. *Physiol. Rev.* 99, 1079–1151. doi:10.1152/physrev.00052.2017

Benzinger, G. R., Kyle, J. W., Blumenthal, K. M., and Hanck, D. A. (1998). A Specific Interaction between the Cardiac Sodium Channel and Site-3 Toxin Anthopleurin B. *J. Biol. Chem.* 273, 80–84. doi:10.1074/jbc.273.1.80

Boiteux, C., Vorobyov, I., French, R. J., French, C., Yarov-Yarovoy, V., and Allen, T. W. (2014). Local Anesthetic and Antiepileptic Drug Access and Binding to a Bacterial Voltage-Gated Sodium Channel. *Proc. Natl. Acad. Sci. U. S. A.* 111, 13057–13062. doi:10.1073/pnas.1408710111

Capes, D. L., Goldschen-Ohm, M. P., Arcisio-Miranda, M., Bezanilla, F., and Chanda, B. (2013). Domain IV Voltage-Sensor Movement Is Both Sufficient and Rate Limiting for Fast Inactivation in Sodium Channels. *J. Gen. Physiol.* 142, 101–112. doi:10.1085/jgp.201310998

Catterall, W. A., Cestèle, S., Yarov-Yarovoy, V., Yu, F. H., Konoki, K., and Scheuer, T. (2007). Voltage-gated Ion Channels and Gating Modifier Toxins. *Toxicon* 49, 124–141. doi:10.1016/j.toxicon.2006.09.022

Catterall, W. A., Dib-Hajj, S., Meisler, M. H., and Pietrobon, D. (2008). Inherited Neuronal Ion Channelopathies: New Windows on Complex Neurological Diseases. *J. Neurosci.* 28, 11768–11777. doi:10.1523/JNEUROSCI.3901-08.2008

Catterall, W. A. (2000). From Ionic Currents to Molecular Mechanisms: the Structure and Function of Voltage-Gated Sodium Channels. *Neuron* 26, 13–25. doi:10.1016/s0896-6273(00)81133-2

Catterall, W. A., Goldin, A. L., and Waxman, S. G. (2005). International Union of Pharmacology. XLVII. Nomenclature and Structure-Function Relationships of Voltage-Gated Sodium Channels. *Pharmacol. Rev.* 57, 397–409. doi:10.1124/pr.57.4.4

Catterall, W. A., Lenaeus, M. J., and Gamal El-Din, T. M. (2020a). Structure and Pharmacology of Voltage-Gated Sodium and Calcium Channels. *Annu. Rev. Pharmacol. Toxicol.* 60, 133–154. doi:10.1146/annurev-pharmtox-010818-021757

Catterall, W. A. (1986). Molecular Properties of Voltage-Sensitive Sodium Channels. *Annu. Rev. Biochem.* 55, 953–985. doi:10.1146/annurev.bi.55.070186.004513

Catterall, W. A. (2014). Sodium Channels, Inherited Epilepsy, and Antiepileptic Drugs. *Annu. Rev. Pharmacol. Toxicol.* 54, 317–338. doi:10.1146/annurev-pharmtox-011112-140232

Catterall, W. A., Wisedchaisri, G., and Zheng, N. (2017). The Chemical Basis for Electrical Signaling. *Nat. Chem. Biol.* 13, 455–463. doi:10.1038/nchembio.2353

Catterall, W. A., Wisedchaisri, G., and Zheng, N. (2020b). The Conformational Cycle of a Prototypical Voltage-Gated Sodium Channel. *Nat. Chem. Biol.* 16, 1314–1320. doi:10.1038/s41589-020-0644-4

Cestèle, S., Qu, Y., Rogers, J. C., Rochat, H., Scheuer, T., and Catterall, W. A. (1998). Voltage Sensor-Trapping: Enhanced Activation of Sodium Channels by Beta-Scorpion Toxin Bound to the S3-S4 Loop in Domain II. *Neuron* 21, 919–931. doi:10.1016/s0896-6273(00)80606-6

Chakrabarti, N., Ing, C., Payandeh, J., Zheng, N., Catterall, W. A., and Pomès, R. (2013). Catalysis of Na+ Permeation in the Bacterial Sodium Channel Na(V)Ab. *Proc. Natl. Acad. Sci. U. S. A.* 110, 11331–11336. doi:10.1073/pnas.1309452110

Chanda, B., Asamoah, O. K., and Bezanilla, F. (2004). Coupling Interactions between Voltage Sensors of the Sodium Channel as Revealed by Site-specific Measurements. *J. Gen. Physiol.* 123, 217–230. doi:10.1085/jgp.200308971

Chanda, B., and Bezanilla, F. (2002). Tracking Voltage-dependent Conformational Changes in Skeletal Muscle Sodium Channel during Activation. *J. Gen. Physiol.* 120, 629–645. doi:10.1085/jgp.20028679

Chen, H., and Heinemann, S. H. (2001). Interaction of Scorpion Alpha-Toxins with Cardiac Sodium Channels: Binding Properties and Enhancement of Slow Inactivation. *J. Gen. Physiol.* 117, 505–518. doi:10.1085/jgp.117.6.505

Clairfeuille, T., Cloake, A., Infield, D. T., Llongueras, J. P., Arthur, C. P., Li, Z. R., et al. (2019). Structural Basis of α-scorpion Toxin Action on Nav Channels. *Science* 363. doi:10.1126/science.aav8573

Clancy, C. E., and Kass, R. S. (2005). Inherited and Acquired Vulnerability to Ventricular Arrhythmias: Cardiac Na+ and K+ Channels. *Physiol. Rev.* 85, 33–47. doi:10.1152/physrev.00005.2004

Clatot, J., Ziyadeh-Isleem, A., Maugenre, S., Denjoy, I., Liu, H., Dilanian, G., et al. (2012). Dominant-negative Effect of SCN5A N-Terminal Mutations through the Interaction of Na(v)1.5 α-subunits. *Cardiovasc Res.* 96, 53–63. doi:10.1093/cvr/cvs211

Corry, B., and Thomas, M. (2012). Mechanism of Ion Permeation and Selectivity in a Voltage Gated Sodium Channel. *J. Am. Chem. Soc.* 134, 1840–1846. doi:10.1021/ja210020h

Das, S., Gilchrist, J., Bosmans, F., and Van Petegem, F. (2016). Binary Architecture of the Nav1.2-β2 Signaling Complex. *Elife* 5. doi:10.7554/eLife.10960

Deuis, J. R., Mueller, A., Israel, M. R., and Vetter, I. (2017). The Pharmacology of Voltage-Gated Sodium Channel Activators. *Neuropharmacology* 127, 87–108. doi:10.1016/j.neuropharm.2017.04.014

Dib-Hajj, S. D., and Waxman, S. G. (2019). Sodium Channels in Human Pain Disorders: Genetics and Pharmacogenomics. *Annu. Rev. Neurosci.* 42, 87–106. doi:10.1146/annurev-neuro-070918-050144

Doyle, D. A., Morais Cabral, J., Pfuetzner, R. A., Kuo, A., Gulbis, J. M., Cohen, S. L., et al. (1998). The Structure of the Potassium Channel: Molecular Basis of K+ Conduction and Selectivity. *Science* 280, 69–77. doi:10.1126/science.280.5360.69

Dufton, M. J., and Rochat, H. (1984). Classification of Scorpion Toxins According to Amino Acid Composition and Sequence. *J. Mol. Evol.* 20, 120–127. doi:10.1007/BF02257372

Eaholtz, G., Scheuer, T., and Catterall, W. A. (1994). Restoration of Inactivation and Block of Open Sodium Channels by an Inactivation Gate Peptide. *Neuron* 12, 1041–1048. doi:10.1016/0896-6273(94)90312-3

Favre, I., Moczydlowski, E., and Schild, L. (1996). On the Structural Basis for Ionic Selectivity Among Na+, K+, and Ca2+ in the Voltage-Gated Sodium Channel. *Biophysical J.* 71, 3110–3125. doi:10.1016/S0006-3495(96)79505-X

Gamal El-Din, T. M., Lenaeus, M. J., Zheng, N., and Catterall, W. A. (2018). Fenestrations Control Resting-State Block of a Voltage-Gated Sodium Channel. *Proc. Natl. Acad. Sci. U. S. A.* 115, 13111–13116. doi:10.1073/pnas.1814928115

Gilchrist, J., Das, S., Van Petegem, F., and Bosmans, F. (2013). Crystallographic Insights into Sodium-Channel Modulation by the β4 Subunit. *Proc. Natl. Acad. Sci. U. S. A.* 110, E5016–E5024. doi:10.1073/pnas.1314557110

Goldin, A. L. (2003). Mechanisms of Sodium Channel Inactivation. *Curr. Opin. Neurobiol.* 13, 284–290. doi:10.1016/s0959-4388(03)00065-5

Goldschen-Ohm, M. P., Capes, D. L., Oelstrom, K. M., and Chanda, B. (2013). Multiple Pore Conformations Driven by Asynchronous Movements of Voltage Sensors in a Eukaryotic Sodium Channel. *Nat. Commun.* 4, 1350. doi:10.1038/ncomms2356

Guy, H. R., and Seetharamulu, P. (1986). Molecular Model of the Action Potential Sodium Channel. *Proc. Natl. Acad. Sci. U. S. A.* 83, 508–512. doi:10.1073/pnas.83.2.508

Hartshorne, R. P., and Catterall, W. A. (1984). The Sodium Channel from Rat Brain. Purification and Subunit Composition. *J. Biol. Chem.* 259, 1667–1675. doi:10.1016/s0021-9258(17)43460-0

Helliwell, K. E., Chrachri, A., Koester, J. A., Wharam, S., Taylor, A. R., Wheeler, G. L., et al. (2020). A Novel Single-Domain Na+-Selective Voltage-Gated Channel in Photosynthetic Eukaryotes. *Plant Physiol.* 184, 1674–1683. doi:10.1104/pp.20.00889

Helliwell, K. E., Chrachri, A., Koester, J. A., Wharam, S., Verret, F., Taylor, A. R., et al. (2019). Alternative Mechanisms for Fast Na+/Ca2+ Signaling in Eukaryotes via a Novel Class of Single-Domain Voltage-Gated Channels. *Curr. Biol.* 29, 1503–e6.e1506. doi:10.1016/j.cub.2019.03.041

Hille, B. (2001). *Ionic Channels in Excitable Membranes*. 3rd edition. United States: OUP.

Hille, B. (1975). Ionic Selectivity, Saturation, and Block in Sodium Channels. A Four-Barrier Model. *J. Gen. Physiol.* 66, 535–560. doi:10.1085/jgp.66.5.535

Hille, B. (1977). Local Anesthetics: Hydrophilic and Hydrophobic Pathways for the Drug-Receptor Reaction. *J. Gen. Physiol.* 69, 497–515. doi:10.1085/jgp.69.4.497

Hille, B. (1971a). The Hydration of Sodium Ions Crossing the Nerve Membrane. *Proc. Natl. Acad. Sci. U. S. A.* 68, 280–282. doi:10.1073/pnas.68.2.280

Hille, B. (1972). The Permeability of the Sodium Channel to Metal Cations in Myelinated Nerve. *J. Gen. Physiol.* 59, 637–658. doi:10.1085/jgp.59.6.637

Hille, B. (1971b). The Permeability of the Sodium Channel to Organic Cations in Myelinated Nerve. *J. Gen. Physiol.* 58, 599–619. doi:10.1085/jgp.58.6.599

Hodgkin, A. L., and Huxley, A. F. (1952a). Currents Carried by Sodium and Potassium Ions through the Membrane of the Giant Axon of Loligo. *J. Physiol.* 116, 449–472. doi:10.1113/jphysiol.1952.sp004717

Hodgkin, A. L., and Huxley, A. F. (1952b). The Components of Membrane Conductance in the Giant Axon of Loligo. *J. Physiol.* 116, 473–496. doi:10.1113/jphysiol.1952.sp004718

Hondeghem, L. M., and Katzung, B. G. (1984). Antiarrhythmic Agents: the Modulated Receptor Mechanism of Action of Sodium and Calcium Channel-Blocking Drugs. *Annu. Rev. Pharmacol. Toxicol.* 24, 387–423. doi:10.1146/annurev.pa.24.040184.002131

Huang, C. L., Wu, L., Jeevaratnam, K., and Lei, M. (2020). Update on Antiarrhythmic Drug Pharmacology. *J. Cardiovasc Electrophysiol.* 31, 579–592. doi:10.1111/jce.14347

Huang, W., Liu, M., Yan, S. F., and Yan, N. (2017). Structure-based Assessment of Disease-Related Mutations in Human Voltage-Gated Sodium Channels. *Protein Cell.* 8, 401–438. doi:10.1007/s13238-017-0372-z

Ishii, H., Kinoshita, E., Kimura, T., Yakehiro, M., Yamaoka, K., Imoto, K., et al. (1999). Point-mutations Related to the Loss of Batrachotoxin Binding Abolish the Grayanotoxin Effect in Na(+) Channel Isoforms. *Jpn. J. Physiol.* 49, 457–461. doi:10.2170/jjphysiol.49.457

Isom, D. G., Castañeda, C. A., Cannon, B. R., and García-Moreno, B. (2011). Large Shifts in pKa Values of Lysine Residues Buried inside a Protein. *Proc. Natl. Acad. Sci. U. S. A.* 108, 5260–5265. doi:10.1073/pnas.1010750108

Isom, L. L., De Jongh, K. S., and Catterall, W. A. (1994). Auxiliary Subunits of Voltage-Gated Ion Channels. *Neuron* 12, 1183–1194. doi:10.1016/0896-6273(94)90436-7

Jiang, D., Banh, R., Gamal El-Din, T. M., Tonggu, L., Lenaeus, M. J., Pomès, R., et al. (2021a). Open-state Structure and Pore Gating Mechanism of the Cardiac Sodium Channel. *Cell.* 184, 5151–e11.e5111. doi:10.1016/j.cell.2021.08.021

Jiang, D., Gamal El-Din, T., Zheng, N., and Catterall, W. A. (2021b). Expression and Purification of the Cardiac Sodium Channel NaV1.5 for Cryo-EM Structure Determination. *Methods Enzymol.* 653, 89–101. doi:10.1016/bs.mie.2021.01.030

Jiang, D., Gamal El-Din, T. M., Ing, C., Lu, P., Pomès, R., Zheng, N., et al. (2018). Structural Basis for Gating Pore Current in Periodic Paralysis. *Nature* 557, 590–594. doi:10.1038/s41586-018-0120-4

Jiang, D., Shi, H., Tonggu, L., Gamal El-Din, T. M., Lenaeus, M. J., Zhao, Y., et al. (2020). Structure of the Cardiac Sodium Channel. *Cell.* 180, 122–e10. doi:10.1016/j.cell.2019.11.041

Jiang, D., Tonggu, L., Gamal El-Din, T. M., Banh, R., Pomès, R., Zheng, N., et al. (2021c). Structural Basis for Voltage-Sensor Trapping of the Cardiac Sodium Channel by a Deathstalker Scorpion Toxin. *Nat. Commun.* 12, 128. doi:10.1038/s41467-020-20078-3

Kao, C. Y. (1966). Tetrodotoxin, Saxitoxin and Their Significance in the Study of Excitation Phenomena. *Pharmacol. Rev.* 18, 997–1049.

Kellenberger, S., Scheuer, T., and Catterall, W. A. (1996). Movement of the Na+ Channel Inactivation Gate during Inactivation. *J. Biol. Chem.* 271, 30971–30979. doi:10.1074/jbc.271.48.30971

Kingwell, K. (2019). Nav1.7 Withholds its Pain Potential. *Nat. Rev. Drug Discov.* doi:10.1038/d41573-019-00065-0

Kohlhardt, M., and Fichtner, H. (1988). Block of Single Cardiac Na+ Channels by Antiarrhythmic Drugs: the Effect of Amiodarone, Propafenone and Diprafenone. *J. Membr. Biol.* 102, 105–119. doi:10.1007/BF01870449

Koishi, R., Xu, H., Ren, D., Navarro, B., Spiller, B. W., Shi, Q., et al. (2004). A Superfamily of Voltage-Gated Sodium Channels in Bacteria. *J. Biol. Chem.* 279, 9532–9538. doi:10.1074/jbc.M313100200

Kopeyan, C., Martinez, G., Lissitzky, S., Miranda, F., and Rochat, H. (1974). Disulfide Bonds of Toxin II of the Scorpion Androctonus Australis Hector. *Eur. J. Biochem.* 47, 483–489. doi:10.1111/j.1432-1033.1974.tb03716.x

Kowey, P. R. (1998). Pharmacological Effects of Antiarrhythmic Drugs. Review and Update. *Arch. Intern Med.* 158, 325–332. doi:10.1001/archinte.158.4.325

Lazdunski, M., Frelin, C., Barhanin, J., Lombet, A., Meiri, H., Pauron, D., et al. (1986). Polypeptide Toxins as Tools to Study Voltage-Sensitive Na+ Channels. *Ann. N. Y. Acad. Sci.* 479, 204–220. doi:10.1111/j.1749-6632.1986.tb15571.x

Lenaeus, M. J., Gamal El-Din, T. M., Ing, C., Ramanadane, K., Pomès, R., Zheng, N., et al. (2017). Structures of Closed and Open States of a Voltage-Gated Sodium Channel. *Proc. Natl. Acad. Sci. U. S. A.* 114, E3051–E3060. doi:10.1073/pnas.1700761114

Lerche, H., Peter, W., Fleischhauer, R., Pika-Hartlaub, U., Malina, T., Mitrovic, N., et al. (1997). Role in Fast Inactivation of the IV/S4-S5 Loop of the Human Muscle Na+ Channel Probed by Cysteine Mutagenesis. *J. Physiol.* 505 (Pt 2) (Pt 2), 345–352. doi:10.1111/j.1469-7793.1997.345bb.x

Li, X., Xu, F., Xu, H., Zhang, S., Gao, Y., Zhang, H., et al. (2022). Structural Basis for Modulation of Human NaV1.3 by Clinical Drug and Selective Antagonist. *Nat. Commun.* 13, 1286. doi:10.1038/s41467-022-28808-5

Li, Z., Jin, X., Wu, T., Huang, G., Wu, K., Lei, J., et al. (2021a). Structural Basis for Pore Blockade of the Human Cardiac Sodium Channel Nav 1.5 by the Antiarrhythmic Drug Quinidine*. *Angew. Chem. Int. Ed. Engl.* 60, 11474–11480. doi:10.1002/anie.202102196

Li, Z., Jin, X., Wu, T., Zhao, X., Wang, W., Lei, J., et al. (2021b). Structure of Human Na V 1.5 Reveals the Fast Inactivation-Related Segments as a Mutational Hotspot for the Long QT Syndrome. *Proc. Natl. Acad. Sci. U.S.A.* 118. doi:10.1073/pnas.2100069118

Liu, H., Atkins, J., and Kass, R. S. (2003). Common Molecular Determinants of Flecainide and Lidocaine Block of Heart Na+ Channels: Evidence from Experiments with Neutral and Quaternary Flecainide Analogues. *J. Gen. Physiol.* 121, 199–214. doi:10.1085/jgp.20028723

Long, S. B., Campbell, E. B., and Mackinnon, R. (2005). Crystal Structure of a Mammalian Voltage-dependent Shaker Family K+ Channel. *Science* 309, 897–903. doi:10.1126/science.1116269

Makita, N., Behr, E., Shimizu, W., Horie, M., Sunami, A., Crotti, L., et al. (2008). The E1784K Mutation in SCN5A Is Associated with Mixed Clinical Phenotype of Type 3 Long QT Syndrome. *J. Clin. Invest.* 118, 2219–2229. doi:10.1172/JCI34057

Makita, N., Bennett, P. B., and George, A. L. (1994). Voltage-gated Na+ Channel Beta 1 Subunit mRNA Expressed in Adult Human Skeletal Muscle, Heart, and Brain Is Encoded by a Single Gene. *J. Biol. Chem.* 269, 7571–7578. doi:10.1016/s0021-9258(17)37325-8

Männikkö, R., Shenkarev, Z. O., Thor, M. G., Berkut, A. A., Myshkin, M. Y., Paramonov, A. S., et al. (2018). Spider Toxin Inhibits Gating Pore Currents Underlying Periodic Paralysis. *Proc. Natl. Acad. Sci. U. S. A.* 115, 4495–4500. doi:10.1073/pnas.1720185115

Mantegazza, M., Yu, F. H., Catterall, W. A., and Scheuer, T. (2001). Role of the C-Terminal Domain in Inactivation of Brain and Cardiac Sodium Channels. *Proc. Natl. Acad. Sci. U. S. A.* 98, 15348–15353. doi:10.1073/pnas.211563298

Marcotte, P., Chen, L. Q., Kallen, R. G., and Chahine, M. (1997). Effects of Tityus Serrulatus Scorpion Toxin Gamma on Voltage-Gated Na+ Channels. *Circ. Res.* 80, 363–369. doi:10.1161/01.res.80.3.363

Martin, M. F., Rochat, H., Marchot, P., and Bougis, P. E. (1987). Use of High Performance Liquid Chromatography to Demonstrate Quantitative Variation in Components of Venom from the Scorpion Androctonus Australis Hector. *Toxicon* 25, 569–573. doi:10.1016/0041-0101(87)90293-5

McCormack, K., Santos, S., Chapman, M. L., Krafte, D. S., Marron, B. E., West, C. W., et al. (2013). Voltage Sensor Interaction Site for Selective Small Molecule Inhibitors of Voltage-Gated Sodium Channels. *Proc. Natl. Acad. Sci. U. S. A.* 110, E2724–E2732. doi:10.1073/pnas.1220844110

McDonnell, A., Collins, S., Ali, Z., Iavarone, L., Surujbally, R., Kirby, S., et al. (2018). Efficacy of the Nav1.7 Blocker PF-05089771 in a Randomised, Placebo-Controlled, Double-Blind Clinical Study in Subjects with Painful Diabetic Peripheral Neuropathy. *Pain* 159, 1465–1476. doi:10.1097/j.pain.0000000000001227

McPhee, J. C., Ragsdale, D. S., Scheuer, T., and Catterall, W. A. (1998). A Critical Role for the S4-S5 Intracellular Loop in Domain IV of the Sodium Channel Alpha-Subunit in Fast Inactivation. *J. Biol. Chem.* 273, 1121–1129. doi:10.1074/jbc.273.2.1121

McPhee, J. C., Ragsdale, D. S., Scheuer, T., and Catterall, W. A. (1994). A Mutation in Segment IVS6 Disrupts Fast Inactivation of Sodium Channels. *Proc. Natl. Acad. Sci. U. S. A.* 91, 12346–12350. doi:10.1073/pnas.91.25.12346

Meisler, M. H., and Kearney, J. A. (2005). Sodium Channel Mutations in Epilepsy and Other Neurological Disorders. *J. Clin. Invest.* 115, 2010–2017. doi:10.1172/JCI25466

Middleton, R. E., Warren, V. A., Kraus, R. L., Hwang, J. C., Liu, C. J., Dai, G., et al. (2002). Two Tarantula Peptides Inhibit Activation of Multiple Sodium Channels. *Biochemistry* 41, 14734–14747. doi:10.1021/bi026546a

Namadurai, S., Balasuriya, D., Rajappa, R., Wiemhöfer, M., Stott, K., Klingauf, J., et al. (2014). Crystal Structure and Molecular Imaging of the Nav Channel β3 Subunit Indicates a Trimeric Assembly. *J. Biol. Chem.* 289, 10797–10811. doi:10.1074/jbc.M113.527994

Namadurai, S., Yereddi, N. R., Cusdin, F. S., Huang, C. L., Chirgadze, D. Y., and Jackson, A. P. (2015). A New Look at Sodium Channel β Subunits. *Open Biol.* 5, 140192. doi:10.1098/rsob.140192

Naylor, C. E., Bagnéris, C., DeCaen, P. G., Sula, A., Scaglione, A., Clapham, D. E., et al. (2016). Molecular Basis of Ion Permeability in a Voltage-Gated Sodium Channel. *EMBO J.* 35, 820–830. doi:10.15252/embj.201593285

Nguyen, P. T., DeMarco, K. R., Vorobyov, I., Clancy, C. E., and Yarov-Yarovoy, V. (2019). Structural Basis for Antiarrhythmic Drug Interactions with the Human Cardiac Sodium Channel. *Proc. Natl. Acad. Sci. U. S. A.* 116, 2945–2954. doi:10.1073/pnas.1817446116

Noda, M., Shimizu, S., Tanabe, T., Takai, T., Kayano, T., Ikeda, T., et al. (1984). Primary Structure of Electrophorus Electricus Sodium Channel Deduced from cDNA Sequence. *Nature* 312, 121–127. doi:10.1038/312121a0

Noda, M., Suzuki, H., Numa, S., and Stühmer, W. (1989). A Single Point Mutation Confers Tetrodotoxin and Saxitoxin Insensitivity on the Sodium Channel II. *FEBS Lett.* 259, 213–216. doi:10.1016/0014-5793(89)81531-5

O'Brien, J. E., and Meisler, M. H. (2013). Sodium Channel SCN8A (Nav1.6): Properties and De Novo Mutations in Epileptic Encephalopathy and Intellectual Disability. *Front. Genet.* 4, 213. doi:10.3389/fgene.2013.00213

O'Malley, H. A., and Isom, L. L. (2015). Sodium Channel β Subunits: Emerging Targets in Channelopathies. *Annu. Rev. Physiol.* 77, 481–504. doi:10.1146/annurev-physiol-021014-071846

Olesen, M. S., Jespersen, T., Nielsen, J. B., Liang, B., Møller, D. V., Hedley, P., et al. (2011). Mutations in Sodium Channel β-subunit SCN3B Are Associated with Early-Onset Lone Atrial Fibrillation. *Cardiovasc Res.* 89, 786–793. doi:10.1093/cvr/cvq348

Pajouhesh, H., Beckley, J. T., Delwig, A., Hajare, H. S., Luu, G., Monteleone, D., et al. (2020). Discovery of a Selective, State-independent Inhibitor of NaV1.7 by Modification of Guanidinium Toxins. *Sci. Rep.* 10, 14791. doi:10.1038/s41598-020-71135-2

Pan, X., Li, Z., Huang, X., Huang, G., Gao, S., Shen, H., et al. (2019). Molecular Basis for Pore Blockade of Human Na+ Channel Nav1.2 by the μ-conotoxin KIIIA. *Science* 363, 1309–1313. doi:10.1126/science.aaw2999

Pan, X., Li, Z., Zhou, Q., Shen, H., Wu, K., Huang, X., et al. (2018). Structure of the Human Voltage-Gated Sodium Channel Nav1.4 in Complex with β1. *Science* 362. doi:10.1126/science.aau2486

Pan, X., Li, Z., Jin, X., Zhao, Y., Huang, G., Huang, X., et al. (2021). Comparative Structural Analysis of Human Na V 1.1 and Na V 1.5 Reveals Mutational Hotspots for Sodium Channelopathies. *Proc. Natl. Acad. Sci. U.S.A.* 118. doi:10.1073/pnas.2100066118

Patino, G. A., Brackenbury, W. J., Bao, Y., Lopez-Santiago, L. F., O'Malley, H. A., Chen, C., et al. (2011). Voltage-gated Na+ Channel β1B: a Secreted Cell Adhesion Molecule Involved in Human Epilepsy. *J. Neurosci.* 31, 14577–14591. doi:10.1523/JNEUROSCI.0361-11.2011

Payandeh, J., Gamal El-Din, T. M., Scheuer, T., Zheng, N., and Catterall, W. A. (2012). Crystal Structure of a Voltage-Gated Sodium Channel in Two Potentially Inactivated States. *Nature* 486, 135–139. doi:10.1038/nature11077

Payandeh, J., Scheuer, T., Zheng, N., and Catterall, W. A. (2011). The Crystal Structure of a Voltage-Gated Sodium Channel. *Nature* 475, 353–358. doi:10.1038/nature10238

Peng, K., Shu, Q., Liu, Z., and Liang, S. (2002). Function and Solution Structure of Huwentoxin-IV, a Potent Neuronal Tetrodotoxin (TTX)-sensitive Sodium Channel Antagonist from Chinese Bird Spider Selenocosmia Huwena. *J. Biol. Chem.* 277, 47564–47571. doi:10.1074/jbc.M204063200

Peng, S., Chen, M., Xiao, Z., Xiao, X., Luo, S., Liang, S., et al. (2021). A Novel Spider Toxin Inhibits Fast Inactivation of the Nav1.9 Channel by Binding to Domain III and Domain IV Voltage Sensors. *Front. Pharmacol.* 12, 778534. doi:10.3389/fphar.2021.778534

Qu, Y., Isom, L. L., Westenbroek, R. E., Rogers, J. C., Tanada, T. N., McCormick, K. A., et al. (1995). Modulation of Cardiac Na+ Channel Expression in Xenopus Oocytes by Beta 1 Subunits. *J. Biol. Chem.* 270, 25696–25701. doi:10.1074/jbc.270.43.25696

Quandt, F. N., and Narahashi, T. (1982). Modification of Single Na+ Channels by Batrachotoxin. *Proc. Natl. Acad. Sci. U. S. A.* 79, 6732–6736. doi:10.1073/pnas.79.21.6732

Ragsdale, D. S., McPhee, J. C., Scheuer, T., and Catterall, W. A. (1996). Common Molecular Determinants of Local Anesthetic, Antiarrhythmic, and Anticonvulsant Block of Voltage-Gated Na+ Channels. *Proc. Natl. Acad. Sci. U. S. A.* 93, 9270–9275. doi:10.1073/pnas.93.17.9270

Ragsdale, D. S., McPhee, J. C., Scheuer, T., and Catterall, W. A. (1994). Molecular Determinants of State-dependent Block of Na+ Channels by Local Anesthetics. *Science* 265, 1724–1728. doi:10.1126/science.8085162

Rahnama, S., Deuis, J. R., Cardoso, F. C., Ramanujam, V., Lewis, R. J., Rash, L. D., et al. (2017). The Structure, Dynamics and Selectivity Profile of a NaV1.7 Potency-Optimised Huwentoxin-IV Variant. *PLoS One* 12, e0173551. doi:10.1371/journal.pone.0173551

Raman, I. M., and Bean, B. P. (1997). Resurgent Sodium Current and Action Potential Formation in Dissociated Cerebellar Purkinje Neurons. *J. Neurosci.* 17, 4517–4526. doi:10.1523/jneurosci.17-12-04517.1997

Raman, I. M., Sprunger, L. K., Meisler, M. H., and Bean, B. P. (1997). Altered Subthreshold Sodium Currents and Disrupted Firing Patterns in Purkinje Neurons of Scn8a Mutant Mice. *Neuron* 19, 881–891. doi:10.1016/s0896-6273(00)80969-1

Ren, D., Navarro, B., Xu, H., Yue, L., Shi, Q., and Clapham, D. E. (2001). A Prokaryotic Voltage-Gated Sodium Channel. *Science* 294, 2372–2375. doi:10.1126/science.1065635

Revell, J. D., Lund, P. E., Linley, J. E., Metcalfe, J., Burmeister, N., Sridharan, S., et al. (2013). Potency Optimization of Huwentoxin-IV on hNav1.7: a Neurotoxin TTX-S Sodium-Channel Antagonist from the Venom of the Chinese Bird-Eating Spider Selenocosmia Huwena. *Peptides* 44, 40–46. doi:10.1016/j.peptides.2013.03.011

Rochat, H., Bernard, P., and Couraud, F. (1979). Scorpion Toxins: Chemistry and Mode of Action. *Adv. Cytopharmacol.* 3, 325–334.

Rogers, J. C., Qu, Y., Tanada, T. N., Scheuer, T., and Catterall, W. A. (1996). Molecular Determinants of High Affinity Binding of Alpha-Scorpion Toxin and Sea Anemone Toxin in the S3-S4 Extracellular Loop in Domain IV of the Na+ Channel Alpha Subunit. *J. Biol. Chem.* 271, 15950–15962. doi:10.1074/jbc.271.27.15950

Rohl, C. A., Boeckman, F. A., Baker, C., Scheuer, T., Catterall, W. A., and Klevit, R. E. (1999). Solution Structure of the Sodium Channel Inactivation Gate. *Biochemistry* 38, 855–861. doi:10.1021/bi9823380

Rothenberg, M. E., Tagen, M., Chang, J. H., Boyce-Rustay, J., Friesenhahn, M., Hackos, D. H., et al. (2019). Safety, Tolerability, and Pharmacokinetics of GDC-0276, a Novel NaV1.7 Inhibitor, in a First-In-Human, Single- and Multiple-Dose Study in Healthy Volunteers. *Clin. Drug Investig.* 39, 873–887. doi:10.1007/s40261-019-00807-3

Ruan, Y., Liu, N., and Priori, S. G. (2009). Sodium Channel Mutations and Arrhythmias. *Nat. Rev. Cardiol.* 6, 337–348. doi:10.1038/nrcardio.2009.44

Sato, C., Ueno, Y., Asai, K., Takahashi, K., Sato, M., Engel, A., et al. (2001). The Voltage-Sensitive Sodium Channel Is a Bell-Shaped Molecule with Several Cavities. *Nature* 409, 1047–1051. doi:10.1038/35059098

Scheuer, T. (2011). Regulation of Sodium Channel Activity by Phosphorylation. *Semin. Cell. Dev. Biol.* 22, 160–165. doi:10.1016/j.semcdb.2010.10.002

Schmalhofer, W. A., Calhoun, J., Burrows, R., Bailey, T., Kohler, M. G., Weinglass, A. B., et al. (2008). ProTx-II, a Selective Inhibitor of NaV1.7 Sodium Channels, Blocks Action Potential Propagation in Nociceptors. *Mol. Pharmacol.* 74, 1476–1484. doi:10.1124/mol.108.047670

Shen, H., Li, Z., Jiang, Y., Pan, X., Wu, J., Cristofori-Armstrong, B., et al. (2018). Structural Basis for the Modulation of Voltage-Gated Sodium Channels by Animal Toxins. *Science* 362. doi:10.1126/science.aau2596

Shen, H., Liu, D., Wu, K., Lei, J., and Yan, N. (2019). Structures of Human Nav1.7 Channel in Complex with Auxiliary Subunits and Animal Toxins. *Science* 363, 1303–1308. doi:10.1126/science.aaw2493

Shen, H., Yan, N., and Pan, X. (2021). Structural Determination of Human Nav1.4 and Nav1.7 Using Single Particle Cryo-Electron Microscopy. *Methods Enzymol.* 653, 103–120. doi:10.1016/bs.mie.2021.03.010

Shen, H., Zhou, Q., Pan, X., Li, Z., Wu, J., and Yan, N. (2017). Structure of a Eukaryotic Voltage-Gated Sodium Channel at Near-Atomic Resolution. *Science* 355. doi:10.1126/science.aal4326

Sivilotti, L., Okuse, K., Akopian, A. N., Moss, S., and Wood, J. N. (1997). A Single Serine Residue Confers Tetrodotoxin Insensitivity on the Rat Sensory-neuron-specific Sodium Channel SNS. *FEBS Lett.* 409, 49–52. doi:10.1016/s0014-5793(97)00479-1

Smith, M. R., and Goldin, A. L. (1997). Interaction between the Sodium Channel Inactivation Linker and Domain III S4-S5. *Biophys. J.* 73, 1885–1895. doi:10.1016/S0006-3495(97)78219-5

Sokolov, S., Kraus, R. L., Scheuer, T., and Catterall, W. A. (2008). Inhibition of Sodium Channel Gating by Trapping the Domain II Voltage Sensor with Protoxin II. *Mol. Pharmacol.* 73, 1020–1028. doi:10.1124/mol.107.041046

Sokolov, S., Scheuer, T., and Catterall, W. A. (2007). Gating Pore Current in an Inherited Ion Channelopathy. *Nature* 446, 76–78. doi:10.1038/nature05598

Stühmer, W., Conti, F., Suzuki, H., Wang, X. D., Noda, M., Yahagi, N., et al. (1989). Structural Parts Involved in Activation and Inactivation of the Sodium Channel. *Nature* 339, 597–603. doi:10.1038/339597a0

Stühmer, W., Methfessel, C., Sakmann, B., Noda, M., and Numa, S. (1987). Patch Clamp Characterization of Sodium Channels Expressed from Rat Brain cDNA. *Eur. Biophys. J.* 14, 131–138. doi:10.1007/BF00253837

Sula, A., Booker, J., Ng, L. C., Naylor, C. E., DeCaen, P. G., and Wallace, B. A. (2017). The Complete Structure of an Activated Open Sodium Channel. *Nat. Commun.* 8, 14205. doi:10.1038/ncomms14205

Sun, Y. M., Favre, I., Schild, L., and Moczydlowski, E. (1997). On the Structural Basis for Size-Selective Permeation of Organic Cations through the Voltage-Gated Sodium Channel. Effect of Alanine Mutations at the DEKA Locus on Selectivity, Inhibition by Ca2+ and H+, and Molecular Sieving. *J. Gen. Physiol.* 110, 693–715. doi:10.1085/jgp.110.6.693

Sunami, A., Glaaser, I. W., and Fozzard, H. A. (2000). A Critical Residue for Isoform Difference in Tetrodotoxin Affinity Is a Molecular Determinant of the External Access Path for Local Anesthetics in the Cardiac Sodium Channel. *Proc. Natl. Acad. Sci. U. S. A.* 97, 2326–2331. doi:10.1073/pnas.030438797

Tamkun, M. M., and Catterall, W. A. (1981). Reconstitution of the Voltage-Sensitive Sodium Channel of Rat Brain from Solubilized Components. *J. Biol. Chem.* 256, 11457–11463. doi:10.1016/s0021-9258(19)68422-x

Tang, L., Gamal El-Din, T. M., Payandeh, J., Martinez, G. Q., Heard, T. M., Scheuer, T., et al. (2014). Structural Basis for Ca2+ Selectivity of a Voltage-Gated Calcium Channel. *Nature* 505, 56–61. doi:10.1038/nature12775

Tang, L., Gamal El-Din, T. M., Swanson, T. M., Pryde, D. C., Scheuer, T., Zheng, N., et al. (2016). Structural Basis for Inhibition of a Voltage-Gated Ca2+ Channel by Ca2+ Antagonist Drugs. *Nature* 537, 117–121. doi:10.1038/nature19102

Tang, X. C., Liu, X. J., Lu, W. H., Wang, M. D., and Li, A. L. (1986). Studies on the Analgesic Action and Physical Dependence of Bulleyaconitine A. *Yao Xue Xue Bao* 21, 886–891.

Thomsen, W. J., and Catterall, W. A. (1989). Localization of the Receptor Site for Alpha-Scorpion Toxins by Antibody Mapping: Implications for Sodium Channel Topology. *Proc. Natl. Acad. Sci. U. S. A.* 86, 10161–10165. doi:10.1073/pnas.86.24.10161

Ulbricht, W. (1969). The Effect of Veratridine on Excitable Membranes of Nerve and Muscle. *Ergeb Physiol.* 61, 18–71. doi:10.1007/BFb0111446

Vassilev, P. M., Scheuer, T., and Catterall, W. A. (1988). Identification of an Intracellular Peptide Segment Involved in Sodium Channel Inactivation. *Science* 241, 1658–1661. doi:10.1126/science.241.4873.1658

Vijayaragavan, K., O'Leary, M. E., and Chahine, M. (2001). Gating Properties of Na(v)1.7 and Na(v)1.8 Peripheral Nerve Sodium Channels. *J. Neurosci.* 21, 7909–7918. doi:10.1523/jneurosci.21-20-07909.2001

Wang, C. F., Gerner, P., Wang, S. Y., and Wang, G. K. (2007). Bulleyaconitine A Isolated from Aconitum Plant Displays Long-Acting Local Anesthetic Properties In Vitro and In Vivo. *Anesthesiology* 107, 82–90. doi:10.1097/01.anes.0000267502.18605.ad

Wang, G. K., Quan, C., Seaver, M., and Wang, S. Y. (2000). Modification of Wild-type and Batrachotoxin-Resistant Muscle Mu1 Na+ Channels by Veratridine. *Pflugers Arch.* 439, 705–713. doi:10.1007/s004249900229

Wang, G. K., Russell, C., and Wang, S. Y. (2003). State-dependent Block of Wild-type and Inactivation-Deficient Na+ Channels by Flecainide. *J. Gen. Physiol.* 122, 365–374. doi:10.1085/jgp.200308857

Wang, S. Y., Barile, M., and Wang, G. K. (2001). Disparate Role of Na(+) Channel D2-S6 Residues in Batrachotoxin and Local Anesthetic Action. *Mol. Pharmacol.* 59, 1100–1107. doi:10.1124/mol.59.5.1100

Wang, S. Y., and Wang, G. K. (1999). Batrachotoxin-resistant Na+ Channels Derived from Point Mutations in Transmembrane Segment D4-S6. *Biophys. J.* 76, 3141–3149. doi:10.1016/S0006-3495(99)77465-5

Wang, S. Y., and Wang, G. K. (1998). Point Mutations in Segment I-S6 Render Voltage-Gated Na+ Channels Resistant to Batrachotoxin. *Proc. Natl. Acad. Sci. U. S. A.* 95, 2653–2658. doi:10.1073/pnas.95.5.2653

Watanabe, H., Darbar, D., Kaiser, D. W., Jiramongkolchai, K., Chopra, S., Donahue, B. S., et al. (2009). Mutations in Sodium Channel β1- and β2-subunits Associated with Atrial Fibrillation. *Circ. Arrhythm. Electrophysiol.* 2, 268–275. doi:10.1161/CIRCEP.108.779181

Weigele, J. B., and Barchi, R. L. (1982). Functional Reconstitution of the Purified Sodium Channel Protein from Rat Sarcolemma. *Proc. Natl. Acad. Sci. U. S. A.* 79, 3651–3655. doi:10.1073/pnas.79.11.3651

Weiss, J., Pyrski, M., Jacobi, E., Bufe, B., Willnecker, V., Schick, B., et al. (2011). Loss-of-function Mutations in Sodium Channel Nav1.7 Cause Anosmia. *Nature* 472, 186–190. doi:10.1038/nature09975

West, J. W., Numann, R., Murphy, B. J., Scheuer, T., and Catterall, W. A. (1991). A Phosphorylation Site in the Na+ Channel Required for Modulation by Protein Kinase C. *Science* 254, 866–868. doi:10.1126/science.1658937

West, J. W., Patton, D. E., Scheuer, T., Wang, Y., Goldin, A. L., and Catterall, W. A. (1992). A Cluster of Hydrophobic Amino Acid Residues Required for Fast Na(+)-Channel Inactivation. *Proc. Natl. Acad. Sci. U. S. A.* 89, 10910–10914. doi:10.1073/pnas.89.22.10910

Wisedchaisri, G., Tonggu, L., Gamal El-Din, T. M., McCord, E., Zheng, N., and Catterall, W. A. (2021). Structural Basis for High-Affinity Trapping of the NaV1.7 Channel in its Resting State by Tarantula Toxin. *Mol. Cell.* 81, 38–e4. doi:10.1016/j.molcel.2020.10.039

Wisedchaisri, G., Tonggu, L., McCord, E., Gamal El-Din, T. M., Wang, L., Zheng, N., et al. (2019). Resting-State Structure and Gating Mechanism of a Voltage-Gated Sodium Channel. *Cell.* 178, 993–e12.e1012. doi:10.1016/j.cell.2019.06.031

Xiao, Y., Bingham, J. P., Zhu, W., Moczydlowski, E., Liang, S., and Cummins, T. R. (2008). Tarantula Huwentoxin-IV Inhibits Neuronal Sodium Channels by Binding to Receptor Site 4 and Trapping the Domain Ii Voltage Sensor in the Closed Configuration. *J. Biol. Chem.* 283, 27300–27313. doi:10.1074/jbc.M708447200

Xiao, Y., Blumenthal, K., Jackson, J. O., Liang, S., and Cummins, T. R. (2010). The Tarantula Toxins ProTx-II and Huwentoxin-IV Differentially Interact with Human Nav1.7 Voltage Sensors to Inhibit Channel Activation and Inactivation. *Mol. Pharmacol.* 78, 1124–1134. doi:10.1124/mol.110.066332

Xu, H., Li, T., Rohou, A., Arthur, C. P., Tzakoniati, F., Wong, E., et al. (2019). Structural Basis of Nav1.7 Inhibition by a Gating-Modifier Spider Toxin. *Cell.* 176, 702–e14. doi:10.1016/j.cell.2019.01.047

Yan, Z., Zhou, Q., Wang, L., Wu, J., Zhao, Y., Huang, G., et al. (2017). Structure of the Nav1.4-β1 Complex from Electric Eel. *Cell.* 170, 470–e11.e411. doi:10.1016/j.cell.2017.06.039

Yellen, G. (2002). The Voltage-Gated Potassium Channels and Their Relatives. *Nature* 419, 35–42. doi:10.1038/nature00978

Yue, L., Navarro, B., Ren, D., Ramos, A., and Clapham, D. E. (2002). The Cation Selectivity Filter of the Bacterial Sodium Channel, NaChBac. *J. Gen. Physiol.* 120, 845–853. doi:10.1085/jgp.20028699

Zhang, X., Ren, W., DeCaen, P., Yan, C., Tao, X., Tang, L., et al. (2012). Crystal Structure of an Orthologue of the NaChBac Voltage-Gated Sodium Channel. *Nature* 486, 130–134. doi:10.1038/nature11054

Zuliani, V., Fantini, M., and Rivara, M. (2012). Sodium Channel Blockers as Therapeutic Target for Treating Epilepsy: Recent Updates. *Curr. Top. Med. Chem.* 12, 962–970. doi:10.2174/156802612800229206

Conflict of Interest: The authors declare that the research was conducted in the absence of any commercial or financial relationships that could be construed as a potential conflict of interest.

frontiers | Frontiers in Pharmacology

ORIGINAL RESEARCH
published: 09 June 2022
doi: 10.3389/fphar.2022.888308

Identification of a Subtype-Selective Allosteric Inhibitor of GluN1/GluN3 NMDA Receptors

Yue Zeng[1,2†], Yueming Zheng[1†], Tongtong Zhang[2,3], Fei Ye[4], Li Zhan[1], Zengwei Kou[3], Shujia Zhu[2,3]* and Zhaobing Gao[1,2,5]*

[1]Center for Neurological and Psychiatric Research and Drug Discovery, Shanghai Institute of Materia Medica, Chinese Academy of Sciences, Shanghai, China, [2]College of Pharmacy, University of Chinese Academy of Sciences, Beijing, China, [3]State Key Laboratory of Neuroscience, CAS Center for Excellence in Brain Science and Intelligence Technology, Institute of Neuroscience, Chinese Academy of Sciences, Shanghai, China, [4]College of Life Sciences and Medicine, Zhejiang Sci-Tech University, Hangzhou, China, [5]Zhongshan Institute of Drug Discovery, Institution for Drug Discovery Innovation, Chinese Academy of Sciences, Zhongshan, China

Edited by:
Jinwei Zhang,
University of Exeter, United Kingdom

Reviewed by:
Andreas Reiner,
Ruhr University Bochum, Germany
Dan Monaghan,
University of Nebraska Medical Center, United States

***Correspondence:**
Shujia Zhu
shujiazhu@ion.ac.cn
Zhaobing Gao
zbgao@simm.ac.cn

†These authors have contributed equally to this work

Specialty section:
This article was submitted to Pharmacology of Ion Channels and Channelopathies, a section of the journal Frontiers in Pharmacology

Received: *02 March 2022*
Accepted: *13 May 2022*
Published: *09 June 2022*

Citation:
Zeng Y, Zheng Y, Zhang T, Ye F, Zhan L, Kou Z, Zhu S and Gao Z (2022) Identification of a Subtype-Selective Allosteric Inhibitor of GluN1/GluN3 NMDA Receptors. Front. Pharmacol. 13:888308. doi: 10.3389/fphar.2022.888308

N-methyl-D-aspartate receptors (NMDARs) are Ca^{2+}-permeable ionotropic glutamate receptors (iGluRs) in the central nervous system and play important roles in neuronal development and synaptic plasticity. Conventional NMDARs, which typically comprise GluN1 and GluN2 subunits, have different biophysical properties than GluN3-containing NMDARs: GluN3-containing NMDARs have smaller unitary conductance, less Ca^{2+}-permeability and lower Mg^{2+}-sensitivity than those of conventional NMDARs. However, there are very few specific modulators for GluN3-containing NMDARs. Here, we developed a cell-based high-throughput calcium assay and identified 3-fluoro-1,2-phenylene bis (3-hydroxybenzoate) (WZB117) as a relatively selective inhibitor of GluN1/GluN3 receptors. The IC_{50} value of WZB117 on GluN1/GluN3A receptors expressed in HEK-293 cells was 1.15 ± 0.34 μM. Consistently, WZB117 exhibited strong inhibitory activity against glycine-induced currents in the presence of CGP-78608 but only slightly affected the NMDA-, KA- and AMPA-induced currents in the acutely isolated rat hippocampal neurons. Among the four types of endogenous currents, only the first one is primarily mediated by GluN1/GluN3 receptors. Mechanistic studies showed that WZB117 inhibited the GluN1/GluN3A receptors in a glycine-, voltage- and pH-independent manner, suggesting it is an allosteric modulator. Site-directed mutagenesis and chimera construction further revealed that WZB117 may act on the GluN3A pre-M1 region with key determinants different from those of previously identified modulators. Together, our study developed an efficient method to discover modulators of GluN3-containing NMDARs and characterized WZB117 as a novel allosteric inhibitor of GluN1/GluN3 receptors.

Keywords: N-methyl-D-aspartate (NMDA) receptors, GluN3 subunits, WZB117, allosteric modulator, ion channels, drug discovery

INTRODUCTION

N-methyl-D-aspartate receptors (NMDARs) are glutamate-gated ion channels that play pivotal roles in neuronal development and synaptic plasticity in the central nervous system (Traynelis et al., 2010; Paoletti et al., 2013; Hansen et al., 2018). Seven NMDAR subunits have been identified, including GluN1, GluN2 (2A-2D) and GluN3 (3A-3B) subunits. Conventional NMDARs are heterotetramers comprising two glycine-binding GluN1 subunits and two glutamate-binding GluN2 (2A-2D) subunits, with high Ca^{2+}-permeability and voltage-dependent Mg^{2+} blockage (Ulbrich and Isacoff, 2007; Paoletti et al., 2013; Karakas and Furukawa, 2014). Over the past 3 decades, conventional NMDARs have been intensively studied as potential therapeutic targets for various psychiatric or neurological disorders (Hansen et al., 2021).

Much less is known about GluN3-containing NMDARs (hereafter GluN3-NMDARs) than about conventional NMDARs (Crawley et al., 2022). Coassembly with GluN3 (3A-3B) subunits dramatically changes the biophysical properties of NMDARs by promoting smaller unitary conductance, less Ca^{2+}-permeability and lower Mg^{2+}-sensitivity. Thus, GluN3A and GluN3B have been proposed to be dominant negative subunits of NMDARs (Das et al., 1998; Perez-Otano et al., 2001; Chatterton et al., 2002). Under physiological conditions, GluN3A expression is maintained in a narrow time window in early postnatal development and remains at a low level in adults (Ciabarra et al., 1995; Sucher et al., 1995; Sasaki et al., 2002; Wong et al., 2002). Multiple studies have reported that GluN3A may regulate synaptic maturation and pruning (Perez-Otano et al., 2006; Roberts et al., 2009; Fiuza et al., 2013; Kehoe et al., 2013; Kehoe et al., 2014). Dysfunction of GluN3A due to failure of downregulation or aberrant reactivation beyond the physiological time window is implicated in multiple neurological diseases, such as Huntington's disease (Marco et al., 2013; Wesseling and Perez-Otano, 2015; Mahfooz et al., 2016; Marco et al., 2018), addiction (Yuan and Bellone, 2013; Yuan et al., 2013; Jin et al., 2014), and schizophrenia (Glantz and Lewis, 2000; Mueller and Meador-Woodruff, 2004; Takata et al., 2013). Different from that of GluN3A, the expression of GluN3B increases slowly throughout the developmental stages but appreciably in caudal areas (Chatterton et al., 2002). Limited studies have suggested that GluN3B may be involved in motor function, as the expression of GluN3B is restricted to the motor neurons of spinal cord and brainstem (Chatterton et al., 2002). The pharmacological and physiological functions of these two GluN3 subunits need to be further studied, especially regarding whether they can be drug targets for the treatment of neurological diseases, in which GluN3-specific modulators may serve as pharmacological tools.

In contrast to conventional NMDARs, GluN1/GluN3 receptors belong to a special class of NMDARs that only require glycine for activation, since the endogenous ligands are glycine for both GluN1 and GluN3 (Ciabarra et al., 1995; Sucher et al., 1995; Chatterton et al., 2002; Sasaki et al., 2002; Kehoe et al., 2014). However, the glycine-induced currents measured with conventional methods such as whole-cell patch-clamp recording of GluN1/GluN3 receptors are negligible, possibly due to their rapid desensitization caused by the preferential binding of glycine to the GluN1 subunit (Grand et al., 2018). Mutagenesis of the glycine-binding sites ($GluN1^{F484A/T518L}$) (Kvist et al., 2013) or pre-incubation with CGP-78608, a competitive antagonist of GluN1 (Grand et al., 2018), can prevent desensitization, which has enabled the discovery of GluN3-specific modulators, including TK series compounds (TK13, TK30, TK80) and EU1180-438 (Kvist et al., 2013; Zhu et al., 2020). Although TK compounds are less active and relatively mediocre in selectivity, their discovery suggests that the glycine-binding pocket in the GluN3A subunit could be suitable for GluN3-specific pharmaceutical development, as reflected in a 650-fold higher affinity of glycine for GluN3A than for GluN1 (Yao and Mayer, 2006). EU1180-438 was reported as a negative allosteric modulator of GluN1/GluN3 receptors with high potency and selectivity acting on the Glu3A pre-M1 region, a linker between the ligand binding domains (LBDs) and the first transmembrane helix (M1) (Zhu et al., 2020). In short, pharmacological tools targeting GluN3 are still scarce. Thus, it is important to develop a more efficient method to identify novel and potent modulators targeting GluN3-NMDARs.

Here, we developed a cell-based high throughput calcium assay and identified multiple novel inhibitors of GluN3-NMDARs from 2560 compounds. Most of the compounds were obtained from the Approved Drug Library (originally from Topscience, MCE, ApexBio and Selleck), and the rest that are in clinical or preclinical stages were collected by our lab. These compounds generally have known and well-characterized biological activity, safety and bioavailability. Among the identified hits, WZB117 was characterized as an allosteric inhibitor with high selectivity for recombinant and native GluN1/GluN3 receptors.

MATERIAL AND METHODS

Molecular Biology

To establish GluN1/GluN3A stable cell lines, the human GluN1-1a (GenBank: NP_015566.1) and the rat GluN3A (GenBank: NP_612555.1) genes were subcloned into the pcDNA5-FRT-To and pcDNA3.1 vectors, respectively. An EGFP tag was added to the C-terminus of GluN1 or GluN3A using a T2A linker for identification of transfected cells during transient transfection. Point mutations were introduced by site-directed mutagenesis using PrimeSTAR (Takara). The human GluN2A (GenBank: NP_000824.1) gene was subcloned into the pcDNA3.1 vector. The chimeras $GluN3A^{670\text{-}673\ MWPL/LEPF}$ and $GluN2A^{550\text{-}553\ LEPF/MWPL}$ were generated using In-Fusion HD Cloning kits (Takara). All constructs were confirmed by DNA sequencing (Beijing Genomics Institute).

Cell Culture and Transfection

The Flp-in T-Rex 293 cell lines (Invitrogen), stably expressing GluN1/GluN3A were grown in DMEM basal medium (Gibco) supplemented with 10% fetal bovine serum (FBS, Invitrogen), 15 μg/ml blasticidin S (Invitrogen), 50 μg/ml hygromycin B (Invitrogen) and 500 μg/ml G418 (Gibco). Expression in cell lines was induced with 1 μg/ml doxycycline (Invitrogen) 24–28 h prior to the experiments. Chinese hamster ovary (CHO) cells were grown in DMEM-F12 basal medium (Gibco) supplemented with 10% FBS. In the study on the action sites of WZB117, all whole-cell patch-clamp recordings were performed on CHO cells. The transfections were carried out using Lipofectamine 3000 transfection reagent (Thermo Fisher) according to the manufacturer's instructions. All cells mentioned above were cultured in a 5% CO_2 incubator at 37°C and passaged every other day at a ratio of 1:3.

qRT-PCR

Total RNA was extracted from cells using TRIzol (Invitrogen) and reverse-transcribed into cDNA using PrimeScript RT Master Mix (Takara) following the manufacturer's instructions. The quantifications were performed using the SYBR Green Master Mix kit (Yeasen) in the Fast Real-Time PCR system (Applied Biosystems 7500, CA, United States). The results were processed with the mean values of delta Ct and Standard Error of Mean (SEM). The primers used for quantification are as follows:

GluN1-F: 5′-CCAGTCAAGAAGGTGATCTGCAC-3′;
GluN1-R: 5′-TTCATGGTCCGTGCCAGCTTGA-3′;
GluN3A-F: 5′-GCATAGTGCGCCACGAGTT-3′;
GluN3A-R: 5′-GGTCAGGATTGAGACAGTGACAT-3′;
GAPDH-F: 5′-GTCAAGGCTGAGAACGGGAA-3′;
GAPDH-R: 5′-AAATGAGCCCCAGCCTTCTC-3′.

Western Blot Analysis

Total protein was extracted with strong RIPA lysis buffer (Yeasen), quantified with the BCA protein quantification kit (Thermo Fisher) and separated by 8% SDS-PAGE electrophoresis, and then the membrane was incubated with primary antibodies against GluN3A (at a working concentration of 10 μg/ml) and GAPDH (Yeasen, at a working concentration of 1 μg/ml). The primary antibody against GluN3A was produced by our own lab. Briefly, GluN3A-NTD protein was used as an antigen to immunize Balb/c mice. Seropositive splenocytes detected by ELISA were fused with myeloma cells (SP2/0) to obtain hybridoma cells. Total RNA was extracted from hybridoma cells and reverse-transcribed into cDNA. The sequence of the heavy and light chains of the antibody were cloned and sequenced using multiple mixed primers (von Boehmer et al., 2016), and the antibody was expressed and purified in HEK-293T cells *in vitro*. The second antibody was peroxidase AffiniPure goat anti-mouse IgG (H + L) (Yeasen).

High-Throughput Screening Assay

The HEK-293 cells stably expressing GluN1/GluN3A receptors were seeded at a density of 10,000 cells/well in the 384-well plates, and expression was induced with 1 μg/ml doxycycline for 24–28 h. Then the culture medium was removed, Fluo-4 (Invitrogen) was loaded and the cells were incubated in the 37°C incubator away from light for 1 h (Gee et al., 2000). The plates were gently washed twice with Ca^{2+}-free buffer and then incubated with one of the 2560 compounds (from the Chinese National Compound Library) or DMSO (1% and 0.33%) for 20 min. A fixed concentration of 30 μM and dual concentrations of 10 μM and 30 μM were applied in the primary and secondary screening, respectively. Two replicates were set up for each condition. After incubating 30 μl of the tested compounds, 10 μl of CGP-78608 (Tocris, at a working concentration of 500 nM) was added and incubated for 3 min, and the cells were subsequently stimulated by 10 μl of glycine (Amresco, at a working concentration of 100 μM). A FDSS/μCell platform (Hamamatsu) was used to measure the fluorescence signals. The excitation (Ex) and emission (Em) wavelengths were set to 480 and 540 nm, respectively. The inhibitory effects of tested compounds were compared by the ratios of fluorescence (F) with (F_{drug}) and without (F_{control}) the compounds. The F_{control} value in these assays represented the value of basal Fluo-4 fluorescence plus glycine-stimulated fluorescence, and the F_{drug} indicated the total Fluo-4 fluorescence after treatment of the drugs. Both the F_{drug} and F_{control} values were taken at the peak. The Ca^{2+}-free buffer used to dilute Fluo-4 and wash cell-plates contained (in mM): 140 NaCl, 5 KCl, 1 $MgCl_2$, 10 glucose, 10 HEPES, and 0.5 EGTA. The pH was adjusted to 7.2 using NaOH. To dilute the compounds, 2 mM of free Ca^{2+} was added in addition to the other components of the buffer.

Acutely Isolated Hippocampal Neuron Preparations

Hippocampal neurons were obtained from Sprague-Dawley rats (aged P7-14). Briefly, the isolated hippocampal tissues were cut into approximately 800 μM slices along the sagittal plane and were digested with 3 mg/ml proteinase (Sigma-Aldrich) at 32°C for 8 min. Then 1 mg/ml bovine serum albumin (Sangon Biotech) and 1 mg/ml trypsin inhibitor (Sigma-Aldrich) were used to stop the digestion. A few slices of the hippocampus were gently blown into single cells with the dissecting solution, then transferred to a dish and left to rest for 20 min before experiments. The dishes were preprocessed. Essentially, the bottom of the dish was covered with discarded cell suspension the day before the experiment and was washed and dried the next day, which prevented the neurons from sticking to the bottom too tightly. The dissecting solution contained (in mM): 82 Na_2SO_4, 30 K_2SO_4, 5 $MgCl_2$, 1 Na pyruvate, 10 HEPES, and 20 glucose. The pH was adjusted to 7.2 using NaOH (Xie et al., 2020).

Whole-Cell Patch-Clamp Recording

Whole-cell patch-clamp recordings were performed at room temperature (22–25°C) using an EPC-10 amplifier and Patch Master Software (HEKA). Pipettes were pulled from borosilicate glass capillaries (World Precision Instruments), and the resistances were 3–5 MΩ when filled with the intracellular solution. The extracellular solution contained (in mM): 140 NaCl, 2.8 KCl, 1 $CaCl_2$, 10 HEPES and 20 sucrose (290–300 mOsm), pH adjusted to 7.3 using NaOH. The pipette solution contained (in mM): 115 CsF, 10 CsCl, 10 HEPES and 10 BAPTA (280–290 mOsm), pH adjusted to 7.2 using CsOH (Grand et al., 2018). When recording in hippocampal neurons, the extracellular solution contained (in mM): 140 NaCl, 5 KCl, 1 $CaCl_2$, 1.25

$MgCl_2$, 10 glucose, and 10 HEPES, and the pH was adjusted to 7.4 using NaOH, and the pipette solution contained (in mM): 140 KCl, 1 $MgCl_2$, 10 EGTA, and 10 HEPES, and the pH was adjusted to 7.2 using KOH (Xie et al., 2020). Drug-containing solutions were applied through an RSC-200 Rapid Solution Changer with a 9-tube head (BioLogic Co., France), in which the cell is positioned close to the output of a capillary. The solution, containing either one drug or a combination of different drugs, to be assayed flows out of the capillary at a moderate flow rate by gravity. The lifted cell, exposed to this stream, rapidly equilibrates in the perfusion solution. Whole-cell patch-clamp recordings in heterologous cells and hippocampal neurons were performed at a holding potential of −60 mV. Currents were sampled at 10 kHz and low pass filtered at 2.9 kHz. To record the native GluN1/GluN3 receptor-mediated currents, the extracellular solution was supplemented with 10 μM bicuculline (Sigma-Aldrich), 2 μM NBQX (Topscience), 100 μM D-APV (MCE), and 50 μM strychnine (UHN Shanghai) to block γ-aminobutyric acid type A ($GABA_A$), α-amino-3-hydroxy-5-methylisoxazole-4-propionate (AMPA), GluN1/GluN2 NMDA and glycine receptors, respectively. To record the native GluN2-NMDARs-mediated currents, 10 μM bicuculline and 2 μM NBQX were added into the extracellular solution to block $GABA_A$ receptors and AMPA receptors, respectively (Grand et al., 2018; Otsu et al., 2019; Zhu et al., 2020).

Two-Electrode Voltage-Clamp Recordings

Two-electrode voltage-clamp (TEVC) recordings were performed on *Xenopus* oocytes expressing various subtypes of recombinant NMDARs. Each oocyte was injected with a mixture of 0.5–1.0 ng cDNAs or cRNAs encoding wild-type (WT) or mutant GluN1 (GluN1-1a or GluN1-4a) and GluN2 (2A-2D) or GluN3 (3A-3B) at a ratio of 1:1. The mutant GluN1-4a$^{F484A/T518L}$ was injected together with GluN3B to boost the currents of GluN1/GluN3B receptors, and WT GluN1-1a was used unless otherwise stated. The cRNAs of GluN1-4a, GluN3A and GluN3B were transcribed from corresponding DNAs using the mMESSAGE mMACHINE T7 Ultra kit (Life Technologies) according to the manufacturer's instructions, and the others not specified were cDNAs. TEVC recording was performed 24–72 h post injection in extracellular solution containing (in mM): 100 NaCl, 0.3 $BaCl_2$, 2.5 KCl, 0.01 DTPA and 5 HEPES, and the pH was adjusted to 7.3 using NaOH. All recordings were carried out at a holding potential of −60 mV.

Molecular Modeling

The structural model of GluN1/GluN3A receptor was generated using Modeller 9.24 (Webb and Sali, 2016) based on two templates, the diheteromeric GluN1/GluN2B receptor structure (PDB ID: 6WHS) (Chou et al., 2020) and the truncated GluN3A-LBD structure (PDB ID: 2RC7) (Yao et al., 2008). Then, the structure was refined using the Protein Preparation Wizard Workflow embedded in the Maestro 9.0, and all the parameters were set as the default. The potential binding pockets around the pre-M1 region of GluN1/GluN3A receptors were predicted using the Fpocket program (Le Guilloux et al., 2009). Afterward, the program Glide (Friesner et al., 2004) integrated in Maestro was employed to perform molecular docking. The residues in the range of 10 Å around the residue W671 were defined as the binding sites. The compound WZB117 was prepared through LigPrep provided by Maestro to generate protonation states with Epik (Shelley et al., 2007) with a pH value of 7.0 ± 2.0. The Glide XP mode was used to dock the prepared ligand into the defined docking grid of GluN1/GluN3A receptors.

Statistical Analysis

Patch-clamp data were processed using Clampfit 10.4 (Molecular Device, Sunnyvale, CA, United States) and analyzed with GraphPad Prism 5.0 (GraphPad Software, San Diego, CA, United States). Concentration-response curves were fitted using the following 3-parameter Hill equation: Y=Bottom + (Top-Bottom)/(1 + 10^(X-LogIC$_{50}$)), where Top and Bottom, respectively, represent the channel's maximum and minimum responses to the compounds, X is the value of the logarithm of the concentration, Y is the $I_{drug}/I_{control}$ value, and IC_{50} is the drug concentration producing a half-maximum response. All results are given as the mean ± SEM. Statistical analyses were performed using Student's t-test or two-way ANOVA. Asterisks (*) indicate statistically significant differences from the control group ($*p < 0.05$, $**p < 0.01$ and $***p < 0.001$).

RESULTS

Establishment of a HTS Method for GluN1/GluN3A Receptors

To discover GluN3A-specific modulators, we have developed a cell-based HTS method by measuring Ca^{2+} influx using Fluo-4 as fluorescent indicator. First, a cell line stably expressing GluN1/GluN3A receptors was established using the Flp-in T-REx system (**Figure 1A**). To induce GluN1/GluN3A expression, 1 μg/ml doxycycline was added into the culture medium 24–28 h before the experiments. The GluN1/GluN3A Flp-in T-REx 293 stable cell lines remained healthy despite the induction. Unlike in the host cells, qRT-PCR (**Figure 1B**) and Western blot assays (**Figure 1C**) showed that both GluN1 and GluN3A were well expressed in the GluN1/GluN3A stable cell lines with induction. As illustrated in **Figure 1D**, after administration of CGP-78608 and glycine, only the GluN1/GluN3A stable cell line yielded fluorescence signal, whereas neither GluN1 stable cell lines nor host cells did. These data showed that a functional HTS method was successfully established.

Identification of Modulators for GluN1/GluN3A Receptors

Taking advantage of the established HTS method, we carried out two rounds of screening (**Figure 2A**). The appropriate concentrations of CGP-78608 were optimized in a preliminary experiment and we found that the saturated concentration of CGP-78608 was approximately 500 nM (**Supplementary Figure S1**). The tested compounds were incubated for 20 min before the administration of 500 nM CGP-78608. In the first round, a total of 2560 compounds

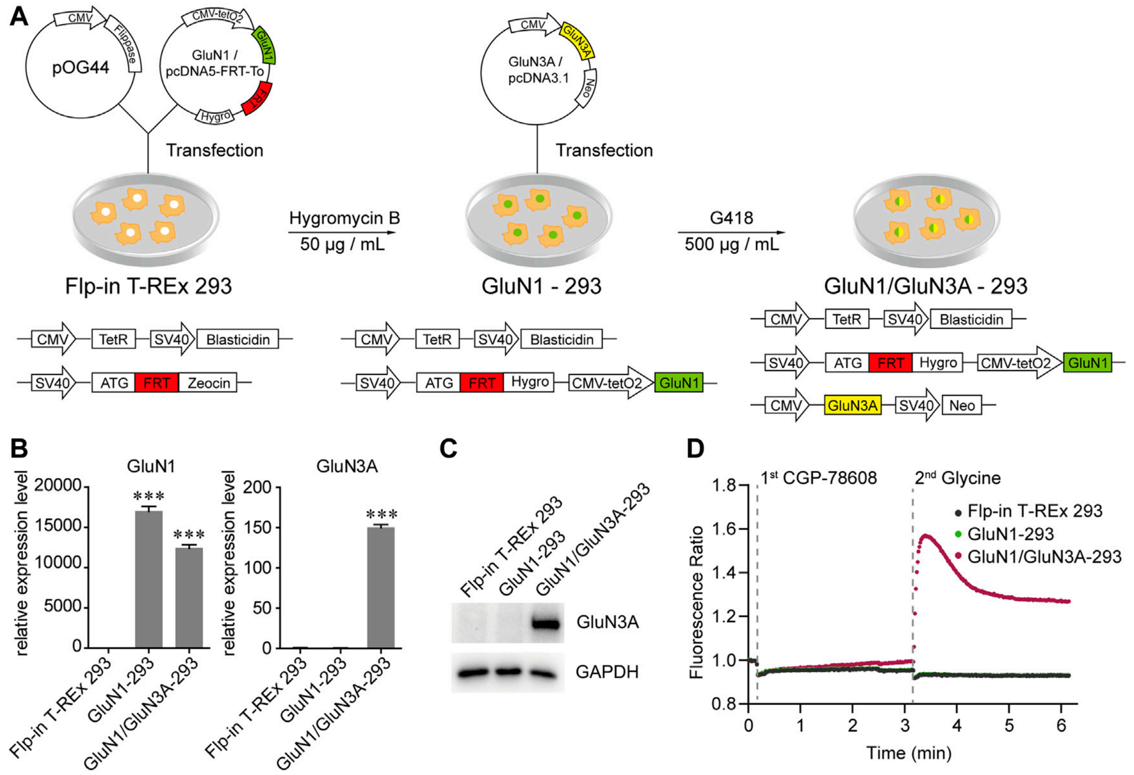

FIGURE 1 | Generation and functional verification of GluN1/GluN3A Flp-in T-REx 293 stable cell lines. **(A)** Schematic graph showing the generation of GluN1/GluN3A Flp-in T-REx 293 stable cell lines. **(B and C)** Expression levels of GluN1 and GluN3A in the GluN1/GluN3A stable cell lines verified by qRT-PCR **(B)** and Western Blot **(C)**. **(D)** GluN1/GluN3A stable cell lines formed functional ion channels. When the channels were activated by CGP-78608 and glycine, Ca^{2+} flowed into cells and bound to Fluo-4, resulting in a fluorescence signal detected by a FDSS/µCell platform. The basal fluorescence value was automatically normalized to 1 in the FDSS/µCell platform, so the real-time fluorescence response was displayed as a fluorescence ratio. Significance was tested using one-way ANOVA; $*p < 0.05$, $**p < 0.01$ and $***p < 0.001$.

were tested at a fixed dose of 10 µM, and 160 compounds with $F_{drug}/F_{control} < 0.75$ were defined as the pre-hits (**Figure 2B**). To improve the accuracy of screening, the pre-hits were further examined at 10 µM and 30 µM in the second round. After the secondary screening, 13 hits were obtained, which met the following criteria: 1) $F_{drug}/F_{control} < 0.75$ at 10 µM; 2) a dose-dependent change in the Ca^{2+} fluorescence between 10 µM and 30 µM. Notably, although this relatively strict criterion will reduce false positive ratio, it is also possible to miss some potential hits because their effects have been saturated at 10 µM; 3) No effect on NMDARs has been reported previously (**Figures 2C,D**). As shown in **Figure 2D**, a substantial fluorescence increase was visible upon CGP-78608 addition in the control condition, which appeared to depend on the concentration of Ca^{2+} and expression of GluN3A (**Supplementary Figure S2**). The inhibitory effects of these 13 hits were validated at a concentration of 3 µM using whole-cell patch-clamp recording. Among them, 2-chloro-N-[2'-(N-cyanosulfamoyl) biphenyl-4-ylmethyl]-N-(4-methylbenzyl) benzamide (S0859), 7-bromo-2-(4-hydroxyphenyl) benzoxazol-5-ol (WAY200070) and 3-fluoro-1,2-phenylene bis(3-hydroxybenzoate) (WZB117) showed relatively strong inhibitory activity, among which WZB117 was the most potent one (**Table 1**; **Figure 2E**). Notably, both the positive control (5,7-DCKA) and four previously reported NMDAR modulators, including L-701324 (Priestley et al., 1996), flupirtine maleate (Osborne et al., 1998; Kornhuber et al., 1999), riluzole (Debono et al., 1993) and D-serine (Wolosker, 2007), were also identified in both the primary screening and secondary screening, suggesting that the HTS method is relatively reliable. Together, our results showed that the HTS method enables the identification of potential modulators targeting GluN1/GluN3A receptors.

WZB117 Selectively Inhibits the Activity of GluN1/GluN3 Receptors

To fully understand the influences of WZB117 on NMDA receptors, the inhibitory activity and subtype selectivity of WZB117 were evaluated in HEK-293 cells stably expressing GluN1/GluN3A receptors and *Xenopus* oocytes transiently expressing NMDARs, respectively. As shown in **Figure 3A**, WZB117 dose-dependently suppressed the GluN1/GluN3A receptor-mediated currents in the presence of 100 µM glycine. The inhibitory data were fitted to the Hill equation, revealing an IC_{50} value of 1.15 ± 0.34 µM (**Figure 3B**). The selectivity of WZB117 against other NMDARs was examined in *Xenopus* oocytes. Consistent with the inhibitory effect observed in the GluN1/GluN3A stable cell line, 30 µM WZB117 potently

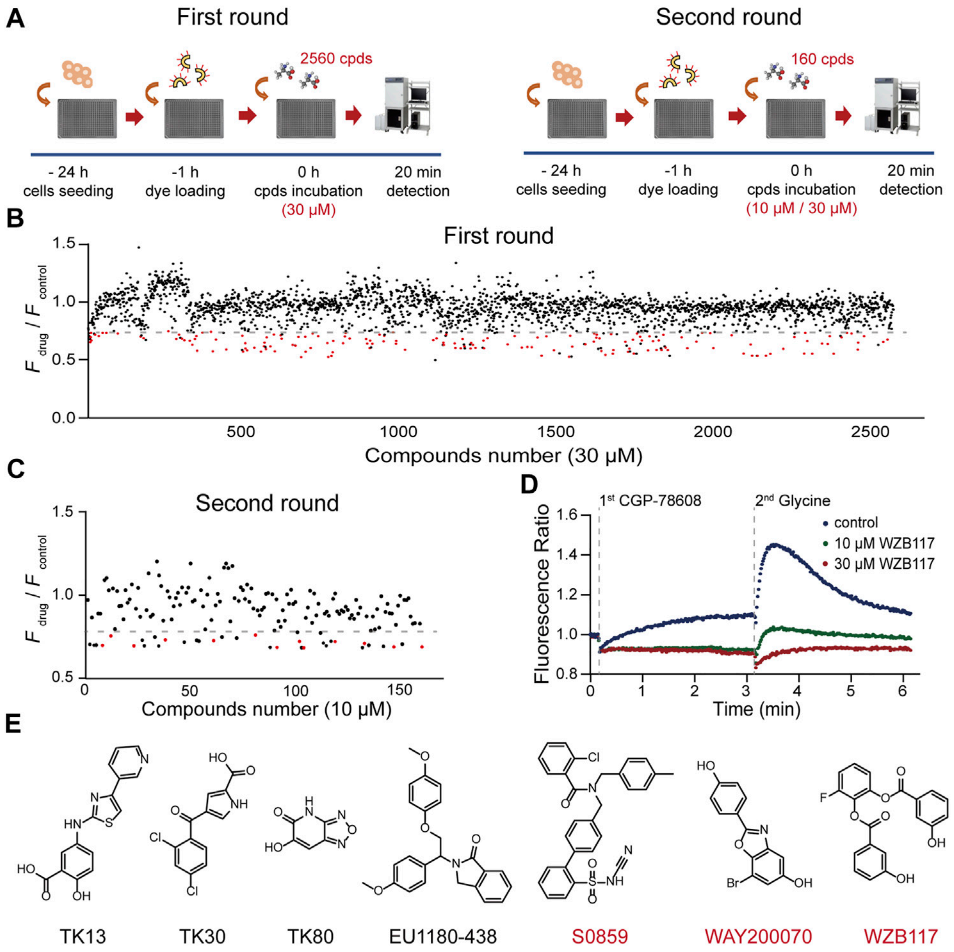

FIGURE 2 | HTS for GluN1/GluN3A modulators. **(A)** Flow chart of the HTS. **(B)** Overview of the first round results. The Ca^{2+} fluorescence signal ratio ($F_{drug}/F_{control}$) of all compounds (2560) is represented by a circle. Compounds (30 μM) with a ratio less than 0.75 (the dashed line) were considered as the pre-hits and are displayed as red circles. Data represent the mean of the duplicate results. **(C)** Discovery of hits. A total of 160 pre-hits were selected for the second round. Compounds (10 μM) with a ratio less than 0.75 (the dashed line) and showing a dose-dependent inhibitory activity were considered as potent hits of GluN1/GluN3A receptors. **(D)** Representative fluorescence signal of a hit in the FDSS/μCell. The well-to-well variation was 0.01 at 10 μM and 0.02 at 30 μM (calculated with standard deviation). **(E)** Chemical structures of previously reported (black) and newly discovered (red) modulators.

TABLE 1 | Inhibitory effects of 13 compounds on GluN1/GluN3A receptors.

Compound	$I_{drug}/I_{control}$	n	Compound	$I_{drug}/I_{control}$	n
DMSO	0.94 ± 0.01	3	Rhein	0.80 ± 0.04	4
Avasimibe	0.86 ± 0.03	3	S0859	0.48 ± 0.02	6
GSK2334470	0.84 ± 0.04	6	TAK285	0.92 ± 0.06	3
IC261	0.88 ± 0.01	3	Tirapazamine	1.03 ± 0.05	3
KN93 Phosphate	0.90 ± 0.02	6	WAY200070	0.53 ± 0.02	3
Lonafarnib	0.98 ± 0.02	3	WZB117	0.08 ± 0.02	9
NH125	0.84 ± 0.03	3	SU6668	0.89 ± 0.04	3

Data are shown as the mean ± SEM. All recordings were performed on GluN1/GluN3A Flp-in T-REx 293 stable cell lines. The order of drug application was the same as in FDSS/μCell Ca^{2+} imaging, and the representative current traces are given in ***Supplementary Figure S4****.*

suppressed the currents recorded in the *Xenopus* oocytes expressing GluN1/GluN3A receptors (**Figures 3C,D**). Due to the failure to record currents of WT GluN1/GluN3B receptors, GluN1-4a$^{F484A/T518L}$/GluN3B mutants were used here, which had been reported to delay desensitization and amplify the currents (Kvist et al., 2013). We found that 30 μM WZB117 showed inhibitory effects on the GluN1-4a$^{F484A/T518L}$/GluN3B receptor-mediated currents similar to those on the GluN1/GluN3A receptors-mediated currents (**Figures 3C,D**). To induce the GluN1/GluN2 (2A-2D) receptors-mediated currents, 100 μM glycine and 100 μM glutamate were coapplied. Infusion of 30 μM WZB117 produced relatively weak inhibition on the GluN1/GluN2 (2A-2D) receptors (**Figures 3C,D**). Our results indicated that WZB117 is a relatively selective inhibitor of GluN1/GluN3 receptors.

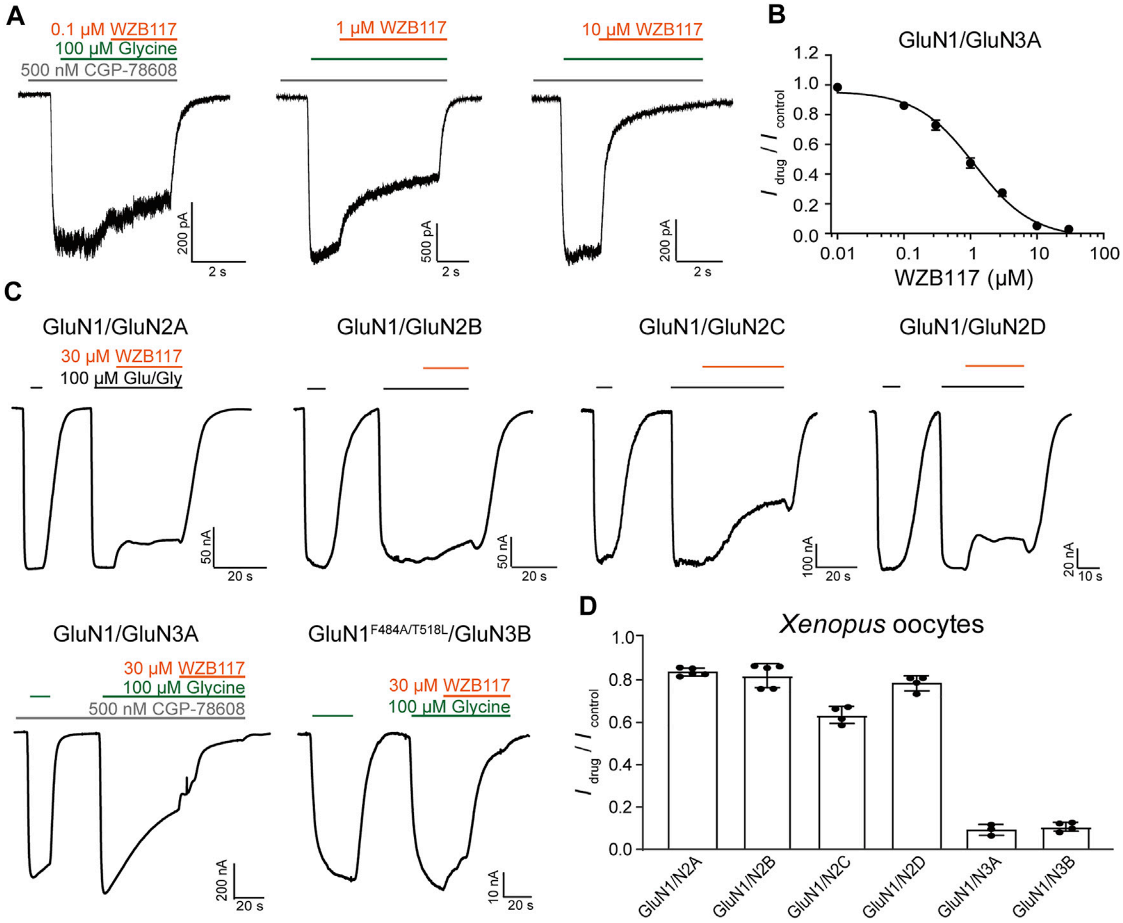

FIGURE 3 | Effects of WZB117 on GluN1/GluN3A receptors. **(A)** Representative traces of GluN1/GluN3A receptors with WZB117 application at the indicated concentrations. Whole-cell patch-clamp recording was performed on HEK-293 cells stably expressing GluN1/GluN3A receptors. **(B)** Dose-response curve of WZB117 on recombinant GluN1/GluN3A receptors (IC_{50} = 1.15 ± 0.34 μM, *n* = 6-7). **(C)** Representative traces of indicated receptors with WZB117 application. TEVC recording was performed on *Xenopus* oocyte expressing indicated receptors. Since currents were not observed for WT GluN1/GluN3B receptors, the mutant channel GluN1-4a$^{F484A/T518L}$/GluN3B was used instead (Kvist et al., 2013). GluN1-1a was always used unless otherwise stated. **(D)** Inhibitory effects of WZB117 on various NMDAR subtypes in *Xenopus* oocytes.

WZB117 Inhibits GluN3-NMDARs Neuronal Responses

The potent and selective inhibition of WZB117 on GluN1/GluN3 receptors expressed in the heterologous system prompted us to study whether WZB117 could inhibit native GluN1/GluN3 receptors in juvenile hippocampal neurons (Grand et al., 2018; Zhu et al., 2020). Consistent with the results obtained in HEK-293 cells stably expressing GluN1/GluN3A receptors, after incubation with CGP-78608, perfusion of 10 μM WZB117 produced a strong inhibition ($I_{drug}/I_{control}$ = 0.18 ± 0.03) of glycine-induced currents in neurons (**Figures 4A–C**). In contrast, administration of 10 μM WZB117 showed a relatively weak inhibition ($I_{drug}/I_{control}$ = 0.73 ± 0.01) on the native currents primarily mediated by GluN2-containing NMDARs (**Figures 4D–F**). However, this inhibitory effect was still larger than that of 30 μM WZB117 on the recombinant GluN1/GluN2 receptors on *Xenopus* oocytes (**Figures 3C,D**), suggesting that the native currents are possibly not only derived from GluN1/GluN2 receptors, but are also partially originated from GluN1/GluN2/GluN3 receptors. This speculation was then examined in the HEK-293 cells transiently transfected with GluN1/GluN2/GluN3 (1:1:2 ratio) plasmids. We found that the inhibitory effect of 30 μM WZB117 on GluN1/GluN2A/GluN3A (I_{drug}/I_{cotrol} = 0.22 ± 0.04) was indeed higher than those of GluN1/GluN2A (I_{drug}/I_{cotrol} = 0.84 ± 0.01) (**Supplementary Figure S3**). Notably, when the three plasmids were expressed simultaneously, there was a mixture of GluN1/GluN2A, GluN1/GluN3A and GluN1/GluN2A/GluN3A receptors on the plasma membranes, making it difficult to conclude the real effects on GluN1/GluN2A/GluN3A receptors. AMPA and KA receptors are also important iGluRs expressed in the central nervous system. We found that, at 10 μM, WZB117 showed little effect on the KA-induced currents (**Figures 4G–I**) and was almost ineffective on the AMPA -induced currents (**Figures 4J–L**). Our data revealed that WZB117 preferentially suppresses native GluN1/GluN3 currents over those of the other iGluRs.

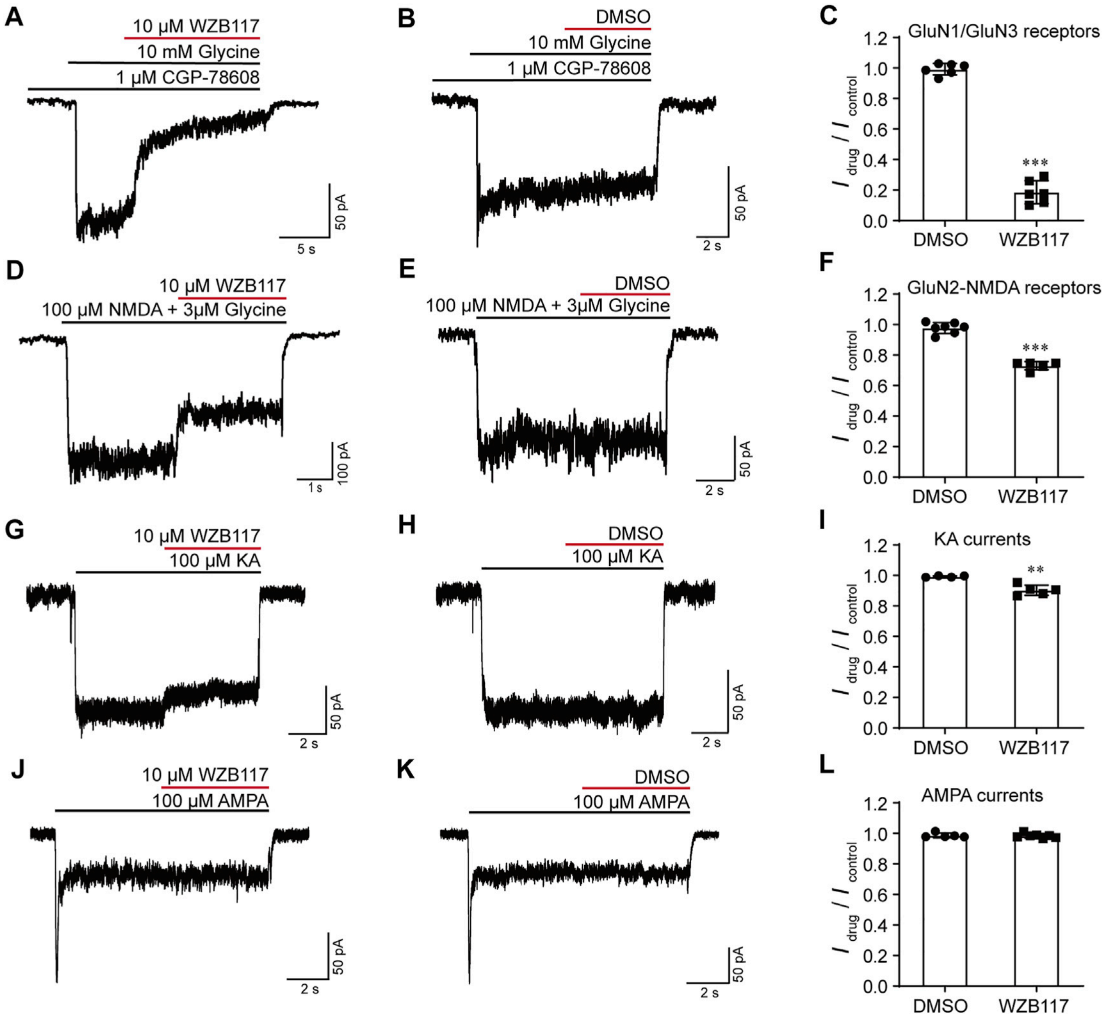

FIGURE 4 | Effects of WZB117 on the native iGluRs. **(A–C)** WZB117 (10 μM) potently inhibited GluN1/GluN3 receptors on acutely isolated rat hippocampal neurons. **(D–L)** WZB117 (10 μM) showed relatively weak inhibition of GluN2-NMDARs **(D–F)** and non-NMDA receptors **(G–L)**. Significance was tested using a t-test; $*p < 0.05$, $**p < 0.01$ and $***p < 0.001$.

WZB117 is a Negative Allosteric Modulator of GluN1/GluN3A Receptors

To understand how WZB117 inhibits GluN1/GluN3A receptors, the dose-response curves of WZB117 were compared in the presence of 10 μM and 100 μM glycine individually. The similar IC_{50} values indicated that WZB117 is not a competitive antagonist for the glycine binding sites (IC_{50} = 1.15 ± 0.34 μM at 100 μM glycine; IC_{50} = 1.08 ± 0.31 μM at 10 μM glycine) (**Figure 5B**). The voltage-dependence of WZB117 was also evaluated. As shown in **Figure 5C**, there was no significant change of inhibition activity at +40 mV and −60 mV. The current-voltage relationship (*I-V* curve) of WZB117 also argued against the possibility that WZB117 is a voltage-dependent pore blocker (**Figure 5D**). Given that extracellular pH conditions can affect the current amplitudes of GluN1/GluN3 receptors (Cummings and Popescu, 2016), we generated dose-response curves for WZB117 at pH values of 6.9, 7.3, and 8.3, respectively. The comparable IC_{50} values under different pH conditions indicated that WZB117 is a pH-independent antagonist (IC_{50} = 1.27 ± 0.39 μM at pH 6.9; IC_{50} = 1.15 ± 0.34 μM at pH 7.3; IC_{50} = 1.09 ± 0.22 μM at pH 8.3) (**Figures 5E,F**). Together, our data showed that WZB117 is a negative allosteric modulator which inhibits GluN1/GluN3A receptors in a glycine-, voltage- and pH-independent manner.

Molecular Determinants of WZB117 Modulation

To explore the potential action sites of WZB117, we investigated whether the pre-M1 region, previously known to be critical for other inhibitors such as EU1180-438 (Zhu et al., 2020), contributes to WZB117 inhibition. Pre-M1 is a helix connecting the LBD and M1 with poor homology between GluN3 and other subunits of NMDARs (**Figure 6A**). Alanine-scanning mutagenesis across the pre-M1 region of GluN1 and GluN3A subunits was performed

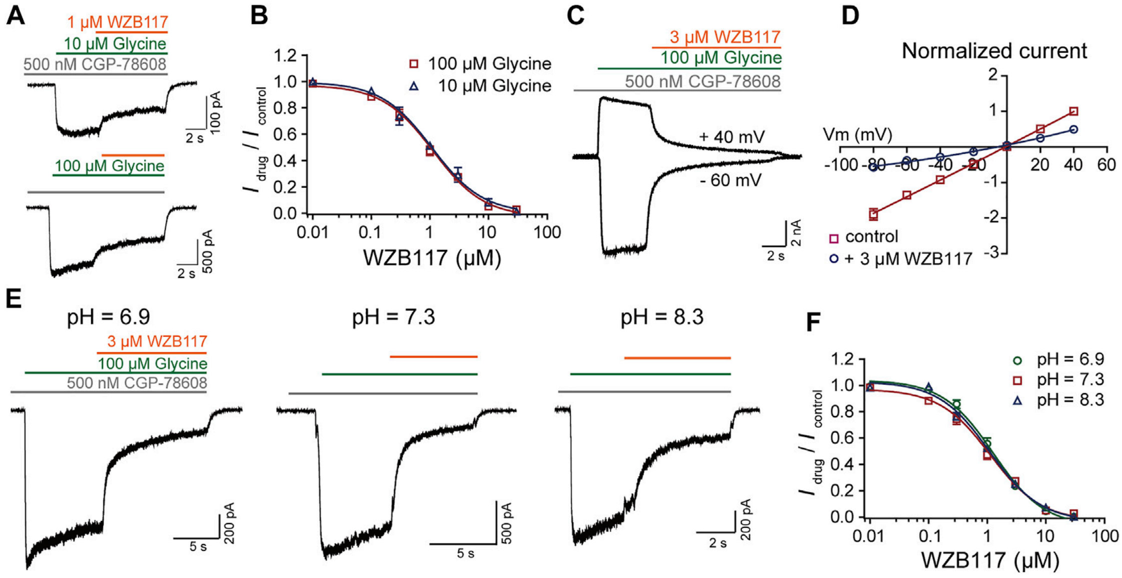

FIGURE 5 | Inhibition mechanism of WZB117 on GluN1/GluN3A receptors. **(A)** Representative traces of GluN1/GluN3A receptors in the presence of glycine at the indicated concentrations. **(B)** Dose-response curves of WZB117 under agonistic conditions of 10 μM (blue) and 100 μM (red) glycine. **(C)** Representative traces of GluN1/GluN3A receptors in the presence of 3 μM WZB117 at membrane potentials of −60 mV and +40 mV. **(D)** Effect of 3 μM WZB117 on the current-voltage relationship of GluN1/GluN3A receptors. The *I-V* curves were recorded at membrane potentials ranging from −80 mV to +40 mV, and the current amplitudes were normalized to the response of control at +40 mV. **(E)** Representative traces following 3 μM WZB117 inhibition of GluN1/GluN3A receptors at pH values of 6.9, 7.3, and 8.3. **(F)** Dose-response curves of WZB117 on GluN1/GluN3A receptors at pH of 6.9 (green), 7.3 (red) and 8.3 (blue). All data were recorded from GluN1/GluN3A Flp-in T-REx 293 stable cell lines.

individually. We found that the mutations W671A and L673A of the GluN3A subunit significantly influenced the inhibitory effect of WZB117 (**Figure 6C**), while none of the mutations in the pre-M1 region of the GluN1 subunit showed a detectable influence on WZB117 activity (**Figure 6B**), which preliminarily indicated that GluN3A might be the dominant subunit for WZB117 activity. Then, we generated two chimeras of GluN3A$^{670\text{-}673\ \mathrm{MWPL/LEPF}}$ and GluN2A$^{550\text{-}553\ \mathrm{LEPF/MWPL}}$ based on the distinct effects of WZB117 between GluN1/GluN3A and GluN1/GluN2A (**Figures 3C,D**). Interestingly, after swapping the four amino acids in the pre-M1 regions of GluN2A and GluN3A, the chimera GluN1/GluN2A$^{550\text{-}553\ \mathrm{LEPF/MWPL}}$ acquired higher sensitivity to WZB117 (**Figure 6E**), while the inhibition on the chimera GluN3A$^{670\text{-}673\ \mathrm{MWPL/LEPF}}$ was greatly reduced (**Figure 6D**), which validated that pre-M1 of GluN3A is a key region for the inhibitory effect of WZB117.

In Silico Modeling of WZB117 Binding Sites

We have shown that the pre-M1 region in GluN3A contributes to WZB117 inhibition. Then WZB117 was docked into the potential binding pocket at pre-M1 region based on the homology model of GluN1/GluN3A receptors (**Figure 6A**). As shown in **Supplementary Figure S5A**, there are two neighboring cavities in the pre-M1 region. Cavity C1 refers to the potential binding pocket of EU1180-438 (Zhu et al., 2020), while WZB117 might bind to the Cavity C2 since it is surrounded by residues affecting WZB117 inhibition, which are W671 and L673 of GluN3A. For GluN1/GluN2A receptors, there is no obvious pocket located at the corresponding sites (**Supplementary Figure S5B**), which may account for the lower inhibitory activity of WZB117 against GluN1/GluN2A receptors. The putative binding mode of WZB117 suggested that the compound WZB117 may form hydrogen bonds with W671 as well as hydrophobic interactions with L673 (**Figures 6F,G**), confirming the important roles of the two residues. As substitutions of the two residues by glutamate, alanine or phenylalanine might lead to conformational changes of the main chain, thereby destroying the hydrogen bond and the hydrophobic interactions, the reduction of the inhibitory efficacy of WZB117 on the corresponding mutants might be ascribed to the destruction of these original interactions. Together, the molecular docking study supported the notion that pre-M1 is a key region for WZB117 activity.

DISCUSSION

To date, only few GluN3 modulators have been reported (Crawley et al., 2022). Due to the low sequence identity and structural conservation between GluN3 and the other NMDAR subunits, GluN3 subunits are hyposensitive to both competitive modulators acting on GluN2 subunits and broad-spectrum channel blockers (Chatterton et al., 2002; McClymont et al., 2012). GluN3A seems to be an attractive target compared to other NMDAR subunits. First, the expression level of GluN3A was found to be abnormally elevated in pathological conditions while low expression levels were found in healthy adults (Kehoe et al., 2013; Wesseling and Perez-Otano, 2015; Pérez-Otaño et al.,

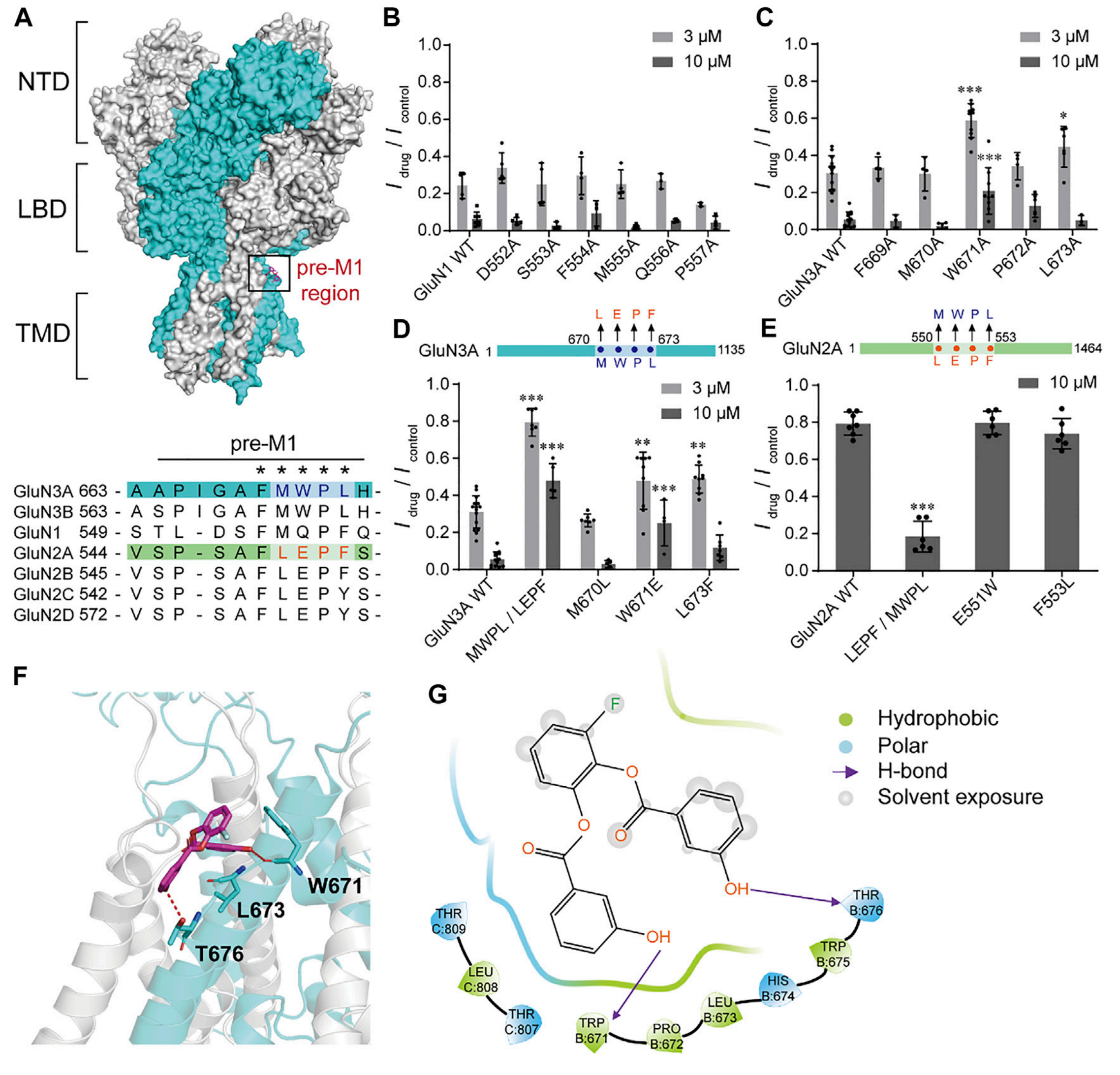

FIGURE 6 | Critical residues for WZB117 inhibition. **(A)** Homology model of the GluN1/GluN3A structure based on the structures of GluN1/GluN2B receptor (PDB ID: 6WHS) and the LBD of GluN3A subunit (PDB ID: 2RC7). GluN1 and GluN3A subunits are shown in gray and cyan, respectively (NTD: the N-terminal domain; LBD: the ligand binding domain; TMD: the transmembrane domain). The black box indicates the pre-M1 region. The bottom panel shows the sequence alignment of pre-M1 in all NMDAR subunits. Residues marked with an asterisk were selected for mutagenesis and whole-cell patch-clamp recordings. **(B and C)** Scanning mutagenesis across the pre-M1 region of GluN1 **(B)** and GluN3A **(C)** subunits. **(D and E)** Inhibition of WZB117 after amino acid substitutions in the pre-M1 regions between GluN3A **(D)** and GluN2A **(E)** subunits. **(F)** Putative binding mode of WZB117. The compound is shown as magenta sticks, and key residues are shown as cyan sticks. Hydrogen bonds are shown as a red dashed line. **(G)** 2D diagram of the interactions between compounds WZB117 and GluN1/GluN3A receptors. All recordings were carried out in transiently transfected CHO cells. Significance was tested using one-way ANOVA; $*p < 0.05$, $**p < 0.01$ and $***p < 0.001$.

2016). Second, inhibition of GluN3A by genetic intervention at different developmental stages can prevent or rescue kinds of Huntington's disease symptoms ranging from neuronal survival to cognitive and motor functions in mouse models (Marco et al., 2013; Marco et al., 2018). However, the feasibility of GluN3A as a therapeutic target has not been investigated from the perspective of molecular blockade. Similarly, the physiological roles of GluN3B are unclear due to limited research. Therefore, the discovery of GluN3-specific small-molecule modulators is of great significance.

Here, we established a cell-based calcium assay for screening GluN1/GluN3A modulators. First, the Ca^{2+} fluorescence signal is stable with good temporal resolution and sensitivity, and the screening window can be flexibly optimized by changing the stimulation conditions. Second, comparing to the isolated LBD of GluN3A applied in the screening (Kvist et al., 2013), the full length of GluN1/GluN3A receptors may greatly facilitate the discovery of new molecules with different characteristics. In our study, a total of 2560 compounds were tested, and finally 3 compounds (≥50% inhibition at 3 μM) were identified as GluN1/GluN3A receptor antagonists with completely different structures than those of the previously reported molecules (**Figure 2**; **Table 1**). Based on both the positive experiences and negative experiences learned from this pilot screening, a large-scale HTS would accelerate the identification of more GluN3 modulators.

Among the three identified hits in the pilot screening, WZB117 showed strong inhibitory potency with an IC_{50} value of 1.15 ± 0.34 μM (**Figure 3**), which is similar to that of EU1180-438 (IC_{50} = 1.80 ± 0.30 μM) (Zhu et al., 2020) and much higher than that of TK compounds (Kvist et al., 2013). Due to the desensitization of the GluN1/GluN3 receptors (Grand et al., 2018), the inhibitory effect of WZB117 could be overestimated in the TEVC and whole-cell patch clamp experiments. In addition, WZB117 exhibited a good subtype selectivity for GluN1/GluN3 receptors relative to GluN1/GluN2 receptors and other iGluRs in acutely isolated rat hippocampal neurons (**Figure 3**; **Figure 4**). However, to define WZB117 as a good pharmacological tool, a more comprehensive evaluation of selectivity is needed. For example, WZB117 has been reported to be a glucose transporter (GluT) inhibitor with antitumor activity. Besides, S0859 is a high-affinity inhibitor of Na^+/HCO_3^- cotransporter (NBC) with potential activity in the regulation of cardiac function, and WAY-200070 is an agonist of estrogen receptor beta (ERRβ) with potential anxiolytic and antidepressant activity (Ch'en et al., 2008; Hughes et al., 2008; Liu et al., 2012; Xintaropoulou et al., 2015; Wei et al., 2018). Accordingly, it appears difficult to identify an ideal probe with potent activity and excellent selectivity for GluN3A or GluN3B simply through HTS. Further structural modifications would help to improve both potency and selectivity and eliminate potential side effects of these lead compounds.

In the past 30 years, clinical studies have shown that competitive antagonists and channel blockers of NMDARs commonly display severe side effects, possibly due to their broad-spectrum inhibitory effects, and thereby greatly limiting their clinical development (Kalia et al., 2008; Hardingham and Bading, 2010; Traynelis et al., 2010; Hansen et al., 2012). Allosteric modulators generally show strong subunit-selectivity and better clinical development prospects as they bind to less conserved pockets (Hansen et al., 2012; Zhu and Paoletti, 2015; Burnell et al., 2019; Strong et al., 2021). Our data indicated that WZB117 is a negative allosteric modulator inhibiting GluN1/GluN3A receptors in a glycine-, voltage- and pH-independent manner (**Figure 5**). We further demonstrated that GluN3A pre-M1 is a potential binding pocket for WZB117, which was profoundly implicated by the significant changes in the activity of WZB117 against the chimeras $GluN1/GluN3A^{670\text{-}673\ MWPL/LEPF}$ and $GluN1/GluN2A^{550\text{-}553\ LEPF/MWPL}$. Particularly, the chimera $GluN1/GluN2A^{550\text{-}553\ LEPF/MWPL}$, owning a short motif containing only four amino acids from the GluN3A pre-M1 region, gained sensitivity towards WZB117 inhibition, which further confirmed the importance of the pre-M1 region (**Figure 6**). Recent structural pharmacological studies of NMDARs have provided cogent evidence for the important contribution of the linkers between the LBDs and the transmembrane domains (TMDs) to channel gating (Wang et al., 2021). In addition, many *de novo* mutations related to neurological diseases, such as epilepsy and developmental delay, are associated with the pre-M1 regions of both GluN1 and GluN2 subunits, which also appear to affect the kinetics of the channels (Sobolevsky et al., 2007; Ogden et al., 2017; Vyklicky et al., 2018; XiangWei et al., 2019; McDaniel et al., 2020). Although no studies about GluN3A pre-M1 related structures or pathogenic mutations have been reported, our work provides insights from a pharmacological perspective that GluN3A pre-M1 is a potential target for drug development. Considering that the critical residues of WZB117 are different from those of EU1180-438, there may be different drug binding pockets near to each other (**Supplementary Figure S5A**).

In conclusion, we have established a cell-based high-throughput screening and identified WZB117 as a novel and potent allosteric modulator against GluN1/GluN3 receptors. WZB117 exhibited relative selectivity for GluN1/GluN3 inhibition over other iGluRs. A mechanistic study revealed that multiple residues located at pre-M1 region of the GluN3A subunit are critical for the activity of WZB117. Our study provided new active molecules for channel function research and drug development targeting GluN3-NMDARs.

DATA AVAILABILITY STATEMENT

The raw data supporting the conclusion of this article will be made available by the authors, without undue reservation.

ETHICS STATEMENT

The animal study was reviewed and approved by IACUC (Institutional Animal Care and Use Committees) of Shanghai Institute of Materia Medica (permission number: 2021-02-GZB-09).

AUTHOR CONTRIBUTIONS

ZG and SZ conceived the project; YZe, TZ, FY, LZ, and ZK performed the experiments; all authors analyzed the data; YZe, YZh, SZ, and ZG wrote the manuscript; all authors have approved the final version of the manuscript.

FUNDING

This work was supported by the National Science Fund for Distinguished Young Scholars (81825021), the Youth Innovation Promotion Association of the Chinese Academy of Sciences (2020284), the Fund of Science and Technology Commission of Shanghai Municipality (19431906000), the Lin Gang Laboratory, the Strategic Priority Research Program of the Chinese Academy of Sciences (XDB32020000), and the National Natural Science Foundation of China (32100762).

SUPPLEMENTARY MATERIAL

The Supplementary Material for this article can be found online at: https://www.frontiersin.org/articles/10.3389/fphar.2022.888308/full#supplementary-material

REFERENCES

Burnell, E. S., Irvine, M., Fang, G., Sapkota, K., Jane, D. E., and Monaghan, D. T. (2019). Positive and Negative Allosteric Modulators of N-Methyl-D-Aspartate (NMDA) Receptors: Structure-Activity Relationships and Mechanisms of Action. *J. Med. Chem.* 62 (1), 3–23. doi:10.1021/acs.jmedchem.7b01640

Ch'en, F. F., Villafuerte, F. C., Swietach, P., Cobden, P. M., and Vaughan-Jones, R. D. (2008). S0859, an N-Cyanosulphonamide Inhibitor of Sodium-Bicarbonate Cotransport in the Heart. *Br. J. Pharmacol.* 153 (5), 972–982. doi:10.1038/sj.bjp.0707667

Chatterton, J. E., Awobuluyi, M., Premkumar, L. S., Takahashi, H., Talantova, M., Shin, Y., et al. (2002). Excitatory glycine Receptors Containing the NR3 Family of NMDA Receptor Subunits. *Nature* 415 (6873), 793–798. doi:10.1038/nature715

Chou, T. H., Tajima, N., Romero-Hernandez, A., and Furukawa, H. (2020). Structural Basis of Functional Transitions in Mammalian NMDA Receptors. *Cell* 182 (2), 357. doi:10.1016/j.cell.2020.05.052

Ciabarra, A. M., Sullivan, J. M., Gahn, L. G., Pecht, G., Heinemann, S., and Sevarino, K. A. (1995). Cloning and Characterization of Chi-1: a Developmentally Regulated Member of a Novel Class of the Ionotropic Glutamate Receptor Family. *J. Neurosci.* 15 (10), 6498–6508. doi:10.1523/jneurosci.15-10-06498.1995

Crawley, O., Conde-Dusman, M. J., and Pérez-Otaño, I. (2022). GluN3A NMDA Receptor Subunits: More Enigmatic Than Ever? *J. Physiol.* 600 (2), 261–276. doi:10.1113/jp280879

Cummings, K. A., and Popescu, G. K. (2016). Protons Potentiate GluN1/GluN3A Currents by Attenuating Their Desensitisation. *Sci. Rep.* 6, 23344. doi:10.1038/srep23344

Das, S., Sasaki, Y. F., Rothe, T., Premkumar, L. S., Takasu, M., Crandall, J. E., et al. (1998). Increased NMDA Current and Spine Density in Mice Lacking the NMDA Receptor Subunit NR3A. *Nature* 393 (6683), 377–381. doi:10.1038/30748

Debono, M. W., Le Guern, J., Canton, T., Doble, A., and Pradier, L. (1993). Inhibition by Riluzole of Electrophysiological Responses Mediated by Rat Kainate and NMDA Receptors Expressed in Xenopus Oocytes. *Eur. J. Pharmacol.* 235 (2-3), 283–289. doi:10.1016/0014-2999(93)90147-a

Fiuza, M., González-González, I., and Pérez-Otaño, I. (2013). GluN3A Expression Restricts Spine Maturation via Inhibition of GIT1/Rac1 Signaling. *Proc. Natl. Acad. Sci. U. S. A.* 110 (51), 20807–20812. doi:10.1073/pnas.1312211110

Friesner, R. A., Banks, J. L., Murphy, R. B., Halgren, T. A., Klicic, J. J., Mainz, D. T., et al. (2004). Glide: a New Approach for Rapid, Accurate Docking and Scoring. 1. Method and Assessment of Docking Accuracy. *J. Med. Chem.* 47 (7), 1739–1749. doi:10.1021/jm0306430

Gee, K. R., Brown, K. A., Chen, W. N., Bishop-Stewart, J., Gray, D., and Johnson, I. (2000). Chemical and Physiological Characterization of Fluo-4 Ca(2+)-Indicator Dyes. *Cell Calcium* 27 (2), 97–106. doi:10.1054/ceca.1999.0095

Glantz, L. A., and Lewis, D. A. (2000). Decreased Dendritic Spine Density on Prefrontal Cortical Pyramidal Neurons in Schizophrenia. *Arch. Gen. Psychiatry* 57 (1), 65–73. doi:10.1001/archpsyc.57.1.65

Grand, T., Abi Gerges, S., David, M., Diana, M. A., and Paoletti, P. (2018). Unmasking GluN1/GluN3A Excitatory glycine NMDA Receptors. *Nat. Commun.* 9 (1), 4769. doi:10.1038/s41467-018-07236-4

Hansen, K. B., Ogden, K. K., and Traynelis, S. F. (2012). Subunit-selective Allosteric Inhibition of glycine Binding to NMDA Receptors. *J. Neurosci.* 32 (18), 6197–6208. doi:10.1523/jneurosci.5757-11.2012

Hansen, K. B., Wollmuth, L. P., Bowie, D., Furukawa, H., Menniti, F. S., Sobolevsky, A. I., et al. (2021). Structure, Function, and Pharmacology of Glutamate Receptor Ion Channels. *Pharmacol. Rev.* 73 (4), 298–487. doi:10.1124/pharmrev.120.000131

Hansen, K. B., Yi, F., Perszyk, R. E., Furukawa, H., Wollmuth, L. P., Gibb, A. J., et al. (2018). Structure, Function, and Allosteric Modulation of NMDA Receptors. *J. Gen. Physiol.* 150 (8), 1081–1105. doi:10.1085/jgp.201812032

Hardingham, G. E., and Bading, H. (2010). Synaptic versus Extrasynaptic NMDA Receptor Signalling: Implications for Neurodegenerative Disorders. *Nat. Rev. Neurosci.* 11 (10), 682–696. doi:10.1038/nrn2911

Hughes, Z. A., Liu, F., Platt, B. J., Dwyer, J. M., Pulicicchio, C. M., Zhang, G., et al. (2008). WAY-200070, a Selective Agonist of Estrogen Receptor Beta as a Potential Novel Anxiolytic/antidepressant Agent. *Neuropharmacology* 54 (7), 1136–1142. doi:10.1016/j.neuropharm.2008.03.004

Jin, Z., Bhandage, A. K., Bazov, I., Kononenko, O., Bakalkin, G., Korpi, E. R., et al. (2014). Selective Increases of AMPA, NMDA, and Kainate Receptor Subunit mRNAs in the hippocampus and Orbitofrontal Cortex but Not in Prefrontal Cortex of Human Alcoholics. *Front. Cell Neurosci.* 8, 11. doi:10.3389/fncel.2014.00011

Kalia, L. V., Kalia, S. K., and Salter, M. W. (2008). NMDA Receptors in Clinical Neurology: Excitatory Times Ahead. *Lancet Neurol.* 7 (8), 742–755. doi:10.1016/s1474-4422(08)70165-0

Karakas, E., and Furukawa, H. (2014). Crystal Structure of a Heterotetrameric NMDA Receptor Ion Channel. *Science* 344 (6187), 992–997. doi:10.1126/science.1251915

Kehoe, L. A., Bellone, C., De Roo, M., Zandueta, A., Dey, P. N., Pérez-Otaño, I., et al. (2014). GluN3A Promotes Dendritic Spine Pruning and Destabilization during Postnatal Development. *J. Neurosci.* 34 (28), 9213–9221. doi:10.1523/JNEUROSCI.5183-13.2014

Kehoe, L. A., Bernardinelli, Y., and Muller, D. (2013). GluN3A: an NMDA Receptor Subunit with Exquisite Properties and Functions. *Neural Plast.* 2013, 145387. doi:10.1155/2013/145387

Kornhuber, J., Bleich, S., Wiltfang, J., Maler, M., and Parsons, C. G. (1999). Flupirtine Shows Functional NMDA Receptor Antagonism by Enhancing Mg2+ Block via Activation of Voltage Independent Potassium Channels. Rapid Communication. *J. Neural Transm. (Vienna)* 106 (9-10), 857–867. doi:10.1007/s007020050206

Kvist, T., Greenwood, J. R., Hansen, K. B., Traynelis, S. F., and Bräuner-Osborne, H. (2013). Structure-based Discovery of Antagonists for GluN3-Containing N-Methyl-D-Aspartate Receptors. *Neuropharmacology* 75, 324–336. doi:10.1016/j.neuropharm.2013.08.003

Le Guilloux, V., Schmidtke, P., and Tuffery, P. (2009). Fpocket: an Open Source Platform for Ligand Pocket Detection. *BMC Bioinforma.* 10, 168. doi:10.1186/1471-2105-10-168

Liu, Y., Cao, Y., Zhang, W., Bergmeier, S., Qian, Y., Akbar, H., et al. (2012). A Small-Molecule Inhibitor of Glucose Transporter 1 Downregulates Glycolysis, Induces Cell-Cycle Arrest, and Inhibits Cancer Cell Growth *In Vitro* and *In Vivo*. *Mol. Cancer Ther.* 11 (8), 1672–1682. doi:10.1158/1535-7163.Mct-12-0131

Mahfooz, K., Marco, S., Martínez-Turrillas, R., Raja, M. K., Pérez-Otaño, I., and Wesseling, J. F. (2016). GluN3A Promotes NMDA Spiking by Enhancing Synaptic Transmission in Huntington's Disease Models. *Neurobiol. Dis.* 93, 47–56. doi:10.1016/j.nbd.2016.04.001

Marco, S., Giralt, A., Petrovic, M. M., Pouladi, M. A., Martínez-Turrillas, R., Martínez-Hernández, J., et al. (2013). Suppressing Aberrant GluN3A Expression Rescues Synaptic and Behavioral Impairments in Huntington's Disease Models. *Nat. Med.* 19 (8), 1030–1038. doi:10.1038/nm.3246

Marco, S., Murillo, A., and Pérez-Otaño, I. (2018). RNAi-Based GluN3A Silencing Prevents and Reverses Disease Phenotypes Induced by Mutant Huntingtin. *Mol. Ther.* 26 (8), 1965–1972. doi:10.1016/j.ymthe.2018.05.013

McClymont, D. W., Harris, J., and Mellor, I. R. (2012). Open-channel Blockade Is Less Effective on GluN3B Than GluN3A Subunit-Containing NMDA Receptors. *Eur. J. Pharmacol.* 686 (1-3), 22–31. doi:10.1016/j.ejphar.2012.04.036

McDaniel, M. J., Ogden, K. K., Kell, S. A., Burger, P. B., Liotta, D. C., and Traynelis, S. F. (2020). NMDA Receptor Channel Gating Control by the Pre-M1 Helix. *J. Gen. Physiol.* 152 (4), e201912362. doi:10.1085/jgp.201912362

Mueller, H. T., and Meador-Woodruff, J. H. (2004). NR3A NMDA Receptor Subunit mRNA Expression in Schizophrenia, Depression and Bipolar Disorder. *Schizophr. Res.* 71 (2-3), 361–370. doi:10.1016/j.schres.2004.02.016

Ogden, K. K., Chen, W., Swanger, S. A., McDaniel, M. J., Fan, L. Z., Hu, C., et al. (2017). Molecular Mechanism of Disease-Associated Mutations in the Pre-M1 Helix of NMDA Receptors and Potential Rescue Pharmacology. *PLoS Genet.* 13 (1), e1006536. doi:10.1371/journal.pgen.1006536

Osborne, N. N., Cazevieille, C., Wood, J. P., Nash, M. S., Pergande, G., Block, F., et al. (1998). Flupirtine, a Nonopioid Centrally Acting Analgesic, Acts as an NMDA Antagonist. *Gen. Pharmacol.* 30 (3), 255–263. doi:10.1016/s0306-3623(97)00355-8

Otsu, Y., Darcq, E., Pietrajtis, K., Mátyás, F., Schwartz, E., Bessaih, T., et al. (2019). Control of Aversion by Glycine-Gated GluN1/GluN3A NMDA Receptors in the Adult Medial Habenula. *Science* 366 (6462), 250–254. doi:10.1126/science.aax1522

Paoletti, P., Bellone, C., and Zhou, Q. (2013). NMDA Receptor Subunit Diversity: Impact on Receptor Properties, Synaptic Plasticity and Disease. *Nat. Rev. Neurosci.* 14 (6), 383–400. doi:10.1038/nrn3504

Pérez-Otaño, I., Larsen, R. S., and Wesseling, J. F. (2016). Emerging Roles of GluN3-Containing NMDA Receptors in the CNS. *Nat. Rev. Neurosci.* 17 (10), 623–635. doi:10.1038/nrn.2016.92

Pérez-Otaño, I., Luján, R., Tavalin, S. J., Plomann, M., Modregger, J., Liu, X. B., et al. (2006). Endocytosis and Synaptic Removal of NR3A-Containing NMDA Receptors by PACSIN1/syndapin1. *Nat. Neurosci.* 9 (5), 611–621. doi:10.1038/nn1680

Perez-Otano, I., Schulteis, C. T., Contractor, A., Lipton, S. A., Trimmer, J. S., Sucher, N. J., et al. (2001). Assembly with the NR1 Subunit Is Required for Surface Expression of NR3A-Containing NMDA Receptors. *J. Neurosci.* 21 (4), 1228–1237. doi:10.1523/jneurosci.21-04-01228.2001

Priestley, T., Laughton, P., Macaulay, A. J., Hill, R. G., and Kemp, J. A. (1996). Electrophysiological Characterisation of the Antagonist Properties of Two Novel NMDA Receptor glycine Site Antagonists, L-695,902 and L-701,324. *Neuropharmacology* 35 (11), 1573–1581. doi:10.1016/s0028-3908(96)00141-4

Roberts, A. C., Díez-García, J., Rodriguiz, R. M., López, I. P., Luján, R., Martínez-Turrillas, R., et al. (2009). Downregulation of NR3A-Containing NMDARs Is Required for Synapse Maturation and Memory Consolidation. *Neuron* 63 (3), 342–356. doi:10.1016/j.neuron.2009.06.016

Sasaki, Y. F., Rothe, T., Premkumar, L. S., Das, S., Cui, J., Talantova, M. V., et al. (2002). Characterization and Comparison of the NR3A Subunit of the NMDA Receptor in Recombinant Systems and Primary Cortical Neurons. *J. Neurophysiol.* 87 (4), 2052–2063. doi:10.1152/jn.00531.2001

Shelley, J. C., Cholleti, A., Frye, L. L., Greenwood, J. R., Timlin, M. R., and Uchimaya, M. (2007). Epik: a Software Program for pK(a) Prediction and Protonation State Generation for Drug-like Molecules. *J. Comput. Aided Mol. Des.* 21 (12), 681–691. doi:10.1007/s10822-007-9133-z

Sobolevsky, A. I., Prodromou, M. L., Yelshansky, M. V., and Wollmuth, L. P. (2007). Subunit-specific Contribution of Pore-Forming Domains to NMDA Receptor Channel Structure and Gating. *J. Gen. Physiol.* 129 (6), 509–525. doi:10.1085/jgp.200609718

Strong, K. L., Epplin, M. P., Ogden, K. K., Burger, P. B., Kaiser, T. M., Wilding, T. J., et al. (2021). Distinct GluN1 and GluN2 Structural Determinants for Subunit-Selective Positive Allosteric Modulation of N-Methyl-D-Aspartate Receptors. *ACS Chem. Neurosci.* 12 (1), 79–98. doi:10.1021/acschemneuro.0c00561

Sucher, N. J., Akbarian, S., Chi, C. L., Leclerc, C. L., Awobuluyi, M., Deitcher, D. L., et al. (1995). Developmental and Regional Expression Pattern of a Novel NMDA Receptor-like Subunit (NMDAR-L) in the Rodent Brain. *J. Neurosci.* 15 (10), 6509–6520. doi:10.1523/jneurosci.15-10-06509.1995

Takata, A., Iwayama, Y., Fukuo, Y., Ikeda, M., Okochi, T., Maekawa, M., et al. (2013). A Population-specific Uncommon Variant in GRIN3A Associated with Schizophrenia. *Biol. Psychiatry* 73 (6), 532–539. doi:10.1016/j.biopsych.2012.10.024

Traynelis, S. F., Wollmuth, L. P., McBain, C. J., Menniti, F. S., Vance, K. M., Ogden, K. K., et al. (2010). Glutamate Receptor Ion Channels: Structure, Regulation, and Function. *Pharmacol. Rev.* 62 (3), 405–496. doi:10.1124/pr.109.002451

Ulbrich, M. H., and Isacoff, E. Y. (2007). Subunit Counting in Membrane-Bound Proteins. *Nat. Methods* 4 (4), 319–321. doi:10.1038/nmeth1024

von Boehmer, L., Liu, C., Ackerman, S., Gitlin, A. D., Wang, Q., Gazumyan, A., et al. (2016). Sequencing and Cloning of Antigen-specific Antibodies from Mouse Memory B Cells. *Nat. Protoc.* 11 (10), 1908–1923. doi:10.1038/nprot.2016.102

Vyklicky, V., Krausova, B., Cerny, J., Ladislav, M., Smejkalova, T., Kysilov, B., et al. (2018). Surface Expression, Function, and Pharmacology of Disease-Associated Mutations in the Membrane Domain of the Human GluN2B Subunit. *Front. Mol. Neurosci.* 11, 110. doi:10.3389/fnmol.2018.00110

Wang, H., Lv, S., Stroebel, D., Zhang, J., Pan, Y., Huang, X., et al. (2021). Gating Mechanism and a Modulatory Niche of Human GluN1-GluN2A NMDA Receptors. *Neuron* 109 (15), 2443. doi:10.1016/j.neuron.2021.05.031

Webb, B., and Sali, A. (2016). Comparative Protein Structure Modeling Using MODELLER. *Curr. Protoc. Protein Sci.* 86, 21–375. doi:10.1002/cpbi.3

Wei, M., Lu, L., Sui, W., Liu, Y., Shi, X., and Lv, L. (2018). Inhibition of GLUTs by WZB117 Mediates Apoptosis in Blood-Stage Plasmodium Parasites by Breaking Redox Balance. *Biochem. Biophys. Res. Commun.* 503 (2), 1154–1159. doi:10.1016/j.bbrc.2018.06.134

Wesseling, J. F., and Pérez-Otaño, I. (2015). Modulation of GluN3A Expression in Huntington Disease: a New N-Methyl-D-Aspartate Receptor-Based Therapeutic Approach? *JAMA Neurol.* 72 (4), 468–473. doi:10.1001/jamaneurol.2014.3953

Wolosker, H. (2007). NMDA Receptor Regulation by D-Serine: New Findings and Perspectives. *Mol. Neurobiol.* 36 (2), 152–164. doi:10.1007/s12035-007-0038-6

Wong, H. K., Liu, X. B., Matos, M. F., Chan, S. F., Pérez-Otaño, I., Boysen, M., et al. (2002). Temporal and Regional Expression of NMDA Receptor Subunit NR3A in the Mammalian Brain. *J. Comp. Neurol.* 450 (4), 303–317. doi:10.1002/cne.10314

XiangWei, W., Kannan, V., Xu, Y., Kosobucki, G. J., Schulien, A. J., Kusumoto, H., et al. (2019). Heterogeneous Clinical and Functional Features of GRIN2D-Related Developmental and Epileptic Encephalopathy. *Brain* 142 (10), 3009–3027. doi:10.1093/brain/awz232

Xie, Z. Q., Tian, X. T., Zheng, Y. M., Zhan, L., Chen, X. Q., Xin, X. M., et al. (2020). Antiepileptic Geissoschizine Methyl Ether Is an Inhibitor of Multiple Neuronal Channels. *Acta Pharmacol. Sin.* 41 (5), 629–637. doi:10.1038/s41401-019-0327-4

Xintaropoulou, C., Ward, C., Wise, A., Marston, H., Turnbull, A., and Langdon, S. P. (2015). A Comparative Analysis of Inhibitors of the Glycolysis Pathway in Breast and Ovarian Cancer Cell Line Models. *Oncotarget* 6 (28), 25677–25695. doi:10.18632/oncotarget.4499

Yao, Y., Harrison, C. B., Freddolino, P. L., Schulten, K., and Mayer, M. L. (2008). Molecular Mechanism of Ligand Recognition by NR3 Subtype Glutamate Receptors. *Embo J.* 27 (15), 2158–2170. doi:10.1038/emboj.2008.140

Yao, Y., and Mayer, M. L. (2006). Characterization of a Soluble Ligand Binding Domain of the NMDA Receptor Regulatory Subunit NR3A. *J. Neurosci.* 26 (17), 4559–4566. doi:10.1523/jneurosci.0560-06.2006

Yuan, T., and Bellone, C. (2013). Glutamatergic Receptors at Developing Synapses: the Role of GluN3A-Containing NMDA Receptors and GluA2-Lacking AMPA Receptors. *Eur. J. Pharmacol.* 719 (1-3), 107–111. doi:10.1016/j.ejphar.2013.04.056

Yuan, T., Mameli, M., O'Connor, E. C., O' Connor, E. C., Dey, P. N., Verpelli, C., et al. (2013). Expression of Cocaine-Evoked Synaptic Plasticity by GluN3A-Containing NMDA Receptors. *Neuron* 80 (4), 1025–1038. doi:10.1016/j.neuron.2013.07.050

Zhu, S., and Paoletti, P. (2015). Allosteric Modulators of NMDA Receptors: Multiple Sites and Mechanisms. *Curr. Opin. Pharmacol.* 20, 14–23. doi:10.1016/j.coph.2014.10.009

Zhu, Z., Yi, F., Epplin, M. P., Liu, D., Summer, S. L., Mizu, R., et al. (2020). Negative Allosteric Modulation of GluN1/GluN3 NMDA Receptors. *Neuropharmacology* 176, 108117. doi:10.1016/j.neuropharm.2020.108117

Conflict of Interest: The authors declare that the research was conducted in the absence of any commercial or financial relationships that could be construed as a potential conflict of interest.

frontiers | Frontiers in Pharmacology

REVIEW
published: 17 June 2022
doi: 10.3389/fphar.2022.925880

Molecular Pharmacology of P2X Receptors: Exploring Druggable Domains Revealed by Structural Biology

Adam C. Oken[1], Ipsita Krishnamurthy[1], Jonathan C. Savage[1], Nicolas E. Lisi[1], Michael H. Godsey[1] and Steven E. Mansoor[1,2]*

[1]Department of Chemical Physiology and Biochemistry, Oregon Health & Science University, Portland, OR, United States, [2]Knight Cardiovascular Institute, Oregon Health & Science University, Portland, OR, United States

Extracellular ATP is a critical signaling molecule that is found in a wide range of concentrations across cellular environments. The family of nonselective cation channels that sense extracellular ATP, termed P2X receptors (P2XRs), is composed of seven subtypes ($P2X_1$-$P2X_7$) that assemble as functional homotrimeric and heterotrimeric ion channels. Each P2XR is activated by a distinct concentration of extracellular ATP, spanning from high nanomolar to low millimolar. P2XRs are implicated in a variety of physiological and pathophysiological processes in the cardiovascular, immune, and central nervous systems, corresponding to the spatiotemporal expression, regulation, and activation of each subtype. The therapeutic potential of P2XRs is an emerging area of research in which structural biology has seemingly exceeded medicinal chemistry, as there are several published P2XR structures but currently no FDA-approved drugs targeting these ion channels. Cryogenic electron microscopy is ideally suited to facilitate structure-based drug design for P2XRs by revealing and characterizing novel ligand-binding sites. This review covers structural elements in P2XRs including the extracellular orthosteric ATP-binding site, extracellular allosteric modulator sites, channel pore, and cytoplasmic substructures, with an emphasis on potential therapeutic ligand development.

Keywords: purinergic receptors, P2X, ion channels, cryo-EM, X-ray crystallography, antagonist, allosteric modulator, structure-based drug design

Edited by:
Shujia Zhu,
Shanghai Institute for Biological Sciences (CAS), China

Reviewed by:
Ye Yu,
China Pharmaceutical University, China
Motoyuki Hattori,
Fudan University, China
Thomas Grutter,
Université de Strasbourg, France

****Correspondence:***
Steven E. Mansoor
mansoors@ohsu.edu

Specialty section:
This article was submitted to Pharmacology of Ion Channels and Channelopathies,
a section of the journal Frontiers in Pharmacology

Received: *22 April 2022*
Accepted: *10 May 2022*
Published: *17 June 2022*

Citation:
Oken AC, Krishnamurthy I, Savage JC, Lisi NE, Godsey MH and Mansoor SE (2022) Molecular Pharmacology of P2X Receptors: Exploring Druggable Domains Revealed by Structural Biology.
Front. Pharmacol. 13:925880.
doi: 10.3389/fphar.2022.925880

INTRODUCTION

Membrane proteins that recognize extracellular purine nucleotides, termed purinergic receptors, are grouped into three unique families: G-protein coupled P1 receptors that recognize adenosine, G-protein coupled P2Y receptors that recognize ADP and ATP, and ligand-gated P2X receptor (P2XR) ion channels that recognize ATP exclusively (Burnstock, 1976; van Calker et al., 1979; Londos et al., 1980; Webb et al., 1993; Brake et al., 1994; Valera et al., 1994). The seven P2XR subtypes, denoted $P2X_1$-$P2X_7$, are trimeric non-selective cation channels that are activated by distinct extracellular concentrations of ATP, a key signaling molecule released from cells in a broad range of physiological and pathophysiological states, from low concentrations during homeostasis to high concentrations in chronic inflammation or ischemia (Burnstock, 1972; Roman and Fitz, 1999; Taylor et al., 1999; Burnstock, 2004). Individual P2XR subtypes are activated by a wide range of distinct extracellular ATP (eATP) concentrations, from high nanomolar to low millimolar (Jarvis and Khakh, 2009; Illes et al., 2021). The binding of eATP to the receptor induces a conformational change, opening the ion channel and facilitating the influx of Na^+ and Ca^{2+} ions and the efflux of K^+ ions (Samways et al., 2014). The resultant net inward current following P2XR activation plays a significant role in downstream signaling and cellular function.

The functional and clinical significance of P2XR subtypes is related to both their individualized affinity to eATP and the cell types in which they are expressed. These include, but are not limited to, platelets ($P2X_1$), smooth muscle cells ($P2X_{1\text{-}7}$, predominantly $P2X_1$), sensory neurons ($P2X_{1\text{-}7}$, predominantly $P2X_3$), epithelial cells ($P2X_4$, $P2X_5$, $P2X_6$, $P2X_7$), and immune cells ($P2X_4$ and $P2X_7$) (Burnstock and Kennedy, 2011). Accordingly, P2XRs are implicated in an array of pathological conditions. For instance, in animal models of Alzheimer's disease (AD), pharmacologic inhibition or genetic depletion of $P2X_7$ significantly improves the symptoms and neuropathology of AD (Francistiova et al., 2020). Several other examples of P2XR-implicated pathological conditions include: platelet aggregation ($P2X_1$), hearing loss ($P2X_2$), asthma ($P2X_3$), vascular inflammation ($P2X_7$), and cancer ($P2X_7$) (Kamei et al., 2005; Baroni et al., 2007; Burnstock and Kennedy, 2011; Furlan-Freguia et al., 2011; Mahaut-Smith et al., 2011; North and Jarvis, 2013; Yan et al., 2013; Burnstock and Knight, 2018; Lara et al., 2020; Illes et al., 2021). As a result, P2XRs are an active area of therapeutic research with several subtype-specific antagonists currently in clinical trials to treat persistent cough (clinicaltrials.gov: NCT02502097), rheumatoid arthritis (clinicaltrials.gov: NCT00628095), and depression (clinicaltrials.gov: NCT04116606), among others (Kamei et al., 2005; Pfizer, 2008; Keystone et al., 2012; Abdulqawi et al., 2015; Afferent Pharmaceuticals, 2015; CCTU-Core et al., 2019; Richards et al., 2019).

P2XRs assemble as both homotrimeric and heterotrimeric channels. The known heterotrimeric assemblies include: $P2X_{1/2}$, $P2X_{1/4}$, $P2X_{1/5}$, $P2X_{2/3}$, $P2X_{2/6}$, $P2X_{4/5}$, $P2X_{4/6}$, and $P2X_{4/7}$ (Murrell-Lagnado and Qureshi, 2008). Very little is known about heterotrimeric composition, stoichiometry, and function. This is compounded by the increased pharmacologic complexity of heterotrimeric receptors, which poses an additional challenge to therapeutic targeting of P2XR activity. For example, heterotrimeric $P2X_{2/3}$ has a ligand dose-response profile that is distinct from either homotrimeric $P2X_2$ or $P2X_3$ (Lewis et al., 1995). Currently, there are published structures for only three of seven homotrimeric subtypes and none for heterotrimeric receptors. The first P2XR structure, solved by X-ray crystallography, characterized the apo (unbound) closed state, defined the overall architecture of this receptor family, and confirmed three-fold symmetry for the homotrimeric assembly (Kawate et al., 2009). Subsequent crystallographic studies have identified the extracellular orthosteric ATP-binding site, revealed two distinct extracellular allosteric binding sites, and defined the molecular mechanisms of P2XR gating (Hattori and Gouaux, 2012; Karasawa and Kawate, 2016; Mansoor et al., 2016; Kasuya et al., 2017; Wang et al., 2018). While these crystallographic studies established a foundational understanding of P2XR structure and function, truncation of the cytoplasmic N- and C- termini (necessary for crystallization) limited the scope of our understanding of P2XR biology. The application of single-particle cryogenic electron microscopy (cryo-EM) to rat $P2X_7$ overcame these limitations and provided visualization of the first full-length, wild-type P2XR, revealing novel features in the cytoplasmic domain that are essential for receptor function (McCarthy et al., 2019).

The "resolution revolution" in cryo-EM is advancing the ability of researchers to solve high-resolution protein structures (Kuhlbrandt, 2014). Compared to X-ray crystallography, cryo-EM requires less protein, tolerates more sample heterogeneity, and allows for the study of proteins in more native-like membrane environments, all of which are challenges in studying membrane protein structure (Su et al., 2021). Moreover, cryo-EM structures of wild-type proteins and protein complexes are consistently reaching sufficient resolutions to discover novel ligands and identify post-translational modifications (McCarthy et al., 2019; Flores et al., 2020; Nakane et al., 2020; Rahman et al., 2020). In turn, these new high-resolution structures of therapeutically relevant proteins have accelerated structure-based drug design (SBDD) efforts, which are significantly more efficient and generate higher-specificity ligands when compared to classical *in vitro* based assays (Lionta et al., 2014; Batool et al., 2019; Ballante et al., 2021; Ford et al., 2021; Lees et al., 2021). Cryo-EM is well suited to visualize novel receptor structures and receptor-ligand interactions for use in SBDD techniques, ultimately leading to more potent therapeutic compounds with fewer and less severe side effects for patients.

Careful examination of the available P2XR structures provides insights into the molecular pharmacology of this therapeutically relevant receptor family. This review highlights both known and potentially targetable sites within P2XRs that are critical to modulate receptor function.

OVERALL P2XR DOMAIN ARCHITECTURE

The first P2XR structure to be solved, the apo closed state of a truncated zebrafish $P2X_4$ ($zfP2X_4$), defined the architecture of the extracellular and transmembrane regions for this receptor family (Kawate et al., 2009). Within each protomer of a trimeric receptor, the extracellular and transmembrane domains were imagined to resemble a breaching dolphin (**Figure 1A**) (Kawate et al., 2009). This overall architecture was confirmed to be conserved for apo closed states of the human $P2X_3$ ($hP2X_3$), giant panda $P2X_7$ ($pdP2X_7$), and rat $P2X_7$ ($rP2X_7$) receptors in successive structural studies (Karasawa and Kawate, 2016; Mansoor et al., 2016; McCarthy et al., 2019). Comparing the molecular architecture of several P2XRs reveals conserved sites that are targetable across this receptor family and highlights the structural differences across subtypes.

The Extracellular Domain

The extracellular domain, which has been likened to a dolphin's head and body, is composed of thirteen β-strands and four α-helices (**Figure 1A**). The β-sheets of the lower and upper body compose the central backbone of the extracellular domain of all P2XRs, with peripheral α-helices and loops variable between subtypes. Tucked within the loops, β-sheets, and α-helices of the extracellular domain are several ligand-binding pockets that modulate P2XR function. The orthosteric ATP-binding site,

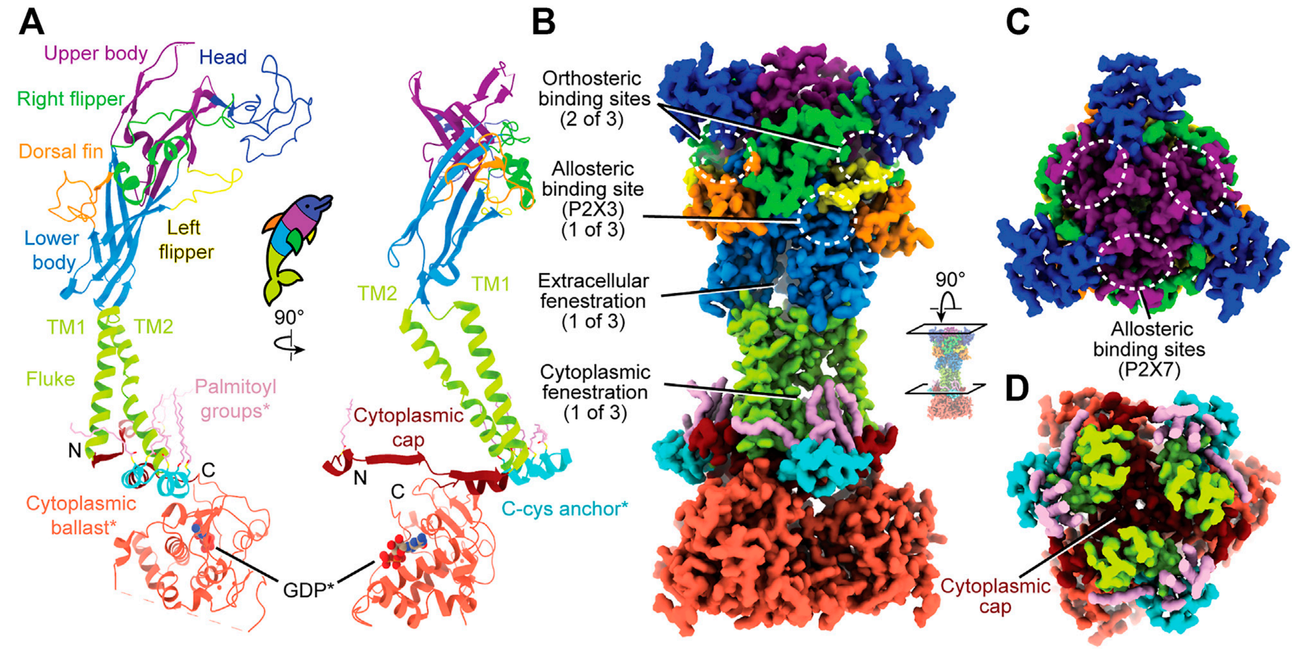

FIGURE 1 | Overall, dolphin-resembling architecture of P2XRs exemplified by $rP2X_7$ (PDB: 6U9V). **(A)** *Left:* Ribbon representation of one subunit of $rP2X_7$ colored by domain architecture. *Right:* Orthogonal view colored by domain architecture. **(B)** Surface representation of the biological trimeric assembly of $rP2X_7$ colored by domain architecture, viewed parallel to the membrane and with select structural elements labeled. The orthosteric ATP-binding site and the extracellular and cytoplasmic fenestrations are structurally conserved amongst P2XRs. The allosteric site found in $hP2X_3$ is mapped to its respective spatial position on the presented $P2X_7$ model. This allosteric site has not been confirmed to exist in $P2X_7$, but the structural similarity amongst P2XRs allows visualization of its relative position. **(C)** Top-down view of the trimeric assembly of the $rP2X_7$ extracellular domain colored by domain architecture, with denoted symmetry-related allosteric site confirmed in $P2X_7$. This view highlights the three identical, symmetry-related, allosteric binding sites found on top of the extracellular domain of homotrimeric $P2X_7$. **(D)** Biological trimeric assembly of $rP2X_7$, colored by domain architecture, viewed perpendicular to the membrane from the center of the transmembrane domain into the cytoplasm. *Denotes structural elements found only in the $P2X_7$ subtype.

defined as the location of endogenous ligand (eATP) binding, has been structurally characterized for three P2XR subtypes: $hP2X_3$, $zfP2X_4$, and $rP2X_7$ (Mansoor et al., 2016; Kawate et al., 2009; Hattori and Gouaux, 2012; McCarthy et al., 2019). This site is found in all P2XRs at an interface formed by the head, left flipper, and upper body of one protomer and the lower body of the neighboring protomer (**Figures 1A,B**). Thus, a functional trimeric P2XR has three symmetry-related orthosteric binding sites. However, it is generally accepted that the occupation of all three of these binding sites by ATP is not necessary to activate the channel (Friel and Bean, 1988; Coddou et al., 2011; Kawate, 2017).

In addition, extracellular allosteric binding sites—distinct from the orthosteric binding site—have been structurally confirmed in $hP2X_3$ and $pdP2X_7$ and are predicted in other P2XRs (**Figures 1B,C**) (Ase et al., 2019; Bidula et al., 2022; Karasawa and Kawate, 2016; Obrecht et al., 2019; Wang et al., 2018). One structurally confirmed allosteric site in $hP2X_3$ is found towards the base of the extracellular domain, formed by the left flipper of one subunit and the lower body and dorsal fin of another (**Figure 1B**) (Wang et al., 2018). Due to symmetry, there are three such allosteric sites in homotrimeric $hP2X_3$ (**Figure 1B**). Another allosteric site, structurally confirmed in $pdP2X_7$, is located on top of the extracellular domain and is formed by the upper body between neighboring protomers (**Figure 1C**) (Karasawa and Kawate, 2016). Similarly, due to symmetry, there are three such allosteric sites in homotrimeric $pdP2X_7$ (**Figure 1C**). Ligand binding at allosteric sites modulates protein activity through structural rearrangements, resulting in either inhibited (negative allostery) or enhanced (positive allostery) orthosteric ligand binding. Negative allosteric modulators are non-competitive antagonists as they do not compete with orthosteric ligand binding. The orthosteric and two distinct allosteric sites are critical targets to consider when developing potential therapeutic ligands that modulate P2XR activity.

The Transmembrane Domain

The transmembrane (TM) domain, the dolphin's tail, is composed of two α-helices (the peripheral TM1 and internal, pore-lining TM2) that span the membrane, connecting the extracellular and cytoplasmic domains (**Figures 1A,B**). Together, the six TM helices of the trimeric receptor form the pore and undergo distinct conformational rearrangements upon ATP binding (Li et al., 2010). The three conformational states of the gating cycle include the apo closed state, the ATP-bound open state, and the ATP-bound desensitized (closed) state (Mansoor et al., 2016). Desensitization refers to progressive pore closure during sustained agonist binding, which has been thoroughly reviewed for P2XRs (Werner et al., 1996; North, 2002; Kawate,

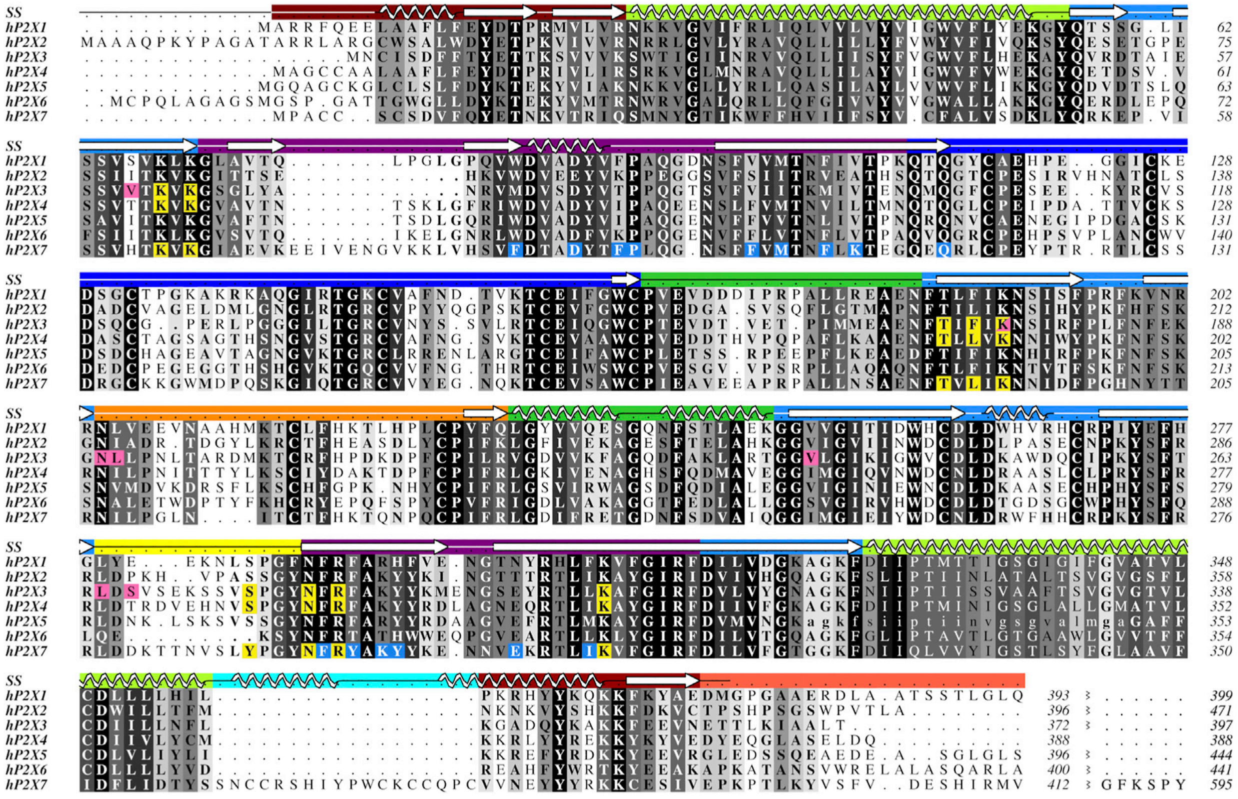

FIGURE 2 | Protein sequence alignment of the seven human P2XR subtypes, P2X$_1$-P2X$_7$. Amino acids are shown in grayscale by level of sequence conservation across human subtypes as calculated with Alscript (Barton, 1993) (white text on black background denotes full sequence conservation). Residues with direct ligand interactions are highlighted, with the orthosteric ATP-binding site residues in yellow and the residues of the two distinct allosteric sites in pink and blue. These residues are highlighted only for subtypes for which there are published structures. Secondary structure (SS) is denoted in the top row and is colored by domain architecture corresponding to the color scheme in **Figure 1**. The break at the end of the sequence alignment condenses the divergent cytoplasmic domains. The ancestral difference in TM2 of hP2X$_5$, as described in the text, is indicated with lower case letters. The sequence alignment was generated in Clustal Omega and the figure created using Aline (Bond and Schuttelkopf, 2009; Sievers and Higgins, 2018). Sequences were obtained from the UniProt database with accession numbers P51575, Q9UBL9, P56373, Q99571, Q93086, O15547, and Q99572 for hP2X$_1$-hP2X$_7$, respectively.

2017; Mansoor, 2022, in press). The rearrangements of the pore during the gating cycle are described in the helical recoil model of receptor desensitization, first proposed from the published structures of hP2X$_3$ (Mansoor et al., 2016). The P2X$_7$ subtype is the only P2XR that does not undergo desensitization. Currently, there are no structures characterizing P2XR pore-modulating ligands, but such a class of antagonists would have therapeutic potential for modulating P2XR function.

The Cytoplasmic Domains

Not much is known about the structure of cytoplasmic domains for the majority of P2XR subtypes. However, the hP2X$_3$ ATP-bound open state structure and the full-length rP2X$_7$ structures highlight aspects of intracellular elements (Mansoor et al., 2016; McCarthy et al., 2019). The first segment of the cytoplasmic domain was elucidated by the hP2X$_3$ ATP-bound open state structure, which revealed the cytoplasmic ends of the TM helices are flanked by a substructure termed the “cytoplasmic cap” (**Figures 1A,D**) (Mansoor et al., 2016). The cytoplasmic cap is a product of domain swapping, composed of intertwining β-strands from all three protomers knitted together to form β-sheets that run parallel to the membrane. The stability of the cytoplasmic cap plays a pivotal role in the gating cycle of distinct subtypes by setting the rate of desensitization (Mansoor et al., 2016). Two additional cytoplasmic structural features unique to P2X$_7$ were revealed by cryo-EM, a cysteine rich domain termed the “C-cys anchor“ and a ~200 residue C-terminal domain termed the “cytoplasmic ballast” (**Figures 1A,B**) (McCarthy et al., 2019). Further elucidation of P2XR cytoplasmic structural diversity by cryo-EM will provide invaluable information about receptor biology.

The array of P2XR structures to date have supplemented our understanding of P2XR function and defined orthosteric and allosteric ligand binding, the path of ion flow through the pore, and the helical recoil model of desensitization. The recent discoveries of the previously unknown cytoplasmic elements of rP2X$_7$, facilitated by cryo-EM, have raised new questions regarding its metabotropic signaling properties (Surprenant et al., 1996; Wilson et al., 2002; Cheewatrakoolpong et al., 2005; Adinolfi et al., 2010; Costa-Junior et al., 2011; McCarthy et al., 2019). The nuances of the structural elements contained within the P2XR architecture are discussed below, focusing on potential strategies to target them therapeutically with ligands.

P2XR SEQUENCE CONSERVATION

Protein sequence alignments of human P2XRs reveal these receptors share ~35–53% sequence identity between any two subtypes (**Figure 2**). P2XRs vary in length by up to 207 amino acids per protomer, with $P2X_7$ having the longest sequence and $P2X_4$ having the shortest (595 and 388 amino acids per protomer, respectively). The most significant variations between P2XR sequences lay in their cytoplasmic termini, which are known to play a critical role in receptor desensitization, trafficking, and signaling (Brandle et al., 1997; Koshimizu et al., 1999; Boue-Grabot et al., 2000; North, 2002; Chaumont et al., 2004; Jarvis and Khakh, 2009; Hausmann et al., 2014; Mansoor et al., 2016; Sattler and Benndorf, 2022). The N-termini vary in length by up to 18 amino acids, with $P2X_2$ having the longest N-terminus at 20 residues before the first α-helix of the cytoplasmic cap and $P2X_3$ having the shortest at only two residues. The C-termini vary in length by up to 191 amino acids after the last β-strand in the cytoplasmic cap, with $P2X_7$ having the longest C-terminus at 203 residues and $P2X_4$ having the shortest at 12 residues. Despite significant sequence similarity between P2XRs, subtype-specific sequence differences confer distinct receptor functionality. As our interests lie in human specific drug design, unless stated otherwise, all residues discussed will be from the register of human orthologs.

There is no published structure of $P2X_5$ but this subtype is known to be expressed in humans predominantly as a non-functional isoform (Kotnis et al., 2010). A single-nucleotide polymorphism leads to the canonical isoform which lacks 22 residues (328–349) encoded by exon 10, including the N-terminal (outer leaflet) portion of TM2 (**Figure 2**) (Le et al., 1997). Without a significant portion of TM2, this isoform is prone to subunit aggregation (Duckwitz et al., 2006). Restoration of the amino acids encoded by exon 10 is found to re-establish $P2X_5$ function, producing strong currents in response to ATP (Bo et al., 2003). While, in humans, the allele encoding the non-functional protein is predominant, alleles encoding full-length, functional $P2X_5$ have also been reported (Kotnis et al., 2010). Notably, the full-length, functional $P2X_5$ isoform predominates in other species. Structures of the truncated and full-length isoforms might provide insight into the evolution of this P2XR subtype and the structural basis for the corresponding pharmacological effects.

While the sequence of $hP2X_6$ appears to be quite similar to other P2XRs, this subtype lacks nine residues that compose the main portion of the left flipper, a key element in the activation of P2XRs (**Figure 2**) (Wang et al., 2017; Zhao et al., 2014; Li et al., 2010; Kawate, 2017; Jiang et al., 2012). These missing residues might explain why $P2X_6$ homotrimers do not produce currents in response to ATP (Soto et al., 1996; Le et al., 1998; King et al., 2000). However, all residues that are known to coordinate ATP in other P2X subtypes are conserved within $hP2X_6$ (**Figure 2**). This suggests that while ATP may be able to bind in the orthosteric binding site of $hP2X_6$, the lack of a functional left flipper may be the cause of this subtype's inability to transition to an ATP-bound open state. The functional significance of $hP2X_6$ may be found in its ability to form heterotrimers, thereby expanding the pharmacological complexity of purinergic signaling (Le et al., 1998; King et al., 2000; Antonio et al., 2014).

Easily seen in the sequence alignment, $P2X_7$ has several features that are specific to this subtype, including the C-cys anchor (residues 360–377) and its uniquely large cytoplasmic domain, referred to as the cytoplasmic ballast (**Figure 2**) (McCarthy et al., 2019). Post-translational palmitoylation of residues on the C-cys anchor explains the distinct ability of $P2X_7$ to remain open without undergoing desensitization (McCarthy et al., 2019). Mapping the unique features of $P2X_7$ from sequence to structure demonstrates the importance of resolving the cytoplasmic domains for each of the other P2XRs.

ORTHOSTERIC LIGAND BINDING

It is crucial to elucidate how ATP interacts with the orthosteric binding site in order to understand the mechanism and modulation of P2XR activation. One approach to inhibit P2XR function is to develop competitive antagonists that target the orthosteric ATP-binding site (**Figure 1B**). The residues that compose the orthosteric pocket are positively charged, hydrophilic, and highly conserved across all receptor subtypes (**Figures 2**, **3A,B**) (Chataigneau et al., 2013). Similarity of the orthosteric site across P2XRs might impede the development of subtype-selective competitive antagonists. However, structural studies can provide crucial insights into the subtle differences in molecular pharmacology between P2XR subtypes at the orthosteric site.

The published structures of $hP2X_3$, $zfP2X_4$, and $rP2X_7$ receptors in an ATP-bound open state define the orthosteric binding site (**Figure 3**). A close look at these structures reveals that ATP occupies a virtually identical U-shaped pose and the principal residues responsible for ATP coordination are highly conserved: four lysines, a threonine, an asparagine, and an arginine (**Figures 2**, **3C–E**) (Hattori and Gouaux, 2012; Mansoor et al., 2016; McCarthy et al., 2019). Despite this conservation, the molecular pharmacology of P2XR activation by ATP is remarkably variable across subtypes. For example, $P2X_7$ requires ~200-fold higher concentration of eATP than $P2X_3$ for activation (Jarvis and Khakh, 2009; Illes et al., 2021). A comparison of the ATP-bound open state structures of $hP2X_3$, $zfP2X_4$, and $rP2X_7$ reveals there are differences in only two of the residues that directly coordinate ATP. The first difference is a hydrophobic residue that interacts with the adenosine base (F174, L191, and L191 in $hP2X_3$, $zfP2X_4$, and $rP2X_7$, respectively) (**Figures 2**, **3**). The second variable residue is on a loop within the left flipper which differs between a serine (S275) in $hP2X_3$ that interacts with the α-phosphate of ATP, an alanine (A292) in $zfP2X_4$ that makes no contacts to ATP, or a phenylalanine (F288) in $rP2X_7$ that interacts with C5 on the ribose of ATP. These minor variations in the principal residues of the orthosteric binding site between subtypes seem unlikely to fully explain the dramatic

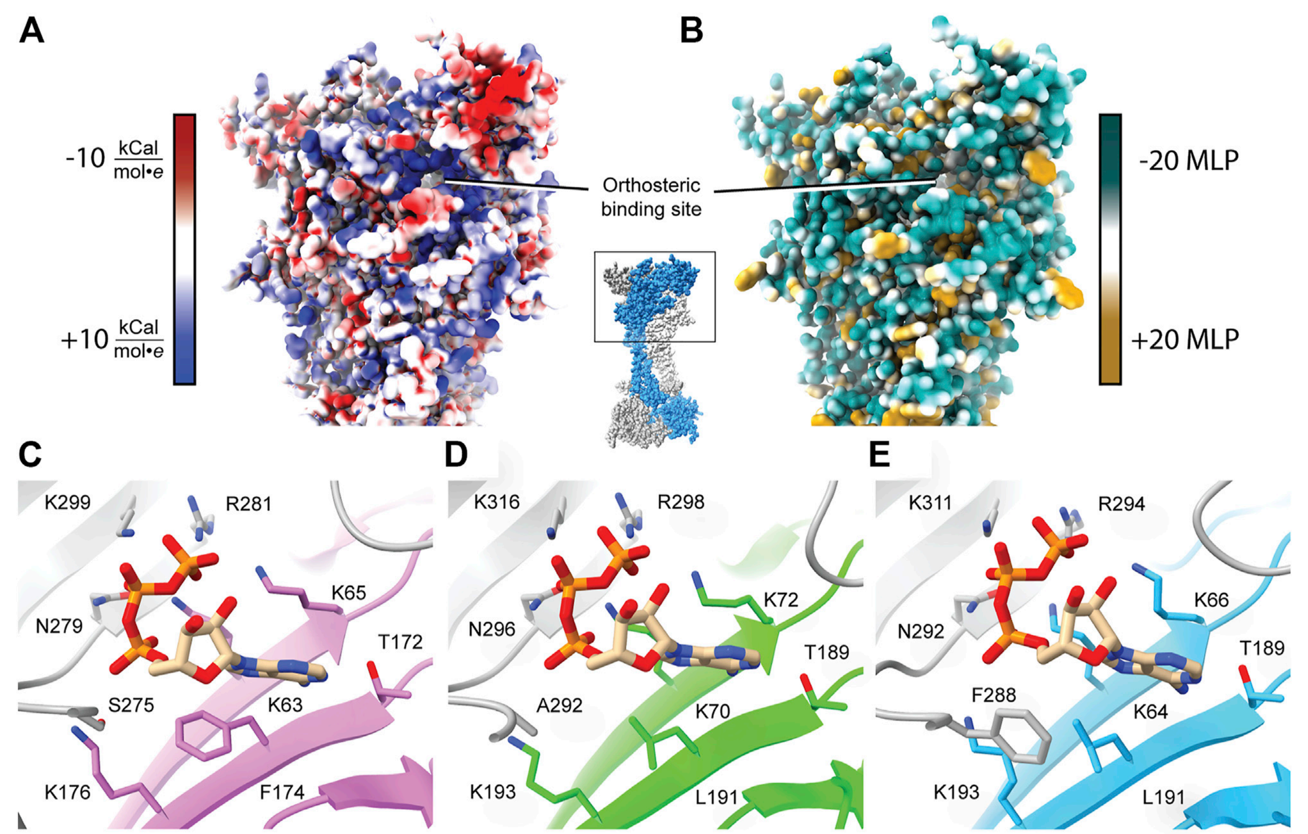

FIGURE 3 | Characteristics of the orthosteric binding site of $hP2X_3$, $zfP2X_4$, and $rP2X_7$. **(A)** Electrostatic surface rendering of $rP2X_7$ (PDB: 6U9V) with blue and red coloring representing positive and negative electrostatic potential, respectively, highlighting the electropositive nature of the P2XR orthosteric ATP-binding site. **(B)** Hydrophobic surface rendering of $rP2X_7$ (PDB: 6U9V) with hydrophobic regions colored brown and hydrophilic regions colored turquoise, each defined by positive and negative molecular lipophilicity potential (MLP), respectively (Laguerre et al., 1997). This rendering highlights the hydrophilic nature of the orthosteric ATP-binding pocket. **(C–E)** Conserved residues involved in the coordination of ATP in the orthosteric binding pocket across structurally characterized P2XRs. Panels are annotated with ortholog-specific residue numbering. Orthosteric site of **(C)** the ATP-bound open state $hP2X_3$ structure (light purple, PDB: 5SVK), **(D)** the ATP-bound open state $zfP2X_4$ structure (green, PDB: 4DW1), and **(E)** the ATP-bound open state $rP2X_7$ structure (blue, PDB: 6U9W). All bound ATP molecules occupy a nearly identical U-shaped pose. The MLP and electrostatic surface potential were calculated in ChimeraX (Pettersen et al., 2021).

differences in ATP sensitivity, suggesting there are other factors at play.

A kinetic limitation to ATP-binding may be one such factor contributing to differential ATP sensitivities between P2XR subtypes. Solvent accessibility to the orthosteric binding site in the apo closed state structures of $hP2X_3$, $zfP2X_4$, and $rP2X_7$ are strikingly different (**Figure 4**) (Stank et al., 2016; McCarthy et al., 2019). The surface-accessible volume of the orthosteric binding site in $rP2X_7$ is approximately 44% smaller than in $hP2X_3$ and 32% smaller than in $zfP2X_4$ (**Figure 4**) (Tian et al., 2018). The effects of variable accessibility can perhaps be explained by small side-chain fluctuations and backbone or interdomain vibrational movements, referred to as "pocket breathing" (Ferrari et al., 2003; Stank et al., 2016). Local protein dynamics and flexibility would affect the kinetics of ligand binding by restricting pocket accessibility, thereby requiring higher concentrations of ATP to activate $P2X_7$. The identity of the coordinating residues and the accessibility of the orthosteric site are valuable insights gained from structural analysis, both of which are necessary considerations during the design of subtype-selective antagonists.

The effect that divalent cations have on the activity of select P2XRs is another consideration for the difference in ATP sensitivities between subtypes. The presence of divalent cations in the extracellular environment shifts the activation requirements for $P2X_2$, $P2X_4$, and $P2X_7$ to higher concentrations of ATP (Garcia-Guzman et al., 1997; Virginio et al., 1997; Li et al., 2013). In $P2X_2$, the affinity and efficacy of $MgATP^{2-}$ is lower than that of free ATP, suggesting Mg^{2+} acts as an inhibitor and constrains receptor function. In contrast, $MgATP^{2-}$ effectively agonizes $P2X_1$ and $P2X_3$ at similar concentrations to free ATP (Li et al., 2013). The crystal structures of the apo closed state and ATP-bound open state of $hP2X_3$ confirm that Mg^{2+} binds in two distinct conformations at an acidic chamber near the orthosteric binding site (Mansoor et al., 2016; Li et al., 2019). Functional data for $hP2X_3$ suggest that Mg^{2+} slows ATP release and receptor recovery from desensitization (Li et al., 2019). However, direct equilibrium

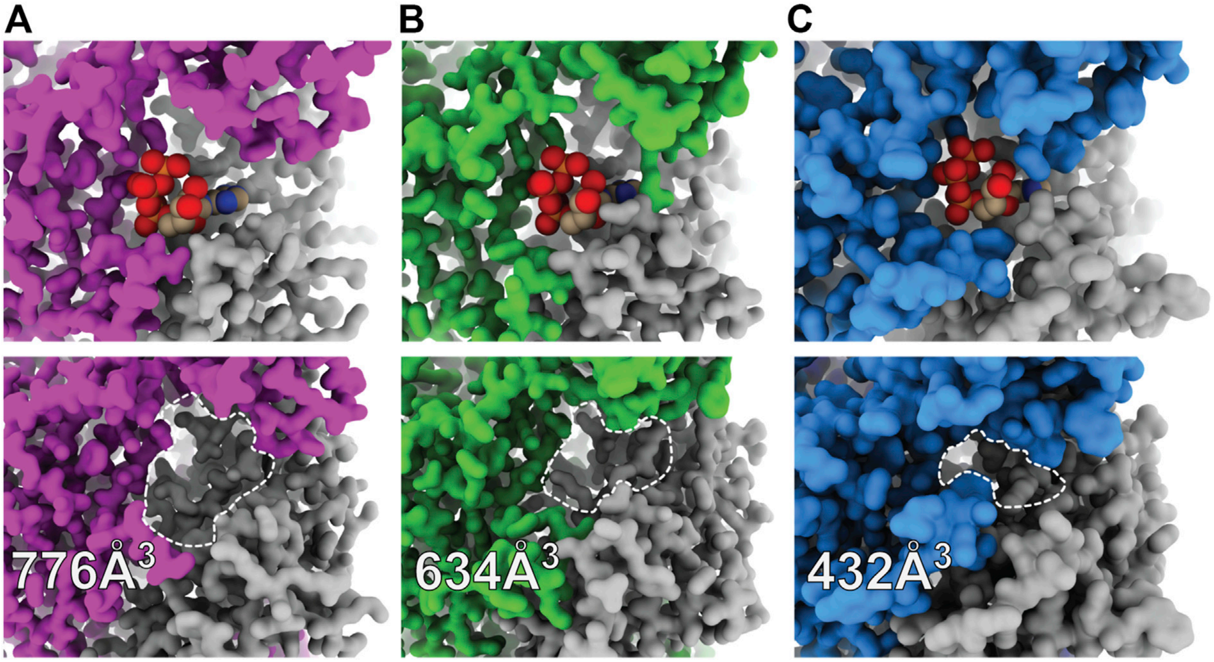

FIGURE 4 | Surface representations of orthosteric ATP-binding pockets highlight differential ligand accessibility between P2XR subtypes. **(A)** ATP-bound open (top) and apo closed (bottom) states of $hP2X_3$ (light purple, PDBs: 5SVK and 5SVJ) reveal the highly accessible pocket. **(B)** ATP-bound open (top) and apo closed (bottom) states of $zfP2X_4$ (green, PDBs: 4DW1 and 4DW0) reveal a slightly less accessible pocket. **(C)** ATP-bound open (top) and apo closed (bottom) states of $rP2X_7$ (blue, PDBs: 6U9W and 6U9V) reveal the least accessible pocket. The approximate binding pockets are outlined with dashed lines for visual clarity. Reported solvent accessible pocket volumes of the orthosteric ATP-binding site in the apo states of $hP2X_3$, $zfP2X_4$, and $rP2X_7$ were calculated with CASTp (using a 2.0 Å probe radius) to be 776, 634, and 432 $Å^3$, respectively (Tian et al., 2018).

binding data demonstrate the presence of Mg^{2+} does not influence the affinity of $hP2X_3$ for ATP (Mansoor et al., 2016). The subtype-specific effects of divalent cations on P2XR activation and gating need to be investigated further.

The information gained from the few known competitive antagonists that target P2XRs provides crucial insight into receptor modulation (Wolf et al., 2011; North and Jarvis, 2013; Muller, 2015; Muller and Namasivayam, 2021; Illes et al., 2021). The two structures of competitive antagonists bound to $hP2X_3$ (TNP-ATP and A-317491) reveal these high-affinity antagonists bind at the orthosteric binding site in a Y-shaped pose, distinct from the U-shaped pose of ATP (**Figures 5A,B**) (Mansoor et al., 2016). This shift in ligand pose allows for deeper penetration into the binding pocket and is postulated to prevent the conformational changes necessary for channel opening (Mansoor et al., 2016). Residues D158 and F174 ($hP2X_3$) are theorized to confer high specificity of TNP-ATP for $hP2X_3$ and $hP2X_1$, as this pair of key residues is only conserved in these two P2XR subtypes (**Figure 2**) (Mansoor et al., 2016). TNP-ATP occupies a different, extended conformational pose in the orthosteric binding site of $ckP2X_7$, distinct from both the U-shaped pose of ATP in $rP2X_7$ and Y-shaped pose of TNP-ATP in $hP2X_3$ (**Figures 5B,C**) (Kasuya et al., 2017). The phosphate groups of TNP-ATP in $ckP2X_7$ are stabilized in this extended conformation by hydrogen bond interactions from residues K236 and K298. Notably, while TNP-ATP inhibits $P2X_1$ and $P2X_3$ with low nanomolar affinity, hundreds of micromolar of TNP-ATP are required to antagonize $P2X_7$ (Virginio et al., 1998). This drastic difference in apparent affinity and the distinct binding poses of TNP-ATP between $hP2X_3$ and $ckP2X_7$ may be correlated. The multitude of poses occupied by ATP, TNP-ATP, and A-317491 reveal the targetable space within the orthosteric pocket, providing knowledge that should be used in development of general and subtype-specific competitive antagonists. These structures reveal the importance of subtype-specific residues and pocket accessibility as critical factors for consideration in SBDD.

ALLOSTERIC LIGAND BINDING

Identification of allosteric binding sites in P2XRs is crucial for the development of novel therapeutic ligands (Muller, 2015; Muller and Namasivayam, 2021). These sites bind secondary ligands non-competitively, promoting structural conformations that enhance or suppress orthosteric ligand binding. From a therapeutic perspective, allosteric modulators are advantageous as they often have fewer side effects compared to orthosteric ligands due to higher receptor specificity, resulting in less disruption of other functional pathways (Coddou et al., 2011; Nussinov and Tsai, 2012; Wenthur et al., 2014; Muller, 2015; Changeux and Christopoulos, 2016; Wang et al., 2018). This is particularly important when targeting a protein whose orthosteric ligand is ATP, a common substrate for proteins

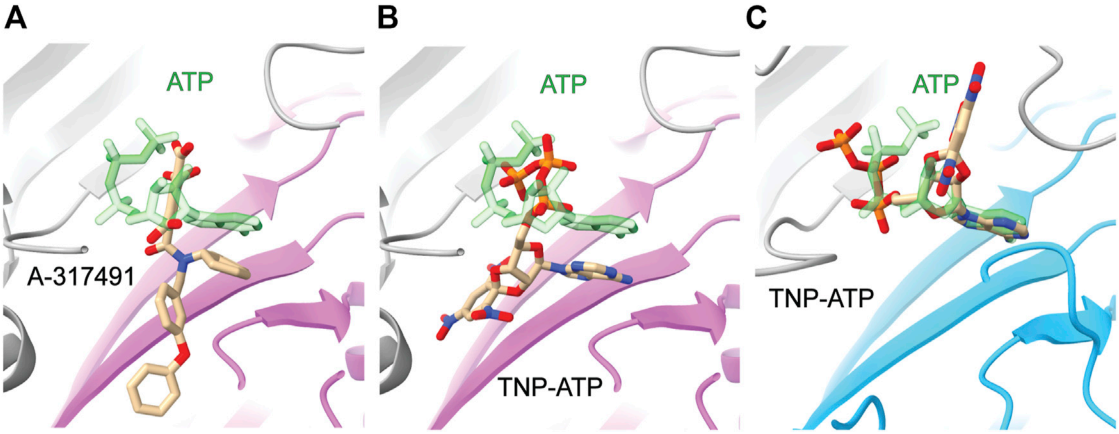

FIGURE 5 | Comparative ligand poses of competitive antagonist-bound closed state and ATP-bound open state P2XR structures. **(A)** The Y-shaped pose of competitive antagonist A-317491 (tan) bound to $hP2X_3$ contrasts with the U-shaped pose of ATP (green) bound to $hP2X_3$ (purple). Superimposed PDBs: 5SVR and 5SVK. **(B)** The Y-shaped pose of competitive antagonist TNP-ATP (tan) bound to $hP2X_3$ contrasts with the U-shaped pose of ATP (green) bound to $hP2X_3$ (purple). Superimposed PDBs: 5SVQ and 5SVK. **(C)** The extended pose of competitive antagonist TNP-ATP (tan) bound to $ckP2X_7$ contrasts with the U-shaped pose of ATP (green) bound to $rP2X_7$ (blue). Superimposed PDBs: 5XW6 and 6U9W.

involved in metabolism and neurotransmission. Until recently, all known allosteric modulators against P2XRs were non-natural synthetic ligands. Current data now indicate bilirubin is an endogenous ligand that acts as a negative allosteric modulator of $P2X_7$, suggesting the possibility for native cellular mechanisms of P2XR allosteric regulation (Zhao et al., 2021). It would be intriguing to discover other endogenous ligands that modulate P2XRs, determine their role in physiological or pathophysiological states, and adapt their chemical scaffold for the development of novel ligands. In support of the proposed therapeutic value of the P2XR allosteric sites, there are numerous small-molecule antagonists of P2XRs in various phases of clinical trials (Kamei et al., 2005; Pfizer, 2008; Keystone et al., 2012; Abdulqawi et al., 2015; Afferent Pharmaceuticals, 2015; CCTU-Core et al., 2019; Richards et al., 2019).

There are currently two distinct allosteric binding sites within P2XRs that have been confirmed with high-resolution structures, one near the orthosteric binding site and another on the top of the extracellular domain, visualized in $hP2X_3$ and $pdP2X_7$, respectively (**Figures 1B,C**) (Karasawa and Kawate, 2016; Wang et al., 2018). Electrophysiological and biochemical studies additionally show allosteric sites exist in $P2X_1$ and $P2X_4$ (Muller, 2015; Ase et al., 2019; Obrecht et al., 2019; Illes et al., 2021; Muller and Namasivayam, 2021; Bidula et al., 2022). Sequence analysis further suggests the remaining P2XRs also contain allosteric sites (**Figure 2**). Since each distinct allosteric site exists at the interface of two protomers, it is unclear to what extent similar allosteric sites exist within heterotrimeric receptors where the interface between subtypes might be markedly different. Examination of the available P2XR structures in complex with allosteric modulators provides pivotal insights into the regulation of P2XRs.

One of the visualized allosteric sites in P2XRs was revealed in the structure of $hP2X_3$ bound to the nanomolar-affinity negative allosteric modulator gefapixant (Wang et al., 2018). This site is composed of residues at a protomer interface formed by the left flipper of one subunit and the lower body and dorsal fin of another (**Figures 1A,B**, **6A,B**). This allosteric site is located on the opposite side of the left flipper as the orthosteric binding site. Movement of the left flipper is an essential step in the transition to an ATP-bound open state (Wang et al., 2017; Zhao et al., 2014; Li et al., 2010; Kawate, 2017; Jiang et al., 2012). Negative allosteric modulators that bind this site, including gefapixant, restrict left flipper mobility and thereby inhibit channel opening. Analysis of the gefapixant-bound $hP2X_3$ structure indicates that residue K176, which is fully conserved across all human P2XRs, is of particular importance (**Figure 2**). It is the only residue in common between this allosteric site and the orthosteric ATP-binding site, interacting with the two oxygens of the sulfonyl nitrene moiety of gefapixant or with an oxygen on the α-phosphate of ATP (**Figures 3C**, **6B**). More biochemical experimentation is required to determine if both ligands can occupy their respective binding sites simultaneously. Several other residues interacting with gefapixant in $hP2X_3$ are of note; N190 is fully conserved and L191, V238, and L265 display hydrophobicity across all P2XR subtypes (**Figures 2**, **6B**). Interestingly, all residues in this allosteric site (except V61 and S267) are conserved between $hP2X_3$ and $hP2X_1$, suggesting this allosteric site is present and quite similar in both subtypes. To support this idea, the ligand aurintricarboxylic acid (ATA) is a high-affinity negative allosteric modulator of $hP2X_1$ and $hP2X_3$ (proposed to bind the same site as gefapixant), but does not effectively antagonize other subtypes (Obrecht et al., 2019). The characterization of this allosteric site within $P2X_3$ (and potentially $P2X_1$) provides a structural template for the development of P2XR subtype-specific antagonists to this novel site.

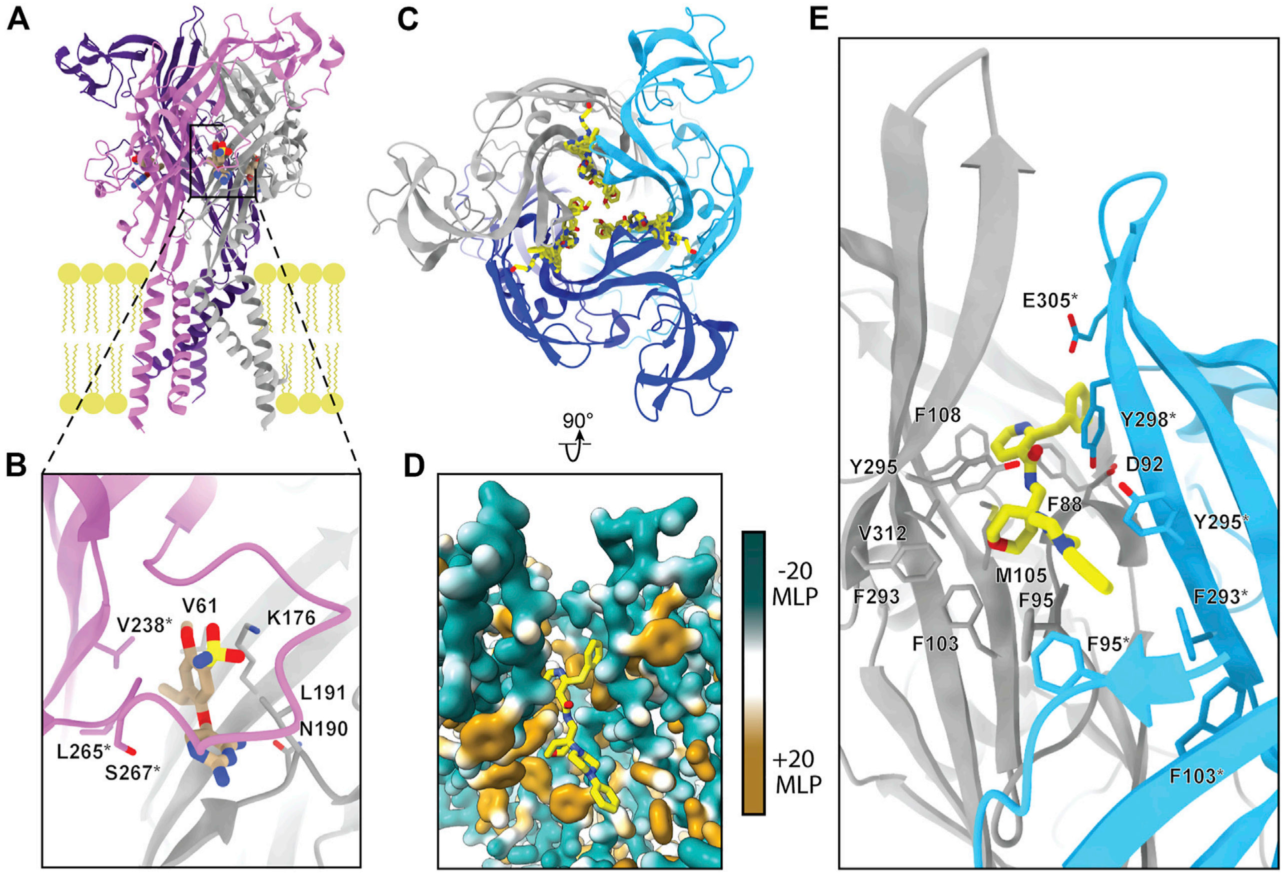

FIGURE 6 | The two known allosteric sites of P2XRs. **(A)** Ribbon representation of the negative allosteric modulator gefapixant (tan) bound to hP2X$_3$ (PDB: 5YVE). **(B)** Magnified view of panel A showing gefapixant interacting with residues at the interface of the left flipper of one protomer (purple) and lower body of another (grey) in hP2X$_3$. **(C)** Top-down view of five superimposed negative allosteric modulators (yellow) bound to a ribbon representation of pdP2X$_7$, highlighting the nearly identical binding mode of the chemically distinct ligands (PDBs: 5U1W, 5U1X, 5U1Y, 5U1V, and 5U1U). **(D)** Magnified and rotated view of panel C showing one of the five negative allosteric modulators (JNJ-47965567) bound to the hydrophobic pocket of pdP2X$_7$ (PDB: 5U1X). Hydrophobic surface rendering of pdP2X$_7$ with hydrophobic regions colored brown and hydrophilic regions colored turquoise, each defined by positive and negative molecular lipophilicity potential (MLP), respectively (Laguerre et al., 1997). **(E)** Ribbon representation of panel D with negative allosteric modulator JNJ-47965567 bound to pdP2X$_7$ highlighting interacting residues (PDB: 5U1X). *Demarcating residues in the purple and blue protomers in panel B and in panel E, respectively. The MLP was calculated in ChimeraX (Pettersen et al., 2021).

Crystallographic structures of five unique negative allosteric modulators bound to pdP2X$_7$ provide a view of another allosteric site present in P2XRs (Karasawa and Kawate, 2016). Located on the top of the extracellular domain, ligands bound at this allosteric site prevent a conformational rearrangement required for all P2XRs to undergo transition to an ATP-bound open state (**Figures 1C**, **6C**) (Karasawa and Kawate, 2016; Kawate, 2017). This binding pocket is generally hydrophobic and the entrance is lined by charged residues (**Figures 6D,E**). The five negative allosteric modulators structurally characterized in complex with pdP2X$_7$, despite varying in size, share a common scaffold that generally complements the properties of the pocket, with a mostly hydrophobic tail and a hydrophilic head connected through a narrow, nitrogenous linker (**Figure 6D**) (Karasawa and Kawate, 2016). The residues at this allosteric binding pocket of pdP2X$_7$ are similar or conserved in hP2X$_7$ and across other human P2XRs, suggesting this site may be present in other subtypes. In support of this, the proposed negative allosteric modulator 5-(3-Bromophenyl)-1,3-dihydro-2*H*-benzofuro [3,2-*e*]-1,4-diazepin-2-one (5-BDBD) is reported to bind to P2X$_4$ at the equivalent allosteric site (Bidula et al., 2022). Altogether, the structures of allosteric modulators bound to pdP2X$_7$ and the biochemical experiments on P2X$_4$ suggest this site is a promising target for the development of novel high-affinity and subtype-specific P2XR antagonists by SBDD.

P2XR PORE ARCHITECTURE

As the primary function of P2XRs is to serve as non-selective cation channels in response to activation by eATP, another approach to inhibit ion channel function is by obstructing the ion path through the protein. The pore through the transmembrane region of P2XRs is formed by a bundle of TM helices in a structure similar to those found in acid-sensing ion channels (ASICs) and epithelial Na$^+$ channels (ENaCs) (Noreng

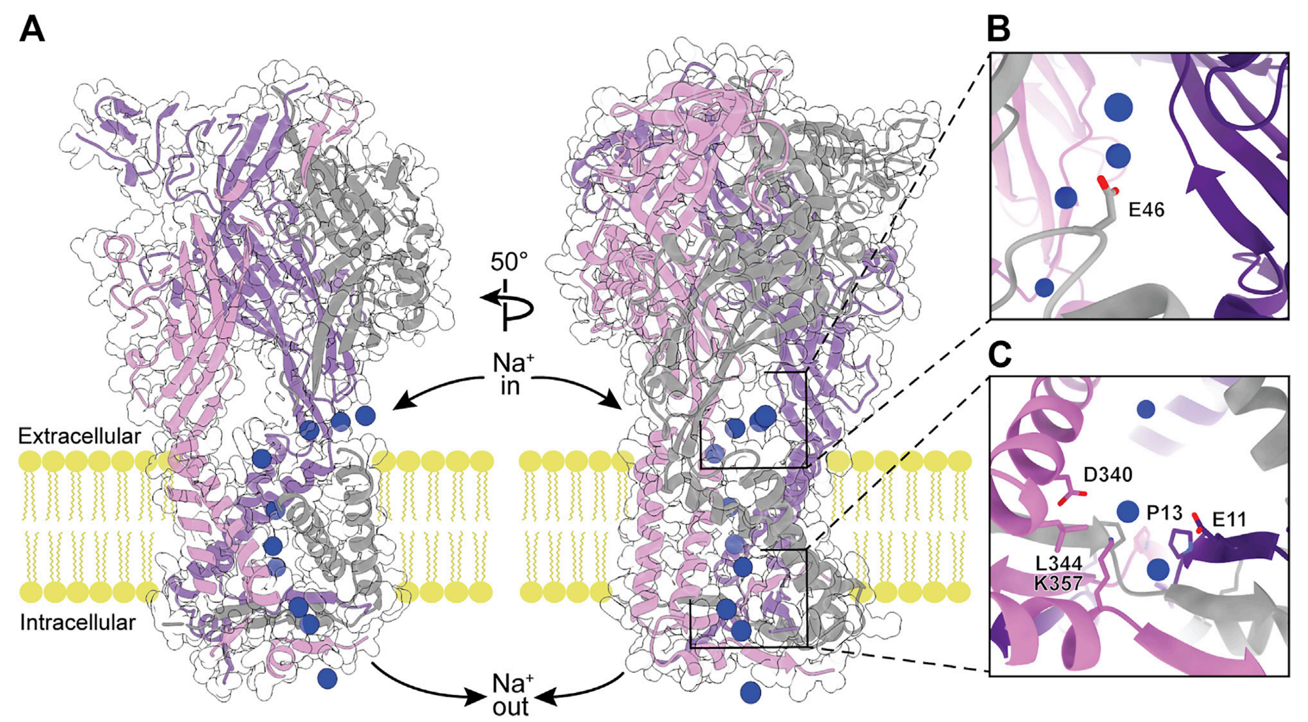

FIGURE 7 | The modeled flow of Na$^+$ ions through the ATP-bound open state hP2X$_3$ structure (PDB: 5SVK). **(A)** Molecular dynamic simulations show Na$^+$ ions (blue spheres) enter the receptor through the extracellular fenestrations, pass through the extracellular vestibule and the pore, and enter the cell via the cytoplasmic fenestrations (Mansoor et al., 2016). *Left:* View highlighting the flow of Na$^+$ ions through the pore. *Right:* 50° rotated view highlighting the flow of Na$^+$ ions through extracellular and cytoplasmic fenestrations. **(B)** Magnified view of Na$^+$-coordinating residue (E46) within the extracellular fenestration. **(C)** Magnified view of key residues in the cytoplasmic fenestration. Mutations T13P/S15V/V16I were needed to slow the rate of desensitization and capture the ATP-bound open state hP2X$_3$ crystal structure (Hausmann et al., 2014).

et al., 2018; Jasti et al., 2007; Baconguis et al., 2014). Ions flow through lateral, phospholipid-lined fenestrations into vestibules on both sides of the TM helices (**Figures 1**, **7**, **8**) (Samways et al., 2011; Samways et al., 2014). To validate the ion flow path, hP2X$_3$ was crystallized in the presence of CsCl and probed for the location of Cs$^+$ ions by anomalous signal (Mansoor et al., 2016). Glutamate E46 was found to coordinate a Cs$^+$ ion at the entrance to each of the three extracellular fenestrations, indicating this residue similarly coordinates Na$^+$ ions under physiological conditions (**Figure 7B**). The residue at this position is a glutamate or aspartate in four of the human subtypes (P2X$_1$, P2X$_3$, P2X$_4$, and P2X$_7$), but a glutamine in hP2X$_2$ and a lysine in hP2X$_5$ and hP2X$_6$ (**Figure 2**). In hP2X$_2$, hP2X$_5$, and hP2X$_6$, this ion-coordinating role in the fenestrations is likely fulfilled by a nearby acidic residue on an alternate protomer (E69, D57, or E66, respectively). This conserved charge at the lateral extracellular fenestrations could be targeted by designing ligands that prevent ion entry, regardless of whether the pore is open or closed. Such a ligand would need to selectively bind and block each extracellular fenestration, which are large surface domains with substantial void space in the ATP-bound open state (**Figures 1B**, **7A**). This may be one instance where P2XR modulation is best achieved by a larger biologic therapeutic, such as an antibody or an aptamer (Nelson et al., 2010; Zhou and Rossi, 2017). These structured protein and nucleic acid affinity reagents are ideally suited for targeting large extracellular epitopes, where accessing small binding pockets is not necessary and diffusion across the cell membrane is not desired.

Ions travel from one of the extracellular fenestrations to the extracellular/central vestibule lined by the first β-strand after TM1 and the last β-strand before TM2 (**Figures 1A**, **8A,B**). Through molecular modeling and mutagenesis studies, this large vestibule has been found to be a binding site for ginsenoside ("steroid-like" dammarane triterpenoid glycosides) allosteric modulators of hP2X$_7$ (Bidula et al., 2019). Simulations suggest these molecules bind in the upper part of this vestibule (central vestibule), making key interactions to the β-strand immediately preceding TM2. While no structures of ginsenoside molecules bound to P2XRs exist at this time, this site may prove to be an attractive target for new allosteric modulators due to its location near the transmembrane pore. The upper vestibule is also the location of a Zn^{2+}-binding site seen in the tick P2X structure (AmP2X) (Kasuya et al., 2016). Of the human subtypes, only hP2X$_4$ has residues (Q94, E95) similar to the Zn^{2+}-coordinating residues (E105, E106) of AmP2X (**Figure 2**). The activity of hP2X$_4$ has been shown to be modulated by Zn^{2+}, an interesting consideration for development of P2X$_4$-specific ligands (Garcia-Guzman et al., 1997).

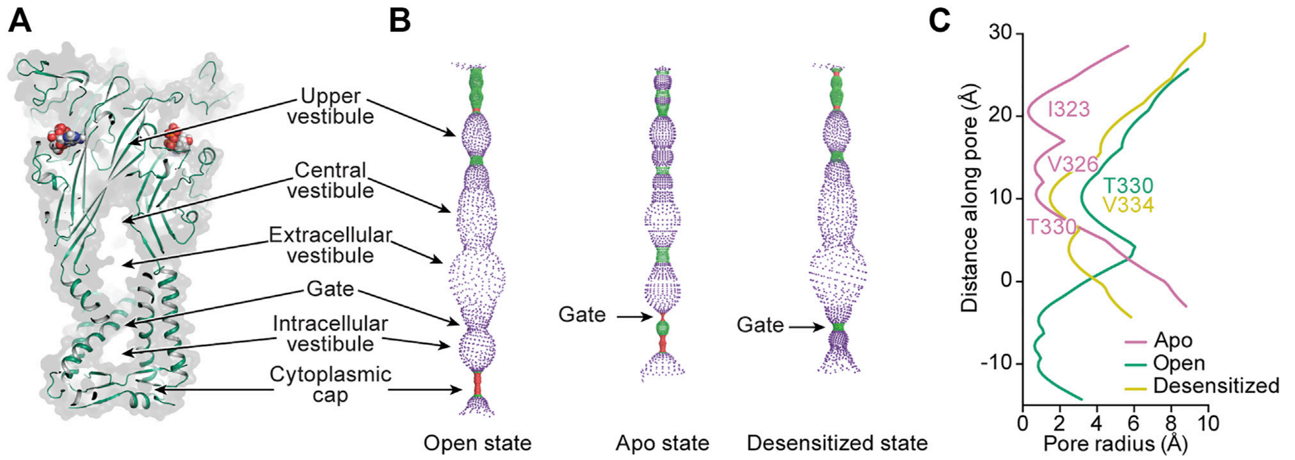

FIGURE 8 | Mapping the interior space of the hP2X$_3$ pore in different conformational states. **(A)** A coronal section of a surface representation of the ATP-bound open state of hP2X$_3$ (PDB: 5SVK) reveals the upper, central, extracellular, and intracellular vestibules. **(B)** Pore-lining surface along the axis of hP2X$_3$ for the ATP-bound open, apo closed, and ATP-bound desensitized states (PDBs: 5SVK, 5SVJ, and 5SVL, respectively), calculated by the program HOLE: red <1.15 Å radius, green between 1.15–2.30 Å radius, and purple >2.30 Å radius (Smart et al., 1996). **(C)** Plot of pore radius as a function of distance along the pore axis for the ATP-bound open, apo closed, and ATP-bound desensitized states of hP2X$_3$. The positions of the residues making up the narrowest radius in each conformational state are labeled. The Cα position of I341 in hP2X$_3$ is set as zero. This figure was from adapted from Mansoor et al. (2016).

From the extracellular/central vestibule, ions cross the membrane through a channel (the pore) at the symmetry axis formed by a set of six TM helices consisting of two antiparallel helices from each protomer (**Figures 1**, **8A**). In each protomer, the N-terminal α-helix (TM1) is oriented from cytosolic to extracellular and TM2 is oriented oppositely, forming a short section of antiparallel coiled-coil. The interior of the bundle is formed by TM2 from each protomer. The pore of the apo closed state is gated towards the extracellular side of the transmembrane region, with minimum radii of 0.3 Å at symmetry-related I323 in hP2X$_3$ and 0.1 Å at S339 in rP2X$_7$ (**Figures 8B,C**). Interestingly, these residues are on different turns of TM2 in the superimposed structures, showing there is some variability in the placement of the extracellular gate between subtypes. Upon the binding of ATP, movement of the three TM2 helices opens the channel to a pore radius large enough for passage of partially hydrated sodium ions (minimum radii of 3.2 Å in hP2X$_3$ and 2.5 Å in rP2X$_7$) (Degrève et al., 1996). Desensitization of P2X$_3$, and presumably other P2XRs (except P2X$_7$ which does not desensitize), occurs through another movement of the TM2 helices, whereby disassembly of the cytoplasmic cap leads to a new gate near the center of the transmembrane region at V334 in hP2X$_3$ (radius of 1.5 Å). This new gate is too narrow to allow passage of hydrated sodium ions (**Figures 8B,C**) (Mansoor et al., 2016).

ASICs and ENaCs have known pore-blocking molecules such as amiloride, which binds near the extracellular end of the TM2 helices (PDB: 4NTX) (Kleyman and Cragoe, 1988; Baconguis et al., 2014). Considering the structural similarities between ASICs, ENaCs, and P2XRs, it is conceivable that amiloride derivatives or other molecules might also be found to target this region in P2XRs. Deeper areas of the pore, elucidated by cryo-EM, could also prove to be attractive drug targets despite being less accessible to extracellular molecules.

At the cytosolic end of the P2XR pore, the cytoplasmic cap forces the ions to egress laterally through the three cytoplasmic fenestrations (**Figures 7A,C**) (Mansoor et al., 2016). These fenestrations are roughly triangular in shape, with two sides formed by the ends of TM1 and TM2 from adjacent protomers and the third (distal) side formed by part of the cytoplasmic cap. The distal sides of the fenestrations are lined with charged side chains from each of the protomers, providing a favorable path for ions to exit the pore and enter the cell. The residues D340 and K357 form a salt bridge in the cytoplasmic fenestration of hP2X$_3$ (Mansoor et al., 2016). Of note, these two residues are absolutely conserved across human subtypes while there is diversity in the other residues of the fenestrations (**Figures 2**, **7C**). As in the extracellular fenestrations, these conserved charges may be useful in designing drugs to target the cytosolic fenestrations.

The P2XR ion path contains several locations that may prove to be attractive drug targets, including the extracellular and cytoplasmic fenestrations, the extracellular vestibule, and the transmembrane portion of the pore. The existing P2XR structures provide starting points for SBDD. Structures of the other human P2XRs would prove extremely useful in designing ligands that effectively and specifically target the pore.

P2XR CYTOPLASMIC C-TERMINAL DOMAINS

P2XR C-terminal domains are divergent in sequence and size and their impacts on receptor function remain poorly understood. These domains dramatically vary from approximately 3%–34% of total protomer length, corresponding to 12 residues per protomer for hP2X$_4$ and 203 residues per protomer for hP2X$_7$, respectively (**Figure 2**). Unfortunately, the full C-terminal domains were not present in any of the constructs used to obtain crystal structures (Mansoor et al., 2016; Hattori and Gouaux, 2012; Kawate et al., 2009;

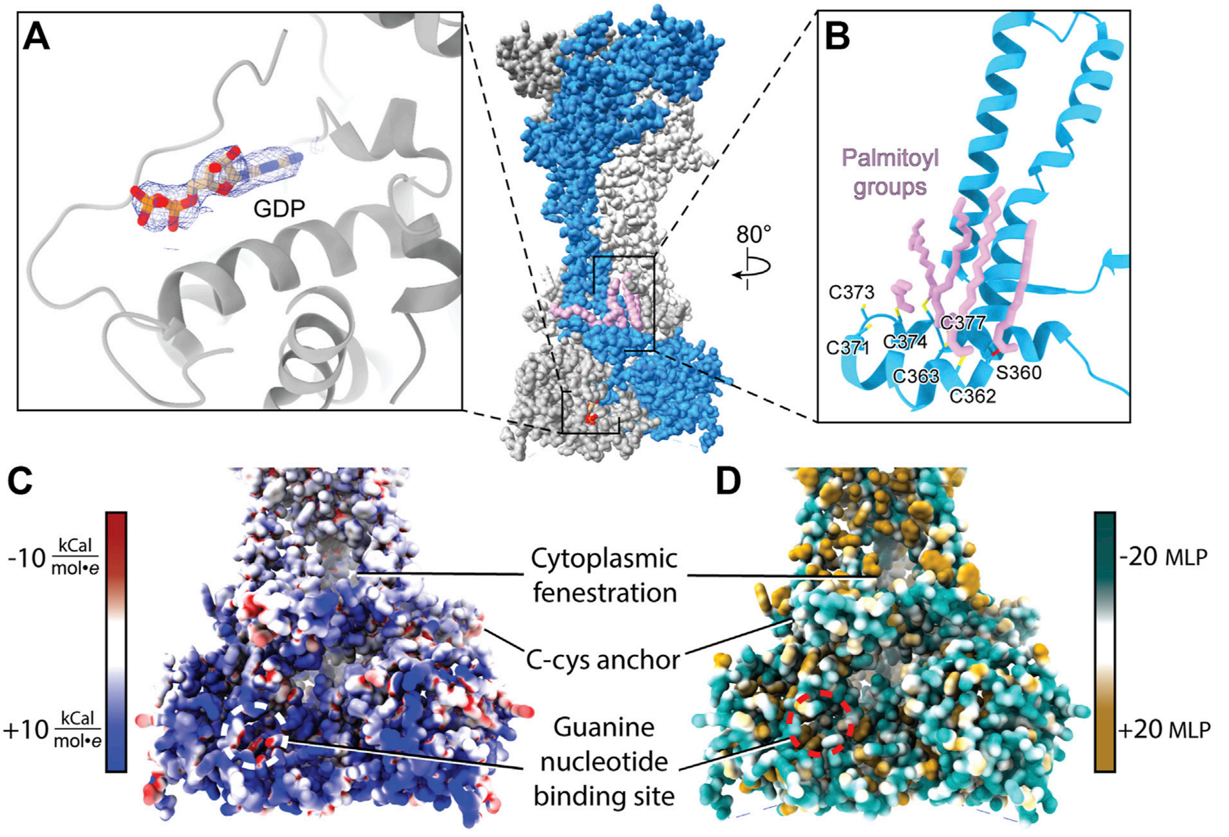

FIGURE 9 | Attributes of the cytoplasmic domain of $rP2X_7$ (PDB: 6U9V). **(A)** GDP bound to the cytoplasmic ballast of $rP2X_7$ with its cryo-EM density shown in blue mesh (EMDB: 20702). **(B)** The C-cys anchor of $rP2X_7$ contains palmitoyl groups (light purple) that extend into the membrane and prevent desensitization. **(C)** Electrostatic surface rendering of the $rP2X_7$ cytoplasmic domain (PDB: 6U9V) with blue and red coloring representing positive and negative electrostatic potential, respectively, highlighting the electropositive nature of the cytoplasmic ballast. **(D)** Hydrophobic surface rendering of the $rP2X_7$ cytoplasmic domain with hydrophobic regions colored brown and hydrophilic regions colored turquoise, each defined by positive and negative molecular lipophilicity potential (MLP), respectively, highlighting the hydrophilic nature of the cytoplasmic ballast (Laguerre et al., 1997). The location of the guanine nucleotide-binding site is outlined in white and red in panel C and in panel D, respectively. The MLP and electrostatic surface potential were calculated in ChimeraX (Pettersen et al., 2021).

Karasawa and Kawate, 2016; Kasuya et al., 2017; Wang et al., 2018). The recent full-length cryo-EM structures of $rP2X_7$ contain the only structurally characterized P2XR cytoplasmic domain beyond the cytoplasmic cap, including the subtype-unique C-cys anchor and cytoplasmic ballast (**Figure 9**) (McCarthy et al., 2019).

Within each protomer of $P2X_7$ is a C-cys anchor which contains six cysteines and one serine that can be palmitoylated (**Figure 9B**). The palmitoyl moieties extend into the inner leaflet of the membrane, preventing the helical recoil movement of TM2 that would otherwise result in channel desensitization (McCarthy et al., 2019). When the C-cys anchor is removed or mutated to prevent palmitoylation, $rP2X_7$ desensitizes similarly to each of the other P2XR subtypes (McCarthy et al., 2019). While the role of the C-cys anchor in the gating cycle has been characterized, details surrounding post-translational modifications to this element remain unclear. For example, it is currently unknown in what stage of folding or trafficking the palmitoyl groups are added, nor which specific palmitoyl acyl transferase (PAT) enzyme or adapter protein is responsible for this post-translational modification. PATs generally target specific substrates and are localized to the ER, the Golgi, the plasma membrane, and endosomes, providing precise spatial regulation to their activity (Charollais and Van Der Goot, 2009). Modifications to the palmitoylation of $P2X_7$ have a dramatic effect on receptor gating and would presumably alter downstream signaling (Allsopp and Evans, 2015). As a result, modulating C-cys anchor palmitoylation poses as an interesting therapeutic avenue to pursue, despite the significant challenges. As with any drug that has an intracellular target, the membrane is a barrier to delivery (Aungst, 1993; Di and Kerns, 2003; Naylor et al., 2018). Given that many other proteins are also palmitoylated, selectively preventing $P2X_7$ palmitoylation would require determining and specifically targeting the correct PAT(s) at the appropriate point in post-translational processing. A greater understanding of the basic biology of $P2X_7$ maturation is necessary before such a pharmacological strategy can be attempted.

The discovery of a nanomolar-affinity guanine nucleotide-binding site in the cytoplasmic ballast of $rP2X_7$, the residues of which are conserved in $hP2X_7$, is quite intriguing (**Figure 9A**). While only GDP is visualized in the apo closed and ATP-bound open state $rP2X_7$

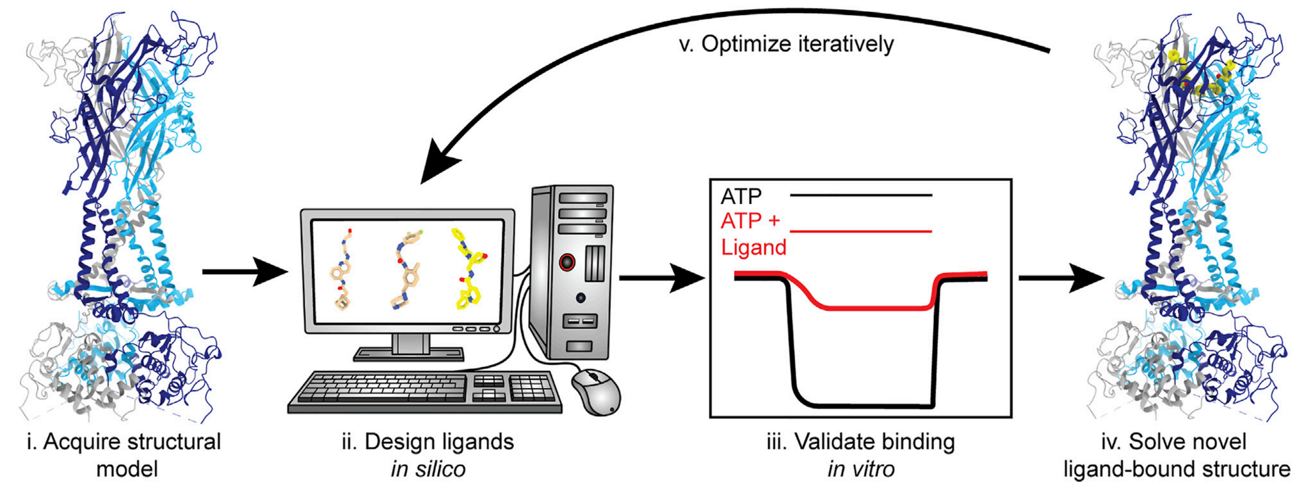

FIGURE 10 | Structure-based drug design (SBDD) workflow using P2XRs as an example. SBDD includes five broad steps. (i) Solve receptor structure to high-resolution or use a reliable theoretical model to identify and define ligand-binding sites; (ii) Use molecular docking and modeling software (*in silico*) to identify and optimize small molecules capable of occupying a binding pocket; (iii) Chemically synthesize the most promising *in silico* "hits" and validate binding and selectivity by biochemical and electrophysiological methods; (iv) Solve the structure of the ligand-bound receptor complex empirically; and (v) Iterate steps (ii–iv) until ligand(s) with satisfactory properties are obtained and fully characterized. Representative structures generated from PDBs: 6U9V (for protein backbone) and 5U1X (for the bound ligand).

structures following purification, both GTP and GDP were shown to bind with equally high affinity (McCarthy et al., 2019). The pose of GDP is such that the ribose and nucleobase are positioned internally and the phosphate tail is on the periphery of the cytoplasmic ballast and easily accessible to the intracellular environment and potential accessory proteins (**Figure 9A**). The guanine nucleotide-binding site is electropositive, hydrophilic, and exposed, making it an accessible docking site for protein-protein interactions (**Figures 9C,D**). It would be interesting if P2X$_7$, like G-protein coupled receptors (GPCRs), has associated guanine nucleotide exchange factors (GEFs) that facilitate GDP release (Cherfils and Zeghouf, 2013). The presence of the cytoplasmic ballast is necessary for the metabotropic properties of P2X$_7$, including the release of cytokines as well as activation of various lipases and kinases (El-Moatassim and Dubyak, 1992; Humphreys and Dubyak, 1996; Surprenant et al., 1996; Wilson et al., 2002; Cheewatrakoolpong et al., 2005; Costa-Junior et al., 2011; Kopp et al., 2019). While there is no direct data regarding a role of the guanine nucleotide-binding site in P2X$_7$ signaling, it is intriguing to imagine the metabotropic signaling properties of the cytoplasmic ballast are dependent on guanine nucleotide binding. If, similar to GPCRs, guanine nucleotide binding proves to be critical for P2X$_7$ signaling, then guanine nucleotide analog ligands (such as abacavir, acyclovir, and entecavir) may be applied to study and therapeutically target P2X$_7$-mediated signaling (Seley-Radtke and Yates, 2018). As with targeting the orthosteric ATP-binding site, targeting intracellular guanine nucleotide-binding sites must be done carefully as GTP and GDP are crucial metabolic and signaling molecules for numerous biological processes. Altogether, cryo-EM facilitated the study of full-length rP2X$_7$ and thus revealed the cytoplasmic domain in its entirety and the therapeutic potential it holds. With the unique cytoplasmic domains of the remaining six P2XRs yet to be structurally characterized, there are more avenues for novel subtype-specific therapeutic development to be discovered.

P2XR STRUCTURAL ELUCIDATION BY CRYO-EM

The recent structures of full-length rP2X$_7$ facilitated key discoveries that were exclusively enabled by cryo-EM. The guanine nucleotide-binding site was identified only after the cryo-EM map revealed an unexplained non-protein density of sufficient quality to accurately predict ligand identity without *a priori* knowledge of its existence (**Figure 9A**) (McCarthy et al., 2019). The identity of the guanine nucleotide was subsequently validated to be GDP by mass spectrometry. The cryo-EM reconstructions similarly revealed the precise location of the palmitoylated residues in the C-cys anchor (including the unexpected palmitoylation of a serine residue), a task that proved to be challenging by other methods (Gonnord et al., 2009). Altogether, the discoveries empowered by cryo-EM have unveiled novel elements that will further our understanding of the biological functions of P2X$_7$.

There remain four homotrimeric P2XR subtypes without published structures: P2X$_1$, P2X$_2$, P2X$_5$, and P2X$_6$. Given that these receptors are implicated in a wide range of physiological and pathophysiological states, it is crucial to understand the molecular pharmacology of each receptor subtype (Burnstock and Kennedy, 2011; North and Jarvis, 2013; Burnstock and Knight, 2018; Lara et al., 2020). Obtaining cryo-EM structures of these receptors will not only reveal their subtype-specific features but also facilitate SBDD to improve ligand selectivity. It is important to note that while homology modeling and machine-learning programs like AlphaFold are improving, there is no replacement for the certainty afforded by empirically determined ligand-bound or protein-protein complexed structures (Jumper et al., 2021). To this point, there are also many known P2XR ligands for which we do not know how (or even where) they bind receptors. These ligands dramatically vary in size, shape, and chemical identity—even between ligands known to be selective for a specific receptor subtype—suggesting there are additional uncharacterized allosteric sites present in P2XRs. Structures of each receptor subtype in complex with these different ligands will help define the molecular pharmacology of P2XRs and confirm the locations of novel allosteric sites.

To date, the published P2XR structures are predominantly of non-human orthologs. While these structures are helpful and enable more accurate homology models, it is known that P2XR orthologs have unique pharmacological features which can significantly impact drug development. For example, human, mouse, and rat $P2X_7$ dramatically differ in response to known allosteric modulators. The negative allosteric modulator AZ11645373 is a high-affinity antagonist for $hP2X_7$, yet is ~100-fold less effective against mouse $P2X_7$ ($mP2X_7$) and >500-fold less effective against $rP2X_7$ (Stokes et al., 2006; Michel et al., 2009). There are also negative allosteric modulators such as A-438079 and A-740003 that antagonize all three of these $P2X_7$ orthologs with similar efficacy (Donnelly-Roberts et al., 2009). Therefore, using cryo-EM to understand the structural basis for the pharmacologic variability across P2XR orthologs is crucial for the development of novel therapeutics that effectively target human P2XRs.

The feasibility of SBDD has dramatically increased with access to more advanced computational tools and the availability of structures for therapeutically relevant membrane proteins, largely due to the cryo-EM resolution revolution (Kuhlbrandt, 2014; Lionta et al., 2014; Lees et al., 2021). With the information gained from the currently published P2XR structures, SBDD can facilitate the discovery of ligands that target this receptor family (**Figure 10**). Molecular docking and *in silico* screening can probe any of the targetable sites within P2XRs for potential "hit" compounds (Ballante et al., 2021). Then, structure-based modeling can be used to optimize chemical groups, adding or substituting different moieties to improve affinity and specificity. Once computationally optimized, a ligand can be synthesized, evaluated *in vitro*, and (if validated) structurally solved in complex with its target receptor to high-resolution. This process will be repeated iteratively until a threshold of affinity and specificity is reached (**Figure 10**). Even though the use of cryo-EM has led to a dramatic number of new structures, the application of SBDD driven by this structural method is still an emerging area of research. Some recent successful cases that exemplify this approach include ligands that specifically target the TRPV5 channel, μ-opioid receptor, and the 80S ribosome (Wong et al., 2017; Hughes et al., 2019; Wang et al., 2022). Cryo-EM is currently the best method to solve ligand-bound P2XR structures and empower the use of SBDD.

CONCLUDING REMARKS

The substantial body of work characterizing P2XR structures has provided invaluable information on the biology and molecular pharmacology for this receptor family, however there remain many unanswered questions. Little is known about the structure and function of P2XR cytoplasmic domains and even less about heterotrimeric P2XRs. While the structural determination of the $P2X_7$ cytoplasmic domain provided valuable insights, unexpected findings raised even more questions about its biological function. Most importantly, we have yet to fully understand how to selectively modulate the seven homotrimeric P2XRs or how effective such modulators would be against heterotrimeric P2XRs, considering their pharmacological complexity. The recent advancements in cryo-EM make this technique ideally suited to study P2XRs, including novel receptor structures and ligand-bound receptor complexes. While P2XRs are implicated in a host of physiological and pathophysiological conditions found within the cardiovascular, central nervous, and immune systems, there are no FDA-approved drugs targeting this receptor family. The success of antiplatelet drugs which antagonize the related P2Y GPCR family exemplifies the therapeutic value of targeting purinergic signaling (Kamran et al., 2021). To this point, there remains substantial untapped therapeutic potential for P2XR modulation. Using the currently published structures as a roadmap, we have discussed the known targetable sites and postulated potential areas for SBDD targeting P2XRs. Continued structural investigation will advance our understanding of P2XR biology and reveal novel approaches for receptor modulation and therapeutic intervention.

AUTHOR CONTRIBUTIONS

SM and AO outlined the manuscript. AO, IK, MG, and JS wrote the manuscript. AO, NL, and MG made the figures. All authors edited the manuscript.

ACKNOWLEDGMENTS

We want to thank David L. Farrens for reading the manuscript and providing constructive feedback.

REFERENCES

Abdulqawi, R., Dockry, R., Holt, K., Layton, G., Mccarthy, B. G., Ford, A. P., et al. (2015). P2x3 Receptor Antagonist (Af-219) in Refractory Chronic Cough: A Randomised, Double-Blind, Placebo-Controlled Phase 2 Study. *Lancet* 385, 1198–1205. doi:10.1016/S0140-6736(14)61255-1

Adinolfi, E., Cirillo, M., Woltersdorf, R., Falzoni, S., Chiozzi, P., Pellegatti, P., et al. (2010). Trophic Activity of A Naturally Occurring Truncated Isoform of the P2x7 Receptor. *Faseb J.* 24, 3393–3404. doi:10.1096/fj.09-153601

Afferent Pharmaceuticals, I. (2015). A Study of Gefapixant (Af-219/Mk-7264) in Participants with Idiopathic Pulmonary Fibrosis (Ipf) with Persistent Cough (Mk-7264-016). Available at: https://Clinicaltrials.Gov/Show/Nct02502097.

Allsopp, R. C., and Evans, R. J. (2015). Contribution of the Juxtatransmembrane Intracellular Regions to the Time Course and Permeation of Atp-Gated P2x7 Receptor Ion Channels. *J. Biol. Chem.* 290, 14556–14566. doi:10.1074/jbc.M115.642033

Antonio, L. S., Stewart, A. P., Varanda, W. A., and Edwardson, J. M. (2014). Identification of P2x2/P2x4/P2x6 Heterotrimeric Receptors Using Atomic Force Microscopy (Afm) Imaging. *Febs Lett.* 588, 2125–2128. doi:10.1016/j.febslet.2014.04.048

Ase, A. R., Therrien, É., and Séguéla, P. (2019). An Allosteric Inhibitory Site Conserved in the Ectodomain of P2x Receptor Channels. *Front. Cell Neurosci.* 13, 121. doi:10.3389/fncel.2019.00121

Aungst, B. J. (1993). Novel Formulation Strategies for Improving Oral Bioavailability of Drugs with Poor Membrane Permeation or Presystemic Metabolism. *J. Pharm. Sci.* 82, 979–987. doi:10.1002/jps.2600821008

Baconguis, I., Bohlen, C. J., Goehring, A., Julius, D., and Gouaux, E. (2014). X-Ray Structure of Acid-Sensing Ion Channel 1-Snake Toxin Complex Reveals Open State of A Na(+)-Selective Channel. *Cell* 156, 717–729. doi:10.1016/j.cell.2014.01.011

Ballante, F., Kooistra, A. J., Kampen, S., De Graaf, C., and Carlsson, J. (2021). Structure-Based Virtual Screening for Ligands of G Protein-Coupled Receptors: What Can Molecular Docking Do for You? *Pharmacol. Rev.* 73, 527–565. doi:10.1124/pharmrev.120.000246

Baroni, M., Pizzirani, C., Pinotti, M., Ferrari, D., Adinolfi, E., Calzavarini, S., et al. (2007). Stimulation of P2 (P2x7) Receptors in Human Dendritic Cells Induces the Release of Tissue Factor-Bearing Microparticles. *Faseb J.* 21, 1926–1933. doi:10.1096/fj.06-7238com

Barton, G. J. (1993). ALSCRIPT: A Tool to Format Multiple Sequence Alignments. *Prot. Eng.* 6 (1), 37–40. doi:10.1093/protein/6.1.37

Batool, M., Ahmad, B., and Choi, S. (2019). A Structure-Based Drug Discovery Paradigm. *Int. J. Mol. Sci.* 20. doi:10.3390/ijms20112783

Bidula, S., Nadzirin, I. B., Cominetti, M., Hickey, H., Cullum, S. A., Searcey, M., et al. (2022). Structural Basis of the Negative Allosteric Modulation of 5-Bdbd at Human P2x4 Receptors. *Mol. Pharmacol.* 101, 33–44. doi:10.1124/molpharm.121.000402

Bidula, S. M., Cromer, B. A., Walpole, S., Angulo, J., and Stokes, L. (2019). Mapping A Novel Positive Allosteric Modulator Binding Site in the Central Vestibule Region of Human P2x7. *Sci. Rep.* 9, 3231. doi:10.1038/s41598-019-39771-5

Bo, X., Jiang, L. H., Wilson, H. L., Kim, M., Burnstock, G., Surprenant, A., et al. (2003). Pharmacological and Biophysical Properties of the Human P2x5 Receptor. *Mol. Pharmacol.* 63, 1407–1416. doi:10.1124/mol.63.6.1407

Bond, C. S., and Schüttelkopf, A. W. (2009). Aline: A Wysiwyg Protein-Sequence Alignment Editor for Publication-Quality Alignments. *Acta Crystallogr. D. Biol. Crystallogr.* 65, 510–512. doi:10.1107/S0907444909007835

Boué-Grabot, E., Archambault, V., and Séguéla, P. (2000). A Protein Kinase C Site Highly Conserved in P2x Subunits Controls the Desensitization Kinetics of P2x(2) Atp-Gated Channels. *J. Biol. Chem.* 275, 10190–10195. doi:10.1074/jbc.275.14.10190

Brake, A. J., Wagenbach, M. J., and Julius, D. (1994). New Structural Motif for Ligand-Gated Ion Channels Defined by an Ionotropic Atp Receptor. *Nature* 371, 519–523. doi:10.1038/371519a0

Brändle, U., Spielmanns, P., Osteroth, R., Sim, J., Surprenant, A., Buell, G., et al. (1997). Desensitization of the P2x(2) Receptor Controlled by Alternative Splicing. *Febs Lett.* 404, 294–298. doi:10.1016/s0014-5793(97)00128-2

Burnstock, G. (1976). Do Some Nerve Cells Release More Than One Transmitter? *Neuroscience* 1, 239–248. doi:10.1016/0306-4522(76)90054-3

Burnstock, G. (2004). Introduction: P2 Receptors. *Curr. Top. Med. Chem.* 4, 793–803. doi:10.2174/1568026043451014

Burnstock, G., and Kennedy, C. (2011). P2x Receptors in Health and Disease. *Adv. Pharmacol.* 61, 333–372. doi:10.1016/B978-0-12-385526-8.00011-4

Burnstock, G. (1972). Purinergic Nerves. *Pharmacol. Rev.* 24, 509–581.

Burnstock, G., and Knight, G. E. (2018). The Potential of P2x7 Receptors as A Therapeutic Target, Including Inflammation and Tumour Progression. *Purinergic Signal.* 14, 1–18. doi:10.1007/s11302-017-9593-0

CCTU-CorePharmaceuticals, J.Cambridgeshire and Peterborough NHS Foundation Trust (2019). Antidepressant Trial with P2x7 Antagonist Jnj-54175446. Available at: https://Clinicaltrials.Gov/Show/Nct04116606.

Changeux, J. P., and Christopoulos, A. (2016). Allosteric Modulation as A Unifying Mechanism for Receptor Function and Regulation. *Cell* 166, 1084–1102. doi:10.1016/j.cell.2016.08.015

Charollais, J., and Van Der Goot, F. G. (2009). Palmitoylation of Membrane Proteins (Review). *Mol. Membr. Biol.* 26, 55–66. doi:10.1080/09687680802620369

Chataigneau, T., Lemoine, D., and Grutter, T. (2013). Exploring the Atp-Binding Site of P2x Receptors. *Front. Cell Neurosci.* 7, 273. doi:10.3389/fncel.2013.00273

Chaumont, S., Jiang, L. H., Penna, A., North, R. A., and Rassendren, F. (2004). Identification of A Trafficking Motif Involved in the Stabilization and Polarization of P2x Receptors. *J. Biol. Chem.* 279, 29628–29638. doi:10.1074/jbc.M403940200

Cheewatrakoolpong, B., Gilchrest, H., Anthes, J. C., and Greenfeder, S. (2005). Identification and Characterization of Splice Variants of the Human P2x7 Atp Channel. *Biochem. Biophys. Res. Commun.* 332, 17–27. doi:10.1016/j.bbrc.2005.04.087

Cherfils, J., and Zeghouf, M. (2013). Regulation of Small Gtpases by Gefs, Gaps, and Gdis. *Physiol. Rev.* 93, 269–309. doi:10.1152/physrev.00003.2012

Coddou, C., Stojilkovic, S. S., and Huidobro-Toro, J. P. (2011). Allosteric Modulation of Atp-Gated P2x Receptor Channels. *Rev. Neurosci.* 22, 335–354. doi:10.1515/RNS.2011.014

Costa-Junior, H. M., Sarmento Vieira, F., and Coutinho-Silva, R. (2011). C Terminus of the P2x7 Receptor: Treasure Hunting. *Purinergic Signal.* 7, 7–19. doi:10.1007/s11302-011-9215-1

Degrève, L., Vechi, S. M., and Junior, C. Q. (1996). The Hydration Structure of the Na+ and K+ Ions and the Selectivity of Their Ionic Channels. *Biochimica Biophysica Acta (Bba) - Bioenergetics* 1274, 149–156.

Di, L., and Kerns, E. H. (2003). Profiling Drug-like Properties in Discovery Research. *Curr. Opin. Chem. Biol.* 7, 402–408. doi:10.1016/s1367-5931(03)00055-3

Donnelly-Roberts, D. L., Namovic, M. T., Han, P., and Jarvis, M. F. (2009). Mammalian P2x7 Receptor Pharmacology: Comparison of Recombinant Mouse, Rat and Human P2x7 Receptors. *Br. J. Pharmacol.* 157, 1203–1214. doi:10.1111/j.1476-5381.2009.00233.x

Duckwitz, W., Hausmann, R., Aschrafi, A., and Schmalzing, G. (2006). P2x5 Subunit Assembly Requires Scaffolding by the Second Transmembrane Domain and A Conserved Aspartate. *J. Biol. Chem.* 281, 39561–39572. doi:10.1074/jbc.M606113200

El-Moatassim, C., and Dubyak, G. R. (1992). A Novel Pathway for the Activation of Phospholipase D by P2z Purinergic Receptors in Bac1.2f5 Macrophages. *J. Biol. Chem.* 267, 23664–23673. doi:10.1016/s0021-9258(18)35890-3

Ferrari, S., Costi, P. M., and Wade, R. C. (2003). Inhibitor Specificity via Protein Dynamics: Insights from the Design of Antibacterial Agents Targeted against Thymidylate Synthase. *Chem. Biol.* 10, 1183–1193. doi:10.1016/j.chembiol.2003.11.012

Flores, J. A., Haddad, B. G., Dolan, K. A., Myers, J. B., Yoshioka, C. C., Copperman, J., et al. (2020). Connexin-46/50 in a Dynamic Lipid Environment Resolved by CryoEM at 1.9 Å. *Nat. Commun.* 11, 4331. doi:10.1038/s41467-020-18120-5

Ford, A. P., Dillon, M. P., Kitt, M. M., and Gever, J. R. (2021). The Discovery and Development of Gefapixant. *Auton. Neurosci.* 235, 102859. doi:10.1016/j.autneu.2021.102859

Francistiová, L., Bianchi, C., Di Lauro, C., Sebastián-Serrano, Á., de Diego-García, L., Kobolák, J., et al. (2020). The Role of P2x7 Receptor in Alzheimer's Disease. *Front. Mol. Neurosci.* 13, 94. doi:10.3389/fnmol.2020.00094

Friel, D. D., and Bean, B. P. (1988). Two Atp-Activated Conductances in Bullfrog Atrial Cells. *J. Gen. Physiol.* 91, 1–27. doi:10.1085/jgp.91.1.1

Furlan-Freguia, C., Marchese, P., Gruber, A., Ruggeri, Z. M., and Ruf, W. (2011). P2x7 Receptor Signaling Contributes to Tissue Factor-dependent Thrombosis in Mice. *J. Clin. Invest.* 121, 2932–2944. doi:10.1172/JCI46129

Garcia-Guzman, M., Soto, F., Gomez-Hernandez, J. M., Lund, P. E., and Stühmer, W. (1997). Characterization of Recombinant Human P2x4 Receptor Reveals Pharmacological Differences to the Rat Homologue. *Mol. Pharmacol.* 51, 109–118. doi:10.1124/mol.51.1.109

Gonnord, P., Delarasse, C., Auger, R., Benihoud, K., Prigent, M., Cuif, M. H., et al. (2009). Palmitoylation of the P2x7 Receptor, an Atp-Gated Channel, Controls its Expression and Association with Lipid Rafts. *Faseb J.* 23, 795–805. doi:10.1096/fj.08-114637

Hattori, M., and Gouaux, E. (2012). Molecular Mechanism of Atp Binding and Ion Channel Activation in P2x Receptors. *Nature* 485, 207–212. doi:10.1038/nature11010

Hausmann, R., Bahrenberg, G., Kuhlmann, D., Schumacher, M., Braam, U., Bieler, D., et al. (2014). A Hydrophobic Residue in Position 15 of the Rp2x3 Receptor Slows Desensitization and Reveals Properties Beneficial for Pharmacological

Analysis and High-Throughput Screening. *Neuropharmacology* 79, 603–615. doi:10.1016/j.neuropharm.2014.01.010

Hughes, T. E., Del Rosario, J. S., Kapoor, A., Yazici, A. T., Yudin, Y., Fluck, E. C., 3rd, et al. (2019). Structure-Based Characterization of Novel Trpv5 Inhibitors. *Elife* 8. doi:10.7554/eLife.49572

Humphreys, B. D., and Dubyak, G. R. (1996). Induction of the P2z/P2x7 Nucleotide Receptor and Associated Phospholipase D Activity by Lipopolysaccharide and Ifn-Gamma in the Human Thp-1 Monocytic Cell Line. *J. Immunol.* 157, 5627–5637.

Illes, P., Müller, C. E., Jacobson, K. A., Grutter, T., Nicke, A., Fountain, S. J., et al. (2021). Update of P2x Receptor Properties and Their Pharmacology: Iuphar Review 30. *Br. J. Pharmacol.* 178, 489–514. doi:10.1111/bph.15299

Jarvis, M. F., and Khakh, B. S. (2009). Atp-Gated P2x Cation-Channels. *Neuropharmacology* 56, 208–215. doi:10.1016/j.neuropharm.2008.06.067

Jasti, J., Furukawa, H., Gonzales, E. B., and Gouaux, E. (2007). Structure of Acid-Sensing Ion Channel 1 at 1.9 A Resolution and Low Ph. *Nature* 449, 316–323. doi:10.1038/nature06163

Jiang, R., Taly, A., Lemoine, D., Martz, A., Cunrath, O., and Grutter, T. (2012). Tightening of the Atp-Binding Sites Induces the Opening of P2x Receptor Channels. *Embo J.* 31, 2134–2143. doi:10.1038/emboj.2012.75

Jumper, J., Evans, R., Pritzel, A., Green, T., Figurnov, M., Ronneberger, O., et al. (2021). Highly Accurate Protein Structure Prediction with Alphafold. *Nature* 596, 583–589. doi:10.1038/s41586-021-03819-2

Kamei, J., Takahashi, Y., Yoshikawa, Y., and Saitoh, A. (2005). Involvement of P2x Receptor Subtypes in Atp-Induced Enhancement of the Cough Reflex Sensitivity. *Eur. J. Pharmacol.* 528, 158–161. doi:10.1016/j.ejphar.2005.10.030

Kamran, H., Jneid, H., Kayani, W. T., Virani, S. S., Levine, G. N., Nambi, V., et al. (2021). Oral Antiplatelet Therapy after Acute Coronary Syndrome: A Review. *Jama* 325, 1545–1555. doi:10.1001/jama.2021.0716

Karasawa, A., and Kawate, T. (2016). Structural Basis for Subtype-specific Inhibition of the P2x7 Receptor. *Elife* 5. doi:10.7554/eLife.22153

Kasuya, G., Fujiwara, Y., Takemoto, M., Dohmae, N., Nakada-Nakura, Y., Ishitani, R., et al. (2016). Structural Insights into Divalent Cation Modulations of Atp-Gated P2x Receptor Channels. *Cell Rep.* 14, 932–944. doi:10.1016/j.celrep.2015.12.087

Kasuya, G., Yamaura, T., Ma, X. B., Nakamura, R., Takemoto, M., Nagumo, H., et al. (2017). Structural Insights into the Competitive Inhibition of the Atp-Gated P2x Receptor Channel. *Nat. Commun.* 8, 876. doi:10.1038/s41467-017-00887-9

Kawate, T., Michel, J. C., Birdsong, W. T., and Gouaux, E. (2009). Crystal Structure of the Atp-Gated P2x(4) Ion Channel in the Closed State. *Nature* 460, 592–598. doi:10.1038/nature08198

Kawate, T. (2017). P2x Receptor Activation. *Adv. Exp. Med. Biol.* 1051, 55–69. doi:10.1007/5584_2017_55

Keystone, E. C., Wang, M. M., Layton, M., Hollis, S., Mcinnes, I. B., and Team, D. C. S. (2012). Clinical Evaluation of the Efficacy of the P2x7 Purinergic Receptor Antagonist Azd9056 on the Signs and Symptoms of Rheumatoid Arthritis in Patients with Active Disease Despite Treatment with Methotrexate or Sulphasalazine. *Ann. Rheum. Dis.* 71, 1630–1635. doi:10.1136/annrheumdis-2011-143578

King, B. F., Townsend-Nicholson, A., Wildman, S. S., Thomas, T., Spyer, K. M., and Burnstock, G. (2000). Coexpression of Rat P2x2 and P2x6 Subunits in Xenopus Oocytes. *J. Neurosci.* 20, 4871–4877. doi:10.1523/jneurosci.20-13-04871.2000

Kleyman, T. R., and Cragoe, E. J., Jr. (1988). Amiloride and its Analogs as Tools in the Study of Ion Transport. *J. Membr. Biol.* 105, 1–21. doi:10.1007/BF01871102

Kopp, R., Krautloher, A., Ramírez-Fernández, A., and Nicke, A. (2019). P2x7 Interactions and Signaling - Making Head or Tail of it. *Front. Mol. Neurosci.* 12, 183. doi:10.3389/fnmol.2019.00183

Koshimizu, T., Koshimizu, M., and Stojilkovic, S. S. (1999). Contributions of the C-Terminal Domain to the Control of P2x Receptor Desensitization. *J. Biol. Chem.* 274, 37651–37657. doi:10.1074/jbc.274.53.37651

Kotnis, S., Bingham, B., Vasilyev, D. V., Miller, S. W., Bai, Y., Yeola, S., et al. (2010). Genetic and Functional Analysis of Human P2x5 Reveals A Distinct Pattern of Exon 10 Polymorphism with Predominant Expression of the Nonfunctional Receptor Isoform. *Mol. Pharmacol.* 77, 953–960. doi:10.1124/mol.110.063636

Kühlbrandt, W. (2014). Biochemistry. The Resolution Revolution. *Science* 343, 1443–1444. doi:10.1126/science.1251652

Laguerre, M., Saux, M., Dubost, J., and Carpy, A. (1997). Mlpp: A Progarm for the Calculation of Molecular Lipophilicity Potential in Proteins. *Pharm. Pharmacol. Commun.* 3 (5-6), 217–222.

Lara, R., Adinolfi, E., Harwood, C. A., Philpott, M., Barden, J. A., Di Virgilio, F., et al. (2020). P2x7 in Cancer: From Molecular Mechanisms to Therapeutics. *Front. Pharmacol.* 11, 793. doi:10.3389/fphar.2020.00793

Lê, K. T., Babinski, K., and Séguéla, P. (1998). Central P2x4 and P2x6 Channel Subunits Coassemble into A Novel Heteromeric Atp Receptor. *J. Neurosci.* 18, 7152–7159. doi:10.1523/jneurosci.18-18-07152.1998

Lê, K. T., Paquet, M., Nouel, D., Babinski, K., and Séguéla, P. (1997). Primary Structure and Expression of A Naturally Truncated Human P2x Atp Receptor Subunit from Brain and Immune System. *Febs Lett.* 418, 195–199. doi:10.1016/s0014-5793(97)01380-x

Lees, J. A., Dias, J. M., and Han, S. (2021). Applications of Cryo-Em in Small Molecule and Biologics Drug Design. *Biochem. Soc. Trans.* 49, 2627–2638. doi:10.1042/BST20210444

Lewis, C., Neidhart, S., Holy, C., North, R. A., Buell, G., and Surprenant, A. (1995). Coexpression of P2x2 and P2x3 Receptor Subunits Can Account for Atp-Gated Currents in Sensory Neurons. *Nature* 377, 432–435. doi:10.1038/377432a0

Li, M., Kawate, T., Silberberg, S. D., and Swartz, K. J. (2010). Pore-Opening Mechanism in Trimeric P2x Receptor Channels. *Nat. Commun.* 1, 44. doi:10.1038/ncomms1048

Li, M., Silberberg, S. D., and Swartz, K. J. (2013). Subtype-Specific Control of P2x Receptor Channel Signaling by Atp and Mg2+. *Proc. Natl. Acad. Sci. U. S. A.* 110, E3455–E3463. doi:10.1073/pnas.1308088110

Li, M., Wang, Y., Banerjee, R., Marinelli, F., Silberberg, S., Faraldo-Gómez, J. D., et al. (2019). Molecular Mechanisms of Human P2x3 Receptor Channel Activation and Modulation by Divalent Cation Bound Atp. *Elife* 8. doi:10.7554/eLife.47060

Lionta, E., Spyrou, G., Vassilatis, D. K., and Cournia, Z. (2014). Structure-Based Virtual Screening for Drug Discovery: Principles, Applications and Recent Advances. *Curr. Top. Med. Chem.* 14, 1923–1938. doi:10.2174/1568026614666140929124445

Londos, C., Cooper, D. M., and Wolff, J. (1980). Subclasses of External Adenosine Receptors. *Proc. Natl. Acad. Sci. U. S. A.* 77, 2551–2554. doi:10.1073/pnas.77.5.2551

Mahaut-Smith, M. P., Jones, S., and Evans, R. J. (2011). The P2x1 Receptor and Platelet Function. *Purinergic Signal* 7, 341–356. doi:10.1007/s11302-011-9224-0

Mansoor, S. E., Lü, W., Oosterheert, W., Shekhar, M., Tajkhorshid, E., and Gouaux, E. (2016). X-Ray Structures Define Human P2x(3) Receptor Gating Cycle and Antagonist Action. *Nature* 538, 66–71. doi:10.1038/nature19367

Mansoor, S. E. (2022). "How Structural Biology Has Directly Impacted Our Understanding of P2x Receptor Function and Gating," in *The* P2x7 Receptor. Editor A. Nicke. 1 Ed. (New York: Humana). in Press.

McCarthy, A. E., Yoshioka, C., and Mansoor, S. E. (2019). Full-Length P2x7 Structures Reveal How Palmitoylation Prevents Channel Desensitization. *Cell* 179, 659–e13. doi:10.1016/j.cell.2019.09.017

Michel, A. D., Ng, S. W., Roman, S., Clay, W. C., Dean, D. K., and Walter, D. S. (2009). Mechanism of Action of Species-Selective P2x(7) Receptor Antagonists. *Br. J. Pharmacol.* 156, 1312–1325. doi:10.1111/j.1476-5381.2009.00135.x

Müller, C. E. (2015). Medicinal Chemistry of P2x Receptors: Allosteric Modulators. *Curr. Med. Chem.* 22, 929–941. doi:10.2174/0929867322666141210155610

Müller, C. E., and Namasivayam, V. (2021). Recommended Tool Compounds and Drugs for Blocking P2x and P2y Receptors. *Purinergic Signal* 17, 633–648. doi:10.1007/s11302-021-09813-7

Murrell-Lagnado, R. D., and Qureshi, O. S. (2008). Assembly and Trafficking of P2x Purinergic Receptors (Review). *Mol. Membr. Biol.* 25, 321–331. doi:10.1080/09687680802050385

Nakane, T., Kotecha, A., Sente, A., Mcmullan, G., Masiulis, S., Brown, P. M. G. E., et al. (2020). Single-Particle Cryo-Em at Atomic Resolution. *Nature* 587, 152–156. doi:10.1038/s41586-020-2829-0

Naylor, M. R., Ly, A. M., Handford, M. J., Ramos, D. P., Pye, C. R., Furukawa, A., et al. (2018). Lipophilic Permeability Efficiency Reconciles the Opposing Roles of Lipophilicity in Membrane Permeability and Aqueous Solubility. *J. Med. Chem.* 61, 11169–11182. doi:10.1021/acs.jmedchem.8b01259

Nelson, A. L., Dhimolea, E., and Reichert, J. M. (2010). Development Trends for Human Monoclonal Antibody Therapeutics. *Nat. Rev. Drug Discov.* 9, 767–774. doi:10.1038/nrd3229

Noreng, S., Bharadwaj, A., Posert, R., Yoshioka, C., and Baconguis, I. (2018). Structure of the Human Epithelial Sodium Channel by Cryo-Electron Microscopy. *Elife* 7. doi:10.7554/eLife.39340

North, R. A., and Jarvis, M. F. (2013). P2x Receptors as Drug Targets. *Mol. Pharmacol.* 83, 759–769. doi:10.1124/mol.112.083758

North, R. A. (2002). Molecular Physiology of P2x Receptors. *Physiol. Rev.* 82, 1013–1067. doi:10.1152/physrev.00015.2002

Nussinov, R., and Tsai, C. J. (2012). The Different Ways through Which Specificity Works in Orthosteric and Allosteric Drugs. *Curr. Pharm. Des.* 18, 1311–1316. doi:10.2174/138161212799436377

Obrecht, A. S., Urban, N., Schaefer, M., Röse, A., Kless, A., Meents, J. E., et al. (2019). Identification of Aurintricarboxylic Acid as A Potent Allosteric Antagonist of P2x1 and P2x3 Receptors. *Neuropharmacology* 158, 107749. doi:10.1016/j.neuropharm.2019.107749

Pettersen, E. F., Goddard, T. D., Huang, C. C., Meng, E. C., Couch, G. S., Croll, T. I., et al. (2021). Ucsf Chimerax: Structure Visualization for Researchers, Educators, and Developers. *Protein Sci.* 30, 70–82. doi:10.1002/pro.3943

Pfizer (2008). Study of Ce-224,535 A Twice Daily Pill to Control Rheumatoid Arthritis in Patients Who Have Not Totally Improved with Methotrexate. Available at: https://Clinicaltrials.Gov/Show/Nct00628095.

Rahman, M. M., Teng, J., Worrell, B. T., Noviello, C. M., Lee, M., Karlin, A., et al. (2020). Structure of the Native Muscle-type Nicotinic Receptor and Inhibition by Snake Venom Toxins. *Neuron* 106, 952–e5. doi:10.1016/j.neuron.2020.03.012

Richards, D., Gever, J. R., Ford, A. P., and Fountain, S. J. (2019). Action of Mk-7264 (Gefapixant) at Human P2x3 and P2x2/3 Receptors and *In Vivo* Efficacy in Models of Sensitisation. *Br. J. Pharmacol.* 176, 2279–2291. doi:10.1111/bph.14677

Roman, R. M., and Fitz, J. G. (1999). Emerging Roles of Purinergic Signaling in Gastrointestinal Epithelial Secretion and Hepatobiliary Function. *Gastroenterology* 116, 964–979. doi:10.1016/s0016-5085(99)70081-8

Samways, D. S., Khakh, B. S., Dutertre, S., and Egan, T. M. (2011). Preferential Use of Unobstructed Lateral Portals as the Access Route to the Pore of Human Atp-Gated Ion Channels (P2x Receptors). *Proc. Natl. Acad. Sci. U. S. A.* 108, 13800–13805. doi:10.1073/pnas.1017550108

Samways, D. S., Li, Z., and Egan, T. M. (2014). Principles and Properties of Ion Flow in P2x Receptors. *Front. Cell Neurosci.* 8, 6. doi:10.3389/fncel.2014.00006

Sattler, C., and Benndorf, K. (2022). Enlightening Activation Gating in P2x Receptors. *Purinergic Signal.* doi:10.1007/s11302-022-09850-w

Seley-Radtke, K. L., and Yates, M. K. (2018). The Evolution of Nucleoside Analogue Antivirals: A Review for Chemists and Non-chemists. Part 1: Early Structural Modifications to the Nucleoside Scaffold. *Antivir. Res.* 154, 66–86. doi:10.1016/j.antiviral.2018.04.004

Sievers, F., and Higgins, D. G. (2018). Clustal Omega for Making Accurate Alignments of Many Protein Sequences. *Protein Sci.* 27, 135–145. doi:10.1002/pro.3290

Smart, O. S., Neduvelil, J. G., Wang, X., Wallace, B. A., and Sansom, M. S. (1996). Hole: A Program for the Analysis of the Pore Dimensions of Ion Channel Structural Models. *J. Mol. Graph* 14, 354376–376. doi:10.1016/s0263-7855(97)00009-x

Soto, F., Garcia-Guzman, M., Karschin, C., and Stühmer, W. (1996). Cloning and Tissue Distribution of A Novel P2x Receptor from Rat Brain. *Biochem. Biophys. Res. Commun.* 223, 456–460. doi:10.1006/bbrc.1996.0915

Stank, A., Kokh, D. B., Fuller, J. C., and Wade, R. C. (2016). Protein Binding Pocket Dynamics. *Acc. Chem. Res.* 49, 809–815. doi:10.1021/acs.accounts.5b00516

Stokes, L., Jiang, L. H., Alcaraz, L., Bent, J., Bowers, K., Fagura, M., et al. (2006). Characterization of A Selective and Potent Antagonist of Human P2x(7) Receptors, Az11645373. *Br. J. Pharmacol.* 149, 880–887. doi:10.1038/sj.bjp.0706933

Su, C. C., Lyu, M., Morgan, C. E., Bolla, J. R., Robinson, C. V., and Yu, E. W. (2021). A 'Build and Retrieve' Methodology to Simultaneously Solve Cryo-Em Structures of Membrane Proteins. *Nat. Methods* 18, 69–75. doi:10.1038/s41592-020-01021-2

Surprenant, A., Rassendren, F., Kawashima, E., North, R. A., and Buell, G. (1996). The Cytolytic P2z Receptor for Extracellular Atp Identified as A P2x Receptor (P2x7). *Science* 272, 735–738. doi:10.1126/science.272.5262.735

Taylor, A. L., Schwiebert, L. M., Smith, J. J., King, C., Jones, J. R., Sorscher, E. J., et al. (1999). Epithelial P2x Purinergic Receptor Channel Expression and Function. *J. Clin. Invest.* 104, 875–884. doi:10.1172/JCI7270

Tian, W., Chen, C., Lei, X., Zhao, J., and Liang, J. (2018). Castp 3.0: Computed Atlas of Surface Topography of Proteins. *Nucleic Acids Res.* 46, W363–W367. doi:10.1093/nar/gky473

Valera, S., Hussy, N., Evans, R. J., Adami, N., North, R. A., Surprenant, A., et al. (1994). A New Class of Ligand-Gated Ion Channel Defined by P2x Receptor for Extracellular Atp. *Nature* 371, 516–519. doi:10.1038/371516a0

van Calker, D., Müller, M., and Hamprecht, B. (1979). Adenosine Regulates via Two Different Types of Receptors, the Accumulation of Cyclic Amp in Cultured Brain Cells. *J. Neurochem.* 33, 999–1005. doi:10.1111/j.1471-4159.1979.tb05236.x

Virginio, C., Church, D., North, R. A., and Surprenant, A. (1997). Effects of Divalent Cations, Protons and Calmidazolium at the Rat P2x7 Receptor. *Neuropharmacology* 36, 1285–1294. doi:10.1016/s0028-3908(97)00141-x

Virginio, C., Robertson, G., Surprenant, A., and North, R. A. (1998). Trinitrophenyl-Substituted Nucleotides Are Potent Antagonists Selective for P2x1, P2x3, and Heteromeric P2x2/3 Receptors. *Mol. Pharmacol.* 53, 969–973.

Wang, H., Hetzer, F., Huang, W., Qu, Q., Meyerowitz, J., Kaindl, J., et al. (2022). Structure-Based Evolution of G Protein-Biased μ-Opioid Receptor Agonists. *Angew. Chem. Int. Ed. Engl.* 6, E202200269. doi:10.1002/anie.202200269

Wang, J., Sun, L. F., Cui, W. W., Zhao, W. S., Ma, X. F., Li, B., et al. (2017). Intersubunit Physical Couplings Fostered by the Left Flipper Domain Facilitate Channel Opening of P2x4 Receptors. *J. Biol. Chem.* 292, 7619–7635. doi:10.1074/jbc.M116.771121

Wang, J., Wang, Y., Cui, W. W., Huang, Y., Yang, Y., Liu, Y., et al. (2018). Druggable Negative Allosteric Site of P2x3 Receptors. *Proc. Natl. Acad. Sci. U. S. A.* 115, 4939–4944. doi:10.1073/pnas.1800907115

Webb, T. E., Simon, J., Krishek, B. J., Bateson, A. N., Smart, T. G., King, B. F., et al. (1993). Cloning and Functional Expression of A Brain G-Protein-Coupled Atp Receptor. *Febs Lett.* 324, 219–225. doi:10.1016/0014-5793(93)81397-i

Wenthur, C. J., Gentry, P. R., Mathews, T. P., and Lindsley, C. W. (2014). Drugs for Allosteric Sites on Receptors. *Annu. Rev. Pharmacol. Toxicol.* 54, 165–184. doi:10.1146/annurev-pharmtox-010611-134525

Werner, P., Seward, E. P., Buell, G. N., and North, R. A. (1996). Domains of P2x Receptors Involved in Desensitization. *Proc. Natl. Acad. Sci. U. S. A.* 93, 15485–15490. doi:10.1073/pnas.93.26.15485

Wilson, H. L., Wilson, S. A., Surprenant, A., and North, R. A. (2002). Epithelial Membrane Proteins Induce Membrane Blebbing and Interact with the P2x7 Receptor C Terminus. *J. Biol. Chem.* 277, 34017–34023. doi:10.1074/jbc.M205120200

Wolf, C., Rosefort, C., Fallah, G., Kassack, M. U., Hamacher, A., Bodnar, M., et al. (2011). Molecular Determinants of Potent P2x2 Antagonism Identified by Functional Analysis, Mutagenesis, and Homology Docking. *Mol. Pharmacol.* 79, 649–661. doi:10.1124/mol.110.068700

Wong, W., Bai, X. C., Sleebs, B. E., Triglia, T., Brown, A., Thompson, J. K., et al. (2017). Mefloquine Targets the Plasmodium Falciparum 80s Ribosome to Inhibit Protein Synthesis. *Nat. Microbiol.* 2, 17031. doi:10.1038/nmicrobiol.2017.31

Yan, D., Zhu, Y., Walsh, T., Xie, D., Yuan, H., Sirmaci, A., et al. (2013). Mutation of the Atp-Gated P2x(2) Receptor Leads to Progressive Hearing Loss and Increased Susceptibility to Noise. *Proc. Natl. Acad. Sci. U. S. A.* 110, 2228–2233. doi:10.1073/pnas.1222285110

Zhao, W. S., Wang, J., Ma, X. J., Yang, Y., Liu, Y., Huang, L. D., et al. (2014). Relative Motions between Left Flipper and Dorsal Fin Domains Favour P2x4 Receptor Activation. *Nat. Commun.* 5, 4189. doi:10.1038/ncomms5189

Zhao, Y., Chen, X., He, C., Gao, G., Chen, Z., and Du, J. (2021). Discovery of Bilirubin as Novel P2x7r Antagonist with Anti-tumor Activity. *Bioorg Med. Chem. Lett.* 51, 128361. doi:10.1016/j.bmcl.2021.128361

Zhou, J., and Rossi, J. (2017). Aptamers as Targeted Therapeutics: Current Potential and Challenges. *Nat. Rev. Drug Discov.* 16, 440–202. doi:10.1038/nrd.2017.86

Conflict of Interest: The authors declare that the research was conducted in the absence of any commercial or financial relationships that could be construed as a potential conflict of interest.

ORIGINAL RESEARCH
published: 21 June 2022
doi: 10.3389/fphar.2022.898670

Differential Activation of TRPM8 by the Stereoisomers of Menthol

Xiaoying Chen[1], *Lizhen Xu*[1], *Heng Zhang*[1], *Han Wen*[2] *and Fan Yang*[1,3]*

[1]Department of Biophysics, Kidney Disease Center of the First Affiliated Hospital, Zhejiang University School of Medicine, Hangzhou, China, [2]DP Technology, Beijing, China, [3]Alibaba-Zhejiang University Joint Research Center of Future Digital Healthcare, Hangzhou, China

The stereoisomers of menthol elicit cooling sensation to various levels. Though the high-resolution three-dimensional structures of the menthol receptor, the transient receptor potential melastatin 8 (TRPM8) ion channels, have been revolved in different states, the menthol-bound state structure is not determined and how the stereoisomers of menthol interact with TRPM8 remains largely elusive. Taking advantage of the identical atom composition but distinct spatial orientation of chemical groups in menthol stereoisomers, we performed thermodynamic mutant cycle analysis (TMCA) with patch-clamp recordings to probe the interaction between these ligands and TRPM8. By comparing (–)-menthol with (+)-neoisomenthol or (+)-neomenthol, we observed that the isopropyl or hydroxyl group in menthol interacts with the S4 or S3 helix in TRPM8, respectively. These interactions were also corroborated in our molecular docking of the stereoisomers, though the predicted structural details in the interactions of these ligands with TRPM8 residues are different. Therefore, we suggest similar molecular mechanisms of TRPM8 activation by the stereoisomers of menthol, while the binding configuration of an individual stereoisomer is varied.

Keywords: menthol, stereoisomers, TRPM8, electrophysiology, gating

Edited by:
Shujia Zhu,
Institute of Neuroscience, Shanghai Institute for Biological Sciences (CAS), China

Reviewed by:
Wuyang Wang,
Xuzhou Medical University, China
Horacio Poblete,
University of Talca, Chile

****Correspondence:***
Fan Yang
fanyanga@zju.edu.cn

Specialty section:
This article was submitted to Pharmacology of Ion Channels and Channelopathies, a section of the journal Frontiers in Pharmacology

Received: *17 March 2022*
Accepted: *09 May 2022*
Published: *21 June 2022*

Citation:
Chen X, Xu L, Zhang H, Wen H and Yang F (2022) Differential Activation of TRPM8 by the Stereoisomers of Menthol. Front. Pharmacol. 13:898670. doi: 10.3389/fphar.2022.898670

INTRODUCTION

Menthol in mint is known to elicit a cool sensation. As a terpenoid alcohol, there are three chiral centers within the menthol molecule, leading to eight possible stereoisomers. Among these stereoisomers, the (−)-menthol, which is the most abundant in nature, also exhibits the lowest cooling thresholds in human taste dilution studies (Hopp, 1993; Barel et al., 2009). Some of the other stereoisomers, such as (+)-neoisomenthol, are less intense in cooling sensation with much higher cooling thresholds. As the stereoisomers of menthol are identical in the number, types, and connectivity of atoms, how they could differentially activate their receptor in humans, the transient receptor potential melastatin 8 (TRPM8) ion channel (McKemy et al., 2002; Peier et al., 2002), to cause differences in cooling sensation remains to be explored.

To investigate the menthol-TRPM8 interactions, functional studies such as thermodynamic mutant cycle analysis (TMCA) with patch-clamp recordings are critical. Though several high-resolution three-dimensional structures of TRPM8 have been resolved by cryo-electron microscopy (cryo-EM) (Yin et al., 2018; Diver et al., 2019; Yin et al., 2019), none of the menthol stereoisomers has been directly observed to be complexed with the channel protein. To probe how menthol binds to TRPM8, by combining molecular docking and TMCA, our previous study showed that (−)-menthol binds to the cytosol-facing cavity formed by the S1–S4 in TRPM8, using its hydroxyl and isopropyl groups as "hand" and "legs," respectively, to grab and stand on TRPM8 (Xu et al., 2020). TMCA has been successfully applied to reveal the interaction between ion channels and peptide toxins (Ranganathan et al., 1996; Yang et al., 2017) and small molecules (Yang et al., 2015; Xu et al., 2020). A prerequisite for TMCA is that the perturbation introduced to the ligand should not be too large to alter the overall binding configuration of the ligand. Therefore, as the stereoisomers of menthol differ only in the orientation of hydroxyl and/or isopropyl groups, we expect that they are suited for TMCA to probe the ligand-protein interaction in TRPM8.

Moreover, because the TRPM8 channel is a polymodal activated by a plethora of stimuli, ligand–protein interactions are also modulated by these stimuli (Zheng, 2013). For instance, membrane depolarization also directly opens this channel. Previous work has demonstrated that the charged residue R842 on the S4 of TRPM8 contributes to the total gating charge in voltage activation (Voets et al., 2007), so as R842 and other residues of the S1–S4 constitute the (−)-menthol-binding pocket (Xu et al., 2020), and transmembrane voltage is expected to alter menthol-TRPM8 interactions. Therefore, in this study to reveal the mechanisms of TRPM8 activation by the menthol stereoisomers, we systematically investigated their interactions by performing TMCA with patch-clamp recordings at either hyperpolarization or depolarization voltages.

MATERIALS AND METHODS

Molecular Biology and Cell Transfection

Murine TRPM8 was used in this study. Mouse TRPM8 channel was used in this study as mouse and human TRPM8 channels are highly conserved in sequence. Specifically, in the S1 to S4 domains where the menthol stereoisomers are bound, the sequence identity is 96.1% (**Supplementary Figure S1A**). Point mutations were made by Fast Mutagenesis Kit V2 (SBS Genetech). Primers were used to generate point mutations. All mutations were confirmed by sequencing.

HEK293T cells were cultured in Dulbecco's modified eagle medium supplemented (DMEM) with 10% fetal bovine serum and 1% penicillin-streptomycin solution at 37°C with 5% CO_2. When cells grow up to 60%–70%, plasmids were transfected with lipofectamine 2000 following the manufacturer's protocol. Patch-clamp recordings were performed 18–24 h after transfection.

Chemicals

(−)-menthol (CAS: 2216-51-5) was purchased from BBI Life Sciences; (+)-menthol (CAS: 15356-60-2) and (+)-neomenthol (CAS: 2216-52-6) were purchased from TCI; (+)-isomenthol (CAS: 23283-97-8) was purchased from Phytolab, and (+)-neoisomenthol (CAS: 20752-34-5) was purchased from Toronto Research Chemicals.

Electrophysiology

Patch-clamp recordings were performed using a HEKA EPC10 amplifier driven by PatchMaster software (HEKA). Patch pipettes were prepared from borosilicate glass and fire-polished to a resistance of 4–6MΩ. A solution (pH 7.25) containing 130 mM NaCl, 0.2 mM EDTA, and 3 mM HEPES was used in both bath and pipette for recording. For whole-cell recording, cells were detached by trypsin and plated on the microscope cover glass for 30–60 min before the experiment. Transfected cells could be identified by green fluorescence. Cells were clamped at +80 mV and −80 mV for 350 ms, respectively, during recording, and the average current in the last 40 ms was performed. All recordings were performed at room temperature (~25°C).

To perfuse (−)-menthol and other isomers during the patch-clamp recording, a rapid solution changer with a gravity-driven perfusion system was used (RSC-200, Bio-Logic). Each solution was delivered through a separate tube, so there was no mixing of solutions. The pipette tip was placed right in front of the perfusion outlet during recording to ensure the solution exchange was complete.

Data Analysis

Data from whole-cell recordings were analyzed in Igor Pro (WaveMatrix). EC_{50} values were derived from fitting a Hill equation to the concentration–response relationship. Changes in EC_{50} by point mutation may be caused by either perturbation of ligand binding or channel gating or both. To distinguish these possibilities, the dissociation constant (K_d) for ligand binding is estimated assuming the following gating scheme:

$$C_0 \overset{K_d}{\leftrightarrow} C_1 \overset{L}{\leftrightarrow} O,$$

where L is the equilibrium constant for the final closed-to-open transition.

The P_o of mouse TRPM8 activated by (−)-menthol was measured through single-channel recordings as in our previous study (Xu et al., 2020), and P_o of TRPM8 mutant channels activated by (−)-menthol was estimated from noise analysis through whole-cell recordings. The mean current amplitude (I), the squared deviations in current amplitude from the mean value (σ^2), and the single-channel current (i) were measured experimentally from a membrane patch of ion channels. Then, the number of ion channels clamped into that patch (N) is determined as

$$N = \frac{I^2}{i \cdot I - \sigma^2}.$$

The maximum current when each of the ion channel is at the open state with a P_o of 1 is equal to $i \times N$. Then, the open probability was calculated as the ratio between the measured macroscopic current and the maximum current calculated by noise analysis.

For TRPM8 activation by other stereoisomers, $P_{o\ max}$ was measured from the concentration–response curve and L was determined from $P_{o\ max}$ by $L = P_{o\ max}/(1 - P_{o\ max})$. Both K_d and L contribute to the measured apparent affinity by the equation $EC_{50} = K_d/(1 + L)$.

To perform thermodynamic cycle analysis, K_d values of four channel–ligand combinations (WT channel, menthol: K_d _1; Mutant channel, menthol: K_d _2; WT channel, menthol analog: K_d _3; Mutant channel, menthol analog: K_d _4) were determined separately. The strength of coupling was determined by the coupling energy (kT multiplied by $Ln\Omega$, where k is the Boltzmann constant and T is the temperature in Kelvin). $Ln\Omega$ is calculated by the following equation:

$$\mathrm{Ln}\Omega = \mathrm{Ln}\left(\frac{K_d\text{-}1 \cdot K_d\text{-}4}{K_d\text{-}2 \cdot K_d\text{-}3}\right).$$

Molecular Docking

The RosettaLigand application (Meiler and Baker, 2006; Davis and Baker, 2009; Davis et al., 2009) from Rosetta program suite version 2019.12 was used to dock ligand to TRPM8. TRP domain is important for ligand gating in TRPM8 as revealed by a previous study (Xu et al., 2020), so this domain is included in our docking experiments. For docking of stereoisomers, the TRPM8 model (PDB ID: 6BPQ) was first relaxed in the membrane environment using the RosettaMembrane application (Yarov-Yarovoy et al., 2006a; Yarov-Yarovoy et al., 2006b; Yarov-Yarovoy et al., 2012), and the model with lowest energy score was chosen for docking of menthol stereoisomers. Menthol stereoisomer conformers were generated using the FROG2 (Miteva et al., 2010) (http://mobyle.rpbs.univ-paris-diderot.fr/cgi-bin/portal.py#forms::Frog2) server before docking.

As menthol stereoisomers bind to the transmembrane region of TRPM8, the molecular docking approach must consider the energetic effects of the lipid membrane. The membrane environment was set up using the RosettaMembrane energy function (Yarov-Yarovoy et al., 2006a; Yarov-Yarovoy et al., 2006b; Yarov-Yarovoy et al., 2012) in an XML style script in RosettaScripts (Fleishman et al., 2011) (**Supplementary Methods**). The script also allowed us to control the details of docking. A total of 10,000 models were generated for a docking trial of each ligand. To determine the best docking model, these models were first screened with the total energy score (Rosetta energy term name: *score*). Top 1,000 models with the lowest total energy score were selected. They were further scored with the binding energy between menthol stereoisomers and the channel. Binding energy was calculated as the difference in total energy between the menthol-bounded state and the corresponding apo state models. The top 10 models with the lowest binding energy (*interface_delta_X*) were identified as the candidates. The hydrogen bond between menthol stereoisomers and TRPM8 was determined by UCSF Chimera software. The distance of hydrogen bond was measured between the O1 atom in menthol stereoisomers and the hydrogen atom in the sidechain of R842.

Molecular Dynamic Simulation

Starting from the transmembrane domain (residue ID 733-977) of the modeled closed-state structure, we used the Membrane Builder function (Jo et al., 2007; Jo et al., 2009; Wu et al., 2014) of the CHARMM-GUI web server (Jo et al., 2008; Lee et al., 2016) to embed the protein in a bilayer of 1-palmitoyl-2-oleoyl phosphatidylcholine (POPC) lipids surrounded by a box of water and ions (with a 15-A° buffer of water/lipids extending from the protein in each direction). The system has a dimension of 110 Å × 110 Å × 85 Å and contains a total of ~93400 atoms, including 15873 water molecules and 219 POPC molecules. To ensure 0.15 M ionic concentration and zero net charge, 54 K^+ and 42 Cl^- ions were added. A menthol-bound system was built following the same settings except one menthol molecule was docked to each subunit as previously described. After energy minimization, six steps of equilibration were performed (with gradually reduced harmonic restraints applied to protein, lipids, water, and ions). Finally, we conducted production MD runs in the NPT ensemble. The Nosé–Hoover method (Nosé, 1984; Hoover, 1985) was used with a temperature of T = 30°C. The Parrinello–Rahman method (Parrinello and Rahman, 1981) was used for pressure coupling. For nonbonded interactions, a 10- A° switching distance and a 12-A° cutoff distance were used. The particle mesh Ewald method (Darden et al., 1993) was used for electrostatics calculations. The LINCS algorithm (Hess et al., 1997) was used to constrain the hydrogen-containing bond lengths, which allowed a 2-fs time step for MD simulation. The energy minimization and MD simulation were performed with the GROMACS program (Pronk et al., 2013) version 5.1.1-gpu using the CHARMM36 force field (Klauda et al., 2010; Huang and MacKerell, 2013) and the TIP3P water model (Jorgensen et al., 1983). The parameters for the menthol molecules were generated with the CHARMM General Force Field (Vanommeslaeghe et al., 2010).

RESULTS

Differential Activation of TRPM8 by the Stereoisomers

We first measured TRPM8 activation by the five commercially available menthol stereoisomers with whole-cell patch-clamp recordings (**Figures 1A–E**). TRP channels, including TRPM8, are polymodal receptors activated by ligands, depolarization, or temperature. Therefore, when we performed patch-clamp recordings, we kept the recording temperature (~25°C) and clamping voltage (±80 mV) constant, so that only the concentration of ligand (menthol stereoisomers) was changed. Moreover, at 25°C and −80 mV, the TRPM8 channel was barely activated if no menthol was perfused (**Supplementary Figure S1B**). Though at 25°C and +80 mV, we observed a small current in the absence of menthol, perfusion of menthol elicited a much larger current. Therefore, the changes in current we measured from patch-clamp recordings were indeed caused by channel activation by menthol stereoisomers but not by other stimuli.

We observed that while all these stereoisomers activated TRPM8 current in a concentration–dependent manner, current activation was differentially modulated by transmembrane voltage. At +80 mV, the maximum current amplitudes induced by the stereoisomers normalized to that of (−)-menthol were similar except for (+)-neomenthol (**Figure 1F**). Their concentration-dependent curves were also shifted to higher concentrations as compared to that of (−)-menthol, but the changes in EC_{50} values were less than ten-fold (**Figure 1G**). EC_{50} of (−)-menthol and (+)-neomenthol was 62.64 ± 1.2 μM and 206.22 ± 11.4 μM, respectively) (**Figure 1G**).

To quantify the ligand–protein interactions, we employed the simple gating scheme (**Figure 1H**) that successfully described the

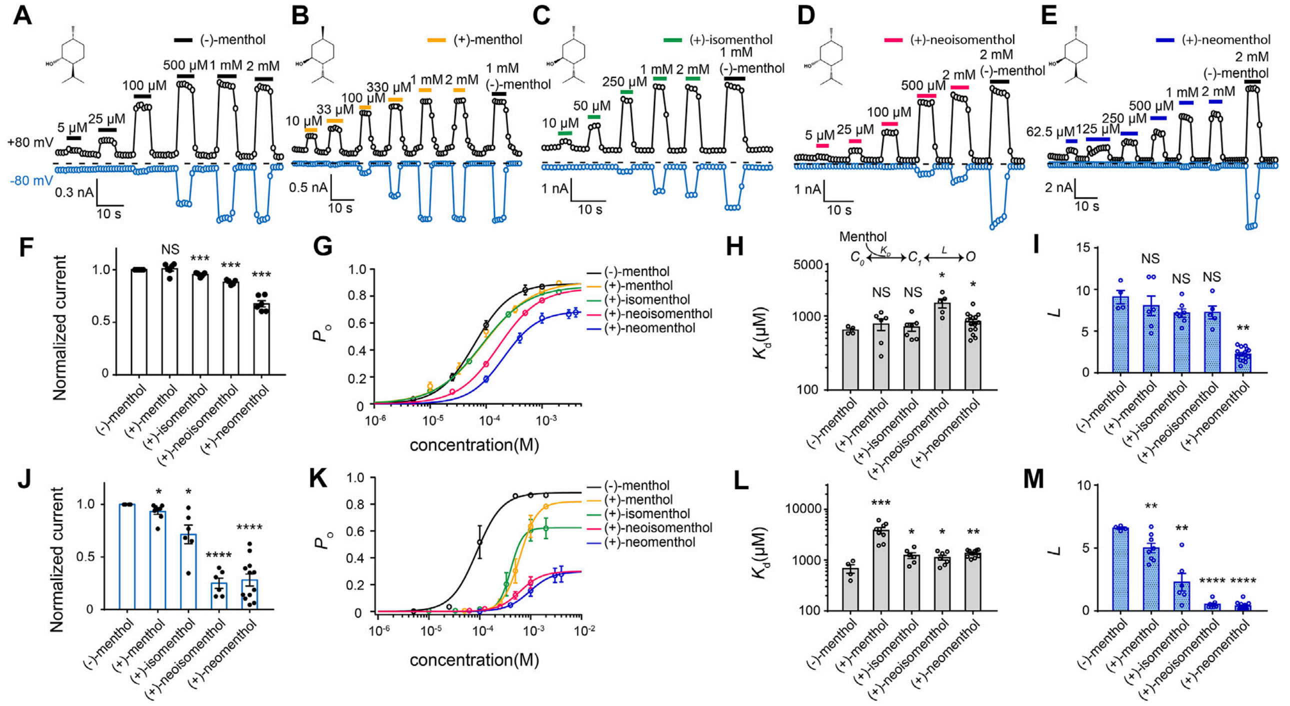

FIGURE 1 | Differential activation of mouse TRPM8 by menthol stereoisomers. **(A–E)** Representative whole-cell recordings of mouse TRPM8 activated by different menthol stereoisomers in a concentration-dependent manner. The chemical structures of menthol stereoisomers are shown on upper left. **(F)** Bar graph of normalized currents induced by menthol stereoisomers at +80 mV from HEK293T cells transfected with mouse TRPM8 recorded in whole-cell configuration (n = 4–7 for each isomer, two-sided t-test, $^{*}p < 0.05$; $^{**}p < 0.01$; $^{***}p < 0.001$; $^{****}p < 0.0001$; NS, not statistically significant). Stereoisomers invoked max current amplitudes that were normalized to the response to 2 mM (–)-menthol. **(G)** Concentration–response curve of menthol stereoisomers activation measured from whole-cell patch-clamp recordings at +80 mV (n = 4–7). **(H,I)** General gating scheme where the ligand binding is represented by K_d, and the equilibrium constant between the closed and open states upon ligand binding is represented by L. For different stereoisomers, K_d and L values were calculated from concentration–response curves in **(G)** (n = 4–7, two-sided t-test, $^{*}p < 0.05$; $^{**}p < 0.01$; $^{***}p < 0.001$; $^{****}p < 0.0001$; NS, not statistically significant). All statistical data are given as mean ± s.e.m. **(J)** Bar graph of normalized currents induced by menthol stereoisomers from HEK293T cells transfected with mouse TRPM8 recorded in whole-cell configuration (n = 4–7 for each isomer, two-sided t-test, $^{*}p < 0.05$; $^{**}p < 0.01$; $^{***}p < 0.001$; $^{****}p < 0.0001$; NS, not statistically significant). Stereoisomers invoked max current amplitudes that were normalized to the response to 2 mM (–)-menthol. **(K)** Concentration–response curve of menthol stereoisomers activation measured from whole-cell patch-clamp recordings at –80 mV (n = 4–7, two-sided t-test, $^{*}p < 0.05$; $^{**}p < 0.01$; $^{***}p < 0.001$; $^{****}p < 0.0001$; NS, not statistically significant). **(L,M)** At –80 mV, K_d and L values of different stereoisomers were calculated from concentration–response curves in **(K)**. All statistical data are given as mean ± s.e.m.

(−)-menthol and capsaicin binding and activation of TRPM8 (Xu et al., 2020) and TRPV1 (Yang et al., 2015), respectively. In this scheme, K_d and L reflect the binding affinity and gating capability of the ligand, respectively. These parameters were determined from EC50 values and the maximum open probability (P_o_max) (see Methods for details). As we have measured the P_o_max of wild-type TRPM8 activated by (−)-menthol with single-channel recordings (Xu et al., 2020), we normalized the current amplitude induced by a stereoisomer to that of (−)-menthol to calculate the P_o_max of this ligand. In this way, we calculated the K_d and L values of the stereoisomers based on their concentration-dependent curves (**Figures 1H,I**). Surprisingly, the K_d values of all stereoisomers were similar, except that (+)-neoisomenthol and (+)-neomenthol exhibited a slightly decreased affinity (**Figure 1H**). Only the L value of (+)-neomenthols was significantly reduced as compared to that of (−)-menthol (**Figure 1I**).

In contrast, at −80 mV, the maximum current activated by (+)-neoisomenthol and (+)-neomenthol was much reduced (**Figure 1J**), with their concentration–dependence curves largely shifted to higher concentrations (**Figure 1K**). As a result, the K_d values of stereoisomers were slightly but significantly increased, while their L values were much reduced (**Figures 1L, M**). The increase in K_d for (+)-menthol at −80 mV is more apparent as compared to the increase in other stereoisomers. We reason that such an increase in K_d for (+)-menthol is due to the relatively large P_o_max (therefore the smaller decrease in L value) induced by (+)-menthol at −80 mV (**Figure 1K**, lines in yellow and black, respectively). These observations clearly suggest that the less intense cooling sensation and higher cooling thresholds of the stereoisomers (Barel et al., 2009), such as (+)-neoisomenthol as compared to (−)-menthol, are due to both reduced binding affinity and ability in opening TRPM8 channel, especially at the more physiologically relevant −80 mV. Moreover, the further decreased gating capability (L values) of the stereoisomers at −80 mV as compared to those measured at +80 mV (**Figures 1I, M**, respectively) indicated that the ligand–protein interactions were modulated by transmembrane voltage.

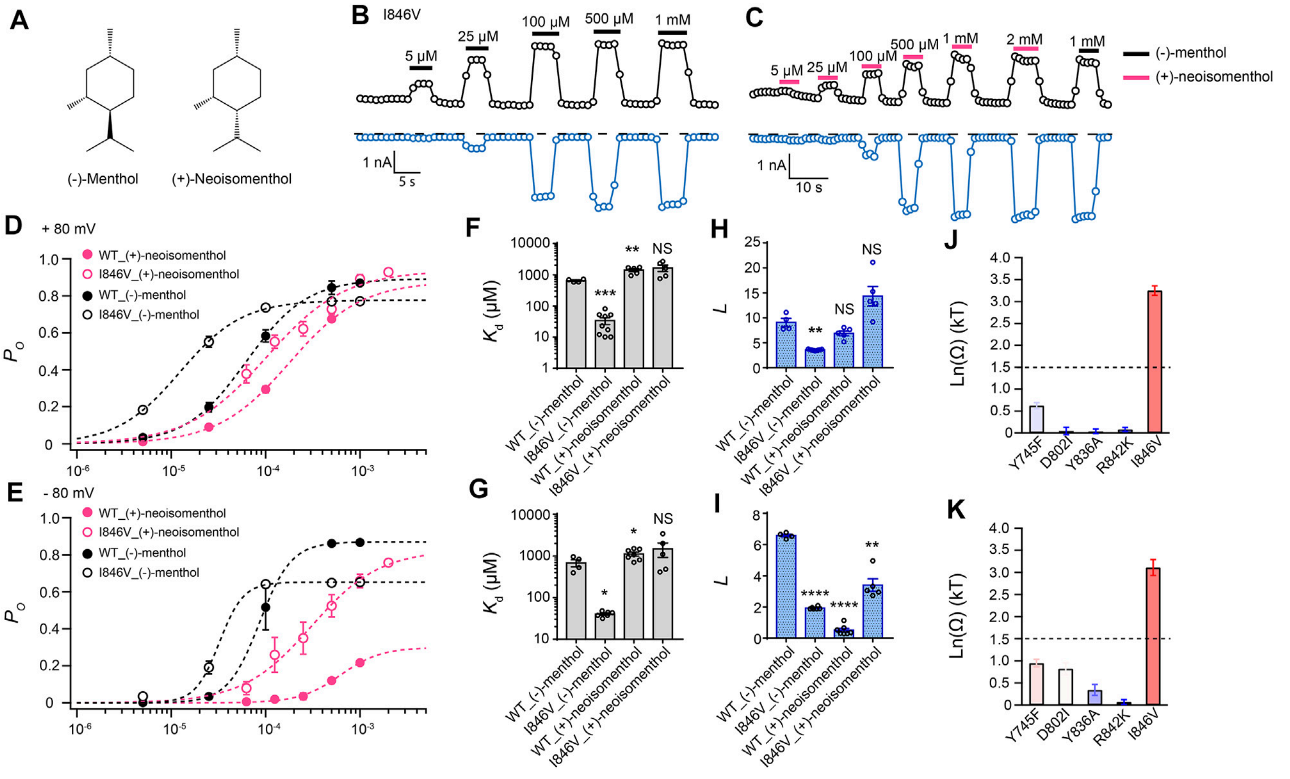

FIGURE 2 | Differential interactions between mouse TRPM8 and (–)-menthol or (+)-neoisomenthol revealed by TMCA. **(A)** Comparison of chemical structures of (–)-menthol and (+)-neoisomenthol is shown. **(B)** Representative whole-cell recordings of the I846V mutant channel activated by (–)-menthol in a concentration-dependent manner. **(C)** Representative whole-cell recordings of the I846V mutant channel by (+)-neoisomenthol in a concentration-dependent manner. **(D)** Concentration–response curves of wild type and mutant such as I846V with either (-)-menthol or (+)-neoisomenthol activation were measured from whole-cell patch-clamp recordings at +80 mV ($n = 5$–9). **(F)** and **(H)** For wild type and I846V channel, K_d and L values at +80mV were calculated from the concentration–response curves in **(D)** (two-sided *t*-test, $^*p < 0.05$; $^{**}p < 0.01$; $^{***}p < 0.001$; $^{****}p < 0.0001$; NS, not statistically significant). **(J)** Summary of coupling energy measurements at +80 mV. Coupling energy was calculated from the K_d values. Mutants showing a coupling energy larger than 1.5 kT (dashed line) were colored in red. Those with less energy were colored in different shades of blue. At least four independent trials were performed for each chemical at each concentration. **(E)** Concentration–response curves of wild type and mutant such as I846V with either (–)-menthol or (+)-neoisomenthol activation were measured from whole-cell patch-clamp recordings at –80 mV ($n = 5$–9). **(G)** and **(I)** For wild type and I846V channel, K_d and L values at -80 mV were calculated from the concentration–response curves in **(E)** (two-sided *t*-test, $^*p < 0.05$; $^{**}p < 0.01$; $^{***}p < 0.001$; $^{****}p < 0.0001$; NS, not statistically significant). **(K)** Summary of coupling energy measurements at -80 mV. Coupling energy was calculated from the K_d values. Mutants showing a coupling energy larger than 1.5 kT (dashed line) were colored in red. Those with less energy were colored in different shades of blue. At least four independent trials were performed for each chemical at each concentration.

Interactions Between TRPM8 and the Stereoisomers Revealed by TMCA

To understand the origin of the differential activation of TRPM8 by the stereoisomers, we performed TMCA with patch-clamp recordings. Previously, we have employed this strategy to study the binding of (–)-menthol by replacing its hydroxyl group with an oxygen atom (the menthol analog menthone) or its isopropyl group with a methylethenyl group (the menthol analog isopulegol) (Xu et al., 2020). However, by using the menthol analogs, the chemical identity of a functional group in menthol was altered. To keep the chemical identity of functional groups and introduce perturbation of the chemical structure of menthol for TMCA, we employed the stereoisomers of menthol.

By comparing (–)-menthol and (+)-neoisomenthol (**Figure 2A**), we observed that they are only different in the orientation of the isopropyl group, while the special orientations of hydroxyl and methyl groups are identical. So these two stereoisomers are well-suited for probing the interaction between the isopropyl group and channel protein. By further measuring current activation by either (–)-menthol or (+)-neoisomenthol in WT TRPM8 and mutants like the I846V at ± 80 mV (**Figures 2B,C**), we first established the concentration dependence of channel open probability at either +80 mV or –80 mV (**Figures 2D,E**), and then calculated the corresponding K_d (**Figures 2F,G**) and L (**Figures 2H,I**) values of the stereoisomers based on their concentration–dependence curves. We further calculated the coupling energy of different mutants and observed that there is a large coupling (**Figures 2J,K**. 3.25 ± 0.11 kT and 3.10 ± 0.18 kT for +80 mV and – 80 mV, respectively) between the isopropyl group of menthol stereoisomers and residue I846 in the S4 of TRPM8. This is consistent with our previous findings that the isopropyl group of (-)-menthol interacts with L843 and I846 in TRPM8 (Xu et al.,

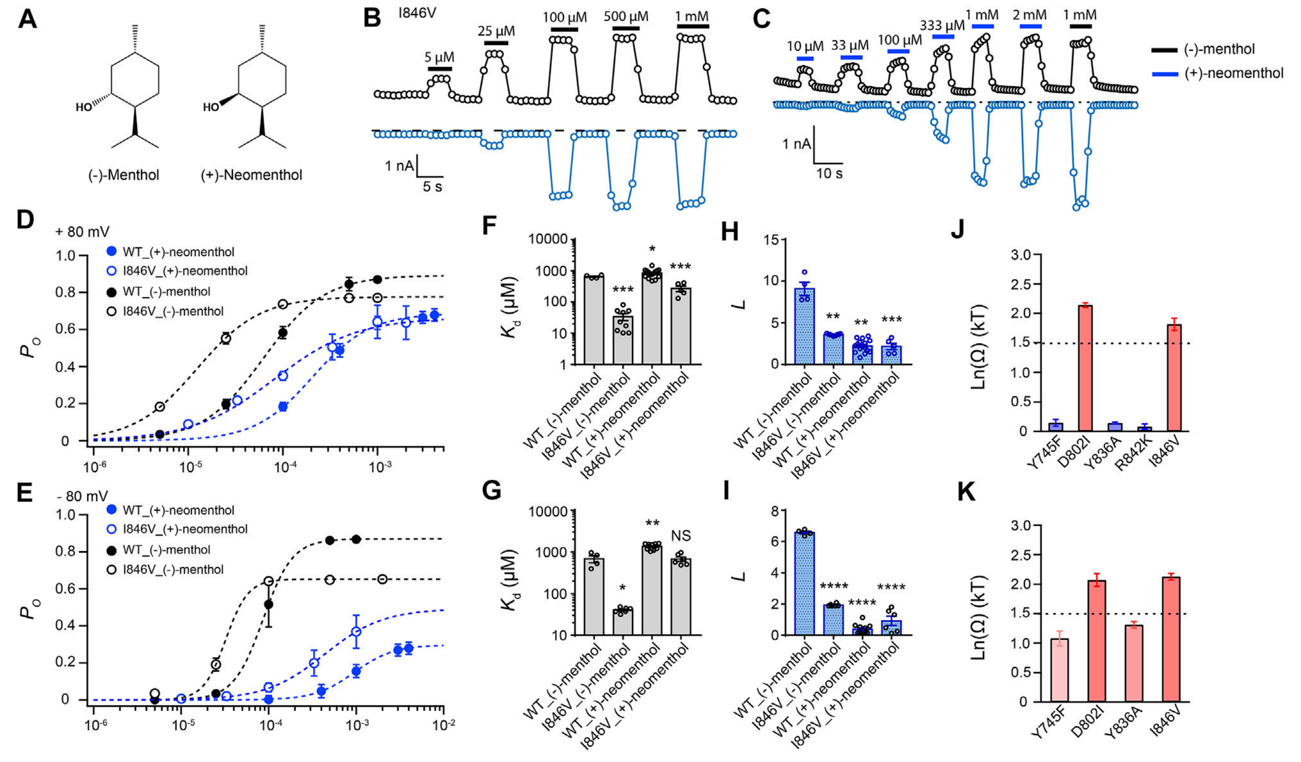

FIGURE 3 | Differential interactions between mouse TRPM8 and (–)-menthol or (+)-neomenthol revealed by TMCA. **(A)** Comparison of chemical structures of (–)-menthol and (+)-neomenthol is shown. **(B)** Representative whole-cell recordings of the I846V mutant channel activated by (–)-menthol in a concentration-dependent manner. **(C)** Representative whole-cell recordings of the I846V mutant channel activated by (+)-neomenthol in a concentration-dependent manner. **(D)** Concentration–response curves of wild type and mutant such as I846V with either (–)-menthol or (+)-neomenthol activation were measured from whole-cell patch-clamp recordings at +80 mV ($n = 5$–9). **(F)** and **(H)** For wild type and I846V channel, K_d and L at +80 mV values were calculated from the concentration–response curves in **(D)** (two-sided t-test, $^*p < 0.05$; $^{**}p < 0.01$; $^{***}p < 0.001$; $^{****}p < 0.0001$; NS, not statistically significant). **(J)** Summary of coupling energy measurements at +80 mV. Coupling energy was calculated from the K_d values. Mutants showing a coupling energy larger than 1.5 kT (dashed line) were colored in red. Those with less energy were colored in different shades of blue. At least four independent trials were performed for each chemical at each concentration. **(E)** Concentration–response curves of wild type and mutant such as I846V with either (–)-menthol or (+)-neomenthol activation were measured from whole-cell patch-clamp recordings at –80 mV ($n = 5$–9). **(G)** and **(I)** For wild type and I846V channel, K_d and L values at -80 mV were calculated from the concentration–response curves in **(E)** (two-sided t-test, $^*p < 0.05$; $^{**}p < 0.01$; $^{***}p < 0.001$; $^{****}p < 0.0001$; NS, not statistically significant). **(K)** Summary of coupling energy measurements at –80 mV. Coupling energy was calculated from the K_d values. Mutants showing a coupling energy larger than 1.5 kT (dashed line) were colored in red. Those with less energy were colored in different shades of blue. At least four independent trials were performed for each chemical at each concentration.

2020). Moreover, the coupling energy values measured at either +80 mV or –80 mV were similarly large, indicating that though the S4 serves as, at least partially, a voltage sensor in TRPM8 channel (Voets et al., 2007), the interaction between the isopropyl group and TRPM8 is not affected by the transmembrane potential.

To investigate the interaction between the hydroxyl group of the stereoisomers and TRPM8, we measured current activation by either (–)-menthol or (+)-neomenthol in WT TRPM8 and mutants like the I846V at ± 80 mV (**Figures 3A–C**), as only the hydroxyl group in these two stereoisomers differs in spatial orientation. We also determined the concentration dependence of channel open probability at either +80 mV or –80 mV (**Figures 3D,E**), and then calculated the corresponding K_d (**Figures 3F,G**) and L (**Figures 3H,I**) values of the stereoisomers based on their concentration–dependence curves. We further calculated the coupling energy of different mutants and observed that there is a large coupling (**Figures 3J,K.** 1.81 ± 0.10 kT and 2.12 ± 0.06 kT for +80 mV and –80 mV, respectively) between the hydroxyl group of menthol stereoisomers and residue D802 in the S3 of TRPM8. We also found that at -80 mV, (+)-neomenthol cannot activate the R842K mutant, preventing the determination of coupling energy at this residue. Our previous study detected large coupling energy between the hydroxyl group of (–)-menthol and D802 or R842 in TRPM8 by using the menthol analog menthone in TMCA (Xu et al., 2020), which is consistent with our observations.

Interestingly, we observed that the coupling energy at I846 was also larger than the 1.5 kT threshold, indicating that the orientation of the hydroxyl group may also affect how the isopropyl group interacts with the channel protein.

Putative Binding Configurations of the Stereoisomers Suggested by Docking

As the menthol-bound state of TRPM8 has not been directly revealed by cryo-EM despite the fact that several TRPM8

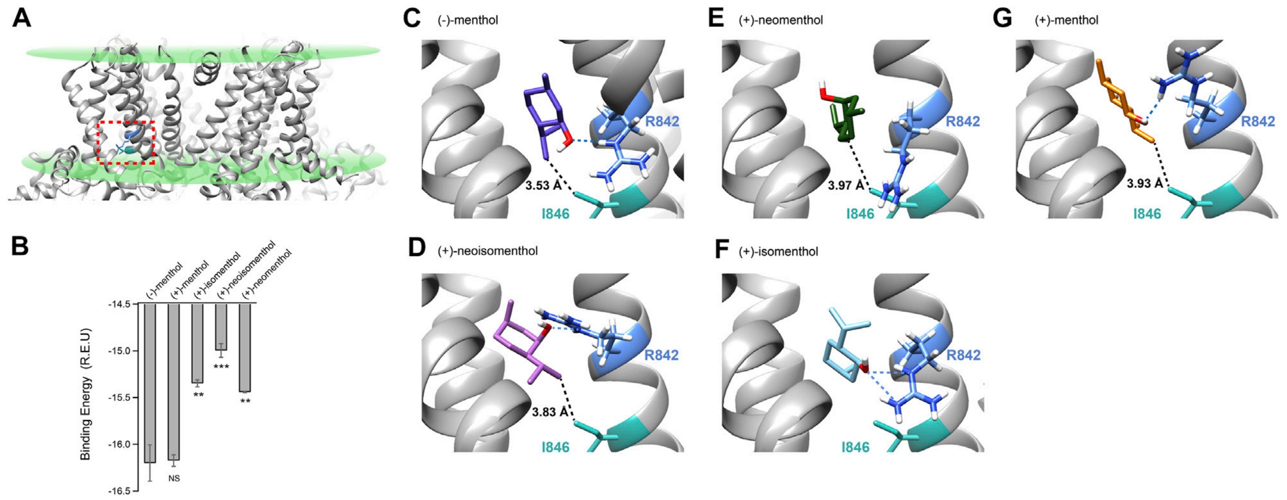

FIGURE 4 | Molecular docking suggested that menthol stereoisomers activated mouse TRPM8 in different binding configurations. **(A)** Putative menthol-binding pocket located within the transmembrane domains of the TRPM8 channel as revealed by cryo-EM in apo state (PDB ID: 6BPQ). R842 and I846 are highlighted in blue and green, respectively. **(B)** Menthol stereoisomers were docked into the binding pocket. Averaged binding energy of the top ten binding models of each stereoisomer was measured. All statistical data are given as mean ± s.e.m. ($n = 10$, two-sided t-test, $^{*}p < 0.05$; $^{**}p < 0.01$; $^{***}p < 0.001$; $^{****}p < 0.0001$; NS, not statistically significant). **(C–G)** Docking of menthol stereoisomers into the binding pocket. The hydroxyl group of stereoisomers was predicted to form a hydrogen bond with sidechain R842 (dashed line in blue), and the distance of the isopropyl group with sidechain I846 is shown with dashed lines in black.

structures have been reported (Yin et al., 2018; Diver et al., 2019; Yin et al., 2019), we employed molecular docking in the Rosetta suite (Leaver-Fay et al., 2011) to investigate the possible binding configurations of menthol stereoisomer. We computationally docked (−)-menthol, (+)-neoisomenthol, (+)-neomenthol, or (+)-isomenthol into the pocket formed by the S1 to S4 transmembrane helices in the apo state of TRPM8 (**Figures 4A,B**, dashed box in red, PDB ID: 6BPQ) because this site has been validated as the menthol binding pocket in previous studies (Bandell et al., 2006; Xu et al., 2020). We then performed a statistical analysis of the docking models by plotting their binding energy against the rmsd of the best scoring models (**Supplementary Figures S1C–G**). The docking models exhibited a funnel-shaped distribution of binding energy, supporting the validity of the docking results. Moreover, we performed cluster analysis (**Supplementary Figures S1H–L**). We observed that the docking models we originally showed in **Figure 4** are indeed clustered with a converged ligand binding configuration among the top 10 binding energy models. Specifically, the cluster of the representative (-)-menthol model shown in **Figure 4** contained 9 out of the top 10 models (**Supplementary Figure S1H**). The cluster of representative (+)-menthol, (+)-isomenthol, (+)-neoisomenthol, and (+)-neomenthol contained 3, 6, 4, and 6 models among the top 10 models, respectively. Therefore, the representative docking models shown in **Figure 4** are reliable.

To validate our docking results, we performed a molecular dynamics simulation as suggested by the reviewer (see Methods for details). Starting from our (−)-menthol docking model, the S1–S4 domains remained stable during the 378 ns simulation with RMSD being around 3 Å (**Supplementary Figure S2A**). The menthol molecule is bound stably within its binding pocket inside the S1–S4 domains, as illustrated in the ensemble plot of the menthol molecule with snapshots of the simulation from the beginning to the end (**Supplementary Figure S2B**, red and blue, respectively; **Supplementary Movie S1**). The distance between the oxygen atom in menthol and the OD atom of D802, as well as the distance between the C9 atom in menthol and the CD atom of I846, remained stable during the 378 ns simulation, indicating the docking configuration of menthol is stable.

Our previous study has shown that for (−)-menthol, its hydroxyl group forms a hydrogen bond with the sidechain of R842, while the isopropyl group is within 4 Å of the sidechain of I846 (**Figure 4C**, dashed lines in blue or black, respectively) (Xu et al., 2020). For (+)-neoisomenthol, which differs from (-)-menthol in the orientation of the isopropyl group (**Figures 1A,D**), its hydroxyl group also formed a hydrogen bond with the sidechain of R842 (**Figure 4D**, dashed line in blue). Though the isopropyl group of (+)-neoisomenthol points in the opposite direction as compared to that in (−)-menthol, it was still in contact with the sidechain of I846 (3.83 Å, **Figure 4D**, dashed line in black). These observations suggested that the "grab and stand" binding mechanism we established in (−)-menthol (Xu et al., 2020) is also applicable to (+)-neoisomenthol, validating the use of TMCA as these two stereoisomers shared similar binding configurations. Moreover, the binding energy of the top 10 (+)-neoisomenthol docking models (−14.99 ± 0.07 Rosetta Energy Unit (R.E.U.)) was predicted to be smaller than that of (−)-menthol (−16.20 ± 0.19 R.E.U.) (**Figure 4B**), which was consistent with the increased K_d values measured from patch-clamp recordings (**Figures 1H, L**). The upward-pointing sidechain of R842 upon (+)-neoisomenthol binding as compared to the downward-point conformation in (−)-menthol bound model may offer clues to understand the reduced channel opening capability (reduced *L* values measured from patch-clamp recordings) of (+)-neoisomenthol (**Figure 1M**).

However, when (+)-neomenthol, which differs from (−)-menthol in the orientation of hydroxyl group (**Figures 1A,E**), was docked into TRPM8, the models with the top 10 largest binding energy were converged into a different configuration (**Figure 4E**). The orientation of hydroxyl group in (+)-neomenthol pointed away from the sidechain of R842, so that the hydrogen bond between the hydroxyl group of (-)-menthol and R842 was disrupted. Indeed, the binding energy of (+)-neomenthol was significantly smaller than that of (-)-menthol (**Figure 4B**), which is consistent with the increased K_d values measured from patch-clamp recordings (**Figures 1H, L**). As R842 was no longer "grabbed" by the hydroxyl group, the channel opening capability (reflected in *L* values) of (+)-neomenthol was likely reduced (**Figures 1I, M**). Furthermore, as the isopropyl group of (+)-neomenthol pointed away from I846 with an increased distance of 3.97 Å (**Figure 4E**, dashed line in black), the interaction between the isopropyl group and I846 was most likely perturbed, so that it is not surprising that we observed large coupling energy values between (+)-neomenthol and I846 (**Figures 3J,K**).

Furthermore, we also docked (+)-isomenthol or (+)-menthol into TRPM8. As these two stereoisomers contain either two or three chemical groups with distinct spatial orientations compared to (-)-menthol, it is not feasible to perform TMCA by comparing (-)-menthol and these ligands to directly probe molecular interactions with TRPM8. Nevertheless, from docking, we gained insights into their binding and activation of the channel. For (+)-isomenthol, the top 10 docking models with the largest binding energy well converged into a configuration where the isopropyl group pointed upward away from I846, while the hydroxyl group still formed a hydrogen bond with the sidechain of R842 (**Figure 4F**, dashed lines in blue). The reduced binding energy of (+)-isomenthol (**Figure 4B**) was consistent with the increased K_d measured at -80 mV (**Figure 1L**).

For (+)-menthol, though its chemical groups differ from (−)-menthol in all three chiral centers, the docking figuration was similar to that of (−)-menthol. Its hydroxyl group formed a hydrogen bond between the sidechain of R842 and its isopropyl group pointed toward I846 (**Figure 4G**, dashed line in blue and black, respectively). Such a similar binding configuration of (+)-menthol was in line with its unchanged binding energy predicted from docking (**Figure 4B**) and K_d measured at +80 mV (**Figure 1H**), though K_d and *L* measured at −80 mV were still significantly changed as compared to (−)-menthol (**Figures 1L, M**).

DISCUSSION

In this study, we systematically investigated how the five commercially available stereoisomers of menthol bind and activate the TRPM8 channel with patch-clamp recordings and molecular docking. We observed that (−)-menthol, which is the most abundant menthol stereoisomer in mints, best activated the TRPM8 channel with the largest P_o_max (therefore the largest *L* value) and the lowest K_d, while (+)-menthol exhibited slightly altered current activation properties (**Figure 1**). Such a similarity in TRPM8 activation by (−)-menthol and (+)-menthol could be explained by their similar putative binding configuration, where the hydroxyl group "grabs" the D802/R842 with a hydrogen bond and the isopropyl group "stands on" I846 (**Figure 4**). In contrast, (+)-isomenthol, (+)-neoisomenthol, and (+)-neomenthol showed significantly reduced P_o_max (therefore smaller *L* values) and increased K_d, especially at −80 mV (**Figure 1**), which is likely due to altered binding configurations where the "grab and stand" mechanism is disrupted (**Figure 4**). Therefore, our observations lead to mechanistical insights regarding the differential activation of TRPM8 by the menthol stereoisomers.

TMCA by patch-clamp recording has been widely used to probe ligand-protein interactions. For instance, this approach was employed to study how peptide toxin bind to the outer pore of voltage-gated potassium channel (Ranganathan et al., 1996) and TRPV1 channel (Yang et al., 2017). TMCA is applicable to investigate how small molecules such as capsaicin (Yang et al., 2015) or (−)-menthol (Xu et al., 2020) interact with TRP channels. However, we observed that when the ligand is small in a chemical structure like menthol, altering one chemical group of the ligand may affect how another group interacts with the protein. When the orientation of the hydroxyl group in (−)-menthol is changed as in (+)-neomenthol, we observed that besides the hydrogen-bounding D802 residue, I846 residue also showed large coupling energy (**Figures 3J,K**). We reason that most likely in (+)-neoisomenthol, its overall binding configuration was slightly changed so that how its isopropyl group interacted with I846 was accordingly altered. Indeed, our docking results suggested that the distance between the isopropyl group of (+)-neoisomenthol and the sidechain of I846 was increased as compared to that of (−)-menthol (**Figures 4C,D**). Therefore, caution must be taken regarding the interpretation of coupling energy values measured from TMCA for small molecules.

TRP channels like TRPM8, are polymodal receptors modulated by a plethora of physical and chemical stimuli (Julius, 2013; Zheng, 2013), including the transmembrane voltage. For TRPM8 activation by the stereoisomers of menthol, we clearly found that the P_o _max of TRPM8 (therefore the *L* values of the ligands) was reduced at a hyperpolarized voltage (−80 mV) as compared to that at depolarization (+80 mV) (**Figures 1G,K**). For (+)-neoisomenthol and (+)-neomenthol, such a reduction in P_o _max was even larger, which may explain the less intense cooling sensation elicited by (+)-neoisomenthol because the physiologically relevant transmembrane voltage resides within the hyperpolarized range (Hopp, 1993; Hille, 2001; Barel et al., 2009). Mechanistically, given menthol interacts with the voltage-sensing residue R842 (Voets et al., 2007; Xu et al., 2020) in S4 or D802 in S3 (**Figures 3J,K**), it is not surprising that the menthol activation is drastically affected by voltage. However, because the cryo-EM structures of TRPM8 channel were determined at zero transmembrane voltage, they do not represent the deactivated structural state of the voltage sensing S1 to S4 domains.

Therefore, it will require more work in the future to deduce the structural basis for the voltage modulation of the menthol stereoisomer binding and activation of TRPM8.

DATA AVAILABILITY STATEMENT

The original contributions presented in the study are included in the article/**Supplementary Material**; further inquiries can be directed to the corresponding author.

AUTHOR CONTRIBUTIONS

XC, LX, and HZ conducted the experiments including patch-clamp recordings and molecular docking; HW performed MD simulation and analysis; FY conceived and supervised the project and prepared the manuscript; XC and FY participated in data analysis and manuscript writing.

FUNDING

This study was supported by the National Natural Science Foundation of China (32122040 and 31971040 to FY) and Natural Science Foundation of Zhejiang Province (LR20C050002 to FY). This work was also supported by Alibaba Cloud.

ACKNOWLEDGMENTS

We are grateful to our lab members for assistance and discussion.

SUPPLEMENTARY MATERIAL

The Supplementary Material for this article can be found online at: https://www.frontiersin.org/articles/10.3389/fphar.2022.898670/full#supplementary-material

Supplementary Figure S1 | Binding energy contribution from menthol stereoisomers docking results. **(A)** Alignment of the amino acid sequence of S1–S4 in murine TRPM8 (mTRPM8) and human TRPM8 (hTRPM8). The S1 to S4 regions (wave line in blue) are indicated. The protein sequence between mTRPM8 and hTRPM8 is highly conserved with the identity of 96.61%. **(B)** Representative whole-cell recordings showed that (–)-menthol activated mTRPM8 at ± 80 mV. **(C–G)** Menthol stereoisomers docking models exhibited a funnel-shaped distribution of binding energy versus the ligand RMSD as calculated by Rosetta (R.E.U., Rosetta energy unit). The top one models with the lowest binding energy, which was the docking model presented in **Figure 4**, were highlighted in red. **(H–L)** Docking models with the best binding scores are clustered in a converged configuration. The cluster of representative (–)-menthol, (+)-menthol, (+)-isomenthol, (+)-neoisomenthol, and (+)-neomenthol contained 9, 3, 6, 4, and 6 models among the top ten models, respectively.

Supplementary Figure S2 | Molecular dynamic analysis of TRPM8 and menthol ligand. **(A)** RMSD of S1–S4 domains calculated by molecular dynamic stimulation during 378 ns is around 3 Å. **(B)** Ensemble plot of (**–**)-menthol molecule during stimulation. The configuration from the beginning is shown in red, and the configuration at the end is shown in blue. **(C)** Distance between specific atoms of (**–**)-menthol and residues is displayed. The distance between the oxygen atom in menthol and the OD atom of D802 is shown in blue line, and the distance between the C9 atom in menthol and CD atom of I846 is shown in gray line.

REFERENCES

Bandell, M., Dubin, A. E., Petrus, M. J., Orth, A., Mathur, J., Hwang, S. W., et al. (2006). High-throughput Random Mutagenesis Screen Reveals TRPM8 Residues Specifically Required for Activation by Menthol. *Nat. Neurosci.* 9 (4), 493–500. doi:10.1038/nn1665

Barel, A. O., Paye, M., and Maibach, H. I. (2009). *Handbook of Cosmetic Science and Technology*. New York: Informa Healthcare.

Darden, T., York, D., and Pedersen, L. (1993). Particle Mesh Ewald: AnN·Log(N) Method for Ewald Sums in Large Systems. *J. Chem. Phys.* 98 (12), 10089–10092. doi:10.1063/1.464397

Davis, I. W., and Baker, D. (2009). RosettaLigand Docking with Full Ligand and Receptor Flexibility. *J. Mol. Biol.* 385 (2), 381–392. doi:10.1016/j.jmb.2008.11.010

Davis, I. W., Raha, K., Head, M. S., and Baker, D. (2009). Blind Docking of Pharmaceutically Relevant Compounds Using RosettaLigand. *Protein Sci.* 18 (9), 1998–2002. doi:10.1002/pro.192

Diver, M. M., Cheng, Y., and Julius, D. (2019). Structural Insights into TRPM8 Inhibition and Desensitization. *Science* 365 (6460), 1434–1440. doi:10.1126/science.aax6672

Fleishman, S. J., Leaver-Fay, A., Corn, J. E., Strauch, E. M., Khare, S. D., Koga, N., et al. (2011). RosettaScripts: a Scripting Language Interface to the Rosetta Macromolecular Modeling Suite. *PLoS One* 6 (6), e20161. doi:10.1371/journal.pone.0020161

Hess, B., Bekker, H., Berendsen, H. J. C., and Fraaije, J. G. E. M. (1997). LINCS: A Linear Constraint Solver for Molecular Simulations. *J. Comput. Chem.* 18 (12), 1463–1472. doi:10.1002/(sici)1096-987x(199709)18:12<1463::aid-jcc4>3.0.co;2-h

Hille, B. (2001). *Ion Channels of Excitable Membranes*. Sunderland, Mass: Sinauer.

Hoover, W. G. (1985). Canonical Dynamics: Equilibrium Phase-Space Distributions. *Phys. Rev. A Gen. Phys.* 31 (3), 1695–1697. doi:10.1103/physreva.31.1695

Hopp, R. (1993). Menthol. Its Origins, Chemistry, Physiology and Toxicological Properties. *Rec. Adv. Tob. Sci.* 19, 3–46.

Huang, J., and MacKerell, A. D., Jr. (2013). CHARMM36 All-Atom Additive Protein Force Field: Validation Based on Comparison to NMR Data. *J. Comput. Chem.* 34 (25), 2135–2145. doi:10.1002/jcc.23354

Jo, S., Kim, T., and Im, W. (2007). Automated Builder and Database of Protein/Membrane Complexes for Molecular Dynamics Simulations. *Plos One* 2 (9), e880. doi:10.1371/journal.pone.0000880

Jo, S., Kim, T., Iyer, V. G., and Im, W. (2008). CHARMM-GUI: a Web-Based Graphical User Interface for CHARMM. *J. Comput. Chem.* 29 (11), 1859–1865. doi:10.1002/jcc.20945

Jo, S., Lim, J. B., Klauda, J. B., and Im, W. (2009). CHARMM-GUI Membrane Builder for Mixed Bilayers and its Application to Yeast Membranes. *Biophys. J.* 97 (1), 50–58. doi:10.1016/j.bpj.2009.04.013

Jorgensen, W. L., Chandrasekhar, J., Madura, J. D., Impey, R. W., and Klein, M. L. (1983). Comparison of Simple Potential Functions for Simulating Liquid Water. *J. Chem. Phys.* 79 (2), 926–935. doi:10.1063/1.445869

Julius, D. (2013). TRP Channels and Pain. *Annu. Rev. Cell. Dev. Biol.* 29, 355–384. doi:10.1146/annurev-cellbio-101011-155833

Klauda, J. B., Venable, R. M., Freites, J. A., O'Connor, J. W., Tobias, D. J., Mondragon-Ramirez, C., et al. (2010). Update of the CHARMM All-Atom Additive Force Field for Lipids: Validation on Six Lipid Types. *J. Phys. Chem. B* 114 (23), 7830–7843. doi:10.1021/jp101759q

Leaver-Fay, A., Tyka, M., Lewis, S. M., Lange, O. F., Thompson, J., Jacak, R., et al. (2011). ROSETTA3: an Object-Oriented Software Suite for the Simulation and Design of Macromolecules. *Methods Enzymol.* 487, 545–574. doi:10.1016/B978-0-12-381270-4.00019-6

Lee, J., Cheng, X., Swails, J. M., Yeom, M. S., Eastman, P. K., Lemkul, J. A., et al. (2016). CHARMM-GUI Input Generator for NAMD, GROMACS, AMBER, OpenMM, and CHARMM/OpenMM Simulations Using the CHARMM36 Additive Force Field. *J. Chem. Theory Comput.* 12 (1), 405–413. doi:10.1021/acs.jctc.5b00935

McKemy, D. D., Neuhausser, W. M., and Julius, D. (2002). Identification of a Cold Receptor Reveals a General Role for TRP Channels in Thermosensation. *Nature* 416 (6876), 52–58. doi:10.1038/nature719

Meiler, J., and Baker, D. (2006). ROSETTALIGAND: Protein-Small Molecule Docking with Full Side-Chain Flexibility. *Proteins* 65 (3), 538–548. doi:10.1002/prot.21086

Miteva, M. A., Guyon, F., and Tufféry, P. (2010). Frog2: Efficient 3D Conformation Ensemble Generator for Small Compounds. *Nucleic Acids Res.* 38, W622–W627. doi:10.1093/nar/gkq325

Nosé, S. (1984). A Molecular Dynamics Method for Simulations in the Canonical Ensemble. *Mol. Phys.* 52 (2), 255–268. doi:10.1080/00268978400101201

Parrinello, M., and Rahman, A. (1981). Polymorphic Transitions in Single Crystals: A New Molecular Dynamics Method. *J. Appl. Phys.* 52 (12), 7182–7190. doi:10.1063/1.328693

Peier, A. M., Moqrich, A., Hergarden, A. C., Reeve, A. J., Andersson, D. A., Story, G. M., et al. (2002). A TRP Channel that Senses Cold Stimuli and Menthol. *Cell.* 108 (5), 705–715. doi:10.1016/s0092-8674(02)00652-9

Pronk, S., Páll, S., Schulz, R., Larsson, P., Bjelkmar, P., Apostolov, R., et al. (2013). GROMACS 4.5: a High-Throughput and Highly Parallel Open Source Molecular Simulation Toolkit. *Bioinformatics* 29 (7), 845–854. doi:10.1093/bioinformatics/btt055

Ranganathan, R., Lewis, J. H., and MacKinnon, R. (1996). Spatial Localization of the K+ Channel Selectivity Filter by Mutant Cycle-Based Structure Analysis. *Neuron* 16 (1), 131–139. doi:10.1016/s0896-6273(00)80030-6

Vanommeslaeghe, K., Hatcher, E., Acharya, C., Kundu, S., Zhong, S., Shim, J., et al. (2010). CHARMM General Force Field: A Force Field for Drug-like Molecules Compatible with the CHARMM All-Atom Additive Biological Force Fields. *J. Comput. Chem.* 31 (4), 671–690. doi:10.1002/jcc.21367

Voets, T., Owsianik, G., Janssens, A., Talavera, K., and Nilius, B. (2007). TRPM8 Voltage Sensor Mutants Reveal a Mechanism for Integrating Thermal and Chemical Stimuli. *Nat. Chem. Biol.* 3 (3), 174–182. doi:10.1038/nchembio862

Wu, E. L., Cheng, X., Jo, S., Rui, H., Song, K. C., Dávila-Contreras, E. M., et al. (2014). CHARMM-GUI Membrane Builder toward Realistic Biological Membrane Simulations. *J. Comput. Chem.* 35 (27), 1997–2004. doi:10.1002/jcc.23702

Xu, L., Han, Y., Chen, X., Aierken, A., Wen, H., Zheng, W., et al. (2020). Molecular Mechanisms Underlying Menthol Binding and Activation of TRPM8 Ion Channel. *Nat. Commun.* 11 (1), 3790. doi:10.1038/s41467-020-17582-x

Yang, F., Xiao, X., Cheng, W., Yang, W., Yu, P., Song, Z., et al. (2015). Structural Mechanism Underlying Capsaicin Binding and Activation of the TRPV1 Ion Channel. *Nat. Chem. Biol.* 11 (7), 518–524. doi:10.1038/nchembio.1835

Yang, S., Yang, F., Zhang, B., Lee, B. H., Li, B., Luo, L., et al. (2017). A Bimodal Activation Mechanism Underlies Scorpion Toxin-Induced Pain. *Sci. Adv.* 3 (8), e1700810. doi:10.1126/sciadv.1700810

Yarov-Yarovoy, V., Baker, D., and Catterall, W. A. (2006a). Voltage Sensor Conformations in the Open and Closed States in ROSETTA Structural Models of K(+) Channels. *Proc. Natl. Acad. Sci. U. S. A.* 103 (19), 7292–7297. doi:10.1073/pnas.0602350103

Yarov-Yarovoy, V., DeCaen, P. G., Westenbroek, R. E., Pan, C. Y., Scheuer, T., Baker, D., et al. (2012). Structural Basis for Gating Charge Movement in the Voltage Sensor of a Sodium Channel. *Proc. Natl. Acad. Sci. U. S. A.* 109 (2), E93–E102. doi:10.1073/pnas.1118434109

Yarov-Yarovoy, V., Schonbrun, J., and Baker, D. (2006b). Multipass Membrane Protein Structure Prediction Using Rosetta. *Proteins* 62 (4), 1010–1025. doi:10.1002/prot.20817

Yin, Y., Le, S. C., Hsu, A. L., Borgnia, M. J., Yang, H., and Lee, S. Y. (2019). Structural Basis of Cooling Agent and Lipid Sensing by the Cold-Activated TRPM8 Channel. *Science* 363 (6430), eaav9334. doi:10.1126/science.aav9334

Yin, Y., Wu, M., Zubcevic, L., Borschel, W. F., Lander, G. C., and Lee, S. Y. (2018). Structure of the Cold- and Menthol-Sensing Ion Channel TRPM8. *Science* 359 (6372), 237–241. doi:10.1126/science.aan4325

Zheng, J. (2013). Molecular Mechanism of TRP Channels. *Compr. Physiol.* 3 (1), 221–242. doi:10.1002/cphy.c120001

Conflict of Interest: Author HW was employed by the company DP Technology, Beijing, China.

The remaining authors declare that the research was conducted in the absence of any commercial or financial relationships that could be construed as a potential conflict of interest.

frontiers | Frontiers in Pharmacology

REVIEW
published: 28 June 2022
doi: 10.3389/fphar.2022.939555

Simulation and Machine Learning Methods for Ion-Channel Structure Determination, Mechanistic Studies and Drug Design

*Zhengdan Zhu[1,2†], Zhenfeng Deng[3,4†], Qinrui Wang[3‡], Yuhang Wang[3‡], Duo Zhang[1,3], Ruihan Xu[3,5], Lvjun Guo[3] and Han Wen[3]**

[1]Academy for Advanced Interdisciplinary Studies, Peking University, Beijing, China, [2]Beijing Institute of Big Data Research, Beijing, China, [3]DP Technology, Beijing, China, [4]School of Pharmaceutical Sciences, Peking University, Beijing, China, [5]National Engineering Research Center of Visual Technology, Peking University, Beijing, China

Edited by:
Chia-Hsueh Lee,
St. Jude Children's Research Hospital,
United States

Reviewed by:
Hongtu Zhao,
St. Jude Children's Research Hospital,
United States
Jing Huang,
Westlake University, China

****Correspondence:***
Han Wen
wenh@dp.tech

†These authors have contributed equally to this work and share the first authorship

‡These authors have contributed equally to this work and share senior authorship

Specialty section:
This article was submitted to Pharmacology of Ion Channels and Channelopathies, a section of the journal Frontiers in Pharmacology

Received: *09 May 2022*
Accepted: *07 June 2022*
Published: *28 June 2022*

Citation:
Zhu Z, Deng Z, Wang Q, Wang Y, Zhang D, Xu R, Guo L and Wen H (2022) Simulation and Machine Learning Methods for Ion-Channel Structure Determination, Mechanistic Studies and Drug Design. Front. Pharmacol. 13:939555. doi: 10.3389/fphar.2022.939555

Ion channels are expressed in almost all living cells, controlling the in-and-out communications, making them ideal drug targets, especially for central nervous system diseases. However, owing to their dynamic nature and the presence of a membrane environment, ion channels remain difficult targets for the past decades. Recent advancement in cryo-electron microscopy and computational methods has shed light on this issue. An explosion in high-resolution ion channel structures paved way for structure-based rational drug design and the state-of-the-art simulation and machine learning techniques dramatically improved the efficiency and effectiveness of computer-aided drug design. Here we present an overview of how simulation and machine learning-based methods fundamentally changed the ion channel-related drug design at different levels, as well as the emerging trends in the field.

Keywords: ion channel, cryo-EM, machine learning, molecular dynamics, computer-aided drug design

INTRODUCTION

Ion channels are a group of pore-forming proteins located at the membrane of cells or intracellular organelles, controlling the flow of ions across the membranes. Such transportation of ions plays a critical role in the physiology of all living cells (Hille, 1978; Hille, 1986), thus the malfunction of ion channels leads to numerous diseases at the fundamental level. Although spanning a broad spectrum of families, ion channels can be roughly categorized into the voltage-gated and the ligand-gated based on activation mechanisms and structural similarities (**Figure 1**). Most voltage-gated ion channels contain four individual subunits or four repeats within one continuous polypeptide, each includes a similar six-transmembrane-helix core architecture, which can be further divided into a four-helix voltage sensor domain S1-S4 and the pore domain S5-S6 connected by the pore loop (Gulbis et al., 1999). The typical voltage-gated ion channels, mainly the sodium (Catterall, 2000), potassium (Wulff et al., 2009), and calcium channels (Catterall, 2011), are mostly depolarization activated and responsible for fast reactions upon voltage changes at the cell membrane, thereby playing a key part in electric signaling (Catterall, 2000; Sands et al., 2005; Catterall, 2010). While some members of the transient receptor potential (TRP) family, mainly facilitate their biological function via other stimuli including temperature, force, and chemical compounds. They serve as the vanguard of the sensory system (Clapham, 2003). As for ligand-gated ion channels, they are mostly activated by ligands like neurotransmitters and are crucial for nervous activities. There are three families in

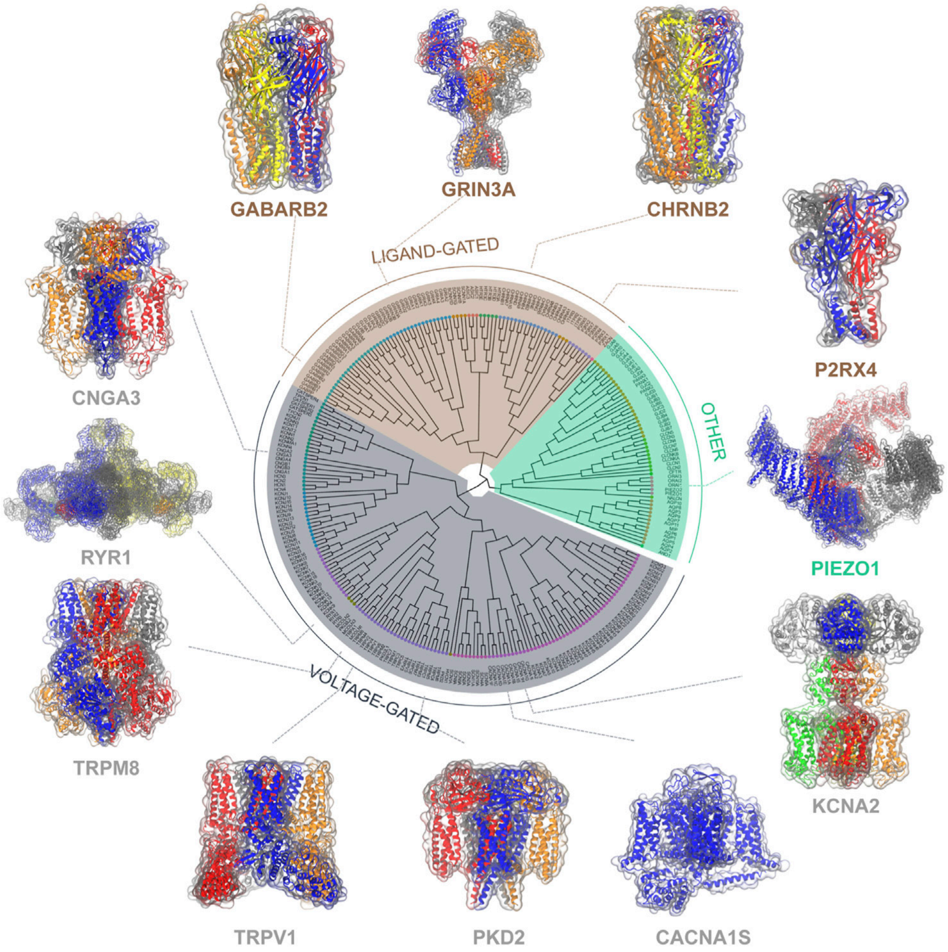

FIGURE 1 | Classification of ion channels based on activation mechanisms and structural similarities. The evolutionary relationships among these ion channels are measured by the phylogenetic tree of ion channels (Alexander et al., 2019) with representative channel structures (center). Representative ion channels selected from each class are shown with their 3D molecular structures.

mammals: Cys-loop receptor ion channels (Sine and Engel, 2006), Glutamate receptor ion channels (Traynelis et al., 2010), and ATP gated ion channels (Schmid and Evans, 2019), they are typically composed of a transmembrane domain forming the pore and an extracellular domain carrying the ligand-binding sites. Besides, some other ion channels are beyond these two types, for example, the ubiquitously expressed trimeric Piezo 1/2 channels that respond to mechanical stimuli (Coste et al., 2010).

Due to the vital function of ion channels in physiology, mutations of ion channels were identified to be responsible for various diseases: inherited neuronal diseases like epilepsy (Escayg et al., 2000), cardiac diseases like Long-QT syndrome (Keating, 1996), muscle diseases like Hyperkalemic periodic paralysis (Brugnoni et al., 2022) and many others (Ackerman and Clapham, 1997). Also, the blockage of ion channels can directly regulate sensory perception such as pain (Tominaga and Caterina, 2004; Bourinet et al., 2014; Bennett et al., 2019). Consequently, ion channels are among the most pursued drug targets in the past decades (Bagal et al., 2013) and several drugs were developed against a wide range of diseases (Clare, 2010). To be specific, for the most related central nervous system (CNS) diseases: Diazepam, the famous anxiolytic launched in 1963 and the best-seller in the United States between 1968 and 1982 (Calcaterra and Barrow, 2014), was identified as a positive allosteric modulator of the gamma-aminobutyric acid (GABA) type-A receptors in 1977 (Braestrup and Squires, 1977; Mohler and Okada, 1977). A detoured but successful development of ketamine, the *N*-methyl-D-aspartate (NMDA) receptor antagonist (Alessandri et al., 1989; Zhang et al., 2021) into an anti-depressant drug is even considered a sign of a renaissance in the psychiatric drug industry (Daly et al., 2018; Reardon, 2018). Recent studies also revealed more potential applications of channel modulators in Parkinson's (Daniel et al., 2021) and Alzheimer's diseases (Tan et al., 2012; Gonzales and Sumien, 2017; Lu et al., 2017). Additionally, the prevalent expression makes ion channels adequate targets for other diseases as well. Varenicline is derived from the modification of (-)-cytisine, an alkaloid that could be found in nature (Coe et al., 2005). As a partial agonist of nicotinic receptors with the beta 2 subunit (Papke and Heinemann, 1994), Chantix (varenicline tartrate) was launched by Pfizer in 2006 for smoking cessation (Coe et al., 2005) and is still one of the best-selling drugs in the world with annual sales of 919 million dollars in the year of 2020 (McGrath et al., 2010; Njardarson et al., 2020). In addition, cystic fibrosis, a heritable disease, is caused by a defect in the ATP-activated chloride channel, cystic fibrosis transmembrane conductance regulator (CFTR) which is involved in water flow control during the production of sweat, digestive fluids, and mucus (Bobadilla et al., 2002). The latest treatment for cystic fibrosis, Trikafta, was developed by Vertex Pharmaceuticals and hit the market in 2019, and was considered at the top of 2019's new approvals by expected revenue (Mullard, 2020). Another case for diabetes treatment is the blocking of ATP-sensitive potassium channel KATP by Glipizide leads to depolarization of beta cells, resulting in the opening of voltage-gated calcium channels which encourages insulin release (Shuman, 1983). Ion channels were also reported to be potential anti-cancer targets. Their role in proliferation, migration, and metastasis of cancer was well-explored (Litan and Langhans, 2015) and the over-expression of TRPA1 and TRPV1 channels was observed in several tumors suitable for topical administration, allowing for a safe and efficient therapy (Kiss et al., 2020).

Despite the vast opportunities, the discovery of drugs targeting ion channels faces unique obstacles. To begin with, the development of biological assays for ion channels is usually challenging, and the low expression rates further hindered the high-throughput screening. Ever since Hodgkin and Huxley firstly described the movement of ions in nerve cells of squid axons during an action potential (Hodgkin and Huxley, 1952), electrophysiology has been used to study the function of ion channels. Yet, such methods require considerable expertise and are labor-intensive and time-consuming, therefore not realistic for large-scale screening, even with the great advancement in automated patch clamp devices (Dunlop et al., 2008; Kodandaramaiah et al., 2012). Another major stumbling block is ligand selectivity because channels from the same or close families usually share great similarities in sequence and structure yet bear diverse functions. Lead compounds, especially channel blockers, often suffer from side effects due to poor selectivity (Vandenberg et al., 2017; Flood et al., 2019). As the "low-hanging fruit" is becoming rare in modern drug discovery, cases like carbamazepine, a pan-ion-channel inhibitor with broad pharmacological properties (Bagal et al., 2013), may be very rare and not welcomed nowadays, for which mechanism studies came several decades later than discovery (Schindler and Hafliger, 1954; Grant and Faulds, 1992).

Because of the aforementioned problems, the rational design of drugs is critical for the efficiency and efficacy of ion channel drug discovery. Such designs require precise structural information, which is largely missing until the rise of single-particle cryo-electron microscopy (cryo-EM) (Li et al., 2013; Liao et al., 2013). Starting from the high-resolution structures, computer-aided drug design (CADD) can be applied to perform large scale virtual screenings before the costly wet-lab experiments to greatly narrow down the size of the library to an affordable range (Lyne, 2002); molecular dynamics (MD) simulations can be performed to further model the structures and study the mechanism at atomistic details (Maffeo et al., 2012). On the other hand, recent advancement in machine learning begins to demonstrate their power in cryo-EM and drug development. Towards accelerating the ion channel drug discovery, in this review, we will provide a broad overview of the current machine-learning and simulation-based techniques in structural biology and drug design, and discuss how they can be applied to ion channel research.

COMPUTATIONAL METHODS FOR SINGLE-PARTICLE CRYO-EM

While being essential for mechanistic studies and rational drug design, molecular structures for ion channels are more difficult to purify and crystallize than soluble proteins, mainly due to the necessity and difficulty of preserving the membrane-like environment. Detergents, amphipols, and nanodiscs have been commonly used to extract membrane proteins such as ion channels, and also serve as substitutes for the local membrane to stabilize the transmembrane domains (Zampieri et al., 2021). In recent years, the single-particle cryo-EM technique has rapidly evolved as a powerful method for structure determination for various ion channels (Martin et al., 2017; Basak et al., 2019; Dang et al., 2019; Masiulis et al., 2019; Zhao et al., 2019; Wang Q. et al., 2020; Sun and MacKinnon, 2020; Lin et al., 2021; Song et al., 2021; Yu et al., 2021). Cryo-EM eliminates the need for protein crystallization and is capable of resolving multiple protein conformations within a single cryo-EM dataset (Frank and Ourmazd, 2016; Frank, 2017; Cheng, 2018; Wu and Lander, 2020). The structural resolution of cryo-EM experiments has also been improved over the years, with the highest resolution reaching ~1.2 Å (Nakane et al., 2020; Yip et al., 2020). High-resolution cryo-EM enables its use in target identification and lead-optimization for developing drugs targeting ion channels.

A typical single-particle cryo-EM experiment includes sample purification, vitrification via plunge freezing, electron microscopy data collection, image processing, and structural model building (**Figure 2**) (Lyumkis, 2019; Wu and Lander, 2020). We will focus on the last two steps in this review, which rely heavily on computational techniques.

Cryo-EM Image Analysis

The goal of cryo-EM image analysis is to reconstruct the three-dimensional (3D) structure of the target proteins represented as statistically estimated density maps. A large collection of two-dimensional (2D) projection maps are subjected to image preprocessing, particle picking, 2D image classifications, 3D classifications, and 3D reconstructions (Singer and Sigworth, 2021). Many software programs are available for building cryo-EM density maps from 2D projection maps, such as RELION (Scheres, 2012; Kimanius et al., 2021), cryoSPARC (Punjani et al., 2017), Xmipp (Sorzano et al., 2004), Warp (Tegunov and Cramer, 2019), CisTEM (Grant et al., 2018), EMAN2 (Tang et al., 2007). Although these programs are sufficient for most cryo-EM experiments, their output density maps are mostly limited to a few representative classes of particles

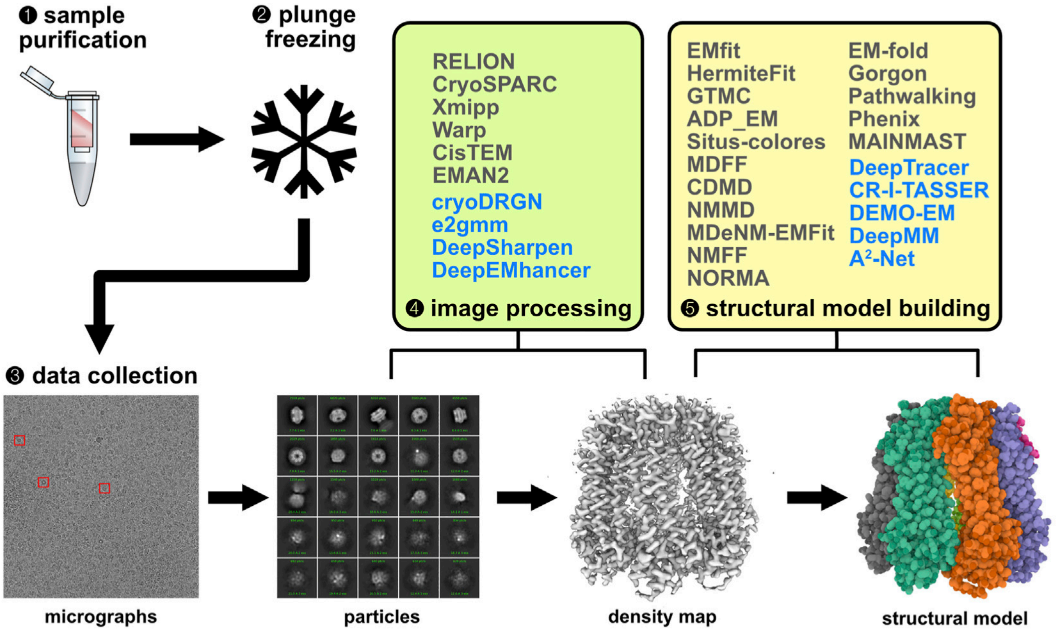

FIGURE 2 | Singe-particle cryo-EM workflow and relevant computational methods. Traditional methods for image processing and structural model building are shown in grey and ML-based methods in blue. Electron micrographs and particle images were visualized using cryoSPARC (Punjani et al., 2017). The density map and structural model were generated using Mol* viewer (Sehnal et al., 2021).

in the projection map dataset. Recent machine-learning-based methods focus on characterizing the continuous distribution of particle distributions within a cryo-EM experiment, e.g., cryoDRGN (Zhong et al., 2020; Zhong ED. et al., 2021; Zhong E. D. et al., 2021) and e2gmm (Chen and Ludtke, 2021). CryoDRGN is a method for heterogeneous cryo-EM reconstruction based on deep neural networks. It is powerful and general for analyzing structural heterogeneity in macromolecular complexes of various sizes and degrees of heterogeneity. The cryoDRGN model consists of two neural networks structured in an image-encoder-volume-decoder architecture with a continuous latent variable representation for describing the sample heterogeneity. Although the initial version of cryoDRGN (Zhong et al., 2020) can optimize image poses together with image reconstruction/classification, for better efficiency and accuracy, the pose estimation component was dropped and pre-computed image poses estimated from an upstream homogeneous reconstruction were used (Zhong ED. et al., 2021). CryoDRGN2 combines a traditional cryo-EM image pose search algorithm with deep neural networks, which eliminates the need for pre-computed image poses (Zhong E. D. et al., 2021). Compared with the initial version of cryoDRGN, both the speed and accuracy are increased significantly in pose estimation. The e2gmm algorithm can also find the structural variability of target macromolecules captured by cryo-EM experiments. In this method, each structural domain is modeled by a 3-dimensional (3D) Gaussian function, parameterized by its center coordinates, amplitude, and width. Autoencoder-like neural network architecture is used to generate a latent vector representation of each projection image through an encoder. Then the decoder component converts each latent vector into a set of 3D Gaussian function parameters which represents a Gaussian mixture model (GMM). This GMM representation is converted back to a 2D projection image through a projection operation. In e2gmm, training was first done for the decoder only, then for the encoder and decoder together. Unlike the standard autoencoder, the input to the encoder is not the projection image, but the gradient of loss function score with respect to the GMM parameters (Chen and Ludtke, 2021). The projection orientation of each image must be given as inputs which can be refined later once the network has been trained. The conformational variability of the cryo-EM dataset can be visualized through dimension reduction of the 4D latent space based on the latent vectors from the encoder. The cryoDRGN and e2gmm algorithms are similar in terms of the use of latent vectors for characterizing the structure variability, although latent vectors are obtained differently.

Reconstructed cryo-EM density maps usually suffer from loss of contrast at high resolution due to factors such as specimen movement, radiation damage, particle flexibility/heterogeneity, and deficiencies in extracting/averaging micrograph signals in the reconstruction algorithms (Rosenthal and Henderson, 2003). Algorithms, known as sharpening, have been designed to reduce this type of contrast loss. A commonly used sharpening method is based on global B-factor correction (Rosenthal and Henderson, 2003). Other methods, such as LocScale (Jakobi et al., 2017), LocalDeblur (Ramirez-Aportela et al., 2020), and LocSpiral (Kaur et al., 2021), improved upon the previous method by considering local variations in B-factors. Instead of explicitly performing sharpening calculations, deep-learning-based methods can implicitly encode the sharpening transformation. One example is DeepSharpen (Zehni et al., 2020), which uses a Convolutional Neural Network (CNN) trained on ~15,000 pairs of low and high-resolution synthetic cryo-EM density maps. The benefit of this approach is that sharpening on a new density map only requires inference through trained CNN parameters which can be very fast. Deep cryo-EM Map Enhancer (DeepEMhancer) is another deep-learning-based sharpening method (Sanchez-Garcia et al., 2021). It uses a 3D U-net architecture (Ronneberger et al., 2015) to learn the local sharpening effect of the LocScale algorithm by training on paired map datasets from the Electron Microscopy Data Bank (EMDB). Each map pair consists of an experimental density map and a post-processed map using LocScale. DeepSharpen and DeepEMhancer share similar deep learning designs, although their training strategies and training targets differ. More realistic and better-labeled training datasets can further improve these supervised-learning-based methods.

Cryo-EM Structural Model Building

In the final step of cryo-EM experiments, 3D atomic structural models are built based on the reconstructed 3D density maps. The goal is to search for the most probable 3D atomic structure that can best interpret the reconstructed density map. Traditionally, these atomic structural models are built semi-automatically using software like Coot (Casañal et al., 2020) and Phenix (Liebschner et al., 2019). These types of methods require the users to have extensive knowledge of the biochemical compositions of the target biological entities. More automated methods can be roughly divided into three categories. The first class of automated methods performs rigid-body fitting of initial structures into the density maps. Examples of such methods include EMfit (Rossmann et al., 2001), HermiteFit (Derevyanko and Grudinin, 2014), GTMC (Wu et al., 2003), ADP_EM (Garzón et al., 2007), and Situs-colores (Chacón and Wriggers, 2002). These methods solve the problem of placing an atomic structure model into a target cryo-EM density map as a rigid body and they differ in their specific implementation of translational/rotational search. Most of these methods are developed for low-resolution maps before the so-called “resolution revolution” during the development of cryo-EM (Crowther, 2016; Frank, 2017; Alnabati and Kihara, 2019).

As the average resolution of cryo-EM increased, the second class of automated methods emerged which allows flexible fitting of initial structures into density maps. One type of flexible fitting method combines molecular dynamics (MD) simulations and the experimental density maps to automatically fit some initial structural models into density maps. Examples of such methods include molecular dynamics flexible fitting (MDFF) and correlation-driven molecular dynamics (CDMD). In MDFF (Trabuco et al., 2008; Chan et al., 2011; Singharoy et al., 2016), an additional potential energy term derived from the density map was added to the simulation force field. The derivative of this potential generates forces that drive the initial structural model into the target density map. CDMD acts similarly (Igaev et al., 2019). Instead of directly adding a density-map-derived potential energy term, the cross-correlation coefficient (ccc) between the intermediate structures and the target density map is calculated. Forces derived from ccc drive the initial structure into the density map. Although both methods are equivalent, CDMD is more sensitive to the quality of initial structures and noises in the density maps compared to MDFF in practice. ISOLDE is a hybrid method that combines user interactions and MDFF to achieve a semi-automated structure modeling (Croll, 2018). The same hybrid modeling can also be performed using interactive MDFF (iMDFF) (McGreevy et al., 2016). NMMD is another MD-based cryo-EM structural fitting method (Vuillemot et al., 2022). Compared to CDMD and MDFF, NMMD combines normal mode analysis (NMA) and MD to perform global structural fitting with NMA and local structural fitting with MD. Other NMA-based flexible fitting methods include MDeNM-EMFit (Costa et al., 2020), NMFF (Tama et al., 2004a; b), NORMA (Suhre et al., 2006), and a coarse-grained fitting method with a modified elastic network model (Zheng, 2011). Besides MD, Monte Carlo (MC) simulations together with MD can also be used to fit structures into density maps (Topf et al., 2008).

Another approach to building cryo-EM structures is *de novo* modeling, which doesn’t require any initial structural models. This class of methods includes RosettaES (Frenz et al., 2017), EM-fold (Lindert et al., 2009; Lindert et al., 2012a; Lindert et al., 2012b), Gorgon (Baker et al., 2011), Pathwalking (Baker et al., 2012; Chen et al., 2016), Phenix (Terwilliger et al., 2018; Terwilliger et al., 2020), MAINMAST (Terashi and Kihara, 2018b; a), etc. (see the recent review (Alnabati and Kihara, 2019)). More recently, deep-learning-based *de novo* cryo-EM structural model building has been gaining much ground, such as DeepTracer (Pfab et al., 2021), CR-I-TASSER (Zhang et al., 2022), DeepMM (He and Huang, 2021), and A^2-Net (Xu et al., 2019). DeepTracer (Pfab et al., 2021) uses four U-Net-based neural networks to extract structural information from the input density amp. Each network can classify each density map voxel into a certain category. The Atoms U-Net predicts four classes: C-alpha, nitrogen, carbon (non-C-alpha), and non-atom. The Backbone U-Net predicts three classes: backbone, side chain, and neither. The Secondary Structure U-Net predicts four classes: loop, helix, sheet, and none of these. The Amino Acid Type U-Net predicts 21 classes: 20 types of amino acids and non-protein density. Then, protein backbone tracing is done in three steps: identifying protein chains based on Backbone U-Net outputs, estimating C-alpha atom coordinates, and connecting C-alpha atoms into chains using a modified traveling salesman algorithm. The assignment of amino acid residue types to each C-alpha atom was done through a customized sequence alignment algorithm based on the U-Net-predicted and input protein sequences. The all-atom backbone structure is subsequently reconstructed based on information from the Atoms U-Net predictions and some assumptions on the peptide bond geometries. One of the major limitations of DeepTracer is its inability to predict the side-chain conformations, which is delegated to an external program called SCWRL4 (Krivov et al., 2009). CR-I-TASSER (cryo-EM iterative threading assembly refinement) is a hybrid method that uses information from both homology modeling and density-map-based *de novo* C-alpha tracing (Zhang et al., 2022). Like DeepTracer, C-alpha atom positions are predicted based on density maps using machine learning techniques, which is a deep convolutional network (3D-CNN) in this case. Then, CR-I-TASSER solves the problem of C-alpha tracing using a local meta-threading server (LOMETS). After that, the atom structure models are built using the iterative threading assembly refinement method (I-TASSER) driven by model-map correlation under deep-learning boosted template restraints. The novelty of this method is the C-alpha position prediction using 3D-CNN and the use of C-alpha locations for better template reselection in LOMETS. CR-I-TASSER shows good performance in terms of TM scores compared to other methods such as MAINMAST and MDFF. However, its accuracy is limited for low-resolution cryo-EM data, and its C-alpha tracing method is also problematic in long-loop/tail or disordered regions. Another major limitation of CR-I-TASSER is that it can only handle single-chain proteins, thus the density maps have to be manually segmented first. DeepMM takes a workflow design similar to DeepTracer (He and Huang, 2021). Based on cryo-EM density maps, it uses one Densely Connected Convolutional Network (DenseNet) to predict the main chain (backbone N, C, and C-alpha atoms) and C-alpha probabilities at each density map voxel. Using the MAINMAST method, the main-chain paths are determined based on the main-chain probability map. Then, another DenseNet is used to predict the residue identities and secondary structure types for each main chain point. Smith-Waterman dynamic programming is used to align the target sequence to the main-chain paths. Finally, all-atom structure models are based on the top-10 C-alpha models using the ctrip program (Xiang and Honig, 2001; Petrey et al., 2003) and refined by energy minimization using Amber (Case et al., 2005). Like CR-I-TASSER, DeepMM can only handle building single protein chains and segmentation tools, such as Segger (Pintilie et al., 2010) are needed to preprocess multi-chain density maps into individual chain map segments. Compared to DeepTracer, DeepMM's main feature is the ability to build full-length protein structures from high-resolution EM maps, while DeepTracer only builds backbone segments in high-resolution map regions. All these methods only apply machine learning techniques to convert cryo-EM maps into basic protein structural models without side chains. A2-Net (Xu et al., 2019) is another *de novo* structure building method based on a deep Convolutional Neural Network (Srivastava et al., 2015). Like the methods mentioned above, it contains neural networks for amino acid residue identity detection. The main difference is that A2-net also contains a poseNet based on the 3D stacked hourglass network (Newell et al., 2016) for estimating the coordinates of each residue (side chain included). Then, these residues are connected to form the target protein using a Monte Carlo tree search algorithm. In the advent of accurate protein structure prediction methods such as AlphaFold2 (Jumper et al., 2021) and RoseTTAFold (Baek et al., 2021), new possibilities are brought to cryo-EM structure building. For example, ChimeraX added a new feature to allow users to start cryo-EM structure modeling from AlphaFold predictions[1]. Phenix also added a new workflow[2] (Terwilliger et al., 2022), to iteratively refine cryo-EM structural models by integrating AlphaFold predictions using ColabFold (Mirdita et al., 2022). Recently, Yan and Shen reported that AlphaFold2-predicted structure could help model the density map regions with moderate resolutions in voltage-gated sodium channel $Na_V1.7$ (Huang et al., 2022). With the rapid progress in the field of machine learning, more accurate and efficient *de novo* cryo-EM structure modeling methods are expected in the near future.

Evaluation of the Cryo-EM Structural Model Quality

Evaluation of the quality of the density-map-derived molecular structural models is yet another challenge. Global metrics (such as map-model cross-correlation coefficient and FSC curve) between the experimental density map and a simulated map converted from the structural model are often insensitive to local mis-fittings (Hryc et al., 2017). Moreover, these metrics usually do not account for densities not modeled by the atomic structural models such as lipids and detergents, and masks are usually needed to access local features (Pintilie et al., 2016). EMRinger and Z-scores are metrics defined based on how well the structure models interpret the experimental density maps. EMRinger score is based on the expectation that the map density values near the beta-carbon atoms should peak at certain angles when rotating the side-chain chi-1 dihedral angle (Barad et al., 2015). Although the EMRinger score correlates well with the protein backbone modeling quality and map density quality near the beta-carbons, it is suspectable to noise and lacks assessment of the rest of the side chains. Z-score has been proposed to quantify the density map quality at the secondary structure element level and side-chain level (Pintilie and Chiu, 2018). Its definition is based on the cross-correlation coefficients between the experimental and simulated maps of the secondary structure elements or side chains with and without some geometric displacements (Pintilie and Chiu, 2018). To make even finer-scale assessments, Q-score is established to quantify the resolvability of individual atoms in cryo-EM maps (Pintilie et al., 2020). The basic idea of the Q-score is to measure the cross-correlation coefficient between experimental density map values for individual atoms and ideal densities represented by a three-dimensional (3D) Gaussian-like function centered at each atom in the structure model (Pintilie et al., 2020). FSC-Q is another method that can also assess structure modeling quality on a per-atom basis (Ramírez-Aportela et al., 2021). FSC-Q calculates the difference between two local resolution maps calculated using the blocres program. The first local resolution

---

[1] https://www.rbvi.ucsf.edu/chimerax/data/stanford-sep2021/alphafold.html

[2] https://phenix-online.org/documentation/reference/alphafold_in_colab.html

map is calculated using the full density map and the simulated map based on the structure model, while the second is calculated using the half maps. Then the FSC-Q difference map can be projected onto atomic models to obtain an FSC-Q score for each atom. Alternatively, the FSC-Q map can be normalized by dividing by the local resolution map based on the half maps for better cross-comparison between experimental density maps of different resolutions.

Challenges in Cryo-EM Structure Determination for Ion Channels

Ion channels naturally reside in biological membranes which means preserving the amphiphilic local environment for the channel transmembrane domains is essential during cryo-EM sample preparation. Techniques such as nanodiscs can serve as good replacement for the membrane (Zampieri et al., 2021). However, the disordered nature of these membrane memetics also add difficulties to the cryo-EM structural analysis. In cryo-EM image analysis, algorithms such as non-uniform refinement can reduce the negative impact of the disordered detergent/lipid molecules (Punjani et al., 2020). In addition, certain ion channels, such as mechanosensitive channels, have flexible transmembrane domains and often require specific protein-lipid interactions for structural stability (Kefauver et al., 2020). Preserving their local membrane environment can be very difficult. For example, it has been reported that mechanosensitive channel YnaI's transmembrane domain couldn't be resolved using cryo-EM with membrane-active polymer SMA2000 except for core helices TM4 and TM5 (Catalano et al., 2021). Computational techniques such as normal model analysis and molecular dynamics can offer additional insights into these protein-lipid interactions required for the structural stability and functions of mechanosensitive channels (Jojoa-Cruz et al., 2018; Argudo et al., 2019). In addition, the application of toxins, truncation of flexible regions and mutations are often introduced in cryo-EM studies of ion channels (Jiang D. et al., 2021). Although sometimes intended by the researchers for their specific projects, these conditions have also been used to artificially stabilize ion channels to capture a certain conformation during structure determination (Rook et al., 2021). Computational techniques can reverse these effects if needed and can also be used to evaluate the impact of such conditions (Gupta and Vadde, 2021; Saikia et al., 2021).

COMPUTER-AIDED DRUG DESIGN APPROACHES TARGETING ION CHANNELS

In the glorious history of the era driven by occasions and classic synthetic chemistry, numerous ion-channel modulators were discovered. For example, the series of "-caine" analogues was inspired and chemically modified from cocaine, an alkaloid derived from plants (Plowman, 1982), including benzocaine, amylocaine, procaine, procainamide, and lignocaine (lidocaine), which showed potency as sodium channel inhibitors and were approved for medical use as anesthetics and/or antiarrhythmics (Cox, 2015). Typical cases also include the previously mentioned varenicline and carbamazepine, and maybe even ethanol and neurotoxic peptides in venoms. Ethanol was proved to be able to interact with various post-synaptic ion channel receptors (Howard et al., 2011; Murail et al., 2012; Zhang et al., 2016), while neurotoxic peptides in venoms were sometimes regarded as good starting points for modification as modulators targeting ion channels such as voltage-gated sodium, potassium, and calcium channels as well as some ligand-gated channels (Clark et al., 2010; Dutertre and Lewis, 2010; Bagal et al., 2013; Wulff et al., 2019).

In recent years, under the concept of rational drug design, considering the features of ligands, the structures of receptors, and the motions and dynamics of the system becomes more and more important. Accordingly, numerous computational methods and machine-learning algorithms have been developed (**Figure 3**).

Ligand-Based Approaches

Benefit from these data collected in the early era, ligand-based approaches could be applied to build relatively reliable models to describe the relationship between modulators and the corresponding ion channels, especially when the experimentally-resolved protein structures are absent. One of the typical cases should be the development of ligand-based models for the prediction of human ether-a-go-go related gene hERG potassium ion channel blockage, which is believed to be important in avoiding sudden cardiac death considering its relationship with drug-induced long QT syndrome. In the past few years, a considerable amount of associated data was collected (Konda et al., 2019) and numerous quantitative structure-activity relationship (QSAR) or classification models (Cavalli et al., 2002; Ekins et al., 2002; Roche et al., 2002; Keseru, 2003; Nisius and Goller, 2009; Braga et al., 2015; Siramshetty et al., 2018; Konda et al., 2019) were built for hEGR blockage prediction based on the traditional regression models such as partial least squares, machine learning algorithms including support vector machines (SVM), random forest (RF), gradient boosting machine (GBM) or neural network models. These models have been systematically discussed in the previous reviews (Aronov, 2005; Taboureau and Jorgensen, 2011; Villoutreix and Taboureau, 2015; Vandenberg et al., 2017; Menke et al., 2021).

Actually, besides hERG, the application of the mentioned models is also a common strategy in ligand-based drug design of ion channel modulators when facing abundant research data. For example, in the study of structural-activity relationships of $Na_v1.4$ blockers, both traditional two-dimensional and advanced three-dimensional QSAR models were applied by Carrieri et al. to reveal the structural characteristics of bioactive molecules (Carrieri et al., 2009). Further design of sodium channel blockers was thus inspired. Consequently, a series of tocainide analogues were designed and one of them was verified to have a favorable pharmacodynamic profile and was proposed to be a valid $Na_v1.4$ blocker (Muraglia et al., 2014). Based on the data collected from ChEMBL, BindingDB, and in-house databases, various machine learning-based QSAR models were built by

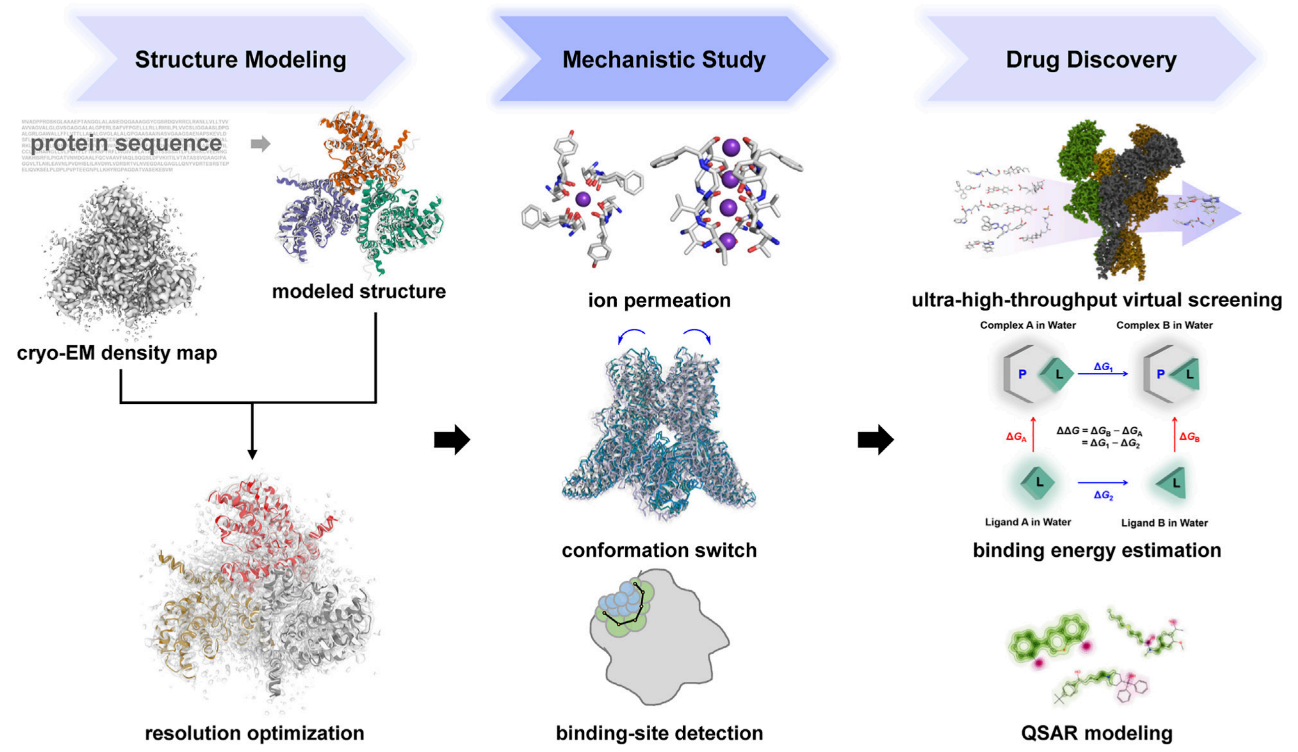

FIGURE 3 | Computational approaches in the structure modeling, mechanistic study and drug discovery of ion channels. Several subplots were collected using Hermite (https://hermite.dp.tech), Mol* viewer (Sehnal et al., 2021), PyMOL (https://github.com/schrodinger/pymol-open-source) and the Pred-hERG web-server (Braga et al., 2015).

Kristam et al. to predict blockers of the voltage-gated sodium ion channel $Na_v1.5$, with the balanced accuracy of 0.88 (at the threshold of 1 μM) and predicted R^2 of 0.71 (RMSE = 0.73 for pIC50) for the classification and regression models, respectively (Khalifa et al., 2020). Similarly, Huang and Xie et al. trained and filtered a classification model based on the data from ChEMBL and BindingDB for the discovery of $Na_v1.7$ blockers (Kong et al., 2020). The Grammar Variational Autoencoder, the trained classification model, and simulated annealing were combined to conduct the molecular optimization and an active compound was found and identified experimentally (Kong et al., 2020). Li et al. studied the pharmacophore hypothesis of ligands that bind at the benzodiazepine site of $GABA_A$ receptors based on ligand-based pharmacophore, 3D-QSAR analysis, and Bayesian models, which might provide useful viewpoints in the discovery of $GABA_A$ modulators (Yang Y. et al., 2013). Because of the potentially limited chemical space the pore-blockers could adapt, approaches based on the three-dimensional similarity between the ligands and reference molecules that take the spatial molecular shape and electrostatic features into consideration (Cleves et al., 2019; Jiang Z. et al., 2021) are possibly another practical ligand-based method in discovering ion channel modulators. Additionally, Bahar et al. proposed a probabilistic matrix factorization (PMF) based scheme to predict unknown drug-target interactions, which focused on the phenotypic similarity of the drugs by grouping the drugs according to the corresponding therapeutic effects (Cobanoglu et al., 2013). The obtained model showed good performance when applied to large data sets of ion-channel-drug pairs (Cobanoglu et al., 2013).

Structure-Based Approaches

In terms of the structural-based approaches, recent computational and machine-learning technologies have empowered the exploration of ion channel modulators mainly in three aspects, viz., structures with higher quality, binding affinity prediction with higher accuracy, and virtual screening with higher throughput (**Figure 3**).

The recent rapid development of protein structure modeling, as well as structural biology, possibly enables the rational design and exploration of ion channel modulators with atomic-resolution structures. Taking again the case of hERG as an example, in the past, owing to the lack of solved hERG channel structure, structural-based exploration mainly relies on structures from homology modeling. With the modeled structure and docked model, Vaz et al. illustrated that the π-stacking formed between the blockers and Phe656 in the protein as well as that of the cation-π interaction involving Tyr652 might be the potential key elements of the pharmacophore (Pearlstein et al., 2003). Similar conclusions associated with the important character of Phe656 were also drawn by the work of Åqvist et, al., which explored the binding of potential hERG blockers using docking and molecular dynamics combined with the linear interaction energy method to evaluate the binding affinities of the potential blockers (Osterberg and Aqvist, 2005). However, numerous experimental ion channel structures have been determined with the cryo-EM technique nowadays, including the human hERG structures that were resolved in 2017 (Wang and MacKinnon, 2017), which might provide a significant cornerstone of the structure-based prediction. Beneficial from the high-resolution structures of the TRPM8 channel in various states (Yin et al., 2018; Diver et al., 2019; Yin et al., 2019), Yang et al. conducted a rational design of the TRPM8 channel and developed a modality-specific inhibitor DeC-1.2, which showed the potential as a novel analgesic against oxaliplatin-induced neuropathic pain (Aierken et al., 2021). Additionally, various protein-folding and modeling tools were also developed (Baek et al., 2021; Jumper et al., 2021), which provide an alternative way for protein structure modeling besides the classic homology modeling approach (Huang et al., 2022), and may also contribute as a start point for the construction of single-particle cryo-EM structures (**Figure 3**). The application of molecular dynamics may be another powerful approach to structural exploration and refinement (Hollingsworth and Dror, 2018; Carnevale et al., 2021). For example, following a multistep protocol, Noskov et al. modeled the open, closed and open-inactive states of the hERG channel to explore the molecular mechanisms behind the state-dependent binding of potential hERG blockers (Durdagi et al., 2012). The missing elements in the homology model were complemented with Rosetta, following all-atom molecular dynamics simulation to refine the obtained structure. The Poisson-Boltzmann calculations conducted based on the ligand-channel complex obtained by the Glide induced-fit docking (IFD) protocol showed a good correlation with the experimental results (Durdagi et al., 2012). Also, starting from the modeled structure, Barakat et al. performed the structural refinement of the $Na_v1.5$ ion channel based on a long-time molecular dynamics simulation of 680 ns in the lipid membrane bilayer (Ahmed et al., 2017). The binding affinities between the reported molecules and the obtained model of the channel were evaluated with AMBER-MM/GBSA. The results demonstrated a good computational-experimental correlation (Pearson coefficient = 0.7) to distinguishing drugs that block or not block the $Na_v1.5$ channel (Ahmed et al., 2017).

Binding affinities of the ion channel modulators are usually evaluated after the construction of reliable modulator-channel complexes. As discussed above, numerous algorithms are available in the historical explorations for binding affinity prediction, including LIE, MM/PBSA, and MM/GBSA, and showed relatively satisfactory results (Osterberg and Aqvist, 2005; Durdagi et al., 2012; Ahmed et al., 2017). Nevertheless, to derive the theoretically more accurate results, the more rigorous defined alchemical methods such as free energy perturbation (FEP) could also be applied to access the binding potency of the channel modulators (Limongelli, 2020). Based on the extensive search for the isoflurane binding sites in the proton gated Gloeobacter violaceus ligand-gated ion channel (GLIC) in their previous study (Brannigan et al., 2010), Klein and Brannigan et al. performed free energy perturbations to evaluate the binding affinities of two anesthetics against GLIC, viz., isoflurane and propofol (LeBard et al., 2012). The evaluated affinities demonstrated good correlations with the previous electrophysiology data (LeBard et al., 2012). In the work of Rempe and Ren et al., FEP was used to determine accurately the thermodynamic stabilities of ion configurations for the potassium channel of *streptomyces* A (KcsA), by comparing the relative free energy difference between various configurations (Jing et al., 2021). The computation results showed good agreement with evidence derived from crystal structures, ion binding experiments, and mutagenesis experiments (Jing et al., 2021). Moreover, machine learning techniques could be introduced in large-scale screening considering the large computational cost of alchemical methods. Bhat et al. showed that it is possible and acceptable to perform more than 5000 FEP calculations in one lead optimization task with the acceleration of active learning (Konze et al., 2019). System-specific scoring functions might provide another efficient way for discovering ion channel modulators. These scoring functions could be constructed either with deep learning or machine learning methods alone or combined with physical-based models (Ain et al., 2015; Wang et al., 2019; Guedes et al., 2021). Numerous studies have demonstrated that the application of target-specific scoring functions outperforms the universal scoring functions on the validation set of DUD-E, which usually covers the major druggable target classes and ion channels are also included (Ain et al., 2015; Wojcikowski et al., 2017; Wang et al., 2019; Guedes et al., 2021).

The development of ultra-high-throughput virtual screening might also be a chance to accelerate the discovery of ion channel modulators. Though various experimental techniques including ion-flux or fluorescence-based assays and electrophysiology measurements are developed for discovering ion channel modulators, however, most of the options are time-consuming and costly for high-throughput screening (Zhang et al., 2016). Under the logic that screening of larger libraries could generally lead to higher quality results (Gorgulla et al., 2020), a variety of programs and algorithms have been developed for ultra-high throughput virtual screening. Generally, the ideas for these approaches include optimization in algorithm engineering to enable high-performance computing (Alhossary et al., 2015; Hassan et al., 2017) and the usage of graphics processing units (Santos-Martins et al., 2021; Shidi et al., 2022), the development of highly-organized workflows (Gorgulla et al., 2020), the application of deep learning which trained QSAR models on docking scores of subsets of the library (Gentile et al., 2020), and the improvement in searching efficiency in a fragment-based manner with the idea partial similar with dynamic programming (Sadybekov et al., 2022). These methods have pushed the limit of virtual screening throughput to libraries with more than tens of billion compounds, and may potentially help the drug discovery of various target classes including ion channels.

COMPUTATIONAL APPROACHES FOR FUNCTIONAL ANALYSIS OF ION CHANNELS

Recent advances in structural biology such as high-resolution cryo-EM have enabled the in-depth study of the functions and mechanisms of ion channels at the molecular scale. However, protein dynamics is essential for the functions of ion channels, which is difficult to infer from static structures. Therefore, computational approaches have been widely applied to explore the dynamic responses and microscopic interactions of macromolecules (**Figure 3**).

Simulation of Ion Conductance

Since the first ion channel structure was published in 1998 by Doyle et al. in their study of the KcsA channel (Doyle et al., 1998), scientists have been using molecular dynamics (MD) simulations to study the interactions between ion channels and their solvent environment. In 2000, Berneche et al. simulated the KcsA K^+ channel in dipalmitoylphosphatidylcholine (DPPC) phospholipid bilayer with KCl aqueous salt solution (Bernèche and Roux, 2000). Their work showed that the translocation of K^+ ion along the ion conductance pathway is facilitated by the structural movements of the extracellular residues Glu 71, Asp80, Arg89, and the selectivity filter residues Val76, Gly77. The dynamics of water and K^+ ions were reported in several simulation studies, where a single file of potassium with water molecules interspersed in between passes along the channel pore (Guidoni et al., 2000; Shrivastava and Sansom, 2000). The observed interactions with the fluctuating selectivity filter laid the foundation for understanding the basis for K^+ selectivity over Na^+. Later, Shrivastava et al. showed that K^+ ions are preferentially coordinated by eight carbonyl oxygens of the filter (Shrivastava et al., 2002), which mimics the salvation shell of hydrated K^+, while the smaller Na^+ ion interacts with four carbonyl organs and two water molecules, which exerts larger distortion on the selectivity filter. Further simulation studies revealed that to accommodate the smaller ionic radius of Na^+ and provide the expected coordination, the dynamic carbonyl groups need to adapt to a "collapsed" state, which builds up unfavorable strain energy. The local interaction mediated by the filter residues and coordinating waters provides a molecular mechanism for ion selectivity in KcsA (Noskov et al., 2004; Noskov and Roux, 2006; Bostick and Brooks, 2007; Noskov and Roux, 2007). After the initial surge of both experimental and simulation studies of the KcsA channel with the availability of its structural information, research has been continuously growing in studying the structures and ion conductance of potassium channels. Long before the crystal structure of the inward rectifier potassium channel Kir6.2 was solved, MD simulation studies had already been conducted on its homology model, which represents another field of computational applications in pursuing structure-based approaches to research (John and Sali, 2003). Capener et al. showed that the Kir6.2 channel model has a similar ion passing motion with KcsA (Capener et al., 2000).

Despite the success of these early studies, a complete permeation event was not described until Khalili-Araghi et al., who applied an electric field of 1 V across the membrane bilayer for the open state of $K_v1.2$ channel during 25 ns of MD simulations, and observed permeation events that are consistent with previous studies, where K^+ ions pass the channel pore through the water-mediated knock-on mechanism (Khalili-Araghi et al., 2006). With increasing computation power, more detailed studies of the ion conductance mechanisms have been carried out. In 2010, Jensen et al. performed simulations on $K_v1.2$ with the voltage ranging between −180 and 180 mV over a total of ~30 μs(Jensen et al., 2010). In this work, not only do they show that the rate-limiting step of K^+ conductance is the formation of the knock-on intermediate, where two ions form direct contact but also revealed a then-novel gating mechanism that at reverse or zero voltage, the channel undergoes a dewetting transition into the intrinsically more stable closed state.

In addition to the direct application of electric field across the membrane, computational electrophysiology has also been used to study ion permeation. This approach uses a double membrane to separate the system into two isolated compartments, and different ion concentrations are created in each compartment to directly form an electrochemical gradient across the membrane. Köpfer et al. used this method to study the K^+ conductance of the archaeal MthK channel from *Methanobacterium thermoautotrophicum* and the eukaryotic $K_v1.2$-$K_v2.1$ chimeric channel in the physiological voltage range (Köpfer et al., 2014). Their results suggest that direct ion-ion contacts instead of co-translocation of alternating ion and water is the key to highly efficient K^+ conductance. Several subsequent studies reported this direct knock-on mechanism for different potassium channels under a variety of simulation conditions (Schewe et al., 2016; Kopec et al., 2018; Kopec et al., 2019; Lolicato et al., 2020). These studies proposed that strong electrostatic repulsion between ions is the main driving force for the fasting permeation of K^+ ions, and the higher energetic penalty for complete desolvation of Na^+ over K^+ contributes to the ion selectivity. The two permeation mechanisms are still under debate. Both experimental and computational research has been providing various support for either of the mechanisms. It cannot be excluded that a mixture of these mechanisms exists depending on the channel and its physiological conditions.

In contrast to K^+ channels, the studies of ion conductance of sodium selective channels have been hindered by relatively fewer structural information. The publication of the prokaryotic voltage-gated sodium channel Na_vAb from *Arcobacter butzleri* with an activated voltage sensor and a closed pore first provided a structural basis for investigations of the selectivity and transport of Na^+ ions (Payandeh et al., 2011). A notable difference between K_v and Na_v channels lies in the selectivity filter. The backbone carbonyl oxygens of the K_v channel selectivity filter loop form the cation binding sites to coordinate and pass on K^+ ions. However, Na_v channel selectivity filters are lined by the side chains, which contribute to the relatively wider and more diversely shaped ion pathways in Na_v channels. This difference puzzled scientists as to how the wider filter provides selectivity for the ion with a smaller atomic radius and prevents K^+ and Ca^{2+} to permeate. Corry and Thomas (Corry and Thomas, 2012) calculated the energetics of ion permeation in Na_vAb via MD simulations, and showed that a plane formed by four of the filter lining glutamate residues prohibits K^+ to be rightly coordinated with water molecule bridging between the cation and the carboxylate groups.

Similar binding geometry of partially-hydrated Na^+ has also been reported in the open state sodium channel from the marine bacterium *Magnetococcus* sp. (Na_vMs) (McCusker et al., 2012), showing that the glutamate side chains form the high field strength ion binding site, which has a lower permeation barrier for Na^+ over K^+ (Ulmschneider et al., 2013). However, the timescale of these studies hampered the observation of concerted movement between ions and proteins. Simulations on the microsecond scale showed that the selectivity filter fluctuates in a coordinated way with ion translocation (Chakrabarti et al., 2013; Boiteux et al., 2014; Ke et al., 2014; Furini and Domene, 2018). With the ion moving across the narrowest part of the pore, the GLU side chains break the symmetric arrangement to coordinate multiple ions to facilitate the passage of the ion into the cavity (Chakrabarti et al., 2013; Boiteux et al., 2014; Guardiani et al., 2017; Callahan and Roux, 2018; Chen et al., 2021). Although simulation studies of bacterial Na_v channels have provided valuable insights into the selectivity and ion conductance of Na_v channels, structures of eukaryotic Na_v channels were not available until 2017 (Shen et al., 2017; Yan et al., 2017; Pan et al., 2018; Shen et al., 2018; Pan et al., 2019; Shen et al., 2019; Jiang et al., 2020). Instead of the homo-tetrameric configuration of the bacterial Na_v channels, the four domains of eukaryotic Na_v channels are formed by a single polypeptide chain, which gives rise to an asymmetrical pore structure. Compared to the EEEE motif of the prokaryotic SF, eukaryotic SF is constituted by aspartic acid, glutamic acid, lysine, and alanine (DEKA), each from one channel domain. Simulation studies suggested that despite this striking structural difference, the asymmetrical SF functions similarly to the symmetrical prokaryotic counterpart. The ASP and GLU residues coordinate the Na^+ ion, and the protonated LYS has been proposed to act as another cation in the knock-on or pass-by mechanism (Zhang J. et al., 2018; Flood et al., 2018).

Analysis of Functional States

Ion channels control the flux of ions by changing between their active and inactive states, which relies on changes between different conformations. Such transitions have proven to be difficult to capture by experimental methods, and even when structures of different states are available, the process of induction and transformation of conformational changes is still hard to explain with the static pictures, which might be important for rational drug design. As a result, computational techniques, especially MD simulations, become useful in studying different function states of ion channels.

As an example, Wen and Zheng performed extensive simulations on the wild-type closed state and the constitutively active mutant of the heat-sensitive cation channel TRPV1 at different temperatures (Wen and Zheng, 2018). They observed a range of hydrogen-bonding network rearrangement between domains in the WT simulations, which are consistent with previous mutational studies, providing a mechanistic explanation of the transition between a closed to pre-open state. Simulations of the gain-of-function mutant complete the process from pre-open to an open state. Similar propagation of movements in the S2-S3 and S4-S5 linkers were observed, suggesting that the dynamic motions in these domains are the key to the channel opening. To study the gating process, Guardiani et al. used targeted molecular dynamics to simulate the transition between closed and open states of the calcium release-activated calcium channel (CRAC) (Guardiani et al., 2021). They reported that upon binding of the activator protein STIM1, a propagation of conformation change occurs from the TM4 to TM1 helices. The extension of TM4 pulls TM3 outward, which in turn moves the lower part of TM1 backward and opens the hydrophobic region of the pore. This result is consistent with patch-clamp experiments on a series of mutants, which showed that disruption of the TM11-TM3 interactions reduces Ca^{2+} influx (Liu et al., 2019).

For mechanosensitive ion channel TREK-2, Aryal et al. simulated changes in membrane tension by changing the area per lipid, and thus studied the effect of lateral pressures on the conformation of the channel (Aryal et al., 2017). They observed that increase in membrane tension induced a transition from the downstate to the upstate. The expansion of the bilayer increases the cross-sectional area of the lower half of the protein, while the upper half remains unchanged to maintain the integrity of the selectivity filter. Interestingly, such membrane stretch does not induce a conformational change in the homologous non-mechanosensitive TWIK-1 channel, indicating that the membrane tension-dependent conformational change is specific to mechanosensitive K2P channels. NOMPC is also a mechanosensitive ion channel, it has, however, been shown to be activated by compression of the intracellular ankyrin repeat domain on the normal plane of the membrane instead of a stretch along the bilayer. In MD simulations, Wang et al. observed that when a pushing force is applied, the TRP domain undergoes an upward movement and clockwise rotation, which induced a rotation in the S6 helices leading to the opening of the channel (Wang et al., 2021). They validated this using patch-clamp experiments and showed that clear electrical signals could be detected when a compressing force was applied, which were abolished with the addition of a NOMPC blocker. Yet, a pulling force was not able to induce a clear NOMPC-dependent current. Another well-known mechanosensitive channel Piezo1 has also attracted a large amount of research attentions. Due to the local bilayer convex curvature imposed by the bowl-like shape of Piezo1, it has been proposed that as membrane tension increases, the protein flattens, which leads to opening of the channel (Guo and MacKinnon, 2017). Since the membrane is a crowded environment, any effects of alteration of the membrane are likely to propagate beyond a single channel. Jiang et al. used a hyperbolic tangent model to study the membrane topology and channel opening as a result of overlapping neighboring Piezo1 membrane footprints. Together with atomistic MD simulations, they found that this overlap decreased bilayer curvature, creating a tension-free opening of Piezo1 (Jiang W. et al., 2021).

Not only has computational methods showed their broad applicability in studying single protein properties, but they also have been used to investigate interactions between channels and their auxiliary proteins. Catte et al. simulated the human $K_v4.3$ channel in complex with one of its auxiliary β-subunits, K_v channel-interacting protein 1 (KChIP1), and detailed the structural and energetic changes of the complex upon mutations in the interfaces of the complex (Catte et al., 2019). By combining computational protein-protein docking, MD simulations, and electrophysiology, Kuenze and co-workers showed that the S1, S4, S5 helices of voltage-gated KCNQ1 potassium channel interacts with a three-amino-acid motif (F57-T58-L59) in the auxiliary protein KCNE1, which modulates the channel gating through an allosteric network with S5-S6 pore helices (Kuenze et al., 2020). With more structures of channel-auxiliary protein complexes available, such as the sodium leak channel NALCN in complex with auxiliary subunit FAM155A (Xie et al., 2020) or the AMPA-subtype ionotropic glutamate receptor with the auxiliary subunit γ2, more computational investigations can be conducted to reveal the underlying mechanistic details of such interactions (Yelshanskaya et al., 2022).

Identification of Binding Site and Allosteric Site

Identifying potential binding sites has become a key step in rational drug discovery. Computational methods for identifying protein-ligand binding sites can be roughly classified into sequence-based and structure-based methods. The main assumption for sequence-based approaches is that functionally important binding sites are highly conserved for proteins to maintain their functionalities. Therefore, these methods scan protein sequences for conserved residues as potential binding sites (Capra and Singh, 2007). However, the lack of spatial and physicochemical information in such predictions limits the ability of these methods in providing reliable binding sites. Consequently, structure-based methods have become the mainstream methods for predicting potential binding sites with the advances in obtaining reliable structures both experimentally and computationally. One of the most common approaches in this category is searching for cavities on protein surfaces. Since such methods were pioneered in the 1990s (Levitt and Banaszak, 1992; Laskowski, 1995), developments in this field have not only incorporated both structural and conservation information (Huang and Schroeder, 2006; Capra et al., 2009), but also allowed predictions regarding properties that are highly relevant to drug discovery such as binding affinities (Laurie and Jackson, 2005; Ngan et al., 2012; Liu et al., 2020) and druggability (Le Guilloux et al., 2009; Volkamer et al., 2012; Yuan et al., 2013; Hussein et al., 2015). Methods that infer binding sites from structurally similar template proteins have also been developed (Brylinski and Skolnick, 2008; Wass et al., 2010; Roy and Zhang, 2012; Yang J. et al., 2013). They take advantage of the quick accumulation of protein structures, and provide relatively reliable binding sites for proteins with templates of high structural similarities. In recent years, artificial intelligence methods have also been applied in the prediction of protein-ligand binding sites, which learned the structural or interaction patterns of the binding sites using schemes such as 3D convolutional neural networks (Jiménez et al., 2017) or grid-based approaches (Pu et al., 2019), and may provide satisfactory results when compared with traditional structure-based methods (Capra et al., 2009; Le Guilloux et al., 2009). Additionally, to consider the dynamic nature of ligand binding, MD simulations are also frequently used besides or together with static pocket detection algorithms (Schmidtke et al., 2011; Ung et al., 2016; Chen et al., 2019).

These methods have been widely applied to investigate ligand binding in ion channels. To validate their deep learning-based binding site detection algorithm BiteNet, Igor and Popov applied it to the ATP-gated cation channel P2X3 (Kozlovskii and Popov, 2020). They were able to successfully identify the binding sites for the endogenous agonist ATP and the antagonist AF-219. It is worth noting that such success depends on the protein conformational state. The difference between the agonist-bound and the antagonist-bound conformations prevents the correct prediction of the agonist binding site in the antagonist-bound conformation and vice versa. This is a common limitation of pocket prediction methods using static structures. Nguyen et al. constructed a homology model of human $Na_v1.5$ based on electric eel $Na_v1.4$ (Yan et al., 2017), and used molecular docking to identify binding locations of antiarrhythmic and local anesthetic drugs, lidocaine, flecainide, and ranolazine (Nguyen et al., 2019). Starting from five different initial locations, they were able to locate binding hot spots of each drug, which are consistent with regions suggested by experimental data. Further multi-microsecond MD simulations revealed detailed mechanistic insights into the dynamic passage and binding of the ligands. Faulkner et al. performed atomistic MD simulations to probe the binding sites of the opioid analgesic fentanyl on the GLIC channel (Faulkner et al., 2019). Fentanyl molecules were placed in a bulk solution to allow free exploration of potential binding sites on the protein, and binding affinities of each site were assessed by molecular mechanics Poisson–Boltzmann surface area (MM/PBSA) calculations (Miller et al., 2012). The newly identified stable binding sites in GLIC are different from previously observed sites for other general anesthetics. They also reported that the binding of fentanyl to one of these novel sites leads to conformational changes, which results in the formation of a hydrophobic gate inhibiting ion conductance through the channel.

Targeting allosteric binding sites of ion channels has aroused more and more attention in recent years considering that the emblematic pore-blocking strategy that targets the highly conserved region might suffer from poor subtype specificity (Marzian et al., 2013). The allosteric effect refers to the phenomenon that the modulation of a binding site (named as allosteric site) differed from the classic active site (referred to as the orthosteric site) resulting in the functional change of the protein. A variety of allosteric sites and the corresponding modulators have been discovered in the field of ion channels, according to that organized in the Allosteric Database (Huang et al., 2011; Huang et al., 2014). Using the comprehensive alanine-scanning mutagenesis, patch-clamp electrophysiological recordings as well as molecular docking and molecular dynamic simulation approaches, Decher et al. showed that the K_v1 inhibitor Psora-4 could bind to another less conserved site of the channel in addition to the central pore cavity, which demonstrated a new allosteric site of the $K_v1.x$ channels and thus provided the molecular basis for the development of novel selective voltage-gated channel inhibitors (Marzian et al., 2013). Under the similar strategies, with TKDC, an inhibitor of the TREK subfamily, as the chemical probe, Yang et al. conducted a study combining molecular simulation, mutagenesis, and electrophysiology, and revealed an allosteric site of the two-pore domain potassium (K2P) channel that located in the extracellular cap of the channel (Luo et al., 2017). Accordingly, virtual screening was performed and a series of new inhibitors were identified (Luo et al., 2017). With the combination of molecular dynamics and oocyte electrophysiology studies, Lindahl et al. revealed the special motion and modulation with the modification of a transmembrane binding site within each subunit of the GLIC channel, which thus supports the multisite model of transmembrane allosteric modulation of the channel (Heusser et al., 2018). Using microseconds long atomistic MD simulations, Botello-Smith et al. identified the binding site of the allosteric agonist Yoda1 of Piezo1 (Botello-Smith et al., 2019). Their study indicated that Yoda1 binds at a site approximately 40 A aways from the channel pore, and modulates the channel activity by facilitating force-induced motions of the bound subunit. Similar research was also conducted in various ion channel systems by different groups, including the voltage-gated KCNQ1 potassium channel (Kuenze et al., 2020) and the large-conductance mechanosensitive channel MscL (Kapsalis et al., 2019).

The prediction of potential allosteric sites might also be empowered with the combination of machine learning or deep learning approaches and molecular simulation strategies. The general idea of these algorithms is to analyze the correlation between the orthogonal site and the allosteric site. The prediction could be conducted based on either a single protein structure or combined with trajectories from molecular simulation. In the former case, the correlation might be analyzed based on perturbation exerted on the orthogonal sites using a network model including an elastic network model, anisotropic network model, and graph-based model (Amor et al., 2016; Dokholyan, 2016; Zhang and Nussinov, 2019; Wang J. et al., 2020; Huang et al., 2021; Mersmann et al., 2021; Zheng, 2021; Wu et al., 2022). In the latter case, as described in the cases mentioned above, the results of the simulation-based approaches rely heavily on sampling efficiency. Recently, the reinforced dynamics scheme was reported by Zhang and Wang et al. by constructing the free energy surface with deep neural network models, which turn out to be highly efficient in sampling high-dimensional free energy landscapes (Zhang L. et al., 2018; Wang et al., 2022), and thus might provide new insights into the allosteric modulation of ion channels based on the comprehensive exploration of the protein structural dynamics. Additionally, the evolutionary-based approach could predict the allosteric communication in proteins as well by analyzing the evolutionarily conserved networks of residues (Suel et al., 2003). Case studies also showed that the evolutionary insights could contribute to the understanding of allosteric regulation of the TRP Ion channels (Hilton et al., 2019). However, an in-depth discussion of the principle of the algorithms is beyond the scope of this paper. Details of the algorithms are referred to in the previous literature (Dokholyan, 2016; Liu and Nussinov, 2016; Zhang and Nussinov, 2019).

CONCLUSION

Ion channels have long been concerned as medically important drug targets. Increasing the ligand screening throughput and ligand binding selectivity are the main challenges in the search for highly potent ion-channel modulators. As the potential key to meeting these challenges, the practice of rational drug design has long been expected.

Resolving the molecular structures of ion channels is getting easier owing to the rapid development of single-particle cryo-EM. Also, the impressive progress in protein structure prediction is bringing fundamental changes to structural biology. Although accurate predictions of multimeric structures, protein-protein interactions and multiple conformations remain challenging, we are already seeing progress in these directions such as the structural prediction of core eukaryotic protein complexes (Humphreys et al., 2021), heterodimeric protein complexes (Bryant et al., 2022) and alternative conformations for receptors and transporters (Del Alamo et al., 2022). Innovations and applications of protein folding algorithms have been accelerated through open-sourcing AlphaFold2-comparable high-performance training code[3], and online tools such as ColabFold (Mirdita et al., 2022) and Uni-Fold[4]. It is expected that protein folding algorithms will soon be used to study ion channel conformational states and channel-modulator interactions, even for new channel discoveries. Results from the exploration in the drug discovery era driven by occasions and classic synthetic chemistry enabled reliable computational models through ligand-based approaches. More abundant and higher quality ion channel structures (obtained either experimentally or computationally), as well as accurate binding affinity predictions and ultra-high-throughput virtual screening, have pushed forward structure-based rational drug design. Besides techniques based on static protein structures, simulation and machine-learning-based methods also allow us to explore the dynamic nature of ion channels and direct the rational drug design process. Various computational studies have revealed the molecular mechanisms of channel functions and potential ligand-binding sites, especially allosteric binding sites. With help from these computational methods, we expect the implementation of a more effective drug discovery paradigm in the coming future (de Oliveira et al., 2021; Lees et al., 2021; Robertson et al., 2022).

---

[3] https://github.com/dptech-corp/Uni-Fold

[4] Hermite platform: https://hermite.dp.tech

AUTHOR CONTRIBUTIONS

ZZ, ZD and HW conceptualized and finalized the manuscript; ZZ, ZD, QW, YW, DZ, RX, LG, HW drafted the manuscript.

REFERENCES

Ackerman, M. J., and Clapham, D. E. (1997). Ion Channels-Bbasic Science and Clinical Disease. *N. Engl. J. Med.* 336, 1575–1586. doi:10.1056/nejm199705293362207

Ahmed, M., Jalily Hasani, H., Ganesan, A., Houghton, M., and Barakat, K. (2017). Modeling the Human Nav1.5 Sodium Channel: Structural and Mechanistic Insights of Ion Permeation and Drug Blockade. *Drug Des. Devel Ther.* 11, 2301–2324. doi:10.2147/dddt.S133944

Aierken, A., Xie, Y. K., Dong, W., Apaer, A., Lin, J. J., Zhao, Z., et al. (2021). Rational Design of a Modality-Specific Inhibitor of TRPM8 Channel against Oxaliplatin-Induced Cold Allodynia. *Adv. Sci.* 8, 2101717. doi:10.1002/advs.202101717

Ain, Q. U., Aleksandrova, A., Roessler, F. D., and Ballester, P. J. (2015). Machine-learning Scoring Functions to Improve Structure-Based Binding Affinity Prediction and Virtual Screening. *Wiley Interdiscip. Rev. Comput. Mol. Sci.* 5, 405–424. doi:10.1002/wcms.1225

Alessandri, B., Bättig, K., and Welzl, H. (1989). Effects of Ketamine on Tunnel Maze and Water Maze Performance in the Rat. *Behav. Neural Biol.* 52, 194–212. doi:10.1016/S0163-1047(89)90313-0

Alexander, S. P. H., Christopoulos, A., Davenport, A. P., Kelly, E., Mathie, A., Peters, J. A., et al. (2019). The Concise Guide to Pharmacology 2019/20: G Protein-Coupled Receptors. *Br. J. Pharmacol.* 176, S21–S141. doi:10.1111/bph.14748

Alhossary, A., Handoko, S. D., Mu, Y., and Kwoh, C. K. (2015). Fast, Accurate, and Reliable Molecular Docking with QuickVina 2. *Bioinformatics* 31, 2214–2216. doi:10.1093/bioinformatics/btv082

Alnabati, E., and Kihara, D. (2019). Advances in Structure Modeling Methods for Cryo-Electron Microscopy Maps. *Molecules* 25, 82. doi:10.3390/molecules25010082

Amor, B. R., Schaub, M. T., Yaliraki, S. N., and Barahona, M. (2016). Prediction of Allosteric Sites and Mediating Interactions through Bond-To-Bond Propensities. *Nat. Commun.* 7, 12477. doi:10.1038/ncomms12477

Argudo, D., Capponi, S., Bethel, N. P., and Grabe, M. (2019). A Multiscale Model of Mechanotransduction by the Ankyrin Chains of the NOMPC Channel. *J. Gen. Physiol.* 151, 316–327. doi:10.1085/jgp.201812266

Aronov, A. M. (2005). Predictive In Silico Modeling for hERG Channel Blockers. *Drug Discov. Today* 10, 149–155. doi:10.1016/s1359-6446(04)03278-7

Aryal, P., Jarerattanachat, V., Clausen, M. V., Schewe, M., McClenaghan, C., Argent, L., et al. (2017). Bilayer-Mediated Structural Transitions Control Mechanosensitivity of the TREK-2 K2P Channel. *Structure* 25, 708–e2. doi:10.1016/j.str.2017.03.006

Baek, M., DiMaio, F., Anishchenko, I., Dauparas, J., Ovchinnikov, S., Lee, G. R., et al. (2021). Accurate Prediction of Protein Structures and Interactions Using a Three-Track Neural Network. *Science* 373, 871–876. doi:10.1126/science.abj8754

Bagal, S. K., Brown, A. D., Cox, P. J., Omoto, K., Owen, R. M., Pryde, D. C., et al. (2013). Ion Channels as Therapeutic Targets: A Drug Discovery Perspective. *J. Med. Chem.* 56, 593–624. doi:10.1021/jm3011433

Baker, M. L., Abeysinghe, S. S., Schuh, S., Coleman, R. A., Abrams, A., Marsh, M. P., et al. (2011). Modeling Protein Structure at Near Atomic Resolutions with Gorgon. *J. Struct. Biol.* 174, 360–373. doi:10.1016/j.jsb.2011.01.015

Baker, M. R., Rees, I., Ludtke, S. J., Chiu, W., and Baker, M. L. (2012). Constructing and Validating Initial Cα Models from Subnanometer Resolution Density Maps with Pathwalking. *Structure* 20, 450–463. doi:10.1016/j.str.2012.01.008

Barad, B. A., Echols, N., Wang, R. Y., Cheng, Y., DiMaio, F., Adams, P. D., et al. (2015). EMRinger: Side Chain-Directed Model and Map Validation for 3D Cryo-Electron Microscopy. *Nat. Methods* 12, 943–946. doi:10.1038/nmeth.3541

ACKNOWLEDGMENTS

ZZ thanks Prof. Weinan E and Prof. Jianfeng Pei for the sponsorship of his postdoctoral research.

Basak, S., Gicheru, Y., Kapoor, A., Mayer, M. L., Filizola, M., and Chakrapani, S. (2019). Molecular Mechanism of Setron-Mediated Inhibition of Full-Length 5-HT3A Receptor. *Nat. Commun.* 10, 3225. doi:10.1038/s41467-019-11142-8

Bennett, D. L., Clark, A. J., Huang, J., Waxman, S. G., and Dib-Hajj, S. D. (2019). The Role of Voltage-Gated Sodium Channels in Pain Signaling. *Physiol. Rev.* 99, 1079–1151. doi:10.1152/physrev.00052.2017

Bernèche, S., and Roux, B. (2000). Molecular Dynamics of the KcsA K(+) Channel in a Bilayer Membrane. *Biophys. J.* 78, 2900–2917. doi:10.1016/s0006-3495(00)76831-7

Bobadilla, J. L., Macek, M., Jr., Fine, J. P., and Farrell, P. M. (2002). Cystic Fibrosis: a Worldwide Analysis of CFTR Mutations-Ccorrelation with Incidence Data and Application to Screening. *Hum. Mutat.* 19, 575–606. doi:10.1002/humu.10041

Boiteux, C., Vorobyov, I., and Allen, T. W. (2014). Ion Conduction and Conformational Flexibility of a Bacterial Voltage-Gated Sodium Channel. *Proc. Natl. Acad. Sci. U. S. A.* 111, 3454–3459. doi:10.1073/pnas.1320907111

Bostick, D. L., and Brooks, C. L. (2007). Selectivity in K+ Channels Is Due to Topological Control of the Permeant Ion's Coordinated State. *Proc. Natl. Acad. Sci. U. S. A.* 104, 9260–9265. doi:10.1073/pnas.0700554104

Botello-Smith, W. M., Jiang, W., Zhang, H., Ozkan, A. D., Lin, Y. C., Pham, C. N., et al. (2019). A Mechanism for the Activation of the Mechanosensitive Piezo1 Channel by the Small Molecule Yoda1. *Nat. Commun.* 10, 4503. doi:10.1038/s41467-019-12501-1

Bourinet, E., Altier, C., Hildebrand, M. E., Trang, T., Salter, M. W., and Zamponi, G. W. (2014). Calcium-Permeable Ion Channels in Pain Signaling. *Physiol. Rev.* 94, 81–140. doi:10.1152/physrev.00023.2013

Braestrup, C., and Squires, R. F. (1977). Specific Benzodiazepine Receptors in Rat Brain Characterized by High-Affinity (3H)diazepam Binding. *Proc. Natl. Acad. Sci. U. S. A.* 74, 3805–3809. doi:10.1073/pnas.74.9.3805

Braga, R. C., Alves, V. M., Silva, M. F., Muratov, E., Fourches, D., Lião, L. M., et al. (2015). Pred-hERG: A Novel Web-Accessible Computational Tool for Predicting Cardiac Toxicity. *Mol. Inf.* 34, 698–701. doi:10.1002/minf.201500040

Brannigan, G., LeBard, D. N., Hénin, J., Eckenhoff, R. G., and Klein, M. L. (2010). Multiple Binding Sites for the General Anesthetic Isoflurane Identified in the Nicotinic Acetylcholine Receptor Transmembrane Domain. *Proc. Natl. Acad. Sci. U. S. A.* 107, 14122–14127. doi:10.1073/pnas.1008534107

Brugnoni, R., Canioni, E., Filosto, M., Pini, A., Tonin, P., Rossi, T., et al. (2022). Mutations Associated with Hypokalemic Periodic Paralysis: from Hotspot Regions to Complete Analysis of CACNA1S and SCN4A Genes. *Neurogenetics* 23, 19–25. doi:10.1007/s10048-021-00673-2

Bryant, P., Pozzati, G., and Elofsson, A. (2022). Improved Prediction of Protein-Protein Interactions Using AlphaFold2. *Nat. Commun.* 13. doi:10.1038/s41467-022-28865-w

Brylinski, M., and Skolnick, J. (2008). A Threading-Based Method (FINDSITE) for Ligand-Binding Site Prediction and Functional Annotation. *Proc. Natl. Acad. Sci. U. S. A.* 105, 129–134. doi:10.1073/pnas.0707684105

Calcaterra, N. E., and Barrow, J. C. (2014). Classics in Chemical Neuroscience: Diazepam (Valium). *ACS Chem. Neurosci.* 5, 253–260. doi:10.1021/cn5000056

Callahan, K. M., and Roux, B. (2018). Molecular Dynamics of Ion Conduction through the Selectivity Filter of the NaVAb Sodium Channel. *J. Phys. Chem. B* 122, 10126–10142. doi:10.1021/acs.jpcb.8b09678

Capener, C. E., Shrivastava, I. H., Ranatunga, K. M., Forrest, L. R., Smith, G. R., and Sansom, M. S. (2000). Homology Modeling and Molecular Dynamics Simulation Studies of an Inward Rectifier Potassium Channel. *Biophys. J.* 78, 2929–2942. doi:10.1016/s0006-3495(00)76833-0

Capra, J. A., Laskowski, R. A., Thornton, J. M., Singh, M., and Funkhouser, T. A. (2009). Predicting Protein Ligand Binding Sites by Combining Evolutionary Sequence Conservation and 3D Structure. *PLoS. Comput. Biol.* 5, e1000585. doi:10.1371/journal.pcbi.1000585

Capra, J. A., and Singh, M. (2007). Predicting Functionally Important Residues from Sequence Conservation. *Bioinformatics* 23, 1875–1882. doi:10.1093/bioinformatics/btm270

Carnevale, V., Delemotte, L., and Howard, R. J. (2021). Molecular Dynamics Simulations of Ion Channels. *Trends biochem. Sci.* 46, 621–622. doi:10.1016/j.tibs.2021.04.005

Carrieri, A., Muraglia, M., Corbo, F., and Pacifico, C. (2009). 2D- and 3D-QSAR of Tocainide and Mexiletine Analogues Acting as Na(v)1.4 Channel Blockers. *Eur. J. Med. Chem.* 44, 1477–1485. doi:10.1016/j.ejmech.2008.10.005

Casañal, A., Lohkamp, B., and Emsley, P. (2020). Current Developments in Coot for Macromolecular Model Building of Electron Cryo-Microscopy and Crystallographic Data. *Protein Sci.* 29, 1069–1078. doi:10.1002/pro.3791

Case, D. A., Cheatham, T. E., Darden, T., Gohlke, H., Luo, R., Merz, K. M., et al. (2005). The Amber Biomolecular Simulation Programs. *J. Comput. Chem.* 26, 1668–1688. doi:10.1002/jcc.20290

Catalano, C., Ben-Hail, D., Qiu, W., Blount, P., des Georges, A., and Guo, Y. (2021). Cryo-EM Structure of Mechanosensitive Channel YnaI Using SMA2000: Challenges and Opportunities. *Membr. (Basel)* 11, 849. doi:10.3390/membranes11110849

Catte, A., Ferbel, L., Bhattacharjee, N., Jan Akhunzada, M., D'Agostino, T., and Brancato, G. (2019). In Silico investigation of the Interaction between the Voltage-Gated Potassium Channel Kv4.3 and its Auxiliary Protein KChIP1. *Phys. Chem. Chem. Phys.* 21, 25290–25301. doi:10.1039/c9cp04082j

Catterall, W. A. (2000). From Ionic Currents to Molecular Mechanisms: the Structure and Function of Voltage-Gated Sodium Channels. *Neuron* 26, 13–25. doi:10.1016/s0896-6273(00)81133-2

Catterall, W. A. (2010). Ion Channel Voltage Sensors: Structure, Function, and Pathophysiology. *Neuron* 67, 915–928. doi:10.1016/j.neuron.2010.08.021

Catterall, W. A. (2011). Voltage-gated Calcium Channels. *Cold Spring Harb. Perspect. Biol.* 3, a003947. doi:10.1101/cshperspect.a003947

Cavalli, A., Poluzzi, E., De Ponti, F., and Recanatini, M. (2002). Toward a Pharmacophore for Drugs Inducing the Long QT Syndrome: Insights from a CoMFA Study of HERG K(+) Channel Blockers. *J. Med. Chem.* 45, 3844–3853. doi:10.1021/jm0208875

Chacón, P., and Wriggers, W. (2002). Multi-resolution Contour-Based Fitting of Macromolecular Structures. *J. Mol. Biol.* 317, 375–384. doi:10.1006/jmbi.2002.5438

Chakrabarti, N., Ing, C., Payandeh, J., Zheng, N., Catterall, W. A., and Pomès, R. (2013). Catalysis of Na+ Permeation in the Bacterial Sodium Channel Na(V) Ab. *Proc. Natl. Acad. Sci. U. S. A.* 110, 11331–11336. doi:10.1073/pnas.1309452110

Chan, K. Y., Gumbart, J., McGreevy, R., Watermeyer, J. M., Sewell, B. T., and Schulten, K. (2011). Symmetry-restrained Flexible Fitting for Symmetric EM Maps. *Structure* 19, 1211–1218. doi:10.1016/j.str.2011.07.017

Chen, A. Y., Brooks, B. R., and Damjanovic, A. (2021). Determinants of Conductance of a Bacterial Voltage-Gated Sodium Channel. *Biophys. J.* 120, 3050–3069. doi:10.1016/j.bpj.2021.06.013

Chen, M., Baldwin, P. R., Ludtke, S. J., and Baker, M. L. (2016). De Novo modeling in Cryo-EM Density Maps with Pathwalking. *J. Struct. Biol.* 196, 289–298. doi:10.1016/j.jsb.2016.06.004

Chen, M., and Ludtke, S. J. (2021). Deep Learning-Based Mixed-Dimensional Gaussian Mixture Model for Characterizing Variability in Cryo-EM. *Nat. Methods* 18, 930–936. doi:10.1038/s41592-021-01220-5

Chen, Z., Zhang, X., Peng, C., Wang, J., Xu, Z., Chen, K., et al. (2019). D3Pockets: A Method and Web Server for Systematic Analysis of Protein Pocket Dynamics. *J. Chem. Inf. Model.* 59, 3353–3358. doi:10.1021/acs.jcim.9b00332

Cheng, Y. (2018). Membrane Protein Structural Biology in the Era of Single Particle Cryo-EM. *Curr. Opin. Struct. Biol.* 52, 58–63. doi:10.1016/j.sbi.2018.08.008

Clapham, D. E. (2003). TRP Channels as Cellular Sensors. *Nature* 426, 517–524. doi:10.1038/nature02196

Clare, J. J. (2010). Targeting Ion Channels for Drug Discovery. *Discov. Med.* 9, 253–260.

Clark, R. J., Jensen, J., Nevin, S. T., Callaghan, B. P., Adams, D. J., and Craik, D. J. (2010). The Engineering of an Orally Active Conotoxin for the Treatment of Neuropathic Pain. *Angew. Chem. Int. Ed. Engl.* 49, 6545–6548. doi:10.1002/anie.201000620

Cleves, A. E., Johnson, S. R., and Jain, A. N. (2019). Electrostatic-field and Surface-Shape Similarity for Virtual Screening and Pose Prediction. *J. Comput. Aided Mol. Des.* 33, 865–886. doi:10.1007/s10822-019-00236-6

Cobanoglu, M. C., Liu, C., Hu, F., Oltvai, Z. N., and Bahar, I. (2013). Predicting Drug-Target Interactions Using Probabilistic Matrix Factorization. *J. Chem. Inf. Model.* 53, 3399–3409. doi:10.1021/ci400219z

Coe, J. W., Brooks, P. R., Vetelino, M. G., Wirtz, M. C., Arnold, E. P., Huang, J., et al. (2005). Varenicline: an Alpha4beta2 Nicotinic Receptor Partial Agonist for Smoking Cessation. *J. Med. Chem.* 48, 3474–3477. doi:10.1021/jm050069n

Corry, B., and Thomas, M. (2012). Mechanism of Ion Permeation and Selectivity in a Voltage Gated Sodium Channel. *J. Am. Chem. Soc.* 134, 1840–1846. doi:10.1021/ja210020h

Costa, M. G. S., Fagnen, C., Vénien-Bryan, C., and Perahia, D. (2020). A New Strategy for Atomic Flexible Fitting in Cryo-EM Maps by Molecular Dynamics with Excited Normal Modes (MDeNM-EMfit). *J. Chem. Inf. Model.* 60, 2419–2423. doi:10.1021/acs.jcim.9b01148

Coste, B., Mathur, J., Schmidt, M., Earley, T. J., Ranade, S., Petrus, M. J., et al. (2010). Piezo1 and Piezo2 Are Essential Components of Distinct Mechanically Activated Cation Channels. *Science* 330, 55–60. doi:10.1126/science.1193270

Cox, B. (2015). "Chapter 1 Ion Channel Drug Discovery: a Historical Perspective," in *Ion Channel Drug Discovery* (Cambridge, United Kingdom: The Royal Society of Chemistry), 1–15.

Croll, T. I. (2018). ISOLDE: a Physically Realistic Environment for Model Building into Low-Resolution Electron-Density Maps. *Acta Crystallogr. D. Struct. Biol.* 74, 519–530. doi:10.1107/s2059798318002425

Crowther, R. A. (2016). *The Resolution Revolution: Recent Advances in cryoEM*. Academic Press.

Daly, E. J., Singh, J. B., Fedgchin, M., Cooper, K., Lim, P., Shelton, R. C., et al. (2018). Efficacy and Safety of Intranasal Esketamine Adjunctive to Oral Antidepressant Therapy in Treatment-Resistant Depression: A Randomized Clinical Trial. *JAMA Psychiatry* 75, 139–148. doi:10.1001/jamapsychiatry.2017.3739

Dang, S., van Goor, M. K., Asarnow, D., Wang, Y., Julius, D., Cheng, Y., et al. (2019). Structural Insight into TRPV5 Channel Function and Modulation. *Proc. Natl. Acad. Sci. U. S. A.* 116, 8869–8878. doi:10.1073/pnas.1820323116

Daniel, N. H., Aravind, A., and Thakur, P. (2021). Are Ion Channels Potential Therapeutic Targets for Parkinson's Disease? *Neurotoxicology* 87, 243–257. doi:10.1016/j.neuro.2021.10.008

de Oliveira, T. M., van Beek, L., Shilliday, F., Debreczeni, J. É., and Phillips, C. (2021). Cryo-EM: The Resolution Revolution and Drug Discovery. *SLAS Discov.* 26, 17–31. doi:10.1177/2472555220960401

Del Alamo, D., Sala, D., McHaourab, H. S., and Meiler, J. (2022). Sampling Alternative Conformational States of Transporters and Receptors with AlphaFold2. *eLife* 11, e75751. doi:10.7554/eLife.75751

Derevyanko, G., and Grudinin, S. (2014). HermiteFit: Fast-Fitting Atomic Structures into a Low-Resolution Density Map Using Three-Dimensional Orthogonal Hermite Functions. *Acta Crystallogr. D. Biol. Crystallogr.* 70, 2069–2084. doi:10.1107/s1399004714011493

Diver, M. M., Cheng, Y., and Julius, D. (2019). Structural Insights into TRPM8 Inhibition and Desensitization. *Science* 365, 1434–1440. doi:10.1126/science.aax6672

Dokholyan, N. V. (2016). Controlling Allosteric Networks in Proteins. *Chem. Rev.* 116, 6463–6487. doi:10.1021/acs.chemrev.5b00544

Doyle, D. A., Morais Cabral, J., Pfuetzner, R. A., Kuo, A., Gulbis, J. M., Cohen, S. L., et al. (1998). The Structure of the Potassium Channel: Molecular Basis of K+ Conduction and Selectivity. *Science* 280, 69–77. doi:10.1126/science.280.5360.69

Dunlop, J., Bowlby, M., Peri, R., Vasilyev, D., and Arias, R. (2008). High-throughput Electrophysiology: an Emerging Paradigm for Ion-Channel Screening and Physiology. *Nat. Rev. Drug Discov.* 7, 358–368. doi:10.1038/nrd2552

Durdagi, S., Deshpande, S., Duff, H. J., and Noskov, S. Y. (2012). Modeling of Open, Closed, and Open-Inactivated States of the hERG1 Channel: Structural Mechanisms of the State-dependent Drug Binding. *J. Chem. Inf. Model.* 52, 2760–2774. doi:10.1021/ci300353u

Dutertre, S., and Lewis, R. J. (2010). Use of Venom Peptides to Probe Ion Channel Structure and Function. *J. Biol. Chem.* 285, 13315–13320. doi:10.1074/jbc.R109.076596

Ekins, S., Crumb, W. J., Sarazan, R. D., Wikel, J. H., and Wrighton, S. A. (2002). Three-dimensional Quantitative Structure-Activity Relationship for Inhibition of Human Ether-A-Go-Go-Related Gene Potassium Channel. *J. Pharmacol. Exp. Ther.* 301, 427–434. doi:10.1124/jpet.301.2.427

Escayg, A., MacDonald, B. T., Meisler, M. H., Baulac, S., Huberfeld, G., An-Gourfinkel, I., et al. (2000). Mutations of SCN1A, Encoding a Neuronal Sodium Channel, in Two Families with GEFS+2. *Nat. Genet.* 24, 343–345. doi:10.1038/74159

Faulkner, C., Plant, D. F., and De Leeuw, N. H. (2019). Modulation of the Gloeobacter Violaceus Ion Channel by Fentanyl: A Molecular Dynamics Study. *Biochemistry* 58, 4804–4808. doi:10.1021/acs.biochem.9b00881

Flood, E., Boiteux, C., and Allen, T. W. (2018). Selective Ion Permeation Involves Complexation with Carboxylates and Lysine in a Model Human Sodium Channel. *PLoS. Comput. Biol.* 14, e1006398. doi:10.1371/journal.pcbi.1006398

Flood, E., Boiteux, C., Lev, B., Vorobyov, I., and Allen, T. W. (2019). Atomistic Simulations of Membrane Ion Channel Conduction, Gating, and Modulation. *Chem. Rev.* 119, 7737–7832. doi:10.1021/acs.chemrev.8b00630

Frank, J. (2017). Advances in the Field of Single-Particle Cryo-Electron Microscopy over the Last Decade. *Nat. Protoc.* 12, 209–212. doi:10.1038/nprot.2017.004

Frank, J., and Ourmazd, A. (2016). Continuous Changes in Structure Mapped by Manifold Embedding of Single-Particle Data in Cryo-EM. *Methods* 100, 61–67. doi:10.1016/j.ymeth.2016.02.007

Frenz, B., Walls, A. C., Egelman, E. H., Veesler, D., and DiMaio, F. (2017). RosettaES: a Sampling Strategy Enabling Automated Interpretation of Difficult Cryo-EM Maps. *Nat. Methods* 14, 797–800. doi:10.1038/nmeth.4340

Furini, S., and Domene, C. (2018). Ion-triggered Selectivity in Bacterial Sodium Channels. *Proc. Natl. Acad. Sci. U. S. A.* 115, 5450–5455. doi:10.1073/pnas.1722516115

Garzón, J. I., Kovacs, J., Abagyan, R., and Chacón, P. (2007). ADP_EM: Fast Exhaustive Multi-Resolution Docking for High-Throughput Coverage. *Bioinformatics* 23, 427–433. doi:10.1093/bioinformatics/btl625

Gentile, F., Agrawal, V., Hsing, M., Ton, A. T., Ban, F., Norinder, U., et al. (2020). Deep Docking: A Deep Learning Platform for Augmentation of Structure Based Drug Discovery. *ACS Cent. Sci.* 6, 939–949. doi:10.1021/acscentsci.0c00229

Gonzales, E. B., and Sumien, N. (2017). Acidity and Acid-Sensing Ion Channels in the Normal and Alzheimer's Disease Brain. *J. Alzheimers Dis.* 57, 1137–1144. doi:10.3233/jad-161131

Gorgulla, C., Boeszoermenyi, A., Wang, Z. F., Fischer, P. D., Coote, P. W., Padmanabha Das, K. M., et al. (2020). An Open-Source Drug Discovery Platform Enables Ultra-large Virtual Screens. *Nature* 580, 663–668. doi:10.1038/s41586-020-2117-z

Grant, S. M., and Faulds, D. (1992). Oxcarbazepine. A Review of its Pharmacology and Therapeutic Potential in Epilepsy, Trigeminal Neuralgia and Affective Disorders. *Drugs* 43, 873–888. doi:10.2165/00003495-199243060-00007

Grant, T., Rohou, A., and Grigorieff, N. (2018). cisTEM, User-Friendly Software for Single-Particle Image Processing. *eLife* 7, e35383. doi:10.7554/eLife.35383

Guardiani, C., Rodger, P. M., Fedorenko, O. A., Roberts, S. K., and Khovanov, I. A. (2017). Sodium Binding Sites and Permeation Mechanism in the NaChBac Channel: A Molecular Dynamics Study. *J. Chem. Theory Comput.* 13, 1389–1400. doi:10.1021/acs.jctc.6b01035

Guardiani, C., Sun, D., and Giacomello, A. (2021). Unveiling the Gating Mechanism of CRAC Channel: A Computational Study. *Front. Mol. Biosci.* 8. doi:10.3389/fmolb.2021.773388

Guedes, I. A., Barreto, A. M. S., Marinho, D., Krempser, E., Kuenemann, M. A., Sperandio, O., et al. (2021). New Machine Learning and Physics-Based Scoring Functions for Drug Discovery. *Sci. Rep.* 11, 3198. doi:10.1038/s41598-021-82410-1

Guidoni, L., Torre, V., and Carloni, P. (2000). Water and Potassium Dynamics inside the KcsA K(+) Channel. *FEBS Lett.* 477, 37–42. doi:10.1016/s0014-5793(00)01712-9

Gulbis, J. M., Mann, S., and MacKinnon, R. (1999). Structure of a Voltage-dependent K+ Channel Beta Subunit. *Cell* 97, 943–952. doi:10.1016/s0092-8674(00)80805-3

Guo, Y. R., and MacKinnon, R. (2017). Structure-based Membrane Dome Mechanism for Piezo Mechanosensitivity. *eLife* 6, e33660. doi:10.7554/eLife.33660

Gupta, M. K., and Vadde, R. (2021). A Computational Structural Biology Study to Understand the Impact of Mutation on Structure-Function Relationship of Inward-Rectifier Potassium Ion Channel Kir6.2 in Human. *J. Biomol. Struct. Dyn.* 39, 1447–1460. doi:10.1080/07391102.2020.1733666

Hassan, N. M., Alhossary, A. A., Mu, Y., and Kwoh, C. K. (2017). Protein-Ligand Blind Docking Using QuickVina-W with Inter-process Spatio-Temporal Integration. *Sci. Rep.* 7, 15451. doi:10.1038/s41598-017-15571-7

He, J., and Huang, S.-Y. (2021). Full-length De Novo Protein Structure Determination from Cryo-EM Maps Using Deep Learning. *Bioinformatics* 37, 3480–3490. doi:10.1093/bioinformatics/btab357

Heusser, S. A., Lycksell, M., Wang, X., McComas, S. E., Howard, R. J., and Lindahl, E. (2018). Allosteric Potentiation of a Ligand-Gated Ion Channel Is Mediated by Access to a Deep Membrane-Facing Cavity. *Proc. Natl. Acad. Sci. U. S. A.* 115, 10672–10677. doi:10.1073/pnas.1809650115

Hille, B. (1978). Ionic Channels in Excitable Membranes. Current Problems and Biophysical Approaches. *Biophys. J.* 22, 283–294. doi:10.1016/s0006-3495(78)85489-7

Hille, B. (1986). Ionic Channels: Molecular Pores of Excitable Membranes. *Harvey Lect.* 82, 47–69.

Hilton, J. K., Kim, M., and Van Horn, W. D. (2019). Structural and Evolutionary Insights Point to Allosteric Regulation of TRP Ion Channels. *Acc. Chem. Res.* 52, 1643–1652. doi:10.1021/acs.accounts.9b00075

Hodgkin, A. L., and Huxley, A. F. (1952). Currents Carried by Sodium and Potassium Ions through the Membrane of the Giant Axon of Loligo. *J. Physiol.* 116, 449–472. doi:10.1113/jphysiol.1952.sp004717

Hollingsworth, S. A., and Dror, R. O. (2018). Molecular Dynamics Simulation for All. *Neuron* 99, 1129–1143. doi:10.1016/j.neuron.2018.08.011

Howard, R. J., Murail, S., Ondricek, K. E., Corringer, P. J., Lindahl, E., Trudell, J. R., et al. (2011). Structural Basis for Alcohol Modulation of a Pentameric Ligand-Gated Ion Channel. *Proc. Natl. Acad. Sci. U. S. A.* 108, 12149–12154. doi:10.1073/pnas.1104480108

Hryc, C. F., Chen, D. H., Afonine, P. V., Jakana, J., Wang, Z., Haase-Pettingell, C., et al. (2017). Accurate Model Annotation of a Near-Atomic Resolution Cryo-EM Map. *Proc. Natl. Acad. Sci. U. S. A.* 114, 3103–3108. doi:10.1073/pnas.1621152114

Huang, B., and Schroeder, M. (2006). LIGSITEcsc: Predicting Ligand Binding Sites Using the Connolly Surface and Degree of Conservation. *BMC Struct. Biol.* 6, 19. doi:10.1186/1472-6807-6-19

Huang, G., Liu, D., Wang, W., Wu, Q., Chen, J., Pan, X., et al. (2022). High-resolution Structures of Human Nav1.7 Reveal Gating Modulation through α-π Helical Transition of S6IV. *Cell Rep.* 39, 110735. doi:10.1016/j.celrep.2022.110735

Huang, Q., Song, P., Chen, Y., Liu, Z., and Lai, L. (2021). Allosteric Type and Pathways Are Governed by the Forces of Protein-Ligand Binding. *J. Phys. Chem. Lett.* 12, 5404–5412. doi:10.1021/acs.jpclett.1c01253

Huang, Z., Mou, L., Shen, Q., Lu, S., Li, C., Liu, X., et al. (2014). ASD v2.0: Updated Content and Novel Features Focusing on Allosteric Regulation. *Nucleic Acids Res.* 42, D510–D516. doi:10.1093/nar/gkt1247

Huang, Z., Zhu, L., Cao, Y., Wu, G., Liu, X., Chen, Y., et al. (2011). ASD: a Comprehensive Database of Allosteric Proteins and Modulators. *Nucleic Acids Res.* 39, D663–D669. doi:10.1093/nar/gkq1022

Humphreys, I. R., Pei, J., Baek, M., Krishnakumar, A., Anishchenko, I., Ovchinnikov, S., et al. (2021). Computed Structures of Core Eukaryotic Protein Complexes. *Science* 374, 1340. doi:10.1126/science.abm4805

Hussein, H. A., Borrel, A., Geneix, C., Petitjean, M., Regad, L., and Camproux, A. C. (2015). PockDrug-Server: a New Web Server for Predicting Pocket Druggability on Holo and Apo Proteins. *Nucleic Acids Res.* 43, W436–W442. doi:10.1093/nar/gkv462

Igaev, M., Kutzner, C., Bock, L. V., Vaiana, A. C., and Grubmüller, H. (2019). Automated Cryo-EM Structure Refinement Using Correlation-Driven Molecular Dynamics. *eLife* 8. doi:10.7554/eLife.43542

Jakobi, A. J., Wilmanns, M., and Sachse, C. (2017). Model-based Local Density Sharpening of Cryo-EM Maps. *eLife* 6, e27131. doi:10.7554/eLife.27131

Jensen, M. Ø., Borhani, D. W., Lindorff-Larsen, K., Maragakis, P., Jogini, V., Eastwood, M. P., et al. (2010). Principles of Conduction and Hydrophobic Gating in K+ Channels. *Proc. Natl. Acad. Sci. U. S. A.* 107, 5833–5838. doi:10.1073/pnas.0911691107

Jiang, D., Gamal El-Din, T., Zheng, N., and Catterall, W. A. (2021a). Expression and Purification of the Cardiac Sodium Channel NaV1.5 for Cryo-EM

Structure Determination. *Methods Enzymol.* 653, 89–101. doi:10.1016/bs.mie.2021.01.030

Jiang, D., Shi, H., Tonggu, L., Gamal El-Din, T. M., Lenaeus, M. J., Zhao, Y., et al. (2020). Structure of the Cardiac Sodium Channel. *Cell* 180, 122–e10. e110. doi:10.1016/j.cell.2019.11.041

Jiang, W., Del Rosario, J. S., Botello-Smith, W., Zhao, S., Lin, Y. C., Zhang, H., et al. (2021b). Crowding-induced Opening of the Mechanosensitive Piezo1 Channel In Silico. *Commun. Biol.* 4, 84. doi:10.1038/s42003-020-01600-1

Jiang, Z., Xu, J., Yan, A., and Wang, L. (2021c). A Comprehensive Comparative Assessment of 3D Molecular Similarity Tools in Ligand-Based Virtual Screening. *Brief. Bioinform* 22. doi:10.1093/bib/bbab231

Jiménez, J., Doerr, S., Martínez-Rosell, G., Rose, A. S., and De Fabritiis, G. (2017). DeepSite: Protein-Binding Site Predictor Using 3D-Convolutional Neural Networks. *Bioinformatics* 33, 3036–3042. doi:10.1093/bioinformatics/btx350

Jing, Z., Rackers, J. A., Pratt, L. R., Liu, C., Rempe, S. B., and Ren, P. (2021). Thermodynamics of Ion Binding and Occupancy in Potassium Channels. *Chem. Sci.* 12, 8920–8930. doi:10.1039/d1sc01887f

John, B., and Sali, A. (2003). Comparative Protein Structure Modeling by Iterative Alignment, Model Building and Model Assessment. *Nucleic Acids Res.* 31, 3982–3992. doi:10.1093/nar/gkg460

Jojoa-Cruz, S., Saotome, K., Murthy, S. E., Tsui, C. C. A., Sansom, M. S., Patapoutian, A., et al. (2018). Cryo-EM Structure of the Mechanically Activated Ion Channel OSCA1.2. *eLife* 7, e41845. doi:10.7554/eLife.41845

Jumper, J., Evans, R., Pritzel, A., Green, T., Figurnov, M., Ronneberger, O., et al. (2021). Highly Accurate Protein Structure Prediction with AlphaFold. *Nature* 596, 583–589. doi:10.1038/s41586-021-03819-2

Kapsalis, C., Wang, B., El Mkami, H., Pitt, S. J., Schnell, J. R., Smith, T. K., et al. (2019). Allosteric Activation of an Ion Channel Triggered by Modification of Mechanosensitive Nano-Pockets. *Nat. Commun.* 10, 4619. doi:10.1038/s41467-019-12591-x

Kaur, S., Gomez-Blanco, J., Khalifa, A. A. Z., Adinarayanan, S., Sanchez-Garcia, R., Wrapp, D., et al. (2021). Local Computational Methods to Improve the Interpretability and Analysis of Cryo-EM Maps. *Nat. Commun.* 12, 1240. doi:10.1038/s41467-021-21509-5

Ke, S., Timin, E. N., and Stary-Weinzinger, A. (2014). Different Inward and Outward Conduction Mechanisms in NaVMs Suggested by Molecular Dynamics Simulations. *PLoS. Comput. Biol.* 10, e1003746. doi:10.1371/journal.pcbi.1003746

Keating, M. T. (1996). The Long QT Syndrome. A Review of Recent Molecular Genetic and Physiologic Discoveries. *Med. Baltim.* 75, 1–5. doi:10.1097/00005792-199601000-00001

Kefauver, J. M., Ward, A. B., and Patapoutian, A. (2020). Discoveries in Structure and Physiology of Mechanically Activated Ion Channels. *Nature* 587, 567–576. doi:10.1038/s41586-020-2933-1

Keserü, G. M. (2003). Prediction of hERG Potassium Channel Affinity by Traditional and Hologram QSAR Methods. *Bioorg. Med. Chem. Lett.* 13, 2773–2775. doi:10.1016/s0960-894x(03)00492-x

Khalifa, N., Kumar Konda, L. S., and Kristam, R. (2020). Machine Learning-Based QSAR Models to Predict Sodium Ion Channel (Nav 1.5) Blockers. *Future Med. Chem.* 12, 1829–1843. doi:10.4155/fmc-2020-0156

Khalili-Araghi, F., Tajkhorshid, E., and Schulten, K. (2006). Dynamics of K+ Ion Conduction through Kv1.2. *Biophys. J.* 91, L72–L74. doi:10.1529/biophysj.106.091926

Kimanius, D., Dong, L., Sharov, G., Nakane, T., and Scheres, S. H. W. (2021). New Tools for Automated Cryo-EM Single-Particle Analysis in RELION-4.0. *Biochem. J.* 478, 4169–4185. doi:10.1042/bcj20210708

Kiss, F., Pohóczky, K., Szállási, A., and Helyes, Z. (2020). *Transient Receptor Potential* (TRP) Channels in Head-And-Neck Squamous Cell Carcinomas: Diagnostic, Prognostic, and Therapeutic Potentials. *Int. J. Mol. Sci.* 21. doi:10.3390/ijms21176374

Kodandaramaiah, S. B., Franzesi, G. T., Chow, B. Y., Boyden, E. S., and Forest, C. R. (2012). Automated Whole-Cell Patch-Clamp Electrophysiology of Neurons *In Vivo*. *Nat. Methods* 9, 585–587. doi:10.1038/nmeth.1993

Konda, L. S. K., Keerthi Praba, S., and Kristam, R. (2019). hERG Liability Classification Models Using Machine Learning Techniques. *Comput. Toxicol.* 12, 100089. doi:10.1016/j.comtox.2019.100089

Kong, W., Tu, X., Huang, W., Yang, Y., Xie, Z., and Huang, Z. (2020). Prediction and Optimization of NaV1.7 Sodium Channel Inhibitors Based on Machine Learning and Simulated Annealing. *J. Chem. Inf. Model.* 60, 2739–2753. doi:10.1021/acs.jcim.9b01180

Konze, K. D., Bos, P. H., Dahlgren, M. K., Leswing, K., Tubert-Brohman, I., Bortolato, A., et al. (2019). Reaction-Based Enumeration, Active Learning, and Free Energy Calculations to Rapidly Explore Synthetically Tractable Chemical Space and Optimize Potency of Cyclin-dependent Kinase 2 Inhibitors. *J. Chem. Inf. Model.* 59, 3782–3793. doi:10.1021/acs.jcim.9b00367

Kopec, W., Köpfer, D. A., Vickery, O. N., Bondarenko, A. S., Jansen, T. L. C., de Groot, B. L., et al. (2018). Direct Knock-On of Desolvated Ions Governs Strict Ion Selectivity in K+ Channels. *Nat. Chem.* 10, 813–820. doi:10.1038/s41557-018-0105-9

Kopec, W., Rothberg, B. S., and de Groot, B. L. (2019). Molecular Mechanism of a Potassium Channel Gating through Activation Gate-Selectivity Filter Coupling. *Nat. Commun.* 10, 5366. doi:10.1038/S41467-019-13227-w

Köpfer, D. A., Song, C., Gruene, T., Sheldrick, G. M., Zachariae, U., and De Groot, B. L. (2014). Ion Permeation in K^+ Channels Occurs by Direct Coulomb Knock-On. *Science* 346, 352–355. doi:10.1126/science.1254840

Kozlovskii, I., and Popov, P. (2020). Spatiotemporal Identification of Druggable Binding Sites Using Deep Learning. *Commun. Biol.* 3, 618. doi:10.1038/s42003-020-01350-0

Krivov, G. G., Shapovalov, M. V., and Dunbrack, R. L. (2009). Improved Prediction of Protein Side-Chain Conformations with SCWRL4. *Proteins* 77, 778–795. doi:10.1002/prot.22488

Kuenze, G., Vanoye, C. G., Desai, R. R., Adusumilli, S., Brewer, K. R., Woods, H., et al. (2020). Allosteric Mechanism for KCNE1 Modulation of KCNQ1 Potassium Channel Activation. *eLife* 9, e57680. doi:10.7554/eLife.57680

Laskowski, R. A. (1995). SURFNET: a Program for Visualizing Molecular Surfaces, Cavities, and Intermolecular Interactions. *J. Mol. Graph.* 13, 323–328. doi:10.1016/0263-7855(95)00073-9

Laurie, A. T., and Jackson, R. M. (2005). Q-SiteFinder: an Energy-Based Method for the Prediction of Protein-Ligand Binding Sites. *Bioinformatics* 21, 1908–1916. doi:10.1093/bioinformatics/bti315

Le Guilloux, V., Schmidtke, P., and Tuffery, P. (2009). Fpocket: An Open Source Platform for Ligand Pocket Detection. *BMC Bioinforma.* 10, 168. doi:10.1186/1471-2105-10-168

LeBard, D. N., Hénin, J., Eckenhoff, R. G., Klein, M. L., and Brannigan, G. (2012). General Anesthetics Predicted to Block the GLIC Pore with Micromolar Affinity. *PLoS. Comput. Biol.* 8, e1002532. doi:10.1371/journal.pcbi.1002532

Lees, J. A., Dias, J. M., and Han, S. (2021). Applications of Cryo-EM in Small Molecule and Biologics Drug Design. *Biochem. Soc. Trans.* 49, 2627–2638. doi:10.1042/bst20210444

Levitt, D. G., and Banaszak, L. J. (1992). POCKET: a Computer Graphics Method for Identifying and Displaying Protein Cavities and Their Surrounding Amino Acids. *J. Mol. Graph.* 10, 229–234. doi:10.1016/0263-7855(92)80074-N

Li, X., Mooney, P., Zheng, S., Booth, C. R., Braunfeld, M. B., Gubbens, S., et al. (2013). Electron Counting and Beam-Induced Motion Correction Enable Near-Atomic-Resolution Single-Particle Cryo-EM. *Nat. Methods* 10, 584–590. doi:10.1038/nmeth.2472

Liao, M., Cao, E., Julius, D., and Cheng, Y. (2013). Structure of the TRPV1 Ion Channel Determined by Electron Cryo-Microscopy. *Nature* 504, 107–112. doi:10.1038/nature12822

Liebschner, D., Afonine, P. V., Baker, M. L., Bunkóczi, G., Chen, V. B., Croll, T. I., et al. (2019). Macromolecular Structure Determination Using X-Rays, Neutrons and Electrons: Recent Developments in Phenix. *Acta Crystallogr. D. Struct. Biol.* 75, 861–877. doi:10.1107/s2059798319011471

Limongelli, V. (2020). Ligand Binding Free Energy and Kinetics Calculation in 2020. *WIREs Comput. Mol. Sci.* 10. doi:10.1002/wcms.1455

Lin, S., Han, S., Cai, X., Tan, Q., Zhou, K., Wang, D., et al. (2021). Structures of Gi-Bound Metabotropic Glutamate Receptors mGlu2 and mGlu4. *Nature* 594, 583–588. doi:10.1038/s41586-021-03495-2

Lindert, S., Alexander, N., Wötzel, N., Karakaş, M., Stewart, P. L., and Meiler, J. (2012a). EM-fold: De Novo Atomic-Detail Protein Structure Determination from Medium-Resolution Density Maps. *Structure* 20, 464–478. doi:10.1016/j.str.2012.01.023

Lindert, S., Hofmann, T., Wötzel, N., Karakaş, M., Stewart, P. L., and Meiler, J. (2012b). Ab Initio protein Modeling into cryoEM Density Maps Using EM-fold. *Biopolymers* 97, 669–677. doi:10.1002/bip.22027

Lindert, S., Staritzbichler, R., Wötzel, N., Karakaş, M., Stewart, P. L., and Meiler, J. (2009). EM-fold: De Novo Folding of Alpha-Helical Proteins Guided by Intermediate-Resolution Electron Microscopy Density Maps. *Structure* 17, 990–1003. doi:10.1016/j.str.2009.06.001

Litan, A., and Langhans, S. A. (2015). Cancer as a Channelopathy: Ion Channels and Pumps in Tumor Development and Progression. *Front. Cell. Neurosci.* 9, 86. doi:10.3389/fncel.2015.00086

Liu, J., and Nussinov, R. (2016). Allostery: An Overview of its History, Concepts, Methods, and Applications. *PLoS. Comput. Biol.* 12, e1004966. doi:10.1371/journal.pcbi.1004966

Liu, X., Wu, G., Yu, Y., Chen, X., Ji, R., Lu, J., et al. (2019). Molecular Understanding of Calcium Permeation through the Open Orai Channel. *PLoS. Biol.* 17, e3000096. doi:10.1371/journal.pbio.3000096

Liu, Y., Grimm, M., Dai, W. T., Hou, M. C., Xiao, Z. X., and Cao, Y. (2020). CB-dock: a Web Server for Cavity Detection-Guided Protein-Ligand Blind Docking. *Acta Pharmacol. Sin.* 41, 138–144. doi:10.1038/s41401-019-0228-6

Lolicato, M., Natale, A. M., Abderemane-Ali, F., Crottès, D., Capponi, S., Duman, R., et al. (2020). K2P Channel C-type Gating Involves Asymmetric Selectivity Filter Order-Disorder Transitions. *Sci. Adv.* 6. doi:10.1126/sciadv.abc9174

Lu, R., He, Q., and Wang, J. (2017). "TRPC Channels and Alzheimer's Disease," in *Transient Receptor Potential Canonical Channels and Brain Diseases*. Editor Y. Wang, 73–83. doi:10.1007/978-94-024-1088-4_7

Luo, Q., Chen, L., Cheng, X., Ma, Y., Li, X., Zhang, B., et al. (2017). An Allosteric Ligand-Binding Site in the Extracellular Cap of K2P Channels. *Nat. Commun.* 8, 378. doi:10.1038/s41467-017-00499-3

Lyne, P. D. (2002). Structure-based Virtual Screening: an Overview. *Drug Discov. Today* 7, 1047–1055. doi:10.1016/s1359-6446(02)02483-2

Lyumkis, D. (2019). Challenges and Opportunities in Cryo-EM Single-Particle Analysis. *J. Biol. Chem.* 294, 5181–5197. doi:10.1074/jbc.REV118.005602

Maffeo, C., Bhattacharya, S., Yoo, J., Wells, D., and Aksimentiev, A. (2012). Modeling and Simulation of Ion Channels. *Chem. Rev.* 112, 6250–6284. doi:10.1021/cr3002609

Martin, G. M., Kandasamy, B., DiMaio, F., Yoshioka, C., and Shyng, S. L. (2017). Anti-diabetic Drug Binding Site in a Mammalian KATP Channel Revealed by Cryo-EM. *eLife* 6, e31054. doi:10.7554/eLife.31054

Marzian, S., Stansfeld, P. J., Rapedius, M., Rinné, S., Nematian-Ardestani, E., Abbruzzese, J. L., et al. (2013). Side Pockets Provide the Basis for a New Mechanism of Kv Channel-specific Inhibition. *Nat. Chem. Biol.* 9, 507–513. doi:10.1038/nchembio.1271

Masiulis, S., Desai, R., Uchański, T., Serna Martin, I., Laverty, D., Karia, D., et al. (2019). GABAA Receptor Signalling Mechanisms Revealed by Structural Pharmacology. *Nature* 565, 454–459. doi:10.1038/s41586-018-0832-5

McCusker, E. C., Bagnéris, C., Naylor, C. E., Cole, A. R., D'Avanzo, N., Nichols, C. G., et al. (2012). Structure of a Bacterial Voltage-Gated Sodium Channel Pore Reveals Mechanisms of Opening and Closing. *Nat. Commun.* 3, 1102. doi:10.1038/ncomms2077

McGrath, N. A., Brichacek, M., and Njardarson, J. T. (2010). A Graphical Journey of Innovative Organic Architectures that Have Improved Our Lives. *J. Chem. Educ.* 87, 1348–1349. doi:10.1021/ed1003806

McGreevy, R., Teo, I., Singharoy, A., and Schulten, K. (2016). Advances in the Molecular Dynamics Flexible Fitting Method for Cryo-EM Modeling. *Methods* 100, 50–60. doi:10.1016/j.ymeth.2016.01.009

Menke, J., Maskri, S., and Koch, O. (2021). Computational Ion Channel Research: from the Application of Artificial Intelligence to Molecular Dynamics Simulations. *Cell. Physiol. biochem.* 55, 14–45. doi:10.33594/000000336

Mersmann, S. F., Strömich, L., Song, F. J., Wu, N., Vianello, F., Barahona, M., et al. (2021). ProteinLens: a Web-Based Application for the Analysis of Allosteric Signalling on Atomistic Graphs of Biomolecules. *Nucleic Acids Res.* 49, W551–W558. doi:10.1093/nar/gkab350

Miller, B. R., McGee, T. D., Swails, J. M., Homeyer, N., Gohlke, H., and Roitberg, A. E. (2012). MMPBSA.py: An Efficient Program for End-State Free Energy Calculations. *J. Chem. Theory Comput.* 8, 3314–3321. doi:10.1021/ct300418h

Mirdita, M., Schütze, K., Moriwaki, Y., Heo, L., Ovchinnikov, S., and Steinegger, M. (2022). ColabFold: Making Protein Folding Accessible to All. *Nat. Methods*. doi:10.1038/s41592-022-01488-1

Mohler, H., and Okada, T. (1977). GABA Receptor Binding with 3H (+) Bicuculline-Methiodide in Rat CNS. *Nature* 267, 65–67. doi:10.1038/267065a0

Mullard, A. (2020). 2019 FDA Drug Approvals. *Nat. Rev. Drug Discov.* 19, 79–84. doi:10.1038/d41573-020-00001-7

Muraglia, M., De Bellis, M., Catalano, A., Carocci, A., Franchini, C., Carrieri, A., et al. (2014). N-Aryl-2,6-dimethylbenzamides, a New Generation of Tocainide Analogues as Blockers of Skeletal Muscle Voltage-Gated Sodium Channels. *J. Med. Chem.* 57, 2589–2600. doi:10.1021/jm401864b

Murail, S., Howard, R. J., Broemstrup, T., Bertaccini, E. J., Harris, R. A., Trudell, J. R., et al. (2012). Molecular Mechanism for the Dual Alcohol Modulation of Cys-Loop Receptors. *PLoS. Comput. Biol.* 8, e1002710. doi:10.1371/journal.pcbi.1002710

Nakane, T., Kotecha, A., Sente, A., McMullan, G., Masiulis, S., Brown, P. M. G. E., et al. (2020). Single-particle Cryo-EM at Atomic Resolution. *Nature* 587, 152–156. doi:10.1038/s41586-020-2829-0

Newell, A., Yang, K., and Deng, J. (2016). in *Stacked Hourglass Networks for Human Pose Estimation*. Editors B. Leibe, J. Matas, N. Sebe, and M. Welling (Cham: Springer International Publishing), 483–499.

Ngan, C. H., Hall, D. R., Zerbe, B., Grove, L. E., Kozakov, D., and Vajda, S. (2012). FTSite: High Accuracy Detection of Ligand Binding Sites on Unbound Protein Structures. *Bioinformatics* 28, 286–287. doi:10.1093/bioinformatics/btr651

Nguyen, P. T., DeMarco, K. R., Vorobyov, I., Clancy, C. E., and Yarov-Yarovoy, V. (2019). Structural Basis for Antiarrhythmic Drug Interactions with the Human Cardiac Sodium Channel. *Proc. Natl. Acad. Sci. U. S. A.* 116, 2945–2954. doi:10.1073/pnas.1817446116

Nisius, B., and Göller, A. H. (2009). Similarity-Based Classifier Using Topomers to Provide a Knowledge Base for hERG Channel Inhibition. *J. Chem. Inf. Model.* 49, 247–256. doi:10.1021/ci800304t

Njardarson, T. G. O. J. T. (2020). Top 200 Brand Name Drugs by Retails Sales in 2020. https://njardarson.lab.arizona.edu/content/top-pharmaceuticals-poster (Accessed March, 2022).

Noskov, S. Y., Bernèche, S., and Roux, B. (2004). Control of Ion Selectivity in Potassium Channels by Electrostatic and Dynamic Properties of Carbonyl Ligands. *Nature* 431, 830–834. doi:10.1038/nature02943

Noskov, S. Y., and Roux, B. (2007). Importance of Hydration and Dynamics on the Selectivity of the KcsA and NaK Channels. *J. Gen. Physiol.* 129, 135–143. doi:10.1085/jgp.200609633

Noskov, S. Y., and Roux, B. (2006). Ion Selectivity in Potassium Channels. *Biophys. Chem.* 124, 279–291. doi:10.1016/j.bpc.2006.05.033

Osterberg, F., and Aqvist, J. (2005). Exploring Blocker Binding to a Homology Model of the Open hERG K+ Channel Using Docking and Molecular Dynamics Methods. *FEBS Lett.* 579, 2939–2944. doi:10.1016/j.febslet.2005.04.039

Pan, X., Li, Z., Huang, X., Huang, G., Gao, S., Shen, H., et al. (2019). Molecular Basis for Pore Blockade of Human Na+ Channel Nav1.2 by the μ-conotoxin KIIIA. *Science* 363, 1309–1313. doi:10.1126/science.aaw2999

Pan, X., Li, Z., Zhou, Q., Shen, H., Wu, K., Huang, X., et al. (2018). Structure of the Human Voltage-Gated Sodium Channel Nav1.4 in Complex with β1. *Science* 362. doi:10.1126/science.aau2486

Papke, R. L., and Heinemann, S. F. (1994). Partial Agonist Properties of Cytisine on Neuronal Nicotinic Receptors Containing the Beta 2 Subunit. *Mol. Pharmacol.* 45, 142–149.

Payandeh, J., Scheuer, T., Zheng, N., and Catterall, W. A. (2011). The Crystal Structure of a Voltage-Gated Sodium Channel. *Nature* 475, 353–358. doi:10.1038/nature10238

Pearlstein, R. A., Vaz, R. J., Kang, J., Chen, X. L., Preobrazhenskaya, M., Shchekotikhin, A. E., et al. (2003). Characterization of HERG Potassium Channel Inhibition Using CoMSiA 3D QSAR and Homology Modeling Approaches. *Bioorg. Med. Chem. Lett.* 13, 1829–1835. doi:10.1016/s0960-894x(03)00196-3

Petrey, D., Xiang, Z., Tang, C. L., Xie, L., Gimpelev, M., Mitros, T., et al. (2003). Using Multiple Structure Alignments, Fast Model Building, and Energetic Analysis in Fold Recognition and Homology Modeling. *Proteins* 53, 430–435. doi:10.1002/prot.10550

Pfab, J., Phan, N. M., and Si, D. (2021). DeepTracer for Fast De Novo Cryo-EM Protein Structure Modeling and Special Studies on CoV-Related Complexes. *Proc. Natl. Acad. Sci. U. S. A.* 118. doi:10.1073/pnas.2017525118

Pintilie, G., Chen, D. H., Haase-Pettingell, C. A., King, J. A., and Chiu, W. (2016). Resolution and Probabilistic Models of Components in CryoEM Maps of Mature P22 Bacteriophage. *Biophys. J.* 110, 827–839. doi:10.1016/j.bpj.2015.11.3522

Pintilie, G., and Chiu, W. (2018). Assessment of Structural Features in Cryo-EM Density Maps Using SSE and Side Chain Z-Scores. *J. Struct. Biol.* 204, 564–571. doi:10.1016/j.jsb.2018.08.015

Pintilie, G., Zhang, K., Su, Z., Li, S., Schmid, M. F., and Chiu, W. (2020). Measurement of Atom Resolvability in Cryo-EM Maps with Q-Scores. *Nat. Methods* 17, 328–334. doi:10.1038/s41592-020-0731-1

Pintilie, G. D., Zhang, J., Goddard, T. D., Chiu, W., and Gossard, D. C. (2010). Quantitative Analysis of Cryo-EM Density Map Segmentation by Watershed and Scale-Space Filtering, and Fitting of Structures by Alignment to Regions. *J. Struct. Biol.* 170, 427–438. doi:10.1016/j.jsb.2010.03.007

Plowman, T. (1982). The Identification of Coca (Erythroxylum Species): 1860-1910. *Bot. J. Linn. Soc.* 84, 329–353. doi:10.1111/j.1095-8339.1982.tb00368.x

Pu, L., Govindaraj, R. G., Lemoine, J. M., Wu, H. C., and Brylinski, M. (2019). DeepDrug3D: Classification of Ligand-Binding Pockets in Proteins with a Convolutional Neural Network. *PLoS. Comput. Biol.* 15, e1006718. doi:10.1371/journal.pcbi.1006718

Punjani, A., Rubinstein, J. L., Fleet, D. J., and Brubaker, M. A. (2017). cryoSPARC: Algorithms for Rapid Unsupervised Cryo-EM Structure Determination. *Nat. Methods* 14, 290–296. doi:10.1038/nmeth.4169

Punjani, A., Zhang, H., and Fleet, D. J. (2020). Non-uniform Refinement: Adaptive Regularization Improves Single-Particle Cryo-EM Reconstruction. *Nat. Methods* 17, 1214–1221. doi:10.1038/s41592-020-00990-8

Ramírez-Aportela, E., Maluenda, D., Fonseca, Y. C., Conesa, P., Marabini, R., Heymann, J. B., et al. (2021). FSC-Q: a CryoEM Map-To-Atomic Model Quality Validation Based on the Local Fourier Shell Correlation. *Nat. Commun.* 12, 42. doi:10.1038/s41467-020-20295-w

Ramírez-Aportela, E., Vilas, J. L., Glukhova, A., Melero, R., Conesa, P., Martínez, M., et al. (2020). Automatic Local Resolution-Based Sharpening of Cryo-EM Maps. *Bioinformatics* 36, 765–772. doi:10.1093/bioinformatics/btz671

Reardon, S. (2018). 'Party Drug' Turned Antidepressant Approaches Approval. *Nat. Rev. Drug Discov.* 17, 773–775. doi:10.1038/nrd.2018.187

Robertson, M. J., Meyerowitz, J. G., and Skiniotis, G. (2022). Drug Discovery in the Era of Cryo-Electron Microscopy. *Trends biochem. Sci.* 47, 124–135. doi:10.1016/j.tibs.2021.06.008

Roche, O., Trube, G., Zuegge, J., Pflimlin, P., Alanine, A., and Schneider, G. (2002). A Virtual Screening Method for Prediction of the hERG Potassium Channel Liability of Compound Libraries. *ChemBioChem* 3, 455–459. doi:10.1002/1439-7633(20020503)3:5<455:AID-CBIC455>3.0.CO;2-L

Ronneberger, O., Fischer, P., and Brox, T. (2015). in *U-net: Convolutional Networks for Biomedical Image Segmentation*. Editors N. Navab, J. Hornegger, W. M. Wells, and A. F. Frangi (Cham: Springer International Publishing), 234–241.

Rook, M. L., Musgaard, M., and MacLean, D. M. (2021). Coupling Structure with Function in Acid-Sensing Ion Channels: Challenges in Pursuit of Proton Sensors. *J. Physiol.* 599, 417–430. doi:10.1113/JP278707

Rosenthal, P. B., and Henderson, R. (2003). Optimal Determination of Particle Orientation, Absolute Hand, and Contrast Loss in Single-Particle Electron Cryomicroscopy. *J. Mol. Biol.* 333, 721–745. doi:10.1016/j.jmb.2003.07.013

Rossmann, M. G., Bernal, R., and Pletnev, S. V. (2001). Combining Electron Microscopic with X-Ray Crystallographic Structures. *J. Struct. Biol.* 136, 190–200. doi:10.1006/jsbi.2002.4435

Roy, A., and Zhang, Y. (2012). Recognizing Protein-Ligand Binding Sites by Global Structural Alignment and Local Geometry Refinement. *Structure* 20, 987–997. doi:10.1016/j.str.2012.03.009

Sadybekov, A. A., Sadybekov, A. V., Liu, Y., Iliopoulos-Tsoutsouvas, C., Huang, X. P., Pickett, J., et al. (2022). Synthon-based Ligand Discovery in Virtual Libraries of over 11 Billion Compounds. *Nature* 601, 452–459. doi:10.1038/s41586-021-04220-9

Saikia, C., Ben-Nissan, G., Reuveny, E., and Karbat, I. (2021). Production of Recombinant Venom Peptides as Tools for Ion Channel Research. *Methods Enzymol.* 654, 169–201. doi:10.1016/bs.mie.2021.01.029

Sanchez-Garcia, R., Gomez-Blanco, J., Cuervo, A., Carazo, J. M., Sorzano, C. O. S., and Vargas, J. (2021). DeepEMhancer: a Deep Learning Solution for Cryo-EM Volume Post-processing. *Commun. Biol.* 4, 874. doi:10.1038/s42003-021-02399-1

Sands, Z., Grottesi, A., and Sansom, M. S. (2005). Voltage-gated Ion Channels. *Curr. Biol.* 15, R44–R47. doi:10.1016/j.cub.2004.12.050

Santos-Martins, D., Solis-Vasquez, L., Tillack, A. F., Sanner, M. F., Koch, A., and Forli, S. (2021). Accelerating AUTODOCK4 with GPUs and Gradient-Based Local Search. *J. Chem. Theory Comput.* 17, 1060–1073. doi:10.1021/acs.jctc.0c01006

Scheres, S. H. (2012). RELION: Implementation of a Bayesian Approach to Cryo-EM Structure Determination. *J. Struct. Biol.* 180, 519–530. doi:10.1016/j.jsb.2012.09.006

Schewe, M., Nematian-Ardestani, E., Sun, H., Musinszki, M., Cordeiro, S., Bucci, G., et al. (2016). A Non-canonical Voltage-Sensing Mechanism Controls Gating in K2P K(+) Channels. *Cell* 164, 937–949. doi:10.1016/j.cell.2016.02.002

Schindler, W., and Häfliger, F. (1954). Über Derivate des Iminodibenzyls. *Hca* 37, 472–483. doi:10.1002/hlca.19540370211

Schmid, R., and Evans, R. J. (2019). ATP-gated P2X Receptor Channels: Molecular Insights into Functional Roles. *Annu. Rev. Physiol.* 81, 43–62. doi:10.1146/annurev-physiol-020518-114259

Schmidtke, P., Bidon-Chanal, A., Luque, F. J., and Barril, X. (2011). MDpocket: Open-Source Cavity Detection and Characterization on Molecular Dynamics Trajectories. *Bioinformatics* 27, 3276–3285. doi:10.1093/bioinformatics/btr550

Sehnal, D., Bittrich, S., Deshpande, M., Svobodová, R., Berka, K., Bazgier, V., et al. (2021). Mol* Viewer: Modern Web App for 3D Visualization and Analysis of Large Biomolecular Structures. *Nucleic Acids Res.* 49, W431–W437. doi:10.1093/nar/gkab314

Shen, H., Li, Z., Jiang, Y., Pan, X., Wu, J., Cristofori-Armstrong, B., et al. (2018). Structural Basis for the Modulation of Voltage-Gated Sodium Channels by Animal Toxins. *Science* 362. doi:10.1126/science.aau2596

Shen, H., Liu, D., Wu, K., Lei, J., and Yan, N. (2019). Structures of Human Nav1.7 Channel in Complex with Auxiliary Subunits and Animal Toxins. *Science* 363, 1303–1308. doi:10.1126/science.aaw2493

Shen, H., Zhou, Q., Pan, X., Li, Z., Wu, J., and Yan, N. (2017). Structure of a Eukaryotic Voltage-Gated Sodium Channel at Near-Atomic Resolution. *Science* 355. doi:10.1126/science.aal4326

Shidi, T., Ruiqi, C., Mengru, L., Qingde, L., Yanxiang, Z., Ji, D., et al. (2022). Accelerating AutoDock VINA with GPUs. *ChemRxiv*. doi:10.26434/chemrxiv-2021-3qvn2

Shrivastava, I. H., and Sansom, M. S. (2000). Simulations of Ion Permeation through a Potassium Channel: Molecular Dynamics of KcsA in a Phospholipid Bilayer. *Biophys. J.* 78, 557–570. doi:10.1016/s0006-3495(00)76616-1

Shrivastava, I. H., Tieleman, D. P., Biggin, P. C., and Sansom, M. S. (2002). K(+) versus Na(+) Ions in a K Channel Selectivity Filter: a Simulation Study. *Biophys. J.* 83, 633–645. doi:10.1016/s0006-3495(02)75197-7

Shuman, C. R. (1983). Glipizide: an Overview. *Am. J. Med.* 75, 55–59. doi:10.1016/0002-9343(83)90254-1

Sine, S. M., and Engel, A. G. (2006). Recent Advances in Cys-Loop Receptor Structure and Function. *Nature* 440, 448–455. doi:10.1038/nature04708

Singer, A., and Sigworth, F. J. (2020). Computational Methods for Single-Particle Electron Cryomicroscopy. *Annu. Rev. Biomed. Data Sci.* 3, 163–190. doi:10.1146/annurev-biodatasci-021020-093826

Singharoy, A., Teo, I., McGreevy, R., Stone, J. E., Zhao, J., and Schulten, K. (2016). Molecular Dynamics-Based Refinement and Validation for Sub-5 Å Cryo-Electron Microscopy Maps. *eLife* 5, e16105. doi:10.7554/eLife.16105

Siramshetty, V. B., Chen, Q., Devarakonda, P., and Preissner, R. (2018). The Catch-22 of Predicting hERG Blockade Using Publicly Accessible Bioactivity Data. *J. Chem. Inf. Model.* 58, 1224–1233. doi:10.1021/acs.jcim.8b00150

Song, K., Wei, M., Guo, W., Quan, L., Kang, Y., Wu, J. X., et al. (2021). Structural Basis for Human TRPC5 Channel Inhibition by Two Distinct Inhibitors. *eLife* 10. doi:10.7554/eLife.63429

Sorzano, C. O., Marabini, R., Velázquez-Muriel, J., Bilbao-Castro, J. R., Scheres, S. H., Carazo, J. M., et al. (2004). XMIPP: a New Generation of an Open-Source Image Processing Package for Electron Microscopy. *J. Struct. Biol.* 148, 194–204. doi:10.1016/j.jsb.2004.06.006

Srivastava, R. K., Greff, K., and Schmidhuber, J. (2015). "Training Very Deep Networks," in *Advances in Neural Information Processing Systems* (Montreal, Canada: Curran Associates, Inc.), 28.

Süel, G. M., Lockless, S. W., Wall, M. A., and Ranganathan, R. (2003). Evolutionarily Conserved Networks of Residues Mediate Allosteric Communication in Proteins. *Nat. Struct. Biol.* 10, 59–69. doi:10.1038/nsb881

Suhre, K., Navaza, J., and Sanejouand, Y. H. (2006). NORMA: a Tool for Flexible Fitting of High-Resolution Protein Structures into Low-Resolution Electron-

Microscopy-Derived Density Maps. *Acta Crystallogr. D. Biol. Crystallogr.* 62, 1098–1100. doi:10.1107/s090744490602244x

Sun, J., and MacKinnon, R. (2020). Structural Basis of Human KCNQ1 Modulation and Gating. *Cell* 180, 340–e9. doi:10.1016/j.cell.2019.12.003

Taboureau, O., and Jørgensen, F. S. (2011). In Silico predictions of hERG Channel Blockers in Drug Discovery: from Ligand-Based and Target-Based Approaches to Systems Chemical Biology. *Comb. Chem. High. Throughput Screen* 14, 375–387. doi:10.2174/138620711795508322

Tama, F., Miyashita, O., and Brooks, C. L. (2004a). Flexible Multi-Scale Fitting of Atomic Structures into Low-Resolution Electron Density Maps with Elastic Network Normal Mode Analysis. *J. Mol. Biol.* 337, 985–999. doi:10.1016/j.jmb.2004.01.048

Tama, F., Miyashita, O., and Brooks, C. L. (2004b). Normal Mode Based Flexible Fitting of High-Resolution Structure into Low-Resolution Experimental Data from Cryo-EM. *J. Struct. Biol.* 147, 315–326. doi:10.1016/j.jsb.2004.03.002

Tan, Y., Deng, Y., and Qing, H. (2012). Calcium Channel Blockers and Alzheimer's Disease. *Neural Regen. Res.* 7, 137–140. doi:10.3969/j.issn.1673-5374.2012.02.010

Tang, G., Peng, L., Baldwin, P. R., Mann, D. S., Jiang, W., Rees, I., et al. (2007). EMAN2: An Extensible Image Processing Suite for Electron Microscopy. *J. Struct. Biol.* 157, 38–46. doi:10.1016/j.jsb.2006.05.009

Tegunov, D., and Cramer, P. (2019). Real-time Cryo-Electron Microscopy Data Preprocessing with Warp. *Nat. Methods* 16, 1146–1152. doi:10.1038/s41592-019-0580-y

Terashi, G., and Kihara, D. (2018a). De Novo main-chain Modeling for EM Maps Using MAINMAST. *Nat. Commun.* 9, 1618. doi:10.1038/s41467-018-04053-7

Terashi, G., and Kihara, D. (2018b). De Novo main-chain Modeling with MAINMAST in 2015/2016 EM Model Challenge. *J. Struct. Biol.* 204, 351–359. doi:10.1016/j.jsb.2018.07.013

Terwilliger, T. C., Adams, P. D., Afonine, P. V., and Sobolev, O. V. (2018). A Fully Automatic Method Yielding Initial Models from High-Resolution Cryo-Electron Microscopy Maps. *Nat. Methods* 15, 905–908. doi:10.1038/s41592-018-0173-1

Terwilliger, T. C., Adams, P. D., Afonine, P. V., and Sobolev, O. V. (2020). Cryo-EM Map Interpretation and Protein Model-Building Using Iterative Map Segmentation. *Protein Sci.* 29, 87–99. doi:10.1002/pro.3740

Terwilliger, T. C., Poon, B. K., Afonine, P. V., Schlicksup, C. J., Croll, T. I., Millán, C., et al. (2022). Improved AlphaFold Modeling with Implicit Experimental Information. *bioRxiv*. doi:10.1101/2022.01.07.475350

Tominaga, M., and Caterina, M. J. (2004). Thermosensation and Pain. *J. Neurobiol.* 61, 3–12. doi:10.1002/neu.20079

Topf, M., Lasker, K., Webb, B., Wolfson, H., Chiu, W., and Sali, A. (2008). Protein Structure Fitting and Refinement Guided by Cryo-EM Density. *Structure* 16, 295–307. doi:10.1016/j.str.2007.11.016

Trabuco, L. G., Villa, E., Mitra, K., Frank, J., and Schulten, K. (2008). Flexible Fitting of Atomic Structures into Electron Microscopy Maps Using Molecular Dynamics. *Structure* 16, 673–683. doi:10.1016/j.str.2008.03.005

Traynelis, S. F., Wollmuth, L. P., McBain, C. J., Menniti, F. S., Vance, K. M., Ogden, K. K., et al. (2010). Glutamate Receptor Ion Channels: Structure, Regulation, and Function. *Pharmacol. Rev.* 62, 405–496. doi:10.1124/pr.109.002451

Ulmschneider, M. B., Bagnéris, C., McCusker, E. C., DeCaen, P. G., Delling, M., Clapham, D. E., et al. (2013). Molecular Dynamics of Ion Transport through the Open Conformation of a Bacterial Voltage-Gated Sodium Channel. *Proc. Natl. Acad. Sci. U. S. A.* 110, 6364–6369. doi:10.1073/pnas.1214667110

Ung, P. M., Ghanakota, P., Graham, S. E., Lexa, K. W., and Carlson, H. A. (2016). Identifying Binding Hot Spots on Protein Surfaces by Mixed-Solvent Molecular Dynamics: HIV-1 Protease as a Test Case. *Biopolymers* 105, 21–34. doi:10.1002/bip.22742

Vandenberg, J. I., Perozo, E., and Allen, T. W. (2017). Towards a Structural View of Drug Binding to hERG K+ Channels. *Trends Pharmacol. Sci.* 38, 899–907. doi:10.1016/j.tips.2017.06.004

Villoutreix, B. O., and Taboureau, O. (2015). Computational Investigations of hERG Channel Blockers: New Insights and Current Predictive Models. *Adv. Drug Deliv. Rev.* 86, 72–82. doi:10.1016/j.addr.2015.03.003

Volkamer, A., Kuhn, D., Rippmann, F., and Rarey, M. (2012). DoGSiteScorer: a Web Server for Automatic Binding Site Prediction, Analysis and Druggability Assessment. *Bioinformatics* 28, 2074–2075. doi:10.1093/bioinformatics/bts310

Vuillemot, R., Miyashita, O., Tama, F., Rouiller, I., and Jonic, S. (2022). NMMD: Efficient Cryo-EM Flexible Fitting Based on Simultaneous Normal Mode and Molecular Dynamics Atomic Displacements. *J. Mol. Biol.* 434, 167483. doi:10.1016/j.jmb.2022.167483

Wang, D., Cui, C., Ding, X., Xiong, Z., Zheng, M., Luo, X., et al. (2019). Improving the Virtual Screening Ability of Target-specific Scoring Functions Using Deep Learning Methods. *Front. Pharmacol.* 10, 924. doi:10.3389/fphar.2019.00924

Wang, D., Wang, Y., Chang, J., Zhang, L., Wang, H., and E., W. (2022). Efficient Sampling of High-Dimensional Free Energy Landscapes Using Adaptive Reinforced Dynamics. *Nat. Comput. Sci.* 2, 20–29. doi:10.1038/s43588-021-00173-1

Wang, J., Jain, A., McDonald, L. R., Gambogi, C., Lee, A. L., and Dokholyan, N. V. (2020a). Mapping Allosteric Communications within Individual Proteins. *Nat. Commun.* 11, 3862. doi:10.1038/s41467-020-17618-2

Wang, Q., Corey, R. A., Hedger, G., Aryal, P., Grieben, M., Nasrallah, C., et al. (2020b). Lipid Interactions of a Ciliary Membrane TRP Channel: Simulation and Structural Studies of Polycystin-2. *Structure* 28, 169–e5. e165. doi:10.1016/j.str.2019.11.005

Wang, W., and MacKinnon, R. (2017). Cryo-EM Structure of the Open Human Ether-À-Go-Go-Related K+ Channel hERG. *Cell* 169, 422–e10. doi:10.1016/j.cell.2017.03.048

Wang, Y., Guo, Y., Li, G., Liu, C., Wang, L., Zhang, A., et al. (2021). The Push-To-Open Mechanism of the Tethered Mechanosensitive Ion Channel NompC. *eLife* 10. doi:10.7554/eLife.58388

Wass, M. N., Kelley, L. A., and Sternberg, M. J. (2010). 3DLigandSite: Predicting Ligand-Binding Sites Using Similar Structures. *Nucleic Acids Res.* 38, W469–W473. doi:10.1093/nar/gkq406

Wen, H., and Zheng, W. (2018). Decrypting the Heat Activation Mechanism of TRPV1 Channel by Molecular Dynamics Simulation. *Biophys. J.* 114, 40–52. doi:10.1016/j.bpj.2017.10.034

Wójcikowski, M., Ballester, P. J., and Siedlecki, P. (2017). Performance of Machine-Learning Scoring Functions in Structure-Based Virtual Screening. *Sci. Rep.* 7, 46710. doi:10.1038/srep46710

Wu, M., and Lander, G. C. (2020). Present and Emerging Methodologies in Cryo-EM Single-Particle Analysis. *Biophys. J.* 119, 1281–1289. doi:10.1016/j.bpj.2020.08.027

Wu, N., Strömich, L., and Yaliraki, S. N. (2022). Prediction of Allosteric Sites and Signaling: Insights from Benchmarking Datasets. *Patterns (N Y)* 3, 100408. doi:10.1016/j.patter.2021.100408

Wu, X., Milne, J. L., Borgnia, M. J., Rostapshov, A. V., Subramaniam, S., and Brooks, B. R. (2003). A Core-Weighted Fitting Method for Docking Atomic Structures into Low-Resolution Maps: Application to Cryo-Electron Microscopy. *J. Struct. Biol.* 141, 63–76. doi:10.1016/s1047-8477(02)00570-1

Wulff, H., Castle, N. A., and Pardo, L. A. (2009). Voltage-gated Potassium Channels as Therapeutic Targets. *Nat. Rev. Drug Discov.* 8, 982–1001. doi:10.1038/nrd2983

Wulff, H., Christophersen, P., Colussi, P., Chandy, K. G., and Yarov-Yarovoy, V. (2019). Antibodies and Venom Peptides: New Modalities for Ion Channels. *Nat. Rev. Drug Discov.* 18, 339–357. doi:10.1038/s41573-019-0013-8

Xiang, Z., and Honig, B. (2001). Extending the Accuracy Limits of Prediction for Side-Chain Conformations. *J. Mol. Biol.* 311, 421–430. doi:10.1006/jmbi.2001.4865

Xie, J., Ke, M., Xu, L., Lin, S., Huang, J., Zhang, J., et al. (2020). Structure of the Human Sodium Leak Channel NALCN in Complex with FAM155A. *Nat. Commun.* 11, 5831. doi:10.1038/s41467-020-19667-z

Xu, K., Wang, Z., Shi, J., Li, H., and Zhang, Q. C. (2019). A2-Net: Molecular Structure Estimation from Cryo-EM Density Volumes. *Aaai* 33, 1230–1237. doi:10.1609/aaai.v33i01.33011230

Yan, Z., Zhou, Q., Wang, L., Wu, J., Zhao, Y., Huang, G., et al. (2017). Structure of the Nav1.4-β1 Complex from Electric Eel. *Cell* 170, 470–e11. e411. doi:10.1016/j.cell.2017.06.039

Yang, J., Roy, A., and Zhang, Y. (2013a). Protein-ligand Binding Site Recognition Using Complementary Binding-specific Substructure Comparison and Sequence Profile Alignment. *Bioinformatics* 29, 2588–2595. doi:10.1093/bioinformatics/btt447

Yang, Y., Zhang, W., Cheng, J., Tang, Y., Peng, Y., and Li, Z. (2013b). Pharmacophore, 3D-QSAR, and Bayesian Model Analysis for Ligands Binding at the Benzodiazepine Site of GABAA Receptors: the Key Roles of

Amino Group and Hydrophobic Sites. *Chem. Biol. Drug Des.* 81, 583–590. doi:10.1111/cbdd.12100

Yelshanskaya, M. V., Patel, D. S., Kottke, C. M., Kurnikova, M. G., and Sobolevsky, A. I. (2022). Opening of Glutamate Receptor Channel to Subconductance Levels. *Nature* 605, 172–178. doi:10.1038/s41586-022-04637-w

Yin, Y., Le, S. C., Hsu, A. L., Borgnia, M. J., Yang, H., and Lee, S. Y. (2019). Structural Basis of Cooling Agent and Lipid Sensing by the Cold-Activated TRPM8 Channel. *Science* 363, 945. doi:10.1126/science.aav9334

Yin, Y., Wu, M., Zubcevic, L., Borschel, W. F., Lander, G. C., and Lee, S. Y. (2018). Structure of the Cold- and Menthol-Sensing Ion Channel TRPM8. *Science* 359, 237–241. doi:10.1126/science.aan4325

Yip, K. M., Fischer, N., Paknia, E., Chari, A., and Stark, H. (2020). Atomic-resolution Protein Structure Determination by Cryo-EM. *Nature* 587, 157–161. doi:10.1038/s41586-020-2833-4

Yu, H., Bai, X. C., and Wang, W. (2021). Characterization of the Subunit Composition and Structure of Adult Human glycine Receptors. *Neuron* 109, 2707–e6. doi:10.1016/j.neuron.2021.08.019

Yuan, Y., Pei, J., and Lai, L. (2013). Binding Site Detection and Druggability Prediction of Protein Targets for Structure-Based Drug Design. *Curr. Pharm. Des.* 19, 2326–2333. doi:10.2174/1381612811319120019

Zampieri, V., Gobet, A., Robert, X., Falson, P., and Chaptal, V. (2021). CryoEM Reconstructions of Membrane Proteins Solved in Several Amphipathic Solvents, Nanodisc, Amphipol and Detergents, Yield Amphipathic Belts of Similar Sizes Corresponding to a Common Ordered Solvent Layer. *Biochim. Biophys. Acta Biomembr.* 1863, 183693. doi:10.1016/j.bbamem.2021.183693

Zehni, M., Do, M. N., and Zhao, Z. (2020). “Deepsharpen: Deep-Learning Based Sharpening of 3D Reconstruction Map from Cryo-Electron Microscopy,” in 2020 IEEE 17th International Symposium on Biomedical Imaging Workshops (Iowa City: ISBI Workshops), 1–4.

Zhang, J., Mao, W., Ren, Y., Sun, R. N., Yan, N., and Gong, H. (2018a). Simulating the Ion Permeation and Ion Selection for a Eukaryotic Voltage-Gated Sodium Channel NaVPaS. *Protein Cell* 9, 580–585. doi:10.1007/s13238-018-0522-y

Zhang, J., and Nussinov, R. (2019). *Protein Allostery in Drug Discovery*. Springer.

Zhang, L., Wang, H., and E, W. (2018b). Reinforced Dynamics for Enhanced Sampling in Large Atomic and Molecular Systems. *J. Chem. Phys.* 148, 124113. doi:10.1063/1.5019675

Zhang, Q., Gao, Z., and Yang, H. (2016). Computer-Aided Drug Discovery and Design Targeting Ion Channels. *Curr. Top. Med. Chem.* 16, 1819–1829. doi:10.2174/1568026616666160315142346

Zhang, X., Zhang, B., Freddolino, P. L., and Zhang, Y. (2022). CR-I-TASSER: Assemble Protein Structures from Cryo-EM Density Maps Using Deep Convolutional Neural Networks. *Nat. Methods* 19, 195–204. doi:10.1038/s41592-021-01389-9

Zhang, Y., Ye, F., Zhang, T., Lv, S., Zhou, L., Du, D., et al. (2021). Structural Basis of Ketamine Action on Human NMDA Receptors. *Nature* 596, 301–305. doi:10.1038/s41586-021-03769-9

Zhao, Y., Huang, G., Wu, J., Wu, Q., Gao, S., Yan, Z., et al. (2019). Molecular Basis for Ligand Modulation of a Mammalian Voltage-Gated Ca2+ Channel. *Cell* 177, 1495–e12. doi:10.1016/j.cell.2019.04.043

Zheng, W. (2011). Accurate Flexible Fitting of High-Resolution Protein Structures into Cryo-Electron Microscopy Maps Using Coarse-Grained Pseudo-energy Minimization. *Biophys. J.* 100, 478–488. doi:10.1016/j.bpj.2010.12.3680

Zheng, W. (2021). Predicting Cryptic Ligand Binding Sites Based on Normal Modes Guided Conformational Sampling. *Proteins* 89, 416–426. doi:10.1002/prot.26027

Zhong, E. D., Bepler, T., Berger, B., and Davis, J. H. (2021a). CryoDRGN: Reconstruction of Heterogeneous Cryo-EM Structures Using Neural Networks. *Nat. Methods* 18, 176–185. doi:10.1038/s41592-020-01049-4

Zhong, E. D., Bepler, T., Davis, J. H., and Berger, B. 2021b. "Reconstructing Continuous Distributions of 3D Protein Structure from Cryo-EM Images", *arXiv*. doi:10.48550/arXiv.1909.05215

Zhong, E. D., Lerer, A., Davis, J. H., and Berger, B. (2020). “"CryoDRGN2: Ab Initio Neural Reconstruction of 3D Protein Structures from Real Cryo-EM Images,” in Proceedings of the IEEE/CVF International Conference on Computer Vision), 4066–4075.

Conflict of Interest: ZD, QW, YW, DZ, RX, LG, HW were employed by the company DP Technology and all authors have participated in the development of the Hermite platform or the Uni-Fold project.

frontiers | Frontiers in Pharmacology

BRIEF RESEARCH REPORT
published: 30 June 2022
doi: 10.3389/fphar.2022.929684

Structural Insights Into the High Selectivity of the Anti-Diabetic Drug Mitiglinide

Mengmeng Wang[1,2,3,4], *Jing-Xiang Wu*[1,4] *and Lei Chen*[1,2,3,4]*

[1]*State Key Laboratory of Membrane Biology, Beijing Key Laboratory of Cardiometabolic Molecular Medicine, College of Future Technology, Institute of Molecular Medicine, Peking University, Beijing, China,* [2]*Peking-Tsinghua Center for Life Sciences, Peking University, Beijing, China,* [3]*Academy for Advanced Interdisciplinary Studies, Peking University, Beijing, China,* [4]*National Biomedical Imaging Center, Peking University, Beijing, China*

Mitiglinide is a highly selective fast-acting anti-diabetic drug that induces insulin secretion by inhibiting pancreatic K_{ATP} channels. However, how mitiglinide binds K_{ATP} channels remains unknown. Here, we show the cryo-EM structure of the SUR1 subunit complexed with mitiglinide. The structure reveals that mitiglinide binds inside the common insulin secretagogue-binding site of SUR1, which is surrounded by TM7, TM8, TM16, and TM17. Mitiglinide locks SUR1 in the NBD-separated inward-facing conformation. The detailed structural analysis of the mitiglinide-binding site uncovers the molecular basis of its high selectivity.

Keywords: K_{ATP}, SUR1, mitiglinide, insulin secretagogues, ABC transporter, diabetes

Edited by:
Tian-Le Xu,
Shanghai Jiao Tong University, China

Reviewed by:
Huaiyu Yang,
East China Normal University, China
Roope Mannikko,
University College London,
United Kingdom

Correspondence:
Lei Chen
chenlei2016@pku.edu.cn

Specialty section:
This article was submitted to Pharmacology of Ion Channels and Channelopathies,
a section of the journal Frontiers in Pharmacology.

Received: *27 April 2022*
Accepted: *25 May 2022*
Published: *30 June 2022*

Citation:
Wang M, Wu J-X and Chen L (2022) Structural Insights Into the High Selectivity of the Anti-Diabetic Drug Mitiglinide.
Front. Pharmacol. 13:929684.
doi: 10.3389/fphar.2022.929684

INTRODUCTION

More than 400 million people are living with diabetes worldwide, and type 2 diabetes (T2DM) accounts for nearly 90% of patients with diabetes (Chatterjee et al., 2017). Dysfunction of insulin secretion is one of the hallmarks of T2DM (Daryabor et al., 2020). Previous studies have established that the K_{ATP} channel plays an essential role in insulin secretion and is a drug target for diabetes (Gribble and Reimann, 2003).

The K_{ATP} channel is a hetero-octamer complex composed of four pore-forming Kir6 (kir6.1 or Kir6.2) subunits and four regulatory sulfonylureas receptor subunits (SUR1 or SUR2). K_{ATP} channels can sense intracellular ATP/ADP ratio using the inhibitory ATP binding site on Kir6 and the activating Mg–ADP binding site on SUR, coupling the metabolism status of the cell to its membrane potential (Ashcroft and Gribble, 1998). K_{ATP} channels are widely distributed in many tissues, including the brain (Ashford et al., 1988), muscles (Noma, 1983; Spruce et al., 1985), and endocrine cells (Cook and Hales, 1984), and perform important physiological functions. In pancreatic β-cells, K_{ATP} channels are mainly formed by Kir6.2 and SUR1, and play key roles in controlling insulin secretion (Ashcroft and Rorsman, 1989). When blood glucose level increases, the intracellular ATP/ADP ratio also increases accordingly, leading to the suppression of the K_{ATP} channel activity. The inhibited potassium efflux through the K_{ATP} channel induces depolarization of the β-cell membrane, resulting in the subsequent activation of voltage-gated calcium channel, calcium influx, and insulin secretion (Rorsman and Trube, 1985; Nichols, 2006). Mutations in genes encoding either Kir6.2 or SUR1 cause disorders in insulin secretion, such as congenital hyperinsulinemia and neonatal diabetes (Ashcroft, 2005). Small-molecule drugs that inhibit the pancreatic K_{ATP} channel are widely used to boost insulin secretion for the treatment of diabetes and are therefore named insulin secretagogues (ISs) (Gribble and Reimann, 2003).

Insulin secretagogues are chemically diverse small molecules, including sulphonylureas, such as glibenclamide (GBM), and glinides, such as repaglinide (RPG) and mitiglinide (MTG) (Wu et al., 2020). ISs bind to the SUR subunits to inhibit the K_{ATP} channels (Wu et al., 2020). MTG ((+)-monocalcium bis [(2S)-2-benzyl-3-(*cis*-hexahydro-2-isoindolinyl carbonyl)propionate]dihydrate), also named KAD-1229, is a glinide that was developed for the treatment of postprandial hyperglycemia (Pratley et al., 2001) and has been approved for the treatment of patients with T2DM in Japan (brand name, Glufast, approved in 2004). MTG has an immediate and short-lasting effect on hypoglycemic action in the postprandial glucose-load state in clinical trials (Phillippe and Wargo, 2013). *In vitro* experiments supported that MTG increases insulin release from a pancreatic β-cell line MIN6 cell (Mogami et al., 1994; Reimann et al., 2001). The insulin responses to chronic MTG treatment were comparable to chronic RPG or GBM treatment in MIN6 cells (Reimann et al., 2001). MTG can displace [^{3}H]-GBM binding to HIT-15 cells with an IC_{50} of 13 nM (Ohnota et al., 1994), suggesting that they might share an overlapped binding site. Notably, MTG is highly selective toward SUR1 over SUR2 (Reimann et al., 2001; Sunaga et al., 2001), and GBM is moderately selective, while RPG is non-selective (Quast et al., 2004). Recent structural studies have uncovered the binding modes of GBM and RPG (Wu et al., 2020), but the exact binding mode of MTG on SUR1 remains unknown. Here, we present the cryo-EM structure of the SUR1 subunit complexed with MTG, allowing the direct visualization of how MTG binds SUR1.

METHODS

Cell Lines

FreeStyle 293-F (Thermo Fisher Scientific) suspension cells were cultured in SMM 293-TI (Sino Biological Inc.) supplemented with 1% fetal bovine serum (FBS) at 37°C, with 6% CO_2 and 70% humidity. Sf9 insect (Thermo Fisher Scientific) suspension cells were cultured in Sf-900 III SFM medium (Thermo Fisher Scientific) at 27°C.

Construct of NGFP_linker_SUR1core

We made a truncated *Mesocricetus auratus* SUR1 construct maSUR1core (from 208 to C terminal) based on the previous work by Ding et al. (2019). We added an N-terminal GFP and MBP tag, a PreScission protease cleavage site, KNtp of mmKir6.2 (Ding et al., 2019), and a GS-rich linker before SUR1core. The construct was made in a modified BacMam vector (Li et al., 2017).

Electrophysiology

Wild-type SUR1 or its mutants together with CGFP-tagged Kir6.2 were transfected into FreeStyle 293F suspension cells using polyethyleneimine at the cell density of 1.0×10^6 cells/ml. Cells were cultured in FreeStyle expression medium supplemented with 1% FBS for 24 h and then seeded into 12-mm dishes for adhesion before recording. Macroscopic currents were recorded in the inside-out mode at +60 mV by Axon-patch 200B amplifier (Axon Instruments, United States). Patch electrodes were pulled by a horizontal microelectrode puller (P-1000, Sutter Instrument Co., United States) to 2.0–3.0 MΩ resistance. Both pipette and bath solution was based on KINT buffer, containing (mM): 140 KCl, 1 EGTA, and 10 HEPES (pH, 7.4, KOH). For mitiglinide (Targetmol) and RPG (Abcam) inhibition, both the stock solutions (10 mM mitiglinide and 100 mM RPG) were dissolved in DMSO, stored at −20°C, and diluted into KINT buffer to the final concentrations before recording. ATP (Sigma) and ADP (Sigma) stocks were prepared on ice, and stored at −20°C. ATP and ADP were dissolved in water and adjusted to pH = 7 by KOH (Sigma). The nucleotide concentration was determined by its extinction coefficient and absorption at A259 nm. Signals were acquired at 5 kHz and low-pass filtered at 1 kHz. Data were further analyzed by pclampfit 10.0 software.

Protein Expression and Purification

SUR1core was expressed as described previously (Ding et al., 2019), and the purification process was carried out with minor modifications. For protein purification, membrane pellets were homogenized in TBS (20 mM Tris–HCl; pH, 7.5; 150 mM NaCl) and solubilized in TBS with 1% GDN (Anatrace), supplemented with protease inhibitors (1 mg/ml leupeptin, 1 mg/ml pepstatin, 1 mg/ml aprotinin, and 1 mM PMSF), 1 mM EDTA, and 1 mM EGTA for 30 min at 4°C. Unsolubilized materials were discarded after centrifugation at 100,000 g for 30 min and the supernatant was loaded onto a 5-ml StrepTactin 4FF (Smart Lifesciences) packed column. The Strep column was washed with TBS buffer supplemented with 0.01% GDN, protease inhibitors (1 mg/ml leupeptin, 1 mg/ml pepstatin, and 1 mg/ml aprotinin), 1 mM EDTA, and 1 mM EGTA. Then the column was washed using TBS supplemented with 0.01% GDN, 3mM $MgCl_2$, and 1 mM ATP. The last washing step buffer was TBS supplemented with 0.01% GDN. The SUR1core was eluted with TBS (50 mM Tris–HCl; pH, 7.5; 150 mM NaCl) supplemented with 0.006% GDN and 5 mM desthiobiotin. The eluate was concentrated and supplemented with PreScission protease overnight. The next day, SUR1core was further purified using Superose 6 increase (GE Healthcare) column running with TBS supplemented with 0.006% GDN. Peak fractions were collected and concentrated to A_{280} = 10 (50 μM). The purified protein was used for cryo-EM sample preparation.

Cryo-EM Sample Preparation

100 μM mitiglinide was added to the sample and incubated for 20 min before centrifugation at 40,000 rpm for 30 min using a TLA55 rotor (Beckman). Cryo-EM grids were prepared with Vitrobot Mark IV (FEI) and GIG R0.6/1 holey carbon grids, which were glow discharged for 120 s using air before adding the protein sample. A 2.5-μl sample was applied to the glow-discharged grid, and then the grid was blotted at blotting force at level 2 for 2 s at 100% humidity and 10°C, before it was plunge frozen in liquid ethane.

Cryo-EM Data Acquisition

Cryo-grids were screened on a Talos Arctica microscope (Thermo Fisher Scientific) operated at 200 kV. Grids of good quality were further loaded onto a Titan Krios microscope (Thermo Fisher Scientific) operated at 300 kV for data collection. Images were collected using a K2 camera (Gatan)

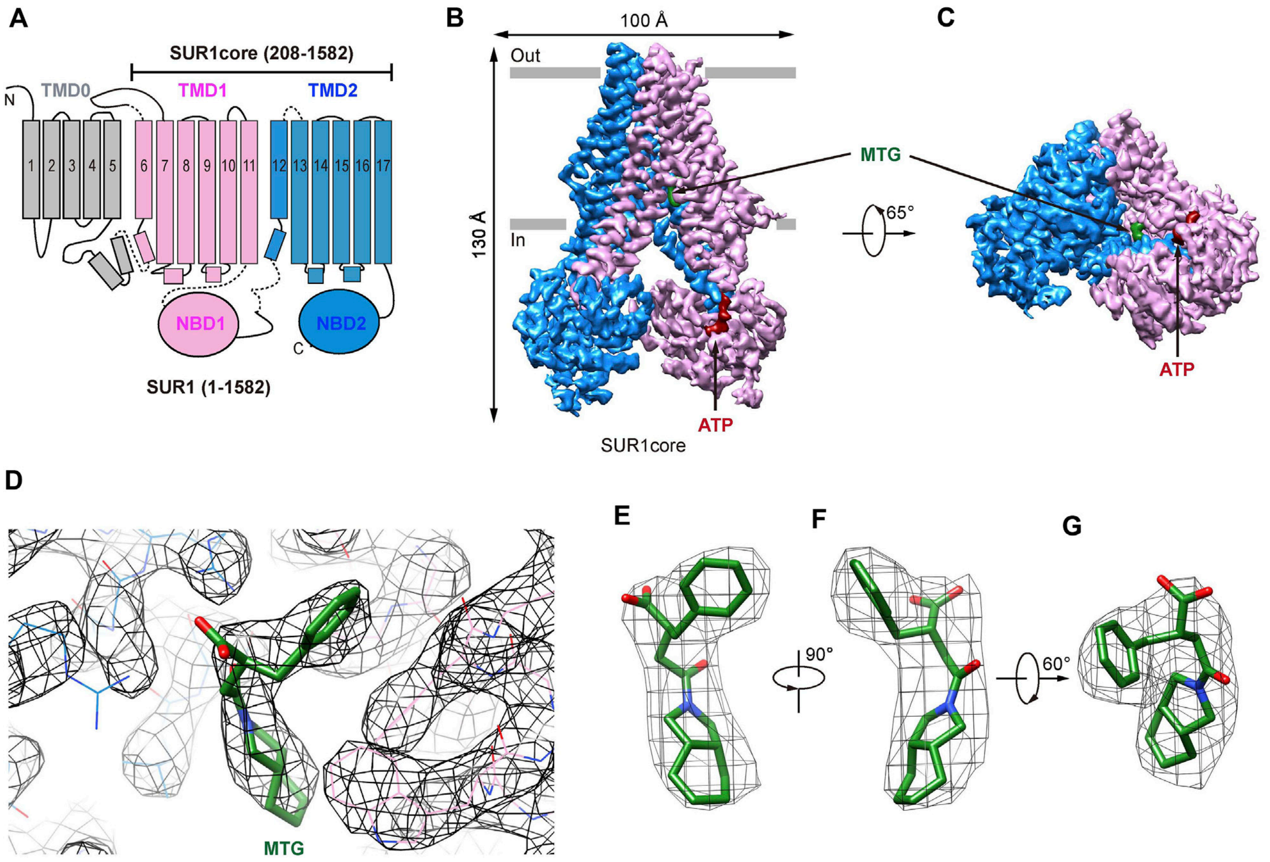

FIGURE 1 | Structure of SUR1 complexed with MTG. **(A)** Topology of SUR1 subunits. TMD, transmembrane domain; NBD, nucleotide-binding domain. Transmembrane helices are shown as cylinders. TMD0 fragment, TMD1-NBD1, and TMD2-NBD2 are shown in gray, pink, and blue, respectively. **(B)** Side view of the cryo-EM density of the SUR1core. ATP and MTG are shown in red and green, respectively. **(C)** Bottom view of the cryo-EM density of the SUR1core. **(D)** Densities of MTG and its surrounding amino acids. **(E–G)** MTG densities viewed from different angles.

mounted post a Quantum energy filter with a 20-eV slit and operated under super-resolution mode with a pixel size of 1.045 Å at the object plane, controlled by software Serial EM. Defocus values were set from −1.5 to −1.8 μm for data collection. The dose rate on the detector was 8.078 e^- pixel^{-1} s^{-1}, and the total exposure was 54.3 e^-A^{-2}. Each 6.72 s movie was dose-fractioned into 32 frames.

Image Processing

A total of 1,181 movies were collected and the movies were exposure filtered, gain corrected, motion corrected, mag-distortion corrected, and binned with MotionCor2 (Zheng et al., 2017), producing dose-weighted and summed micrographs. CTF models of dose-weighted micrographs were determined using Gctf (Zhang, 2016). Gautomatch (developed by Kai Zhang, MRC-LMB) was used for auto-picking. Data processing was initially performed using Relion_3.0 (Zivanov et al., 2018). Particles were extracted from dose-weighted micrographs. After 2D classification (379K particles) and 3D classification with C1 symmetry, 130K particles with good transmembrane domain (TMD) densities were re-extracted and re-centered. In this stage, the mitiglinide density can be observed. The remaining particles were subjected to focused 3D classification with a TMD mask to select around 20K particles (seed particles) with good mitiglinide density. Then the 379K particles were subjected to seed-facilitated 3D classification (Wang et al., 2021) to produce 130K particles in CryoSPARC2 (Punjani et al., 2017). These particles were subjected to non-uniform refinement, CTF refinement, and local non-uniform refinement in cryoSPARC2 to generate a high-resolution map.

Model Building

SUR1 ABC transporter domain in the previously reported K_{ATP} model (PDB ID: 6BJ1) was docked into the density map using UCSF Chimera (Pettersen et al., 2004). The model was manually rebuilt in Coot (Emsley et al., 2010) and refined against the density map using Phenix (Afonine et al., 2018). Figures were prepared using Pymol and UCSF Chimera X (Pettersen et al., 2020).

Quantification and Statistical Analysis

Global resolution estimations of cryo-EM density maps are based on the 0.143 Fourier Shell Correlation criterion (Rosenthal and Henderson, 2003). Electrophysiological data reported were analyzed with pClampfit 10.0 software. The number of

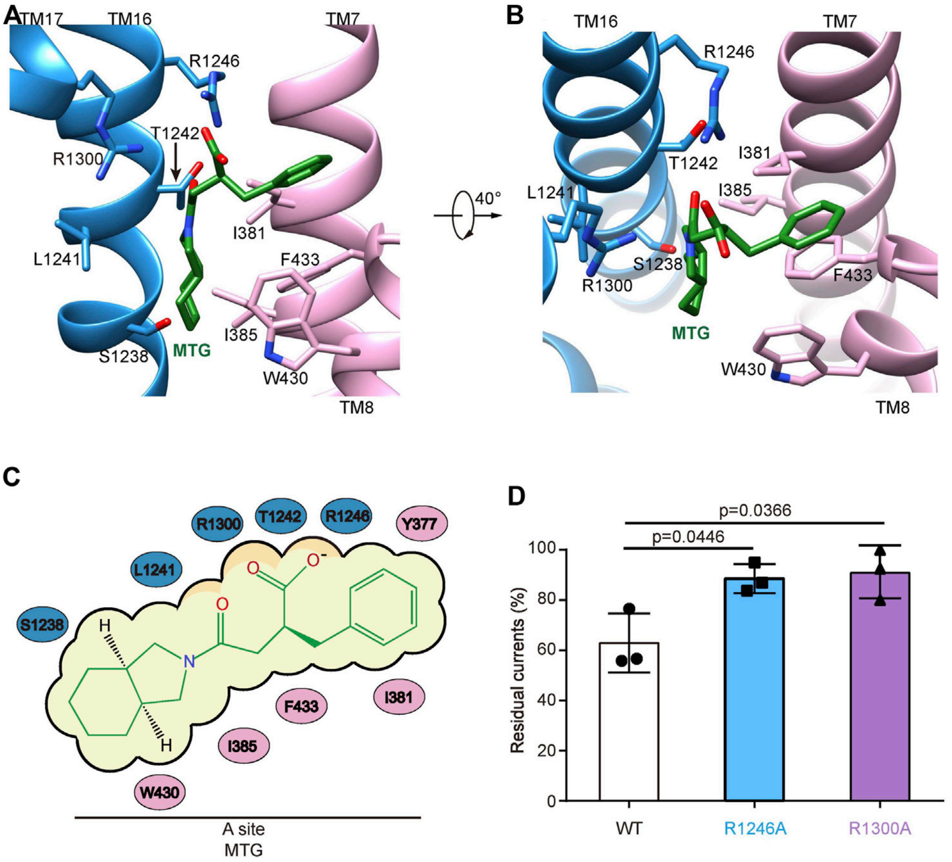

FIGURE 2 | The MTG-binding pocket in SUR1. **(A,B)** Close-up views of the MTG-binding site. TMD1, TMD2, and MTG are shown in pink, blue, and green, respectively. **(C)** Cartoon representation of the interaction between MTG and SUR1. **(D)** Wild-type and mutated K_{ATP} channels inhibition by 10 μM MTG. Data are shown as mean ± SD and *n* = 3 independent patches. *p* was calculated by unpaired two-tailed *t*-test and indicated above.

biological replicates (*N*) and the relevant statistical parameters for each experiment (such as a mean or standard error) are described in figure legends. No statistical methods were used to predetermine sample sizes.

RESULTS

Structure Determination of SUR1core in Complex With Mitiglinide

Previous cryo-EM studies on K_{ATP} channels in complex with GBM (Martin et al., 2017; Wu et al., 2018) or RPG (Ding et al., 2019) have established that the ABC transporter region of the SUR subunit harbors the IS-binding site. Therefore, we used a truncated construct (SUR1core) that encompasses 208-1582 of SUR1, including TMD1, NBD1, TMD2, and NBD2 (**Figure 1A** and **Supplementary Figure S1**), for subsequent structure determination. Purified SUR1core protein was supplemented with ATP and MTG for cryo-EM sample preparation and data collection. Image processing yielded a reconstruction with an overall resolution of 3.27 Å (**Figure 1B,C** and **Supplementary Figure S1,S2**). High-quality local map allows the unambiguous identification of the MTG molecule (**Figure 1D–G**).

The Binding Mode of Mitiglinide

In the presence of ATP and MTG, SUR1core shows an inward-facing conformation with its central vestibule widely open to the cytosol (**Figure 1B,C**). ATP binds to the NBD1 and MTG binds inside a pocket in the central vestibule of SUR1 (**Figure 1B–D**). The MTG-binding pocket is formed by residues on TM7 and TM8 of TMD1 and TM16 and TM17 of TMD2 (**Figure 2A,B**). The interactions between MTG and SUR1 involve both polar interactions and hydrophobic interactions (**Figure 2A,B**). The central negatively charged carboxyl group of MTG makes electrostatic interactions with positively charged R1246 on TM16 and R1300 on TM17 (**Figure 2A,B**). The benzene ring of MTG stacks with the phenyl group of F433 (**Figure 2A,B**). The bulky hexahydro-2-isoindoline group binds in a hydrophobic pocket surrounded by L1241 and T1242 of TMD2 and I381, I385, F433, and W430 of TMD1 (**Figure 2A,B**). To understand the role of R1246 and R1300 on the inhibitory function of MTG, we mutated them into alanines individually. We found that both R1246A and R1300A mutations significantly decreased the inhibitory effect of MTG (**Figure 2D**and **Supplementary Figure S3**), emphasizing their importance on MTG binding and inhibition.

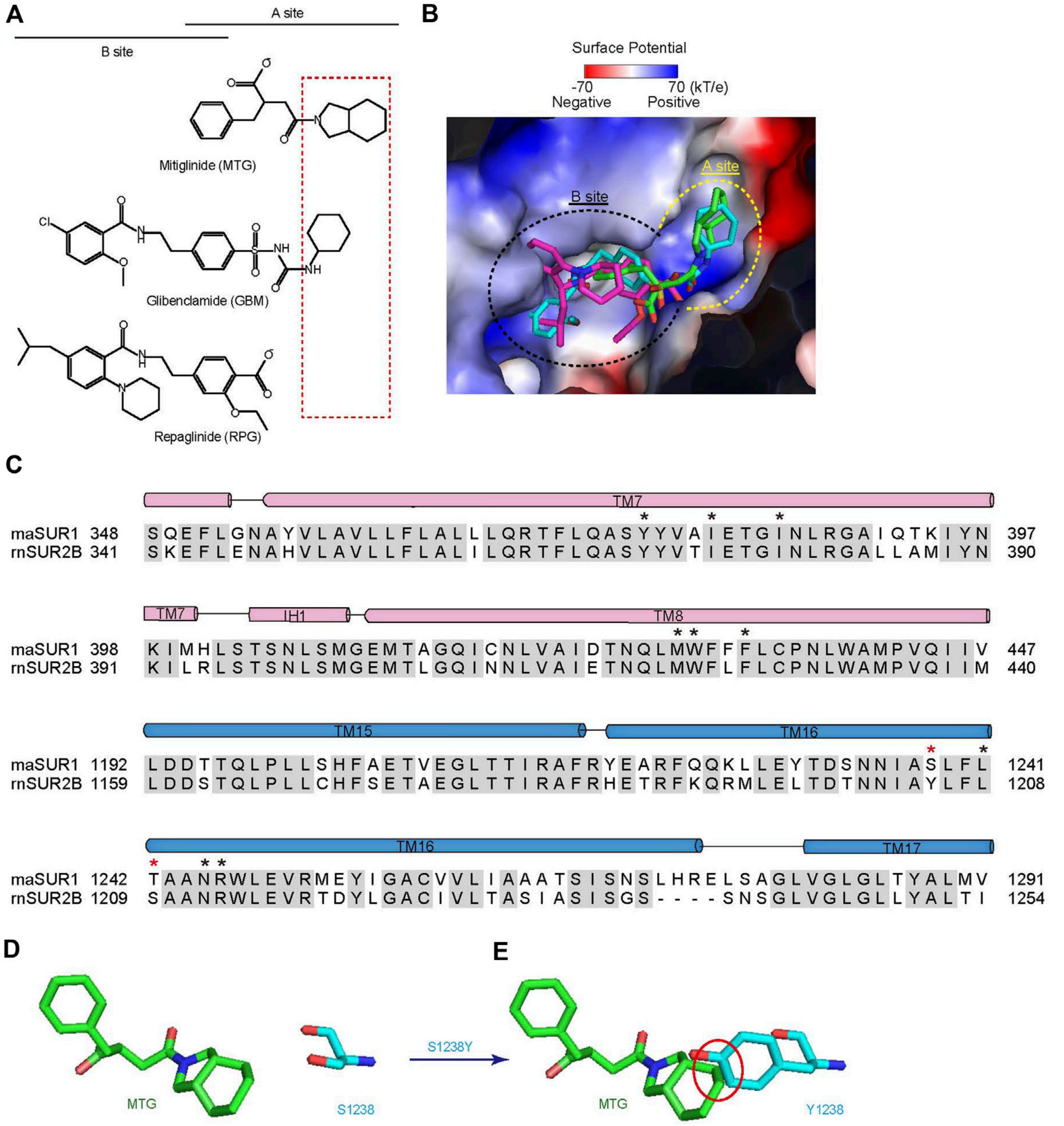

FIGURE 3 | MTG binds in the A-site of SUR1. **(A)** Chemical structures of MTG (A-site ligand), RPG (B-site ligand), and GBM (A + B site ligand). The "SUR Isotype Selectivity Determinative Moiety" (SISDM) is boxed in red. **(B)** Structural superposition of MTG, RPG (PDB ID: 6BJ3), and GBM (PDB ID: 6BAA) in their binding pocket. Insulin secretagogues are shown as sticks. The electrostatic surface of SUR1 is calculated with Pymol. **(C)** Sequence alignment of MTG binding pocket between *Mesocricetus auratus* SUR1 (maSUR1) and *Rattus norvegicus* (rnSUR2). The identical and different MTG-interacting residues are highlighted by black and red asterisks above. **(D)** The relative position of MTG (green) and S1238 side chain (cyan). **(E)** The mutation of S1238 to Tyr (cyan) would generate sterical clashes with MTG (green). Clashes with inter-atom distance smaller than 2.2 Å non-bond distance are circled in red.

Mitiglinide Binds the A-Site of SUR1

Accumulated studies on the structure–activity relationship of IS indicate that there are two overlapping binding sites for IS on SUR, the A-site and the B-site (Yan et al., 2006) (**Figure 3A**). GBM binds in both A- and B-sites (Wu et al., 2018), while RPG binds in the B-site (Ding et al., 2019; Martin et al., 2019). Our structure shows that MTG mainly binds in the A-site (**Figure 3A,B**). MTG-interacting residues are almost identical between SUR1 and SUR2, except that T1242 is replaced by a serine in SUR2 and S1238 is replaced by tyrosine in SUR2 (**Figure 3C**). Notably, S1238 is near the A-site (**Figure 2A,B**), and previous studies found that S1238 is the key determinant for the selectivity of certain IS, such as glibenclamide, tolbutamide, and nateglinide (Ashfield et al., 1999; Hansen et al., 2002). In agreement with this, the hexahydro-2-isoindoline group of MTG is near the S1238, and the replacement of S1238 with a tyrosine would generate sterical clashes with MTG (**Figure 3D,E**), abolishing its binding.

DISCUSSION

The structures of SUR1 in complex with IS are now available for RPG, GBM, and MTG. Among them, MTG has the highest selectivity toward SUR1 over SUR2 (Quast et al., 2004). Notably, SUR isotype-selectivity is highly clinically relevant because SUR1-containing K_{ATP} channels are mainly distributed in pancreatic endocrine cells, while SUR2-containing K_{ATP} channels have broad distribution in cardiac muscles and vascular smooth muscles, participating in several key physiological processes in the cardiovascular system, such as the preservation of cardio-protection under ischemic conditions. Moreover, patients with diabetes often have cardiovascular diseases, such as coronary heart disease. Therefore, it is important to consider the off-target side effect of IS treatment for diabetes. The high selectivity of MTG (1,000×) might mitigate the underlying side effects of inhibiting SUR2-containing K_{ATP} channels. In agreement with this theory, it was reported that MTG could preserve the cardio-protective effect of ischemic preconditioning while GBM could not (Ogawa et al., 2007), emphasizing the potential benefit of using highly selective IS for diabetes. In addition, the high selectivity of MTG is also explored to design ^{18}F-labeled positron emission tomography tracers for the measurement of β-cell mass *in vivo* during the progression of diabetes, aiming to better understand the pathogenesis, to facilitate early diagnosis, and to develop novel therapeutics for diabetes (Kimura et al., 2014). Despite the early observation of high selectivity of MTG, how this is achieved was not well understood previously. Our current structure of SUR1 complexed with MTG shows that the hexahydro-2-isoindoline group is close to S1238, the key residue that is different between SUR1 and SUR2. Therefore, we designate this large hexahydro-2-isoindoline as the "SUR Isotype Selectivity Determinative Moiety" (SISDM). Furthermore, structural comparisons among RPG, GBM, and MTG reveal that the size of SISDM correlates well with their selectivity: larger SISDM confers better SUR-isotype selectivity. Therefore, our structure provides mechanistic insight into the high selectivity of MTG and paves the way for further development of next-generation IS with high selectivity.

DATA AVAILABILITY STATEMENT

The datasets presented in this study can be found in online repositories. The names of the repository/repositories and accession number(s) can be found at http://www.wwpdb.org/, 7WIT. https://www.ebi.ac.uk/pdbe/emdb/, EMD-32535.

AUTHOR CONTRIBUTIONS

LC initiated the project. MW purified protein, prepared the cryo-EM sample, and performed electrophysiology experiments. MW and J-XW collected the data. MW processed the data, and built and refined the model with the help of LC. All authors contributed to the manuscript preparation.

FUNDING

The work is supported by grants from the National Natural Science Foundation of China (91957201, 31870833, and 31821091 LC) and the Center for Life Sciences (CLS). This work is also supported by Peking University Ge Li and Ning Zhao Life Science Research Fund for Young Scientists (LGZNQN202102 to LC).

ACKNOWLEDGMENTS

Cryo-EM data collection was supported by the Electron Microscopy Laboratory and Cryo-EM platform of Peking University with the assistance of Xuemei Li, Zhenxi Guo, Bo Shao, Xia Pei, and Guopeng Wang. Part of the structural computation was also performed on the Computing Platform of the Center for Life Science and High-Performance Computing Platform of Peking University. We thank the National Center for Protein Sciences at Peking University in Beijing, China, for assistance with negative stain EM.

SUPPLEMENTARY MATERIAL

The Supplementary Material for this article can be found online at: https://www.frontiersin.org/articles/10.3389/fphar.2022.929684/full#supplementary-material

REFERENCES

Afonine, P. V., Poon, B. K., Read, R. J., Sobolev, O. V., Terwilliger, T. C., Urzhumtsev, A., et al. (2018). Real-space Refinement in PHENIX for Cryo-EM and Crystallography. *Acta Crystallogr. D. Struct. Biol.* 74, 531–544. doi:10.1107/S2059798318006551

Ashcroft, F. M. (2005). ATP-sensitive Potassium Channelopathies: Focus on Insulin Secretion. *J. Clin. Invest.* 115, 2047–2058. doi:10.1172/JCI25495

Ashcroft, F. M., and Gribble, F. M. (1998). Correlating Structure and Function in ATP-Sensitive K+ Channels. *Trends Neurosci.* 21, 288–294. doi:10.1016/s0166-2236(98)01225-9

Ashcroft, F. M., and Rorsman, P. (1989). Electrophysiology of the Pancreatic Beta-Cell. *Prog. Biophys. Mol. Biol.* 54, 87–143. doi:10.1016/0079-6107(89)90013-8

Ashfield, R., Gribble, F. M., Ashcroft, S. J., and Ashcroft, F. M. (1999). Identification of the High-Affinity Tolbutamide Site on the SUR1 Subunit of the K(ATP) Channel. *Diabetes* 48, 1341–1347. doi:10.2337/diabetes.48.6.1341

Ashford, M. L., Sturgess, N. C., Trout, N. J., Gardner, N. J., and Hales, C. N. (1988). Adenosine-5'-triphosphate-sensitive Ion Channels in Neonatal Rat Cultured Central Neurones. *Pflugers Arch.* 412, 297–304. doi:10.1007/BF00582512

Chatterjee, S., Khunti, K., and Davies, M. J. (2017). Type 2 Diabetes. *Lancet* 389, 2239–2251. doi:10.1016/S0140-6736(17)30058-2

Cook, D. L., and Hales, C. N. (1984). Intracellular ATP Directly Blocks K+ Channels in Pancreatic B-Cells. *Nature* 311, 271–273. doi:10.1038/311271a0

Daryabor, G., Atashzar, M. R., Kabelitz, D., Meri, S., and Kalantar, K. (2020). The Effects of Type 2 Diabetes Mellitus on Organ Metabolism and the Immune System. *Front. Immunol.* 11, 1582. doi:10.3389/fimmu.2020.01582

Ding, D., Wang, M., Wu, J. X., Kang, Y., and Chen, L. (2019). The Structural Basis for the Binding of Repaglinide to the Pancreatic KATP Channel. *Cell Rep.* 27, 1848–e1844. doi:10.1016/j.celrep.2019.04.050

Emsley, P., Lohkamp, B., Scott, W. G., and Cowtan, K. (2010). Features and Development of Coot. *Acta Crystallogr. D. Biol. Crystallogr.* 66, 486–501. doi:10.1107/S0907444910007493

Gribble, F. M., and Reimann, F. (2003). Differential Selectivity of Insulin Secretagogues: Mechanisms, Clinical Implications, and Drug Interactions. *J. Diabetes Complicat.* 17, 11–15. doi:10.1016/s1056-8727(02)00272-6

Hansen, A. M., Christensen, I. T., Hansen, J. B., Carr, R. D., Ashcroft, F. M., and Wahl, P. (2002). Differential Interactions of Nateglinide and Repaglinide on the Human Beta-Cell Sulphonylurea Receptor 1. *Diabetes* 51, 2789–2795. doi:10.2337/diabetes.51.9.2789

Kimura, H., Matsuda, H., Fujimoto, H., Arimitsu, K., Toyoda, K., Mukai, E., et al. (2014). Synthesis and Evaluation of 18F-Labeled Mitiglinide Derivatives as Positron Emission Tomography Tracers for β-cell Imaging. *Bioorg. Med. Chem.* 22, 3270–3278. doi:10.1016/j.bmc.2014.04.059

Li, N., Wu, J. X., Ding, D., Cheng, J., Gao, N., and Chen, L. (2017). Structure of a Pancreatic ATP-Sensitive Potassium Channel. *Cell* 168, 101–e10. doi:10.1016/j.cell.2016.12.028

Martin, G. M., Kandasamy, B., DiMaio, F., Yoshioka, C., and Shyng, S. L. (2017). Anti-diabetic Drug Binding Site in a Mammalian KATP Channel Revealed by Cryo-EM. *Elife* 6, e31054. doi:10.7554/eLife.31054

Martin, G. M., Sung, M. W., Yang, Z., Innes, L. M., Kandasamy, B., David, L. L., et al. (2019). Mechanism of Pharmacochaperoning in a Mammalian KATP Channel Revealed by Cryo-EM. *Elife* 8, e46417. doi:10.7554/eLife.46417

Mogami, H., Shibata, H., Nobusawa, R., Ohnota, H., Satou, F., Miyazaki, J., et al. (1994). Inhibition of ATP-Sensitive K+ Channel by a Non-sulfonylurea Compound KAD-1229 in a Pancreatic Beta-Cell Line, MIN 6 Cell. *Eur. J. Pharmacol.* 269, 293–298. doi:10.1016/0922-4106(94)90036-1

Nichols, C. G. (2006). KATP Channels as Molecular Sensors of Cellular Metabolism. *Nature* 440, 470–476. doi:10.1038/nature04711

Noma, A. (1983). ATP-regulated K+ Channels in Cardiac Muscle. *Nature* 305, 147–148. doi:10.1038/305147a0

Ogawa, K., Ikewaki, K., Taniguchi, I., Takatsuka, H., Mori, C., Sasaki, H., et al. (2007). Mitiglinide, a Novel Oral Hypoglycemic Agent, Preserves the Cardioprotective Effect of Ischemic Preconditioning in Isolated Perfused Rat Hearts. *Int. Heart. J.* 48, 337–345. doi:10.1536/ihj.48.337

Ohnota, H., Koizumi, T., Tsutsumi, N., Kobayashi, M., Inoue, S., and Sato, F. (1994). Novel Rapid- and Short-Acting Hypoglycemic Agent, a Calcium(2s)-2-Benzyl-3-(cis-Hexahydro-2-Isoindolinylcarbonyl) Propionate (KAD-1229) that Acts on the Sulfonylurea Receptor: Comparison of Effects between KAD-1229 and Gliclazide. *J. Pharmacol. Exp. Ther.* 269, 489–495.

Pettersen, E. F., Goddard, T. D., Huang, C. C., Couch, G. S., Greenblatt, D. M., Meng, E. C., et al. (2004). UCSF Chimera-Aa Visualization System for Exploratory Research and Analysis. *J. Comput. Chem.* 25, 1605–1612. doi:10.1002/jcc.20084

Pettersen, E. F., Goddard, T. D., Huang, C. C., Meng, E. C., Couch, G. S., Croll, T. I., et al. (2020). UCSF ChimeraX: Structure Visualization for Researchers, Educators, and Developers. *Protein Sci.* 30 (1), 70–82. doi:10.1002/pro.3943

Phillippe, H. M., and Wargo, K. A. (2013). Mitiglinide for Type 2 Diabetes Treatment. *Expert Opin. Pharmacother.* 14, 2133–2144. doi:10.1517/14656566.2013.834048

Pratley, R. E., Foley, J. E., and Dunning, B. E. (2001). Rapid Acting Insulinotropic Agents: Restoration of Early Insulin Secretion as a Physiologic Approach to Improve Glucose Control. *Curr. Pharm. Des.* 7, 1375–1397. doi:10.2174/1381612013397348

Punjani, A., Rubinstein, J. L., Fleet, D. J., and Brubaker, M. A. (2017). cryoSPARC: Algorithms for Rapid Unsupervised Cryo-EM Structure Determination. *Nat. Methods* 14, 290–296. doi:10.1038/nmeth.4169

Quast, U., Stephan, D., Bieger, S., and Russ, U. (2004). The Impact of ATP-Sensitive K+ Channel Subtype Selectivity of Insulin Secretagogues for the Coronary Vasculature and the Myocardium. *Diabetes* 53 (Suppl. 3), S156–S164. doi:10.2337/diabetes.53.suppl_3.s156

Reimann, F., Proks, P., and Ashcroft, F. M. (2001). Effects of Mitiglinide (S 21403) on Kir6.2/SUR1, Kir6.2/SUR2A and Kir6.2/SUR2B Types of ATP-Sensitive Potassium Channel. *Br. J. Pharmacol.* 132, 1542–1548. doi:10.1038/sj.bjp.0703962

Rorsman, P., and Trube, G. (1985). Glucose Dependent K+-channels in Pancreatic Beta-Cells Are Regulated by Intracellular ATP. *Pflugers Arch.* 405, 305–309. doi:10.1007/BF00595682

Rosenthal, P. B., and Henderson, R. (2003). Optimal Determination of Particle Orientation, Absolute Hand, and Contrast Loss in Single-Particle Electron Cryomicroscopy. *J. Mol. Biol.* 333, 721–745. doi:10.1016/j.jmb.2003.07.013

Spruce, A. E., Standen, N. B., and Stanfield, P. R. (1985). Voltage-dependent ATP-Sensitive Potassium Channels of Skeletal Muscle Membrane. *Nature* 316, 736–738. doi:10.1038/316736a0

Sunaga, Y., Gonoi, T., Shibasaki, T., Ichikawa, K., Kusama, H., Yano, H., et al. (2001). The Effects of Mitiglinide (KAD-1229), a New Anti-diabetic Drug, on ATP-Sensitive K+ Channels and Insulin Secretion: Comparison with the Sulfonylureas and Nateglinide. *Eur. J. Pharmacol.* 431, 119–125. doi:10.1016/s0014-2999(01)01412-1

Wang, N., Jiang, X., Zhang, S., Zhu, A., Yuan, Y., Xu, H., et al. (2021). Structural Basis of Human Monocarboxylate Transporter 1 Inhibition by Anti-cancer Drug Candidates. *Cell* 184, 370–e13. doi:10.1016/j.cell.2020.11.043

Wu, J. X., Ding, D., Wang, M., and Chen, L. (2020). Structural Insights into the Inhibitory Mechanism of Insulin Secretagogues on the Pancreatic ATP-Sensitive Potassium Channel. *Biochemistry* 59, 18–25. doi:10.1021/acs.biochem.9b00692

Wu, J. X., Ding, D., Wang, M., Kang, Y., Zeng, X., and Chen, L. (2018). Ligand Binding and Conformational Changes of SUR1 Subunit in Pancreatic ATP-Sensitive Potassium Channels. *Protein Cell* 9, 553–567. doi:10.1007/s13238-018-0530-y

Yan, F. F., Casey, J., and Shyng, S. L. (2006). Sulfonylureas Correct Trafficking Defects of Disease-Causing ATP-Sensitive Potassium Channels by Binding to the Channel Complex. *J. Biol. Chem.* 281, 33403–33413. doi:10.1074/jbc.M605195200

Zhang, K. (2016). Gctf: Real-Time CTF Determination and Correction. *J. Struct. Biol.* 193, 1–12. doi:10.1016/j.jsb.2015.11.003

Zheng, S. Q., Palovcak, E., Armache, J. P., Verba, K. A., Cheng, Y., and Agard, D. A. (2017). MotionCor2: Anisotropic Correction of Beam-Induced Motion for Improved Cryo-Electron Microscopy. *Nat. Methods* 14, 331–332. doi:10.1038/nmeth.4193

Zivanov, J., Nakane, T., Forsberg, B. O., Kimanius, D., Hagen, W. J., Lindahl, E., et al. (2018). New Tools for Automated High-Resolution Cryo-EM Structure Determination in RELION-3. *Elife* 7, e42166. doi:10.7554/eLife.42166

Conflict of Interest: The authors declare that the research was conducted in the absence of any commercial or financial relationships that could be construed as a potential conflict of interest.

frontiers | Frontiers in Pharmacology

TYPE Original Research
PUBLISHED 04 August 2022
DOI 10.3389/fphar.2022.924661

Molecular mechanism of the spider toxin κ-LhTx-I acting on the bacterial voltage-gated sodium channel NaChBac

Zhen Xiao[1,2†], Yaqi Li[1†], Piao Zhao[1], Xiangyue Wu[1], Guoqing Luo[1], Shuijiao Peng[1], Hongrong Liu[2], Cheng Tang[1*] and Zhonghua Liu[1*]

[1]The National and Local Joint Engineering Laboratory of Animal Peptide Drug Development, College of Life Sciences, Hunan Normal University, Changsha, China, [2]Key Laboratory for Matter Microstructure and Function of Hunan Province, Key Laboratory of Low-dimensional Quantum Structures and Quantum Control, School of Physics and Electronics, Hunan Normal University, Changsha, China

The bacterial sodium channel NaChBac is the prokaryotic prototype for the eukaryotic Na_V and Ca_V channels, which could be used as a relatively simple model to study their structure−function relationships. However, few modulators of NaChBac have been reported thus far, and the pharmacology of NaChBac remains to be investigated. In the present study, we show that the spider toxin κ-LhTx-1, an antagonist of the K_V4 family potassium channels, potently inhibits NaChBac with an IC_{50} of 491.0 ± 61.7 nM. Kinetics analysis revealed that κ-LhTx-1 inhibits NaChBac by impeding the voltage-sensor activation. Site-directed mutagenesis confirmed that phenylalanine-103 (F103) in the S3−S4 extracellular loop of NaChBac was critical for interacting with κ-LhTx-1. Molecular docking predicts the binding interface between κ-LhTx-1 and NaChBac and highlights a dominant hydrophobic interaction between W27 in κ-LhTx-1 and F103 in NaChBac that stabilizes the interface. In contrast, κ-LhTx-1 showed weak activity on the mammalian Na_V channels, with 10 μM toxin slightly inhibiting the peak currents of $Na_V1.2–1.9$ subtypes. Taken together, our study shows that κ-LhTx-1 inhibits the bacterial sodium channel, NaChBac, using a voltage-sensor trapping mechanism similar to mammalian Na_V site 4 toxins. κ-LhTx-1 could be used as a ligand to study the toxin−channel interactions in the native membrane environments, given that the NaChBac structure was successfully resolved in a nanodisc.

KEYWORDS

NaChBac, spider toxin, molecular mechanism, voltage sensor trapping, molecular docking, antagonist

OPEN ACCESS

EDITED BY
Shujia Zhu,
Institute of Neuroscience, Shanghai Institute for Biological Sciences (CAS), China

REVIEWED BY
Hongtu Zhao,
St. Jude Children's Research Hospital, United States
George Chandy,
University of California, Irvine, United States

*CORRESPONDENCE
Cheng Tang,
chengtang@hunnu.edu.cn
Zhonghua Liu,
Liuzh@hunnu.edu.cn

[†]These authors have contributed equally to this work

SPECIALTY SECTION
This article was submitted to Pharmacology of Ion Channels and Channelopathies, a section of the journal Frontiers in Pharmacology

RECEIVED 20 April 2022
ACCEPTED 27 June 2022
PUBLISHED 04 August 2022

CITATION
Xiao Z, Li Y, Zhao P, Wu X, Luo G, Peng S, Liu H, Tang C and Liu Z (2022), Molecular mechanism of the spider toxin κ-LhTx-I acting on the bacterial voltage-gated sodium channel NaChBac.
Front. Pharmacol. 13:924661.
doi: 10.3389/fphar.2022.924661

Introduction

The mammalian voltage-gated sodium (Na_V) channels are the molecular determinants of action potential generation and propagation in excitable cells (Hodgkin and Huxley, 1990; Hille, 2001). To date, nine Na_V channel genes have been identified. $Na_V1.4$ and $Na_V1.5$ are expressed mainly in the skeletal muscle and myocardial muscle cells, respectively. $Na_V1.1$-$Na_V1.3$ and $Na_V1.6$-$Na_V1.9$ are the dominant subtypes in neurons (Goldin, 1999; Catterall et al., 2005; de Lera Ruiz and Kraus, 2015). Their dysfunction causes hyper- or hypo-excitability of the cell types they are expressed in. The altered excitability leads to myotonia ($Na_V1.4$), arrhythmia ($Na_V1.5$), epilepsy ($Na_V1.1$-1.3, $Na_V1.6$), and pain ($Na_V1.7$-1.9) (Andavan and Lemmens-Gruber, 2011; Huang et al., 2017). Therefore, pharmacological modulators regulating the activity of Na_V channels are valuable drug candidates for treating these diseases (Bagal et al., 2015; Wulff et al., 2019). Topologically, the pore-forming Na_V alpha subunit contains 24 transmembrane segments, which could be divided into four homologous domains (DI-DIV). The S1–S4 segments from each domain construct the voltage sensor module (VSM), and the S5–S6 segments make the pore module (PM). The four PMs in DI-DIV form the central Na^+ conducting pathway, with the four VSMs surrounding the pore (Pan et al., 2018; Pan et al., 2019; Shen et al., 2019; Jiang et al., 2020; Pan et al., 2021). Driven by membrane depolarization, the S4 segments, which carry an array of positively charged arginine/lysine residues move outwardly, the local conformation changes were then transmitted into the central pore, resulting in pore opening (de Lera Ruiz and Kraus, 2015). The tremendous progress in cryo-EM structural studies of mammalian Na_V channels has enhanced our understanding of their structure–function relationships (Pan et al., 2018; Pan et al., 2019; Shen et al., 2019; Jiang et al., 2020; Pan et al., 2021; Wisedchaisri et al., 2021).

The prokaryotic Na_V channels, counterparts of the mammalian ones in prokaryotes, were proposed as evolutionary ancestors of mammalian Na_V and Ca_V channels (Charalambous and Wallace, 2011). These channels share the key features of mammalian Na_V channels, such as voltage-gating and Na^+ selectivity. They are involved in specialized functions in prokaryotic organisms, such as motility and chemotaxis (Ren et al., 2001; Ito et al., 2004; Koishi et al., 2004). Structurally, it is assembled by four identical subunits, each of which contains six transmembrane segments, which resembles a single domain of the mammalian Na_V channel (Scheuer, 2014). Several prokaryotic Na_V channels have been identified, including NaChBac from *Bacillus halodurans*, Na_VPZ from *Paracoccus zeaxanthinifaciens*, Na_VSP from *Silicibacter pomeroyi*, and Ns_VBa from *Bacillus alcalophilus* (Ren et al., 2001; Koishi et al., 2004; DeCaen et al., 2014). In light of the simplified topological structure and efficient heterologous expression of prokaryotic Na_V channels, they serve as ideal models for studying the structure–function relationships of mammalian Na_V and Ca_V channels. For example, investigating the structures of the prokaryotic Na_VAb channel in both the resting and activated states uncovered the likely conserved voltage sensing and gating mechanism in mammalian and prokaryotic Na_V channels (Wisedchaisri et al., 2019; Catterall et al., 2020). NaChBac is the first prokaryotic Na_V channel identified from *Bacillus halodurans* (Ren et al., 2001). Recently, the structure of a chimeric NaChBac channel containing the domain II S3-S4 loop of $Na_V1.7$ channel and complexed to the spider toxin HWTx-IV was resolved at high-resolution in a nanodisc. This structure shed light on understanding the toxin–channel interactions in a natural membrane environment (Gao et al., 2020).

Compared to the mammalian Na_V channels, relatively few peptide antagonists have been documented for bacterial Na_V channels. Most of these toxins act on both the mammalian and bacterial Na_V channels. They are either pore-blockers or gating-modifiers based on their mechanisms of action. The mammalian Na_V site 1 modulator, μ-Conotoxin PIIIA, was characterized as a pore-blocker of NaChBac and was suggested to directly occlude the conducting pathway with the side chain of Arg14 (Finol-Urdaneta et al., 2019). We previously purified two potent gating-modifier toxins, JZTx-27 and JZTx-14, from the venom of spider *Chilobrachys jingzhao*. These toxins interact with the S3–S4 loop region of NaChBac and inhibit the channel activity by impeding voltage-sensor activation (Tang et al., 2017; Zhang et al., 2018). A recent study testing the activity of several known peptide modulators of mammalian Na_V channels showed that the site 4 toxins GsAF-I, GrTx1, and GsAF-II also effectively inhibit NaChBac currents, possibly by affecting the voltage-dependent gating of the channel (Zhu et al., 2020). Interestingly, the site 3-toxin BDS-I has opposite effects on the bacterial and mammalian Na_V channels. BDS-I inhibits NaChBac and activates the human $Na_V1.7$ (Zhu et al., 2020). The mechanism of action of these gating-modifier toxins, with the exception of JZTx-27 and JZTx-14, has not been defined to the best of our knowledge. Identifying novel peptide modulators of NaChBac and elucidating their mechanism of action will enhance our understanding of the pharmacology of NaChBac. Such studies will also identify and characterize useful ligands for defining toxin–channel interactions in the native membrane environment with established structural biology approaches (Gao et al., 2020).

In the present study, we identified the spider toxin κ-LhTx-1, which was previously reported as an antagonist of the K_V4 family voltage-gated potassium channel channels (Xiao et al., 2021), as a novel antagonist of the NaChBac channel. Compared with the other known NaChBac peptide inhibitors, κ-LhTx-1 selectively inhibited NaChBac but greatly spared the mammalian Na_V channels. Kinetics analysis demonstrated that κ-LhTx-1 inhibits NaChBac by preventing voltage-sensor activation. Site-directed mutagenesis showed that phenylalanine-F103 (F103) in the S3–S4 extracellular loop of NaChBac was crucial for interacting with κ-LhTx-1. Molecular docking revealed that κ-LhTx-1 bound to NaChBac mainly by the hydrophobic interaction, with W27 in toxin being registered with F103 in the channel. This study describes κ-LhTx-1, a new peptide modulator of NaChBac. This peptide could be used as a tool for characterizing toxin–channel interactions in a native membrane environment using established structural biology methods.

Materials and methods

Toxin

Chemical synthesis and refolding of the linear κ-LhTx-1 was conducted as previously described (Xiao et al., 2021). The purity of synthesized toxins was determined to be >98% by analytic HPLC and MALDI-TOF MS analysis.

Constructs and site-directed mutations

The cDNA of mammalian $Na_V1.2$-1.8 channels was kindly gifted from Professor Theodore R. Cummins (Stark Neurosciences Research Institute, Indiana University School of Medicine, Indianapolis, IN, United States) and subcloned in the pCDNA3.1 or pCMV-blank vectors. The cDNA of $Na_V1.9$ was obtained by gene synthesis and cloned into the pEGFP-N1 vector as previously reported (Zhou et al., 2017). The NaChBac and Na_VPZ expression plasmids were kind gifts from Professor David E. Clapham (Janelia Research Campus, Howard Hughes Medical Institute, Ashburn, VA, United States). NaChBac mutants were made by site-directed mutations. Briefly, the NaChBac plasmid was amplified using a pair of oppositely directed primers harboring the designed mutation site with KOD Fx (TOYOBO Co., Ltd., Osaka, Japan), and the PCR products were treated with FastDigest DpnI (ThermoFisher, Waltham, MA, United States) to remove the methylated template. 10 μl digested product was used to transform 100 μl E. coli DH5α competent cells. Transformants were randomly picked for DNA sequencing to obtain the correct mutants.

Cell culture and transient transfection

HEK293T and ND7/23 cells were cultured in a DMEM medium, and CHO-K1 in a DMEM-F12 medium, supplemented with 10% FBS and 1% PS (all from Gibco; Thermo Fisher Scientific, Inc., Waltham, MA, United States), in standard cell culture conditions (37°C, 5% CO_2, saturated humidity). The Na_V expression plasmid was co-transfected with pEGFP-N1 plasmid into HEK293T (NaChBac and its mutants, Na_VPZ and Na_VPZ/P92F, and $Na_V1.2$–1.7 channels) or ND7/23 ($Na_V1.8$ channel) cells using Lipofectamine 2000 following manufacturer’s instructions (Invitrogen; Thermo Fisher Scientific, Inc., Waltham, MA, United States). $Na_V1.9$-GFP plasmid was transfected into ND7/23 using the X-treme GENE HP DNA Transfection Reagent (Roche, Basel, Switzerland). After 4–6 h transfection, the cells were then seeded onto poly-lysine-coated coverslips. Note that the $Na_V1.9$ transfected ND7/23 cells were maintained at 28°C for additional 20 h to promote the functional expression of the channel after the initial culture at 37°C for 24 h.

Electrophysiology

Whole-cell patch clamp recordings were performed using a MultiClamp 700B amplifier equipped with the Axon Digidata 1550 AD/DA digitizer (Molecular devices, San Jose, CA, United States) at room temperature. The EGFP fluorescence was used to identify the positively transfected cells. The bath solution for sodium currents recording contains (in mM): 140 NaCl, 5 KCl, 1 $MgCl_2$, 2 $CaCl_2$, 10 Glucose, and 10 HEPES; adjust pH to 7.3 with NaOH. The corresponding pipette solution contains (in mM): 140 CsF, 1 EGTA, 10 NaCl, and 10 HEPES; adjust pH to 7.2 with CsOH. All the chemicals were obtained from Sigma-Aldrich (Sigma-Aldrich, Saint Louis, MO, United States). For $Na_V1.8$ and $Na_V1.9$ currents recording, 1 μM TTX was added to the bath solution to eliminate the contamination of endogenous TTX-sensitive Na_V currents in ND7/23 cells. The recording pipettes were made from glass capillaries using a PC-10 puller (NARISHIGE, Tokyo, Japan), and the pipette resistance was adjusted to be between 2 and 3 MΩ after filling with the pipette solution. Whole-cell configuration was established following a standard program. The fast and slow capacitance was sequentially canceled using a computer-controlled circuit of the amplifier. Moreover, series resistance was compensated by 80% to reduce the voltage error, and the cells with series resistance larger than 10 MΩ after break-in were discarded. The steady-state activation curve of NaChBac channels was obtained by calculating the conductance (G) at each depolarizing voltage (V) using the equation: $G = I/(V–V_{rev})$, and plotting G/G_{max} as a function of V, where I, G_{max}, and V_{rev} represent the current amplitude, the maximum conductance, and the reversal potential of the channel, respectively.The G–V curve was fitted using the Boltzmann equation: $y = 1/\{1+\exp[(V_a–V)/K_a]\}$, in which V_a, V, and K_a represent the half maximum activation voltage, test voltage and slope factor, respectively. The steady-state inactivation curve of NaChBac channels was measured using a classical two-pulse protocol: cell was held at −120 mV, and a series of 1 s pre-pulses (−120 to 0 mV, in 10 mV increment) were applied to induce the channel inactivation, followed by a −20 mV/500 ms test pulse to assess the availability of non-inactivated channels (sweep interval was set to 10 s). Currents at the test pulse (I) were normalized to the maximum one (I_{max}) and plotted as a function of the conditional

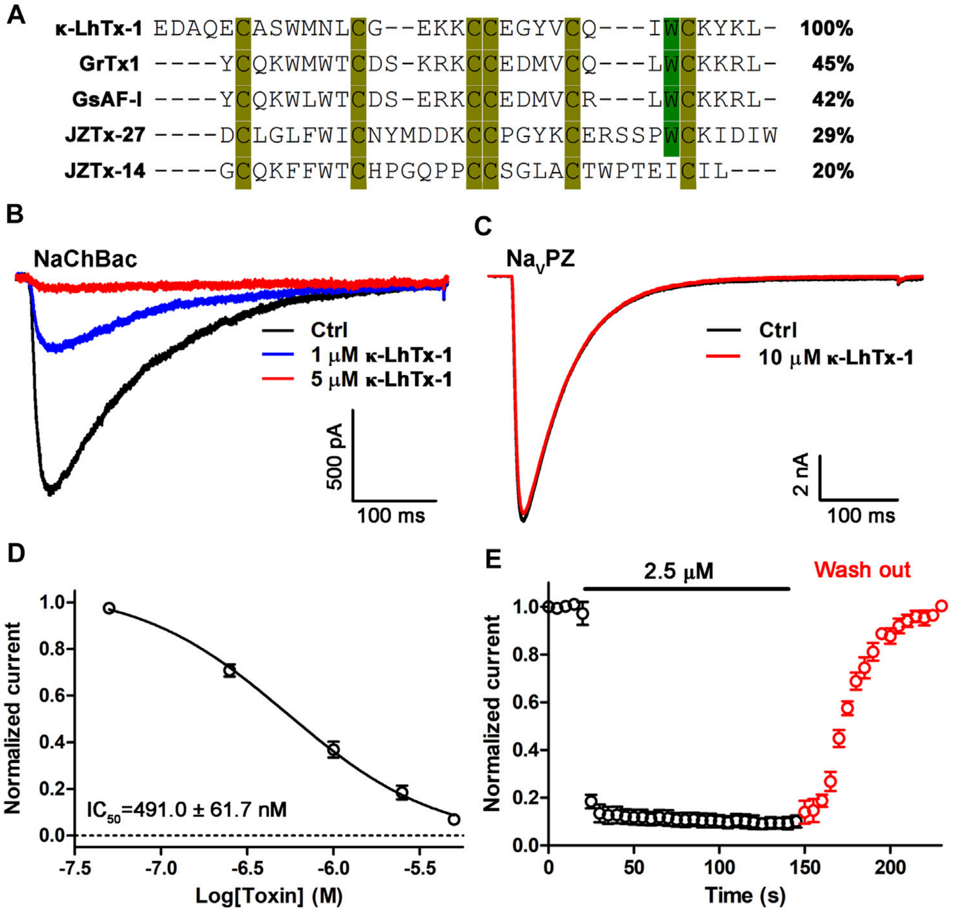

FIGURE 1
Characterization of κ-LhTx-1 as a novel NaChBac antagonist. **(A)** Sequence alignment of κ-LhTx-1 with other known NaChBac peptide antagonists. **(B)** Representative traces showing κ-LhTx -1 dose-dependently inhibited NaChBac currents elicited by depolarization to −20 mV from the holding potential of −100 mV (*n* = 5). **(C)** Representative traces showing that Na_VPZ currents were not affected by 10 μM κ-LhTx-1 treatment (*n* = 4). **(D)** Dose-response curve of κ-LhTx-1 inhibiting NaChBac at −20 mV, and the IC_{50} value was determined as 491.0 ± 61.7 nM (*n* = 5). **(E)** Time course of NaChBac current inhibition by 2.5 μM κ-LhTx-1 and subsequent washing off with bath solution. The association time constant (τ_{on}) and the dissociation time constant (τ_{off}) were determined as 2.0 ± 0.2 s and 34.1 ± 2.5 s, respectively (*n* = 5).

voltage (V), the curve was fitted by the Boltzmann equation: $I/I_{max} = A + (1-A)/\{1 + \exp[(V-V_h)/K_h]\}$, where V_h is the half-maximum inactivation voltage, A represents the minimum channel availability, and K_h is the slope factor. The binding and unbinding kinetics of κ-LhTx-1 with NaChBac were measured by monitoring the time-dependent current rundown after toxin application and recovery upon bath solution perfusion. The association time constant (τ_{on}) was calculated by fitting the decay phase with the one exponential decay equation: $y = y_{steady}+ae^{-x/\tau}$; and the dissociation time constant (τ_{off}) was calculated by fitting the recovery phase with one exponential rising equation: $y = y_{(0)}+a(1-e^{-x/\tau})$. The concentration-response curves were fitted using the following Hill logistic equation: $y = f_{max}-(f_{max}-f_{min})/(1+([Tx]/IC_{50})^n)$, where f_{max} and f_{min} represent the maximum and minimum response of the channel to toxin, [Tx] represents the toxin concentration, IC_{50} represents the half maximum inhibition concentration, and n is an empirical Hill coefficient, respectively. Data were acquired using Clampex 10.5 (Molecular devices, San Jose, CA, United States).

Molecular docking

The structure of κ-LhTx-1 was predicted by C-I-TASSER by using a contact-guided iterative threading assembly refinement (Zheng et al., 2021). The resting-state conformation model of NaChBac channel was generated by modifying the partially activated conformation NaChBac structure (PDB ID: 6VWX) according to the resting-state Na_VAb/Na_V1.7-$_V$S2A chimeric channel structure (PDB ID: 7K48) (Wisedchaisri et al., 2021). The binding mode between NaChBac and κ-LhTx-1 was simulated by *ZDOCK* (ZDOCK 3.0.2) (Mintseris et al., 2007; Pierce et al., 2014). The residues which buried into the membrane were blocked in protein-peptide docking. F103 was selected as the binding site residue according to the results of the patch clamp assay.

Data analysis

Data were presented as the MEAN ± SEM, where *n* represents the number of separate experimental cells. Data were analyzed by using the software Clampfit 10.5 (Axon Instruments, Irvine, CA, United States), Graphpad Prism 5.01 (GraphPad Software, La Jolla, CA, United States), and Excel 2010 (Microsoft Corporation, Redmond, WA, United States). Statistical difference was assessed using the unpaired *t*-test, and the significant difference was accepted at $p < 0.05$.

Results

κ-LhTx-1 is a novel NaChBac antagonist

We screened RP-HPLC fractions of the venom of spider *Pandercetes sp* (the lichen huntsman spider) for potential modulators of NaChBac. We identified κ-LhTx-1, an antagonist of K_V4 family potassium channels, as a potent inhibitor of NaChBac (Figure 1B) (Xiao et al., 2021). The amino acid sequence of κ-LhTx-1 shows relatively low homology to the other known NaChBac peptide inhibitors, including GrTx1 (45%), GsAF-I (42%), JZTx-27 (29%), and JZTx-14 (20%). However, they all share a conserved cysteine framework, which is predicted to fold as an ICK motif (Figure 1A) (Pallaghy et al., 1994). Due to the low abundance of κ-LhTx-1 in the venom, we used the synthetic toxin, which was shown to be correctly refolded as the native one (Xiao et al., 2021), for further experiments. κ-LhTx-1 dose-dependently inhibited the peak current of NaChBac with an IC_{50} of 491.0 ± 61.7 nM at −20 mV (Figures 1B,D). Interestingly, κ-LhTx-1 did not modulate another bacterial sodium channel, Na_VPZ, even at 10 μM (Figure 1C). Toxin-binding kinetics assays showed that κ-LhTx-1 rapidly inhibited NaChBac currents, with a time constant of 2.0 ± 0.2 s for toxin association. Dissociation of κ-LhTx-1 from NaChBac was slow with a time constant of 34.1 ± 2.5 s (Figure 1E).

Effects of κ-LhTx-1 on the gating kinetics of NaChBac

The peptide toxins inhibit Na_V channels possibly by physically occluding the ion conducting pathway or by impeding the voltage-dependent activation of the voltage sensor, which could be assessed by comparing the channels' gating kinetics before and after toxin treatment. We first tested the effect of κ-LhTx-1 on the current–voltage (I-V) relationships of NaChBac. Figure 2A shows the representative current traces of the same cell before and after 1 μM κ-LhTx-1 treatment, demonstrating that the inward currents were partially inhibited, while the outward currents were unaffected. This result was further validated by the I–V curves shown in Figure 2B. Between the depolarization voltages of −50 mV and +30 mV, NaChBac currents were differently inhibited by 1 μM κ-LhTx-1, whereas the inhibition was absent at depolarizing voltages higher than +40 mV. These data suggested that those toxin-bound NaChBac channels were reopened as toxin-free channels at stronger depolarizations, resulting in the phenotype of voltage-dependent inhibition. When normalizing the currents at each depolarizing voltage in the toxin-treated group to its maximum peak current, the I–V relationship showed apparent right-forward shift when compared with the control group. Likewise, 1 μM κ-LhTx-1 caused a significant shift of the G-V curve toward more depolarized direction, and the half maximum activation voltage (V_a) was determined as −35.0 ± 1.3 mV and −22.0 ± 2.8 mV for control and toxin-treated channels, respectively (Figure 2C; $p < 0.001$, unpaired *t*-test). Meanwhile, κ-LhTx-1 treatment also remarkably reduced the slope of the G–V curve (Figure 2C; K_a = 7.3 ± 0.4 mV and 12.5 ± 0.9 mV for control and toxin-treated channels, respectively; $p < 0.001$, unpaired *t*-test), indicating toxin greatly attenuated the channel voltage sensitivity during the voltage-dependent activation. These data strongly suggested that κ-LhTx-1 trapped the voltage sensor of the NaChBac channel in a deactivated state, while the energy barrier of voltage sensor outward movement caused by toxin binding could be counteracted by strengthening membrane depolarization. The steady-state inactivation of NaChBac channels, however, was not affected by κ-LhTx-1 (Figure 2D). Altogether, these results argued that κ-LhTx-1 trapped the voltage sensor of the NaChBac channel in the deactivated state, functioning as a gating modifier.

The molecular determinants in NaChBac for interacting with κ-LhTx-1

Since κ-LhTx-1 is a gating-modifier of NaChBac, we wondered if it might bind to the channel's S3–S4 extracellular loop. The protein sequence-alignment through the S3–S4 region of the κ-LhTx-1-sensitive NaChBac channel and the κ-LhTx-1-resistant Na_VPZ channel is shown in Figure 3A. The alignment in Figure 3A highlights F103 in NaChBac and the corresponding Proline-92 (P92) in Na_VPZ. We used an alanine scan strategy to identify the key residues for interacting with κ-LhTx-1 in this region (Figure 3A). All these NaChBac mutants were functionally expressed in CHO-K1 cells (Figures 3B–F). We tested the inhibitory effect of κ-LhTx-1 on each mutant channel at voltage eliciting its maximum inward peak current. The data showed that F103A, G105A, F108A, and V109A mutations in

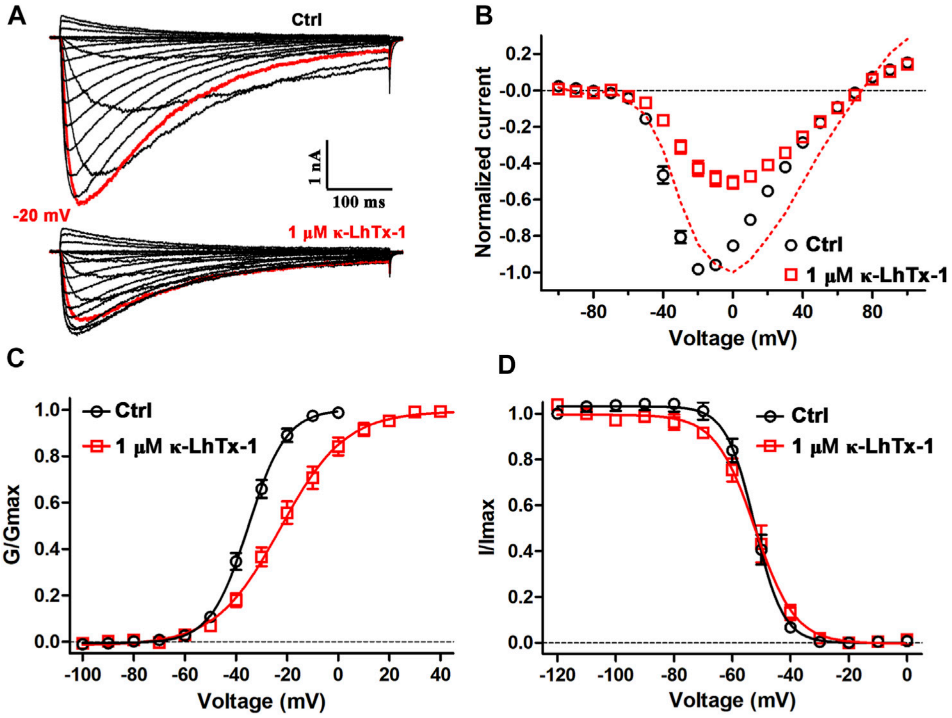

FIGURE 2
Effects of κ-LhTx-1 on the gating kinetics of NaChBac. **(A)** Representative NaChBac currents before (upper panel) and after (lower panel) 1 μM κ-LhTx-1 treatment. Currents were elicited by step depolarizations from −100 to +100 mV from a holding potential of −100 mV. The red traces show the currents at −20 mV (n = 6). **(B)** I−V relationships of NaChBac before and after 1 μM κ-LhTx-1 treatment. The red dashed line shows the I−V relationship of toxin-treated channels by normalizing the currents to their own maximum (n = 6). **(C)** Steady-state activation relationships of NaChBac before and after 1 μM κ-LhTx-1 treatment (V_a = −35.0 ± 1.3 mV and −22.0 ± 2.8 mV, K_a = 7.3 ± 0.4 mV and 12.5 ± 0.9 mV, for control and toxin-treated channels, respectively; $p < 0.001$ when comparing both the V_a and K_a values between the control and toxin groups; unpaired t-test; n = 6). **(D)** Steady-state inactivation relationships of NaChBac before and after 1 μM κ-LhTx-1 treatment (V_h = −52.3 ± 1.3 mV and −53.0 ± 1.9 mV, K_h = −4.6 ± 0.3 mV and −6.0 ± 0.6 mV, for control- and toxin treated channels, respectively; n = 5).

NaChBac all attenuated the inhibitory effect of κ-LhTx-1, with 5 μM toxin not affecting the currents of NaChBac/F103A and only partially inhibiting the currents of NaChBac/G105A, NaChBac/F108A, and NaChBac/V109A by approximately 43.4 ± 8.1%, 40.7 ± 4.2%, and 64.4 ± 4.1%, respectively (Figures 3B,C,E,F). The activity of κ-LhTx-1 on NaChBac/Q107A was not changed a lot when compared with that of the wild type channel (Figure 3D). The dose–response curves in Figure 3G showed that κ-LhTx-1 inhibited the currents of NaChBac/G105A, NaChBac/Q107A, NaChBac/F108A, and NaChBac/V109A with an IC$_{50}$ of 5.5 ± 1.4 μM, 1.0 ± 0.1 μM, 7.8 ± 1.0 μM, and 2.6 ± 0.4 μM, respectively, (Figure 3G). The IC$_{50}$ for NaChBac/F103A could not be determined from the curve as 20 μM κ-LhTx-1 only inhibited its currents by 16.4 ± 2.6% (Figure 3G). Next, we tried to convert the κ-LhTx-1-resistant Na$_V$PZ channel into the κ-LhTx-1-sensitive channel. Since F103 in NaChBac was deemed to be important for κ-LhTx-1 modulation, we decided to replace the corresponding residue in Na$_V$PZ (P92) with phenylalanine. The Na$_V$PZ/P92F mutant was potently inhibited by κ-LhTx-1 (Figure 3H), with an IC$_{50}$ of 6.7 ± 2.3 μM (Figure 3I). Our successful conversion of κ-LhTx-1-resistant Na$_V$PZ into a sensitive channel strongly supports the importance of F103 in NaChBac and the corresponding P92 in Na$_V$PZ.

Effects of κ-LhTx-1 on mammalian Na$_V$ channels

The biological activity of κ-LhTx-1 on the mammalian K$_V$ channels has been systematically examined, which showed it potently inhibited the K$_V$4 family potassium channels without affecting other K$_V$ channels, including K$_V$1.1, K$_V$1.3-1.5, K$_V$2.1, and K$_V$3.1-3.4 (Xiao et al., 2021). Herein, we tested the activity of κ-LhTx-1 on the mammalian Na$_V$ channels. As shown in Figures 4A,B, 10 μM κ-LhTx-1 showed weak inhibition on Na$_V$1.3 (8.4 ± 2.3%), Na$_V$1.5 (17.2 ± 7.3%), Na$_V$1.6 (18.4 ± 15.7%), Na$_V$1.8 (7.1 ± 1.5%), and Na$_V$1.9 (4.8 ± 0.1%) channels and relatively stronger inhibition on Na$_V$1.2 (41.3 ± 6.2%), Na$_V$1.4 (38.7 ± 1.9%), and Na$_V$1.7 (67.4 ± 3.7%) channels. Compared with the

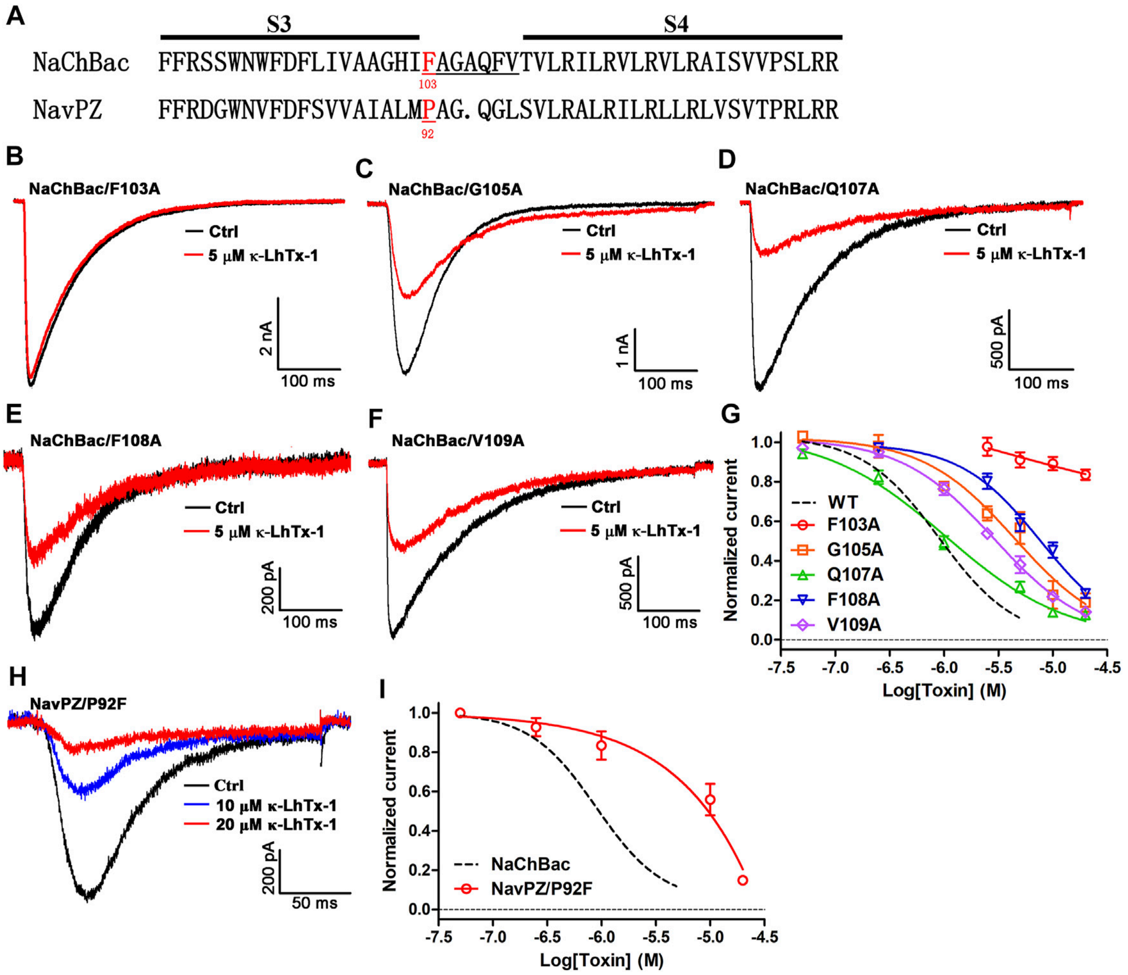

FIGURE 3
Key molecular determinants in NaChBac for interacting with κ-LhTx-1. **(A)** Sequence alignment of the NaChBac and Na$_V$PZ, the number below the residue indicates its location in the sequence. **(B)** Representative traces showing F103A mutation in NaChBac almost fully abolished κ-LhTx-1 inhibition on the channel (*n* = 5). **(C–F)** Representative traces showing the inhibitory effects of 5 μM κ-LhTx-1 on NaChBac mutants as illustrated (*n* = 5–6). **(G)** Dose-response curves of κ-LhTx-1 inhibiting the NaChBac mutant channels, and the IC$_{50}$ values were determined as 5.5 ± 1.4 μM, 1.0 ± 0.1 μM, 7.8 ± 1.0 μM, and 2.6 ± 0.4 μM for NaChBac/G105A, NaChBac/Q107A, NaChBac/F108A, and NaChBac/V109A, respectively (*n* = 5–6). The black dashed line shows the dose-response curve of κ-LhTx-1 against the wild-type NaChBac channel. **(H)** Representative traces showing the κ-LhTx-1 dose-dependently inhibited Na$_V$PZ/P92F currents elicited by depolarization to +30 mV from the holding potential of −100 mV (*n* = 5). **(I)** Dose-response curve of κ-LhTx-1 inhibiting the currents of Na$_V$PZ/P92F at +30 mV, the IC$_{50}$ values were determined as 6.7 ± 2.3 μM (*n* = 4).

potent inhibition of κ-LhTx-1 on the K$_V$4 family potassium channels and NaChBac channels, the toxin showed much weaker activity on the mammalian Na$_V$ channels.

The toxin–channel interface as revealed by molecular docking

The κ-LhTx-1 structure was simulated by C-I-TASSER (Figure 5A). The six cysteines in toxin formed three disulfide bonds as C6-C19, C13-C24, and C18-C28 (number indicates the position of cysteines in toxin sequence). Analyzing the solvent-accessible surface of κ-LhTx-1 showed it is an amphilic molecule, in which most hydrophobic residues are mainly distributed on one side, forming a hydrophobic patch, whereas charged residues are distributed on the other side, forming a hydrophilic surface (Figure 5B). The toxin–channel docking complex is shown in Figure 5C. The modeled resting-state of NaChBac and κ-LhTx-1 is depicted in yellow and green, respectively. The best scoring docking complex showed that the toxin inserted as a wedge into the cleft between S1–S2 and S3–S4 loops (Figure 5C), resembling that of α-scorpion toxin interacting with the voltage sensor of the mammalian Na$_V$ channel (Wang et al., 2011; Clairfeuille et al., 2019). In this docking model, F103 in NaChBac and W27 in κ-

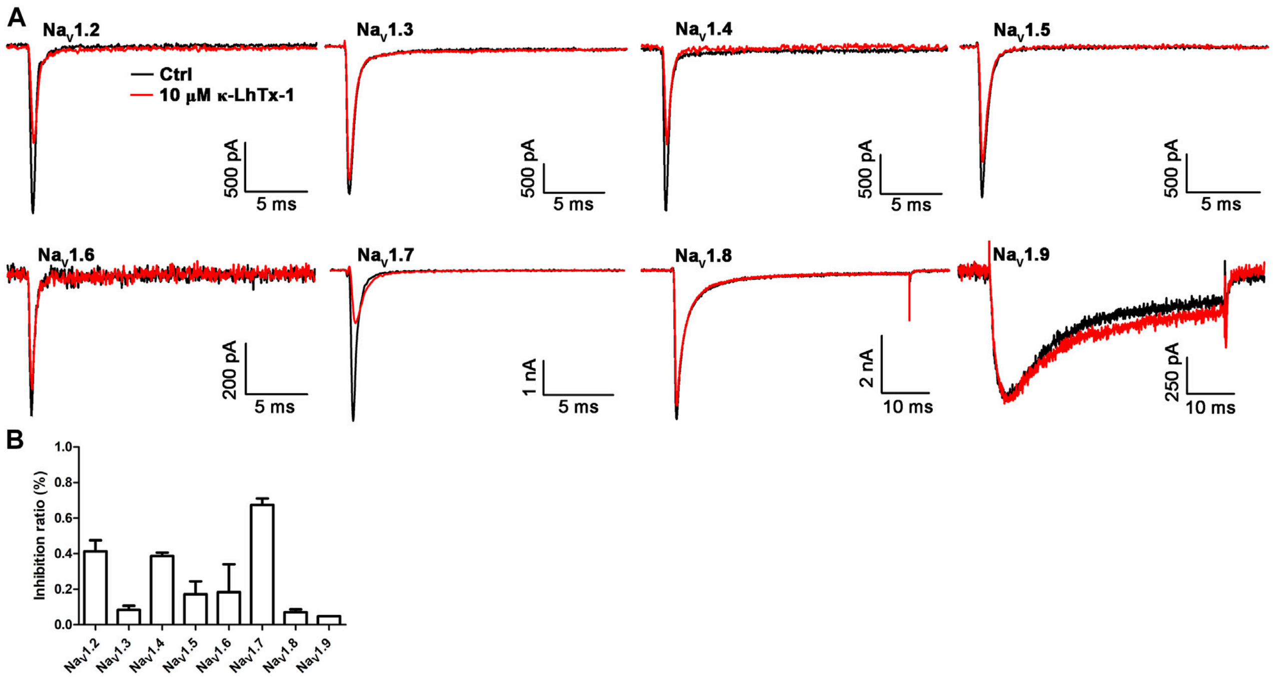

FIGURE 4
Effects of κ-LhTx-1 on the mammalian Na_V channels. **(A)** Representative traces showing the effect of 10 μM κ-LhTx-1 on Na_V1.2–1.9 channels (*n* = 3–5). **(B)** Bar graph showing the inhibition of 10 μM κ-LhTx-1 on the peak currents of Nav1.2–1.9 channels. The inhibition ratio was determined as 41.3 ± 6.2%, 8.4 ± 2.3%, 38.7 ± 1.9%, 17.2 ± 7.3%, 18.4 ± 15.7%, 67.4 ± 3.7%, 7.1 ± 1.5%, and 4.8 ± 0.1% for Na_V1.2, Na_V1.3, Na_V1.4, Na_V1.5, Na_V1.6, Na_V1.7, Na_V1.8, and Na_V1.9 channels, respectively (*n* = 3–5).

LhTx-1 were captured in the channel–toxin interface, in which W27 was registered with F103 by the π–π stacking interaction (Figure 5D). We used site-specific mutagenesis to experimentally verify the functional importance of the phenyl ring of F103 for κ-LhTx-1 binding. The F103A mutation abolished the modulation of NaChBac by κ-LhTx-1 (Figures 3B, 5E). Replacement of F103 with aromatic residues (F103W, F103Y) retained the inhibition by κ-LhTx-1, albeit with lower potency than the wild-type channel. These mutants were inhibited by κ-LhTx-1 with IC_{50s} of 9.5 ± 2.9 μM for NaChBac/F103W (~19-fold lower) and 3.7 ± 1.5 μM for NaChBac/F103Y (~8-fold lower) (Figures 5E,F). Taken together, these results argued that the phenyl ring of F103 in NaChBac played a critical role in binding with κ-LhTx-I, and the association between κ-LhTx-1 and NaChBac likely relies on a hydrophobic interaction.

Discussion

κ-LhTx-1 was demonstrated in our previous study to selectively inhibit the mammalian K_V4 family potassium channels (Xiao et al., 2021). The present study confirmed that κ-LhTx-1 is also a novel NaChBac antagonist. The G–V curve of NaChBac was remarkably shifted to depolarized direction by κ-LhTx-1, indicating κ-LhTx-1 acts on NaChBac as a gating-modifier trapping the deactivated voltage sensor. Moreover, the site-directed mutagenesis and molecular docking showed κ-LhTx-1 bound to the S3–S4 loop of NaChBac, with the phenylalanine-103 (F103) being the most critical residue. Molecular docking also confirmed the W27 residue in κ-LhTx-1 was registered with F103 in NaChBac, likely by the π–π stacking interaction. The action mode of κ-LhTx-1 on NaChBac and its binding site on the channel resembles that of JZTx-27 (Tang et al., 2017). However, unlike JZTx-27, κ-LhTx-1 slightly inhibited the activation but not the inactivation of mammalian Na_V channels. The structure of chimeric NaChBac channel harboring the DII S3-S4 linker of Na_V1.7 channel in complex with the spider toxin HwTx-IV in a nanodisc has been successfully resolved, which has showed greatly improved resolution of the toxin–channel interacting interface and enabled visualization of their binding details (Gao et al., 2020). κ-LhTx-1 in the present study thus provided another useful ligand for studying the toxin and wild-type NaChBac interaction in the native membrane environments.

Historically, NaChBac was shown to pharmacologically resemble the mammalian Na_V and Ca_V channels, as revealed by its inhibition by lots of Ca_V and Na_V channel modulators, such as lidocaine, nifedipine, and various peptide toxins (Ren et al., 2001; Lee et al., 2012; Tang et al., 2017; Zhang et al., 2018; Zhu et al., 2020). κ-LhTx-1 was previously shown to inhibit the

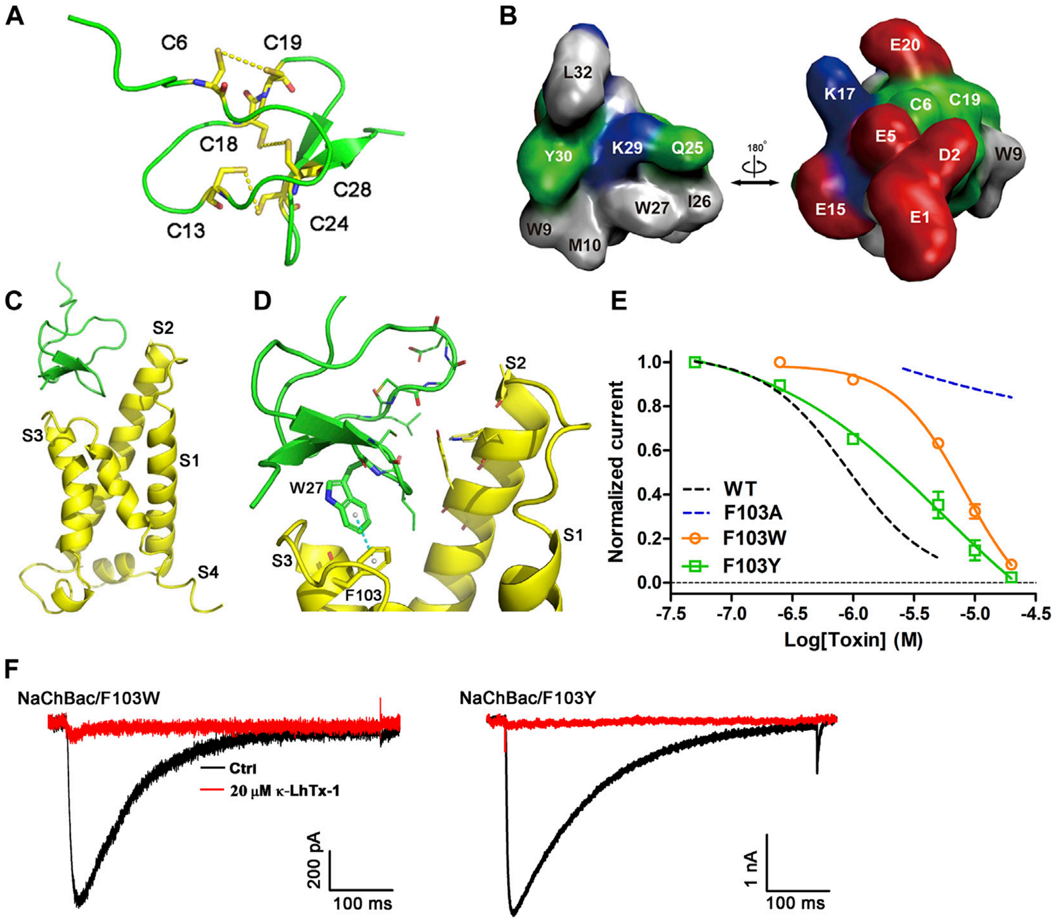

FIGURE 5
Molecular docking of κ-LhTx-1 with NaChBac. **(A)** Predicted structure of the κ-LhTx-1 by *C-I-TASSER*, the peptide toxin GsMTx2 (PDB ID: 1LUP) was used as the template. Cysteines were highlighted in yellow, and the predicted disulfide bonds were shown (C_6 - C_{19}, C_{13} - C_{24}, and C_{18} - C_{28}). **(B)** Surface presentation of κ-LhTx-1 structure. Positively charged residues are shown in blue, negatively charged residues in red, hydrophobic residues in gray, and polar uncharged residues in green. **(C)** Docked κ-LhTx-1-NaChBac complex with the highest score. The resting-state NaChBac channel and the κ-LhTx-1 toxin were shown in yellow and green, respectively. For simplicity, only the S1–S4 region of a single channel subunit was shown. **(D)** Enlarged view of the interaction interface between NaChBac and κ-LhTx-1, in which W27 in toxin captured the experimentally determined key residue in NaChBac, F103, in the toxin–channel interface. **(E)** Dose-response curve of κ-LhTx-1 inhibiting the NaChBac mutants as shown, and the IC_{50} values were determined as 9.5 ± 2.9 μM and 3.7 ± 1.5 μM for NaChBac/F103W and NaChBac/F103Y, respectively. The black and red dashed lines show the dose-response curves of κ-LhTx-1 against the wild-type NaChBac and NaChBac/F103A mutant channel, respectively (n = 5). **(F)** Representative traces showing the inhibition effect of 20 μM κ-LhTx-1 on the currents of NaChBac/F103W and NaChBac/F103Y mutant channels (n = 5).

K_V4 family potassium channels in a voltage-dependent manner (Xiao et al., 2021). Consequently, the present study provided the first example that NaChBac also shares similar pharmacology properties with the K_V channels. Gating currents analysis confirmed that κ-LhTx-1 trapped the voltage sensor of K_V4 channels in a deactivated state (Xiao et al., 2021). Therefore, we concluded that κ-LhTx-1 inhibited the K_V4 and NaChBac channels using the same voltage-sensor trapping mechanism.

Mechanistically, the association between gating-modifier toxins and ion channels relies on electrostatic force and/or hydrophobic interaction between their interface (Bosmans et al., 2008). As that of the HpTx2 binding with the $K_V4.3$ channel solely by hydrophobic force (Zhang et al., 2007; DeSimone et al., 2009), κ-LhTx-1 might also interact with NaChBac mainly by a hydrophobic interaction, as revealed by mutation and molecular docking analyses. Indeed, hydrophobic residues on the S3–S4 loop of NaChBac have been commonly characterized as key molecular determinants in interacting with its gating-modifier toxins, such as F103 for κ-LhTx-1 and JZTx-27 and F108 for JZTx-14 (Tang et al., 2017; Zhang et al., 2018). Interestingly, the hydrophobic residues LF/LV in the S3b region of K_V4 channels were also identified as the key binding determinants for κ-LhTx-1 (Xiao et al., 2021), and it can be rationally presumed that hydrophobic interactions also underlie the interaction between κ-LhTx-1 and K_V4 channels. Additionally, sequence alignment revealed that κ-LhTx-1 and other NaChBac peptide antagonists from spider venom share a conserved cysteine framework, and the critical W27 residue in κ-LhTx-1 is also conserved in most of them (Figure 1A, except for JZTx-14); therefore it is reasonable to speculate that these toxins used this conserved W residue to interact with NaChBac *via* hydrophobic interaction. Indeed, molecular docking analysis in our previous study also showed that this W residue in JZTx-27 interacts with F98 in another bacteria sodium channel, Ns_VBa (Tang et al., 2017).

Data availability statement

The original contributions presented in the study are included in the article/Supplementary Material; further inquiries can be directed to the corresponding authors.

Author contributions

CT, ZX, and ZL designed the study and wrote the manuscript. ZX, YL, PZ, XW, GL, and HL performed the experiments and the data analysis. SP performed the experiments and the data analysis.

Funding

This work was supported by the National Natural Science Foundation of China (Grant Nos. 31600669, 32171271, 32071262, and 31872718), the Science and Technology Innovation Program of Hunan Province (2020RC4023), the Natural Science Foundation of Hunan Province (Grant No. 2018JJ3339), the Research Foundation of the Education Department of Hunan Province (Grant No.18B015), and the Hunan Provincial Innovation Foundation for Postgraduate (CX20190395).

Conflict of interest

The authors declare that the research was conducted in the absence of any commercial or financial relationships that could be construed as a potential conflict of interest.

Publisher's note

References

Andavan, G. S., and Lemmens-Gruber, R. (2011). Voltage-gated sodium channels: Mutations, channelopathies and targets. *Curr. Med. Chem.* 18, 377–397. doi:10.2174/092986711794839133

Bagal, S. K., Marron, B. E., Owen, R. M., Storer, R. I., and Swain, N. A. (2015). Voltage gated sodium channels as drug discovery targets. *Channels (Austin)* 9, 360–366. doi:10.1080/19336950.2015.1079674

Bosmans, F., Martin-Eauclaire, M. F., and Swartz, K. J. (2008). Deconstructing voltage sensor function and pharmacology in sodium channels. *Nature* 456, 202–208. doi:10.1038/nature07473

Catterall, W. A., Goldin, A. L., and Waxman, S. G. (2005). International Union of Pharmacology. XLVII. Nomenclature and structure-function relationships of voltage-gated sodium channels. *Pharmacol. Rev.* 57, 397–409. doi:10.1124/pr.57.4.4

Catterall, W. A., Wisedchaisri, G., and Zheng, N. (2020). The conformational cycle of a prototypical voltage-gated sodium channel. *Nat. Chem. Biol.* 16, 1314–1320. doi:10.1038/s41589-020-0644-4

Charalambous, K., and Wallace, B. A. (2011). NaChBac: The long lost sodium channel ancestor. *Biochemistry* 50, 6742–6752. doi:10.1021/bi200942y

Clairfeuille, T., Cloake, A., Infield, D. T., Llongueras, J. P., Arthur, C. P., Li, Z. R., et al. (2019). Structural basis of α-scorpion toxin action on Na(v) channels. *Science* 363, eaav8573. doi:10.1126/science.aav8573

de Lera Ruiz, M., and Kraus, R. L. (2015). Voltage-gated sodium channels: Structure, function, pharmacology, and clinical indications. *J. Med. Chem.* 58, 7093–7118. doi:10.1021/jm501981g

DeCaen, P. G., Takahashi, Y., Krulwich, T. A., Ito, M., and Clapham, D. E. (2014). Ionic selectivity and thermal adaptations within the voltage-gated sodium channel family of alkaliphilic Bacillus. *eLife* 3, e04387. doi:10.7554/eLife.04387

DeSimone, C. V., Lu, Y., Bondarenko, V. E., and Morales, M. J. (2009). S3b amino acid substitutions and ancillary subunits alter the affinity of Heteropoda venatoria toxin 2 for Kv4.3. *Mol. Pharmacol.* 76, 125–133. doi:10.1124/mol.109.055657

Finol-Urdaneta, R. K., McArthur, J. R., Korkosh, V. S., Huang, S., McMaster, D., Glavica, R., et al. (2019). Extremely potent block of bacterial voltage-gated sodium channels by μ-conotoxin PIIIA. *Mar. Drugs* 17, 510. doi:10.3390/md17090510

Gao, S., Valinsky, W. C., On, N. C., Houlihan, P. R., Qu, Q., Liu, L., et al. (2020). Employing NaChBac for cryo-EM analysis of toxin action on voltage-gated Na(+) channels in nanodisc. *Proc. Natl. Acad. Sci. U. S. A.* 117, 14187–14193. doi:10.1073/pnas.1922903117

Goldin, A. L. (1999). Diversity of mammalian voltage-gated sodium channels. *Ann. N. Y. Acad. Sci.* 868, 38–50. doi:10.1111/j.1749-6632.1999.tb11272.x

Hille, B. (2001). *Ion channels of excitable membranes (Ion channels of excitable membranes).* Sunderland, MA, United States: Sinauer Associates, Inc.

Hodgkin, A. L., and Huxley, A. F. (1990). A quantitative description of membrane current and its application to conduction and excitation in nerve. *Bull. Math. Biol.* 52, 25–23. doi:10.1007/BF02459568

Huang, W., Liu, M., Yan, S. F., and Yan, N. (2017). Structure-based assessment of disease-related mutations in human voltage-gated sodium channels. *Protein Cell* 8, 401–438. doi:10.1007/s13238-017-0372-z

Ito, M., Xu, H., Guffanti, A. A., Wei, Y., Zvi, L., Clapham, D. E., et al. (2004). The voltage-gated Na+ channel NaVBP has a role in motility, chemotaxis, and pH homeostasis of an alkaliphilic Bacillus. *Proc. Natl. Acad. Sci. U. S. A.* 101, 10566–10571. doi:10.1073/pnas.0402692101

Jiang, D., Shi, H., Tonggu, L., Gamal El-Din, T. M., Lenaeus, M. J., Zhao, Y., et al. (2020). Structure of the cardiac sodium channel. *Cell* 180, 122–e10. e110. doi:10.1016/j.cell.2019.11.041

Koishi, R., Xu, H., Ren, D., Navarro, B., Spiller, B. W., Shi, Q., et al. (2004). A superfamily of voltage-gated sodium channels in bacteria. *J. Biol. Chem.* 279, 9532–9538. doi:10.1074/jbc.M313100200

Lee, S., Goodchild, S. J., and Ahern, C. A. (2012). Local anesthetic inhibition of a bacterial sodium channel. *J. Gen. Physiol.* 139, 507–516. doi:10.1085/jgp.201210779

Mintseris, J., Pierce, B., Wiehe, K., Anderson, R., Chen, R., and Weng, Z. (2007). Integrating statistical pair potentials into protein complex prediction. *Proteins* 69, 511–520. doi:10.1002/prot.21502

Pallaghy, P. K., Nielsen, K. J., Craik, D. J., and Norton, R. S. (1994). A common structural motif incorporating a cystine knot and a triple-stranded beta-sheet in toxic and inhibitory polypeptides. *Protein Sci.* 3, 1833–1839. doi:10.1002/pro.5560031022

Pan, X., Li, Z., Huang, X., Huang, G., Gao, S., Shen, H., et al. (2019). Molecular basis for pore blockade of human Na^+ channel Na v 1.2 by the μ-conotoxin KIIIA. *Science* 363, 1309–1313. doi:10.1126/science.aaw2999

Pan, X., Li, Z., Jin, X., Zhao, Y., Huang, G., Huang, X., et al. (2021). Comparative structural analysis of human Na(v)1.1 and Na(v)1.5 reveals mutational hotspots for sodium channelopathies. *Proc. Natl. Acad. Sci. U. S. A.* 118. e2100066118. doi:10.1073/pnas.2100066118

Pan, X., Li, Z., Zhou, Q., Shen, H., Wu, K., Huang, X., et al. (2018). Structure of the human voltage-gated sodium channel Na(v)1.4 in complex with β1. *Science* 362, eaau2486. doi:10.1126/science.aau2486

Pierce, B. G., Wiehe, K., Hwang, H., Kim, B. H., Vreven, T., and Weng, Z. (2014). ZDOCK server: Interactive docking prediction of protein-protein complexes and symmetric multimers. *Bioinformatics* 30, 1771–1773. doi:10.1093/bioinformatics/btu097

Ren, D., Navarro, B., Xu, H., Yue, L., Shi, Q., and Clapham, D. E. (2001). A prokaryotic voltage-gated sodium channel. *Science* 294, 2372–2375. doi:10.1126/science.1065635

Scheuer, T. (2014). Bacterial sodium channels: Models for eukaryotic sodium and calcium channels. *Handb. Exp. Pharmacol.* 221, 269–291. doi:10.1007/978-3-642-41588-3_13

Shen, H., Liu, D., Wu, K., Lei, J., and Yan, N. (2019). Structures of human Na(v) 1.7 channel in complex with auxiliary subunits and animal toxins. *Science* 363, 1303–1308. doi:10.1126/science.aaw2493

Tang, C., Zhou, X., Nguyen, P. T., Zhang, Y., Hu, Z., Zhang, C., et al. (2017). A novel tarantula toxin stabilizes the deactivated voltage sensor of bacterial sodium channel. *FASEB J.* 31, 3167–3178. doi:10.1096/fj.201600882R

Wang, J., Yarov-Yarovoy, V., Kahn, R., Gordon, D., Gurevitz, M., Scheuer, T., et al. (2011). Mapping the receptor site for alpha-scorpion toxins on a Na+ channel voltage sensor. *Proc. Natl. Acad. Sci. U. S. A.* 108, 15426–15431. doi:10.1073/pnas.1112320108

Wisedchaisri, G., Tonggu, L., Gamal El-Din, T. M., McCord, E., Zheng, N., and Catterall, W. A. (2021). Structural basis for high-affinity trapping of the Na(V) 1.7 channel in its resting state by tarantula toxin. *Mol. Cell* 81, 38–e4. e34. doi:10.1016/j.molcel.2020.10.039

Wisedchaisri, G., Tonggu, L., McCord, E., Gamal El-Din, T. M., Wang, L., Zheng, N., et al. (2019). Resting-state structure and gating mechanism of a voltage-gated sodium channel. *Cell* 178, 993–e12. e1012. doi:10.1016/j.cell.2019.06.031

Wulff, H., Christophersen, P., Colussi, P., Chandy, K. G., and Yarov-Yarovoy, V. (2019). Antibodies and venom peptides: New modalities for ion channels. *Nat. Rev. Drug Discov.* 18, 339–357. doi:10.1038/s41573-019-0013-8

Xiao, Z., Zhao, P., Wu, X., Kong, X., Wang, R., Liang, S., et al. (2021). Variation of two S3b residues in K(V)4.1-4.3 channels underlies their different modulations by spider toxin κ-LhTx-1. *Front. Pharmacol.* 12, 692076. doi:10.3389/fphar.2021.692076

Zhang, J., Tang, D., Liu, S., Hu, H., Liang, S., Tang, C., et al. (2018). Purification and characterization of JZTx-14, a potent antagonist of mammalian and prokaryotic voltage-gated sodium channels. *Toxins (Basel)* 10, 408. doi:10.3390/toxins10100408

Zhang, M., Liu, X. S., Diochot, S., Lazdunski, M., and Tseng, G. N. (2007). APETx1 from sea anemone Anthopleura elegantissima is a gating modifier peptide toxin of the human ether-a-go-go- related potassium channel. *Mol. Pharmacol.* 72, 259–268. doi:10.1124/mol.107.035840

Zheng, W., Zhang, C., Li, Y., Pearce, R., Bell, E. W., and Zhang, Y. (2021). Folding non-homologous proteins by coupling deep-learning contact maps with I-TASSER assembly simulations. *Cell Rep. Methods* 1, 100014. doi:10.1016/j.crmeth.2021.100014

Zhou, X., Xiao, Z., Xu, Y., Zhang, Y., Tang, D., Wu, X., et al. (2017). Electrophysiological and pharmacological analyses of Na(v)1.9 voltage-gated sodium channel by establishing a heterologous expression system. *Front. Pharmacol.* 8, 852. doi:10.3389/fphar.2017.00852

Zhu, W., Li, T., Silva, J. R., and Chen, J. (2020). Conservation and divergence in NaChBac and Na(V)1.7 pharmacology reveals novel drug interaction mechanisms. *Sci. Rep.* 10, 10730. doi:10.1038/s41598-020-67761-5

frontiers | Frontiers in Pharmacology

MINI REVIEW
published: 09 August 2022
doi: 10.3389/fphar.2022.925116

Structure and Mechanism of Glycine Receptor Elucidated by Cryo-Electron Microscopy

Hongtao Zhu*

Laboratory of Soft Matter Physics, Institute of Physics, Chinese Academy of Sciences, Beijing, China

Glycine receptors (GlyRs) are pentameric ion channels that mediate fast inhibitory neurotransmission. GlyRs are found in the central nervous system including the spinal cord, brain stem, and cerebellum, as well as in the retina, sperm, macrophages, hippocampus, cochlea, and liver. Due to their crucial roles in counter-balancing excitatory signals and pain signal transmission, GlyR dysfunction can lead to severe diseases, and as a result, compounds that modify GlyR activity may have tremendous therapeutic potential. Despite this potential, the development of GlyR-specific small-molecule ligands is lacking. Over the past few years, high-resolution structures of both homomeric and heteromeric GlyRs structures in various conformations have provided unprecedented details defining the pharmacology of ligand binding, subunit composition, and mechanisms of channel gating. These high-quality structures will undoubtedly help with the development of GlyR-targeted therapies.

Keywords: glycine receptor, cryo-EM, agonist, inhibitory receptor, antagonist, partial agonist, potentiator, gating mechanism

Edited by:
Shujia Zhu,
Shanghai Institute for Biological Sciences (CAS), China

Reviewed by:
Nathan Absalom,
The University of Sydney, Australia
Hans-Georg Breitinger,
German University in Cairo, Egypt

Correspondence:
Hongtao Zhu
hongtao.zhu@iphy.ac.cn

Specialty section:
This article was submitted to Pharmacology of Ion Channels and Channelopathies,
a section of the journal Frontiers in Pharmacology

Received: *21 April 2022*
Accepted: *14 June 2022*
Published: *09 August 2022*

Citation:
Zhu H (2022) Structure and Mechanism of Glycine Receptor Elucidated by Cryo-Electron Microscopy.
Front. Pharmacol. 13:925116.
doi: 10.3389/fphar.2022.925116

INTRODUCTION

Glycine receptors (GlyRs) are ligand-gated ion channel that are members of the Cys-loop superfamily which also includes the $GABA_A$ receptor ($GABA_AR$), nicotinic acetylcholine receptor (nAChR), serotonin type-3 receptor, and zinc-activated ion channel (Lester et al., 2004). GlyRs can be activated by a variety of endogenous ligands including the full agonist glycine as well as the partial agonists taurine, β-alanine, and GABA (Lynch, 2004). The activation of GlyRs caused by agonist binding results in a Cl^- flow across the membrane that is regulated by the Cl^- equilibrium potential and induces the membrane hyperpolarization, which in turn inhibits neuronal activity (Legendre, 2001; Lynch, 2004).

There are four known GlyR α subunits (α1–α4) and one β subunit identified by molecular cloning (Grenningloh et al., 1987; Grenningloh et al., 1990; Akagi et al., 1991; Kuhse et al., 1991; Matzenbach et al., 1994). Each GlyR subunit is composed of an extracellular domain (ECD), a transmembrane domain (TMD), and a long intracellular loop connecting transmembrane domains M3 and M4. The binding pockets are formed by two adjacent subunits located in the ECD (Lynch, 2009). All of the GlyR α subunits have substantial sequence similarity, exceeding 90%, whereas the GlyR β subunit has a considerable sequence variation when compared with GlyR α subunits (Lynch, 2009). Functional GlyRs include homomeric α GlyRs and heteromeric α-β GlyRs. In the prenatal stage, the predominant type of GlyR is homomeric α2, whereas the adult GlyR types are mainly heteromeric α1-β GlyRs (Becker et al., 1988; Lynch, 2009). The GlyR subunit α3 is involved in nociceptive signaling pathways and function as a novel analgesic candidate (Huang et al., 2017b;

TABLE 1 | Summary of GlyR structures.

PDB ID	EMDB ID	Subtype	Resolution	Ligand	State[*]	Method	Membrane-mimic	Reference
Homomeric GlyR								
5CFB	—	α3[$]	3.0 Å	Strychnine	Closed	X-ray	DDM	Huang et al. (2015)
5TIO	—	α3[$]	3.2 Å	Glycine; AM-3607	Desensitized	X-ray	DDM	Huang et al. (2017b)
5TIN	—	α3[$@]	2.6 Å	Glycine; AM-3607	Desensitized	X-ray	DDM	Huang et al. (2017b)
5VDH	—	α3[$]	2.8 Å	AM-3607; glycine; ivermectin	Desensitized	X-ray	DDM	Huang et al. (2017a)
5VDI	—	α3[$@]	3.1 Å	AM-3607; glycine; ivermectin	Desensitized	X-ray	DDM	Huang et al. (2017a)
3JAD	6344	α1[$]	3.9 Å	Strychnine	Closed	Cryo-EM	DDM	Du et al. (2015)
3JAF	6345	α1[$]	3.8 Å	Glycine; ivermectin	Partially-Open	Cryo-EM	DDM	Du et al. (2015)
3JAE	6346	α1[$]	3.9 Å	Glycine	Open	Cryo-EM	DDM	Du et al. (2015)
6PXD	20518	α1[$]	2.9 Å	—	Apo	Cryo-EM	DDM	Yu et al. (2021b)
7MLU	23910	α1	4.1 Å	Glycine	Desensitized	Cryo-EM	DDM	Zhu and Gouaux, (2021)
7MLV[&]	23911[&]	—	3.8 Å	—	—	Cryo-EM	DDM	Zhu and Gouaux, (2021)
—	23912[&]	—	12.3 Å	—	—	Cryo-EM	DDM	Zhu and Gouaux, (2021)
6PLR	20373	α1	3.2 Å	Glycine	Desensitized	Cryo-EM	Nanodisc	Yu et al. (2021b)
6PLS	20374	α1	3.0 Å	Taurine	Desensitized	Cryo-EM	Nanodisc	Yu et al. (2021b)
6PLT	20375	α1	3.2 Å	Taurine	Closed	Cryo-EM	Nanodisc	Yu et al. (2021b)
6PLU	20376	α1	3.3 Å	GABA	Desensitized	Cryo-EM	Nanodisc	Yu et al. (2021b)
6PLV	20377	α1	3.3 Å	GABA	Closed	Cryo-EM	Nanodisc	Yu et al. (2021b)
6UBS	20714	α1	3.3 Å	—	Apo	Cryo-EM	Nanodisc	Kumar et al. (2020)
6UBT	20715	α1	3.4 Å	Glycine	Desensitized	Cryo-EM	Nanodisc	Kumar et al. (2020)
6UD3	20731	α1	3.5 Å	Glycine; picrotoxin	Open	Cryo-EM	Nanodisc	Kumar et al. (2020)
6VM0	21234	α1	3.1 Å	Glycine; ivermectin	Partially-Open	Cryo-EM	Nanodisc	Kumar et al. (2020)
6VM2	21236	α1	3.3 Å	Glycine; ivermectin	Partially-Open	Cryo-EM	Nanodisc	Kumar et al. (2020)
6VM3	21237	α1	3.0 Å	Glycine; ivermectin	Partially-Open	Cryo-EM	Nanodisc	Kumar et al. (2020)
6PM5	20388	α1	3.2 Å	Glycine	Desensitized	Cryo-EM	SMA	Yu et al. (2021b)
6PM6	20389	α1	3.2 Å	Glycine	Open	Cryo-EM	SMA	Yu et al. (2021b)
6PM4	20386	α1	3.2 Å	Glycine	Expanded-Open	Cryo-EM	SMA	Yu et al. (2021b)
6PM1	20383	α1	3.0 Å	Taurine	Desensitized	Cryo-EM	SMA	Yu et al. (2021b)
6PM2	20384	α1	3.2 Å	Taurine	Open	Cryo-EM	SMA	Yu et al. (2021b)
6PM0	20382	α1	3.1 Å	Taurine	Expanded-Open	Cryo-EM	SMA	Yu et al. (2021b)
6PM3	20385	α1	3.2 Å	Taurine	Closed	Cryo-EM	SMA	Yu et al. (2021b)
6PLX	20379	α1	2.9 Å	GABA	Desensitized	Cryo-EM	SMA	Yu et al. (2021b)
6PLY	20380	α1	2.9 Å	GABA	Open	Cryo-EM	SMA	Yu et al. (2021b)
6PLW	20378	α1	3.0 Å	GABA	Expanded-Open	Cryo-EM	SMA	Yu et al. (2021b)
6PLZ	20381	α1	3.0 Å	GABA	Closed	Cryo-EM	SMA	Yu et al. (2021b)
6PLO	20370	α1[%]	3.3 Å	GABA	Open	Cryo-EM	SMA	Yu et al. (2021b)
6PLQ	20372	α1[%]	3.4 Å	GABA	Expanded-Open	Cryo-EM	SMA	Yu et al. (2021b)
6PLP	20371	α1[%]	3.3 Å	GABA	Desensitized	Cryo-EM	SMA	Yu et al. (2021b)
Heteromeric GlyR								
7MLY	23913	α1-β	2.7 Å	Glycine	Desensitized	Cryo-EM	DDM	Zhu and Gouaux, (2021)
7KUY	23041	α2-β[$]	3.6 Å	Strychnine	Closed	Cryo-EM	Nanodisc	Yu et al. (2021a)
7L31	23048	α2-β[$]	3.8 Å	Strychnine	Closed	Cryo-EM	Nanodisc	Yu et al. (2021a)
5BKG	9404	α2-β[$]	3.8 Å	Glycine	Semi-Open	Cryo-EM	Nanodisc	Yu et al. (2021a)
5BKF	9403	α2-β[$]	3.6 Å	Glycine	Desensitized	Cryo-EM	Nanodisc	Yu et al. (2021a)

[*] *State claimed in the literature.*

[$] *The M3M4 Loop is truncated.*

[@] *Carrying the mutation N38Q.*

[%] *Carrying the mutation YGF.*

[&] *Partially assembled homomeric GlyR.*

Hussein et al., 2019; Zeilhofer et al., 2021). In 1982, GlyRs were isolated for the first time *via* strychnine affinity chromatography (Pfeiffer et al., 1982). The structural investigations of GlyR, on the other hand, are behind. Significant progresses have been achieved in studying the structures of GlyR as a result of the development of cryo-EM (Du et al., 2015; Kumar et al., 2020; Yu H. et al., 2021a; Yu J. et al., 2021b; Zhu and Gouaux, 2021). At present, high resolution GlyR structures bound with different ligands have been reported (**Table 1**). Also, these structures have revealed crucial information about the ligand binding and gating mechanism. In this minireview, I have discussed the recent progress in elucidating the structures of GlyR–ligand complexes and progress in elaborating the gating mechanism in GlyRs using single particle cryo-electron microscopy (cryo-EM).

Full Agonist: Glycine

Glycine, the full agonist to GlyR that is co-released with GABA from presynaptic vesicles (Jonas et al., 1998), can efficiently activate GlyRs. The single channel recordings demonstrated that glycine elicits a maximum open probability (P_{open}) of 0.97, much higher than other agonists (Yu J. et al., 2021b). A

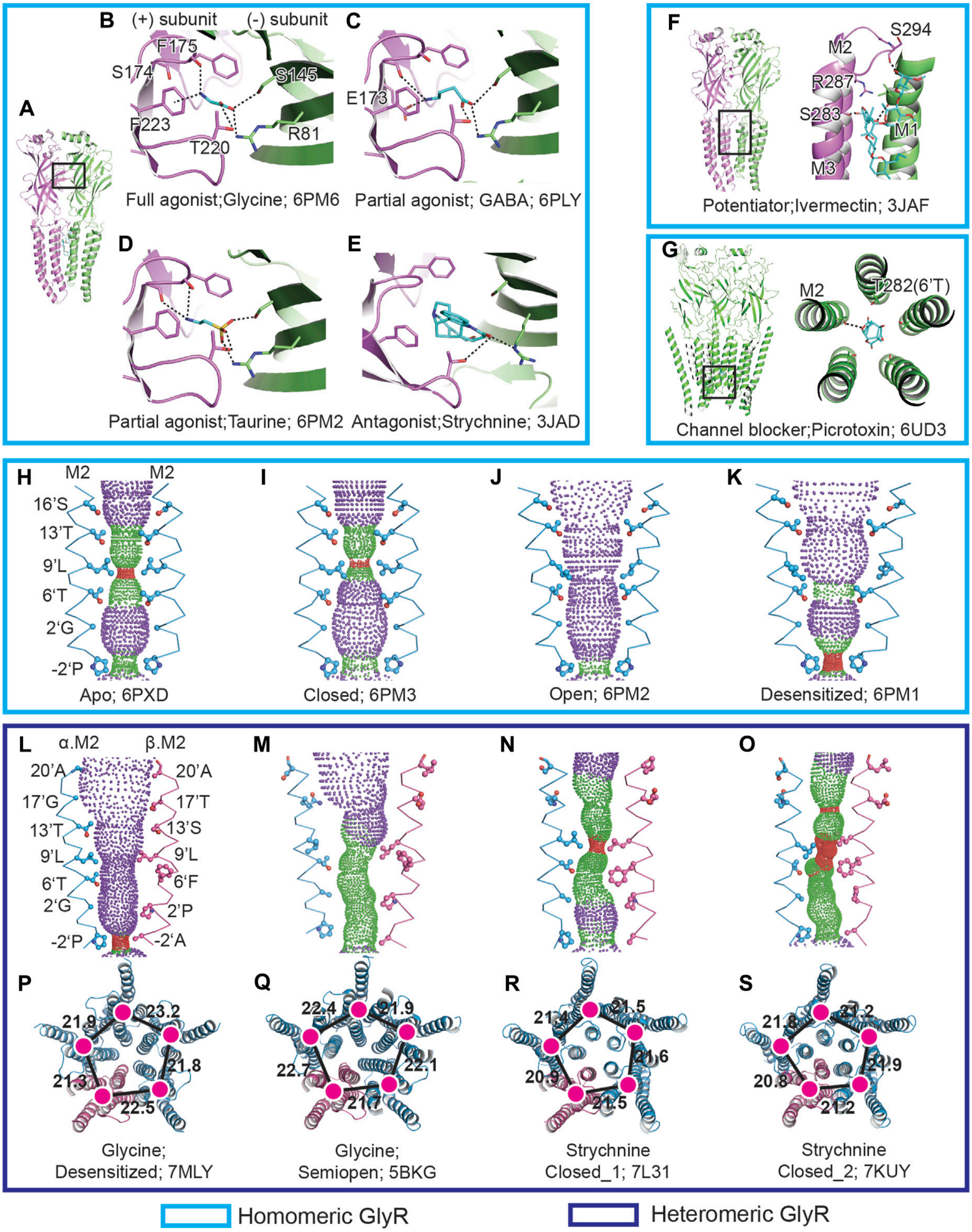

FIGURE 1 | GlyR–ligand interactions and the ion channel permeation pathway. **(A)**, Side view of isolated homomeric GlyR dimer in cartoon representation. The principle (+) and complementary (–) subunit are colored in pink and green, respectively. The boxed area is enlarged in **(B–E)**. **(B–E)** Views of binding pockets of homomeric GlyR bound with glycine **(B)**, GABA **(C)**, taurine **(D)**, and strychnine **(E)**. The ligand molecules are shown in stick representations with oxygen in red, nitrogen in blue, and carbon in cyan. The possible hydrogen bonds are shown as dashed lines. **(F,G)** Views of ivermectin **(F)** and picrotoxin **(G)** binding to homomeric GlyR. **(H–K)** Shape and size of the homomeric GlyR ion permeation pathway for apo **(H)**, closed **(I)**, open **(J)**, and desensitized **(K)** state. M2 helices are shown as cartoons and the side chains of pore-lining residues are in ball and stick representation. Purple, green, and red spheres define radii of >3.3 Å, 1.8–3.3 Å and <1.8 Å, respectively. **(L–O)**

(*Continued*)

FIGURE 1 | Shape and size of the heteromeric GlyR ion permeation pathway for desensitized **(L)**, semi-open **(M)**, strychnine-bound closed state 1 **(N)** and strychnine-bound closed state 1 **(O)**. The M2 helices from the α and β subunits are colored in blue and pink, respectively. **(P–S)** TMD of heteromeric pentamer shown in cartoon representation corresponding to **(L)** to **(O)**. The α and β subunits are colored in blue and pink, respectively. The centers of mass for TMD are shown in magenta. The neighboring distances of centers of mass are denoted in Å.

number of near-atomic resolution glycine-bound zebra fish homomeric GlyR α1 structures identified by cryo-EM have been reported (Du et al., 2015; Kumar et al., 2020; Yu J. et al., 2021b). The structures show that the glycine binding site is located at the subunit interface, with the carboxyl group at the entrance of the binding pockets. The amino group of glycine forms the cation–π interaction with F174 and F223 at the (+) subunit, while the carboxyl group forms several potential hydrogen bonds with the (−) subunit (**Figures 1A,B**).

GlyRs exhibit different conformations in different lipid mimic environments. In detergent, the truncated zebra fish GlyR α1 ($GlyR_{EM}$) adopts an open conformation with the radius of 4.4 Å at −2′P (Du et al., 2015). However, subsequent molecular dynamics simulation discovered that $GlyR_{EM}$ is still ion permeable when docked with the channel blocker picrotoxin, conflicting with the biochemical studies (Wang et al., 2006; Gonzalez-Gutierrez et al., 2017). The full-length GlyR in nanodisc, on the other hand, produced one desensitized state with a diameter ~3 Å at −2′P (Kumar et al., 2020; Yu J. et al., 2021b). Interestingly, for the full-length zebra fish GlyR α1 extracted by 0.5% styrene maleic acid polymer (SMA) at 4°C for 1 h, three conformations, open, desensitized, and expanded-open states, were captured with diameters at −2′P of 5.6 Å, 3.0 Å, and 7.0 Å, respectively. For the expanded-open state in SMA, extra densities were observed at the end of M2 helices, the origin of which needs further investigation (Yu J. et al., 2021b). Given that SMA can preserve the lipid molecules surrounding the receptors, it is possible that these native lipid molecules aid the stabilization of GlyR at different physiological states.

Partial Agonist and Gating Mechanism

Partial agonists, which have efficiency between full agonist and antagonist, are of interest for therapeutics. In the presence of a full agonist, the partial agonist will serve as an antagonist, competing with the full agonist for the same binding sites, as a result, reducing the full agonist's effects (Calvey, 2008). Taurine and GABA are partial agonists on GlyR, featured with eliciting lower maximum P_{open} than the full agonist glycine (De Saint Jan et al., 2001). In 2021, the Sivilotti and Gouaux group performed extensive research on zebra fish GlyR α1 partial agonists combining electrophysiological and cryo-EM approaches (Yu J. et al., 2021b). The single channel recordings revealed that the maximum P_{open} for glycine, taurine, and GABA are 0.98, 0.66, and 0.39, respectively. Furthermore, in the presence of taurine and GABA, the single channel recordings feature with long-lived shut states that are not seen for glycine, implying an additional partial agonist bound closed state. For the partial agonists bound GlyR in SMA, in addition to the open, desensitized and expanded-open states captured for glycine, a partial agonist bound closed state, which is absent for the full agonist glycine, was captured. The partial agonists bound closed state exhibits parallel M2 helices and the side chain of 9′L pointing to the channel axis, creating a contrition less than 3 Å. Compared with glycine, more interactions were observed for taurine and GABA. A potential hydrogen bond was found between the carbonyl group of S174 and the amino group of taurine, as well as an interaction between E173 and GABA (**Figures 1C,D**). These additional interactions for GABA and taurine are possibly due to the ligand's greater length. A comparison of the GlyR structures bound with full and partial agonists shows that the binding of partial agonists induces a lesser extended binding pocket than the full agonist. Moreover, the efficiency of the agonists has a close relationship with the volume of the ligands, with the more efficient of the ligand having a lower ligand volume.

Upon the binding of partial agonists, the gating cycle of GlyRs involves transitions of multiple states (Lape et al., 2008; Lape et al., 2012). At present, three physiological GlyR states bound with partial agonists have been captured: closed, open, and desensitized. The researchers hypothesized that the partial agonists bound closed state is a pre-open state between the apo and open state (Yu J. et al., 2021b). Based on the available structures, the partial agonist gating mechanism was established. During the transition from the apo to the closed state, after the ligand accesses the binding site, a contraction of the binding pocket occurs. But no conformational changes were observed for the TMD, with 9′L functioning as the constriction point (**Figures 1H,I**). From the closed to the open state, the binding pockets shrink more. The conformational changes that happen at the binding pockets travels down to the ECD-TMD interface, which further triggers the tilt of the M2 helices. The tilt of the M2 helices prompts the rotation of the side chain of 9′L and causes the channel to open (**Figure 1J**). After opening, the lower part of the M2 helices will undergo a further tilt, creating a constriction point at −2′P (**Figure 1K**) and blocking the ion permeation (Yu J. et al., 2021b).

Antagonist: Strychnine

Strychnine, an alkaloid that can bind and antagonize GlyR, has been widely employed in radioligand binding and affinity purification experiments (Lynch, 2004, 2009; Breitinger and Breitinger, 2020; Cerdan et al., 2020). According to the human GlyR α3 X-ray crystal and $GlyR_{EM}$ (Du et al., 2015; Huang et al., 2015; Yu H. et al., 2021b), strychnine shares the same binding pocket as glycine (**Figure 1E**). One state was captured for $GlyR_{EM}$ bound with strychnine (Du et al., 2015), which features parallel M2 helices with 9′L pointing to the channel axis, resulting in a diameter of 3 Å and blocking the permeation pathway. In total, two states were obtained for human heteromeric GlyR α2-β bound with strychnine (Yu H. et al., 2021a), and both of the two states exhibit a constriction point at 9′L, but the conformation of their TMD are in markedly different (**Figures 1N,O,R,S**).

Potentiator: Ivermectin

The ivermectin functions as the potentiator to GlyR, which can enhance the glycine sensitivity and increase the P_{open} (Shan et al., 2001a; Breitinger and Breitinger, 2020; Cerdan et al., 2020). There are several ivermectin-bound homomeric GlyR structures available (**Table 1**). The structures demonstrate that ivermectin is bound at the interface of M3 and M1 and forms a polar interaction with M2 (**Figure 1F**). Compared with the glycine-bound $GlyR_{EM}$ open state (Du et al., 2015), when ivermectin binds with GlyR, the M2 helices undergo movement toward the pore lumen and contract the intracellular opening the ion channel at −2′P and enabling chloride ions to pass through. The cryo-EM structures also prove that the binding of ivermectin traps the zebra fish homomeric GlyR α1 at a partially-open state (Du et al., 2015), with the narrowest point at −2′P comparable to glycine bound open state in SMA (Yu J. et al., 2021b).

Channel Blocker: Picrotoxin

Homomeric GlyR is more sensitive than heteromeric GlyR to the inhibition of the channel blocker picrotoxin (Pribilla et al., 1992). The picrotoxin IC_{50} values for homomeric and heteromeric GlyR are 18±1 and 259±44 μM, respectively (Shan et al., 2001b). The zebra fish homomeric GlyR α3 structure bound with picrotoxin (Kumar et al., 2020) shows that picrotoxin is nested between 2′G and 9′L and forms hydrogen bonds with 6′T (**Figure 1G**). The structural basis for heteromeric GlyR's resistance to picrotoxin has been recently revealed (Zhu and Gouaux, 2021). The pig heteromeric GlyR structure demonstrates that the side chain bulk of 6′F on GlyR β subunit, the corresponding residue to 6′T in homomeric GlyR, on the one hand, provides a steric hindrance for picrotoxin accessing the binding site, while, on the other hand, it pushes the M2 helices away from each other and prevents picrotoxin binding.

Heteromeric Glycine Receptors

The predominant type GlyR in adult is heteromeric GlyR (Becker et al., 1988; Lynch, 2009), which is composed of α and β subunits. Since the ligand-binding pockets are located at the interface of the subunits, appropriate knowledge of the subunit stoichiometry of heteromeric GlyRs is thus important to understand the molecular pharmacology. Several subunit stoichiometries have been proposed including 3α:2β, 2α:3β, and 4α:1β obtained by different methods (Langosch et al., 1988; Burzomato et al., 2003; Grudzinska et al., 2005; Durisic et al., 2012; Yang et al., 2012). Because α and β subunits show high similarity in the secondary and tertiary structures (Dutertre et al., 2012), the inconsistent results on the subunit stoichiometry reflect the difficulties in distinguishing these two subunits. The fundamental factor to solve the subunit stoichiometry problem is to precisely tag one of the subunits. In 2021, both the Gouaux group and the Wang group published the near-atomic structures of heteromeric GlyR using tissue-isolated and recombinant pig α1-β GlyR and recombinant human α2-β GlyR, respectively (Yu H. et al., 2021a; Zhu and Gouaux, 2021). A same subunit stoichiometry, which is 4α:1β, was achieved for both groups using different methods, and no other subunit composition was described. In the Gouaux group's research, the native GlyRs were purified from pig's spinal cord and the brain stem by strychnine affinity resin (Graham et al., 1985). A monoclonal antibody specific to GlyR α subunit was prepared to enable differentiation of α and β subunits. Data has suggested that N terminal–fused GFP is tolerated by GlyR (David-Watine et al., 1999). Interestingly, the Wang group employed an EGFP which was inserted between M3 and M4 helices to identify the GlyR β subunit. The 4α:1β stoichiometry provides important implications associated with heteromeric GlyR function and pharmacology, such as the clustering of heteromeric GlyR and drug development specific to heteromeric GlyRs. There are current two states reported for heteromeric GlyR bound with glycine: one is desensitized state and the other is semi-open (**Table 1**). In contrast to the semi-open state, the desensitized state shows a five-fold quasi-symmetrical TMD (**Figures 1L,M,P,Q**), which is similar to the homomeric desensitized state in SMA (**Figures 1K,L**).

Assembly Pathway of Glycine Receptors

Members of the heteromeric Cys-loop family are composed of at least two different types of subunits. The investigation of the assembly intermediates can provide insights into the oligomerization process. Though research on the assembly process of nAChRs (Green and Claudio, 1993) and $GABA_A$Rs (Klausberger et al., 2001) have been reported, little is known regarding the assembly pathway of heteromeric GlyR. Compared with nAChRs and $GABA_A$Rs, the assembly process of heteromeric GlyR is comparatively simple due to the involvement of two types of subunits. By using strychnine affinity resin (Pfeiffer et al., 1982), the GlyR assembly intermediates were successfully isolated from the native materials (Zhu and Gouaux, 2021). A total of two assembly intermediates including a homomeric α tetramer and a homomeric α trimer were captured. However, the homomeric α dimer and β subunit containing assembly intermediates were missing, which might be due to non-functional binding pockets that needs further investigation. Given that GlyR assembly intermediates were captured by strychnine affinity resin, which demonstrates that the functional binding pockets are forming during receptor assembly. The findings reveal that the GlyR oligomerization occurs in steps, with one subunit added at each step. Because all of the assembly intermediates are α homomers, there will be insufficient supply of free α subunit. As a result, in the final step, the chance of homomeric α tetramer assembly with a β subunit to produce a heteromeric pentamer is larger than the likelihood of homomeric pentamer formation. The findings may be relevant for future drug development focusing on the GlyR assembly intermediates.

DISCUSSION

This review summarizes the recent progress of elucidating the structures of GlyR in a complex with different ligands at different conformations by single particle cryo-EM. These structures shed light on the gating mechanism and assembly pathway of GlyR and may provide important details for subsequent GlyR-specific drug design and screening of the authorized drugs. Despite this, little is known about the structural basis of GlyR clustering, GlyR–metal interaction, as well as other GlyR bound ligands (Cerdan et al., 2020), all of which are important goals in future.

AUTHOR CONTRIBUTIONS

HZ designed and wrote the manuscript.

ACKNOWLEDGMENTS

The author thanks Steven Mansoor for discussions and suggestions.

REFERENCES

Akagi, H., Hirai, K., and Hishinuma, F. (1991). Cloning of a glycine Receptor Subtype Expressed in Rat Brain and Spinal Cord during a Specific Period of Neuronal Development. *FEBS Lett.* 281 (1-2), 160–166. doi:10.1016/0014-5793(91)80383-e

Becker, C. M., Hoch, W., and Betz, H. (1988). Glycine Receptor Heterogeneity in Rat Spinal Cord during Postnatal Development. *EMBO J.* 7 (12), 3717–3726. doi:10.1002/j.1460-2075.1988.tb03255.x

Breitinger, U., and Breitinger, H. G. (2020). Modulators of the Inhibitory Glycine Receptor. *ACS Chem. Neurosci.* 11 (12), 1706–1725. doi:10.1021/acschemneuro.0c00054

Burzomato, V., Groot-Kormelink, P. J., Sivilotti, L. G., and Beato, M. (2003). Stoichiometry of Recombinant Heteromeric glycine Receptors Revealed by a Pore-Lining Region Point Mutation. *Recept Channels* 9 (6), 353–361. doi:10.3109/714041016

Calvey, T. N., and Williams, N. E. (2008). *Principles and Practice of Pharmacology for Anaesthetists*. Malden, Mass: Blackwell Pub.

Cerdan, A. H., Sisquellas, M., Pereira, G., Barreto Gomes, D. E., Changeux, J. P., and Cecchini, M. (2020). The Glycine Receptor Allosteric Ligands Library (GRALL). *Bioinformatics* 36 (11), 3379–3384. doi:10.1093/bioinformatics/btaa170

David-Watine, B., Shorte, S. L., Fucile, S., de Saint Jan, D., Korn, H., and Bregestovski, P. (1999). Functional Integrity of Green Fluorescent Protein Conjugated glycine Receptor Channels. *Neuropharmacology* 38 (6), 785–792. doi:10.1016/s0028-3908(99)00015-5

De Saint Jan, D., David-Watine, B., Korn, H., and Bregestovski, P. (2001). Activation of Human Alpha1 and Alpha2 Homomeric glycine Receptors by Taurine and GABA. *J. Physiol.* 535 (Pt 3), 741–755. doi:10.1111/j.1469-7793.2001.t01-1-00741.x

Du, J., Lü, W., Wu, S., Cheng, Y., and Gouaux, E. (2015). Glycine Receptor Mechanism Elucidated by Electron Cryo-Microscopy. *Nature* 526 (7572), 224–229. doi:10.1038/nature14853

Durisic, N., Godin, A. G., Wever, C. M., Heyes, C. D., Lakadamyali, M., and Dent, J. A. (2012). Stoichiometry of the Human glycine Receptor Revealed by Direct Subunit Counting. *J. Neurosci.* 32 (37), 12915–12920. doi:10.1523/JNEUROSCI.2050-12.2012

Dutertre, S., Becker, C. M., and Betz, H. (2012). Inhibitory glycine Receptors: an Update. *J. Biol. Chem.* 287 (48), 40216–40223. doi:10.1074/jbc.R112.408229

Gonzalez-Gutierrez, G., Wang, Y., Cymes, G. D., Tajkhorshid, E., and Grosman, C. (2017). Chasing the Open-State Structure of Pentameric Ligand-Gated Ion Channels. *J. Gen. Physiol.* 149 (12), 1119–1138. doi:10.1085/jgp.201711803

Graham, D., Pfeiffer, F., Simler, R., and Betz, H. (1985). Purification and Characterization of the glycine Receptor of Pig Spinal Cord. *Biochemistry* 24 (4), 990–994. doi:10.1021/bi00325a027

Green, W. N., and Claudio, T. (1993). Acetylcholine Receptor Assembly: Subunit Folding and Oligomerization Occur Sequentially. *Cell.* 74 (1), 57–69. doi:10.1016/0092-8674(93)90294-z

Grenningloh, G., Rienitz, A., Schmitt, B., Methfessel, C., Zensen, M., Beyreuther, K., et al. (1987). The Strychnine-Binding Subunit of the glycine Receptor Shows Homology with Nicotinic Acetylcholine Receptors. *Nature* 328 (6127), 215–220. doi:10.1038/328215a0

Grenningloh, G., Pribilla, I., Prior, P., Multhaup, G., Beyreuther, K., Taleb, O., et al. (1990). Cloning and Expression of the 58 Kd Beta Subunit of the Inhibitory glycine Receptor. *Neuron* 4 (6), 963–970. doi:10.1016/0896-6273(90)90149-a

Grudzinska, J., Schemm, R., Haeger, S., Nicke, A., Schmalzing, G., Betz, H., et al. (2005). The Beta Subunit Determines the Ligand Binding Properties of Synaptic glycine Receptors. *Neuron* 45 (5), 727–739. doi:10.1016/j.neuron.2005.01.028

Huang, X., Chen, H., Michelsen, K., Schneider, S., and Shaffer, P. L. (2015). Crystal Structure of Human glycine Receptor-A3 Bound to Antagonist Strychnine. *Nature* 526 (7572), 277–280. doi:10.1038/nature14972

Huang, X., Chen, H., and Shaffer, P. L. (2017a). Crystal Structures of Human GlyRα3 Bound to Ivermectin. *Structure* 25 (6), 945–950. doi:10.1016/j.str.2017.04.007

Huang, X., Shaffer, P. L., Ayube, S., Bregman, H., Chen, H., Lehto, S. G., et al. (2017b). Crystal Structures of Human glycine Receptor α3 Bound to a Novel Class of Analgesic Potentiators. *Nat. Struct. Mol. Biol.* 24 (2), 108–113. doi:10.1038/nsmb.3329

Hussein, R. A., Ahmed, M., Breitinger, H. G., and Breitinger, U. (2019). Modulation of Glycine Receptor-Mediated Pain Signaling *In Vitro* and *In Vivo* by Glucose. *Front. Mol. Neurosci.* 12, 280. doi:10.3389/fnmol.2019.00280

Jonas, P., Bischofberger, J., and Sandkühler, J. (1998). Corelease of Two Fast Neurotransmitters at a Central Synapse. *Science* 281 (5375), 419–424. doi:10.1126/science.281.5375.419

Klausberger, T., Ehya, N., Fuchs, K., Fuchs, T., Ebert, V., Sarto, I., et al. (2001). Detection and Binding Properties of GABA(A) Receptor Assembly Intermediates. *J. Biol. Chem.* 276 (19), 16024–16032. doi:10.1074/jbc.M009508200

Kuhse, J., Kuryatov, A., Maulet, Y., Malosio, M. L., Schmieden, V., and Betz, H. (1991). Alternative Splicing Generates Two Isoforms of the Alpha 2 Subunit of the Inhibitory glycine Receptor. *FEBS Lett.* 283 (1), 73–77. doi:10.1016/0014-5793(91)80557-j

Kumar, A., Basak, S., Rao, S., Gicheru, Y., Mayer, M. L., Sansom, M. S. P., et al. (2020). Mechanisms of Activation and Desensitization of Full-Length glycine Receptor in Lipid Nanodiscs. *Nat. Commun.* 11 (1), 3752. doi:10.1038/s41467-020-17364-5

Langosch, D., Thomas, L., and Betz, H. (1988). Conserved Quaternary Structure of Ligand-Gated Ion Channels: the Postsynaptic glycine Receptor Is a Pentamer. *Proc. Natl. Acad. Sci. U. S. A.* 85 (19), 7394–7398. doi:10.1073/pnas.85.19.7394

Lape, R., Colquhoun, D., and Sivilotti, L. G. (2008). On the Nature of Partial Agonism in the Nicotinic Receptor Superfamily. *Nature* 454 (7205), 722–727. doi:10.1038/nature07139

Lape, R., Plested, A. J., Moroni, M., Colquhoun, D., and Sivilotti, L. G. (2012). The α1K276E Startle Disease Mutation Reveals Multiple Intermediate States in the Gating of glycine Receptors. *J. Neurosci.* 32 (4), 1336–1352. doi:10.1523/JNEUROSCI.4346-11.2012

Legendre, P. (2001). The Glycinergic Inhibitory Synapse. *Cell. Mol. Life Sci.* 58 (5-6), 760–793. doi:10.1007/pl00000899

Lester, H. A., Dibas, M. I., Dahan, D. S., Leite, J. F., and Dougherty, D. A. (2004). Cys-loop Receptors: New Twists and Turns. *Trends Neurosci.* 27 (6), 329–336. doi:10.1016/j.tins.2004.04.002

Lynch, J. W. (2004). Molecular Structure and Function of the glycine Receptor Chloride Channel. *Physiol. Rev.* 84 (4), 1051–1095. doi:10.1152/physrev.00042.2003

Lynch, J. W. (2009). Native glycine Receptor Subtypes and Their Physiological Roles. *Neuropharmacology* 56 (1), 303–309. doi:10.1016/j.neuropharm.2008.07.034

Matzenbach, B., Maulet, Y., Sefton, L., Courtier, B., Avner, P., Guénet, J. L., et al. (1994). Structural Analysis of Mouse glycine Receptor Alpha Subunit Genes. Identification and Chromosomal Localization of a Novel Variant. *J. Biol. Chem.* 269 (4), 2607–2612. doi:10.1016/s0021-9258(17)41987-9

Pfeiffer, F., Graham, D., and Betz, H. (1982). Purification by Affinity Chromatography of the glycine Receptor of Rat Spinal Cord. *J. Biol. Chem.* 257 (16), 9389–9393. doi:10.1016/s0021-9258(18)34082-1

Pribilla, I., Takagi, T., Langosch, D., Bormann, J., and Betz, H. (1992). The Atypical M2 Segment of the Beta Subunit Confers Picrotoxinin Resistance to Inhibitory glycine Receptor Channels. *EMBO J.* 11 (12), 4305–4311. doi:10.1002/j.1460-2075.1992.tb05529.x

Shan, Q., Haddrill, J. L., and Lynch, J. W. (2001a). Ivermectin, an Unconventional Agonist of the glycine Receptor Chloride Channel. *J. Biol. Chem.* 276 (16), 12556–12564. doi:10.1074/jbc.M011264200

Shan, Q., Haddrill, J. L., and Lynch, J. W. (2001b). A Single Beta Subunit M2 Domain Residue Controls the Picrotoxin Sensitivity of Alphabeta Heteromeric glycine Receptor Chloride Channels. *J. Neurochem.* 76 (4), 1109–1120. doi:10.1046/j.1471-4159.2001.00124.x

Wang, D. S., Mangin, J. M., Moonen, G., Rigo, J. M., and Legendre, P. (2006). Mechanisms for Picrotoxin Block of Alpha2 Homomeric glycine Receptors. *J. Biol. Chem.* 281 (7), 3841–3855. doi:10.1074/jbc.M511022200

Yang, Z., Taran, E., Webb, T. I., and Lynch, J. W. (2012). Stoichiometry and Subunit Arrangement of α1β glycine Receptors as Determined by Atomic Force Microscopy. *Biochemistry* 51 (26), 5229–5231. doi:10.1021/bi300063m

Yu, H., Bai, X. C., and Wang, W. (2021a). Characterization of the Subunit Composition and Structure of Adult Human glycine Receptors. *Neuron* 109 (17), 2707–2716. doi:10.1016/j.neuron.2021.08.019

Yu, J., Zhu, H., Lape, R., Greiner, T., Du, J., Lü, W., et al. (2021b). Mechanism of Gating and Partial Agonist Action in the glycine Receptor. *Cell.* 184 (4), 957–968. doi:10.1016/j.cell.2021.01.026

Zeilhofer, H. U., Werynska, K., Gingras, J., and Yévenes, G. E. (2021). Glycine Receptors in Spinal Nociceptive Control-An Update. *Biomolecules* 11 (6), 846. doi:10.3390/biom11060846

Zhu, H., and Gouaux, E. (2021). Architecture and Assembly Mechanism of Native glycine Receptors. *Nature* 599 (7885), 513–517. doi:10.1038/s41586-021-04022-z

Conflict of Interest: The author declares that the research was conducted in the absence of any commercial or financial relationships that could be construed as a potential conflict of interest.

Advantages of publishing in Frontiers

OPEN ACCESS
Articles are free to read
for greatest visibility
and readership

FAST PUBLICATION
Around 90 days
from submission
to decision

HIGH QUALITY PEER-REVIEW
Rigorous, collaborative,
and constructive
peer-review

TRANSPARENT PEER-REVIEW
Editors and reviewers
acknowledged by name
on published articles

Frontiers
Avenue du Tribunal-Fédéral 34
1005 Lausanne | Switzerland

Visit us: www.frontiersin.org
Contact us: frontiersin.org/about/contact

REPRODUCIBILITY OF RESEARCH
Support open data
and methods to enhance
research reproducibility

DIGITAL PUBLISHING
Articles designed
for optimal readership
across devices

FOLLOW US
@frontiersin

IMPACT METRICS
Advanced article metrics
track visibility across
digital media

EXTENSIVE PROMOTION
Marketing
and promotion
of impactful research

LOOP RESEARCH NETWORK
Our network
increases your
article's readership